A FUNDAMENTAL INVESTIGATION OF MICROFLOW AND ATOMISATION PROCESSES IN AUTOMOTIVE INJECTORS

By

Yong Chuan Khoo
B.Eng. (Hons)

A Doctoral Thesis submitted in partial fulfilment of the requirements for the award of Doctor of Philosophy of Loughborough University

March 2005

ABSTRACT

Recent developments in automotive engines have been directed towards the reduction of engine emissions in order to minimise their effect on the environment. A major part of this advancement has been the improvement of new direct injection injectors providing improved atomisation and better control of the fuel delivery into the combustion chamber. To aid the injector design process, it is vital to understand the fundamental fluid dynamic processes controlling atomisation of high-pressure fluids in Direct Injection injectors. The research effort is directed towards the ability to link changes to the internal nozzle geometry and flow field to the external atomisation processes.

This thesis presents a detailed laser diagnostic investigation of Diesel and gasoline direct injectors for automotive applications. There is a need to increase our understanding of injector flow processes occurring both internally and externally to a high-pressure fuel atomiser and the physical phenomena in generating atomised fuel in the combustion chamber.

The characterisation of Diesel injector flow was achieved by the use of series of real-sized, optically accessible sapphire Diesel injectors, capable of operating at realistic driving pressures through orifice nozzles of 0.15 mm and 0.3 mm diameter. High-speed, laser-illuminated flow visualisation was used to study the effect of injector geometry on the internal flow field and the near-field external spray structure. Data in this thesis shows that operating an injector with a counterbore provides a methodology for controlling spray angle.

The study of gasoline injectors was to develop and apply innovative measurement techniques, using a series of real-sized (1 mm diameter) optical nozzles, to provide data to link the internal flow structure to the external spray development. The investigation of non-swirl flow with sharp-edged inlets nozzle showed that cavitation completely controls the flow development.

Fluorescent Particle Image Velocimetry (FPIV) experiments on all chamfered inlet nozzles (30°, 45° and 60°) showed that the total velocity increased linearly with driving pressure.

High-speed flow visualisation study showed that high-pressure swirl injectors generate tapered aircore in the 30° and 45° chamfered inlet orifice and parallel aircores for 60° chamfered inlet orifices. The results also showed that the film thickness was dependent of driving pressure and nozzle geometry. Application of fluorescent particle image velocimetry (FPIV) was used to provide results for internal flow velocity field for the full range of injector geometries studied. A semi-empirical relationship was used and the empirical constants were modified to fit the current experimental results. For the final optical diagnostic tool, phase Doppler anemometry (PDA) was used to provide profiles of particle size in the external spray. Examples of particle size results were shown that matched findings presented in the literature.

TABLE OF CONTENTS

ACKNOWLEDGEMENTS

I would like to thank my supervisors, Dr Graham Hargrave and Mr Henk Versteeg, for their guidance and assistance throughout the course of this work. I would also like to thank my Director of Research, Dr John Tyrer, for his assistance.

Particular thanks are due to Dr Hargarve for his patience and understanding during the endless discussions and guidance for the whole duration of this thesis work. His support was instrumental in providing laser diagnostic equipments that were essential for the completion of the PhD work.

I am grateful for the financial assistance provided by the Mechanical Engineering faculty for my research.

I would also like to thank all the technical staff in the Wolfson school of Mechanical and Manufacturing Engineering who assisted during this thesis work. I would like to thank my fellow co-workers in optical engineering research laboratory for their support. In particular, I am grateful to Kuberan Anandarajah, Pete Wileman and Simon Jarvis for their assistance.

Not forgetting all my friends in United Kingdom and Singapore for their encouragement and help.

The dedications and the supports that my parents and siblings had given to me, from undergraduate to postgraduate, have been tremendous. The last few months have been a tough time for me, with my dad being struck down by a stroke and this has disrupt my writing up progress. I would like to dedicate this work to him and hope that he will recover.

PUBLICATIONS ARISING FROM THIS WORK

1. Khoo, Y.C., Hargrave, G.K., *An Investigation of the Effect of Nozzle Characteristics on Liquid Atomisation in a GDI Injector*, 1st ICOLAD, City University, (United Kingdom), 16-20 December 2002

2. Allen, J., Khoo, Y.C., Hargrave, G.K., *In-Nozzle and Spray Diagnostic Techniques for Real Sized Pressure Swirl and Plain Orifice Gasoline Direct Injectors*, SAE 2003-01-3151, Pittsburgh (USA), 2003

3. Khoo, Y.C., Allen, J., Hargrave, G.K. *In-Nozzle and Spray Diagnostic Techniques for Real-Sized Pressure Swirl and Plain Orifice Gasoline Direct Injectors*, UnICEG Presentation, Nottingham University (United Kingdom), 31-03-2004

4. Khoo, Y.C., Hargrave, G.K., *Flow Visualisation and PIV study of Real Sized Pressure Swirl GDI injectors*, International Conference on Advanced Optical Diagnostics in Fluids, Solids and Combustion, V0015, Tokyo (Japan), 4-6 December 2004

5. Khoo, Y.C., Hargrave, G.K., Real Sized Pressure Swirl GDI Injectors Investigation with HSFV and FPIV, 2nd ICOLAD, City University, (United Kingdom), September 2005 {Submitted}

NOMENCLATURE

A_p	Tangential inlet port
C_D	Discharge coefficient
d_o	Orifice diameter
D_s	Swirl chamber diameter
D	Characteristic dimension (diameter/length)
D_{32}	Sauter mean diameter
D_u	Inlet pipe diameter
d_o	Nozzle exit diameter
dt	Time shift
h^*	Sheet thickness at break-up location
h	sheet thickness
I_1	First interrogation area
I_2	Second interrogation area
$\hat{I}_1(\xi,\eta)\ I_2(i,j)$	Fourier transform
$\hat{I}_2^*(\xi,\eta)$	Complex conjugate of the Fourier transform
K_v	Nozzle coefficient
K	Atomiser constant
L	Break-up length
$\dot{m}_l$	Liquid mass flow rate
ρ	Density
ρ_l	Liquid density
ρ_g	Density of gas
P_r	Reference pressure,
P_v	Vapour pressure,
P_1	Total pressure upstream
P_{vapour}	Vapour pressure of the fuel
P_2	Downstream (ambient back) pressure
r_{ac}	Radius of aircore
r_o	Radius of orifice

S_{Mie}	Mie signals
S_{LIF}	LIF signals
t	time
U	Nozzle exit radial velocity component
μ	Viscosity
μ_l	liquid viscosity
V	Velocity
V	Nozzle exit axial velocity component
W	Radial velocity
σ	Surface tension stress
λ	Wavelength of dominant wave
θ	Spray angle
ΔP_l	Pressure difference across the nozzle
ρ_g/ρ_l	Density ratio
L_n/d_n	Length/diameter ratio of the nozzle.
C_{spray}	Spray empirical constant
C_{SMD}	Sauter mean diameter equation constant
C_L	Break-up length constant

Abbreviations

CCD	Charged Coupled Device
CFD	Computational Fluid Dynamics
CN	Cavitation Number
CO	Carbon Monoxide
CO_2	Carbon Dioxide
DI	Direct Injection
ECM	Electronic Control Module
FFT	Fast Fourier Transform
FPIV	Fluorescent Particle Image Velocimetry
GDI	Gasoline Direct Injection
GPD	Global Phase Doppler

HC	Hydrocarbons
HCCI	Homogeneous Charge Compression Ignition
HEUI	Hydraulically Actuated Electronically controlled Unit Injector
HSFV	High-speed flow visualisation
IC	Internal Combustion
IMEP	Indicated Mean Effective Pressure
LDA	Laser Doppler Anemometry
LDV	Laser Doppler Velocimetry
LIF	Laser Induced Fluorescence
LSD	Laser Sheet Dropsizing
LSV	Laser Speckle Velocimetry .
MPI	Multi-Point Injection
NO_x	Oxides of Nitrogen
PDA	Phase Doppler Anemometry
PDPA	Phase Doppler Particle Analyser
PIV	Particle Image Velocimetry
PM	Particulates
PTV	Particle Tracking Velocimetry
Re	Reynolds Number
SDI	Spark-ignited Direct Injection
SI	Spark Ignition
SPI	Single Point Injection
SMD	Sauter Mean Diameter
VCO	Valve-Covered Orifice
We	Weber Number

CHAPTER 1

INTRODUCTION

1.1 BACKGROUND

Automotive internal combustion engines have been a significant part of our life for more than a century. With rapidly increasing automotive usage worldwide, the impact of engine emissions on the environment and potential climate changes have become increasingly important. This growing awareness of the problems associated with internal combustion engine emissions has led to political and social pressure to implement more strict legislation to limit pollutant emissions from automotive sources. In 1992, United Nations convened in Kyoto, Japan, to implement the Kyoto Protocol to control the greenhouse gas concentrations in the atmosphere and prevent any adverse effects of climate change on the ecosystem and mankind.

The implementation of the Kyoto Protocol has led to legislation providing stringent controls on emissions and was agreed by every developing and developed country. Regulatory authorities of these countries came to a unanimous decision to adopt a standard emission test procedures for all road vehicles. For Europe, the European Union provides the current directives 94/12/EC on emissions standards ranging from Euro I (1993) to Euro IV (from 2005). The directives regulate the internal combustion engine emissions for the four noxious gases which are carbon monoxide (CO), unburned hydrocarbon (HC), particulates (PM) and oxides of nitrogen (NO_x). Table 1.1 shows the progressive reduction on emissions beyond 2005 for both diesel and gasoline engines in passenger cars [02,05]. Leaded petrol driven cars was also banned in the early 2000, with the focus on unleaded petrol as the main fuel for gasoline passenger cars.

	Fuel (g/km)	CO (g/km)	HC+NOx (g/km)	HC (g/km)	NOx (g/km)	Particulates (g/km)
Euro 93		2.72	0.97	-	-	0.14
Euro 96	Petrol	2.2	0.5	-	-	-
	Diesel	1.0	0.7-0.9	-		0.08-0.1
Euro 2000	Petrol	2.3	-	0.2	0.15	-
	Diesel	0.64	0.56		0.5	0.05
Euro 2005	Petrol	1.0	-	0.1	0.08	-
	Diesel	0.50	0.3		0.25	0.25

Table 1.1 Evolution of European emissions limit values for passenger cars 1993 to 2005 [02,05].

The gradual implementation of more stringent EU policy to combat the impact of transport vehicles on the environment affects all levels within the automotive industry from manufacture and utilisation to end-of-life. A major and significant environmental issue is the engine pollutant emission. This has led to the investigation of several alternatives including hydrogen fuel cells, hydrogen combustion engines, homogeneous charge compression ignition (HCCI) and direct injection.

Fuel cells have always been described as the automotive power plant of the future, but they have not realised their potential after years of research. This potential has become more realistic recently with the launch of a partnership between United States government [04,11] and automotive makers to encourage the growth of hydrogen as a fuel source. This includes developing hydrogen-powered fuel cells in automotive vehicles to replace the internal combustion engine. Although fuel cells are potentially cleaner than IC engines, this system is currently not possible due to the high cost and complications involved [03].

Homogeneous Charge Compression Ignition (HCCI) is another alternative combustion processes developed to provide better efficiencies for future transport vehicles. HCCI allows combustion to take place spontaneously and homogeneously without flame propagation, unlike the traditional Gasoline and Diesel engine where the flame propagates from a small number of ignition points. This lean combustion process allows combustion to take place at lower temperature, thereby reducing NO_x emissions.

With the above two alternatives in their development stages, Direct Injection (DI) provides the best option for improving volumetric efficiency, power output and transient response. Direct Injection involves the direct delivery of fuel into the combustion chamber as compared to the conventional inlet port injection system. Thus, DI can potentially provide better control of the injection process, but to be effective it is essential to gain an understanding of the physical processes involved in the conversion of high pressure liquid fuel to fuel vapour via fuel injection and atomisation.

In real injectors, it is almost impossible to observe and analyse the physical phenomena governing the injection characteristics. Previous studies involved the investigation of the injector flow exiting the nozzle [01,09,10] and the use of large-scale physical models to simulate the actual flow in the nozzles [06,07,08]. However, the technological advances in machining and also the advancements in laser diagnostic techniques provide new measurement capabilities for fluid mechanics research. Improved machining capabilities enabled optical quality nozzles to be easily manufactured from strong, optically transparent materials, such as quartz and sapphire. Laser diagnostics, such as Particle Image Velocimetry (PIV) and Phase Doppler Anemometry (PDA), can provide researchers with more accurate experimental data with the capability of remote and non-intrusive measurements. This is very valuable to allow the comprehensive measurement and study of combustion chamber and injection phenomena.

1.2 THESIS AIMS AND OBJECTIVES

The aim of this PhD thesis is to provide an in-depth analysis of DI injectors. It is vital to understand the fundamental fluid dynamic processes controlling atomisation of high-pressure fluids in Direct Injection injectors. This involves the study of internal and external flow field in high-pressure fuel atomisers and investigation of the physical phenomena associated with liquid jet breakup and atomisation. A major objective is to link changes to the internal nozzle geometry and flow field to the external atomisation processes.

The first step towards achieving this was to design and build an optically accessed nozzle flow rig. To investigate the flow phenomena, optical, laser-based diagnostic techniques were used to provide qualitative and quantitative descriptions of the flow field. These techniques are flow visualisation, particle image velocimetry (PIV) and phase Doppler anemometry (PDA). The application of such optical diagnostic techniques help to provide new insights into the flow behaviour to allow future engine designers and researchers to develop more efficient and environmentally friendly engines.

This thesis also introduces Computational Fluid Dynamics (CFD) modelling as a numerical simulation tool to aid the understanding and the development of injectors. The understanding of flow and atomisation processes gained from the experimental findings was used to aid the development and validation of CFD codes and provide a predictive tool for GDI injector development. This is important for designers and engineers to meet the challenges posed by the Euro IV emissions standards and beyond.

1.3 THESIS OVERVIEW

Chapter 2 presents a review of the previous work on both Diesel and gasoline DI injectors. The review begins with a literature study of DI engines design and operating principles. Current research and technological advances for Diesel and gasoline DI engines are also presented. This is followed by the

description of the fundamentals of sprays and atomisation processes. The chapter concludes with an overview of the numerical tools currently available.

Chapter 3 investigates optical diagnostic techniques applicable in the current DI engine research. The chapter will only discuss diagnostic tools that are applicable in this research. An overview of the experimental setup was also explained.

Chapter 4 provides detailed designs of the injector rig and set-up used in the preliminary experimental studies of DI injectors. This chapter also provides detailed accounts on the use of optical diagnostic techniques.

Chapter 5 describes the detailed investigation of the Diesel injector optical rig. The experiments involved varying the pressure inlet and the pulse width of the injector to study the internal flow characteristics. This was achieved by using non-intrusive, high-speed flow visualisation laser techniques. Later stages of the experiments required pressurising the outlet chamber to investigate the effect on the spray structures and atomisation of the liquid jet.

Chapter 6 describes the flow visualisation study on the gasoline injector optical rig for both internal and external flow, with and without swirlers. Further investigations are presented to quantify the velocity flow field in the nozzles using the Fluorescent Particle Image Velocimetry (FPIV) technique. The data presented are internal velocity flow field for both non-swirl and swirl nozzles. The work is concluded with a Phase Doppler Anemometry (PDA) study to provide detailed analysis of the droplet size and droplet exit velocity of swirl nozzles.

Chapter 7 summaries the contributions of this thesis for diesel and gasoline DI injections. Further discussions are presented for possible future work and improvements to aid the understanding of future DI injections.

1.4 REFERENCE

[01] Arcoumanis, C., Gavaises, M., French, B., *Effect of Fuel Injection Processes on the Structure of Diesel Sprays*, SAE 970799, SP-1219, 1997

[02] Asian Development Bank, *Vehicle Emissions*. (http://www.adb.org/documents/guidelines/Vehicle_Emissions/im_ch03.pdf), 2003. [19.11.2003]

[03] BBC News, Fuel-cell car hopes played down. (http://newsvote.bbc.co.uk/mpapps/pagetools/print/news.bbc.co.uk/1/hi/sci.../2840191.st), 11.03.2003. [13.03.2003]

[04] BBCi News, *The long road for hydrogen*. (http://news.bbc.co.uk/1/hi/sci/tech/2705607.stm), 29.01.2003. [13.03.2003]

[05] Dieselnet, *Emission Standards: European Union*. (http://www.dieselnet.com/standards/eu/ld.html), March 2003. [19.11.2003]

[06] Huang, Z., Shao, Y.M., Shiga, S., Nakamura, H., Karasawa, T., *The role of orifice flow pattern in fuel atomization*, Paper I-12, ICLASS, Rouen (France), July 1994

[07] Jacobsson, L., Winklhofer, E., Chomiak, J., *Injection Orifice Shape: Effects on Spray Characteristics and Heat-Release Rate in a Large-Size Single-Cylinder Diesel Engine*, SAE 1999-01-3490, 1999

[08] Ramamurthi, K., Nandakumar, K., *Effect of injector orifice configurations on atomization*, Paper III-2, ICLASS, Rouen (France), July 1994

[09] Soteriou, C., Andrews, R., Smith, M., *Direct Injection Diesel Sprays and the Effect of Cavitation and Hydraulic Flip on Atomization*, SAE 950080, SP-1065, 1995

[10] Soteriou, C., Andrews, R., Smith, M., *Further Studies of Cavitation and Atomization in Diesel Injection*, SAE 1999-01-1486, SP-1460, 1999

[11] US Department of Energy, *FreedomCar and Fuel Initiative.* (http://www.eere.energy.gov/hydrogenfuel/), 05.02.2003. [13.03.2003]

CHAPTER 2

LITERATURE REVIEWS

2.1 REVIEWS OF INJECTION SYSTEMS

2.1.1 Background

Beau De Rochas first introduced the internal combustion engine concept in 1862 when he published a paper on the operation of a four-stroke engine. In his words, he wrote "*(1) to draw a mixture of gas and air, (2) to compress the mixture, (3) to ignite the mixture at the dead point, thereby producing the power stroke, and (4) to exhaust the products of combustion.*" [36] However, Nikolaus Otto (1832 - 1891) was the pioneer to invent and develop the first working four-stroke spark-ignited engine in 1876 and this was followed by the development of the Diesel cycle, also known as the compression ignition engine, by Rudolph Diesel (1858 – 1913) in 1897.

"An internal combustion engine is defined as an engine in which the chemical energy of the fuel is released inside the engine and used directly for mechanical work, as opposed to an external combustion engine in which a separate combustor is used to burn the fuel." [25]

For over a century, the IC engine has remained fundamentally unchanged apart from improvements made on emissions control and better fuel efficiency. The popularity of the reciprocating engine is due to its simplicity, robust operating characteristics, and higher power to weight ratio. Another major factor is the relatively low operating cost that makes it such an attractive option.

2.1.2 Diesel Injection Engine

Although Diesel compression ignition systems have existed since 1897, the use of Diesel powered vehicle was limited, only gaining momentum in the

early 1980, with the number of vehicles increasing to more than 25% of the market today [31]. This increase in market share was related to a number of advantages such as low fuel consumption; efficiencies comparable to those of gasoline engine. One of the most important factors was the ability to meet all the requirements of the Euro emission standards (Table 1.1) set by the regulatory of the European Union. Raffelsberger [59] highlighted that the injection system was the most influencing part of an engine in terms of efficiency and emissions control. Today injectors are electronically controlled to provide better management of the injection process and the common rail system was developed to provide flexible fuel injection. This system has led to controlled high pressure fuel delivery and controlled fuel injection leading to significant improvements in particulate emission and a reduction in combustion noise.

Stumpp and Ricco [76] believed that the high level of NO_x generated when running lean condition can be tackled by using the common rail system, which not only improves exhaust emissions and engine torque, but also reduces noise levels. The other advantage is the ability to choose the ideal injection fuel quantity and pressure within the limit of the pump, with the pump pressure ranging from 150 bar to 1400 bar. Han *et al* [30] also applied a high-pressure Diesel common-rail system to study the spray characteristics and injection of mini sac and valve-covered orifice (VCO) nozzles. VCO is a long-stem nozzle design that uses a needle valve to cover the injection holes. The sac is eliminated from this design to prevent any fuel retention between the needle valve and the injection holes, thereby reducing emissions caused by this sac. The nozzle hole diameter ranged from 0.147 to 0.180mm, with injection pressure up to 1350 bar. The study found that the injection rate was dependent on the common-rail pressure, the nozzle geometry and the hole diameter, with the nozzle geometry also having an impact on the spray symmetry and structure. Lastly, the mini sac was found to have a higher discharge coefficient than the VCO nozzle and the ability to run at lower injection pressure.

One way of improving engine performance and reducing pollutant emissions was attempted through improving the diesel fuel injection system. Bae and Kang [05] studied the Diesel spray development of VCO nozzles in high speed direct injection (HSDI) engine with special attention paid to low needle lift condition. The VCO nozzle has five identical holes with an inclined angle to generate a spray cone angle of 144°. The study revealed that three different types of spray pattern were identified, puffy spray structure, hollow cone spray and small angle spray at low needle lift regardless of load conditions. Chang and Farrell [13] studied the effects of fuel viscosity and nozzle inlet geometry of a VCO injector on spray characteristics using a common rail injection system under high injection pressure (90 MPa). Sauter mean diameter (SMD) was used to quantify the spray droplets, by using the surface to volume ratio of a droplet. They found that a sharp inlet nozzle gave a bigger spray angle than a round inlet nozzle. Low viscosity fuel in a round inlet nozzle has a smaller SMD compare to high viscosity fuel, but both fuel's SMD were similar in a sharp inlet nozzle. However, with the same injection settings the SMD of sharp inlet nozzle was measured to be smaller than round inlet nozzle.

Yoda and Tsuda [86] also investigated the influence of injection nozzle geometry on DI Diesel engine performance to lower NOx and PM emissions by improving atomisation and flow velocity without increasing the fuel injection pressure. They discovered that higher fuel flow velocity at the spray hole improves atomisation without increasing injection pressure. It was made possible by enlarging the chamfer inlet of the nozzle and this also improved the fuel flow velocity distribution at the nozzle outlet. These test results were applied on an actual engine and it decreased smoke emissions at high load, improved engine power output and lowered NOx-PM.

A major concern is fuel injection cycle-to-cycle variation caused by spray structure abnormalities such as cavitation and hydraulic flip. Although many researchers have noticed this phenomena, it was only in the last decade that it has been possible to understand these spray abnormalities with the help of optical nozzles manufacturing techniques and optical diagnostic

advancements. Soteriou *et al* [74, 75] believed that the use of large scale acrylic direct injection models enabled the interpretation and understanding the results from real sized single hole and VCO nozzles. The experimental results showed that cavitation in the nozzle was the predominant mechanism in causing atomisation in the spray. The authors also believed that the differences in spray characteristic between the large scale models and real size nozzles were caused by asymmetries and imperfections in the real size nozzles. Chaves *et al* [14] were able to remove this ambiguity between single hole and VCO by using real-sized nozzles. Cavitation was also observed by Chaves *et al* [14] in studies of sharp inlet nozzles. They showed that the cavitation developed into supercavitation with increasing injection pressure. They noted that supercavitating flow was unstable and caused velocity fluctuations in the nozzle exit flow. In an investigation of internal flow and spray structure using scaled up VCO models, Laoonual [44] showed that cavitating phenomena can be removed using both bevelled and round inlet nozzles. The experiments were performed using high-speed and single shot imaging systems, with injection pressure ranging from 0.069 MPa to 2.0 MPa. Hydraulic flip was observed only in sharp inlet nozzle and also strong atomisation processes were observed. This was not the case when experiments were conducted on both the bevelled and round inlet nozzles.

2.1.3 Gasoline Injection Engine

Transmission of fuel to the combustion chamber in gasoline engine has gone through a development cycle since Otto first developed the spark-ignition engine. Early engines employed a carburettor system, which premixed the fuel and air to supply a homogeneous charge to the engine. Multi-Point Injection (MPI) system became more prominent in the 1980's as it provides better fuel efficiency and higher power output. However, to control global warming and its effect on the environment, government agencies had introduced tough measures and legislation in order to combat these greenhouse gases (See Table 1.1) like Carbon Dioxide (CO_2). To achieve reduction of greenhouse gases, there is an immediate need to develop and promote the use of a new injection system that emits significantly less CO_2

and Hydrocarbons (HC). These have led to the development of the Gasoline Direct Injection (GDI) system over the last decade. GDI system is able to provide superb controllability in terms of volumetric efficiency and transient response as compared with the current MPI system. The following sections provide a more detail account for conventional injection system and GDI system.

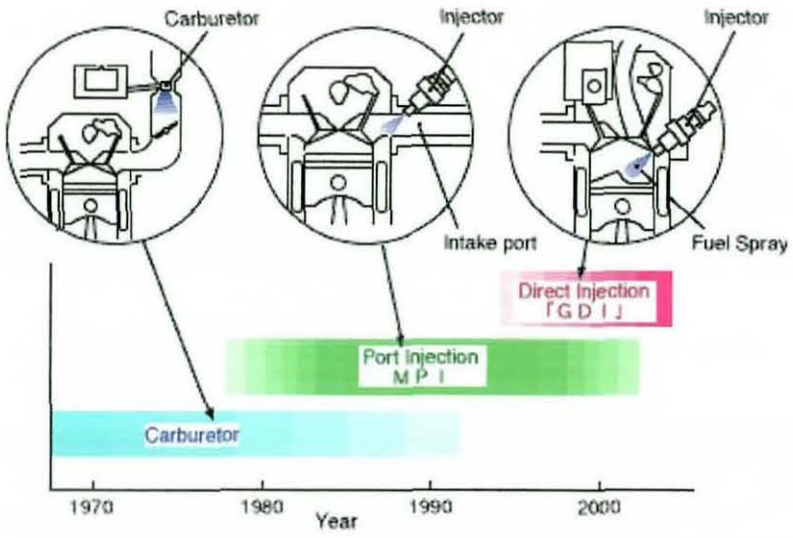

Figure 2.1 Transition of Fuel Systems [48].

2.3.3.1 CONVENTIONAL ENGINE

The fuel-injection systems for conventional spark-ignition engines exist generally in two forms; Multi-point port injection (MPI) and Single-point throttle-body injection (SPI)[17]. Multi-point injection systems involve injecting fuel directly into the intake port of each engine cylinder (See Figure 2.2 "Conventional engine"). The advantages of this system are the increase in power and torque through improved volumetric efficiency of the engine as compared with carburettor system. It also allows more precise control and rapid responses to changes in throttle position which can be controlled both mechanically and electronically. The other conventional fuel injection system is the single-point throttle-body injection that uses electronically controlled injectors to meter the fuel rate into the airflow directly above the throttle body. This method of fuel metering is much more straightforward as compared to multi-point injection system and has the advantage of reduced cost.

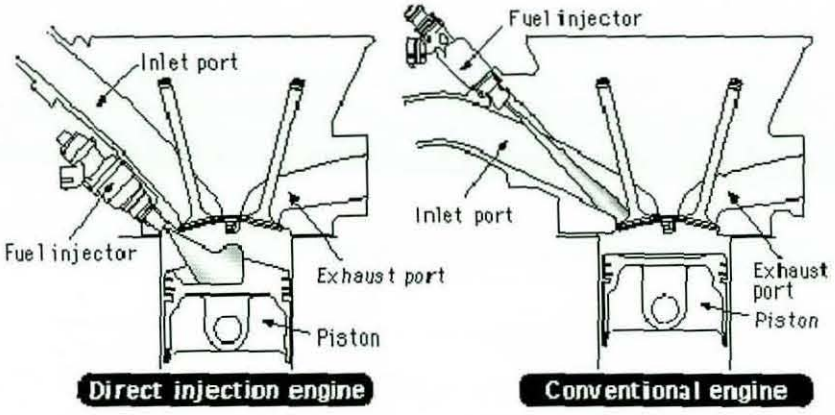

Figure 2.2 Two methods of fuel injection system [26].

The MPI are still the most commonly known engines in use in automotive vehicles, but these engines are being phase out slowly. There are several disadvantages posed by the conventional MPI and the SPI injection systems. As the fuel is not delivered directly into the combustion chamber in the engine, this limits the air/fuel mixing response to different driving conditions. There is the possibility of condensation by the air-fuel mixtures at the inlet valve and affects the fuel efficiency. Gasoline engines are also notorious for generating greenhouse gases (CO and CO_2) and HC emissions, contributing significantly to global warming. Therefore, it is important to search for an alternative solution for gasoline injection system.

2.3.3.2 DIRECT INJECTION ENGINE

Gasoline direct injection (GDI) refers to fuel injected directly into the combustion chamber above the piston. As mentioned in previous section, high levels of CO, CO_2 and HC emissions have always plagued conventional gasoline engines. However, automotive engineers believed that GDI has the greatest potential to correct this problem as shown by Diesel DI and also the ability to deliver better performance and improved efficiency. Several researchers [58, 36, 52, 72, 83] believe that the GDI engine system offer the best solution for gasoline powered automotives for the future. Queiroz and Tomanik [58] provided a bibliographical review on the current GDI developments and offer several ideas used to position the GDI fuel injector in

the combustion chamber as this determines the ability to achieved complete combustion.

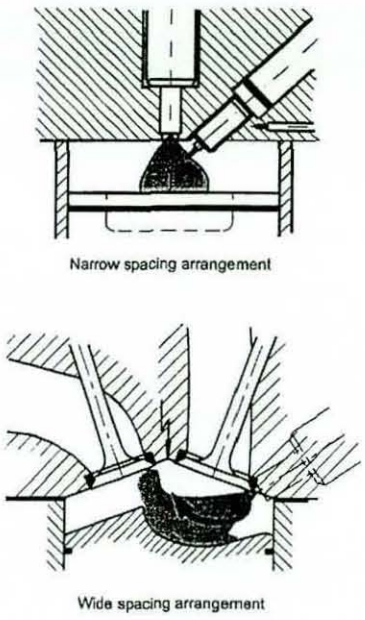

Figure 2.3 GDI concepts with narrow and wide spacing arrangements [72].

The locations of the fuel injector and spark plug are very important in determining the GDI engine's ability to precisely control the mixing of the air and fuel. There are several ways being suggested to locate the GDI injector in the chamber, either by close or wide spacing arrangements. Figure 2.3 showed two different concepts, which were discussed by Spicher *et al* [72]; narrow spacing arrangement and wide spacing arrangement. In the narrow spacing arrangement, the injector is placed in a central position of the cylinder head. This configuration allows better control of stratification at idle and part-load conditions. Experimental results also showed that using a narrow spacing arrangement for the spark plug and injector have a 58% fuel reduction at idle operation. Although this design allows combustion of extremely lean overall mixtures, it suffers from packaging difficulties of the injector and the spark plug and the spark plug electrode might suffer from wetting by the injected fuel. Another narrow spacing arrangement of the fuel injector and spark plug was also investigated by Karl *et al* [36]. The authors acknowledged that proper research into exhaust aftertreatment was essential to meet today emission standards, without compromising the fuel economy offered by this

arrangement. Spicher *et al* [72] believed that the wide spacing arrangement injector was more conveniently located at the side of the cylinder head as compare to the narrow spacing arrangement to enable optimum mixing of gaseous fuel and air. This design uses a special piston cavity and strong tumble or swirl motion generated by the modified cylinder head to transport the fuel from the injector to the spark plug.

Noma *et al* [52] works adopted this wide spacing concept in their research, delivering the atomised fuel to the spark plug via the spherical piston cavity. This arrangement creates an interval long enough for the fuel to vaporise and mixed with the surrounding air before the spark ignition. The authors also introduce a "two-stage mixing" process, which allows the suppression of knock and the ability to varies the air-fuel mixture to suit different driving conditions. The problems associated with this setup are the generation of NO_x and this is reduced by using a catalytic converter. The authors claimed that the GDI engine was able to improve the fuel efficiency by 20% and also increased the air-fuel ratio from 12.5:1 to 20:1. An example of a working Mitsubishi GDI engine development was explained by Iwamoto *et al* [34]. The GDI engine adopted an upright straight intake ports with wide spacing to generate air tumble, spherically shaped compact piston cavity to maintain charge stratification and an electromagnetic swirl injector to achieved optimised spray dispersion and atomisation. The authors claimed that a fuel economy of more than 30% was possible at part load conditions. The only significant problem was NOx emissions under lean burn conditions but using a lean-NOx catalyst was able to overcome this problem.

Shiraishi *et al* [70] also studied the wide angle arrangement of a 2.0 litre GDI engine with flat piston crown to achieved higher power output at open throttle condition and also optimising spray characteristic and in-cylinder flow. This study applied both high-speed flow visualisation and phase Doppler particle analyser (PDPA) techniques to investigate the spray developments in the combustion chamber and droplet size measurements respectively. The experimented results showed that smaller the spray angle of 60 degrees had a droplet size of 50 μm, but bigger penetration and vice versa for 80 degrees

spray angle. The results also showed that low fuel pressure and wide spray angle resulted in low penetration and the air fuel mixture is pushed aside in the combustion chamber. Nogi *et al* [53] used the same 2.0 litre engine to improve combustion stability under lean burn operation. Two fuel injectors were used, narrow and wide spray angle swirl nozzles, and a cavity was introduced on the piston crown. The experimental data showed that narrow spray angle injector contained more smoke because of the impingement on the cavity surface. With spray angle optimisation at about 85 degrees, combustion stability was improved and the amount of smoke decreased. The engine torque also increased by 3.5% compared with the 65 degrees spray angle.

Lake *et al* [43] provided 4 different approaches for combustion system design for GDI engines. These four designs are fuel transport calculations, top entry ports with side injector, side entry port -side injector and side entry ports with central plug and injector. These designs were tested on a rig, using PDA optical technique to obtain comparable data. Although the side entry ports with central plug and injector offers one of the best configuration in part-load and full load conditions, the authors believed that the choice is till dependent on cost, manufacturing requirements, acceptable variable system and control capability.

Besides the arrangement of the spark plug and the fuel injector, GDI engine combustion modes alternated between stratified charge and homogenous charge. During normal driving conditions, the GDI engine operates in stratified mode, as there is no need for sudden acceleration. A spray of fuel is injected over the piston crown during the latter stages of the compression stroke, the resulting spray and air flow within the cylinder cause the spray to vaporise and disperse. The resulting mixture of gaseous fuel and air is then carried up to the spark plug for ignition. The level of fuel efficiency comparable to that of a diesel engine, with an air-fuel ratio of about 30 - 40 (Figure 2.4). This system also enables precise control over the air-fuel ratio at the spark plug, at the point of ignition. In homogeneous combustion, fuel is injected during the intake stroke, when the piston is descending towards the bottom of the

cylinder, vaporising into the air flow and following the piston down. As the piston moves downward and the inside of the cylinder becomes larger in volume, the fuel spray disperses widely, allowing additional air to be drawn in, ensuring a homogenous mixture. This optimises combustion by improving volumetric efficiency and with cooler air-fuel mixture, the possibility of engine knocking is minimised, resulting in higher power output.

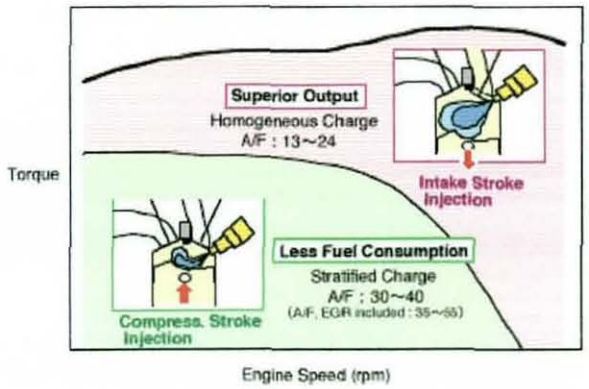

Figure 2.4 A/F ratio with respect to Torque and engine speed [48].

Egermann *et al* [22] employed two different high pressure swirl GDI injectors, with 60° and 90° spray cone angle, to investigate spray formation and evaporation using 2D Mie Scattering and linear Raman spectroscopy. The results showed the 60° injector forms a narrower spray cone, which is more homogeneous (due to stronger evaporation and mixing) and penetrates the chamber faster as compared with the 90° injector. They also noted a stronger turbulent air entry on the radial direction for the 60° spray cone angle injector.

There are several GDI injectors available in the commercial market today from the non-swirl nozzles to the most commonly used swirl injectors. Parrish and Farrell [57] investigated the transient spray characteristic of a single hole, pintle type injector with electronic control. They used Stoddard solvent as it refractive index match those of gasoline and nitrogen was used to pressurise the injector fluid. Particle size measurement technique was used to determine the Sauter mean diameter (SMD) of the droplets for three injection pressures. The results showed that the spray droplets range from 33 to 43 μm for the main spray. Another study of spray development from a single hole nozzle

was investigated by Nouri *et al* [54] using PDA technique. A nitrogen cylinder was used to supply the required injection pressure range from 30 to 100 bar, with injection duration from 3 to 9 ms. The penetration of the injected fuel spray varied from 82 and 116mm for pressure of 30 and 100 bar respectively. At an injection pressure of 70bar, the maximum velocity decreased from 70 to 45 m/s as the spray penetration move from 10 to 60 mm from the injector. However, the Sauter mean diameter remained consistently at 60 μm for the droplet for both distances. De Vita *et al* [21] also investigated the spray characteristics and structures using a single-hole type swirl GDI injector. The measurements were carried out using optical diagnostic techniques on three injection pressures of 5MPa, 7MPa and 9MPa. An initial slug of liquid was observed as the spray exits the nozzle and the spray developed into a large hollow cone angle of about 83°. The results also showed that the SMD values decreases when the injection pressure increases.

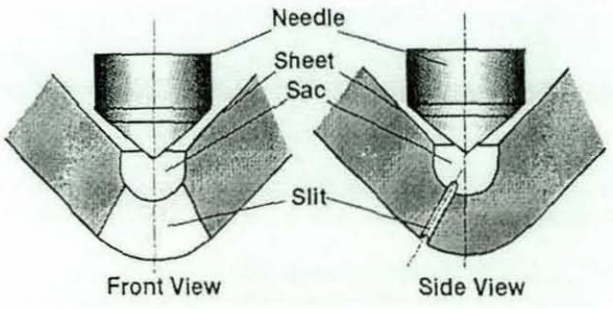

Figure 2.5 Slit Nozzle [77]

One unique concept of a GDI injector was presented by Takeda [77] from a new Toyota production engine. The injector adopted a slit shaped nozzle that produced a thin fan-shaped spray as shown in figure 2.5. The slit nozzle injector allowed the spray to dispersed wider in horizontal direction and thinner in vertical direction when compared with the hollow cone spray. The experimental results showed that this new injector concept has a 20% increase in fuel economy that conventional port injection system. The authors believed this nozzle concept could be easily fitted into any engines, without changing the base characteristic of the spray.

Swirl flow injectors were widely used injectors in the developments of GDI injector technology. The basic principle of the pressure swirl atomiser is presented in figure 2.6. The high-pressure fuel flow is forced to enter the reservoir above the controlling pintle valve via tangential inlets. This generates a swirling flow passing through the pintle and out to the exit nozzle. As the swirling liquid flows through the nozzle and exits the orifice, a vortex is formed which draws air into the centre of the nozzle. This generates an aircore which grows against the outflow until it connects with the pintle, forcing the liquid into a thin annular region on the nozzle wall. In this way, the fuel flow emerges from the nozzle as an annular flow with axial and tangential velocity components and forms a thin, conical liquid sheet, which rapidly disintegrates into ligaments and droplets.

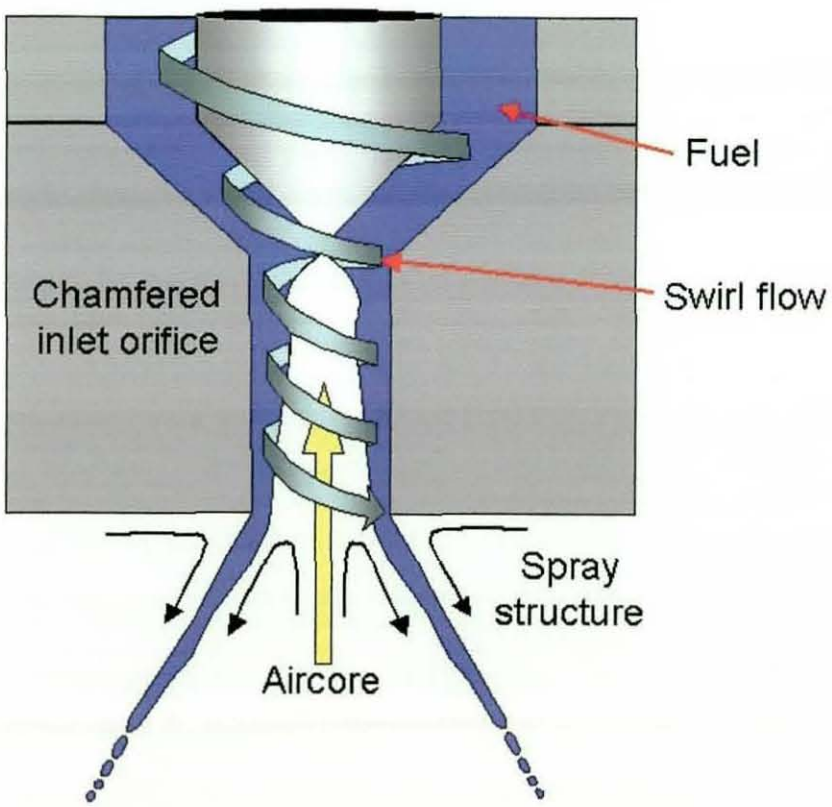

Figure 2.6 The principle of the pressure swirl atomiser.

Evers [23] and Zhao *et al* [88] investigated the spray characteristics of a high pressure swirl injector. Evers [23] used a high pressure (90MPa) swirl injector to quantify the spray regions which were identified as the leading edge, cone,

trailing edge and vortex cloud. The study involved changing the following variables; operation variable of the ambient air pressure surrounding the spray, fluid pressure upstream of the injector and the swirl characteristics. The experimentation results revealed the fluid droplet size decreased with increasing fluid inlet pressure but the droplet size increased with increasing ambient pressure. The droplet size in the leading edge and cone region also increased with increasing nozzle swirl. Zhao *et al* [88] applied almost similar operation variables as Evers [23] in their study on two prototype injectors that is able to generate small and large angle spray. Two addition parameters were the effect of nozzle designs and injection duration. An increased in spray tip penetration was observed with increasing injection pressure but decreases when the ambient temperature was increased. The author also noticed the radial distribution of droplet size for large angle injector was largest at the spray periphery but the spray velocity was constant within the spray envelope.

However, the small angle injector's droplet size showed a trend that was exactly opposite to the large angle nozzle. Abo-Serie *et al* [02] attempted to quantify the spray structures by identifying the spray developments into four stages when the fuel exited the nozzle. These stages are; a poorly atomised asymmetric jet at the central part of the nozzle hole with a tip velocity proportional to the injection pressure, an asymmetric non-hollow spray, a swirl-developing hollow-cone spray with a multi-layer structure, and a fully developed hollow-cone spray with a cone angle almost independent of injection pressure. The authors linked the first two stages to the time before the liquid film was formed in the nozzle hole, with the last two identified as the period of film development. Using high magnification images of the annular liquid sheet at the nozzle exit two modes of droplet formation was revealed. The first being the ligaments formed in the direction of injection and the second was observed wave crest stripping in the radial direction.

In an engine, the air pressure changes in the combustion chamber as the piston moves through the intake, compression, expansion and exhaust strokes. With the change in air pressure in the chamber, this will naturally affect the spray structures in a direct injection engine. Comer *et al* [17] initial

work looked into the spray structure of a high pressure swirl injector into air at ambient and room temperature. The average velocities from the PDA data at the centre of the hollowcone spray were about 50 m/s at about 90mm downstream from the injector. Comer *et al* [18] later investigated the influence of ambient pressure, ranging from 0.1 – 0.6 MPa on GDI sprays. Videos from the experiments showed that the spray structures penetration decreases with increasing ambient pressure. The cone angle decreases by about 20% and the global SMD by about 40% over the range of ambient pressures investigated. The authors believed that a linear trend in penetration, similar to diesel injectors could be approximated. Allen *et al* [01] provided another study on spray characteristic of different fuel injectors under atmospheric and elevated pressure conditions, with the latter as high as 15 bar. The spray results showed air assisted injectors produce the smallest arithmetic droplet diameters (3 μm to 4.5 μm) dependent on the fuel load. For the single fluid atomiser, the high pressure injector is the most effective atomiser with a mean droplet diameter of 4.5 μm to 8 μm and is 1.5 μm to 3 μm smaller than the low pressure injector. Similar mean droplet diameter to the low pressure injector was also observed on the solenoid injector.

2.2 SPRAY AND ATOMISATION

To develop an understanding of automotive engine operation, it is important to gain an insight into the fundamentals of fuel spray and atomisation processes. Scientists and researchers have been studying the mechanisms of liquid spray atomisation extensively for more than a century. There is a wide application of spray phenomena in our daily life and society. There are several ways that a spray can be produced, this can be a simple garden sprinkler, a pharmaceutical inhaler or injection system of a car. Despite numerous studies aimed at developing an understanding of spays and atomisation, there is still uncertainty surrounding the fundamentals of physical processes. Our understanding of sprays and atomisation has improved enormously over the past few years, made possible by the technological advances in laser diagnostic techniques.

Sprays involve the breakup of liquid into droplets, which results in an increase in surface area. Sprays can be created in a number of ways and generate atomisation processes for suitable applications. Nasr *et al* [51] provided a general characterisation of the spray by its shape, patternation and droplet sizes depending on it uses and demands. However this classification is not necessarily the same in all directions as they are time-dependent, but it is possible to categorise the shape of a spray into three general angles; narrow angle ($\theta<30^{\circ}$), medium angle ($30^{\circ}\leq\theta<70^{\circ}$) and wide angle ($\theta\geq70^{\circ}$). This classification can be further divided into three different patternations as shown in Figure 2.7. The hollow cone and full cone sprays are axisymmetric patterns usually achieved with a pressure swirl atomiser or any two-fluid atomisers and the flat fan shape sprays are generated by other atomiser orifice designs.

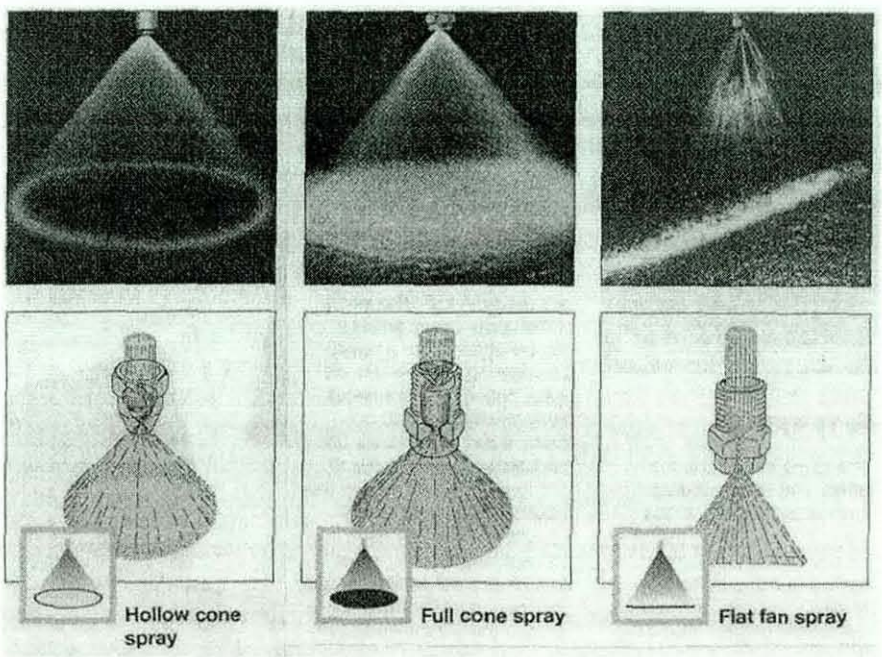

Figure 2.7 Spray patternations [51].

Atomisation is a process in which a liquid jet disintegrates under high velocity flow conditions into surrounding air. Both atomisation and sprays play a very important role in improving combustion efficiency and emissions [15]. For any given combustion application, it is vital that the fuel it transported quickly into the combustion chamber and rapidly mixed with the combustion air. This can be achieved by the use of different fuel injectors, to generate the fuel spray

required as mentioned in figure 2.7 and this promotes rapid vapourisation which determines the spray penetration into the combustion chamber. Spray and atomisation are also strongly influenced by density, viscosity [37] and surface tension of the liquid. The relative importance of these liquid properties can be relates by the Reynolds and Weber numbers equation [51, 45].

For any given flow, Reynolds number is given as

$$\mathrm{Re} = \frac{\rho V D}{\mu} \tag{2.1}$$

and Weber number as

$$We = \frac{\rho V^2 D}{\sigma} \tag{2.2}$$

where ρ is the density, V the velocity, D the characteristic dimension (diameter/length), μ the viscosity and σ is the surface tension stress.

From equation 2.1, it is clear that Reynolds number is strongly influenced by the viscosity of the liquid; any increase in viscosity results in a decrease in the Reynolds number. This hinders the development of turbulence structures during the liquid breakup in turbulent conditions, thereby affecting the spray and increasing the droplet sizes during atomisation. In cases where the surface tension has an important effect, the Weber number (Equation 2.2) is an equation for correlating the size of droplets. Decreasing surface tension results in an increase in the Weber number, which promotes better atomisation process. Therefore, higher values of Reynolds and Weber numbers promote faster and better atomisation.

Another significant parameter is the discharge coefficient (C_D), which is used to express the performances of a nozzle. This is defined as the ratio of actual mass flow rate to the ideal mass flow rate for isentropic flow through a nozzle

with the same inlet and exit conditions [50]. Discharge coefficient can be influenced by the following; the Reynolds number, length/diameter ratio (L/D), pressure difference through the nozzle, inlet geometry, cavitation and ambient pressure. In terms of nozzle geometry, swirl nozzles have a lower discharge coefficient compared with plain nozzles, due to the presence of an air core in the central portion of the nozzle. Ohrn *et al* [56] carried out work on 40 different plain nozzles, with the L/D ratio varying from 2 to 5. Their experiments showed that orifice inlet geometries were sensitive to any small perturbations and changes with inlet radius. Any increase in orifice inlet geometries will rise the discharge coefficient values and this increases the discharge coefficient dependence on Reynolds number. Schmidt [68] developed a 1D model to predict the flow from cavitating nozzles and accurately predicted the coefficient of discharge.

2.2.1 Cavitation

Cavitation is an important phenomenon which has a profound effect on atomisation of a liquid jet. This phenomenon is caused by the local pressure in a liquid dropping below the vapour pressure, which ultimately leads to the growth of cavities or vapours. This was first noticed by Lord Rayleigh [46] while studying the collapse of bubbles when they rose in boiling water. A more detailed account on cavitation can be found in the books published by Knapp *et al* [40] and Young [87]. There are several kinds of cavitation listed by both authors such as hydrodynamic cavitation and acoustic cavitation. However, the study main interest in this study is hydrodynamic cavitation, produced by pressure change in a flow through a pre-determined channel or nozzle.

In the field of hydrodynamics cavitation is often undesirable since it can result in catastrophic effects hydraulic machinery and ship propellers. Bunnell *et al* [11] used a two-phase laminar Navier-Stokes equation to formulate a homogeneous flow model to study the effects of orifice size, pressure drop and site density to understand the effect of cavitation on high-pressure injection flow. Site density is a free variable arising in the homogeneous fluid formulation related to the number of nucleation sites in the flow field used in

the model. The aim of Bunnell *et al* [11] research was to be able to predict and prevent cavitation, however other scientists and researchers believe that cavitation play an important role in generating turbulence structures to improve atomisation in sprays.

From the time of Lord Rayleigh [46], researchers have been trying to provide an understanding of cavitation and it effects on sprays in orifices and nozzles. The uses of new technology such as optical diagnostics have provided researchers with the ability to study cavitation effects more closely. One way of interpreting a cavitation flow is to use the cavitation number, CN, this is a dimensionless number that is the same form as the Euler number (used to measure the ratio of pressure forces to inertia forces) and this cavitation is defined as

$$CN = \frac{(P_r - P_v)}{\frac{1}{2}\rho V^2} \tag{2.3}$$

where P_r is the reference pressure, P_v is the vapour pressure, ρ is the density and V is the velocity.

Several researchers believe that strong turbulence generated by the orifices and nozzles assist in the disintegration of the liquid jet. Bergwerk [10] was one of the earliest researcher to study the spray of a diesel injector. He was able to observe the cavitation effects on the jet appearance by investigating the influence of cavitation number, Reynolds number, sharp inlet geometry and the length/diameter (L/D) ratio. Bergwerk [10] was able to conclude that only the nozzle inlet corners had any effect on the flow characteristics. Under cavitating conditions, the flow was observed to detach from the nozzle wall and emerge as a smooth glass-like jet. This phenomenon is now commonly known as hydraulic flip. This is due to the presences of sharp inlet geometry of the nozzle that causes a low pressure region to fall below the vapour pressure of the fluid.

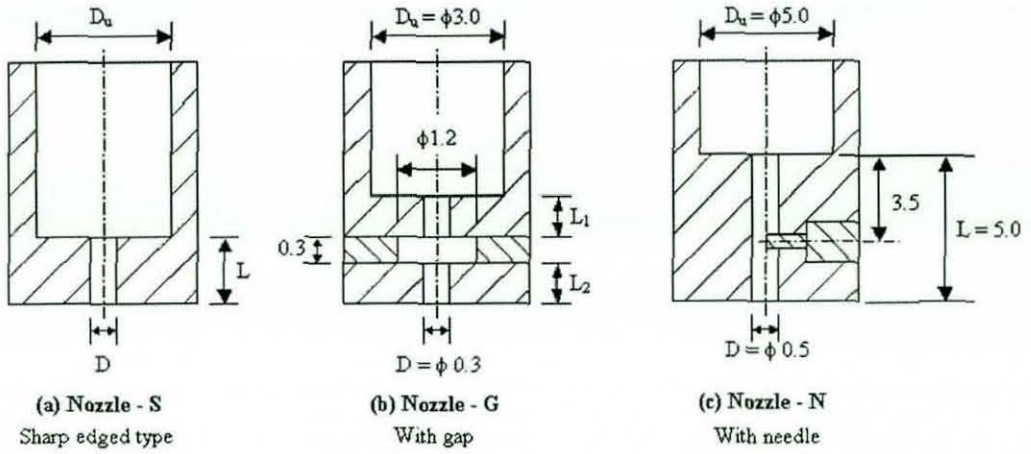

Figure 2.8 Schematic of test nozzles [78]

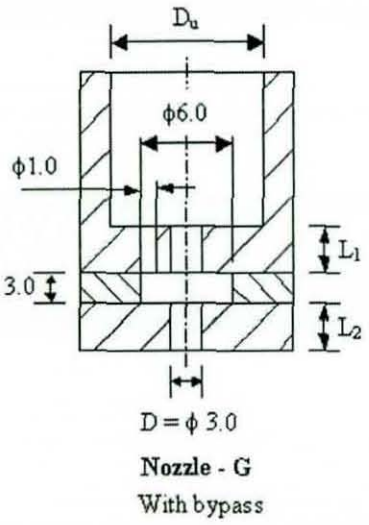

Figure 2.9 Nozzle with bypass [79]

Tamaki *et al* published a series of papers [78, 79, 80] using different nozzle geometries to enhance atomisation by cavitation. Figure 2.8 showed the first investigation by the authors with the installation of a gap in the middle of the nozzle hole. This nozzle design was able to generate strong turbulence flow in the nozzle at low injection pressure condition. The experimental results revealed that the spray angle increased while the breakup length shortened with the gap installed. The same result was also obtained with a smaller L/D ratio (or $(L_1+L_2)/D$). The authors also noted that a smaller L_2 increased the atomisation and Nozzle-N design was able to control the spray direction by the needle in the nozzle gap. In the following paper, Tamaki *et al* [79] incorporated a bypass in the Nozzle-G design as show in figure 2.9. Different

lengths for L_1 and L_2 were used, but no significant results were obtained when compared to the previous paper. As with the previous paper, small $(L_1+L_2)/D$ ratios increased the spray angle and decreased the liquid breakup length. This highlighted that spray and atomisation processes were still dominated by the L/D (L_2) of the final exit orifice.

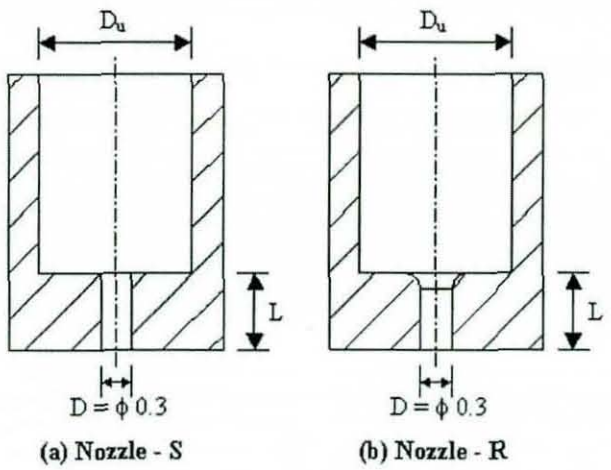

Figure 2.10 Schematic of sharp inlet and radii inlet nozzles [80]

Tamaki *et al* [80] used a single 0.3mm diameter hole nozzle to study atomisation under super-high injection pressure. These injection pressures range from 20MPa to 200 MPa and water was used instead of diesel fuel as the injected liquid. Two set of nozzles were employed in this study, sharp-edged and inlet radius nozzles shown in figure 2.10. At low injection pressure (20MPa), it was found that the inlet pipe diameter D_u and the L/D ratio of the nozzle influenced the disintegration of these liquid jet. The authors also noted that inlet geometry of the nozzles has a profound effect on atomisation processes, independent of the injection pressure. This was true under super-high injection pressure and was believed to be due to the presence of cavitation in the nozzle.

Soteriou *et al* [74] investigated the liquid breakup from 4 different flow geometries, from simple geometry circular orifices to multi-hole nozzles. These nozzles were large-scale acrylic models of actual injectors and intended to enable the interpretation and clarification of the results obtained

with actual nozzles. This work applied simple photographic recording of the flow structure to infer mechanisms for cavitation and atomisation processes in DI diesel sprays. They concluded that cavitation in the nozzles is the predominant mechanism causing atomisation in the sprays. Soteriou *et al* [75] conducted a further study on cavitation and atomisation in Diesel Injection using laser Doppler velocimetry (LDV) technique. They used nozzle rigs with the geometry scale-up by a factor of 20 and the liquid refractive index matched to aid the optical diagnostics. The authors concluded that cavitation in the orifice has a significant effect on the nozzle velocity profiles and boundary layer structure. From this study, cavitation in the hole was classified into 3 stages at high Reynolds number; incipient, plug and developed cavitation. An increase in turbulence was also observed and was shown to have a major effect in producing atomisation and larger spray angle, as mentioned by Tamaki *et al* [78, 79].

Other researchers attempted to generate cavitation in order to provide better understanding of these phenomena [41, 27]. Ganippa *et al* [27] used a simple sharp inlet nozzle in a large scale model. This was to imitate VCO nozzle but with only a single hole. Cavitation growth was observed in the shear layers, which develops into cloud-like coherent structure. This coherent cavitation cloud developed into a glossy sheet cavity under high flow condition. The design of the nozzle also caused asymmetric spray structures as it cavitated more on one side of the nozzle inlet. Ramamurthi [61] studied the inception of cavitation flow by varying the frequency of the solenoid valve and he was able to demonstrate the importance of pressure disturbance in flow transitions of sharp edged nozzle. One other parameter used to describe these turbulence effects was the cavitation number [68, 28, 27]. Goney *et al* [28] stated that cavitation number for multi-phase flow is given as;

$$K = \frac{P_1 - P_{vapour}}{P_1 - P_2} \tag{2.4}$$

where P_1 is the total pressure upstream to the flow passage, P_{vapour} is the vapour pressure of the fuel and P_2 is the downstream (ambient back)

pressure. This is a derivation from Nurick [55] previous work which was also presented by Orhn [56].

One of the earliest researchers to use models to predict cavitating flow was Schmidt *et al* [67, 68]. These models used simplify assumptions associated for flow to predict the momentum of fluid leaving the nozzle and the models accurately predicted the coefficient of discharge for cavitating nozzles. They noted several complex flow phenomena relating to cavitation formation in the nozzle and provided some comparisons with a numerical model of the internal flow.

2.2.2 Nozzles

One other major influences on spray and atomisation was the design of the orifices or nozzles. This plays an important role in controlling the spray structure and atomisation of the fluid. Several papers have been published using different nozzle geometries in order to investigate the effect of nozzle geometry on atomisation, either by either by changes in the flow structure or the generation of cavitation [33, 35, 60, 84]. Huang *et al* [33] and Ramamurthi *et al* [60] investigated the control mechanism in fuel atomisation using different metal orifices. Huang *et al* [33] observed that the flow was found to have two characteristic flow patterns, firstly contraction and reattachment and secondly flow free from the wall. This contraction was what we understand as cavitation and this yielded a smaller droplet size in the atomised fuel. Ramamurthi *et al* [60] looked at the influence of L/D ratio and exit geometry of sharp inlet orifice on atomisation for both swirl and non-swirl water jet. The authors discovered that L/D ratio of less than 5 produced finer droplets for both swirl and non-swirl conditions.

Several authors later used transparent nozzles to further investigate the internal flow structures. Reitz and Bracco [62,63] used different types of transparent nozzles in their study of atomisation processes. The earlier study [62] used plexiglass and stainless steel nozzles, with the latter investigation [63] also used plastic and glass nozzles. Their study found that plastic nozzles

were not able to produce repeatable results of atomisation but the results achieved from the glass nozzles were consistent with those of stainless nozzles. Chaves *et al* [14] used glass nozzles with identical geometry to a DI diesel device and a high efficiency pulsing LED to provide illumination into the flow region. These visualisation studies showed images of the development of cavitation and 'supercavitation' in the fuel nozzles. Data was also provided for the variation in spray cone angle with driving pressure. Other researchers like Soteriou *et al* [74, 75], Dan *et al* [20] and Arcoumanis *et al* [04] used perspex nozzles in their study. Dan *et al* [20] used several nozzles (diameter varies from 0.18 to 0.4mm and length between 0.75 to 1mm) to study the spray divergence angle with different nozzle configuration. They concluded that spray cone angle was controlled by the turbulence generated in the nozzle and the shearing stress was caused by the kinematic viscosity ratio between the fuel and ambient gas. Arcoumanis *et al* [04] used an enlarged (20 times) perspex model of a multi-hole injector to investigate cavitation effects. Their results showed that flow variations occurred between holes after the onset of cavitation, despite the orifices having symmetrical geometry.

2.3 REVIEW OF NUMERICAL TOOLS FOR INJECTION SYSTEMS

2.3.1 Numerical Tools for Diesel Injection

The increasing popularity and advantages of using modelling tools to aid the understanding and also the validation of experimental results have helped to reduce the cost and time invested into developing and building engine prototypes. Balachandra *et al* [07] highlighted the use of both experimental and numerical modelling to optimise a charge injection nozzle and also to understand the atomisation processes for an electro-statically sprayed insulating liquid. A semi-empirical expression was then derived to predict the liquid breakup length, taking into account the liquid volume flow rate and charge mobility which showed good agreement with experimental results. Baumgarten [08] provided a comparison between the use of numerical and experimental techniques for a high pressure VCO Diesel nozzles. The

experimental work involved the use of single and 6-holes nozzles (d=0.22 mm, l = 1 mm). Cavitation was observed in both techniques used, with the 6-holes nozzle appears mostly on one side of the nozzle due to the fuel inlet angle.

Arcoumanis *et al* [03] and Bella *et al* [09] also demonstrated the use of modelling tools in their study of injection processes. Arcoumanis *et al* [04] model was based on a Lagrangian-Eulerian approximation and Navier-Stokes equations, to investigate the physical processes in spray development. The spray model was successfully applied to predict the spray development for a 1.9 litre Diesel engine, with simulated droplet mean radial velocity of up to 200 m/s and these results are almost identical to experimental. The authors also found that cavitating flow produced better atomisation and faster spray evaporation, reducing the chance of wall impingement in the combustion chamber. Bella *et al* [09] presented a modified KIVA 3V model to simulate multiple injection process, the mixture formation and combustion of a high pressure Diesel DI engine. The simulated results were validated using experimental data from a 4 cylinder Turbocharged Diesel DI engine. Bella *et al* [09] found that the computed results were comparable with experimental data for ignition timings, spray penetration and breakup processes in single hole injector spray.

2.3.2 Numerical Tools for Gasoline Injection

In recent years, an increase number of researchers are moving towards the use of numerical tools to study engines and injectors. This was mainly due to the improvement in computation power resulting in an increased use of numerical tools to model actual engine operation or injector spray structures. Most researchers conducted both experimental and numerical simultaneously to provide validation for numerical results. A number of researchers [24, 26, 65 and 12] investigated the in-cylinder flow field in GDI engines using various optical diagnostic techniques and compare with CFD modelling tools. Castagne *et al* [12] developed a methodology using both 3D numerical and experimental tools to characterise air-fuel mixing and combustion for a

Mitsubishi GDI 1.8 litre engine. The authors were able to produce repeatable results despite of the cycle-to-cycle variability for each combustion processes. The IMEP obtained for both calculated and experimental showed a good match in either injection advance or spark advance conditions.

Miyamoto *et al* [49] and Cousin [19] also developed modelling tools to investigate the characteristics of swirl injectors and comparing with the droplet diameters from experimental studies. Miyamoto *et al* [49] was one of the earliest researchers to use numerical models and experiments to study the spray structure of a transient spray using an air-assist hollow cone spray injector. This new method was used to predict the droplet mean size and velocity under different operating conditions and also the influence of fuel atomisation on spray structures. The simulated results showed good agreement with the experimental data. Increasing atomisation leads to the decrease in spray cone angle and droplet size. The results also indicated the evaporating spray structures were also dependent on the degree of atomisation from the injection. Cousin *et al* [19] numerical models were used to validate a large series of tangential injectors with difference internal dimensions. This was also found to be very similar to the SMD for experimental results

Kim *et al* [38] used the Ricardo CFD code, VECTIS, to analyse the in-cylinder flows in a four valve Spark-ignited Direct Injection (SDI) engine. CFD results were successfully used to validate the experimental data obtained from Laser Doppler Velocimetry (LDV) and Particle Image Velocimetry (PIV). CFD analysis was also suggested to replace experimental method during the early stages of development for the Spark-ignited Direct Injection (SDI) engine. Comer *et al* [16] uses similar CFD codes to verify the accuracy of the cone angle, injector orifice size, injection mass and rate and the measure of swirl angle to existing experimental data. A comparison was also done with time-resolved PDA data on droplet velocity profiles, penetrations and etc, with indiscernible difference.

Arcoumanis *et al* [04] used the combination of both modelling and optical diagnostic techniques in the modelling of pressure-swirl atomisers for GDI engines. Using a two-phase KIVA code, the liquid-gas interface developed within the nozzle was used to identify the formation mechanism of the liquid film. This calculation was then extended outside the nozzle to predict the spray cone angle. This had been confirmed by the images obtained from the CCD camera by the experiments conducted.

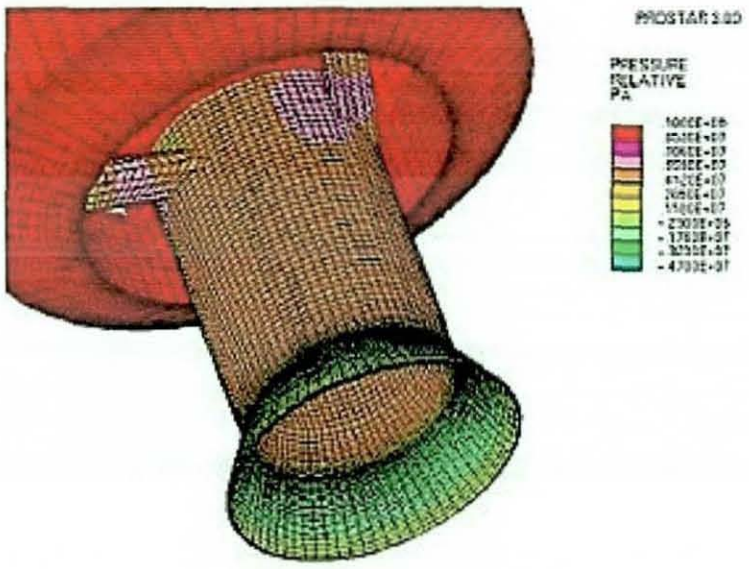

Figure 2.11 Pressure Distribution inside the Delphi DI Injector from Star-CD [85].

STAR-CD is another powerful multipurpose CFD code that can assist you through the complete design and development process. Xu *et al* [85] from Delphi Automotive systems solely used KIVA-3 in conjunction with Star-CD injector flow modelling to develop and produce a model for a high pressure outwardly open fuel injector (Figure 2.11) to predict the spray characteristics. The advantage of producing an outwardly opening nozzle is that the liquid sheet is formed by extrusion through the conical seat annulus, rather than by centrifugal force of swirling liquid as inwardly nozzle. This design also allowed for addition atomisation control by adjusting the initial liquid sheet thickness. The results of the modelling is of acceptable agreement with the subsequent

experimental conducted, therefore highlighted the advantage of this numerical simulations. Topenot *et al* [81] presented experimental results of a GDI swirl injector spray characteristics using different injecting fluids. The experiment results showed that white spirit data matched those of gasoline than water in spray droplet sizes. It also observed that the CFD calculations using STAR-CD also showed similar results in spray droplet sizes.

Another successful application of CFD codes is by Siemens Automotive. Ren *et al* [64] carried out a study on atomisation process of hollow cone sprays from pressure-swirl injector for GDI engine. The objective is to use a three-dimensional FIRE code developed by Advanced Simulation Technologies (AVL) to simulate and understand the effects of nozzle geometry and engine operating conditions on spray characteristics, allowing modification of the injector design to meet the fundamental requirements of GDI engines. The results showed that the spray width and penetration length decreased significantly as the ambient temperature increases, without being affected by the change in injection pressure. This can be seen on Figure 2.10, showing the difference in pressure by the different colours used. VanDerWege *et al* [82] also uses the FIRE code to investigate the physics leading to the flash-boiling hollow-cone spray. They were able to conclude that the interaction of the spray with the surrounding was more important than the original spray characteristics. It was more effective to produce a rapid vaporisation by directing a high momentum, moderately sized droplets spray pattern into wider gas stream (without wall impingement) than atomised spray.

2.4 SUMMARY

This chapter provides a literature reviews on the various works by researchers on both the Diesel and Gasoline engines. The literatures highlighted the current research methodologies many leading industrial corporations and universities are investigating. These include simulations and experimental techniques employed. The review of literature has revealed that there are basically two types of injector used fuel injection in IC engines. For Diesel engines the injectors are basically multi-hole, plain-orifice, non-swirl

atomisers. For single-point and multi-point manifold injection for gasoline engines, atomisers are usually also plain-orifice, non-swirl injectors. However, for GDI engines, where injection, atomisation and mixing must be controlled accurately within the geometry and temporal constraints of combustion chamber, the injector of choice is the pressure swirl atomiser.

A lot of work has also been carried out to investigate the effects of direct injection and it characteristics on the combustion chamber. However, little research is being done or in-depth study on the flow structure before the nozzle exit, and the effects of changes in orifice geometry. These include the input pressure characteristics, different orifice plates, internal flow characteristics and the velocity inside the nozzle before exiting into the combustion chamber. The only notable research is by Arcoumanis *et al* [04] on the modelling of the pressure-swirl injector just before nozzle exit to calculate the location of the liquid-gas interface and estimates the transient response of the liquid film developing on the wall of the discharge hole.

Many of the authors believe that direct injection is the way forward for future engine designers and manufacturers. The potentials offered by direct injection are enormous to the future of automotive industries on improving fuel economy and reducing pollutant, meeting Euro emissions targets. Optical diagnostic techniques were briefly mentioned in the literature works by the researchers. The next chapter provided more in-depth discussions on the various optical diagnostic techniques used in this thesis work, assisting the understanding of both Diesel and gasoline injectors.

To conclude, there is very limited experimental data on the flow structure before the nozzle exit and the effects of changes in orifice geometry, which will be the focus of this investigation.

2.5 REFERENCES

[01] Allen, J, Heath, J., Hargrave, G.K., Wigley, G., *Comparison of the Spray Characteristics of Alternative GDI Fuel Injection Systems Under*

Atmospheric and Elevated Pressure Operation, 15th International Combustion Engine Symposium, 9935086, Seoul (South Korea), July 1999, ISBN 4-915219-25-9

[02] Abo-Serie, E., Arcoumanis, C., Gavaises, M., Argueyrolles, B., Galzin, F., *Structure of Sprays Generated by Pressure Swirl Injectors for Direct-Injection Gasoline Engines*, ILASS-Europe, Toulouse (France), July 1999

[03] Arcoumanis, C., Gavaises, M., French, B., *Effect of Fuel Injection Processes on the Structure of Diesel Sprays*, SAE 970799, SP-1219, 1997

[04] Arcoumanis, C., Gavaises, M., Argueyrolles, B., Galzin, F., *Modeling of Pressure-Swirl Atomisers for GDI Engines*, SAE 1999-01-0500, 1999

[05] Bae, C., Kang, J., *Diesel Spray Development of VCO Nozzles for High Pressure Direct-Injection*, SAE 2000-01-1254, SP-1498, 2000

[06] Bae, C., Yu, J., Kang, J., Kong, J., Lee, K.O., *Effect of Nozzle Geometry on the Common-Rail Diesel Spray*, SAE 2002-01-1625, SP-1713, 2002

[07] Balachandran, W., Hu, D., Yule, A.J., Shrimpton, J.S., Watkins, A.P., *Electrostatically produced Fuel Sprays for Combustion applications*, Paper XII-2, ICLASS, Rouen (France), July 1994

[08] Baumgarten, C., Shi, Y., Busch, R., Merker, G.P. *Numerical and Experimental Investigations of Cavitating Flow in High Pressure Diesel Nozzles*, ILASS Europe, Zurich (Switzerland), Sept 2001

[09] Bella, G., Rocco, V., Ubertini, S., *Combustion and Spray Simulation of a DI Turbocharged Diesel Engine*, SAE 2002-01-2776, SP-1720, 2002

[10] Bergwerk, W., *Flow Pattern in Diesel Nozzle Spray Holes*, Proceedings of the Institution of Mechanical Engineers, Vol. 173, Pg 655-660, 1959

[11] Bunnell, R.A., Heister, S.D., Yen, C., Collicott, S.H., *Cavitating Injector Flows: Validation of Numerical Models and Simulations of Pressure Atomizers*, Atomization and Sprays Journal, Volume 9, No.5, pp 445-465, 1999

[12] Castagne, M., Cheve, E., Dumas, J.P., Henriot, S., *Advanced Tools for Analysis of Gasoline Direct Injection Engines*, SAE 2000-01-1903, 2000

[13] Chang, C.T., Farrell, P.V., *A Study on the Effects of Fuel Viscosity and Nozzle Geometry on High Injection Pressure Diesel Spray Characteristics*, SAE 970353, SP-1219, 1997

[14] Chaves, H., Knapp, M., Kubitzek, A., Obermeier, F., Schneider, T., *Experimental Study of Cavitation in the Nozzle Hole of Diesel Injectors Using Transparent Nozzles*, SAE 950290, SP-1101, 1995.

[15] Chigier, N., *Energy, Combustion, and Environment*, McGraw-Hill Series in Energy, Combustion, and Environment, McGraw-Hill Book company, 1981, ISBN 0-07-010766-1

[16] Comer, M.A., Bowen, P.J., Bates, C.J., Sapsford, S.M., *CFD Modelling of Direct Injection Gasoline Sprays*, ILASS-Europe, Toulouse (France), July 1999

[17] Comer, M.A., Bowen, P.J., Bates, C.J., Sapsford, S.M., Johns, R.J.R., *Transient 3D Analysis of a DI Gasoline Injector Spray, Atomization and Sprays*, Vol.9, No.5, Pg 467-482, 1999

[18] Comer, M.A., Bowen, P.J., Sapsford, S.M., Bates, C.J., *Influence of Ambient Pressure on Transient GDI Sprays*, ILASS-Europe, Zurich (Switzerland), September 2001

[19] Cousin, J., Nuglisch, H.J., *Prediction of Characterisation of Sprays Produced by High Pressure Swirl Injectors*, ILASS-Europe, Toulouse (France), July 1999

[20] Dan, T., Yamamoto, T., Senda, J., Fujimoto, H., *Effect of Nozzle Configurations for Characteristics of Non—Reacting Diesel Fuel Spray*, SAE 970355, SP-1219, 1997

[21] De Vita, A., Di Angelo, L., Alloca, L., Alfuso, S., *Spray Characteristics of a High Pressure Injection for GDI Engines*, 9th International Symposium on Flow Visualisation, Edinburgh (UK), 2000

[22] Egermann, J., Ipp, W., Rabenstein, F., Wensing, M., Leipertz, A., *Spray Formation and Evaporation of High Pressure Swirl Atomizers for Gasoline Direct Injection*, ILASS-Europe, Toulouse (France), July 1999

[23] Evers, L.W., *Characterization of the Transient Spray from a High Pressure Swirl Injector*, SAE 940188, SP-1026, 1994

[24] Faure, M.A., Sandler, M., Oversby, K.K., Stokes, J., Begg, S.M., Pommier, L.S., Heika, M.R., *Application of LDA and PIV Techniques to the Validation of a CFD Model of a Direct Injection Gasoline Engine*, SAE 982705, 1998

[25] Ferguson, C.R., *Internal Combustion Engines*; Applied Thermosciences, John Wiley & Sons, 2001, ISBN 0471356174

[26] Fry, M., King, J., White, C., *A Comparison of Gasoline Direct Injection Systems and Discussion of Development Techniques*, SAE 1999-01-0171, SP-1416, 1999

[27] Ganippa, L.C., Bark, G., Andersson, S., Chomiak, J., *The Structure of Cavitation and its Effect on the Spray Pattern in a Single-Hole Diesel Nozzle*, SAE 2001-01-2008, SP-1630, 2001

[28] Goney, K.H., Corradini, M.L., *Isolated Effects of Ambient Pressure, Nozzle Cavitation and Hole Inlet Geometry on Diesel Injection Spray Characteristics*, SAE 2000-01-2043, 2000

[29] Han, J.S., Lu, P.H., Xie, X.B., Lai, M.C., Henein, N.A., *Investigation of Diesel Spray Primary Break-up and Development for Different Nozzle Geometries*, SAE 2002-01-2775, 2002.

[30] Han, J.S., Wang, T.C., Xie, X.B., Lai, M.C., Henein, N.A., Harringon, D.L., Pinso, J., Miles, P., *Dynamics of Multiple-Injection Fuel Sprays in a small-bore HSDI Diesel Engine*, SAE 2000-01-1256, SP-1498, 2000

[31] Heikal, M., Pethers, P., Gill, S., Shillington, S., Jackson, N., Stone, R., *Future Engine and System Technologies : The Euro IV Challenge*, IMechE Seminar Publication, 1997. ISBN 1-86058-166-8

[32] Heywood, J.B., *Internal Combustion Engine Fundamentals*, McGraw-Hill Book Company, 1988, ISBN 0-07-100499-8

[33] Huang, Z., Shao, Y.M., Shiga, S., Nakamura, H., Karasawa, T., *The role of orifice flow pattern in fuel atomization*, Paper I-12, ICLASS, Rouen (France), July 1994

[34] Iwamoto, Y., Noma, K., Nakayama, O., Yamauchi, T., Ando, H., *Development of Gasoline Direct Injection Engine*, SAE 970541, 1997

[35] Jacobsson, L., Winklhofer, E., Chomiak, J., *Injection Orifice Shape: Effects on Spray Characteristics and Heat-Release Rate in a Large-Size Single-Cylinder Diesel Engine*, SAE 1999-01-3490, 1999

[36] Karl, G., Kemmler, R., Bargende, M., Abthoff, J., *Analysis of a Direct Injected Gasoline Engine*, SAE 970624, 1997

[37] Khavkin, Y., *Can Atomization be Improved by Viscosity Increase?*, 8th ICLASS, Pasadena, California (USA), July 2000

[38] Kim, M., Park, J., Lee, N., Choi, K., *Analysis of In-cylinder Flow in a Spark-Ignited Direct Injection Engine Using PIV and CFD*, 15th International Combustion Engine Symposium, 9935031, Seoul (South Korea), July 1999, ISBN 4-915219-25-9

[39] Kirby, R.S, Withington, S., Darling A.B., Kilgour, F.G., *Engineering in History*, McGraw-Hill Book Company Inc, 1956,LCCN 55-8287

[40] Knapp, R.T., Daily, J.W., Hammitt, F.G., *Cavitation*, McGraw-Hill Inc, 1970, LCCN 77-96428

[41] Koivula, T.S., Ellman, *Cavitation Behaviour of Hydraulic Orifices and Valves*, SAE 982038, SP-1380, 1998

[42] Lading, L., Wigley, G., Buchhave, P., *Optical Diagnostics for Flow Processes*, Plenum Press, 1994, ISBN 0-306-44817-3

[43] Lake, T.H., Stokes, J., Whitaker, P.A., Crump, J.V., *Comparison of Direct Injection Gasoline Combustion Systems*, SAE 980154, 1998

[44] Laoonual, Y., Yule, A.J., Walmsley, S.J., *Internal Fluid Flow and Spray Visualization for a Large Scale Valve Covered Orifice (VCO) Injector Nozzle*, ILASS Europe, Zurich (Switzerland), Sept 2001

[45] Lefebvre, A.H., *Atomization and Sprays*, Combustion: An International Series, Hemisphere Publishing Corporation, 1989, ISBN 0-89116-603-3

[46] Lindsay, R.B., *Lord Rayleigh: The Man and his Works*, Pergamon Press, 1970, ISBN 08-006821-9

[47] Maunoury, B., Duverger, T., Mokaddem, K., Lacas. F., *Optical Investigation of Diesel Spray and Auto-ignition in a Small Direct-injected Diesel Engine*, ILASS Europe, Zurich (Switzerland), Sept 2001

[48] Mitsubishi Technology, *Gasoline Direct Injection Engines* (URL:http://www.mitsubishi-motors.co.jp/inter/technology/GDI/page1.html), 1996, [28.07.2001]

[49] Miyamoto, T., Kobayashi, T., Matsumoto, Y., *Structure of Sprays from an Air-Assist Hollow-Cone Injector* , SAE 960771, SP-1132, 1996

[50] Munson, B.R., Young, D.F., Okiishi, T.H., *Fundamentals of Fluid Mechanics*, John Wiley & Sons Inc, 1998, ISBN 0-471-17024-0

[51] Nasr, G.G., Yule, A.J., Bendig, L., *Industrial sprays and atomisation: design, analysis and application*, Springer publishing, 2002, ISBN 1852334606

[52] Noma, K., Iwamoto, Y., Murakami, N., Lida, K., Nakayama, O., *Optimised Gasoline Direct Injection Engine for the European Market*, SAE 980150, 1998

[53] Nogi, T., Shiraishi, T., Nakayama, Y., Ohsuga, M., Kurihara, N., *Stability Improvement of Direct Fuel Injection Engine under Lean Combustion Operation*, Direct Injection: Engines, Emissions and Aftertreatment, SAE Inc Publishing, SAE 982703, SP-1399, 1998, ISBN 0-7680-0313-X

[54] Nouri, J.M., Brehm, C., Whitelaw, J.H., *The Spray From A Gasoline Direct Injector*, 15th Intl. Liquid Atomisation and Spray Systems (Europe), Toulouse (France), July 1999

[55] Nurick, W.H., *Orifice Cavitation and its Effect on Spray Mixing*, Trans ASME Journal of Fluids Engineering, Volume 98, No.4, pp 681-687, 1976

[56] Ohrn, T.R., Senser, D.W., Lefebvre, A.H., *Geometrical effects on discharge coefficicents for plain-orifice atomisers*, Atomization and Sprays Journal, Volume 1, No.2, pp 137-153, 1991

[57] Parrish, S.E., Farrell, P.V., *Transient Spray Characteristics of a Direct-Injection Spark-Ignited Fuel Injector*, SAE 970629, 1997

[58] Queiroz, C., Tomanik, E., *Gasoline Direct Injection Engines - A Bibliographical Review*, SAE 973113, 1997

[59] Raffelsberger, P., Dolenc, A., Kordesch, V., *Fuel System for the Future High Speed Long Life DI Diesel Engines with Suitable Electronic Control*, SAE 951855, 1995

[60] Ramamurthi, K., Nandakumar, K., *Effect of injector orifice configurations on atomization*, Paper III-2, ICLASS, Rouen (France), July 1994

[61] Ramamurthi, K., Patnaik, S.R., *Influence of periodic disturbances on inception of cavitation in sharp-edged orifices*, Experiments in Fluids Journal, Volume 33, pp 720-727, 2002

[62] Reitz, R.D., Bracco, F.V., *Ultra-high-speed filming of atomising jets*, Physics of Fluids, Volume 22, Pg 1054-1064 ,June 1979

[63] Reitz, R.D., Bracco, F.V., *Ultra-high-speed filming of atomising jets*, Physics of Fluids, Volume 25, Pg 1730-1742 ,October 1982

[64] Ren, W.M., Nally Jr, J.F., *Computations of Hollow-Cone Sprays From A Pressure-Swirl Injector*, SAE 982610, 1998

[65] Richter, M., Axelsson, B., Alden, M., Josefsson, G., Carlsson, L.O., Dahlberg, M., Nisbet, J., Simonsen, H., *Investigation of the Fuel Distribution and the In-cylinder Flow Field in a Stratified Charge Engine Using Laser Techniques and Comparison with CFD Modelling*, SAE 1999-01-3540, 1999

[66] Sasaki, S., Akagawa, H., Tsujimura, K., *A Study on Surrounding Air Flow Induced by Diesel Sprays*, SAE 980805, SP-1316, 1998

[67] Schmidt, D.P., Corradini, M.L., *Analytical prediction of the exit flow of cavitating orifices*, Atomization and Sprays Journal, Volume 7, No.6, 1997

[68] Schmidt, D.P., Corradini, M.L., *One-dimensional analysis of cavitating orifices*, 9th ILASS, San Francisco (USA), 1996

[69] Schwalb, J.A., Ryan III, T.W., Dodge, L.G., *Investigation of Diesel Spray Structure and Spray/Wall Interactions in a Constant Volume Pressure Vessel*, SAE 941918, 1994.

[70] Shiraishi, T., Nakayama, Y., Nogi, T., Ohsuga, M., *Effect of Spray Characteristics on Combustion in a Direct Injection Spark Ignition Engine*, SAE 980156, 1998

[71] Sirignano, W.A., *Fluid Dynamics and Transportation of Droplets and Sprays*, Cambridge University Press, 1999, ISBN 0-521-63036-3

[72] Spicher, U., Reissing, J., Kech, J.M., Gindele, J., *Gasoline Direct Injection (GDI) Engines - Development Potentialities*, SAE 1999-01-2938, SP-1469, 1999

[73] Soteriou, C., Smith, M., Andrews, R., *Diesel injection – laser light sheet illumination of the development of cavitation in orifices*, Combustion Engines and Hybrid Vehicles Conference, Professional Engineering Publishing Limited, pp137-158, 1998, ISBN 1-86058-143-9

[74] Soteriou, C., Andrews, R., Smith, M., *Direct Injection Diesel Sprays and the Effect of Cavitation and Hydraulic Flip on Atomization*, SAE 950080, SP-1065, 1995

[75] Soteriou, C., Andrews, R., Smith, M., *Further Studies of Cavitation and Atomization in Diesel Injection*, SAE 1999-01-1486, SP-1460, 1999

[76] Stumpp, G., Ricco, M., *Common Rail-An Attractive Fuel Injection System for Passenger Car DI Diesel Engines*, SAE 960870, SP-1132, 1996

[77] Takeda, K., Sugimoto, T., Tsuchiya, T., Ogawa, M., Ueda, S., Yoneshige, K., *Slit Nozzle Injector for a New Concept of Direct Injection SI Gasoline Engine*, SAE 2000-01-1902, 2000

[78] Tamaki, N., Nishida, K., Hiroyasu, H., *Promotion of the atomisation of a liquid jet by cavitation in a nozzle hole*, ILASS-Europe, Manchester(UK), July 1998

[79] Tamaki, N., Shimizu, M., Hiroyasu, H., *Enhanced Atomisation of a liquid jet by cavitation in a nozzle hole*, 8th ICLASS, Pasadena (USA), July 2000

[80] Tamaki, N., Shimizu, M., Hiroyasu, H., *Atomisation of super-high injection pressure liquid jet*, ILASS-Europe, Zurich (Switzerland), September 2001

[81] Topenot, E., Le Visage, D., Radenac, C., Tremouliere, G., Carreau, J.L., *Experimental and Numerical Study of Atomisation of Hollow Cone Sheet. Application to Gasoline Direct Injection*, ILASS Europe, Zurich (Switzerland), Sept 2001

[82] VanDerWege, B.A., Lounsberry, T.H., Hochgreb, S., *Numerical Modelling of Fuel Sprays in DISI Engines under Early-Injection Operating Conditions*, SAE 2000-01-0273, SP-1512, 2000

[83] Wirth, M., Piock, W.F., Fraidl, G.K., Schoeggl, P., Winklhofer, E., *Gasoline DI Engines: The Complete System Approach By Interaction of Advanced Development Tools*, SAE 980492. SP-1314, 1998

[84] Wu, K.J., Su, C.C., Steinberger, R.L., Santavicca, D.A., Bracco, F.V., *Measurement of the Spray Angle of Atomizing Jets*, Journal of Fluids Engineerng, Volume 107, Pg 406-413, December 1983

[85] Xu, M., Markle, L.E., *CFD-Aided Development of Spray for an Outwardly Opening Direct Injection Gasoline Injector*, SAE 980493, 1998

[86] Yoda, T., Tsuda, T., *Influence of Injection Nozzle Improvement on DI Diesel Engine*, SAE 970356, SP-1219, 1997

[87] Young, F.R., *Cavitation*, McGraw-Hill Book Company (UK) Limited, 1989, ISBN 0-07-707094-1

[88] Zhao, F.Q., Yoo, J.H., Liu, Y., Lai, M.C., *Spray Dynamics of High Pressure Fuel Injectors for DI Gasoline Engines*, SAE 961925, 1996

CHAPTER 3

OPTICAL DIAGNOSTIC TECHNIQUES AND APPLICATIONS

3.1 INTRODUCTION

In the previous chapter the literature reviews described the works of various researchers in Diesel and gasoline injection systems. Most of the workers employed various diagnostic techniques in their studies to provide detailed analysis of flow and spray structure. Traditionally, physical probing methods have been used to investigate and characterise flow processes. However, the physical presence of the probes can markedly alter the fundamental flow behaviour. Also physical probes can be limited in both spatial resolution and temporal response. For example, in the presence of soot and fuel droplets, their spatial resolution will be reduced and temporal response diminished, resulting in a drop in their accuracy. If the environment of interest is subjected to severe heat transfer, the probe needs to be more robust or else it will be subjected to perturbation.

The ever-expanding role of laser diagnostics in research applications has highlighted its importance to the scientific world and offers an advantageous alternative to physical probing methods. These techniques are non-intrusive and thereby do not affect the flow being studied. Also, these techniques are capable of providing very high spatial and temporal resolution. The measurements are performed *in situ* of the measurement position, therefore without any elaborate and uncertain corrections to the devices. Durst [19] provided a summary of some of these techniques in the fluid mechanics study of various types of flow.

However, laser diagnostic techniques do have their disadvantages. The requirement of optical access to the measurement location results in the addition of windows which may mean compromises to the flow geometry.

Also, no single laser technique is capable of measuring all flow properties such as the species, velocity and temperature simultaneously.

3.2 FLOW VISUALISATION STUDY

3.2.1 Background

Flow visualisation is an experimental technique that can be used to understand the structure of complex flow fields. Ludwig Prandtl [38] was the first person to apply this technique in his study of unsteady flows behind wings and other objects in a water tunnel. This technique is ideal for investigating flow and usually forms the first part of any experimentation involving the use of laser diagnostic tool.

Flow visualisation involves the use of a light source to provide an illumination of the investigated flow field and an imaging system was then used to capture and store the images. Several techniques have been developed over the decades in this application with holography being one of the earliest flow visualisation techniques. Shadowgraphy along with schlieren and holography techniques were the first few techniques used for flow visualisation, using the refractive index changes caused by density gradients. Shadowgraphy detects the changes in the image brightness caused by the redistribution of light rays by variation in refractive index. However, this technique requires a high density gradient for any shadow to be visible. The technique of schlieren imaging uses a parallel beam of light passing through the flow region which is focussed onto a knife-edge. Any change in the density will cause the beam to be refracted, causing the light to be deflected. A detailed explanations of both shadowgraphy and schlieren imaging were provided by Settles [41]. Huang *et al* [25] also provided an example of the shadowgraphy technique in their study of inlet orifice geometry on outlet spray structures. Scaled up models were used for visualising internal flow and metal nozzles for external flow structures. These internal and external flow structures were recorded using a still camera to develop a better understanding in fuel atomisation process. Further applications of shadowgraphy were provided by Kunkulagunta [30], Baumgarten *et al* [07] and Bae *et al* [06] in their study of VCO nozzles.

The simplest form of flow visualisation is single-shot imaging. With this technique a light source is used to illuminate a flow field and a film camera or high resolution CCD camera is used to record images of the flow structure. If the flow to be studied contains inhomogeneities, such as liquid sprays or mixing fields, then the flow can be photographed directly. However, for homogeneous flow tracers maybe added to the flow to make the flow structures visible.

The light source used to illuminate the flow is often a high-energy, short-duration pulsed source to "freeze" the flow motion and allow the imaging of high-speed transient flows. Lasers are most commonly used as the illumination source for flow visualisation since they can provide high intensity light in short duration (nanosecond) pulses. The major advantage of such high energy laser sources is that they can be formed into thin, planar light sheets to allow 2D imaging of complex 3D flows.

Tamaki *et al* [42, 43, 44] and Sasaki *et al* [40] provided examples of the use of flow visualisation in their spray studies. Tamaki *et al* studied the effects of cavitation on atomisation using a ruby laser to provide the light source. This work involved the use of a film camera to record the spray structure and atomisation effects. Sasaki *et al* [40] studied the structure of the surrounding air flow induced by Diesel sprays using a 35mm film camera.

The use of high resolution CCD cameras in gasoline spray studies were presented by Wickers *et al* [48] and Allen *et al* [03, 04]. Wickers *et al* [48] used a Nd:YAG laser to form a 1mm laser sheet into the optical cylinder, synchronised with the high resolution CCD camera using a pulse generator. The authors were able to provide qualitative images to study the fuel spray structures. For the single shot imaging system used by Allen *et al* [03, 04], the authors used a Nd:YAG laser to pump a fluorescence dye cell to provide back illumination to their optical nozzles. Figure 3.1 shows the quality of the internal flow field generated by this technique. The authors were able to provide qualitative data for investigating the internal flow characteristics.

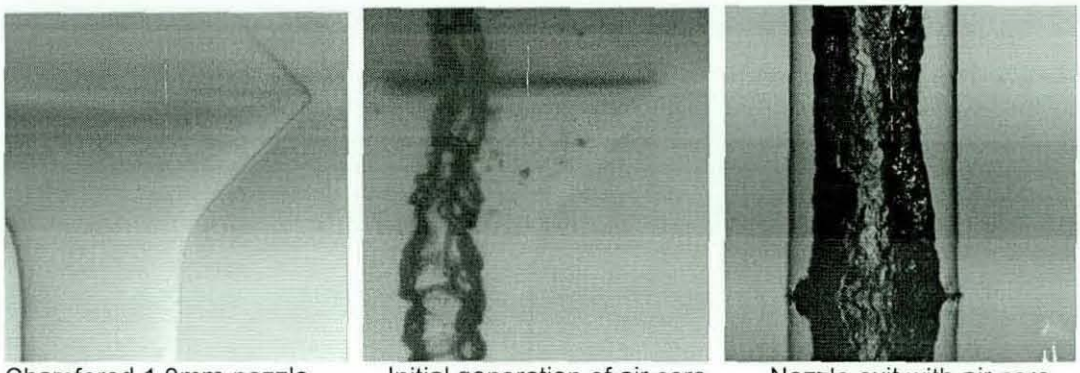

Chamfered 1.0mm nozzle Initial generation of air core Nozzle exit with air core

Fig 3.1 Single shot images of 1.0mm pressure swirl nozzles [04].

Single-shot imaging can provide useful flow visualisation information, but for transient or developing flows the temporal information is important. Advances in laser and camera technology now provide rapidly pulsing lights sources and high-speed digital cameras, which allows flow visualisation imaging at kHz rates. These images provide quantitative data to help researchers understand transient flow processes. Kusakabe [31] and Badock [05] diagnostic method incorporated an Nd:YAG laser to provide a thin laser sheet and a CCD camera for imaging Diesel spray and cavitation phenomena respectively. Cooper *et al* [14] used a helium neon laser to provide illumination, and a high-speed camera operating at 4500 frames per second for imaging. Further investigations used a copper vapour laser as the light source for high-speed imaging studies Laoonual [34], Goney [22]. The authors used the copper vapour laser pulse output and synchronised to the high-speed CCD camera, capturing the spray developments. High-speed imaging enables the authors to visualise and understand the flow structures by playing back the images in slow motion, which was previously undetectable with conventional imaging techniques.

The instrumentation used in the flow visualisation study in this thesis consisted of a number of individual systems; experimental rig, laser system, camera and analysing computer. A schematic of a simple flow visualisation layout is shown in figure 3.2. A flow rig was used to provide the flow to be imaged. The laser system generated an intense and pulsing light source to illuminate the flow field. A digital camera, synchronised with the laser pulse,

was used to capture the flow through the optical rig. The captured images were stored in the computer for processing and analysis. Two flow visualisation techniques are discussed in details in this study, single shot flow visualisation and high-speed flow visualisation. The details of these experimentations will be described in the following sections.

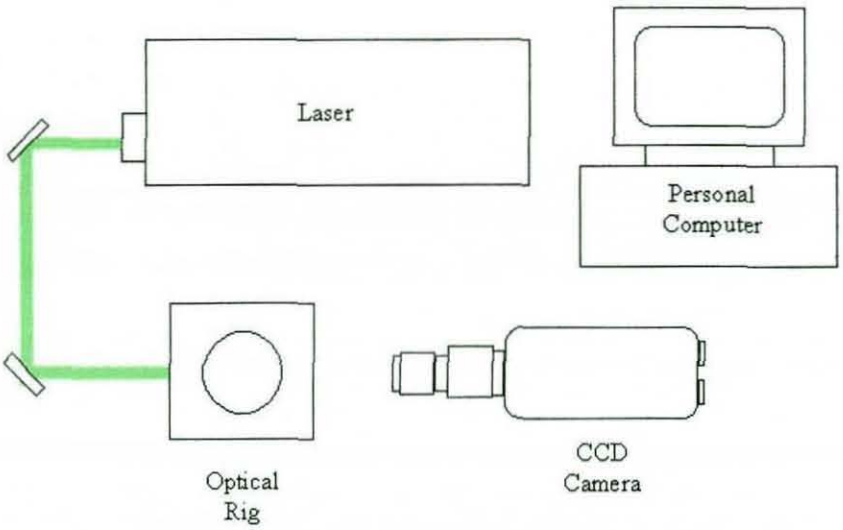

Figure 3.2 A simple flow visualisation layout.

3.2.2 Single Shot Flow Visualisation Experimentation Setup

3.2.2.1 OVERVIEW

The single shot flow visualisation system consisted of an Nd:YAG laser and a Kodak Megaplus ES1.0 CCD camera. The Nd:YAG laser, 532 nm wavelength, was used to pump a fluorescence dye cell to provide back illumination of the optical nozzles. The laser operated with 50 mJ per pulse and the output provided 10 ns light pulses to the dye cell. The dye cell removes coherence from the laser light and eliminates speckle noise to provide a uniform back illumination. The CCD camera was used to record and store all the images captured. The camera was fitted with a Nikon 105mm macro lens with extension bellows, mounted on a two-dimensional traverse system. This technique is predominantly used to provide high resolution images to help identify the internal flow structures in swirl atomisers.

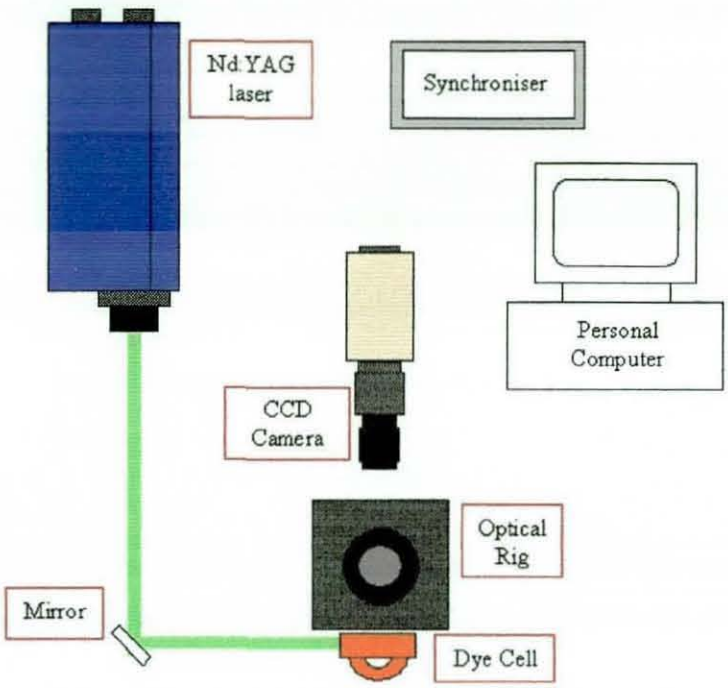

Figure 3.3 Overview of a single shot visualisation.

3.2.2.2 LASER SYSTEM

In single-shot flow visualisation, a New Wave Solo Nd:YAG laser was used. This is a Nd:YAG Q-switch laser producing short duration (10 ns) and high energy (50 mJ) pulses at 532 nm wavelength. The high energy pulse is essential in this study to illuminate micron size particles and short pulse duration to "freeze" the motion of the flows.

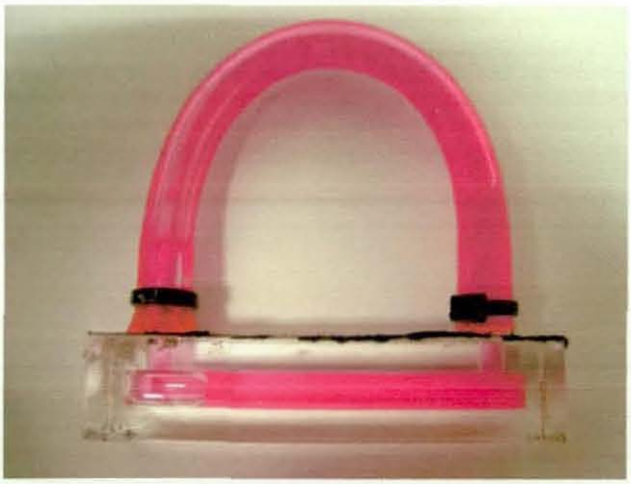

Figure 3.4 Dye cell with Rhodamine 620 dissolved in methanol.

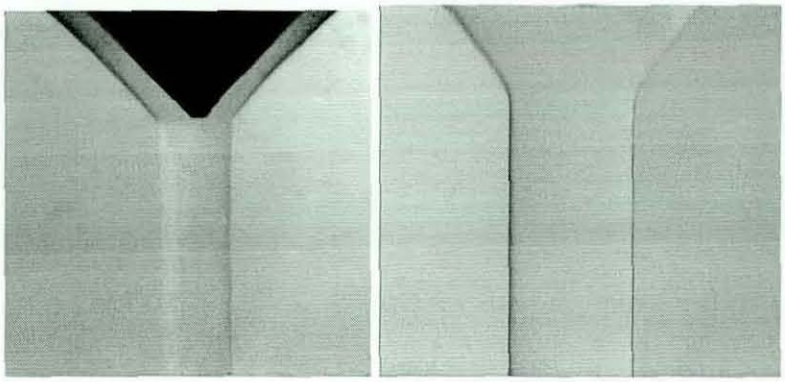

Figure 3.5 Images of two high-resolution 1mm nozzle with and without a pintle valve.

To provide back illumination on the optical section of the rig, a fluorescent dye dissolved in methanol was placed in an enclosed cell (Figure 3.3 and 3.4). Direct illumination of the flow with the ND:YAG laser, or illumination through a diffusion screen, can produce low quality images because of the generation of speckle noise. Using the ND;YAG laser to excite a fluorescing dye cell produces broadband emission and removes the speckle noise. The fluorescence process is approximately 40% efficient, however, the use of a red dye (in this case rhodamine emitting at 620 nm) shifts the imaging into the more responsive part of the imaging detector spectral sensitivity and recovers the efficiency of the imaging. This created a uniform back illumination for the rig, for the CCD camera to capture high-resolution flow images. The images in Figure 3.5 showed two high-resolution images of a 1mm nozzle.

3.2.2.3 IMAGING SYSTEM AND PROCESSING

The imaging camera used in single shot flow visualisation was the Kodak Megaplus ES 1.0 camera shown in figure 3.6. This black and white camera contains a Charge Coupled Device (CCD) sensor array, with a 1008 x 1018 light sensitive elements (pixels) and eight bit digital video output. It also has the ability to perform either a single or dual channel progressive scan with 20MHz pixel clock rate, giving a maximum frame rate of 30 frames per second (fps).

On the rear of the of the CCD camera, a two pin connector is used for supplying DC power between 12 to 28 volts. Two coaxial SMA type connectors are also available at the rear of the camera, trigger and strobe connectors. Trigger connector is used for the camera to synchronise with an external system. A strobe connector is used to send an output pulse signal to trigger a laser light to illuminate the flow field in the camera viewing region. The AIA interface provides the connection to a frame grabber board and communication interface for camera control. The Kodak Megaplus camera also has four modes of operation to select from, continuous, control, trigger or triggered double exposure.

Figure 3.6 An image of the Kodak Megaplus camera with a C-mount lens.

In this study, the CCD camera was fixed with a Nikon 105 mm Macro lens and a bellows to extend the range of the lens. The camera was set to operate in the continuous mode and images captured at 30 fps in dual channel mode. In this mode, the exposure time range from 125 μsec to 33 msec and the camera was synchronised to an external trigger source through the Trigger connector and AIA interface. The system was controlled by a personal computer through an RS323 cable with a serial data link. The operating software provided the signal output to fire the laser and activate the camera capturing sequence. The digital images captured from the CCD camera during the experiments were stored in a personal computer. These images were stored as individual tiff images for analysis and they represent the nozzle geometries and the internal flow structures in each experiment. It is worth noting that all the flow structures in the experiments could be repeated in the

high-speed flow visualisation studies, therefore demonstrates the level of stability and repeatability in this experimental setup.

3.2.3 High-speed Flow Visualisation Experimentation Setup

The second flow visualisation technique is the high-speed flow visualisation. This technique is well established and widely uses to identify the different flow characteristics in various studies highlighted in the literature. The basic setup is similar to the single-shot visualisation technique which consist of a laser, CCD camera and an analysing computer.

3.2.3.1 LASER SYSTEM

The copper vapour laser system used in the high-speed flow visualisation study was a Class 4 high-power pulse laser with a nominal power of 20 Watts, emitting at two wavelengths, 510.6 nm and 578.2 nm, a green and yellow laser light respectively. This laser has a pulse repetition frequency of 4.5 kHz to 20 kHz with a single burst at 50 kHz and pulse duration between 25 ns and 30 ns. Although the standard operating frequency for the laser is 10 kHz, the laser was set to 9 kHz for this study. This allowed the laser to synchronise with the Kodak 4540 High Speed Motion Analyser to a single 30 ns pulse and 2 mJ pulse energy for each frame of the digital camera.

The laser light can be delivered either by direct illumination with mirrors or by the use of an optical fibre cable. The latter was used to minimise any exposed beams in the laboratory and it also does not result in any significant loss of laser power when compared with direct illumination.

3.2.3.2 IMAGING SYSTEM

The Kodak Ektapro HS Motion Analyser was used for the high-speed flow visualisation study because of its ability to visualise and record high-speed flow processes. This system is ideal for recording a continuous flow of images in any experiments. This motion analyser comprises two components, the imager and the processor. The Imager is basically a digital camera with a 256

by 256 pixels CCD array with sensitivity equivalent to ISO 3000 at high gain setting. This camera is connected to the processor by two "python" size data cables. The processor provides the overall commands and functions of the motion analyser through a control keypad. The recording can be done at full frame rate, between 30 and 4500 frames per second, or at frame rate of 9000 through 40500 when a segmented frame is selected. The recorded images are then stored in the random access memory (RAM) in the processor. Whenever the processor is turned on, AUX memory recording was done to clear the RAM and calibrate the motion analyser to remove any fixed pattern noise and shading errors in the pictures, to ensure the quality of the images to be recorded.

The imager required the use of camera lens to be mounted onto the C-mount adapter in front of the CCD chip. In the high-speed visualisation setup, the standard camera lens used was the Nikkor 105mm Macro lens. This is usually accompanied by a series of extension rings and bellows depending on the image magnification required. An example of the imager with a bellows and 105 mm Nikkor lens was mounted is shown on figure 3.7.

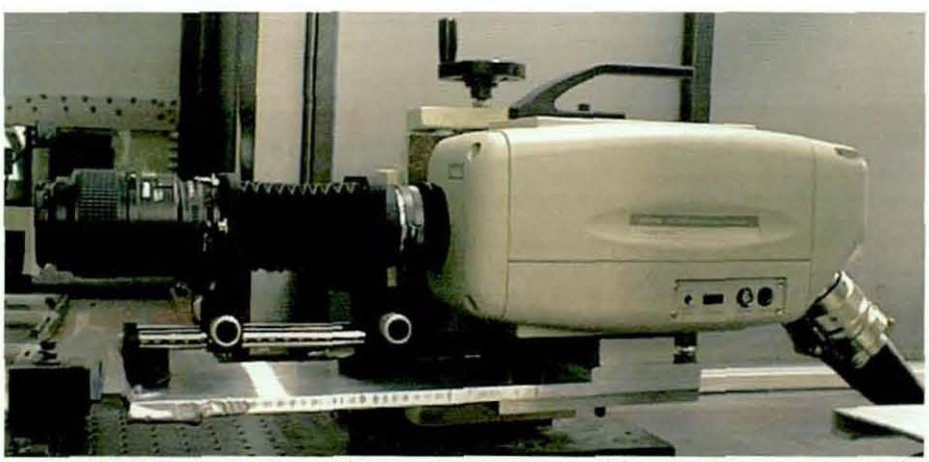

Figure 3.7 Motion Analyser imager attached with a bellows and a Nikkor 105mm macro lens.

3.2.3.3 IMAGE PROCESSING

The high-speed flow visualisation technique provides continuous images of flow structures. This is useful to quantify and understand the fluid

developments through the various channel studied. As mentioned in previous sections, the copper vapour laser is synchronised to a Kodak 4540 high-speed motion analyser at 9 kHz. The motion analyser works like a digital camera and stores the captured images temporarily in the processor unit. These images were then downloaded into a PC connected by a 4-pin video cable via a video-capturing card. This allowed the images to be cropped and digitised to the number of required frames for further analysis. The storage format used was either as a continuous sequence of images (tiff format) or as animation (avi format).

The ability of the motion analyser to produce a sequence of high-speed images resulted in a reduction in image quality, compared with the single-shot flow visualisation technique.

3.3 DIGITAL PARTICLE IMAGE VELOCIMETRY TECHNIQUE

Historically, the devices used for the measurement of velocity are physical probes such as the pitot-structure pressure probes or hot-wire anemometers. However, these techniques are intrusive; the flow may be disturbed by the presence of physical probes. Particle Image Velocimetry (PIV) was developed as a non-intrusive optical technique for indirect measurement of the flow velocity. The technique measures the flow velocity by the means of tracing seeding particles suspended in the flow.

Over the last two decades the PIV technique has developed into one of the most extensively used optical diagnostic tools. The technique has its roots in solid mechanics. Dudderar and Simpkins [18] pioneered the technique of velocimetry measurement known as Laser Speckle Velocimetry (LSV) of the study of solid body motion. However, Adrian [01] explained that applications involving fluid motions are different from solid motions. When a fluid flow containing small particles are illuminated by a pulsed laser light sheet with a known thickness, scattering occurs from a volume distribution of particles sites rather than the surface. Therefore, he renamed the velocimetry technique as particle image velocimetry (PIV). Pickering and Halliwell [38] later examined

the use of high powered laser and noise contributions by film in PIV studies. They noted that this can be reduced by using sensitive films, thus reducing the need for high powered laser, and using a liquid gate during analysis to remove phase distortion. With the PIV systems, improvements were made later to overcome some of it limitations by Coupland *et al* [15, 16]. Cho [11] was able to improve the PIV system further by proposing a new technique called digital image velocimetry, commonly known as digital particle image velocimetry by researchers and scientists today. The technique replaced the photographic film with high speed or video photography, capturing the images digitally. This allowed the images to be analysed almost in real-time compared to the time-consuming photographic film method. This technique has been enhanced today by the development of digital cameras, lasers, processors and software, allowing the analysis to be completed at a fraction of the time.

The DPIV technique is used today in most research facilities and is commonly known as PIV as Pickering *et al* [38] and Adrian [01] first suggested. Wicker *et al* [48] applied this technique in their studies of spray structure in a spark-ignited direct injection (SDI) engine. The authors used an Nd:YAG laser beam, formed into a 1mm thick laser sheet, as the illumination source for the optical research engine. A digital camera was set to capture a sequence of image pairs at 1usec apart. These images were processed using cross-correlation software to calculate the two-dimensional velocity field. Yamakawa *et al* [50] applied 2-D and 3-D PIV techniques to examine the structural behaviour of a swirl type injector. An Nd:YAG laser (25 mJ with 532 nm wavelength) was used to generate a light sheet into the spraying chamber with varying ambient pressure. The authors concluded that the velocity distributions between the 2-D and 3-D PIV techniques at the trailing edge are similar but are different when measurements were taken at the leading edge and central part of the sprays. Kuwahara *et al* [32] used a similar PIV technique to examine the in-cylinder flow field in a wide spacing layout of a GDI engine, known as particle tracking velocimetry (PTV). This technique involved tracking particles individually in the in-cylinder flow, instead of the conventional whole flow field measurement used in PIV. The authors found that the flow field structures can be optimised by using a tumble-control piston

with a curved top surface, promoting eddies and turbulence for mixing in the combustion chamber.

It is clear from the literature that it is essential to understand not only the external flow field, such as the atomising spray, but also the internal flow field, which controls the exit conditions and initial liquid break-up. Allen *et al* [03, 04] and Walther *et al* [47] used real size optical nozzles to investigate the internal flow field in both GDI and Diesel DI studies respectively. Allen and Hargrave [03] examined the internal flow of a 1 mm diameter tangential swirl nozzle with a maximum pressure of 200 bar, using 1 μmm diameter Iriodin III seeding particles. The authors found that a maximum velocity of 160 m/s was calculated with a 90 bar inlet pressure. Allen and Hargrave [04] later developed a new fluorescent PIV technique to provide quantitative data on injector nozzles as small as 0.4 mm diameter. This technique required the use of fluorescent particles to illuminate the flow field. The laser pulse illuminated the fluorescent particles in the flow, providing clear particle images in micro size nozzles without any problems from reflected or refracted laser light when use with a filter. Walther *et al* [47] also used nozzles made from acrylic to investigate Diesel internal flow field using Fluorescent PIV. Real sized nozzles (0.2 mm diameter) were used with injection pressure up to 135MPa. The flow used test oil with physical properties identical to Diesel and the flow is doped with polystyrene tracers of 1 um diameter. They found that the maximum flow velocity at the sac was 150 m/s when the inlet pressure is 10MPa.

DPIV technique is now an important diagnostic tool used to determine the flow velocity from aircraft wind tunnel to laboratory study on injection processes. The following sections provided an insight on the DPIV setup and also a new technique developed using fluorescent particles as the seeding particles.

3.3.1 DPIV Experimental Setup

A simple PIV system is shown in figure 3.8. Small (micro-sized) particles are added to the flow to act as flow tracers. The light source from a laser is formed into a laser sheet and used to illuminate a 2D plane within the flow

field. A camera captures high-resolution images of the particles in the flow field. To capture velocity-coded images, the laser is pulsed twice at a known time separation (Δt) and the camera records the particle positions at two instances as the particles are advected by the flow. The recorded images are subsequently analysed to define the particle displacements over the known time separation and the particle (and thus flow) velocity calculated.

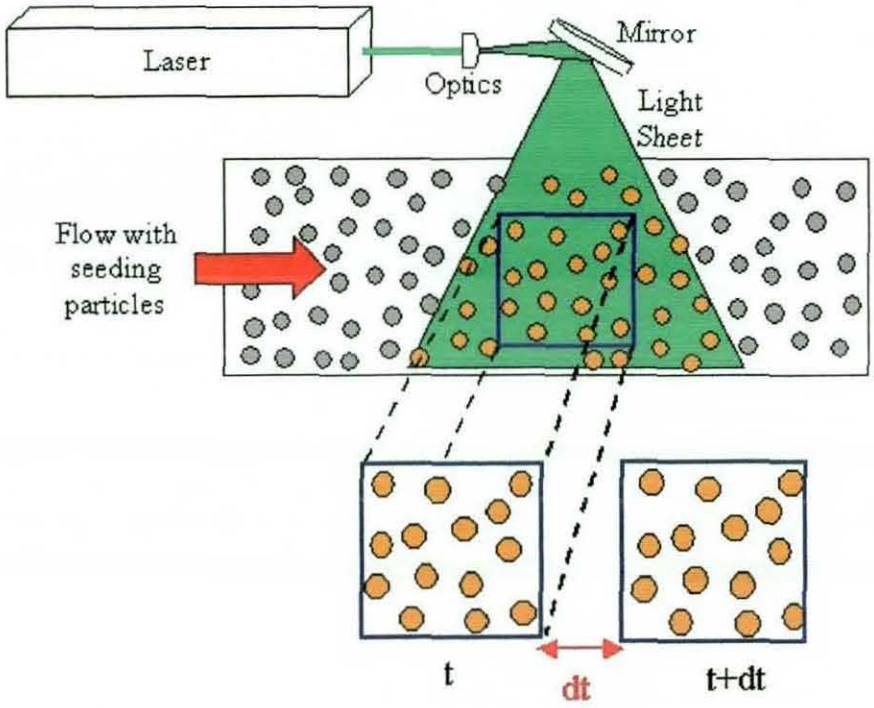

Figure 3.8 Schematic of an experimental arrangement for PIV through a flow channel.

3.3.1.1 SEEDING PARTICLES

The use of seeding particles suspended in the fluid to trace the motion of the flow is an important parameter for any DPIV experiments. The choice of seeding particles used is critical when mapping flow velocity in the experiment. Therefore, the seeding particles selected for each experiment is dependent on a number of parameters. The main consideration are that the particles are small enough to accurately follow the main flow fluctuations and are large enough to scatter sufficient light to be imaged by the PIV camera. Durst *el al* [20] provided a very good particle size estimation using the Hjelmfelt and Mockros method. Following the data presented by Durst *et al*

[20] these particles will follow the flow fluctuations to a frequency of 3 kHz. The interaction between the particle displacement and the fluid motion can be described by the Stoke's law. The motion of a particle in a fluctuating flow structure is governed by a force caused by the viscous drag from the relative motion of the particle and the surrounding fluid. The magnitude of the force in relation to the inertia of the particle determines the response of the particle in an oscillating flow structure investigated.

Several seeding particles were tried and tested in the current study, including: spheriglass, alumina and Iriodin.

The spheriglass particles are glass spheres available in a variety of sizes from 5 to 25 μm. The particle sizes are adequate for the current study, but the density was found to be too high and the particles would not accurately follow the flow.

Alumina (Al_2O_3) can be obtained in particle sizes from sub-micron to millimetre. For the fluids used in the current investigation particle sizes of 1-2 μm were tested. However, it was found that the alumina did not disperse completely and did not provide uniform seeding distribution.

The iriodin (6-10 μm) and Rhodamine 620 fluorescent (5-7 μm) particles provided good dispersion, good light scattering and followed the fluctuations correctly.

3.3.1.2 LASER SYSTEMS

There are several laser systems capable of producing high energy pulsed light for DPIV experiments. These include ruby lasers, Nd:YAG lasers and copper vapour lasers.

The system used in the current study was a doubled-pulsed Nd:YAG laser system, operating frequency doubled with an output at 532 nm. The laser

incorporated two independent oscillators in a single laser head. This arrangement allows the generation of two laser pulses at any time separation. In this study, the laser was operated with a pulse separation ranging from 1 to 2 μs, depending on the flow velocity.

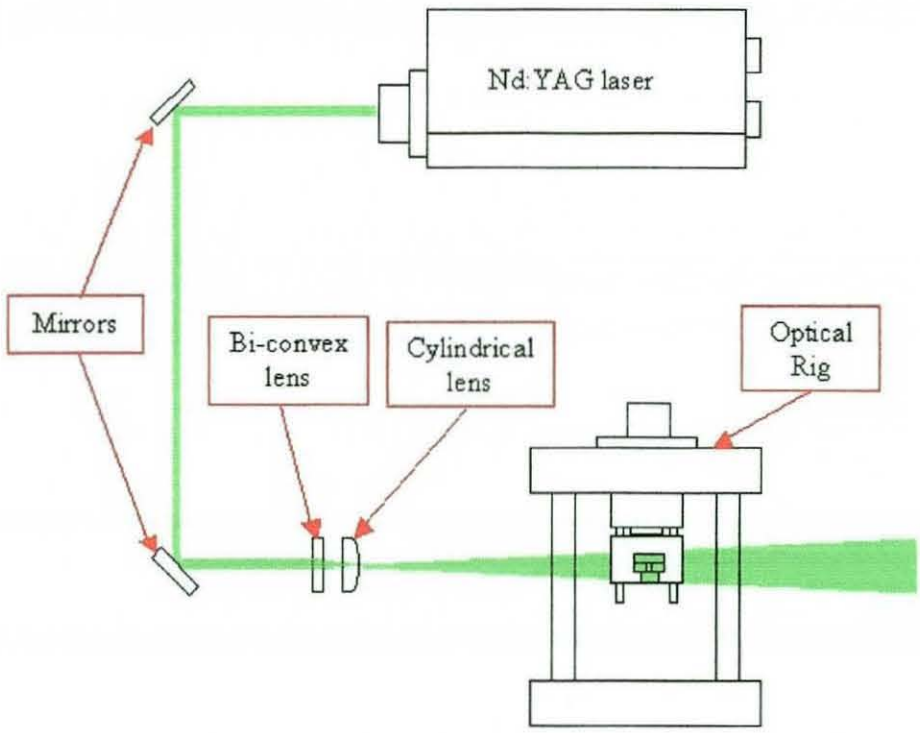

Figure 3.9 Lightsheet optics arrangements.

The formation of the laser beam into a planar lightsheet was easily accomplished using simple optics, as shown in figure 3.9. The beam from the Nd:YAG laser was 4 mm in diameter. A bi-convex spherical lens (f=600 mm) was used to focus the beam to a waist of 1 mm at the point of interest in the flow and a cylindrical lens (f=50 mm) formed the beam into a planar sheet. The size of the lightsheet is an important aspect as it determines the light intensity to which the particles are exposed. A larger cross sectional area created by a lightsheet will reduce the light intensity to expose the seeding particles. Therefore, it is important to use the correct lightsheet dimension on any investigated flow region. In the experimentation used in this research work, the laser light was diverted towards the optical nozzle through a series of Nd:YAG mirrors. A spherical lens was used to focus the laser beam before using a cylindrical lens to generate a 2D 1 mm lightsheet to investigate a 3D

flow. As the nozzle size is 1 mm in diameter, the lightsheet filled the whole nozzle, effectively illuminating the whole nozzle. This is because it is hard to generate a good quality lightsheet thin enough to isolate planes with the 1mm nozzle.

3.3.1.3 CAPTURING AND RECORDING DEVICES

The use of DPIV requires a recording device to capture the seeded particles in the flow. The camera used in this study was the Kodak Megaplus ES 1.0 CCD camera, which is explained in section 3.2.2.3. The CCD camera operation is control by the operating PC through a serial data link. The PC was also connected to the Nd:YAG laser via the synchroniser box and installed with an imaging capturing and processing software known as TSI Insight (version 3) PIV software [46]. This software is a stand-alone, graphical based tool that is able to acquire, display and process DPIV flow images obtained by a CCD camera. The software acts as a control device to "talk" to the Nd:YAG laser and the CCD camera. To use the software, several parameters were needed to be setup using the software.

Figure 3.10 shows the TSI Insight PIV software operating window use for setting up the CCD camera and Nd:YAG laser. To setup the camera the "Capture Dialog" bar, the default camera selected is "Left Camera" for standard PIV setup. "Frame Straddle" exposure mode bar was also selected to allow the CCD camera acquiring two consecutive single-exposure images when a trigger signal was received from the synchroniser. Lastly, the "Sequence" capture mode was selected to control the number of sequence of images captured. The maximum number of images captured was determined by the CCD camera used and PC storage capacity. The "Timing Setup" window located on the bottom left of the image on figure 3.10 controls the laser and camera timings. The first option (dT) set the pulse separation between two laser pulses, with the pulse repetition rate option controlling the frequency of one laser pulse sequence to the next. "Pulse Delay" option is an important parameter in triggering the camera to the first laser pulse which varies for different camera selected. There is also the camera trigger delay

option allows an external trigger to be used if required. Lastly, the laser power for the two laser pulses can be set on the "Pulse Energy Selection" box which includes high, medium and low settings. This allows the synchroniser to control the energy per pulse by changing the Q-switch delay.

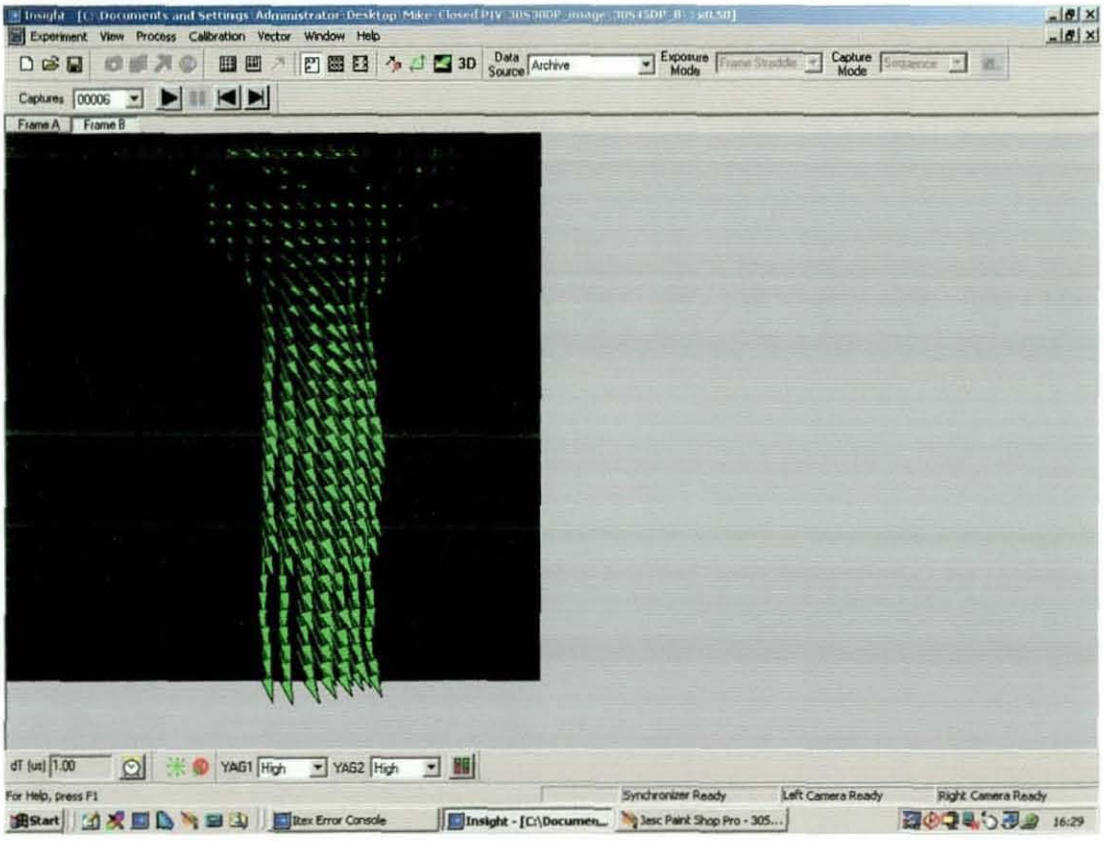

Figure 3.10 TSI Insight (version 3) PIV software operation window.

Once the menu and the various dialog box settings were determined, the laser and camera were ready to record it first sequence of images by clicking the camera icon. The double-pulsed laser system pulsed twice at a known interval, usually microseconds apart between the two laser pulses, generating two laser light sheets to illuminate a plane in the flow. The first pulse of the laser freezes initial positions of the seeding particles onto the first frame of the camera. The camera frame is advanced electronically and the second frame of the camera is exposed to the light scattered by the particles from the second pulse of laser light. This created two camera images; with the first showing the initial positions of the seeding particles and the second their final positions due to the movement of the flow field. This allowed a set of flow

images sequence to be captured and stored in the default folders in the computer for post processing.

3.3.1.4 POST PROCESSING

As mentioned in the previous section, Insight is a Windows NT based software which captures and process PIV images. The processing parameters in the Insight software was determined and post processing was performed on the captured PIV images.

The PIV Images captured were subdivided into interrogation areas. The spatial displacement of the particle images between two consecutive interrogation areas, separated by a small time interval, is determined by a cross-correlation process. The Insight software employs an FFT correlation routine to compute the correlation between the first interrogation area, I_1, and second interrogation area, I_2, where I_2 is a shifted version of I_1. The FFT routine is used in many commercial software codes because the computation is carried out in the frequency domain, and hence, the process is accelerated.

This processing routine was evaluated by a complex conjugate multiplication of two-dimensional Fourier transformed interrogation areas. The FFT correlation routine can be expressed as;

$$I_1(i,j) \otimes I_2(i,j) \Leftrightarrow FFT^{-1}\left(\hat{I}_1(\xi,\eta) \times \hat{I}_2^*(\xi,\eta)\right) \qquad (3.1)$$

where $\hat{I}_1(\xi,\eta)$ denotes the Fourier transform of $I_1(i,j)$ and $\hat{I}_2^*(\xi,\eta)$ represents the complex conjugate of the Fourier transform of $I_2(i,j)$.

The resulting FFT correlation field contains a correlation peak, the location of which represents the displacement between the two interrogation areas. The location of the peak is estimated to sub-pixel accuracy by fitting a Gaussian

curve since the correlation between two Gaussian shaped particle images produces a Gaussian shaped correlation profile.

In the software, cross-correlation is performed by dividing the image into small interrogation regions. The size of the interrogation region was determined based on the maximum particle image displacement to be less than one quarter of the region. The spot size was set at 32 x 32 pixels and 64 x 64 pixels in vertical and horizontal direction and 50% overlap. The next step is to input the parameters for velocity calibration to compute the flow velocity. The measurement option was set to measure velocity vector in meters per second. The dT (μs) is the same pulse separation parameter used in the "Timing Setup" in the previous section to determine the time between two laser pulses. The dT used in the GDI study was set at 1 μs for all the DPIV experiments due to the size of the flow regions. The pixel aspect ratio for x and y direction was set as 1 as the CCD is almost squared. For the entire image size, this can be determined by using the "Field of View" option or the "Measure mm/pixel" option. Both options are essentially the same, the only difference is the latter is based on an object size instead of the entire image in view. The image size depended on the nozzle geometry investigated which varied between 6–8 mm for this thesis study.

With all the parameters setup, the velocity vectors were calculated by the Insight software and were repeated for each interrogation region until a complete 2D-velocity vector map was built. When the velocity map was created, a further post-processing was carried out to remove any spurious velocity vectors to improve the accuracy of the DPIV result. Once all the flow images were analysed and processed, these were built to a complete sequence of flow images with velocity vectors.

3.3.2 Fluorescent Particle Image Velocimetry (FPIV)

The development of the FPIV technique in the Optical Engineering Research Laboratory (OERL) at Loughborough University was due to the difficulty in obtaining quantitative PIV data of the swirl nozzle flow. The fluid film

generated by the swirl injector attached to the sharp inlet wall, resulting in reflection and refraction of the laser sheet. Because of the massive amount of scattering between the glass of the nozzle and the liquid, and also between the liquid and the aircore, the use of fluorescent seeding particles is the only way to remove all these unwanted scattering. The fluorescent seeding particles in this instant allows better tracing of fluid motion in swirl injectors.

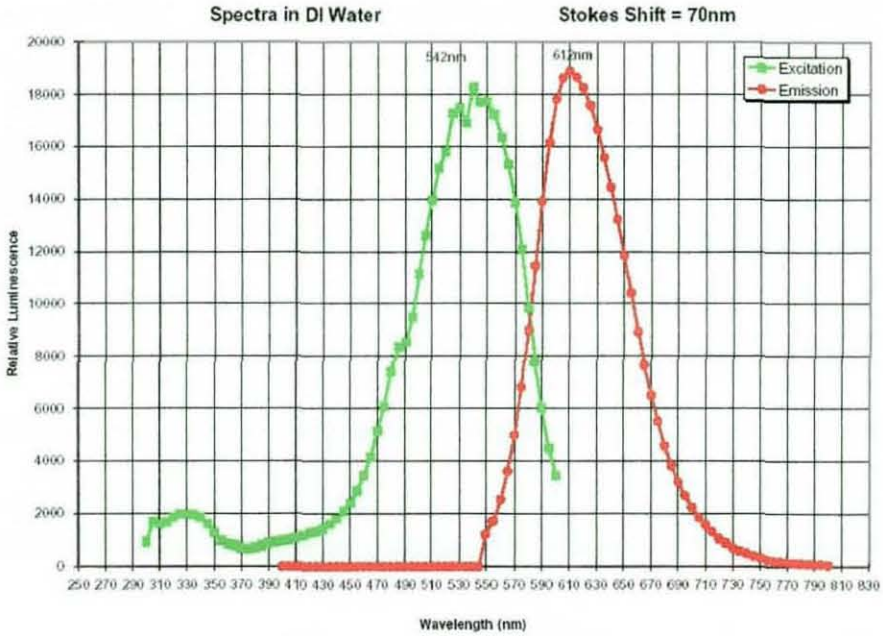

Figure 3.11 Spectral properties of fluorescent microspheres.

Figure 3.12 DPIV image with fluorescent particles.

The fluorescent seeding particles in this instance required the particles to work at the excitation wavelength of the laser which is 532 nm wavelength.

Rhodamine 620 fluorescent particles (5-7 μm) were selected as the seeding particles, which when excited by the laser emits at 620 nm. Figure 3.11 showed the excitation and emission wavelength of the fluorescent seeding particles. The graph showed the peak excitation wavelength for Rhodamine 620 is 542 nm with an emission of 612 nm wavelength.

The FPIV technique uses the same laser and camera system as in DPIV. This system consisted of the laser unit, camera, synchroniser and a processing computer. To achieve the FPIV, the laser was aligned to illuminate the fluorescent seeding particles that were introduced into the flow as tracers. These fluorescent particles were then excited by the laser pulse and emitted at 600 nm wavelength. The fluorescence emitted by the particles was recorded on the CCD camera with a separation between frames varied from 1 μsec to 2 μsec. These were subsequently captured by the CCD camera (figure 3.12) and stored in the processing computer. All the operations were controlled and processed by the TSI Insight (version 3) software mentioned in the previous sections. The FPIV provided a useful diagnostic tool for future swirl flow study.

3.4 PARTICLE SIZE MEASUREMENT

3.4.1 Background

Particle size measurement is an important aspect in determining the droplet size of an injector spray, which helps to improve the engine combustion system efficiencies. Several techniques have been developed to measure spray droplets size, some with the ability to determine droplet velocity.

3.4.1.1 PARTICLE SIZE MEASUREMENT TECHNIQUES

The most common technique used is Phase Doppler Anemometry (PDA), a non-intrusive optical diagnostic technique used to measure the size and velocity of spherical particles in liquid and gaseous flows simultaneously. This is an extension of laser Doppler anemometry (LDA) which measured the velocity from the frequency of the Doppler burst. System like Malvern particle

sizer based on the Fraunhoufer diffraction was used to measure and characterise spray droplets sizes by Sauter Mean Diameter (SMD). The SMD can be definite as

$$SMD = \frac{\Sigma d^3}{\Sigma d^2} \tag{3.2}$$

Where d is the average particle diameter recorded over a number of samples. Gong *et al* [23] and Rashkovan [39] provided examples of this particle sizer on elliptic sprays and gas-dissolved gasoline spray respectively. Gong *et al* [22] found that the spray angle was wider in elliptic nozzle and have smaller SMD than those using circular nozzle. Rashkovan [39] dissolved CO_2 gas into gasoline to study the difference in SMD compared to pure gasoline. The mixture exhibits unstable SMD values under different injection pressure and the results were inconclusive. However, the SMD was half the size of pure gasoline spray when the difference in injection and ambient pressure was about 30 bar.

Konig *et al* [28] was one of the earliest researcher to introduce the PDA technique system. This consisted of a laser to provide the illumination source through a series of transmitting optics. This optics spilt the single laser beam into two before making the two beams crossed using converging optics. The system also consisted of a receiving optics, a signal processor, a personal computer with interface card and a data and processing software. Wigley *et al* [49] applied the PDA technique to characterise GDI spray droplets to obtain Sauter Mean diameters (SMD). One of the papers investigated the effects of compression pressure in the combustion chamber on the spray morphology of the GDI swirl injector. It was found that the spray cone angle and penetration of the hollow cone decreases with increasing combustion chamber pressure. However, no significant changes were noted on the SMD data. The second paper explored the application of PDA technique on dense spray.

Comer *et al* [13] and Alloca *et al* [02] used the PDA method to investigate a swirl-type GDI injector. Comer *et al* [13] aims to used time-resolved data on hollow cone spray generated by high-pressure swirl injector for comparison with CFD models. The spray data obtained stated that the initial fuel injected was sluggish, due to the near-stationary air. It was assumed that the droplets contain within this slug has a SMD of about 50 μm. Alloca *et al* [02] carried out experiments on an electronically controlled swirled GDI injector in an optically accessed chamber using EXXSOL D40 fuel at 70 bar, with an injection duration of 3.0 ms. The authors found that a maximum velocity of 40 m/s and a maximum SMD 0f 20 μm. The SMD also remain fairly constant during the entire injection duration. Chang *et al* [09] studied the effects of refractive index change using PDA system. The results showed that a small collecting angle must be used to increase the sensitivity towards refractive index in forward scattering measurement. For back scattering measurements, a large collecting angle was used to provide a broad refractive index range. Yoda [51] and Kufferath [29] also provided further applications of PDA study on the influence of injection nozzle in Diesel engine and the influence of internal mixing on spray characteristic in a twin fluid atomiser respectively.

Another technique developed to measure spray droplet SMD was the use of light extinction principles. Kamimoto *et al* [27] and El-Beshbeeshy *et al* [21] used this method to quantify their study on fuel sprays. Kamimoto *et al* [27] investigate both Diesel and gasoline sprays using this technique and claimed that the SMD measurement has an accuracy of within 10%. The author discovered that SMD is smaller with increasing injection pressure and this tendency is more prominent in lower injection pressure range. El-Beshbeeshy *et al* [21] used similar technique as Kamimoto *et al* [26] with the exception of using a high speed film camera instead of single shot CCD camera. The information recorded on the film was then digitised using either a projector or CCD camera system. A Lucas-CAV type injector was used in the study and the authors also concluded that the droplet size decreases with increasing injection pressure. Further applications of this technique were applied successfully by Chang *et al* [08] and Goney *et al* [22].

Recently, two new techniques have been developed to look at droplets particle size. The first technique is known as laser sheet dropsizing (LSD), developed by Le Gal [35] as a tool to permit rapid spray characterisation on normal and dense spray. LSD technique requires the characterisation of the elastic and inelastic signals from the illuminated droplets as a function of their diameter, D. For the elastic signal (Mie scattering), it was assumed that the absorbing droplets are spherical and their diameter is greater than 1 μm. In the case of non-elastic scattering or LIF, fluorescence molecules (P-Terphenyl) are seeded into the liquid spray. The Mie signals can be approximated by the equation:

$$S_{Mie} = C_{Mie} D^2 \tag{3.3}$$

The fluorescence signals are expected to be proportional to the concentrations level in the flow in order to define the liquid volume or liquid mass distribution. This can be expressed as:

$$S_{LIF} = C_{LIF} D^3 \tag{3.4}$$

The S_{Mie} and S_{LIF} signals were collected by a laser sheet generated by the Nd:YAG laser and onto the CCD array in the camera. The two images collected were separated by appropriate interference filter and collected simultaneously. This can be either side by side in the camera's chip or by two different cameras. Assuming the S_{Mie} signal follows S_{LIF} signal, then the intensity ratio of the corrected signals will be:

$$\frac{S_{LIF}}{S_{Mie}} = \frac{C_{LIF}\ \Sigma D^3}{C_{Mie}\ \Sigma D^2} \alpha \frac{\Sigma D^3}{\Sigma D^2} : D_{32} \tag{3.5}$$

This ratio gives a 2D map of relative Sauter Mean Diameter (SMD) of the spray. Le Gal [35] gave examples of successful experimentations in the application of this technique. Harding [24] applied this technique as part of his investigation to measure the droplet size of an airspray injector of a gas turbine engine. Jeong *et al* [26] studied the advantageous of the LSD technique on dense spray structure in a pressure swirl atomiser. The authors used a dual imaging system to perform this experiment, and allow the separation of the Mie signals and fluorescence signals. They concluded that this technique has the potential to be applied to both hot and cold sprays. However, erroneous values were produced along the spray border and this was due to the low statistics from the low presence of droplets near the border

The second technique is the Global Phase Doppler (GPD). This is a multi-dimensional particle sizing method that uses out-of-focus images of the particles developed by Tropea [45]. Two laser light sheets were used to illuminate the measurement area at a known intersection angle. With this laser light sheet, it will contribute a glare point for each scattering mode and create a far-field interference pattern similar to those of PDA technique. The difference in GPD to PDA is that the previous captured the fringe patterns simultaneously from the droplets in the illuminated plane, thereby creating a larger measurement volume. These glare points always have the same intensity and created a defocused image. This defocused image was processed using Fourier transform algorithm to determine the particle size. The author highlighted that GPD is able to measure opaque particles was able to obtain good particle size validation. However, Damaschke [17] also noted that any increase in particle concentration lead to many overlapping particles. This resulted in the limitation of this technique to determine the particle size from the images, resulting in constraints being place on the optical system used.

3.4.1.2 SUMMARY OF VARIOUS TECHNQIUES

The availability of different particle size measurement techniques allowed the selection of the best technique suitable for the study of external spray

structure of a GDI spray. Several considerations were made before selecting the right technique of the experiments. These include the availability of the laser system in the laboratory, setting up the diagnostic technique, ability to do spray particle size and velocity measurements and etc.

GPD was not considered as it does not perform velocity measurement of spray particles and the inherent problem of the difficulty in measuring dense spray rendered this technique not suitable in this study. The light extinction method is widely used in measuring droplet size but this technique can be considered as an indirect technique. It uses recorded images and post-processed to determine the spray SMD and this is not ideal in this study. LSD is a new technique similar to the PDA and Jeong *et al* [26] mentioned that the LSD technique is ideal to provide rapid measurement of mean droplet diameter in a 2D plane and also to replace PDA technique in measuring dense spray. However, Wigley *et al* [49] successfully tested the PDA technique on dense sprays with smaller nozzles using high power laser.

PDA is a well established diagnostic tool and widely use in spray studies. In the GDI study, this technique was used to characterise the spray structure exiting the various swirl nozzles investigated as the equipments are readily available for use, and is easy to setup in the laboratory for the GDI spray study.

3.4.2 Phase Doppler Anemometry (PDA)

Phase Doppler Anemometry (PDA) is an optical diagnostic technique derived from a more common and well-established Laser Doppler Anemometer (LDA) as mentioned in the literature. To have a better understanding of PDA, it is ideal to have some background knowledge of the LDA technique.

In the basic LDA system, two light beams from a coherent source are intersected at a point of interest in a flow. The light scattered from particles in the flow is detected using a photomultiplier. The difference between the Doppler shifts of the scattered light from each beam is measured. This

Doppler shift frequency is directly proportional to the flow velocity. A problem with this simple arrangement is directional ambiguity. Lading [33] highlighted that this frequency spectrum is symmetrical around the zero frequency and the changing of frequency signs will not affect the spectrum appearance. Thus, directional ambiguity and this can be overcome by applying a frequency shift to one of the beams. Acoustic-optic Bragg cells are commonly used to generate this frequency shift. This fixed shifting results in a linear phase change from one beam to the other. A non moving particle will caused a signal oscillating with a frequency generates by the moving fringe pattern and this frequency is exactly equal to the acoustic frequency of the Bragg cell. This frequency is increased when the particle is moving in the opposite direction of the fringe pattern and *vice versa*. This is provided that the Doppler frequency is always smaller than those of the Bragg cell. The advantage of frequency shifting is that it is consistent and the dynamic range is also increased. However, LDA does not allow the measurement of particle size, which is essential to quantify the droplet size and flow velocity.

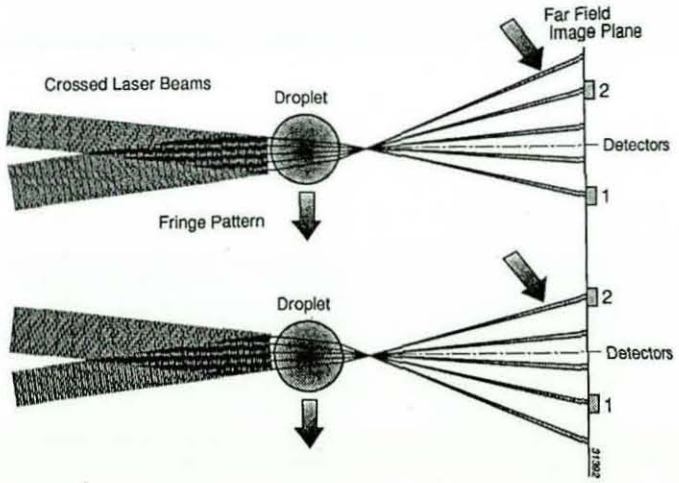

Figure 3.13 Phase of the scattered light signal from two crossed laser beams. [33]

The PDA technique consists an extra component to allow particle size measurement uses the same method in considering the frequency of the scattered light generated by two crossed laser beams and also the phase shift signals from the two scattered light. Wigley [33] provided a simple fringe model to describe the phase shift generated from two signals to determine

particle size. Figure 3.13 shows a droplet moving through the fringe pattern generated by two crossed laser beams at two different locations. The droplet behaves like a spherical lens and projected a magnified fringe pattern (proportional to the droplet radius of curvature) as an image onto the plane in the far field. Wigley [33] described this as the ratio of fringe spacing in the far field to the fringe spacing at the laser beam crossover point and two detectors were required to measure the fringe spacing.

The first image in figure 3.13 showed the droplet moves in the direction of the arrow and through the fringe pattern. From the far field plane, the image also showed the fringes moving past the two detectors, with detector 2 leading 1 by three fringes. However the fringe generated in the near forward scattering angle would be complicated to detect due to the light diffracted from the droplet. Therefore, scattering angles between signal phase and dropsize, where reflection, 1^{st} and 2^{nd} order refraction are dominant, need to be identified. This will allowed the phase shift to be calculated from the path length difference existing between the incident rays. Further in-depth description and formulations of the PDA technique was provided by Wigley [33] and Bachalo *et al* [10].

3.4.2.1 TRANSMITTING AND RECEIVING SYSTEMS

PDA optical diagnostic technique consists of a number of instruments. The two main important components are the transmitting and receiving systems as shown in figure 3.14. The schematic showed an argon-ion laser connected to the transmitting optics via an optical fibre. This is an air-cooled laser that uses very high currents to achieved ionisation and excitation and emits at 514 nm wavelength. The laser has a beam diameter of 1.35 mm and delivered into the transmitting optics with a 40 MHz optical frequency shift by a bragg cell driven by the signal processor. A beam translator in the transmitting optics was used to generate a beam separation of 38 mm and of equal intensity from the single laser. These beams were then focused onto the transmitting lens that also changes the direction of the beams, causing them to cross at a known focal length of 310 mm (Figure 3.14). The intersection point where the beams

crossed is called the measurement volume. Figure 3.14 also shows that the experimental setup was in a forward scattering configuration. The pressurised fluid flows downwards into the fuel collector, with the transmitting and receiving optics perpendicular to it. The effective scattering angle was set at 70° on the receiving optics, determined by the refractive index for air and white spirit as shown in Table 3.1.

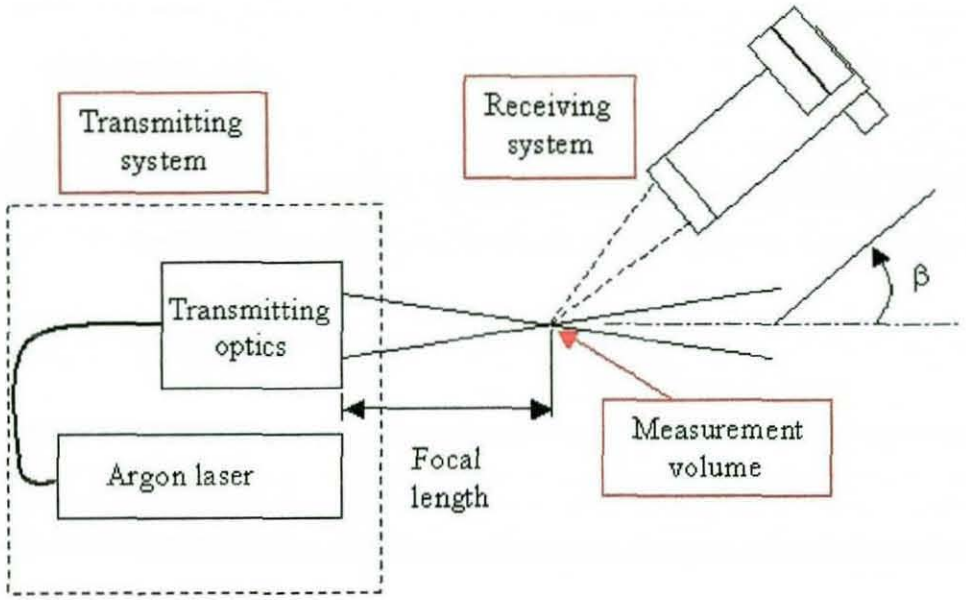

Figure 3.14 Schematic for the optical systems for PDA.

	Refractive Index
Air	1.0
Hydrogen	-
Diesel	1.6
Gasoline	1.45
Perspex	1.49
Quartz	1.5
Sapphire	1.8
White spirit	1.44

Table 3.1 Refractive index for different medium.

The interference of the light beams creates a fringe pattern at the measurement volume that was parallel to the crossed laser beams (Figure 3.15). When a droplet intersects the crossed laser beams, it appeared to

move through the Doppler frequency shift. This Doppler frequency shift is a function of the beam intersection angle, droplet velocity and laser wavelength For the spatial frequency of the fringe pattern, this is dependent on the observation angle, droplet refractive index, drop diameter, laser wavelength and beam intersection angle. The fringe patterns are integrated over the receiving system produced the Doppler burst signals allows the determination of the droplet size. The receiving system consists of series of collecting lens and photomultipliers and configured for use with the argon ion laser, which is equipped 1-D or 2-D measurement. The collecting lens received signals from the scattered fringe pattern in the measurement volume and send to the three photomultiplier detectors. The received signals are dependent on the aperture on the receiver, calibrated drop size, intersection angle and etc. Two of the detectors were placed at different angular positions with respect to the measuring volume when comparing signals collected from the flow and these signals has a phase difference which is linearly dependent on the particle size. This method of size measurement increases the dynamic range and combined with high accuracy which was enhanced by arranging the three detectors in two pairs. The use of three detectors also allows non-spherical particles to be discriminated.

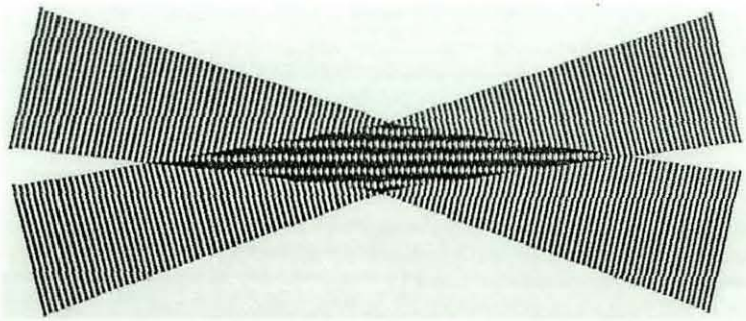

Figure 3.15 Formation of fringe pattern by crossed laser beams in the measurement volume.

3.4.2.2 DATA COLLECTION AND PROCESSING

Data collection and processing were carried out on a PC installed with the PDA software, *SIZEware*. *SIZEware* software was used for setting up, acquiring and processing data from the PDA system and this is connected to

a 58N10 PDA processor. For data acquiring, the software was configured to enabled size measurement with a 1-D velocity component to be measured. This was followed by inputting the parameters for transmitting optics as mentioned in the previous section. The *SIZEware* software was able to determined 36 fringes with a fringe spacing of 4.2051 μm with current setting based on the laser wavelength, beam separation lens focal length and etc.

Figure 3.16 shows the settings used for configuring the receiving optics in this study. The Maximum diameter shown on the display showed two limiting values in the measurement, minimum and maximum values respectively. These values were inter-dependent on the angle adjustment used and vice versa, with the scattering angle and lens focal length determined on the setup used in section 3.4.2. The liquid droplets generated from the injector determined the particle refractive index and density in this instance and the polarisation orientation was set relative to the plane of fringes. When all the parameters were setup, a filename for an experiment was created and "Acquire" option was selected.

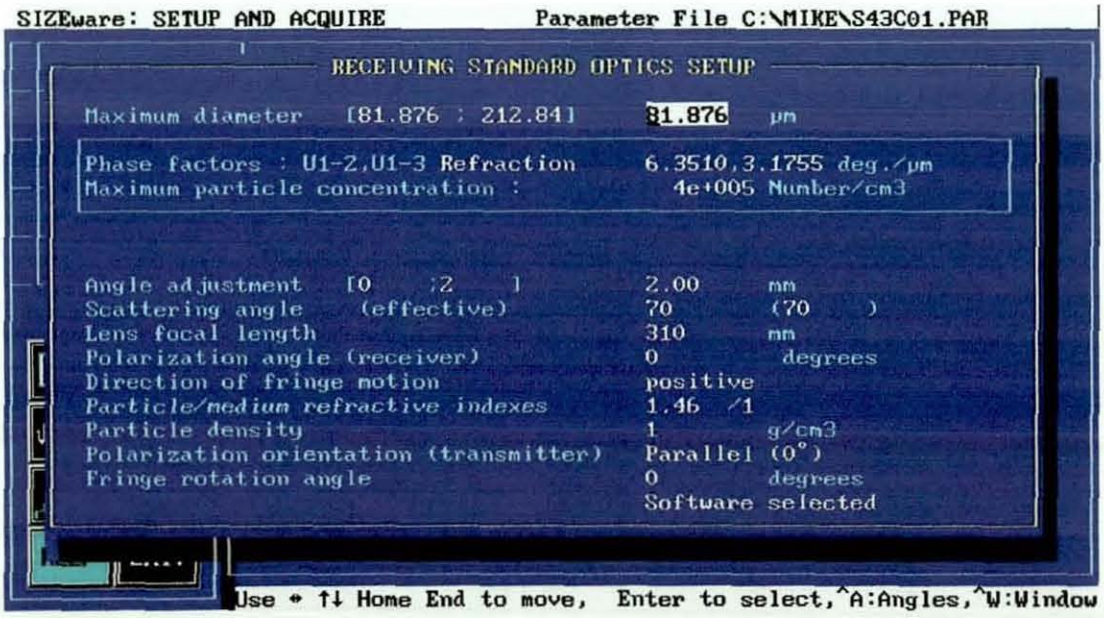

Figure 3.16 Receiving optics setup window.

Data acquisition was performed on the "acquisition" window which includes a number of other options; validation setup, high voltage setup, run and etc.

Validation setup window was used to determine the types of tests and limits for the data to be validated. It allowed the setting of signal to noise ratio to control the rejection level from –6 dB to 3 dB. As a rule of thumb, -6 dB representing the highest number of fringes required and 3 dB as the least number of fringes used (better accuracy). Since both velocity and particle diameter were measured, the velocity, diameter and particle spherically were enabled. The accepted fringe count was set from 0 to 215, the maximum phase error and spherical deviation was set at 10 degrees and 10% respectively. The high voltage setup corresponding to the photomultiplier tube was set between 1000 – 1200 volts. The display window both velocity and particle diameter in real-time histograms, and also providing velocity and diameter as a statistics. Under the run option, the data acquiring mode allowed the data collection to be displayed "live", this was either set as repetitive mode which stored the data in RAM or continuous mode which stored the data permanently in the computer for analysis. With the continuous mode, the number of samples to be collected was set to 3000 with a 60 seconds time out. When activated, the *SIZEware* software will start capturing amplified signals from the particles through the receiving optics.

Once the data were recorded and stored in the computer, the data were first converted from raw into a collection of converted files before being processed. The processor window allowed four different parameters to be selected; velocity, moments, spectrum and correlate and velocity was selected for analysis in the experiment. Once the processing completed, the analysed data can be displayed in a series of histograms in samples distribution, velocity and particles sizes (D_{10} to D_{43}). One disadvantage of the software is it does not support the use of graphs to show the trends of droplet size and velocity distributions. However, the data files can be exported in "ascii" file format and imported in to graph plotting software. This is especially useful to show the trend of the velocity and particle size distribution profiles for different injectors and inlet pressures.

3.5 SUMMARY

This chapter provided detailed reviews on the use of different optical diagnostic techniques applicable in this thesis work. These optical diagnostic techniques provided non-intrusive investigation of flow in an optical rig, allowing in-depth studies of the flow characteristics.

Diesel injectors studies consist of only the use of high speed flow visualisation optical technique to observe the flow structures. For gasoline injectors' studies, these include the use of high speed and single shot flow visualisation, fluorescent particle image velocimetry and phase Doppler anemometry techniques. These diagnostic techniques allowed the link from internal flow structures to the atomisation processes and help to quantify the spray characteristics and atomisation processes.

The following chapter will show the optical rig and the diagnostic setup used in the investigation of Diesel and gasoline injectors. The optical rigs will also show the different optical nozzle configurations available in the studies and the range of pressure used.

3.6 REFERENCES

[01] Adrian, R.J., *Scattering particle characteristics and their effect on pulsed laser measurements of fluid flow: speckle velocimetry vs particle image velocimetry*, Applied Optics, Vol. 24, Pg 1690-1691, 1984

[02] Alloca, L., Corcione, F.E., Valention, G., *Study of the Atomisation Process in a GDI Spray by Laser Light Extinction and Phase Doppler Techniques*, ILASS Europe, Zurich (Switzerland), Sept 2001

[03] Allen, J., Hargrave, G.K., *Fundamental Study of In-nozzle fluid flow and it effect on liquid jet breakup in Gasoline Direct Injectors*, 16th ILASS, Darmstadt, Germany, 2000.

[04] Allen, J. and Hargrave, G. K., *Investigation of internal fluid flow in real sized pressure swirl gasoline direct injectors.* ImechE Conference Transactions Fuel Injection systems, Page 83-94, London, UK, 26-27th November 2002

[05] Badock, C., Wirth, R., Fath, A., Leipertz, A., *Application of Laser Light Sheet Technique for the Investigation of Cavitation Phenomena in Real Size Diesel Injection Nozzles*, ILASS-Europe, Manchester(UK), July 1998

[06] Bae, C., Yu, J., Kang, J., Kong, J., Lee, K.O., *Effect of Nozzle Geometry on the Common-Rail Diesel Spray*, SAE 2002-01-1625, SP-1713, 2002

[07] Baumgarten, C., Shi, Y., Busch, R., Merker, G.P., *Numerical and Experimental Investigations of Cavitating Flow in High Pressure Diesel Nozzles*, ILASS Europe, Zurich (Switzerland), Sept 2001

[08] Chang, C.T., Farrell, P.V., *A Study on the Effects of Fuel Viscosity and Nozzle Geometry on High Injection Pressure Diesel Spray Characteristics*, SAE 970353, SP-1219, 1997

[09] Chang, J.C., Chu, C.S., Chen, C.Y., *The Study of Effects of the Refractive Index Changing on a Phase Doppler Particle Analyser*, 8th ICLASS, Pasadena (USA), July 2000

[10] Chigier, N., *Combustion Measurements*, Combustion: An International Series, Hemisphere Publishing Corporation, 1991, ISBN 1-56032-028-1

[11] Cho, Y.C., *Digital image Velocimetry*, Applied Optics, Vol.28, No.4, Pg 740-748, February 1989

[12] Christopher Outwater & Van Hamersveld, *Practical Holography* (http://www.holo.com/holo/book/book1.html#def), Jan2002 [09.01.2004]

[13] Comer, M.A., Bowen, P.J., Bates, C.J., Sapsford, S.M., *CFD Modelling of Direct Injection Gasoline Sprays*, 15th Intl. Liquid Atomisation and Spray Systems (Europe), 1999

[14] Cooper, D., Yule, A.J., *Waves on the Air Core/Liquid interface of a Pressure Swirl Atomizer*, ILASS-Europe, Zurich (Switzerland), September 2001

[15] Coupland, J.M., Halliwell, N.A., *Particle image velocimetry: rapid transparency analysis using optical correlation*, Applied Optics, Vol. 27, No.10, Pg 1919-1921, 1988

[16] Coupland, J.M., C.J.D., Pickering, *Particle image velocimetry: Estimation of Measurement Confidence at Low Seeding Densities*, Optics and laser in Engineering, Vol. 9, Pg 20-210, 1988

[17] Damaschke, N., Nobach, H., Tropea, C., Optical limits of particle concentration for multi-dmensional particle sizing techniques in fluid mechanics, Experimental in fluids, Vol.32, Pg 143-152, 2002

[18] Dudderar, T.D., Simpkins, P.G., *Laser Speckle photography in a fluid medium*, Nature, Vol. 270, Pg 45-47, 1977

[19] Durst, F., *Fluid Mechanics Developments and Advancements in the 20th Century*, 10th International Symposium on Application Laser Technology to Fluid Mechanics, Lisbon (Portugal), July 2000

[20] Durst, F., Melling, A., Whitelaw.J.H., *Principles and practice of laser-Doppler Anemometry*, Academic Press Inc (London) Ltd, 1976, ISBN 0-12-225250-0

[21] El-Beshbeeshy, M.S., Hodges, J.T., Corradini, M.L., *Image Analysis of Diesel Sprays*, SAE 921628, 1992

[22] Goney, K.H., Corradini, M.L., *Isolated Effects of Ambient Pressure, Nozzle Cavitation and Hole Inlet Geometry on Diesel Injection Spray Characteristics*, SAE 2000-01-2043, 2000

[23] Gong, Y., Liu, C., Huang, Y., Peng Z., *An Experimental Study on Droplet Size Characteristics and Air Entrainment of Elliptic Sprays*, SAE 982546, 1998

[24] Harding, S.C., Farrugia, N., Le Gal, P., Nimmo, G.A., Greenhalgh,D.A., *Fuel Flux, Droplet Size and Velocity Measurements made on Pintle and Airspray Injectors,* ILASS-Europe, Manchester(UK), July 1998

[25] Huang, Z., Shao, Y.M., Shiga, S., Nakamura, H., Karasawa, T., *The role of orifice flow pattern in fuel atomization*, Paper I-12, ICLASS, Rouen (France), July 1994

[26] Jeong, K.S., Jermy, M.C., Greenhalgh, D.A., *Laser Sheet Dropsizing in Evaporating Sprays using Laser Induced Exciplex Fluorescence*, 9th International Symposium on Flow Visualisation, Edinburgh (UK), 2000

[27] Kamimoto, T., Yokota, H., Kobayashi, H., *A New Technique for the Measurement of Sauter Mean Diameter of Droplets in Unsteady Dense Sprays*, SAE 890316, 1989

[28] Konig, G., Anders, K., Frohn, A., *A New Light-scattering Technique to Measure the Diameter of Periodically generated Moving Droplets*, Journal of Aerosol Science, Vol.17, No.2, Pg 157-167, 1986

[29] Kufferath, A., Wende, B., Leuckel, W., *Influence of Liquid Flow Conditions on Spray Characteristics of Internal Mixing Twin Fluid Atomisers*, ILASS-Europe, Manchester (UK), July 1998

[30] Kunkulagunta, K.R., *Video Imaging and Analysis of Common Rail Sprays in an Optical Engine using Shadowgraphy Technique*. SAE 2000-01-1255, SP-1498, 2000

[31] Kusakabe, T., Tsue, M., Kadota, T., *Visualization of Diesel Spray by Laser Sheet Method*, SAE 941920, 1994

[32] Kuwahara, K., Ando, H., *Diagnostic of in-cylinder flow, mixing and combustion in gasoline engines*, Measurement Science and Technology Journal, R95-R111, 2000

[33] Lading, L., Wigley, G., Buchhave, P., *Optical Diagnostics for Flow Processes*, Plenum Press, 1994, ISBN 0-306-44817-3

[34] Laoonual, Y., Yule, A.J., Walmsley, S.J., *Internal Fluid Flow and Spray Visualization for a Large Scale Valve Covered Orifice (VCO) Injector Nozzle*, ILASS Europe, Zurich (Switzerland), Sept 2001

[35] Le Gal, P., *Development of a Laser Sheet Dropsizing Technique for Sprays*, PhD Thesis, School of Mechanical Engineering, Cranfield University, 1999

[36] Maunoury, B., Duverger, T., Mokaddem, K., Lacas. F., *Optical Investigation of Diesel Spray and Auto-ignition in a Small Direct-injected Diesel Engine*, ILASS Europe, Zurich (Switzerland), Sept 2001

[37] Raffel, M., Willert, C.E., Kompenhans, J., *Particle Image Velocimetry: A Practical Guide*, Springer ,1998, ISBN 3-540-63683

[38] Pickering, C.J.D., Halliwell, N.A., *Laser speckle photography and particle image velocimetry: photographic film noise*, Applied Optics, Vol.23, No.17, Pg 2961-2969, September 1984

[39] Rashkovan, A., Kholmer, V., Sher, E., *Gas-dissolved Gasoline Spray – An Experimental Study*, ILASS-Europe, Zurich (Switzerland), September 2001

[40] Sasaki, S., Akagawa, H., Tsujimura, K., *A Study on Surrounding Air Flow Induced by Diesel Sprays*, SAE 980805, SP-1316, 1998

[41] Settles, G.S., *Schlieren and Shadowgraph Techniques*, Springer publishing, 2001, ISBN 3-540-66155-7

[42] Tamaki, N., Nishida, K., Hiroyasu, H., *Promotion of the atomisation of a liquid jet by cavitation in a nozzle hole*, ILASS-Europe, Manchester(UK), July 1998

[43] Tamaki, N., Shimizu, M., Hiroyasu, H., *Enhanced Atomisation of a liquid jet by cavitation in a nozzle hole*, 8th ICLASS, Pasadena (USA), July 2000

[44] Tamaki, N., Shimizu, M., Hiroyasu, H., *Atomisation of super-high injection pressure liquid jet*, ILASS-Europe, Zurich (Switzerland), September 2001

[45] Tropea, C., Damaschke N., Nobach, H., Semidetnov, N., *Multidimensional Particle Sizing Techniques for Two-Phase Flows*, 10th International Symposium on Flow Visualisation, Kyoto (Japan), August 26-29, 2002

[46] TSI Incorporated, *Insight: Particle Image Velocimetry Software*, version 3.3, Dec 2000, P/N 1990010.

[47] Walther, J., Schaller, J.K., Wirth, R., Tropea, C., *Investigation of Internal Flow in Transparent Diesel Injection Nozzles using Fluorescent Particle Image Velocimetry (FPIV)*, 8th ICLASS, Pasadena, California (USA), July 2000

[48] Wicker, R.B., Loya, H.I., Hutchison, P.A., Sakakibara, J., *SIDI Fuel Spray Structure Investigation Using Flow Visualization and Digital Particle Image Velocimetry*, SAE 1999-01-3535, 1999

[49] Wigley, G., Hargrave, G.K., Heath, J., *A High Power, High Resolution LDA/PDA System Applied to Dense Gasoline Direct Injection Spray*, 9th International Symposium on Application Laser Technology to Fluid Mechanics, Paper 9.4, Lisbon (Portugal), 1998

[50] Yamakawa, M., Isshiki, S., Lee, J., Nishida, K., *3-D PIV Analysis of Structural Behaviour of D.I. Gasoline Spray*, SAE 2001-01-3669, SP-1640, 2001

[51] Yoda, T., Tsuda, T., *Influence of Injection Nozzle Improvement on DI Diesel Engine*, SAE 970356, SP-1219, 1997

CHAPTER 4

DEVELOPMENT OF OPTICAL TEST RIGS AND DIAGNOSTIC SETUPS

4.1 INTRODUCTION

The previous chapter provided a generalised methodology for the different optical diagnostics applicable to this research investigation. This was very important for investigating the internal and external flow structures of Diesel and gasoline fuel injectors. The understanding of these flow phenomena are essential in helping to improve the overall performance and efficiency of the automotive engine, as well as understanding their impacts on the environment.

To facilitate the investigation of Diesel and gasoline injection systems, two separate optical test rigs were made for both set of fuelling needs. The first section highlighted the designs of the Diesel optical rig and subsequently made by Caterpillar research with Loughborough University assistance. The nozzle matrix configurations and the optical diagnostic technique employed were discussed in details. The following section provided the detailed designs and developments on Gasoline direct injection optical rig. Different nozzles and swirlers' configurations were used together with three different optical diagnostic techniques. The final section of the chapter summarised any modifications made on both the optical rigs.

4.2 DIESEL INJECTION OPTICAL TEST RIG

4.2.1 Introduction

The literature review highlighted the developments of diesel fuel injection were still an important aspect in engines research. The internal flow characteristics were not yet fully understood but with technological advancements, this was becoming a possibility. This diesel injection study was collaboration between Loughborough University and Caterpillar Research to study the internal flow

with high-speed flow visualisation. This was to aid the understanding and the study of the fuel injection systems, incorporating novel nozzle geometries with HEUI (Hydraulically actuated Electronically controlled Unit Injector) injector. This was because the internal fuel flow regimes in these nozzles, in terms of flow interaction and cavitation were not yet fully understood.

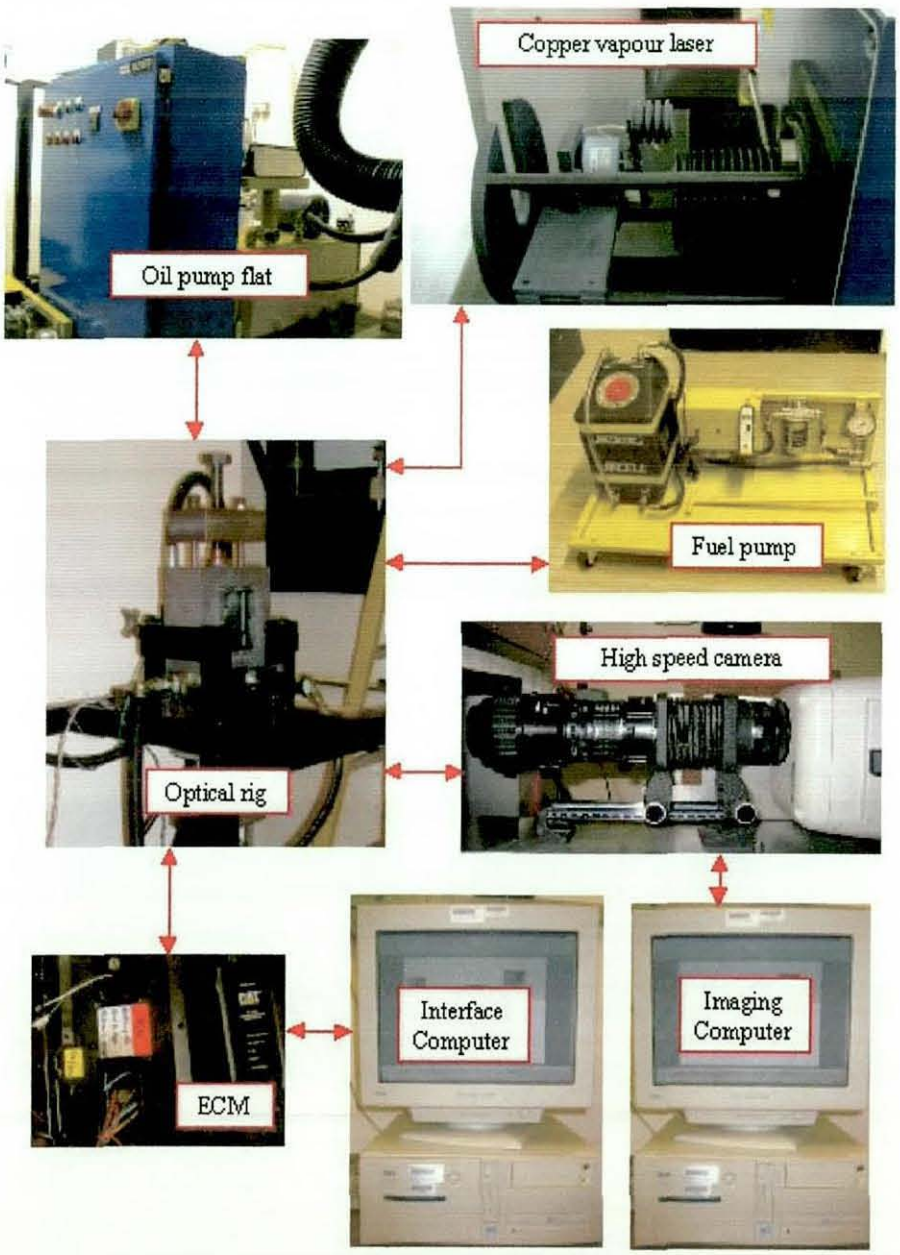

Figure 4.1 Schematic of facility setup

Figure 4.1 shows the overall schematic and the arrangements of the advanced nozzle imaging facility. It consisted of a Diesel optical injector rig, a fuel pump flat, a Oil pump flat and an Electronic Control Module (ECM). The fuel pump providing the fuel into the injector and the oil pump flat supplied the

injection pressure. The ECM unit was used to communicate the injector with the interfacing computer for injection requirements. This facility allowed the optical injector rig to function at operational conditions, while delivering high pressure fuel. The schematic also showed the optical diagnostic setup for high-speed flow visualisation which was applicable in this research investigation.

4.2.2 Oil Pump Flat, Fuel Pump Flat and ECM Unit

This facility required three essential components apart from the HEUI injector and the optical rig, to operate under actual injection cycles. These components were the oil pump flat, fuel pump flat and Electronic Control Module (ECM) unit.

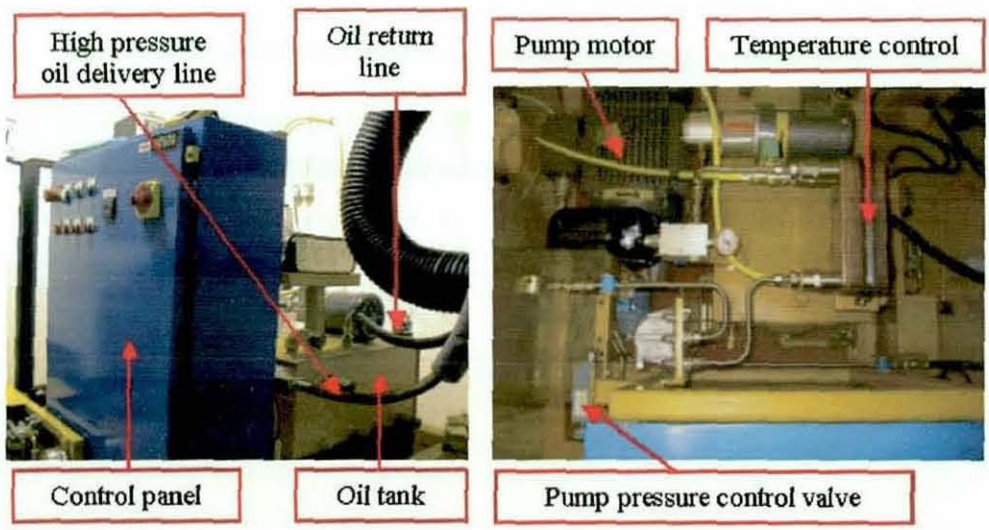

Figure 4.2 Oil Pump Flat.

Figure 4.2 shows a diagram of the oil pump flat installed at the experimental facility in the laboratory. This oil pump flat required a three phase 440V high voltage power supply to operate the pump and used conventional engine lubricating oil to generate enough oil pressure for injection. The engine lubricating oil used to fill the 75 litres reservoir was the Shell Helix Super 15W-40. During operation, the oil pump flat pressurised the oil in the pump reservoir to the required pressure determined by the operator. The pressurised engine lubricating oil controlled the rate of injection by simply

varying the control from the CADetWin software. This pressurised engine oil was sent into the HEUIB injector to pressurise the diesel fuel into the injection system with a capability to deliver up to 300 bar line pressure to the injector but the usual operating range in this study was between 150 bar to 250 bar for the HEUIB injector.

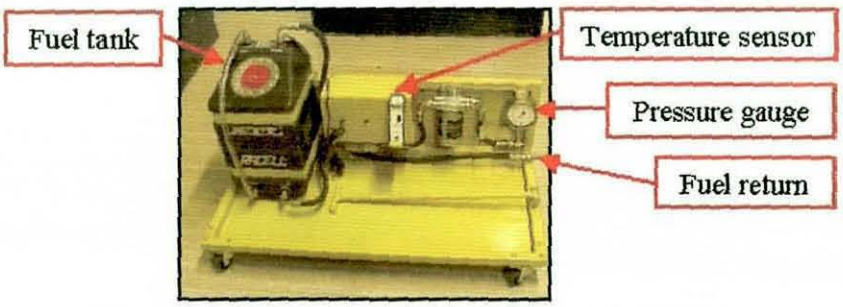

Figure 4.3 Fuel pump flat mounted on a trolley.

Figure 4.4 Electronic Control Module (ECM) unit.

The fuel pump shown in figure 4.3 was mounted on a trolley, with a temperature sensor and a pressure gauge. It primary purpose was to provide a constant supply of diesel fuel into the HEUIB injector. The temperature sensor and pressure gauge allowed the fuel temperature and fuel delivery pressure to be monitored respectively while maintaining the fuel pump delivery within the operating parameters. The initial consideration for diesel fuel used in the experiments was the red diesel. However, initial test of the red diesel showed that it absorbed the 511 nm wavelength of the copper vapour laser. This would affect the use of the laser as the light source for high speed flow visualisation study. Therefore, the alternative choice was to use the

diesel fuel directly from the pump which does not contained any additives in it contents to affect the high-speed flow visualisation study.

Figure 4.4 shows the ECM unit and the CAT communication adapter II. The activation of the HEUI injector required an ECM unit, CAT communication adapter II and the CADeTWin software. The ECM unit and CAT communication adapter II provided the "handshake" to the HEUIB injector by sending an electronic signal using both the communication adapter II software (Figure 4.5) and CADeTWin software as an integrated datalink tool. This electronic signal energised the HEUI injector solenoid, providing precision fuel injection management. The CADeTWin software was a multi-tasking tool developed by Caterpillar to use for testing, performing numerous tasks from software developments, products development and field testing. It has the ability to read and write data, record real-time activities when the program is active. A detail guide of the operation procedures can be found in the manual [2]. In this experimentation, the software was used to control the operation parameters of the HEUIB injector to simulate actual engine operation. Figure 4.6 provides a guide of the operating parameters essential for the operation.

Figure 4.5 CAT communication adapter II software screen.

Channels	Inputs
Internal engine speed override	2000
Injection frequency (Hz)	16.67
Time between injection (msec)	60
cedm (pulse length in μsec)	1500
cedmp {fixed value}	700
Total injection time (msec)	2.2
Oil tank temp.	60
Oil out pressure (bar)	150
Oil out temp	39
Fuel pressure (bar)	6

Figure 4.6 CADeTWin software operation parameters.

4.2.2 Diesel Injector Optical Rig

4.2.2.1 INTRODUCTION

Figure 4.7 shows the Diesel optical injector rig setup with the supporting framework bolting to the floor to prevent any movement generated from the fuel injection cycles. This was also applicable while applying a torque to tighten the bolt when the nozzles were assembled. The picture also showed the engine oil and fuel inlets and outlets were fitted with suitable hoses and fittings for the applications. The optical nozzles shown in figure 4.8 were located between the top jaw and the bottom jaw. The jaws was then closed to tighten the optical nozzles with the help of a tightening nut and a torque wrench located on top of the optical rig (see figure 4.7) and this was achieved by turning the tightening nut in a clockwise direction. This clockwise motion lifted the two jaw guide rods, thereby closing the gap between the top and bottom jaws and locking the optical nozzles with it jaws.

During operation, the pressurised engine oil from the oil pump flat was delivered into the optical rig via a delivery pipe, with an oil drainage pipe to return the engine oil back into the pump. This helps to pressurise the fuel delivered into the HEUI injector via the fuel inlet pipe. To ensure the fuel was delivered with the required pressure, a return valve was fitted on the fuel

return line to regulate the flow. This pressurised fuel was then delivered by the HEUIB injector into the optical nozzles for imaging and analysis.

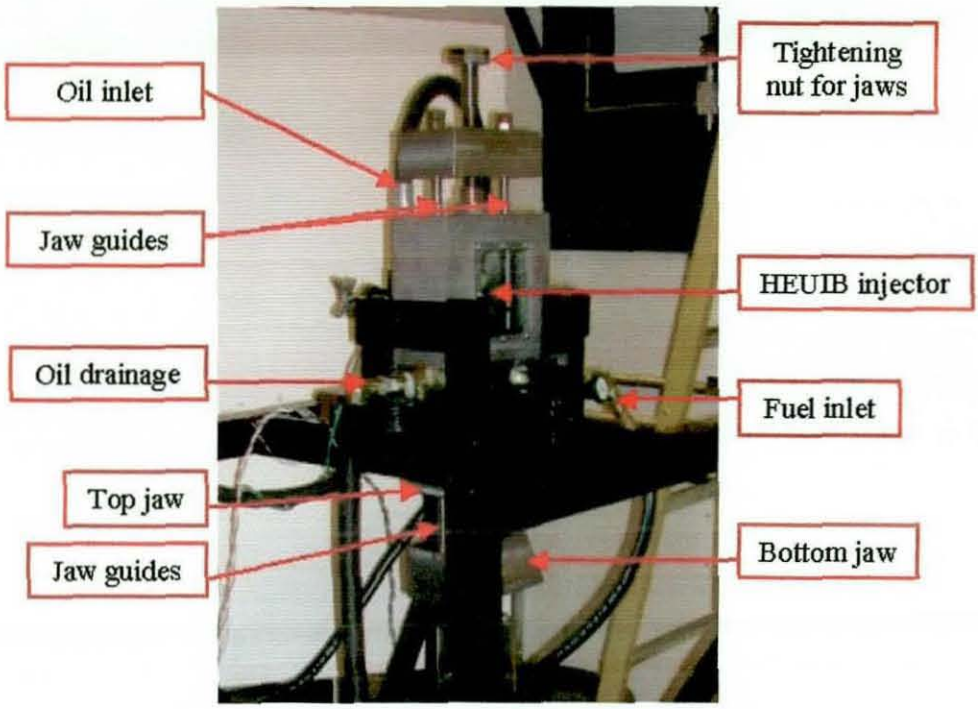

Figure 4.7 Diesel Optical Rig.

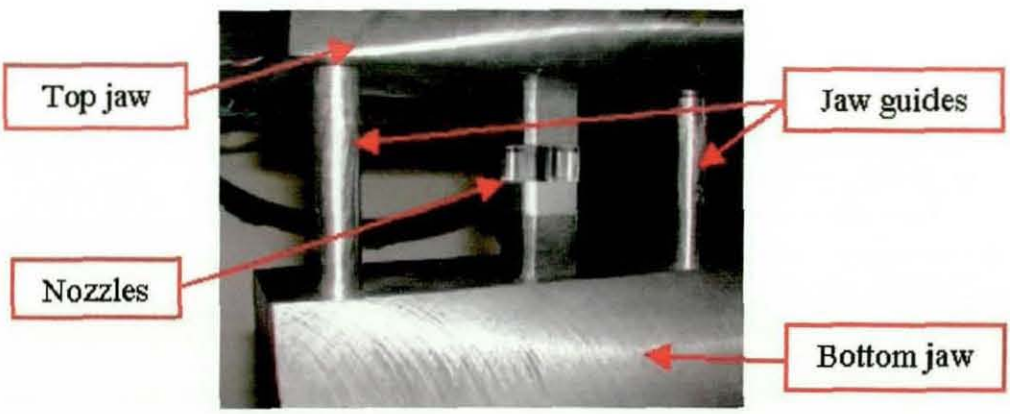

Figure 4.8 Nozzles configuration with top and bottom jaws and guide rods.

4.2.2.2 HEUIB INJECTOR

As mentioned in previous sections, the flow visualisation study of internal flow structures of optical nozzles with high pressure injection required the use of a HEUI diesel injector. The HEUI injector is a commercially available injector for

truck vehicles. The injector is electronically controlled and hydraulically driven. Diesel fuel is supplied to the injector at a pressure of 6 bar and oil is supplied at controlled pressures from 150 to 300 bar. In the injector the oil drives a pressure intensifier providing a 7 fold amplification. In this way the Diesel fuel can be supplied at pressures of 1050 to 2100 bar. This ability to control the injection pressure electronically instead of mechanically provided better fuelling response. In other words, this enabled the injector to operate at operational conditions to simulate actual fuel injection in an enclosed combustion chamber without the need of a crankshaft. This setup makes it feasible to operate the injection system in a laboratory environment.

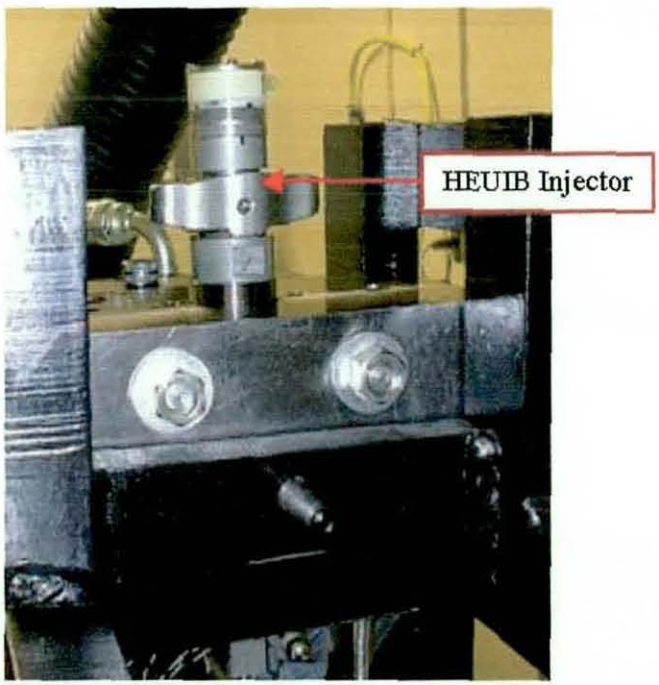

Figure 4.9 HEUIB injector mounted on the diesel optical rig.

4.2.2.3 NOZZLES

The nozzles were mounted between the top and bottom jaws of the optical injector rig (See figure 4.8) was made up of optically accessible sapphire plates. These plates comprised of a series of separate optical sections: an artificial sac, microhole, counterbore and a bottom plate, forming the complete nozzles flow path as shown in Figure 4.10.

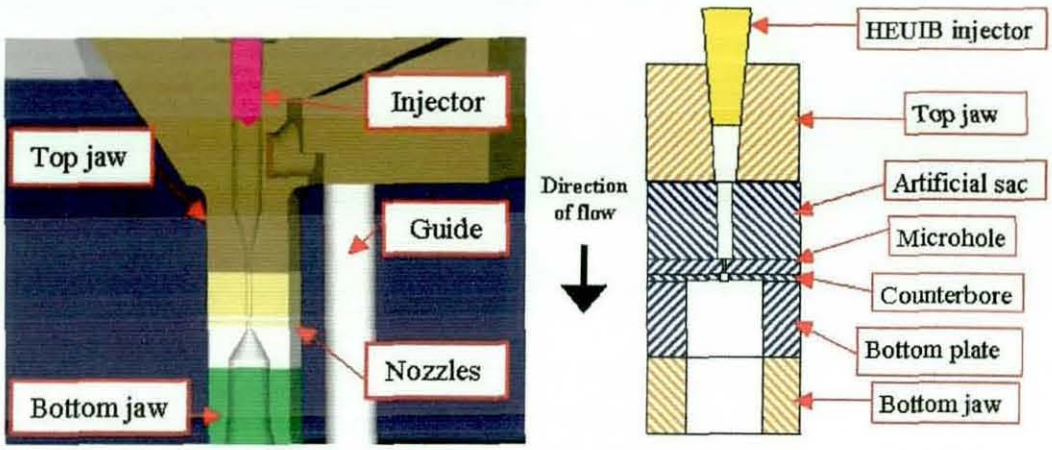

Figure 4.10 Injector nozzles setup schematics.

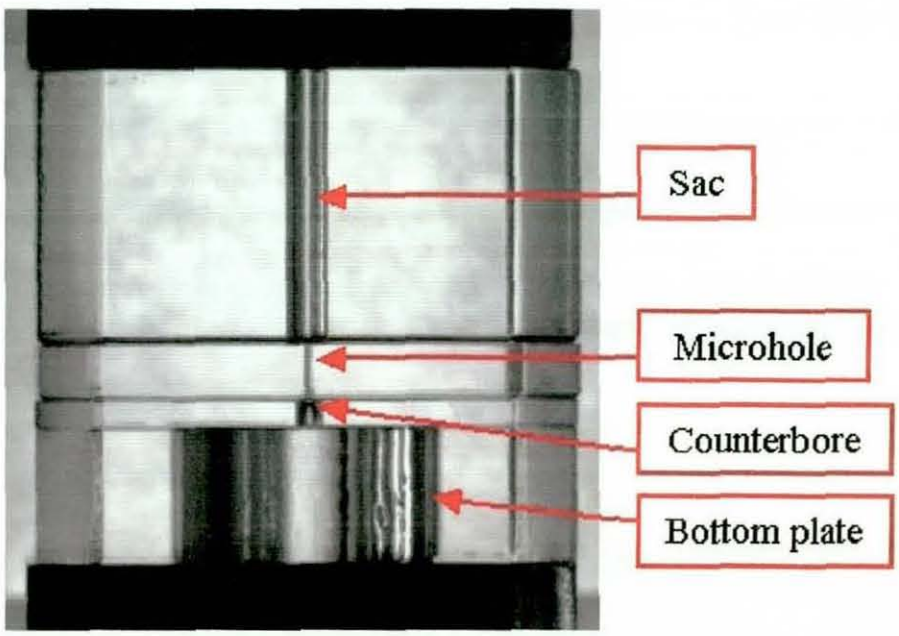

Figure 4.11 Sapphire nozzles matrix assembly on optical rig.

The optical plates were manufactured from optical quality sapphire using electrical discharge machining (EDM) process. This technique is an accurate machining process which allows hard materials to be shaped and with high accuracy. Figure 4.11 shows polished sapphire plates polished with high tolerance, with the holes located centrally in the nozzle. As the sapphire plate matrix was mounted between the top and bottom jaws of the injector rig, a clamping force high enough to seal the optical sections was required to prevent leakage during high pressure diesel fuel injections. A torque of 450Nm was applied through a single centrally mounted lead screw on top of

the optical rig using the torque wrench. This torque applied helped to ensure that the matrix is sealed properly between the jaws and prevent any leakage during full operating pressure conditions.

Plate Name	Thickness (mm)	Diameter (mm)	Inlet Radius (mm)
Sac	10	2	
Thin Microhole	1	0.15	0
	1	0.15	0.02
	1	0.15	0.04
	1	0.15	0.06
Thick Microhole	2	0.3	0
	2	0.3	0.04
	2	0.3	0.06
	2	0.3	0.12
Thick Counterbore	1	1	
	1	0.75	
Thin Counterbore	0.5	0.5	
	0.5	0.75	
Bottom Plate	5	10	

Table 4.1 Sapphire matrix configurations.

The sapphire plate matrix consisted of a series of artificial sac, microhole, counterbore and bottom plate with different thickness, inlet radii and hole diameter were manufactured to understand and improve the nozzles. Table 4.1 shows the numbers of possible matrix configurations with the available plates listed, with the total number of possible configurations stand at 32. The testing of different matrix configurations were conducted in a sequential manner but not all combinations were tested as this was time consuming. However the sapphire nozzles matrix configurations tested were enough to provide a comprehensive study.

4.2.2.4 SAFETY ENCLOSURE

With the use of pump diesel fuel and high pressure injection system, installation of safety screens and proper extraction was essential to ensure safety in the laboratory. The polycarbonate and steel screens protected the rig

operators from any possible rig failure such as fuel or engine oil leaks. Figure 4.12 also showed the safety screens were also attached with red perspex sheet to protect from stray laser beams that might affect operators. These screens also improved the extraction of fuel and engine oil fumes from the optical rig during injection cycles.

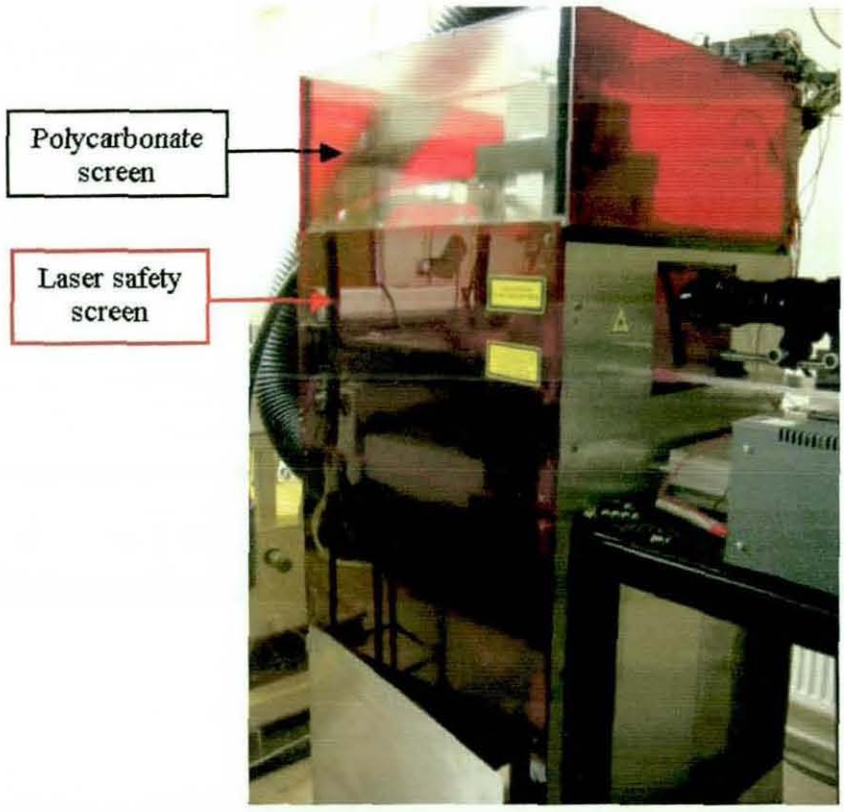

Figure 4.12 The optical rig with polycarbonate and red laser safety screens installed.

4.2.3 Optical Diagnostics Applications

High-speed flow visualisation (HSFV) was the only optical diagnostic tool applied in the Diesel high pressure injection study. This optical diagnostic setup was discussed in details in Chapter 3. Figure 4.12 shows the high-speed flow visualisation setup on the Diesel optical rig. The high-speed camera was mounted on a two-axis traverse system with extension rings, 2X converter and a bellow. This allowed the camera to zoom right up to the nozzles matrix and captured the internal flow structures during the injection process. The fibre optics delivery into the Diesel optical rig using the copper

vapour laser (511 nm wavelength) as the light source was shown in Figure 4.13. A cylindrical lens and a diffuser were placed between the fibre optics and the nozzles to enlarge the laser light and this light was projected onto a curved diffusion screen, providing uniform back illumination to the nozzles matrix.

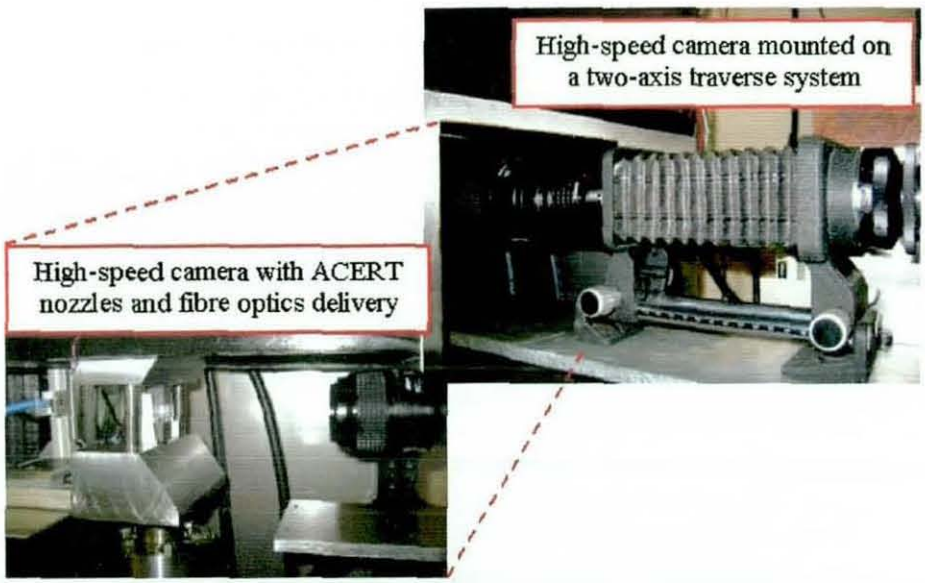

Figure 4.12 High-speed flow visualisation setup on the Diesel rig

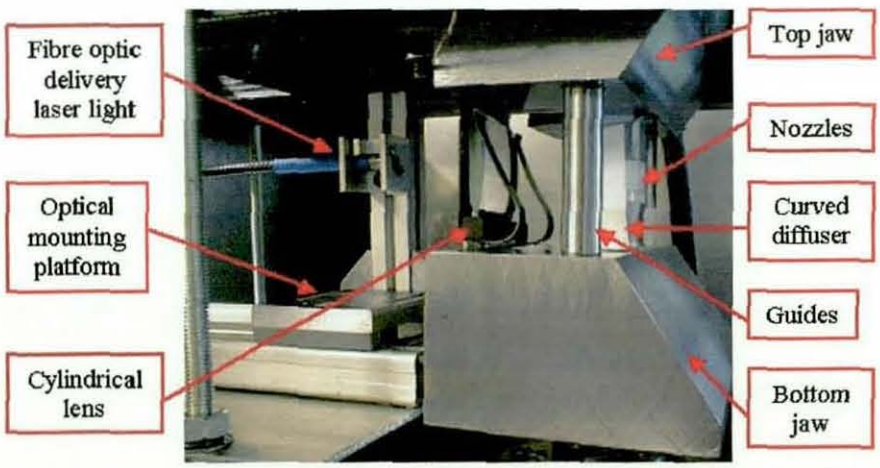

Figure 4.13 The optical back illumination setup with fibre optics delivery.

The copper vapour laser was synchronised with the high speed camera copper vapour laser at both 9 kHz and 18 kHz. High-speed flow imaging at 9 kHz produced an image size of 256 x 128 pixels and running at 18 kHz gave an image of 256 x 64 pixels. The recorded flow videos were stored in an

analysing computer for digitising and analysis. These data were presented as a sequence of images to study the flow characteristic on the investigated nozzle matrix. Due to the amount videos recorded for the various nozzle matrix configurations, only selected flow videos were presented in the following chapter to provide a global view of the internal flow phenomena.

4.2.4 Preliminary Observations and Modifications

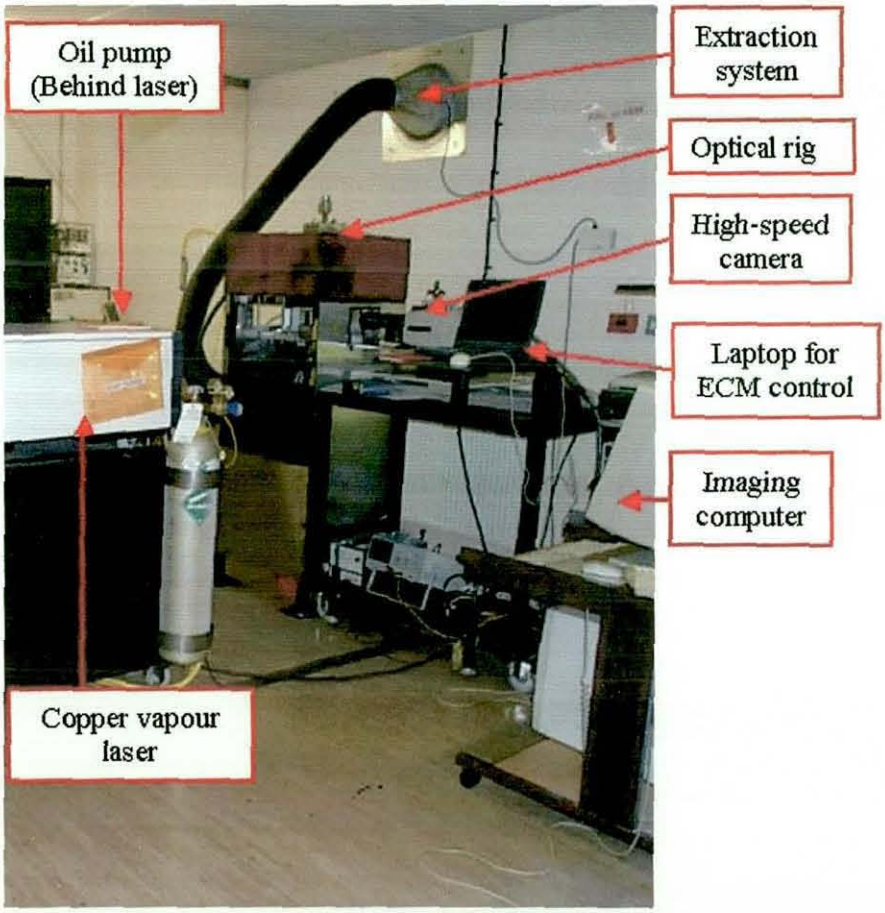

Figure 4.14 The installed diesel injector optical rig.

Figure 4.15 Gasket sealing failure.

The completed Diesel experimental setup was shown in figure 4.14 and preliminary experimental runs were conducted to check the rig operation. This was to ensure the optical rig was able to conduct continuous test runs and also to observe any abnormalities. On the first test run, the oil temperature controller was found to be connected in reverse circuitry on the oil pump flat when the oil began to heat up rather than cool down and vice-versa. To overcome this error, a flow meter close to the heater inlet was installed to monitor the cooling water flow. This also allowed the oil temperature to be changed by adjusting the cooling water flowing through the oil pump flat.

On subsequent test runs in high injection pressure condition, a fuel and oil leak occurred from the injector and oil inlet respectively. A broken O-ring seal from the injector housing caused the fuel leakage into the nozzles and flow abnormalities was observed. The oil leakage was caused by a gasket failure (Figure 4.15) on the optical rig. The spillage could have been worse if not for the installed safety screens, and this prevented a major spill in the laboratory. Improvements to the safety screens were later made to ensure the leakage is fully enclosed.

The most significant problem encountered was the regular rate of sapphire failure in the initial commissioning phase of the experimentation that took several weeks to resolve. The breaking of sapphire plates perpendicular to the line of the steel rod guides shown in Figure 4.16 suggested that the two steel guide rods were not level. This was confirmed by the use of pressure sensitive film to check the flatness of the jaws caused by the steel guide rods. Attempts were made to level the steel guides using stainless steel washer and altering the locking nuts position but to no avail. Inspection of steel artificial sac and bottom plate was conducted and gaskets were also used but these did not help in reducing the breakages. However an inspection on the top and bottom jaws discovered an imprint of the bottom hole could be seen on the top jaw, polishing was attempted but did not make any significant change to the surface. The optical rig was therefore disassembled and the jaw surface flatness measured, and was found to be 10.9 μm for the bottom jaw and 35

μm for the top jaw. The jaws were then reground to a surface roughness and flatness of 1.3 μm (bottom) and 1.6 μm (top). This proved to work effectively as the number of sapphire plates breakage was reduced to the occasional odd one.

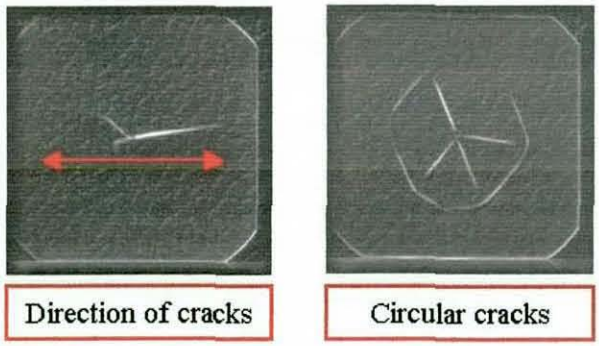

Figure 4.16 Straight line cracks and circular cracks.

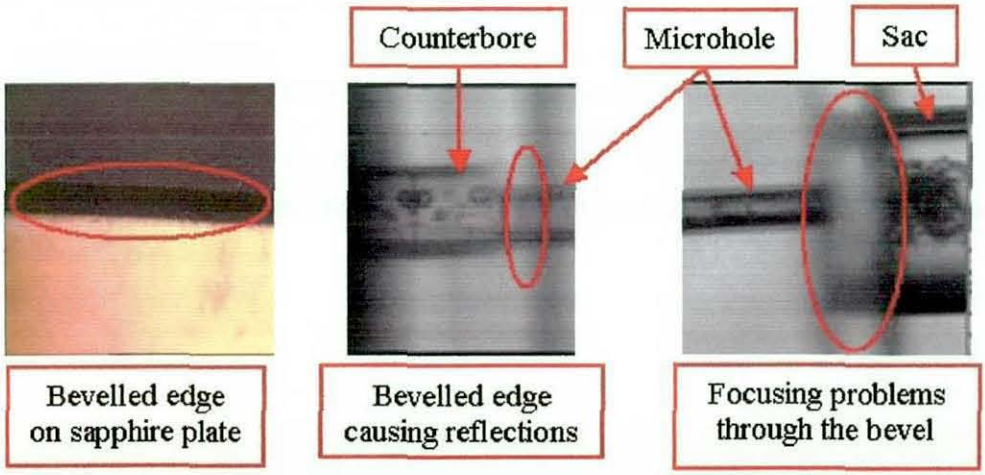

Figure 4.17 The effects of bevelled edge on sapphire nozzle on image quality.

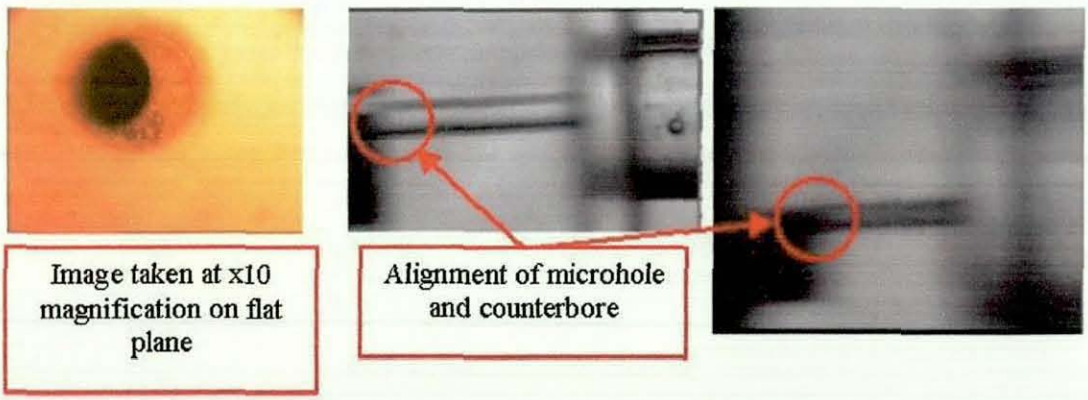

Figure 4.18 Alignment of the sapphire plates.

The use of torque wrench to seal the optical sections was also modified to remove the jerkiness caused by the wrench when the pre-set torque was reached. A minimum of two person were also required to apply the force to the torque wrench at the final stage just prior to a point where the maximum torque (450 Nm) was reached. Stopping just before the maximum torque meant that the final click of the torque wrench did not occur, and therefore did not send a vibration down to the sapphire. One other noticeable cause for sapphire nozzles breakage was the injection rate and pressure. For the thick microhole and thick counterbore this mainly occurred at 250 bar, 2000 rpm (equivalent speed) and 3.3 msec injection period. For the set of thin plates this normally occurred at the lower pressure of 200 bar, 200 rpm and 3.3 msec. This restricted the injection pressure and period used for different sapphire nozzle matrix.

The use of high-speed flow visualisation required the nozzles used to be of optical quality. However the quality of the sapphire plates received by Caterpillar research from the sapphire manufacturer was not up to optical standards. All the edges of the sapphire plates have bevel on them, stopping the optics from focusing on the holes within the plates (Figure 4.17). These edges also created reflections and distort the images captured by the high-speed camera. Some of the plates were noted to be slightly uneven when placed on an optical table top, which meant that they were likely to break once clamped between the jaws. Others sapphire plate's side was noted to be pitted or scratched on the sides when examined under a microscope resulted in poor images obtained. One other flaw discovered on some of the plates were the position of the holes were not located centrally, resulting in misalignment of the plates within the jaws (Figure 4.18).

Despite all the problems associated with the experiments, some of the straightforward problems like o-ring failure and gasket cracks were resolved. For the problems associated with sapphire quality, this was beyond our control. However, it was still possible to obtain some good quality internal flow videos from the existing sapphire plates and observing the flow developments.

This allowed detail analysis of the internal flow structures which was useful in understanding high pressure Diesel injection.

4.3 GASOLINE INJECTION OPTICAL TEST RIG

4.3.1 Developments

The ability to inject fuel directly into the combustion chamber has made the GDI engine the choice for the next generation of passenger cars. As detailed in chapter 2, GDI was preferred with its superior volumetric efficiency, fuel economy, power output and better emission control compared with MPI and SPI system. The main component that has made GDI so successful is the ability to accurately control fuel injection directly into the combustion chamber, instead of the inlet port. When pressurised fuel is pumped into the combustion chamber via the injector, the flow generated depends on the type of injector and the geometry of the piston's crown. These affect the amount of swirl or tumble generated and dictate the shape of the spray structures and atomisation present in the combustion chamber. These promote better mixing of the charges before the ignition of the spark plugs compared to the conventional intake port injector.

A few design considerations were considered before an optically accessed injector test rig was constructed. The first design consideration was the rig must be able to investigate internal and external flow phenomena in a laboratory based environment and able to incorporate two-dimensional and three-dimensional optical nozzles. It must also be easily accessible to employ different optical diagnostic techniques and the ability to withstand high injection pressure up to 150bar. The other major consideration is the fouling to the optical windows should be none or minimum from continuous and multiple injection measurements.

With these design considerations, an optically accessed injector test rig was manufactured as shown in Figure 4.19. The rig was manufactured from aluminium material to limit the weight of the rig, allowing easy transportation

for different optical diagnostic applications. The optical rig has a high pressure fuel inlet fitting for high pressure fuel injection. A separable mounting assembly was also made to enable easy access to optical components for rapid installation and uninstallation between different geometrical arrangements. This allowed non-intrusive optical diagnostic techniques to be employed in the internal flow study.

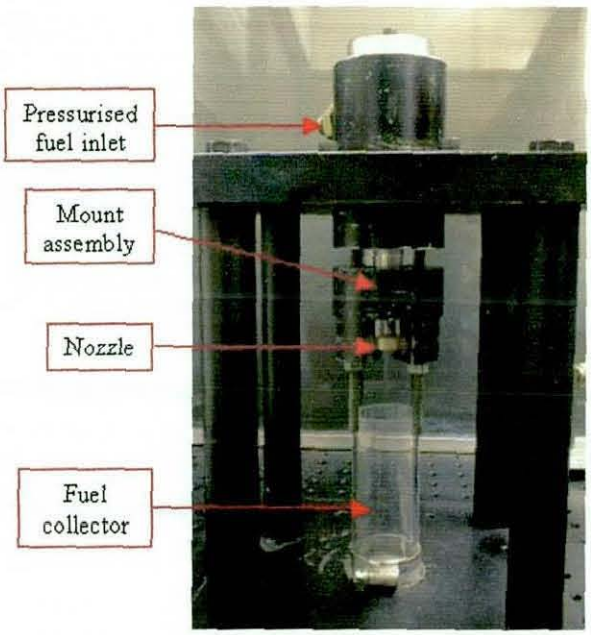

Figure 4.19 GDI optically accessed injector test rig.

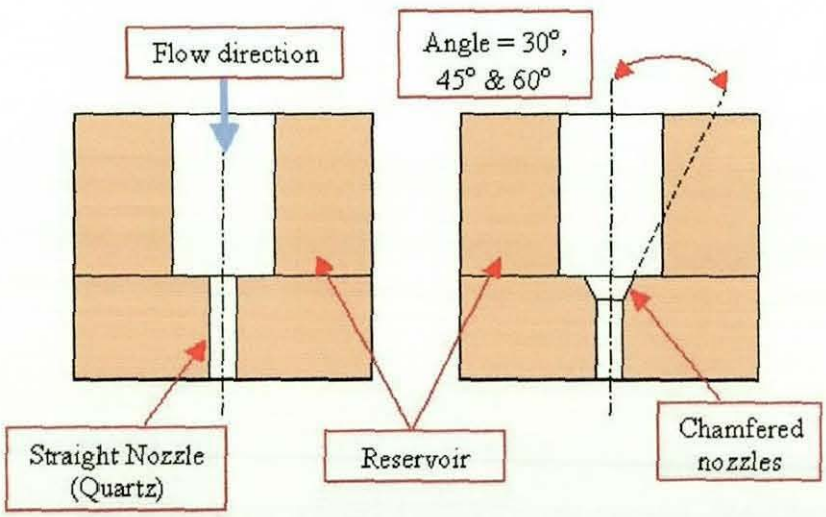

Figure 4.20 Schematic of straight inlet and chamfered inlet nozzles.

The optical nozzles themselves were manufactured from a range of different materials like fused silica and perspex. All were optically polished internally and externally to achieve good surface finishes, to minimise distortion of the fluid flow paths and optical light paths into the nozzles. These nozzles were manufactured from flat plates of the chosen transparent medium in a range of different thickness to accommodate the desired nozzle geometry and structural integrity to allow the working pressures of up to 15MPa to be applied. Length to diameter (L/D) ratios from 4 to 6 and entry conditions from sharp edged to 120° chamfers have been evaluated (Figure 4.20).

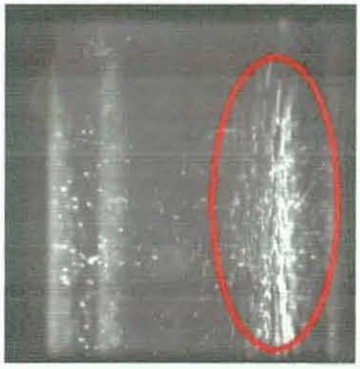

Figure 4.21 Figure showing perspex nozzles with hairline cracks.

The initial optical components were constructed from perspex to study the feasibility of this material under high pressure injections. These perspex nozzles were manufactured in-house with high optical accuracy. However, hairline cracks develops (see figure 4.21) after a few high pressure injection runs which render these nozzles useless for continuous studies. Subsequent nozzles were made from fused silica as real-sized injector components and the reservoir with perspex, as this does not interfere with the investigation of the nozzle flow characteristics.

A schematic diagram to describe the internal arrangement of the nozzle/swirler system is given in figure 4.22. The fluid flow path into the optical nozzle may either be completely unobstructed, which leads to a simple plain orifice flow, or may be directed by the insertion of different flow guiding devices just above the optical orifice. This allows swirl generators of different swirl ratios to be fitted and the inclusion of pintle tips close to the orifice

entrance. These different entry conditions thus allow the same orifices to be studied both as plain orifices and pressure swirl atomisers with varying flow rates and swirl ratios and also allows the accurate reproduction of real GDI nozzle geometries. As well as simple straight orifices alternative entry and exit conditions have been manufactured in order to study the effects of these conditions on the fluid flow. Table 4.2 shows the types of quartz nozzles used in the GDI injector nozzles study.

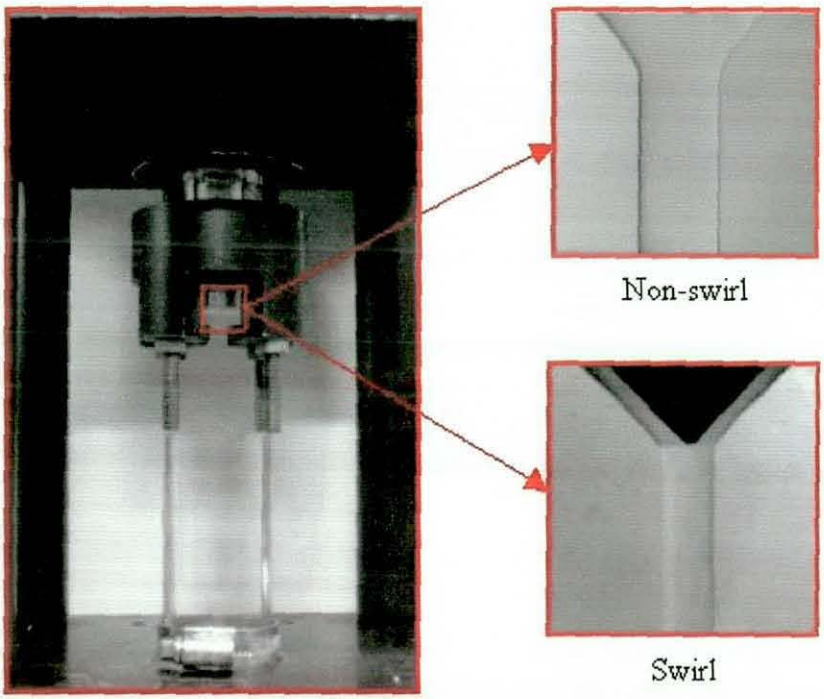

Figure 4.22 Schematic of nozzles with swirlers.

Nozzles	Overall Thickness	Diameter	Inlet Angle	Chamfer Thickness
Sharp inlet	6 mm	1 mm	0°	0 mm
30° chamfer	6 mm	1 mm	30°	2 mm
45° chamfer	6 mm	1 mm	45°	2 mm
60° chamfer	6 mm	1 mm	60°	2 mm

Table 4.2 Nozzles used in experiments.

The fuel delivery system was setup and incorporated onto the optical injector rig via a pipe fitting on the top of the optical rig body. This system enabled any liquid fuel to be supplied at any pressure from 1 MPa to 15 MPa using a controlled supply of nitrogen gas. This was achieved by storing the liquid fuel

in an accumulator (Figure 4.23) which was pressurised by a nitrogen gas supply to the required pressure before each controlled injection. A solenoid control valve (Figure 4.24) was attached to the head of the test rig to simulate actual injection processes to allow better control, of injection timing and pressure in the rig. This was thought to be more reliable and precise than manual actuation to simulate injection process. The optical rig was filled with test fluid and pressurises with nitrogen gas to the required pressure. The integrated solenoid valve was then actuated to activate the injection process, about 40ms-60ms before the solenoid is de-energised and stop.

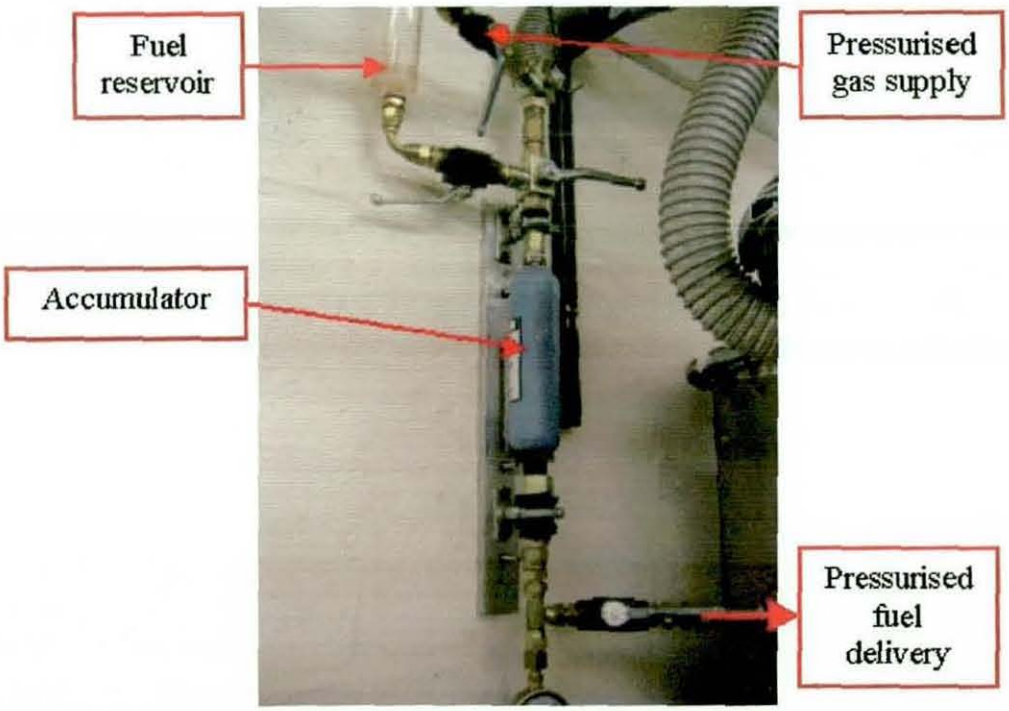

Figure 4.23 Fuel delivery with accumulator setup.

The fuel delivery system allowed any liquid fuel (white spirit, gasoline and diesel) to be supplied into the optical injector rig, with the principle liquid fuel used in all GDI experiments was white spirit. White spirit is a petroleum derivative with a density, viscosity and refractive index (Table 4.3) similar to that of gasoline fuel. However, it is slightly less volatile and flammable than gasoline and offers a safer alternative for laboratory studies. It is also available in low, regular and high flash versions, the latter having a vapour

pressure very similar to gasoline. The whole rig was sealed from any fuel sprays or vapours generated by using suitable extraction system.

Figure 4.24 Optical rig mounted with solenoid control valve.

	Refractive Index	Density (kg/m^3)	Kinematic Viscosity (m^2/s)
Air	1.0	1.23	1.46×10^{-5}
Hydrogen	-	8.38×10^{-2}	1.05×10^{-4}
Diesel	1.6	830	3×10^{-6}
Gasoline	1.45	680	4.6×10^{-7}
Perspex	1.49	-	-
Quartz	1.5	-	-
Sapphire	1.8	3.98×10^{3}	-
White spirit	1.44	780	1.44×10^{-6}

Table 4.3 Properties of different medium.

4.3.2 Optical Diagnostic Applications

4.3.2.1 OVERVIEW

In the previous section, experimental apparatus and procedures for GDI experimentation was detailed. It also highlighted that considerations were made to ensure several laser optical diagnostic techniques could be used to conduct experiments with different optical nozzles. The following sub-sections

provided in-depth discussion and setup details for the three optical diagnostic techniques employed in this study, namely: high speed flow visualisation, fluorescent particle image velocimetry and phase Doppler anemometry.

4.3.2.2 HIGH SPEED FLOW VISUALISATION (HSFV)

High-speed flow visualisation study is a commonly used optical diagnostic tool to provide an insight on the spray characteristics and flow structures of the GDI injector. It has the ability to observe any variations in the internal flow structures and compared with predicted results.

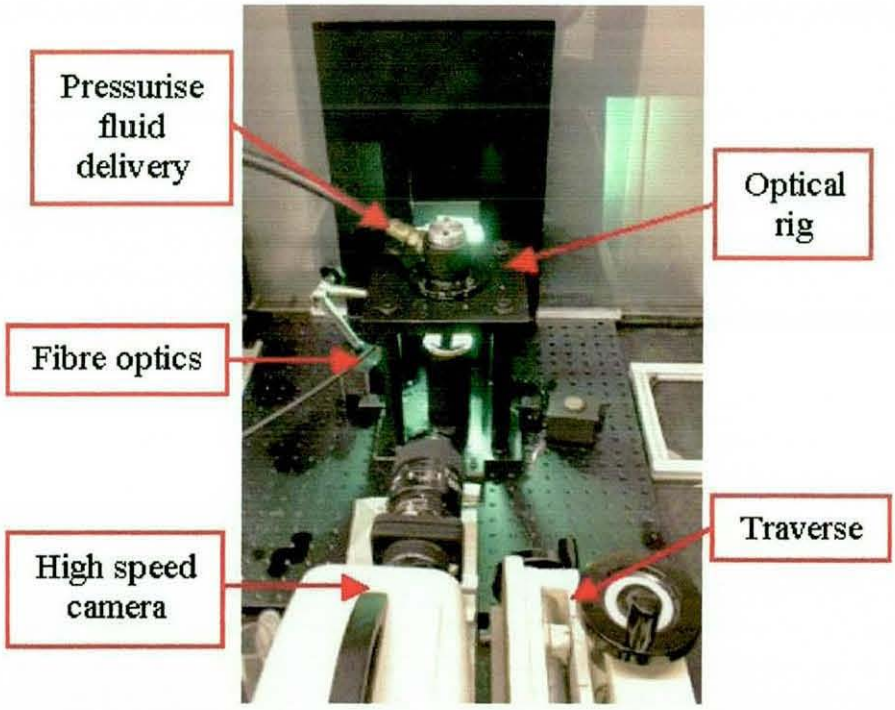

Figure 4.25 HSFV setup for GDI injector nozzle study.

Figure 4.25 showed the HSFV setup used in the study of internal and external flow structures of GDI injector nozzles. Fibre optics was used to deliver the laser light source to the back of the optical rig and provided a uniform back illumination through a diffuser. The same high speed camera mounted on a two-axis traverse system for Diesel injection was used in this study, with the Kodak high speed camera running at 9000 frames per second. The high speed camera was attached with a Nikon 105 mm macro lens, a bellow and a

2x converter to image a region of 6-8 mm square area depending on the optical nozzle geometry investigated. A series of flow videos were recorded based on the nozzle geometry shown on Table 4.2. These videos were stored in the high-speed camera processor before transferring to the analysing computer for converting to images for later analysis. These images will be presented as a series of pictures in Chapter 6 for discussion and analysis.

4.3.2.3 FLUORESCENT PARTICLE IMAGE VELOCIMETRY (FPIV)

Fluorescent particle image velocimetry was the other laser diagnostic used to investigate the optical nozzles internal flow structures. The FPIV system used consisted of a TSI new wave double-pulsed Nd:YAG laser (532 nm wavelength) for the light source and a Kodak Megaplus ES 1.0 camera (1008 x 1018 pixels) to capture a sequence of image pair.

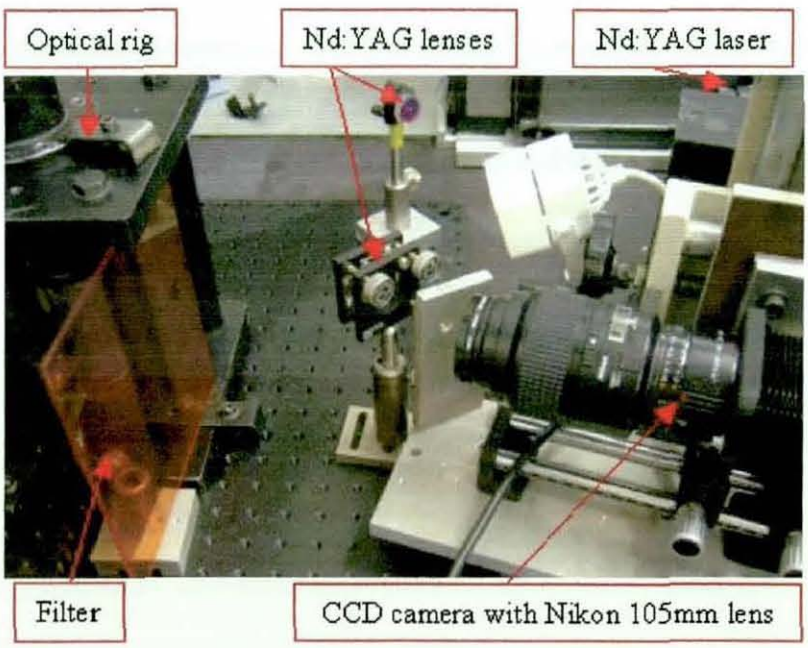

Figure 4.28 FPIV experimental setup.

During experimentation, the Nd:YAG laser was synchronised with the CCD camera through a synchroniser box. With the image region size of 6 to 8 mm, a pulse separation of 1 μsec between frames was set. As mentioned in section 3.3.2 of chapter 3, fluorescent seeding particles (1-6 μm size) was introduced into the flow. This was the only feasible way to remove the

massive amount of scattering caused by the quartz glass and the fluid and also between the liquid and the aircore. The Rhodamine 620 fluorescent seeding particles used also allowed better tracing of fluid motion in high swirl injectors. The light scattered by the fluorescent seeding particles was recorded by the CCD camera and then analysed using cross-correlation method with a 64 x 64 pixels interrogation region and a 50% overlap. A FPIV setup with the optical rig, Nd:YAG laser and the CCD camera was shown in figure 4.28. A filter was placed in front of the CCD camera to prevent speckles from affecting the images recorded.

Following standard DPIV practice [01], the imaging was controlled to ensure the particle image size was between 2.5 and 3 pixels on the CCD to prevent errors from peak locking. Also the laser pulse separation time was controlled to ensure that the maximum displacement was less than a quarter of the interrogation region length. Based on the error analysis provided by Anandarajah *et al* [01] the mean bias error for the velocity measurement was 3%.

4.3.2.4 PHASE DOPPLER ANEMOMETRY (PDA)

With the use both HSFV and FPIV to investigate the internal flow structures of the GDI nozzles, the last optical diagnostic used in this study was the well-established phase Doppler anemometry. These diagnostic techniques helped to link the internal flow structures to the atomisation processes, to quantify the spray characteristics and atomisation processes from the GDI nozzles investigated.

The experimental setup for PDA technique was shown in Figure 4.29. The optical rig was mounted on a 3–axis traverse system, allowing easy movement and positioning of the optical rig for each measurement. The initial position of the transmitting optics allowed the laser beams crossed the centre of the 1 mm nozzle exit. Argon-ion laser with a 514 nm wavelength provided the light source and this single laser beam was spilt into two beams with a separation of 38 mm. These two beams were then transmitted out through the

transmitting optics and onto the optical rig with a focal length of 310 mm and a known distance below the nozzle exit. The receiver in the figure had a scattering angle of 70 degrees, with respect to the transmitting optics.

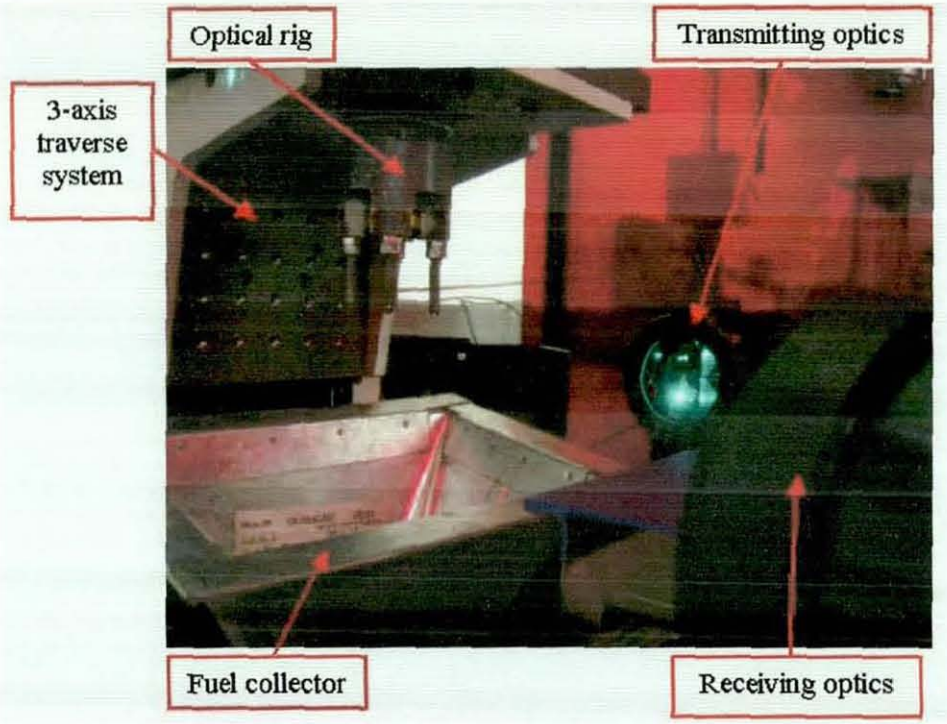

Figure 4.29 PDA technique experimental setup.

Figure 4.30 shows the schematic setup for measuring the particle velocity and dropsize and the measurement was taken at a fixed height below the nozzle outlet. As mentioned from previous paragraph, the GDI optical rig was mounted on a three axis precision traverse system, two horizontal (X-Y axis) and one vertical (Z axis), to position the spray in three dimension relative to the static PDA system. The traverse system calculated it movement in inches due to the nature of this particular system and therefore, all directional movements was done in inches to simplify it use. For every 1000 steps the traverse system travel, this was equivalent to 1.27 mm in any axis direction. Therefore, the measured spray is placed 88.9 mm below the nozzle exit. This distance was used so as to minimise the effect of dense spray affecting data collection as highlighted in the literatures [5,7]. For each radial measurement, it started from the geometric vertical axis through the centre of the nozzle exit and traverse outwards. This radial increment inside the hollow cone of the

spray was set at 1000 steps as shown in figure 4.30, until the external boundary of the spray cone was reached.

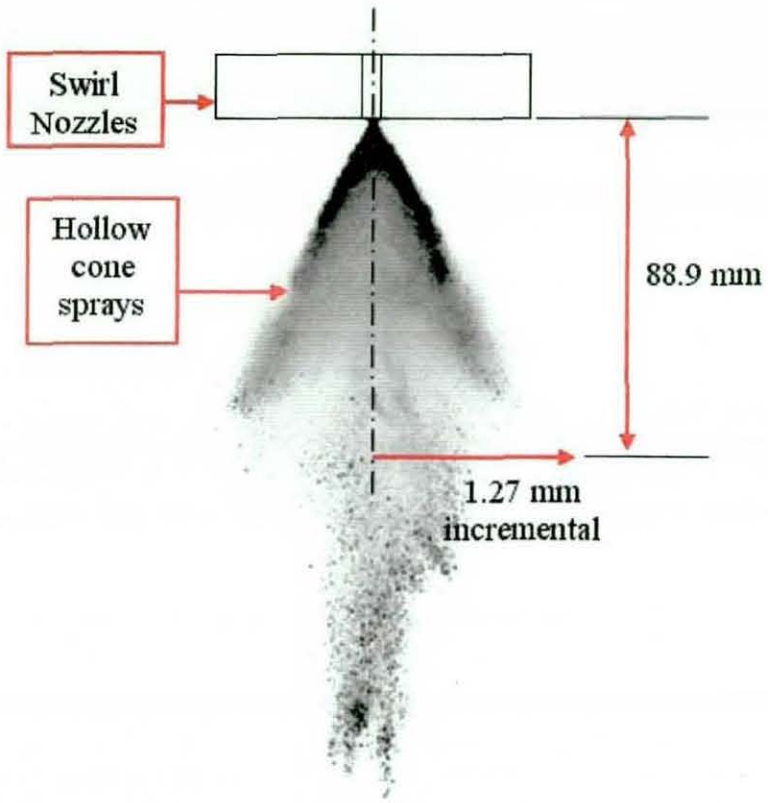

Figure 4.30 Schematic of PDA measurement with hollow cone spray.

With the PDA system setup, data collection and processing was controller by the SIZEware software via the PDA processor. A minimum of 3000 samples of spherical droplets was collected for validation and also with a 60 seconds time out. The samples data was then processed and analysed, to obtain droplets velocities and sizes in D_{10} or D_{32} (Sauter mean diameter). This was useful to provide qualitative data on the exit flow, relative to their position in the hollow cone spray structures.

The accuracy of the velocity and particle size measurements from the PDA system is dependent on the definition of the fringe spacing and the measurement of the Doppler frequency. The fringe spacing is calculated simply from the geometry of the intersecting laser beams and can be defined to ±0.25%. Using the Dantec PDA processor, using burst spectrum analysis,

the frequency and phase change of the Doppler signal can be measured to an accuracy of ±0.5%.

Errors in the measurement arise from:

- High seeding density resulting in multiple scattering within the control volume,
- Non-homogeneous droplets (variable refractive index),
- Non-spherical.

An assessment of the errors for the current measurement has estimated the accuracy of the mean velocity to be ±2% and the SMD to be ±3%.

4.3.3 Preliminary Observations and Modifications

The gasoline optical rig was able to achieve the design requirements and experimental tasks discussed. The initial experiments showed hairline cracks developed from repeated usage of the perspex nozzles under pressurised condition shown in figure 4.21. This resulted in the switch from using perspex nozzles to quartz nozzles. However, quartz nozzles were also susceptible to cracks shown on subsequent experiments. One such crack was during one of the FPIV experiment. The amount of energy generated by the surelite laser caused a crack and burned marks on the quartz nozzle. Extra care was taken later to make sure the energy used for illumination was reduced and also by using another laser (new wave PIV laser) with lower energy. One other issue regarding crack and leaks were discovered under high injection pressure of 60bar. The result of the pressurised fluid flow acting on the nozzle created catastrophic effect to the quartz nozzle. To overcome this problem, a counterbore was added to provide extra support and also with a large enough hole diameter to ensure that it would not affect the flow characteristics. Gaskets were also used to improve the sealing between the optical reservoir and the nozzle, minimising or stopping leaks under high injection pressure.

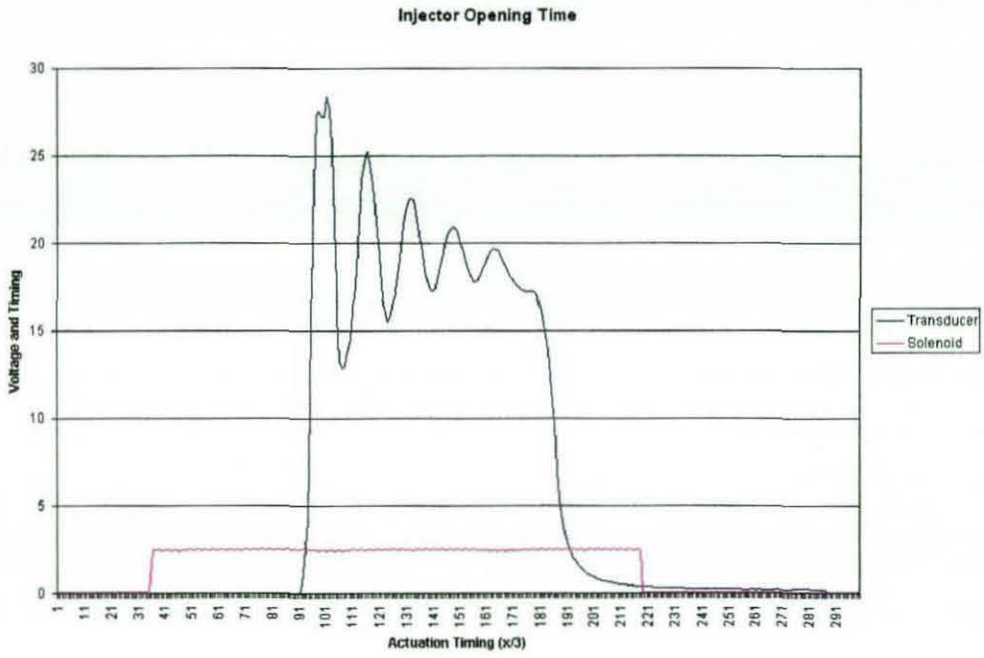

Figure 4.31 Short transducer pressure reading recorded.

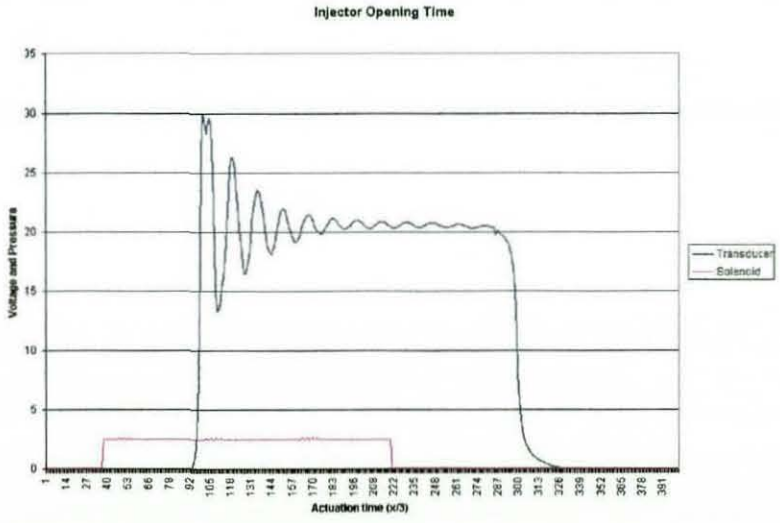

Figure 4.32 Long transducer pressure reading recorded.

As discussed in previous sections, the use of solenoid control valve was abandoned in later experiments as it was not possible to provide consistent and maintain short injection duration throughout the each nozzles configurations. In most initial experimental runs, the actuation timing of the solenoid was set at 60 ms for the whole duration of the injection flow as seen from figure 4.31. However, this actuation timing was not consistent and the some spray structures was not fully developed during recordings. This was

also recorded in the in-house software that was used to track the injection pulse and pressure. Figure 4.31 shows a shorter injection pulse with figure 4.32 showed the actual injection pulse of 60 ms. However this did not affect the injection pressure, as same readings were comparable with those recorded on the pressure gauge. To overcome this deficiency in the solenoid valve, a manual actuated control valve was later attached to the head of the optical rig instead of the solenoid valve to allow manual actuation for each injection process. This allowed relatively slow pressure rise in the reservoir and operates in a steady state condition. This mode of operation is particularly useful for PDA measurements due to the amount of time taken to collect 3000 droplets for measurement.

4.4 SUMMARY

This chapter provided detailed documentation and setup for both Diesel and gasoline injectors studies. These included the various optical diagnostic tools used and their application in both injectors. In Diesel injector optical rig, the only optical diagnostic applicable was the HSFV technique to provide an understanding the effects of cavitation and flow interaction by various matrix configurations and charge pressure used. The use of HSFV, FPIV and PDA techniques for Gasoline DI study allowed the understanding of flow characteristics from the internal flow regimes to the generation of sprays and atomisation as the pressurised fluid exited from different nozzles configuration. The results from both injectors were presented and discussed in the following two chapters.

4.5 REFERENCES

[01] Anandarajah, K., Hargrave, G.K., Halliwell, N.A, *Time-Resolved Digital Particle Image Velocimetry (DPIV): Error Reduction from Normalisation by Signal Strength (NSS)*, International Conference on Advanced Optical Diagnostics in Fluids, Solids and Combustion, V0015, Tokyo (Japan), 4-6 December 2004

[02] Caterpillar Inc, *A Guide to Using CADeTWin*, version 2.78, Measurement Systems Development, 1997-2001

[03] Caterpillar News, *CAT engines with ACERT technology* (http://www.cat.com/about_cat/news/03_products_n_services/getprdata.html?file=enginesepgindustrial051909114.dat&callingdoc=/about_cat/news/03_products_n_services/products_n_services.html&init_section=newsparts&origindoc=/products/engines_n_power_systems/service_n_support/01_press_releases/press_releases.html), 13.05.2003. [16.12.2003]

[04] Caterpillar: HEUI Fuel Systems (http://www.caterpillar.com/products/shared/parts_n_service/03_engine_parts/03_spec_sheet_library/pdf/pehp9526.pdf), 1999, [03.05.2004]

[05] Lading, L., Wigley, G., Buchhave, P., *Optical Diagnostics for Flow Processes*, Plenum Press, 1994, ISBN 0-306-44817-3

[06] Motion Analysis Systems, *Kodak Ektapro HS Motion Analyser: User's Manual Model 4540*, 1993, P/N 91000046-001.

[07] TSI Incorporated, *Insight: Particle Image Velocimetry Software*, version 3.3, Dec 2000, P/N 1990010.

[08] Wigley, G., Hargrave, G.K., Heath, J., *A High Power, High Resolution LDA/PDA System Applied to Dense Gasoline Direct Injection Spray*, 9th International Symposium on Application Laser Technology to Fluid Mechanics 1, Paper 9.4, 1998

CHAPTER 5

DIESEL INJECTION STUDIES

5.1 INTRODUCTION

In the previous chapter, details of the Diesel injection system setup and the optical diagnostic techniques used were presented and discussed. This chapter presents the data collected from the high-speed flow visualisation study. Detailed flow images are presented, with analysis and discussion of the data based on microhole, counterbore sapphire plates and charge air back pressure.

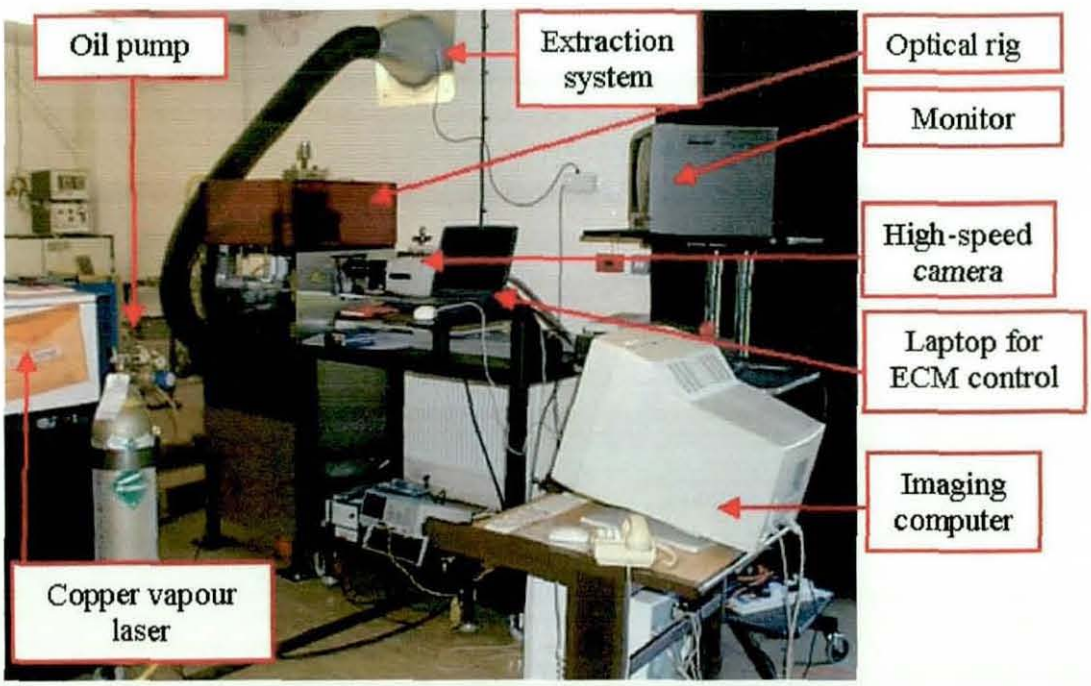

Figure 5.1 Image of the test rig.

Figure 5.1 shows the setup for the whole test facility used in the laboratory for the high-speed flow visualisation study. The Diesel optical rig was enclosed within a protective screen to prevent vapour fumes from leaking into the laboratory and allow the fumes to be removed by the extraction system. The protective screen also prevented stray laser beams.

Pressurised fuel was supplied to the HEUI injector from the oil pump and fuel pump flat. The copper vapour laser provided the light source for back illumination into the nozzles, with the high-speed camera capturing flow field images and storing in the imaging computer. A laptop computer controlled the injection of the HEUI injector through the ECM unit.

5.1.1 Flow Visualisation Study

High speed flow visualisation was the only optical diagnostic technique used in the Diesel injection study. The primary purpose of the flow visualisation was to provide an insight into the spray characteristics and nozzle internal flow structures of the nozzles and to observe any variation in flow structure with different nozzle geometries and operating conditions. Figure 5.2 shows the sapphire nozzles matrix with uniform back illumination through a cylindrical lens and a curved diffuser. The laser light from the copper vapour laser was delivered to the test section via the fibre optic cable shown. Flow videos were recorded at 9,000 frames and 18,000 frames per second, providing in-depth analysis of flow structure with different nozzle geometries. Depending on the final imaged area, the resolution of the imaging ranged from 15 to 45 micron per pixel.

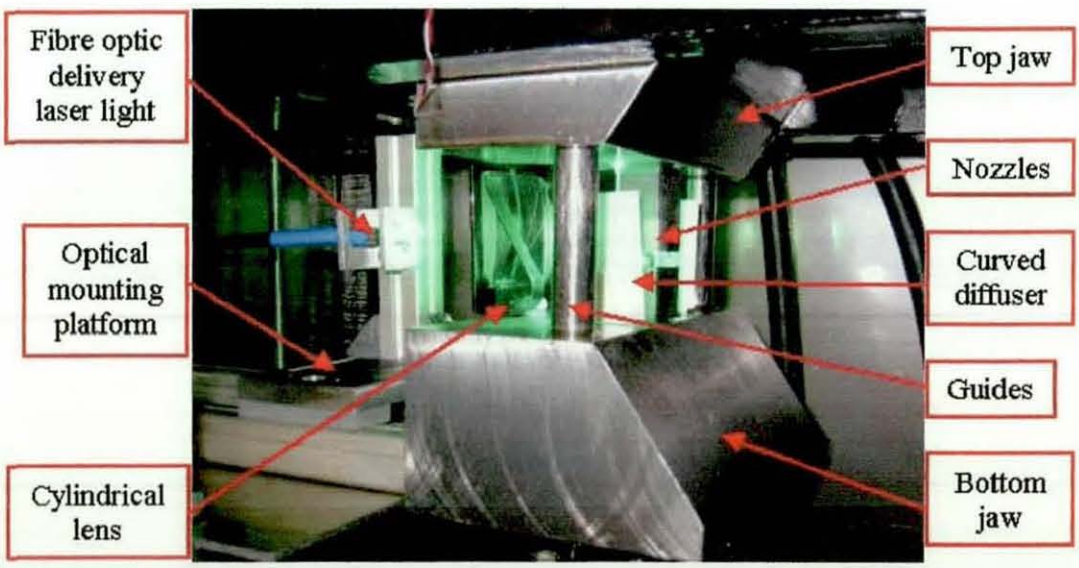

Figure 5.2 Optical fibre delivery to sapphire matrix.

Although Table 4.1 from chapter 4 showed that 32 matrix configurations were possible from the various sapphire plates, it was not necessary to experimentally define the flow structure for every configuration, as some of the geometries are very similar to the each other. The experimental results are presented and analysed based on the microhole, counterbore geometry and charge air back pressure. The microhole section was sub-divided into inlet radii geometry and microhole diameter. The study of charge air back pressure was also sub-divided into sapphire matrix with and without counterbore plate.

5.2 RESULTS AND ANALYSIS

5.2.1 Microhole

The investigation of the microhole is one of the most important parameters in trying to understand the flow characteristics of the injector. The first stage is to look at the microhole inlet radius and diameter to identify trends in the flow. This set of results was conducted under 1 bar charge air pressure conditions.

5.2.1.1 INLET RADII

Microholes of different inlet radii ranging from 0 mm (no radius) to 0.12 mm radius were investigated. Each data set presents a sequence of images of the flow process in the microholes. This is to investigate whether radius has any effects on either cavitation in the microhole or flow in the counterbore.

Figures 5.3 to 5.6 present a sequence of flow images involving the use of a 0.3 mm diameter microhole, with inlet radius ranging from 0.0 mm to 0.12 mm. Figure 5.3 shows the matrix with the sac, microhole (0.0 mm inlet radii) and counterbore, with a driving pressure of 1050 bar. As can be seen in the figure, when the injection sequence starts, the injected fuel flows into the sac and into the microhole, replacing the trapped air in the microhole (0 ms to 21.31 ms). Cavitation can be seen forming from the sharp edge of the nozzle inlet after 35.8 ms. The cavitation, characterised by the bubbly flow that stretches

from the microhole and into the counterbore, can be seen from 35.19 ms to 36.52 ms as the flow develops and reaches peak pressure.

This is illustrated further from figures 5.4 to 5.6, which show similar cavitation phenomena. With increasing inlet radius there was no observed variation in the cavitation in the microholes. However, it is important to note that the radii were not exactly known and much reliance was placed on the manufacturers to provide the design geometry. Although the microholes were examined under a microscope, it was not possible to measure or observe any difference in the radius with sufficient confidence. Ohrn *et al* [06] also have similar problems with the tolerance of their inlet radii study with different nozzle hole size. Despite this uncertainty in absolute values for the radii, it is still possible to note that a large variation in radius did not seem to affect the cavitation structure in the nozzle.

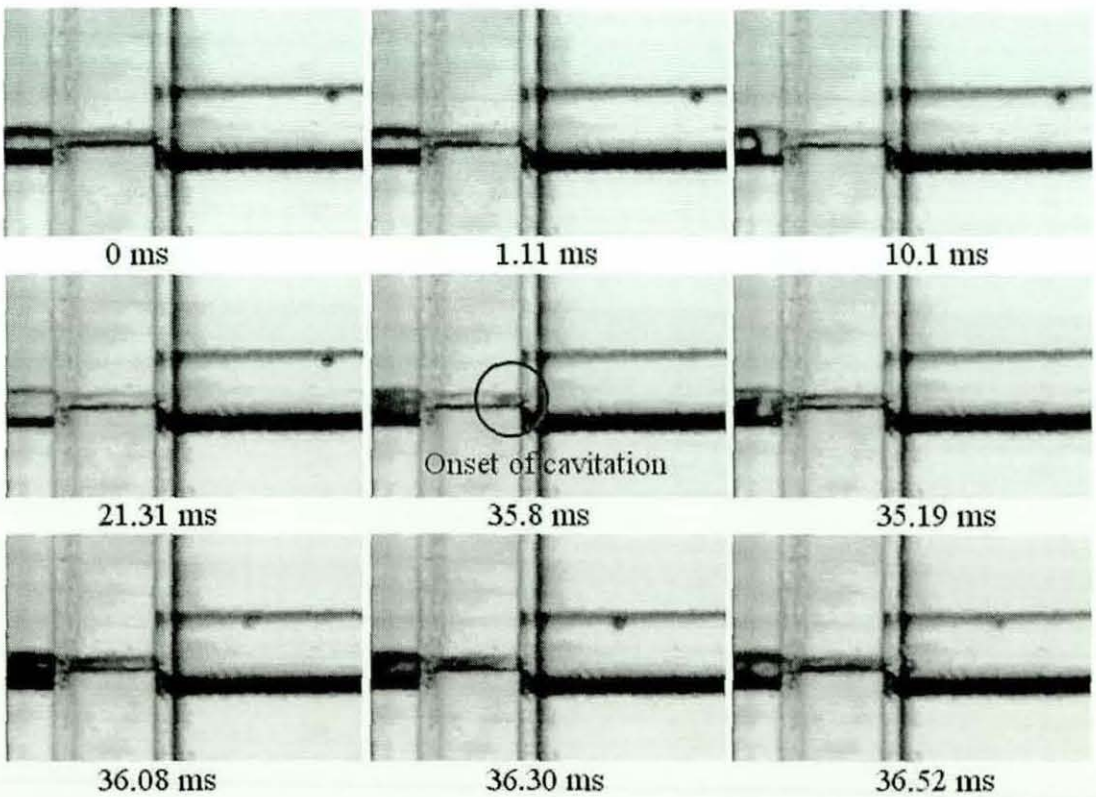

Figure 5.3 Microhole with 0.3mm diameter and sharp inlet radii with driving pressure at 1050 bar. (*M 108 sac_micro_count_1*)

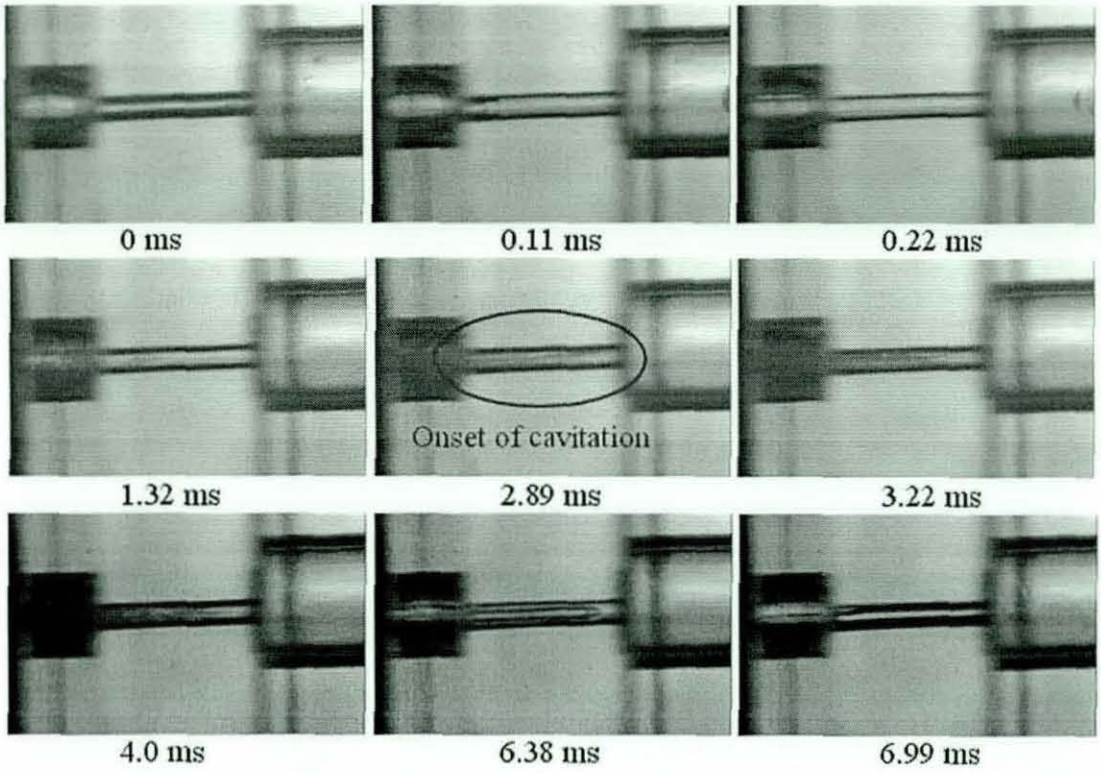

Figure 5.4 Microhole with 0.3mm diameter and 0.04mm inlet radii with driving pressure at 1050 bar. (*M105 1_sac_micro_count*)

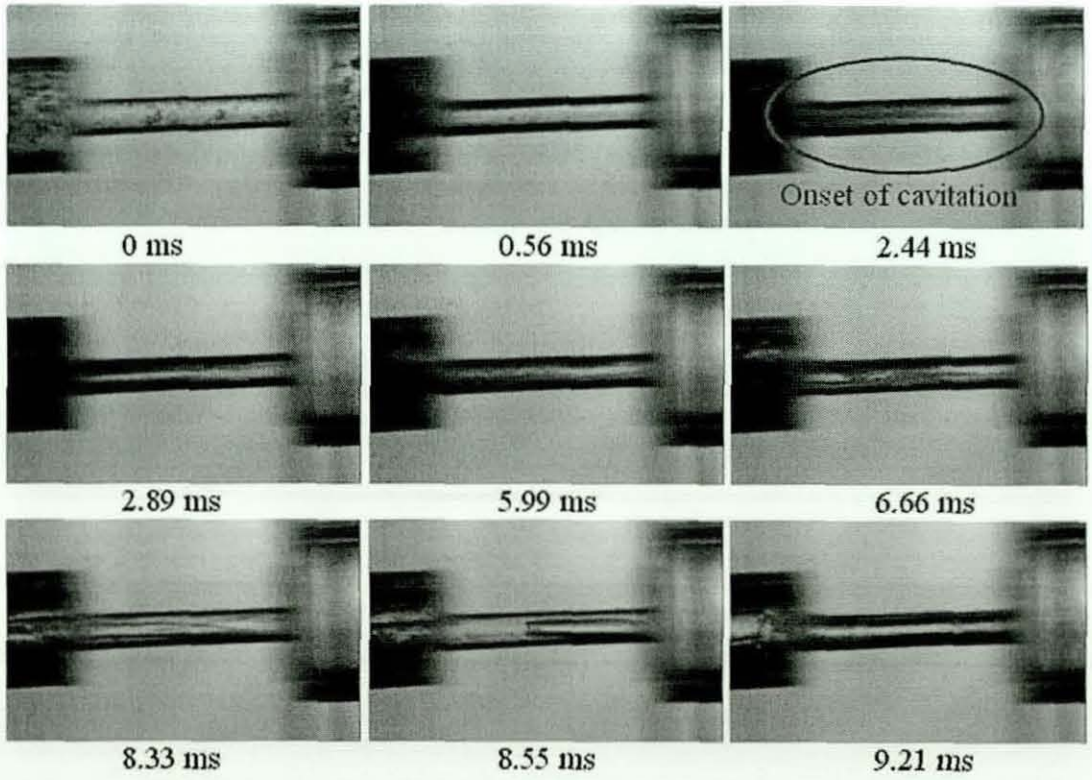

Figure 5.5 Microhole with 0.3mm diameter and 0.06mm inlet radii with driving pressure at 1050 bar. (*M105 8_sac_micro_count*)

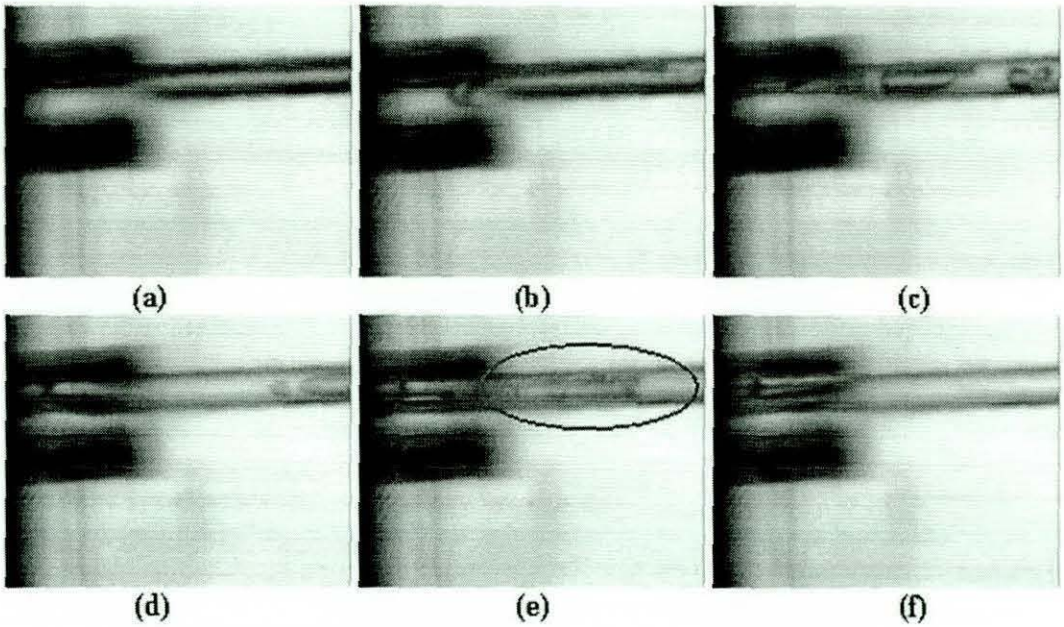

Figure 5.6 Microhole with 0.3mm diameter and 0.12mm inlet radii with 1050 bar driving pressure. (*M101 micro_count_2*)

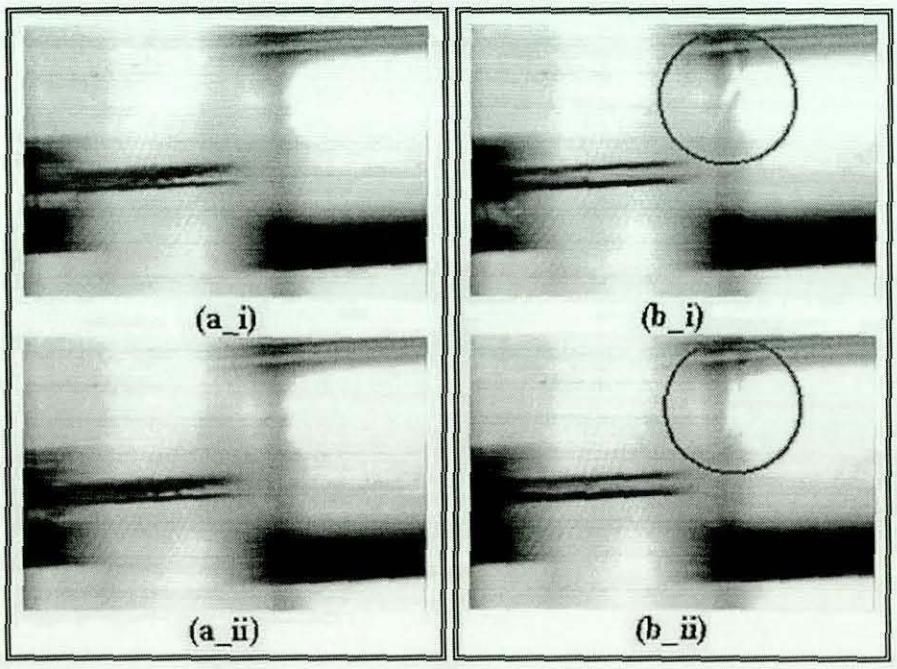

Figure 5.7 The affect of imperfections in the inlet radii of a 0.15 mm diameter microhole, with the left images showing cavitation and the right images without cavitation. (*M209_2 and M209_3*)

For figure 5.7, the test matrix showed a 0.15mm microhole configuration, driving pressure of 1400 bar, with and without cavitation. The first set of flow images on the left show cavitation readily forming in the flow as the pressurised fuel enters the microhole. In the second injection event (shown in figure 5.7b), on the right, under the same running condition cavitation could no longer be seen, indicating that the cavitation seen initially was probably caused by either a small piece of debris or an imperfection on the hole, which was subsequently removed by the flow through repeated injections.

Another notable observation is the presence of "waves" which can be seen in the artificial sac. This was due to the change in the refractive index, either caused by an increase in temperature or change in density of the fluid, indicating that the fluid at the bottom of the artificial sac has higher pressure gradients.

5.2.1.2 MICROHOLE DIAMETER

With the study of the effects of the inlet radius, the next step was to look at the microhole diameter. Figures 5.8 and 5.9 provide a flow characteristic comparison for both 0.15 and 0.3 mm diameter microhole respectively. This allows the effect of the microhole diameter on the internal flow to be studied. The 0.15 mm diameter microhole matrix shows three sequential flow images at 1400 bar driving pressure. The images show no noticeable flow interaction in the microhole, only flow interaction of the fuel and air in the counterbore. The 0.3 mm diameter microhole flow images show more interaction with the flow, with cavitation visible along the nozzle wall. This cavitation could be due to the surface imperfection in the microhole as discussed previously. Apart from the minor cavitation, the microhole diameter did not show any noticeable influence on the flow structures.

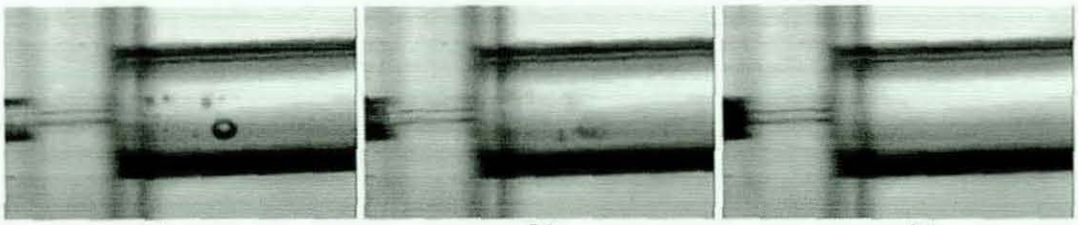

(a) (b) (c)

Figure 5.8 Test matrix consisted of an artificial sac, 0.15 mm diameter microhole at 1400 bar driving pressure. (*M110_3*)

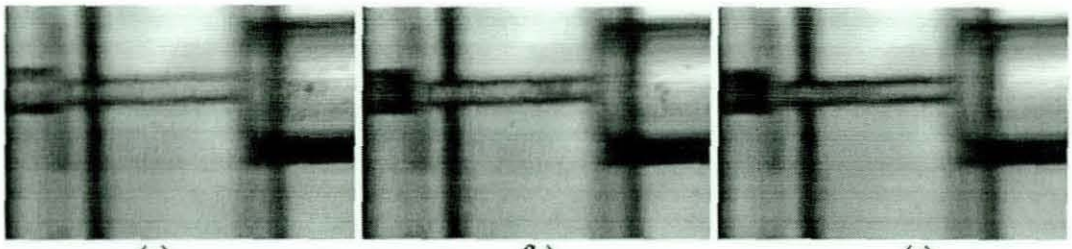

(a) (b) (c)

Figure 5.9 Test matrix consisted of an artificial sac, 0.3 mm diameter microhole at 1400 bar driving pressure. (*M118_2*)

(a) (b) (c)

Figure 5.10 Spray structure from a 0.15 mm diameter microhole and without counterbore at 1050 bar driving pressure. (*M301_1*)

(a) (b) (c)

Figure 5.11 Spray structure from a 0.15 mm diameter microhole and without counterbore at 1750 bar driving pressure. (*M219_1*)

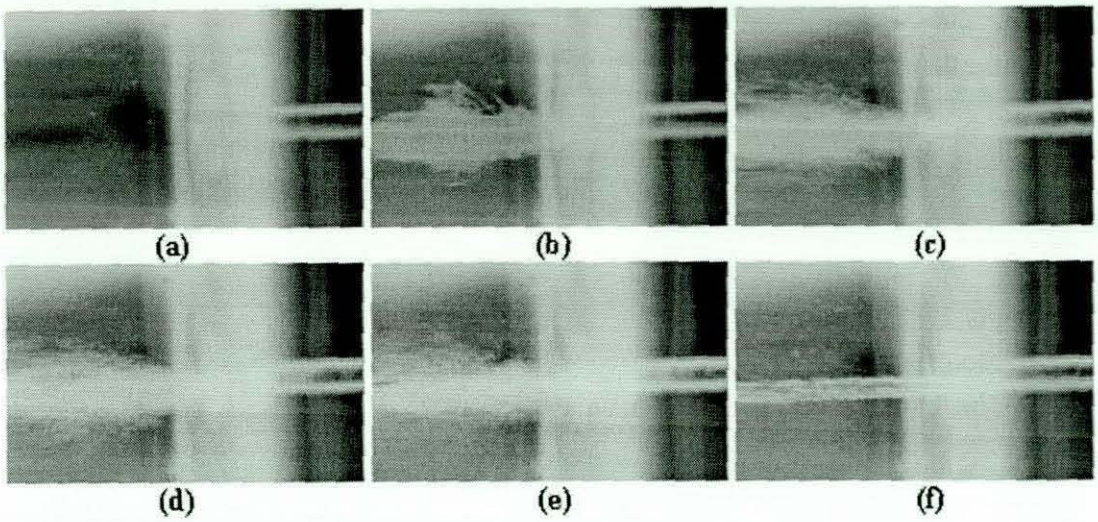

Figure 5.12 Spray structure from a 0.3 mm diameter microhole and without counterbore at 1050 bar driving pressure. (*M311_15*)

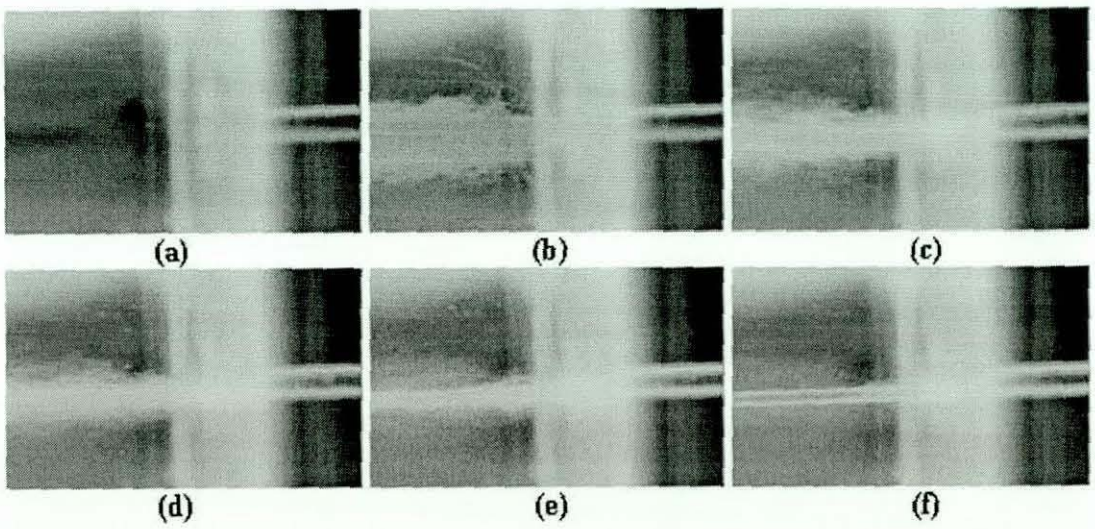

Figure 5.13 Spray structure from a 0.3 mm diameter microhole and without counterbore at 1750 bar driving pressure. (*M311_17*)

Another way of investigating the effects of the microhole diameter was to observe flow exiting the microhole. This was illustrated in figure 5.10 and 5.11, showing 0.15 mm microhole diameter spray structures without counterbore used, low and high injection pressure respectively. The absence of the counterbore was to prevent it from having any effect on the spray structures. Both figures were also converted to a negative image as this provides a better perspective of the spray structure. These figures show that the spray structure remains quite consistent regardless of the change in the driving pressure.

Figure 5.12 and 5.13 shows similar negative effect images for the 0.3 mm microhole diameter and without counterbore. Again, both sprays flow images at different driving pressures looked similar despite the wide difference in driving pressure used. This shows that the driving pressure and microhole diameter has insignificant effect on the flow to affect the spray structures.

5.2.2 Counterbore Geometry

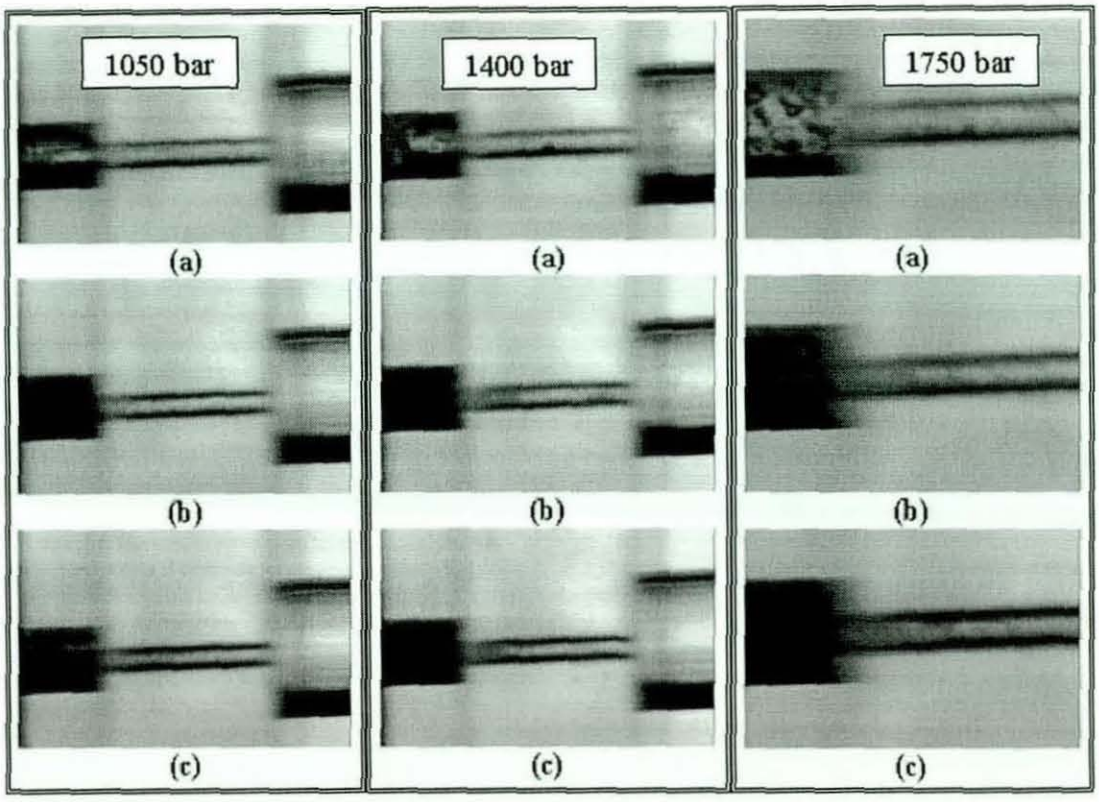

Figure 5.14 0.3 mm diameter microhole with 0.75 mm long and 1 mm diameter counterbore with 1050, 1400 and 1750 driving pressure respectively. (*M214_1, M214_2 and M214_3*)

The second stage of the Diesel Direct Injection studies investigated the counterbore geometry. This study also covered the flow interaction from the microhole exit and it effects on the spray characteristics. Figure 5.14 study the interaction of the microhole and counterbore geometry with 1050, 1400 and 1750 bar driving pressure. The flow videos showed increased interaction in the flow between the microhole and counterbore. In a sequence of still images it is difficult to present this flow interaction but this will be explained in details.

The counterbore images at 1050 bar driving pressure shows strong interactions in the flow as it exits the microhole. This is show by the darker region in image (c) of 1050 bar pressure. This is also show from images at 1400 and 1750 bar driving pressures. This lead to the next set of flow images that studied the flow structures exiting the counterbore.

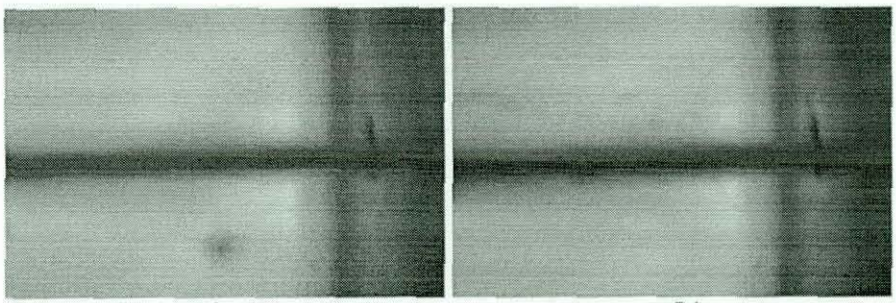

Figure 5.15 Microhole with 0.15 mm diameter and counterbore with 1 mm long and 0.75 mm diameter at 1400 bar driving pressure. (*M221_3*)

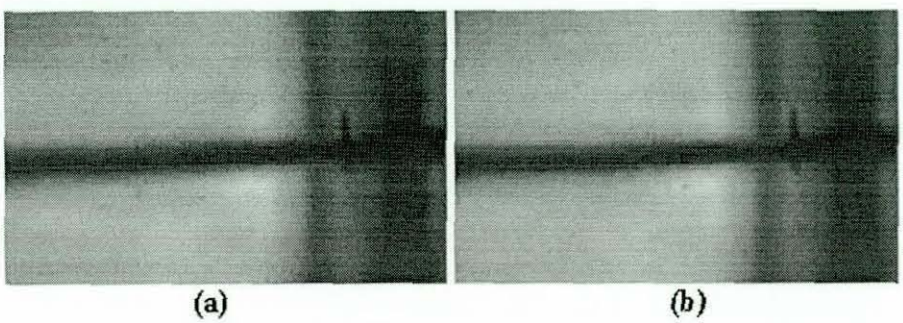

Figure 5.16 Microhole with 0.15 mm diameter and a 1mm long counterbore with 0.75 mm diameter at 1750 bar driving pressure. (*M221_4*)

Figure 5.15 and 5.16 studied the effect of driving pressure on the interaction of spray from a 0.15 mm diameter microhole into a 0.75 mm diameter and 1mm long counterbore. The amount of influence by the counterbore on different driving pressure seems to have a negligible effect on the spray structures. The spray jet appeared to exit on one side of the counterbore but this was noted to be due to misalignment.

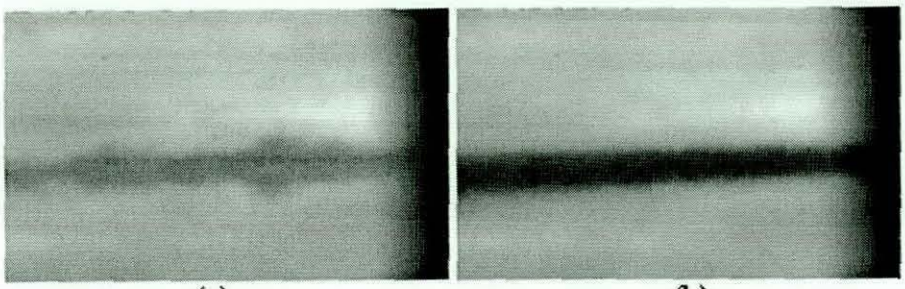

(a) (b)

Figure 5.17 Microhole with 0.3 mm diameter and a 0.75 mm long counterbore with 1 mm diameter at 1750 driving pressure. (*M219_1*)

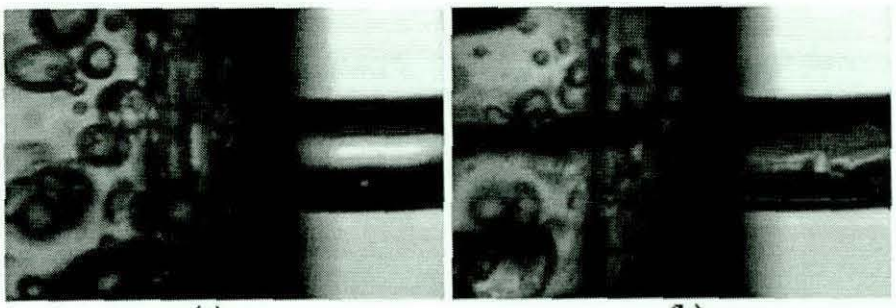

(a) (b)

Figure 5.18 Microhole with 0.3 mm diameter and a 1 mm long counterbore with 0.75 mm diameter at 1750 driving pressure. (*M216_3*)

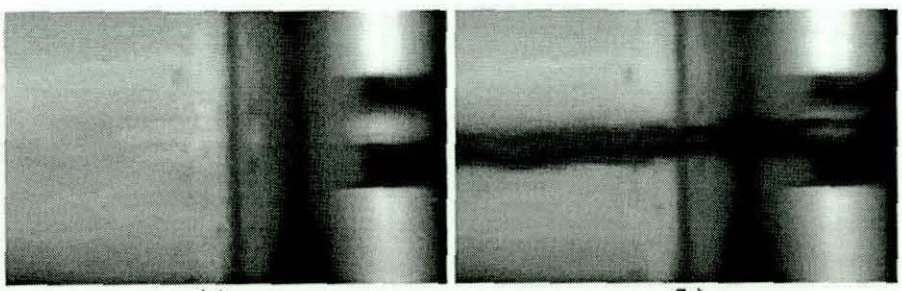

(a) (b)

Figure 5.19 Microhole with 0.3 mm diameter and a 0.5 mm long counterbore with 0.75 mm diameter at 1750 driving pressure. (*M217_3*)

Figures 5.17 to 5.19 provide further data for studying the effect of counterbore geometry on spray structure for a 0.3 mm diameter microhole and a driving pressure of 1750 bar. These images clearly show the counterbore geometry studied had no apparent effect on the spray angle. This was also observed in the 0.15 mm diameter microhole with the same counterbore geometry and

driving pressure of 1400 and 1750 bar. Under these conditions, the spray was a narrow column of approximately the same diameter as the microhole.

5.2.3 Back Pressure

The previous experimental results were all conducted with an atmospheric charge air back pressure conditions. This section looks at the results obtained with charge air back pressures in the bottom chamber ranging from zero to 150 bar (gauge), all at a nominal 20°C. Data for 1050 and 1750 bar results were be presented and discussed. The amount of data collected in this study is enormous, therefore data and results presented will show flow characteristics and trends. These results were presented in the following sub-sections; no counterbore and with counterbore. The figures presented were also displayed in negative image form, providing better display of the flow structures.

The spray angle was measured to record any change in the angle with varying charge back pressure. Figure 5.20 illustrates how the half spray angle was defined. The spray angle is the cone angle determined by adding the two angles, A and B. The cone was measured from the outlet, either from the counterbore or the microhole.

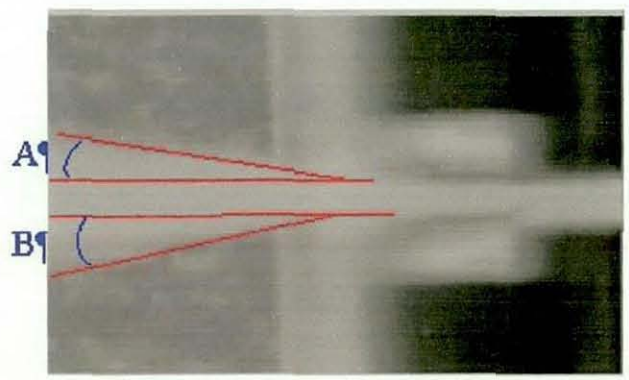

Figure 5.20 Illustration for measuring spray angle (A+B).

5.2.3.1 NO COUNTERBORE

Charge air back pressure from atmospheric to 150 bar (gauge) are shown in figures 5.21 to 5.23 with 1050 bar driving pressures.0.15mm diameter microhole and 150 bar constant driving oil pump pressure. The test matrices used in this study were without counterbore, to study the effect of the microholes on the spray structures with different charge air back pressure. The charge air back pressure range from 20 to 60 bar. The first figure shows the spray angle increases slightly with increasing the microhole diameter. Also, there was a small increase in the spray angle with increasing charge air back pressure but with some degree of fluctuations. This was very distinctive from atmospheric to 60 bar charge air back pressure.

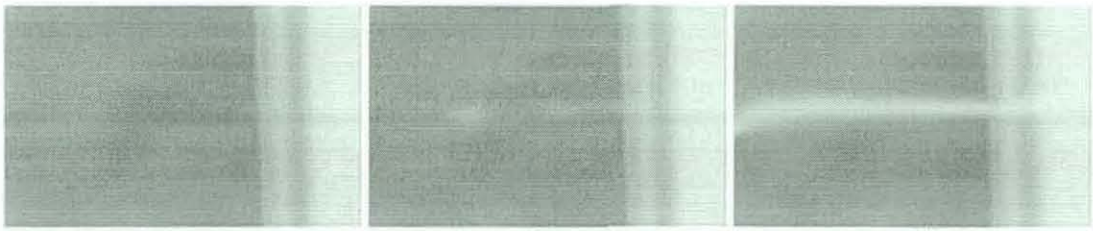

Figure 5.21 0.15mm diameter microhole with 1050 bar driving pressure and atmospheric charge air back pressure. (*M301_1*)

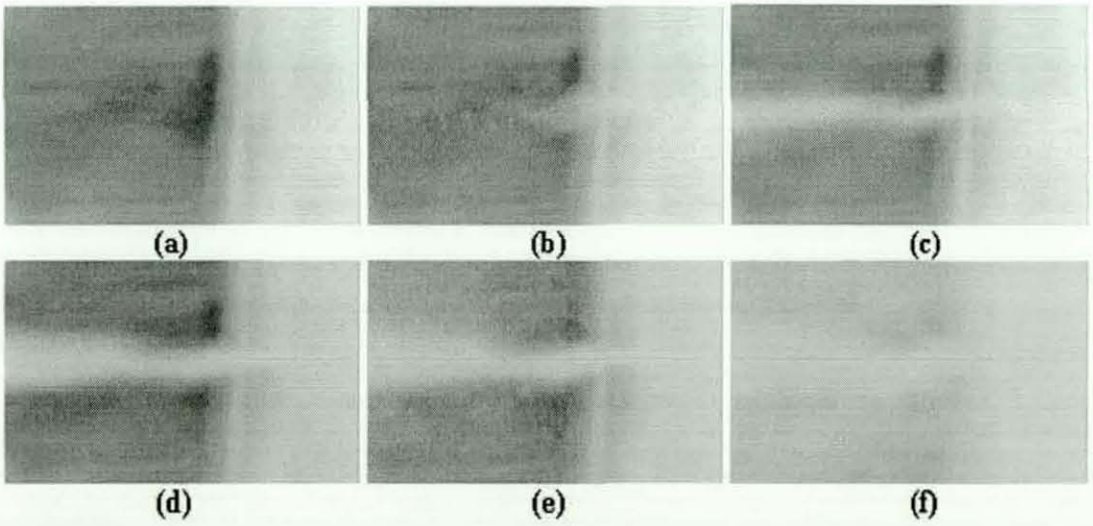

Figure 5.22 0.15mm diameter microhole with 1050 bar driving pressure and 20 bar charge air back pressure. (*M308_1*)

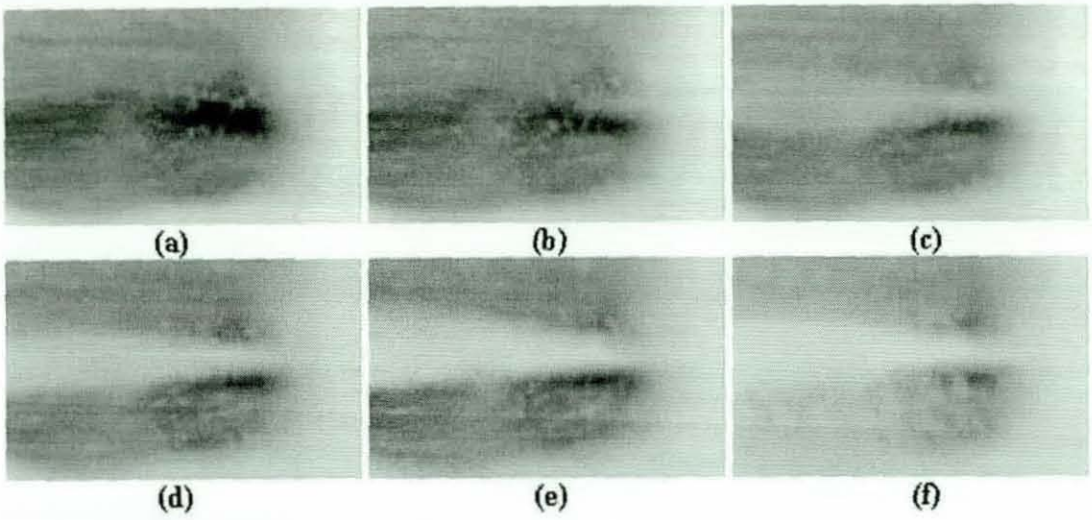

Figure 5.23 0.15mm diameter microhole with 1050 bar driving pressure and 60 bar charge air back pressure. (*M308_3*)

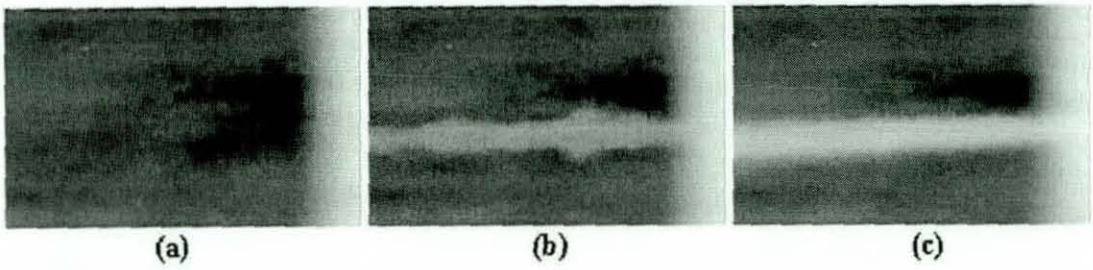

Figure 5.24 0.15mm diameter microhole with 1750 bar driving pressure and atmospheric charge air back pressure. (*M219_1*)

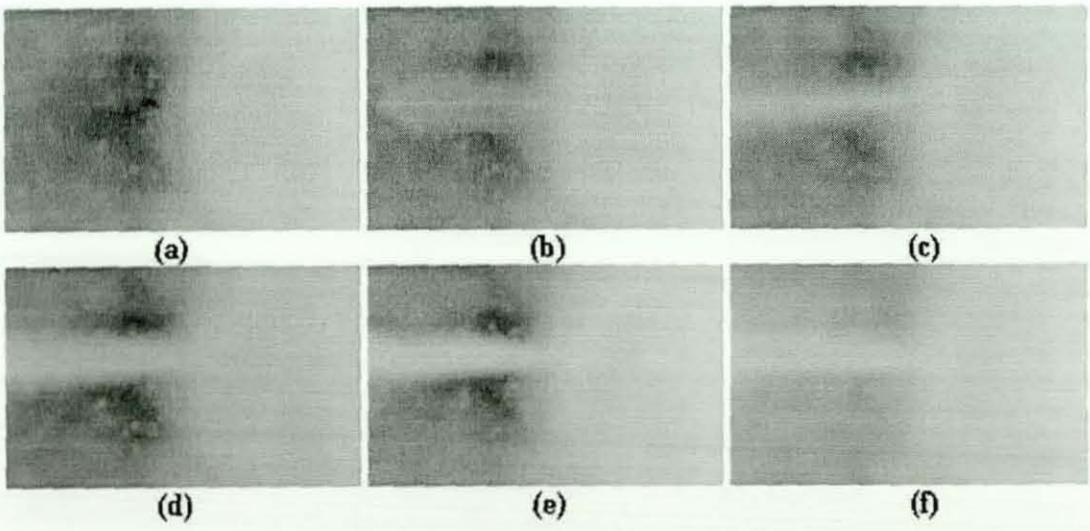

Figure 5.25 0.15mm diameter microhole with 1750 bar driving pressure and 20 bar charge air back pressure. (*M308_8*)

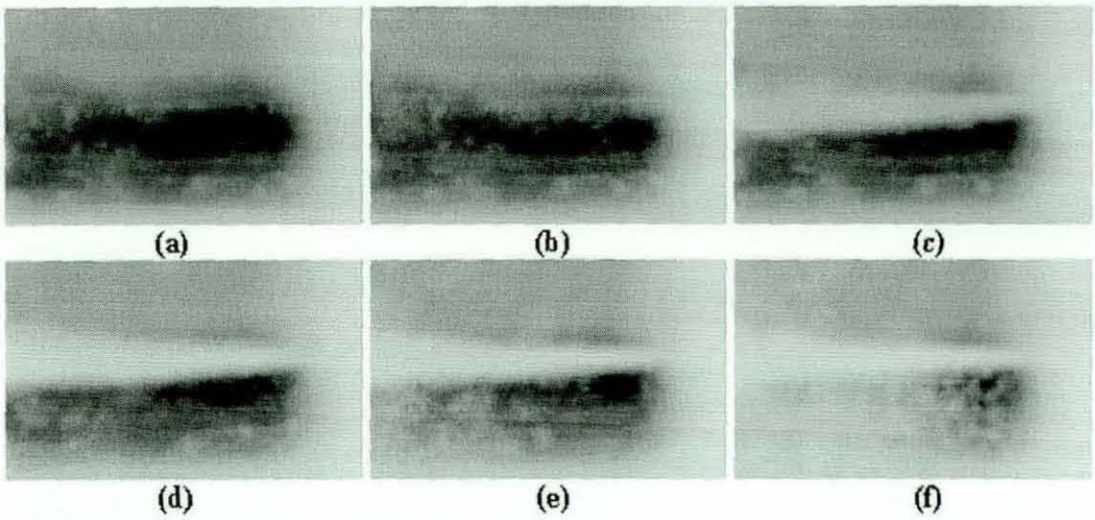

Figure 5.26 0.15mm diameter microhole with 1750 bar driving pressure and 60 bar charge air back pressure. (*M308_10*)

Similar rise in spray angle was also seen from figures 5.24 to 5.26, using the same 0.15 mm microhole but at higher driving pressure of 1750 bar. The rise in spray angle was also distinctive between atmospheric and 20 bar back pressure. However, this change in spray angle appears to be minimum between 20 and 60 bar charge air back pressure.

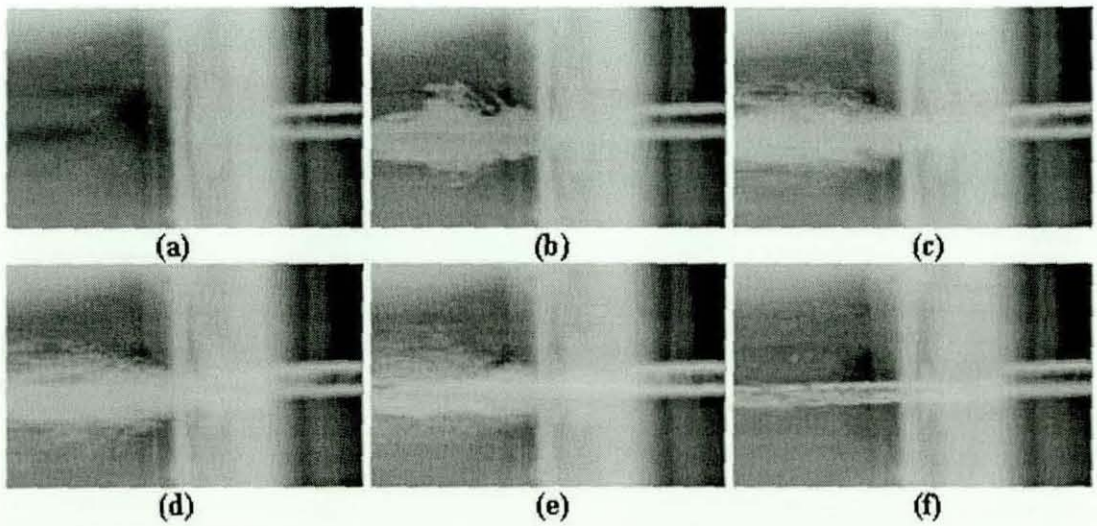

Figure 5.27 0.3mm diameter microhole with 1050 bar driving pressure and atmospheric charge air back pressure. (*M311_15*)

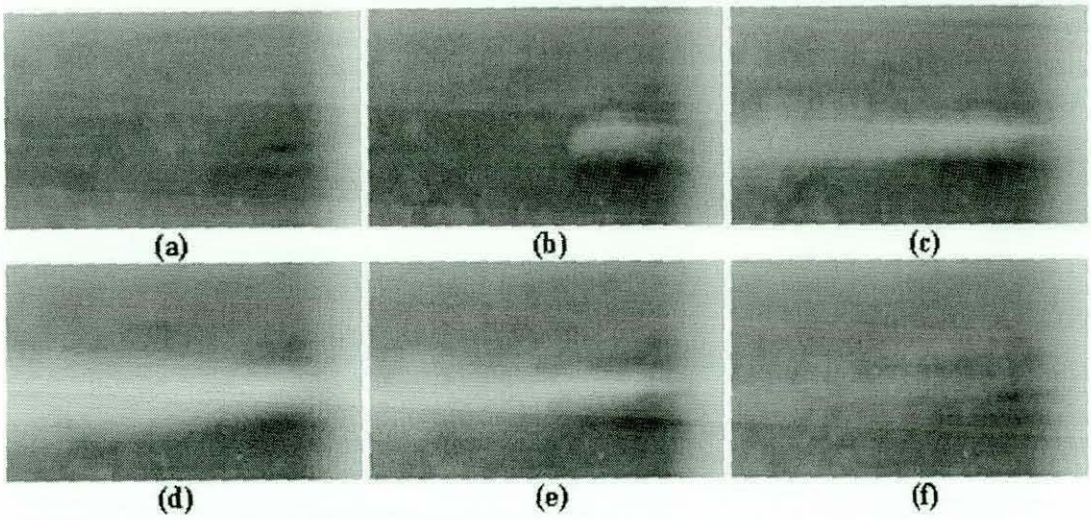

Figure 5.28 0.3mm diameter microhole with 1050 bar driving pressure and 20 bar charge air back pressure. (*M309_1*)

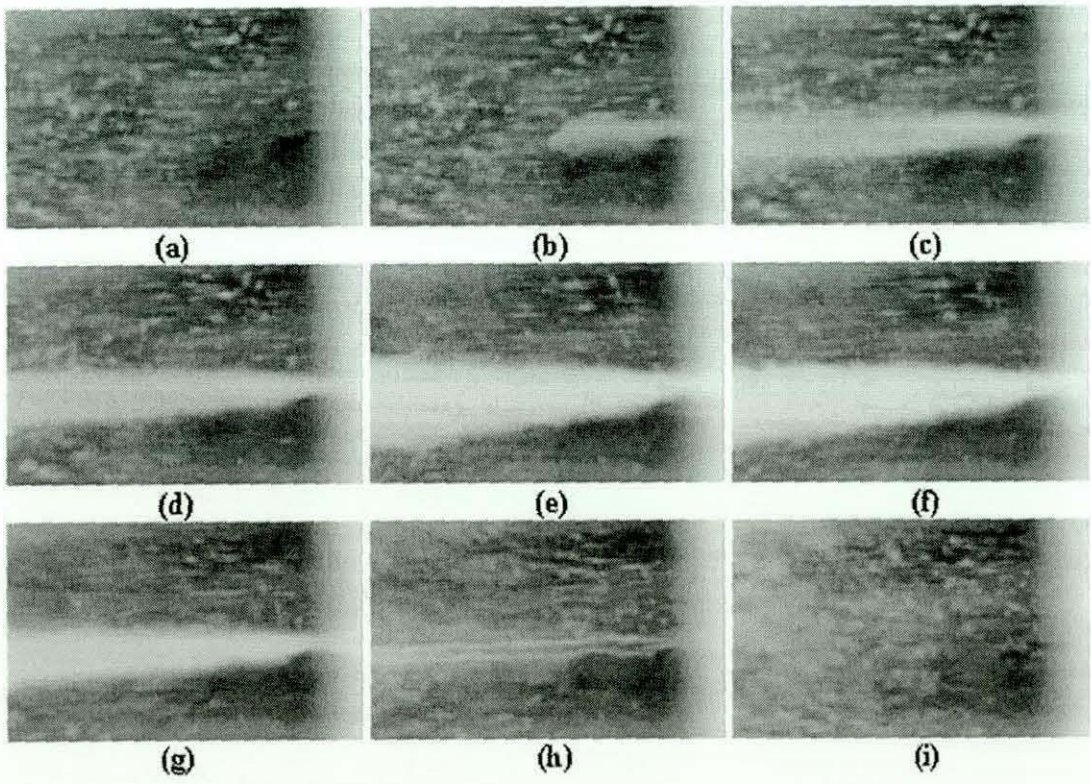

Figure 5.29 0.3mm diameter microhole with 1050 bar driving pressure and 60 bar charge air back pressure. (*M309_3*)

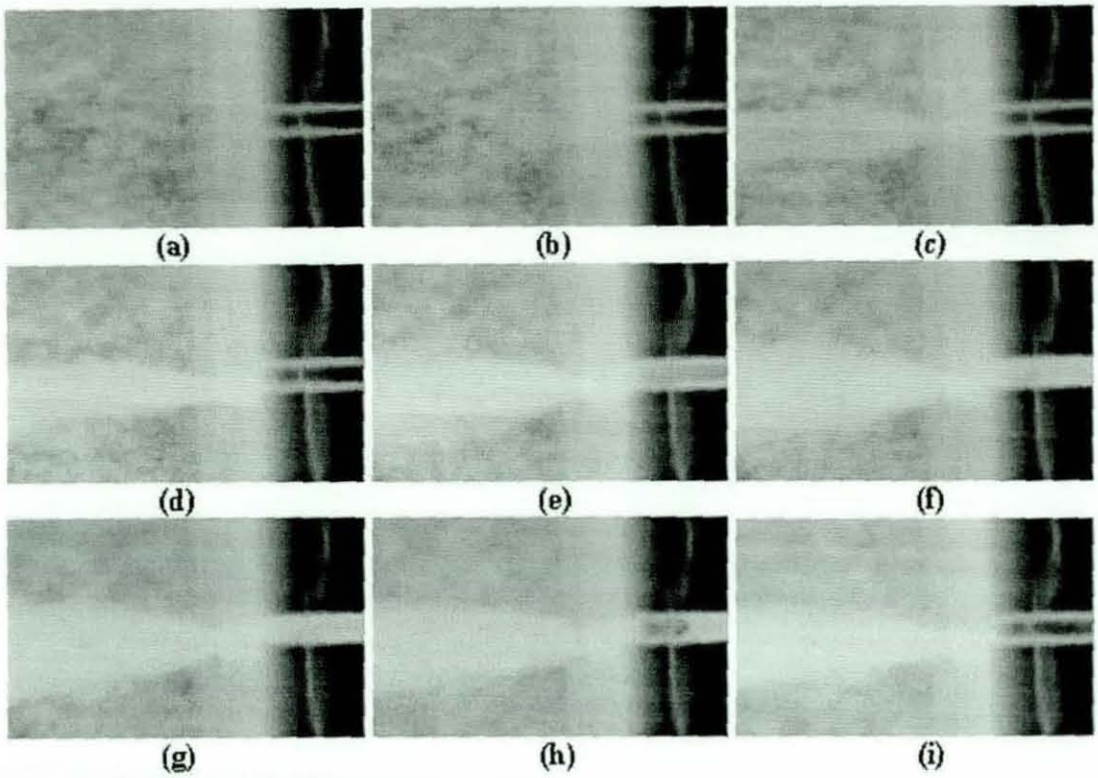

Figure 5.30 0.3mm diameter microhole with 1050 bar driving pressure and 120 bar charge air back pressure. (*M311_11*)

Figures 5.27 to 5.30 show a sequence of flow images for a microhole 0.3 mm with sharp inlet and at 1050 bar driving pressure, with figures 5.31 to 5.34 presenting the same microhole but at a higher driving pressure of 1750 bar. The charge air back pressure ranging from atmospheric to 120 bar (gauge) were considered. Both set of results showed that there was a significant increase in the spray angle between atmospheric and 20 bar charge air back pressure, but between 20 and 150 bar there was little change in the spray angle at 1050 and 1750 bar driving pressure. This was as expected since spray angles were known to typically increase approximately with square root of charge density.

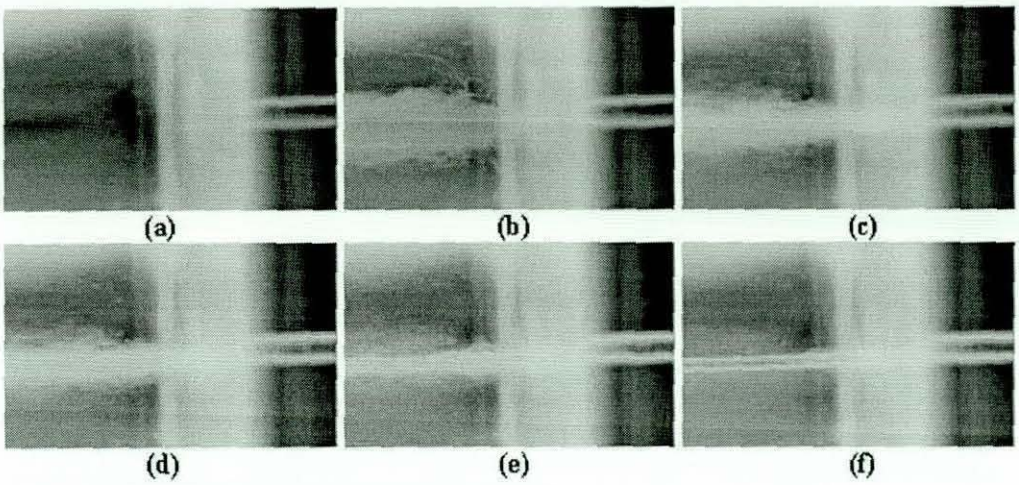

Figure 5.31 0.3mm diameter microhole with 1750 bar driving pressure and atmospheric charge air back pressure. (*M311_17*)

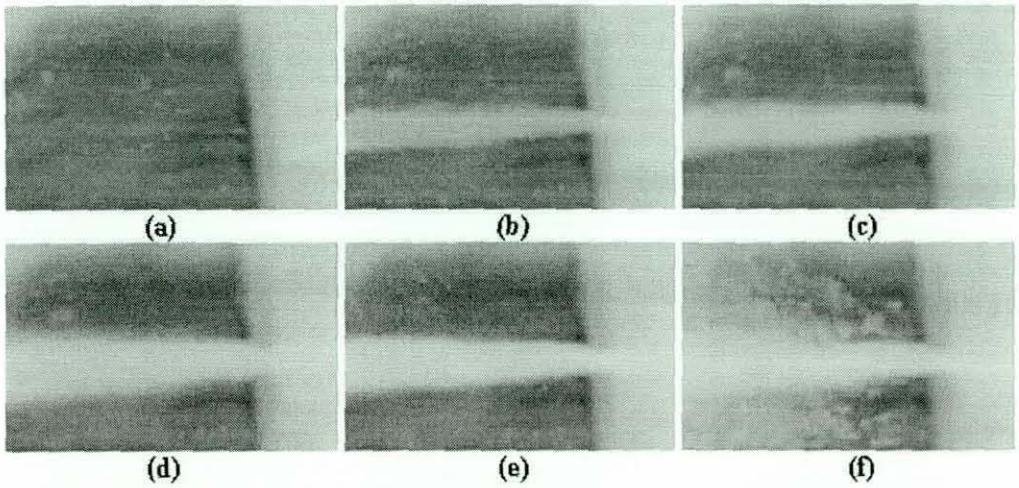

Figure 5.32 0.3mm diameter microhole with 1750 bar driving pressure and 20 bar charge air back pressure. (*M309_7*)

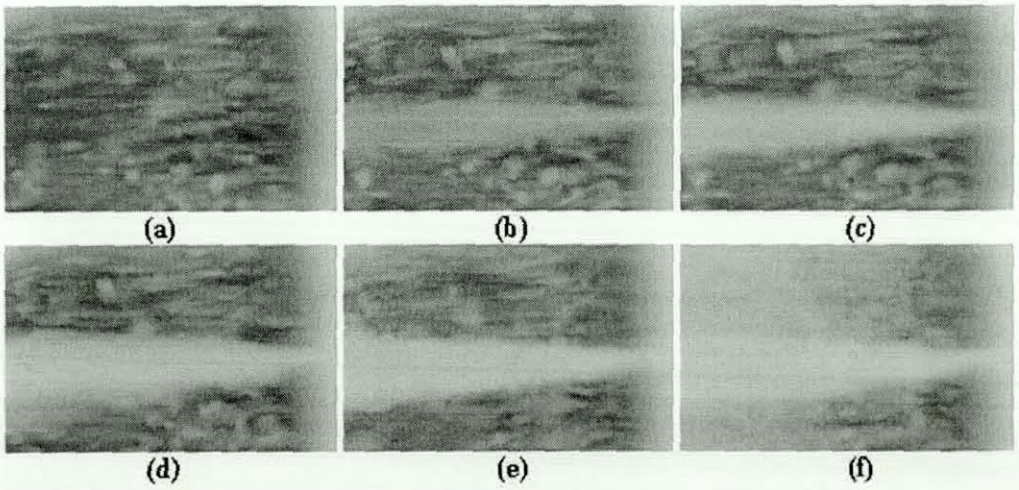

Figure 5.33 0.3mm diameter microhole with 1750 bar driving pressure and 60 bar charge air back pressure. (*M309_9*)

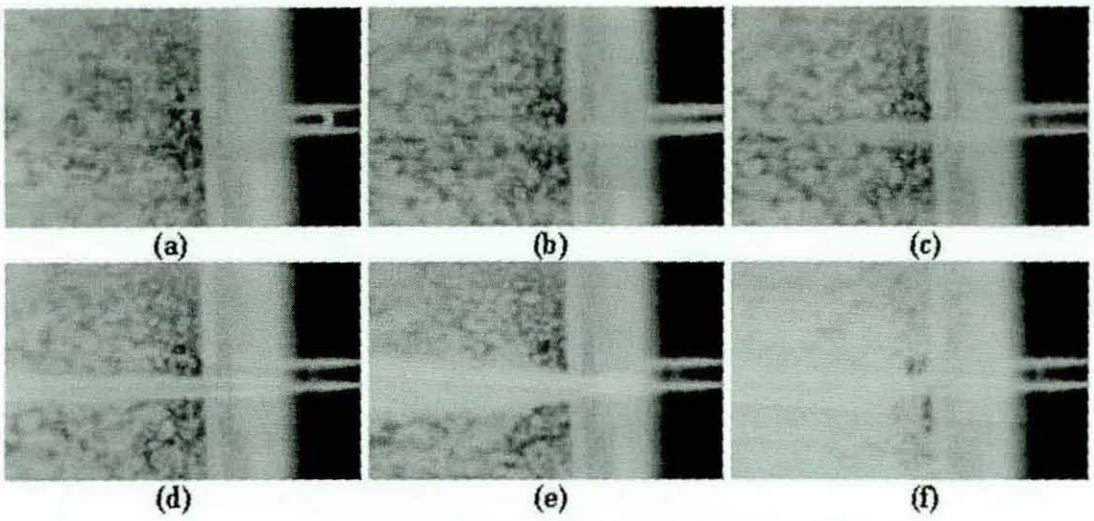

Figure 5.34 0.3mm diameter microhole with 1750 bar driving pressure and 120 bar charge air back pressure. (*M311_3*)

The analysis of these spray data was plotted on a graph to study any visible trends and to provide further understanding of the spray structures. Since the measurements were conducted at different charge air pressure range, only the results for charge air back pressure from 20 to 60 bar were discussed. This will provide further insight of the spray angle using different microhole size. Figure 5.35 shows the trends of the spray angle from 20 to 60 bar for both microhole sizes. In this graph, the charge air back pressure results for 20 bar seems inconclusive as it differs from 40 and 60 bar. The latter charge air back pressure conditions showed that 0.3mm microhole diameter has a bigger spray angle at higher driving pressure. This is in contrast to the 0.15mm microhole which appears to be similar in spray angle regardless of the driving pressure used.

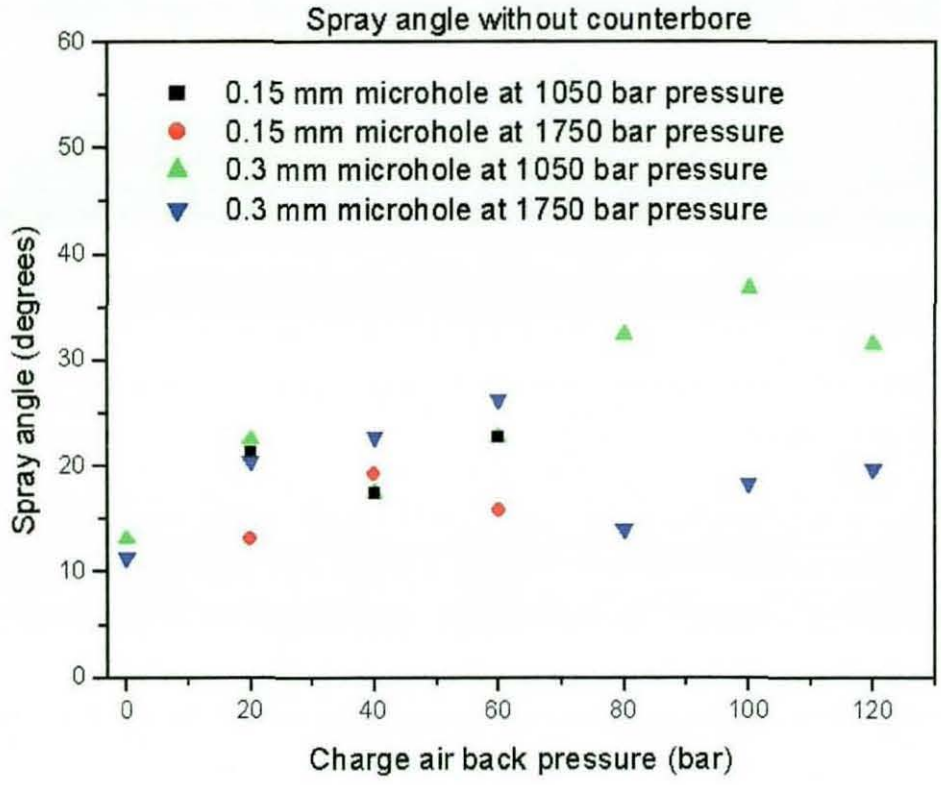

Figure 5.35 Comparison graph for microhole size and driving pressure for no counterbore studies.

5.3.2.2 WITH COUNTERBORE

The charge back air pressure with counterbore incorporated into the sapphire matrices were studied in two driving pressure, the 1050 and 1750 bar with charge air back pressure from atmospheric to 120 bar. Figure 5.36 to 5.39 showed a sapphire matrix with driving pressure at 1050 bar and the charge air pressure of 20, 60, 100 and 120 bar respectively. The sapphire matrix consisted of a 0.3mm diameter microhole with sharp inlet radii and a counterbore with 1mm diameter and 1mm long. The flow images shows that counterbore geometry with charge air back pressure do not have a significant effect on the spray structures. However, it was also recognised that neither the particle diameters were measured, nor the fully developed spray. This was mainly due to the limited access to the spray, with optical access to just over 1mm from the counterbore exit.

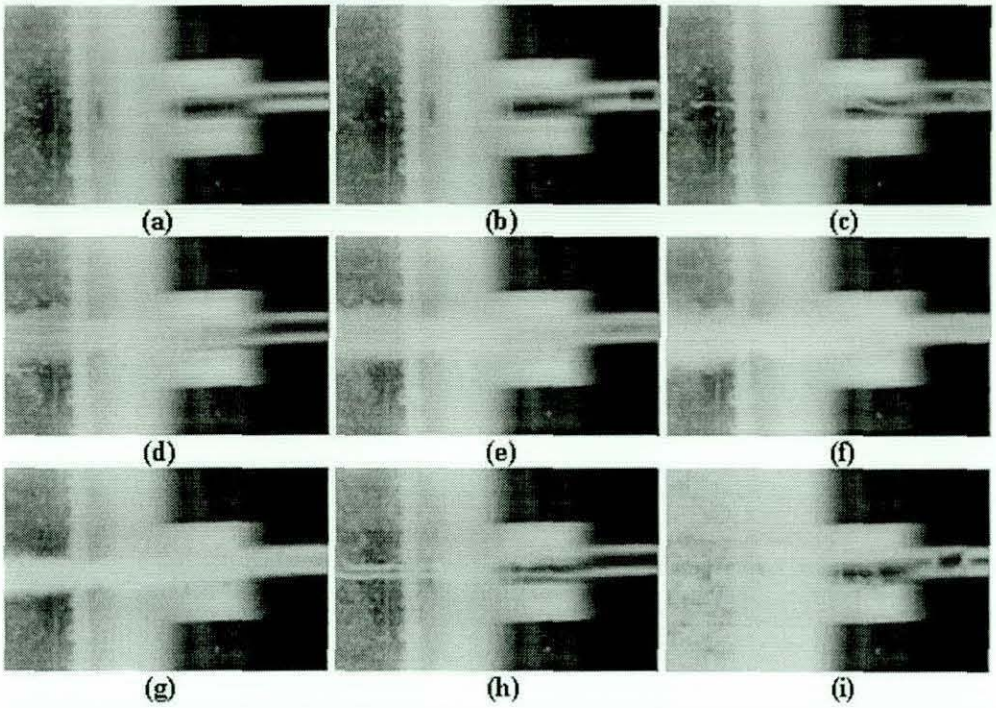

Figure 5.36 Microhole with 0.3mm diameter and a 1 mm long counterbore at 1050 bar driving pressure and 20 bar charge air pressure. (*M306_2*)

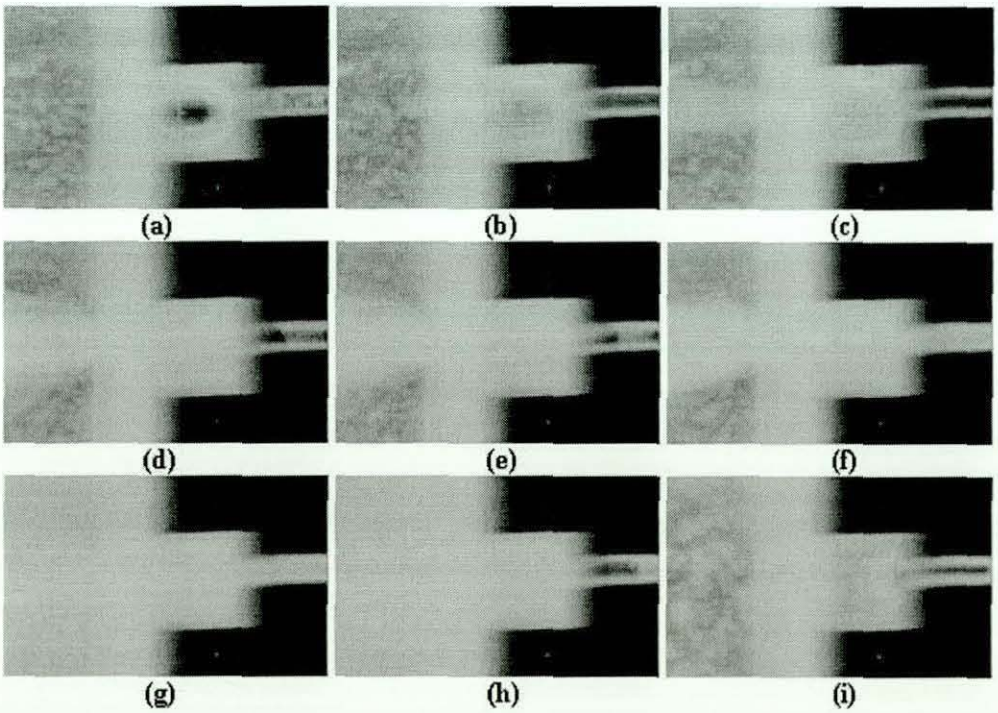

Figure 5.37 Microhole with 0.3mm diameter and a 1 mm long counterbore at 1050 bar driving pressure and 60 bar charge air pressure. (*M306_12*)

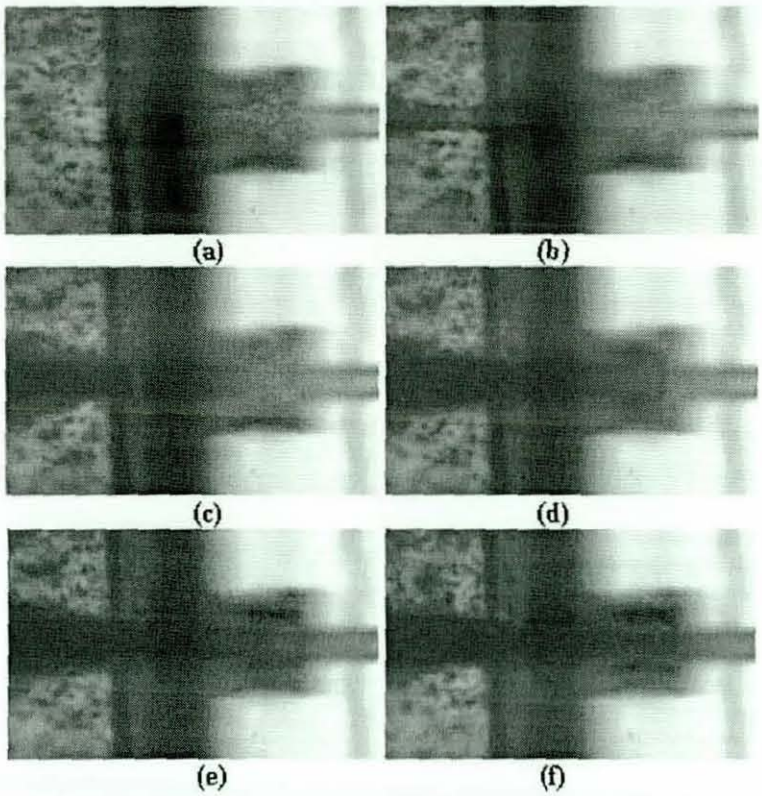

Figure 5.38 Microhole with 0.3mm diameter and a 1 mm long counterbore at 1050 bar driving pressure and 100 bar charge air pressure. (*M310_16*)

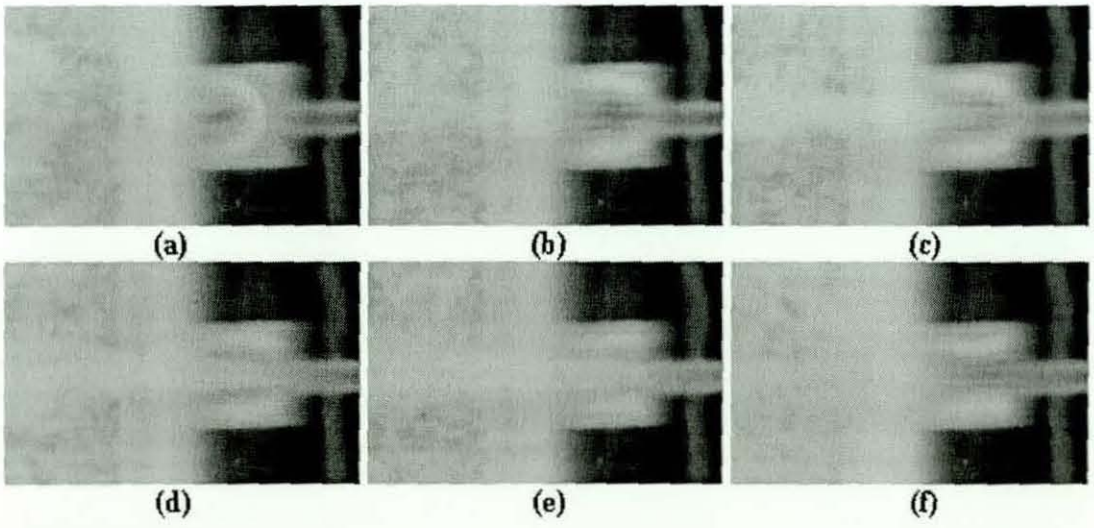

Figure 5.39 Microhole with 0.3mm diameter and a 1 mm long counterbore at 1050 bar driving pressure and 120 bar charge air pressure. (*M310_15*)

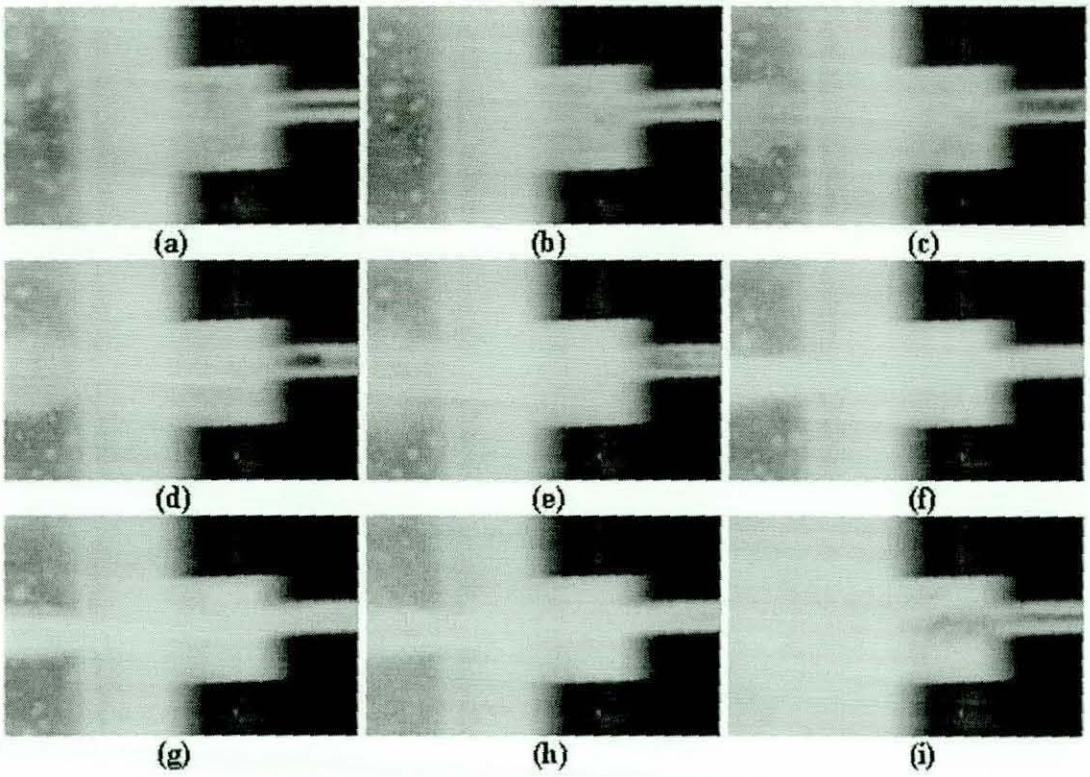

Figure 5.40 Microhole with 0.3mm diameter and a 1 mm long counterbore at 1750 bar driving pressure and 20 bar charge air pressure. (*M306_9*)

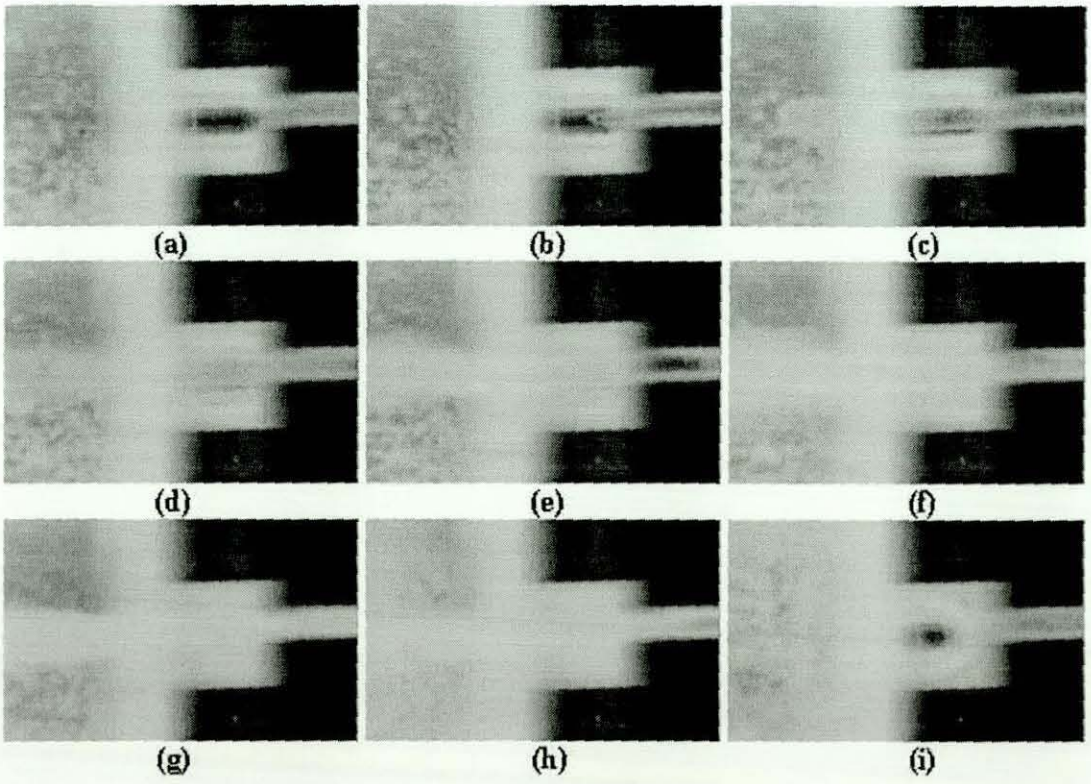

Figure 5.41 Microhole with 0.3mm diameter and a 1 mm long counterbore at 1750 bar driving pressure and 60 bar charge air pressure. (*M306_14*)

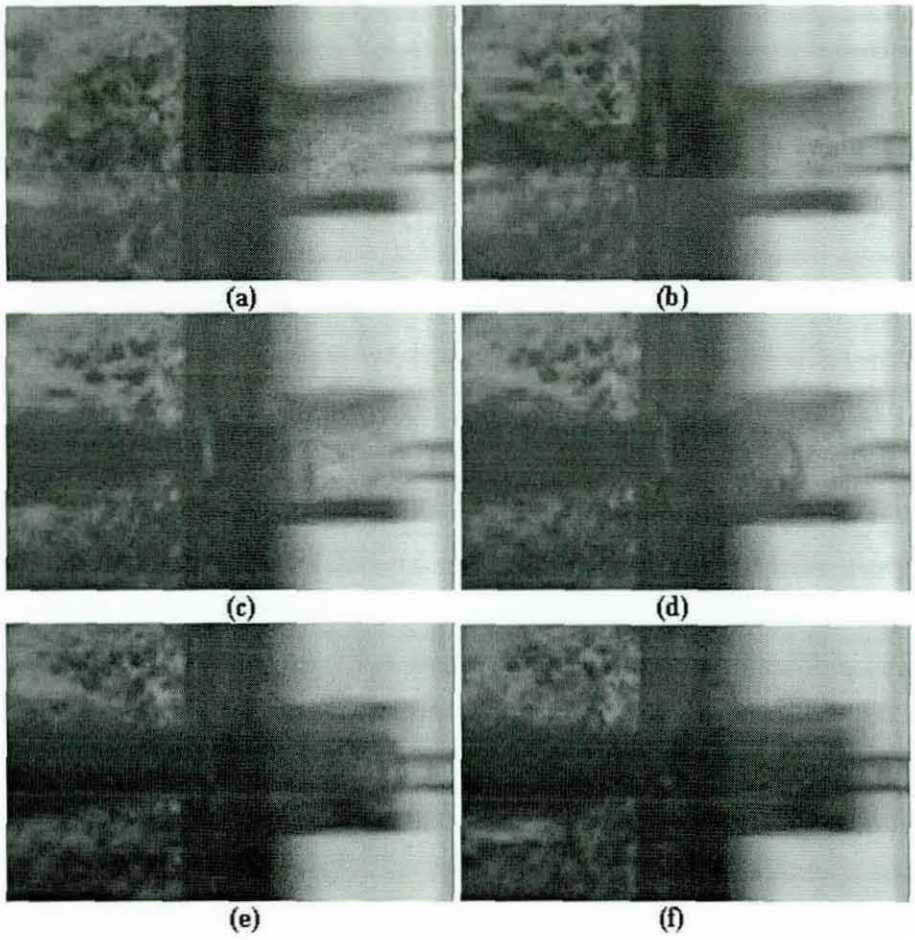

Figure 5.42 Microhole with 0.3mm diameter and a 1 mm long counterbore at 1750 bar driving pressure and 100 bar charge air pressure. (*M310_5*)

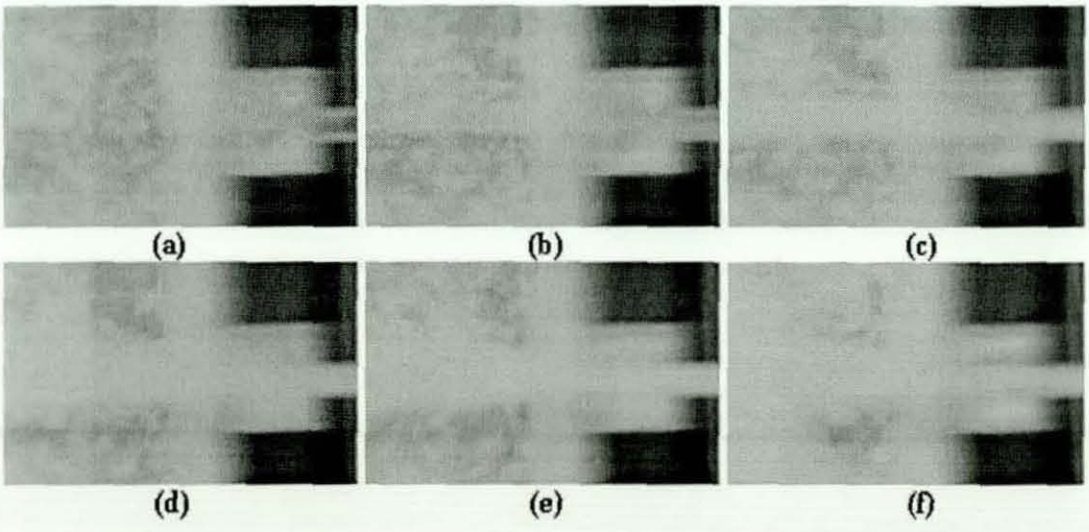

Figure 5.43 Microhole with 0.3mm diameter and a 1 mm long counterbore at 1750 bar driving pressure and 120 bar charge air pressure. (*M310_4*)

Figure 5.40 to 5.43 showed the same sapphire matrix configuration with a 0.3mm microhole but at a higher driving pressure of 1750 bar. This set of flow images also did not show significant increase in spray angle. A bigger spray angle was observed with 20 bar charge air back pressure but this remain fairly consistent at higher charge pressure.

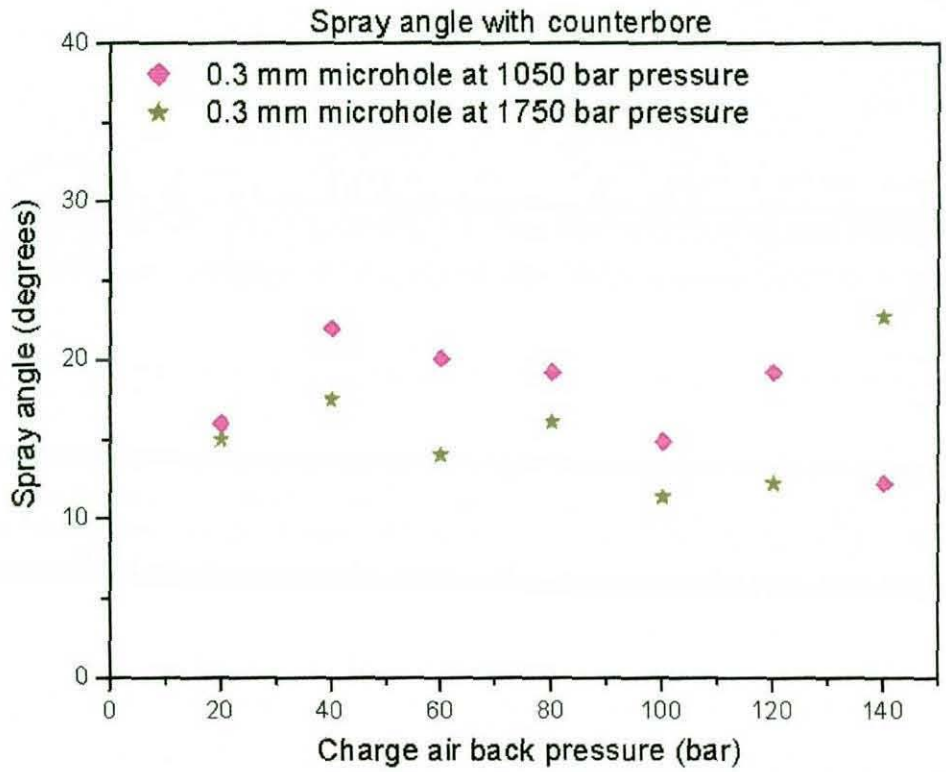

Figure 5.44 Microhole with 0.3 mm diameter at 1050 and 1750 bar driving pressures.

Figure 5.44 provided a graphical analysis of the 0.3mm microhole diameter with counterbore at 2 different driving pressure conditions. The spray angle at 20 bar charge air back pressure is observed to be identical. With higher charge air back pressure, the lower driving pressure seems to produce a higher spray angle. The largest spray angle recorded is about 23° with 40 bar charge air back pressure

5.3 DISCUSSIONS

5.3.1 Effects of Microhole

Inlet radii effects on spray structure were investigated by Bergwerk [01]. He showed that cavitation was a predominant phenomenon in nozzles with sharp inlet radii. To understand the reason the cavitation forms we must consider the flow path. In the sac the flow area is large and the velocity relatively low, producing a high static pressure. As the flow accelerates from the sac into the small area nozzle, the inertia of the fluid prevents it from following a streamline that matches the high degree of curvature of the sharp inlet corner. Thus, the flow separates from the nozzle inlet and forms a vena contracta, where the flow velocity reaches a maximum and the pressure a minimum. If the pressure ratio, and thereby the flow velocity, is high enough, the local pressure in the separated region can fall below the liquid vapour pressure and the cavitation bubbles form.

Clearly, one way to control or limit cavitation is to remove the sharp transition and chamfer or curve the nozzle inlet. In this way the flow streamlines follow the curvature of the nozzle and remain attached to the nozzle walls, thereby preventing separation. However, in an optical study of injector nozzle internal flows, Bergwerk [01] provided data that showed cavitation phenomena in worn (rounded) nozzles. The measured critical cavitation number was higher for the rounded nozzles compared with the sharp inlet nozzles, but cavitation was still seen to be present.

In an experimental study of cavitation in Diesel injectors, Chaves *et al* [02] also provided data that defined the flow conditions differentiating non-cavitating and cavitating flow. Their data suggests that for all realistic operating pressures (ie. above 200 bar) cavitating flow will occur. However, this was not the case in the current research study. It has been shown that the cavitation was removed completely with higher injection pressure. Some initial runs with new, sharp edged inlet did provide some cavitation at driving pressure of 1050 to 1750 bar, but this quickly disappeared after a small number of injections and the extent of the cavitation was minimal.

Bergwerk [01] noted that the onset of cavitation was characterised by a sudden reduction in discharge coefficient. This can be expected since with cavitation present a significant volume of the nozzle flow will be occupied by low density vapour bubbles. Thus, as cavitation increases the nozzle discharge coefficient and mass flow rate will decrease. Ohrn *et al* [06] provided data from a study of the geometrical effects on discharge coefficient for plain orifice atomisers and noted that increasing the inlet radius has a profound effect on the internal flow geometry. Their study measured the mass flow rate from a range of real-sized diesel injector nozzles under varying operating conditions and observed that as the driving pressure was increased from 200 bar to 1000 bar, the nozzle discharge coefficient did not change. They also noted that the discharge coefficient remained constant over a wide range of nozzle Reynolds numbers. However, their data showed, as might be expected, that the discharge coefficient was highly dependent on the nozzle inlet radius.

One conclusion that might be drawn from their data is that the constant discharge coefficient is an indication of either there is no cavitation present in the nozzle, or at least that the level of cavitation is not changing with driving pressure.

To the authors knowledge the current study is the first to provide imaging data in real-sized nozzles operating with driving pressures in excess of 1000 bar and this imaging data supports the conclusion that at such high pressures the cavitation is minimal or non-existent.

5.3.2 Effects of Counterbore Geometry

The aim of incorporating a counterbore was to observe whether this geometry contributes to better atomisation from the spray. Initial observations from the flow videos showed a strong interaction between the fluid and the air in the counterbore. These interactions were observed to increased at higher driving pressures. However, close observation of the spray structure exiting the

counterbore appears to show that the counterbore geometry has no effect on the spray angle and atomisation. This was seen in both 0.15 mm and 0.3mm diameter microhole with the same driving pressure condition. In the 0.15 mm diameter microhole study, the spray structure generated was a narrow column of approximately the same diameter as the microhole.

5.3.3 Effects of Charge Air Back Pressure

The variation in charge air pressure was investigated to determine the effects on spray structure at different driving pressures and microhole sizes. This analysis is further divided into counterbore and no counterbore studies.

Figures 5.45 and 5.46 provide a graphical comparison of the variation of spray angle with density ratio (ρ_g/ρ_l) for both injectors with and without counterbore. The data is presented in density ratio terms to allow comparison with the empirical relationship provided by Heywood [05]:

$$\tan\frac{\theta}{2} = \frac{1}{A}4\pi\left(\frac{\rho_g}{\rho_l}\right)^{\frac{1}{2}}\left(\frac{\sqrt{3}}{6}\right) \qquad (5.1)$$

Where A= 3.0 + 0.28 (L_n/d_n), where L_n/d_n is the length/diameter ratio of the nozzle.

From this figure it is clear that with a driving pressure of 1050 bar and no counterbore the current data agrees well with the data and empirical relation provided by Heywood. However, the higher pressure results (1750 bar) show a discontinuity at a density ratio, (ρ_g/ρ_l) = 110 (equivalent to a air charge pressure of 80 bar). The reason for this distinct, and dramatic, change in spray angle is not completely clear. One possible cause is cavitation behaviour in the nozzle, even though the in-nozzle view provides no indication that this is a problem. As explained earlier the phenomenon of hydraulic flip, where edge cavitation sweeps through the nozzle from input to exit, can

dramatically reduce the spray angle; potentially producing a needle jet with negligible atomisation.

Reviewing the data in Figure 5.45, without counterbore, the injector with the 0.3 mm diameter microhole produced a spray angle of approximately 26° with a 1750 bar driving pressure at a density ratio of 85. This can be compared with the lower spray angle produced at the same operating conditions produced by the 0.15 mm diameter microhole. It is interesting to note that at the lower driving pressure (1050 bar), there is little variation of spray angle with microhole diameter.

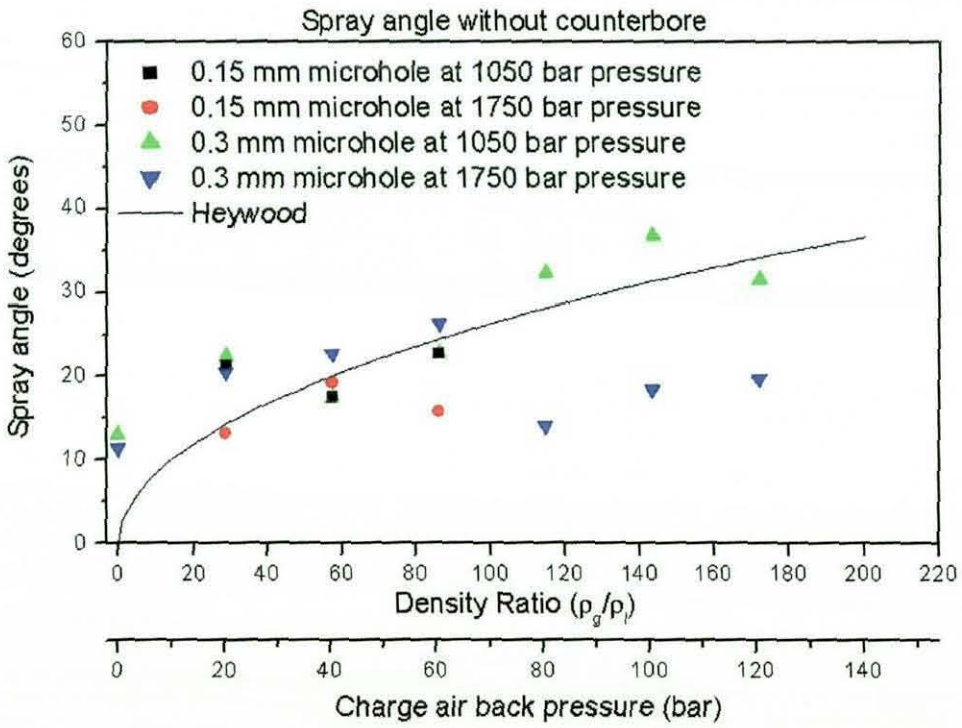

Figure 5.45 Comparison graph of 0.15mm and 0.3mm diameter microhole. [05]

However, the study revealed different trends when the counterbore is inserted in the test matrix. Figure 5.46 presents data for the 0.3 mm diameter microhole, with and without counterbore. The study clearly shows the geometry with no counterbore has a higher spray angle. Reviewing the data at a density ratio of 140, at an operating pressure of 1050 the spray angle is 38°

compared with 15° when the counterbore is inserted. Comparing spray angles at 1750 bar driving pressure we see the angle fall from 18° without counterbore to 11° with counterbore.

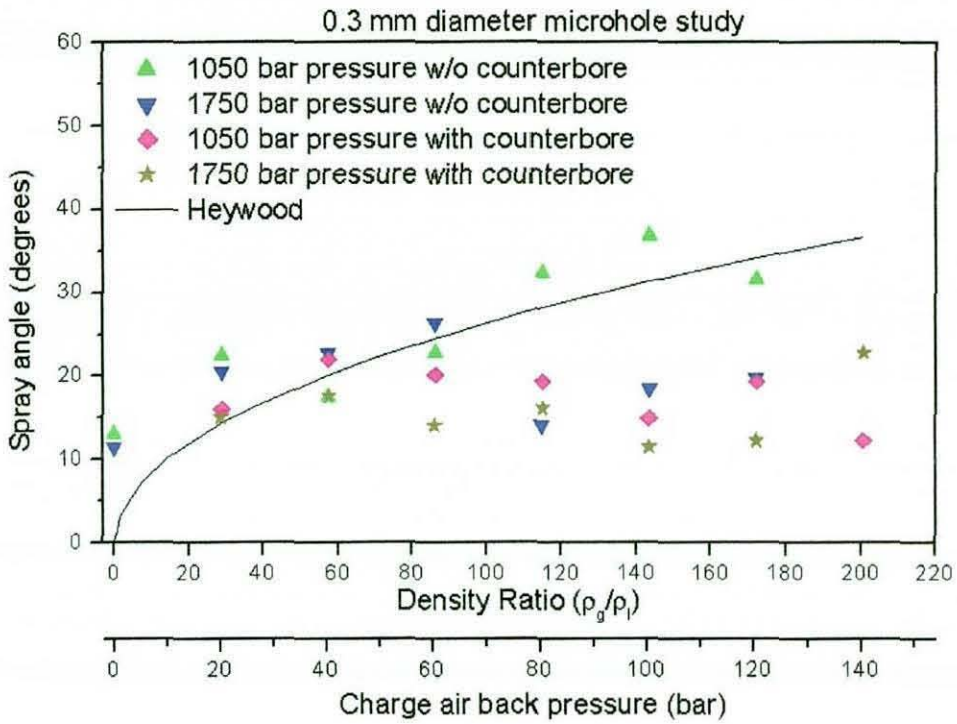

Figure 5.46 Comparison graph of 0.3mm diameter microhole. [05]

Similar studies were performed by Chaves *et al* [02] with the measurement of spray cone angle for varying driving pressure and chamber pressure from a 0.2 mm diameter and 1mm long nozzle. The study found that with a 60 bar charge back pressure the spray angle was the highest at approximately 26°. Their data is compared with the current data in figure 5.47, which shows the variation in spray angle with a driving pressure of 1050 bar and with air charge pressures up to 140 bar. The data provided by Chaves *et al* [02] was for air charge pressures up to 60 bar and has been extrapolated in this figure (dotted line). The figure shows good comparison between Chaves *et al* [02] and the current data and clearly shows the reduction in spray angle with the addition of the counterbore.

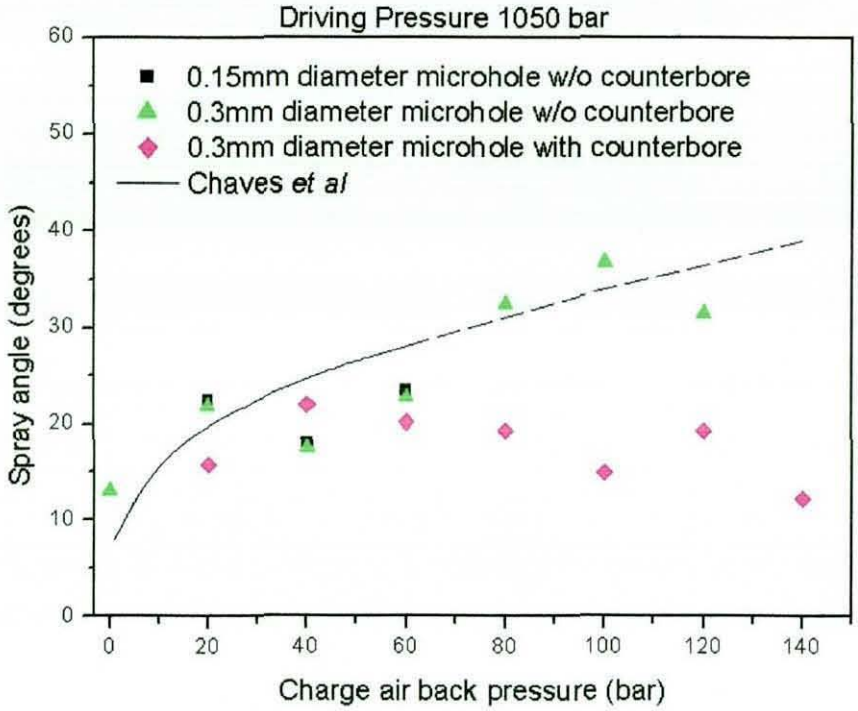

Figure 5.47 Charge back pressure at 1050 driving pressure compared with Chaves *et al* [02]

It is interesting to note that Chaves *et al* [02] reported significant cavitation at all air charge pressures as the driving pressure increases. This was not true for the current study, yet there is still good agreement between their data and the current study for the 0.3 mm diameter microhole.

5.4 SUMMARY

The Diesel injection studies have provided an insight into the internal and near-field external flow characteristics of a high pressure HEUI B injector. These studies used sapphire matrices, consisting of a sac, microhole, counterbore and a bottom plate. To the authors knowledge this is the first study to provide optical data at the driving pressures generated by a HEUI B injector (1750 bar). The experimental work showed that the sapphire matrix system provided significant information and data about internal flow structure.

The optical access allowed a high-speed imaging investigation of the internal and external flow structures. However, this was limited by the optical quality of the sapphire as mentioned in Chapter 4.

The flow visualisation study clearly indicated that cavitation is almost non existent at the higher driving pressures and does not have a significant effect on flow development even with sharp inlet orifices. The counterbore was observed to have significant effects on the external flow development and was shown invariably to reduce the spray angle. The counterbore geometry thereby provides a methodology for controlling the spray angle. This variation in spray angle was attributed to the development of an annular vortex in the counterbore, as shown in figure 5.48, which limits the initial spreading of the jet without the liquid interacting with a solid surface. It is also possible that the rotation of the vortex restricts the shearing at the periphery of the jet, thereby limiting the spray angle.

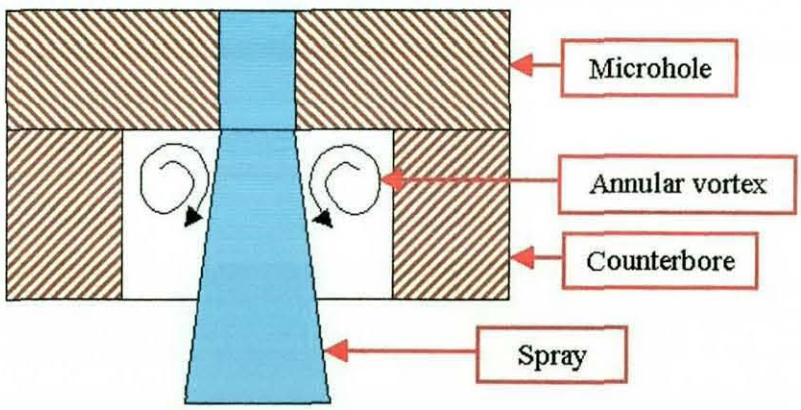

Figure 5.48 Schematic of an annular vortex in a counterbore.

Full engine test data of the nozzle injector in the fuel system of a six-cylinder, medium duty on highway diesel engine was provided by Coldren et al [03]. The advantages of the nozzle counterbore geometry for control of spray angle were clearly demonstrated; the engine showing significant reduction in NOx, HC and smoke emission with little or no fuel consumption penalty.

5.5 REFERENCES

[01] Bergwerk, W., *Flow Pattern in Diesel Nozzle Spray Holes*, Proceedings of the Institution of Mechanical Engineers, Vol. 173, Pg 655-660, 1959

[02] Chaves, H., Knapp, M., Kubitzek, A., Obermeier, F., Schneider, T., *Experimental Study of Cavitation in the Nozzle Hole of Diesel Injectors Using Transparent Nozzles*, SAE 950290, SP-1101, 1995

[03] Coldren, D.R., Schuricht, S.R., Smith, R.A., *Hydraulic Electronic Unit Injector with Rate Shaping Capability*, SAE 2002-01-2890, 2002

[04] El-Hannouny, E.M., Lee, T.W., Farrell, P.V., Reitz, R.D., *An Experimental and Numerical Study of Injector Behavior for HSDI Diesel Engines*, SAE 2003-01-0705, SP-1739, 2003

[05] Heywood, J.B., *Internal Combustion Engine Fundamentals,* McGraw-Hill Book Company, 1988, ISBN 0-07-100499-8

[06] Ohrn, T.R., Senser, D.W., Lefebvre, A.H., *Geometrical effects on discharge coefficicents for plain-orifice atomisers*, Atomization and Sprays Journal, Volume 1, No.2, pp 137-153, 1991

[07] Soteriou, C., Andrews, R., Smith, M., *Direct Injection Diesel Sprays and the Effect of Cavitation and Hydraulic Flip on Atomization*, SAE 950080, SP-1065, 1995

[08] Soteriou, C., Andrews, R., Smith, M., *Further Studies of Cavitation and Atomization in Diesel Injection*, SAE 1999-01-1486, SP-1460, 1999

[09] Tamaki, N., Shimizu, M., Hiroyasu, H., *Atomisation of super-high injection pressure liquid jet*, ILASS-Europe, Zurich (Switzerland), September 2001

CHAPTER 6

GASOLINE DIRECT INJECTION STUDIES

6.1 INTRODUCTION

Researchers and scientists have investigated gasoline direct injection in every major automotive research facility across the globe. As noted in the literature review [14, 15 and 27], this was the next logical step forward for gasoline powered vehicles to solve the environmental and emissions issues related to this engine type. This chapter aims to provide a better understanding in the flow characteristics using optical orifices and diagnostic techniques.

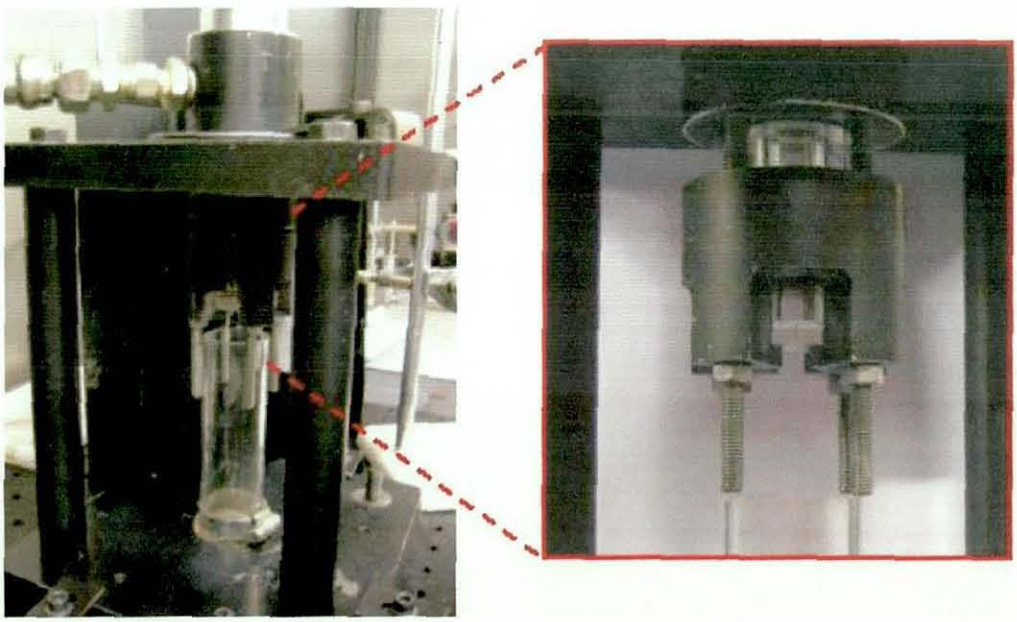

Figure 6.1 GDI optical test rig.

The optical diagnostic investigation was made possible by the designing and building of a GDI optical rig; shown on Figure 6.1. The assembly shows the optical components, shown in the insert, sandwiched between the perspex reservoir and optical holder and secured by four threaded lead screws with locking nuts. Care was taken to ensure equal torque was applied on the four nuts, so as not to exert too much force on the quartz to prevent them from

failing. This facilitates the use of non-intrusive optical diagnostic techniques to be employed in the internal and external flow investigations.

The results from the experiments are presented in three sub sections based on the optical diagnostic tools used. This was further divided into non-swirl and swirl nozzles under each optical diagnostic technique. The size and amount of data collected for the experiments were enormous and difficult to be included in this chapter alone. However, any possible trends from the various non-swirl and swirl orifices investigated will be discussed in detail to provide a global view on the flow characteristics. Full experimental data for the non-swirl and swirl orifices not highlighted in this chapter will be listed in the appendices.

6.2 NON SWIRL INJECTORS STUDY (FLOW VISUALISATION)

6.2.1 Overview

The high-speed flow visualisation setup used in this study was shown previously in figure 4.25 in chapter 4. This was an essential optical technique to provide an understanding of the flow structures through the optical nozzles, using a high-speed camera and a pulsed laser as the light source. The light source was a copper vapour laser with an output at 576 nm and 511 nm wavelength, using an optical fibre to transport the laser light to the optical rig and a diffuser to provide uniform back illumination. The high-speed camera was mounted on a two-axis traverse system and fitted with a Nikon 105 mm macro lens and bellows, allowing the camera to zoom close to the optical nozzles. Depending on the final imaged area, the resolution of the imaging ranged from 30 to 45 micron per pixel. This camera was positioned directly in front of the optical nozzles to capture the flow videos during each injection process. These flow videos were then analysed and stored as individual images. A series of these images was selected and presented in the following sections as a sequence of flow pictures to describe the flow structures on each non-swirl and swirl orifices. Two HSFV images shown in figure 6.2 are

examples showing the chamfered inlet orifice used with the red arrow showing the flow direction, depending on the setup used.

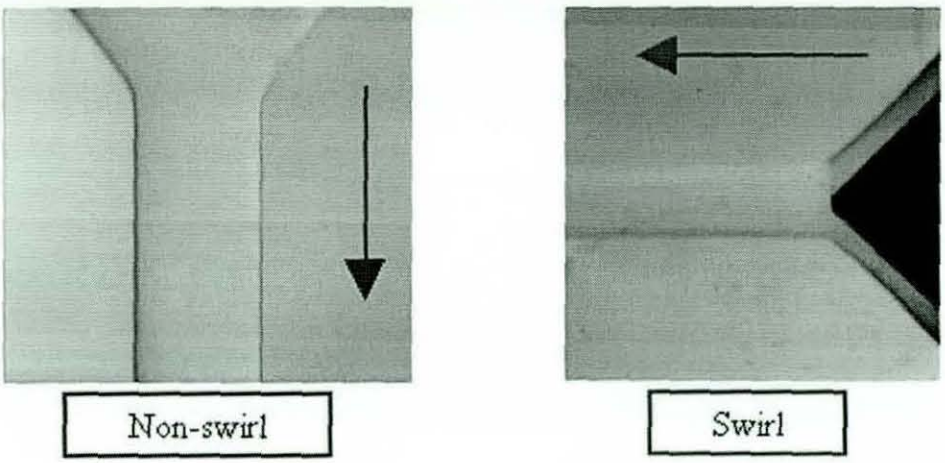

Figure 6.2 Two HSFV images showing the flow direction.

6.2.2 Results and Analysis

The first sequence of images shown in figure 6.3 was a 1 mm diameter nozzle with a sharp inlet from the reservoir to the exit nozzle, with the fluid flow images taken from the high-speed Kodak camera. The timescales indicated in this figure were relative to the first appearance of cavitation, with the flow direction from right to left. Cavitation was clearly visible in the image t+1.1ms as the driving pressure approaches the test pressure of 1MPa. Its formation was due to the generation of a low pressure region at the sharp inlet entry to the nozzle. The low pressure region could fall below the vapour pressure of the fluid, thus creating a vena contracta effect.

Schmidt [24] found that his flow model had an effective area that was significantly smaller than the nominal nozzle area due to the vena contracta effect generated by cavitation. This cavitation region continues to expand until by t+1.7ms it has extended the full length of the nozzle. Images t+1.7ms and t+1.9ms showed the dramatic effect the cavitation has on the spray shape and structure. However, as the cavitation reaches the nozzle exit (super cavitation) the fluid vapour in the cavitation region was replaced with air from outside the

nozzle. This annular structure of air in the nozzle now acts as a sheath around the liquid jet and significantly reduces the effect of aerodynamic shear on the emerging jet and gives rise to a very smooth and straight jet with virtually no break-up; as can be seen in images t+2.0 ms and t+2.2 ms. This phenomenon is widely known as hydraulic flip [25].

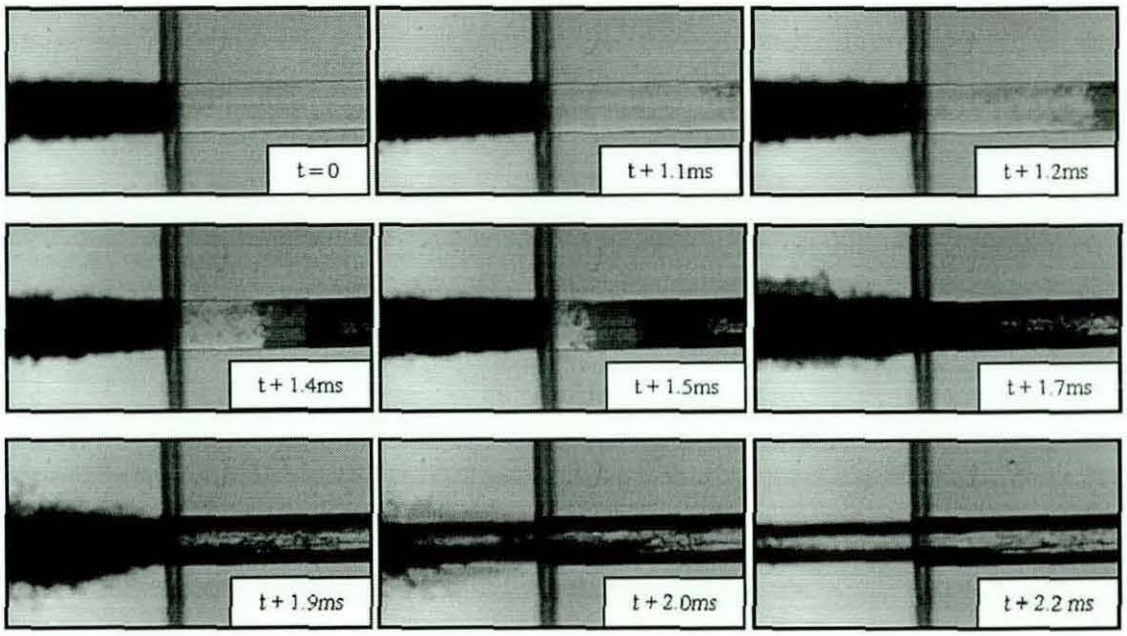

Figure 6.3 Cavitation and hydraulic flip in a 1mm diameter by 4mm long sharp inlet nozzle with a 1MPa driving pressure.

Although hydrodynamic pressure drop induced cavitation can provide control of spray structure, it is not ideal unless complete control of the process can be achieved over a wide range of operating pressures. Also, in this study cavitation obscures the in-nozzle flow and prevents the application of the PIV technique for the quantification of the velocity field in the nozzle. However, Allen *et al* [01] showed that once surface imperfections were removed from GDI nozzles, good quality velocity measurement could be achieved. This led to the development of the chamfered inlet orifices to allow us to quantify the velocity.

Figures 6.4 to 6.6 show three chamfered inlet orifices developed for use in this study, the 30°, 45° and 60° nozzles with flow from the reservoir and into the chamfered section before the nozzle exits. The three figures revealed the

developments of cavitation under different injection pressure condition, whose structure varies from nozzle to nozzle. These orifices were subjected to a series of injection pressure to provide an understanding to the flow characteristics. However due to the amount of data gathered from the flow orifices studied, the majority of the flow under different orifices and injection pressure used were listed in appendix A.

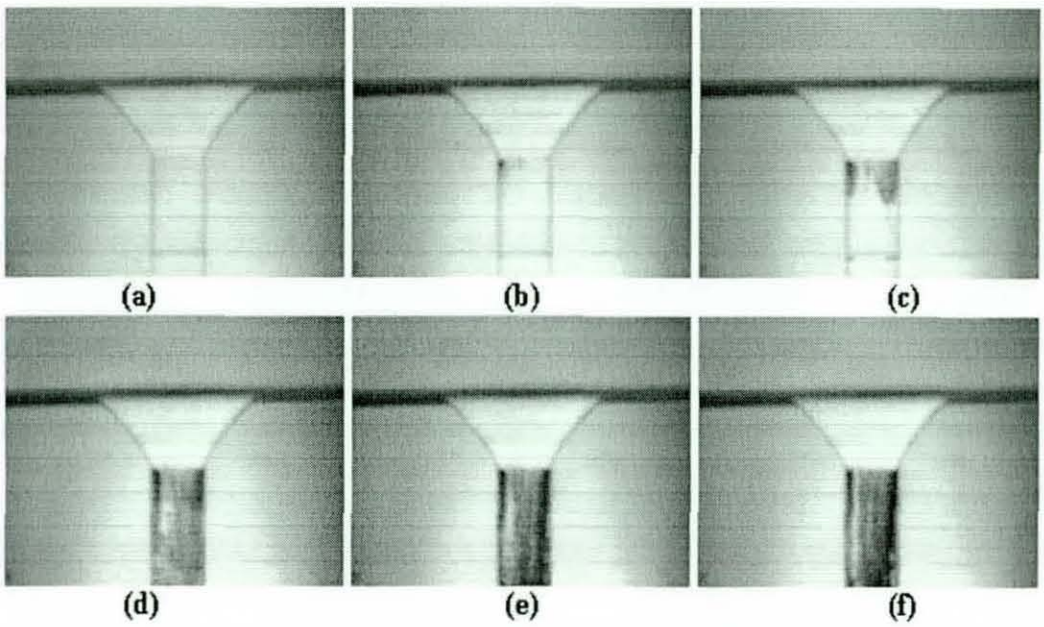

Figure 6.4 30° chamfered inlet orifice flow images at 20bar.

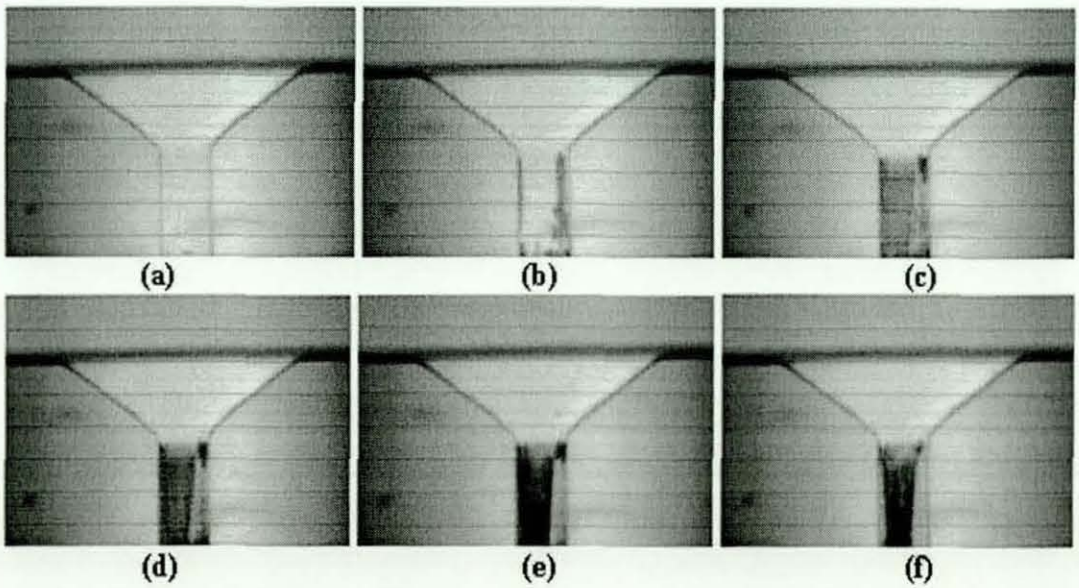

Figure 6.5 45° chamfered inlet orifice flow images at 30bar.

The 30° chamfered inlet orifice in figure 6.4 showed cavitation extends to the nozzle exit and it seems to be more localised than the sharp inlet nozzle. This was also observed with the 45° and 60° chamfered inlet orifices in figure 6.5 and 6.6, respectively. This localised cavitation seems to be caused by surface imperfections or the entry into the straight nozzle. These cavitation structures also increased with driving pressure when compared with those listed in appendix A. One other interesting aspect was no disruption of the flow was observed from the reservoir and into the convergent section of the orifice under different driving pressure conditions, indicating the reservoir does not have any significant effect on the orifice.

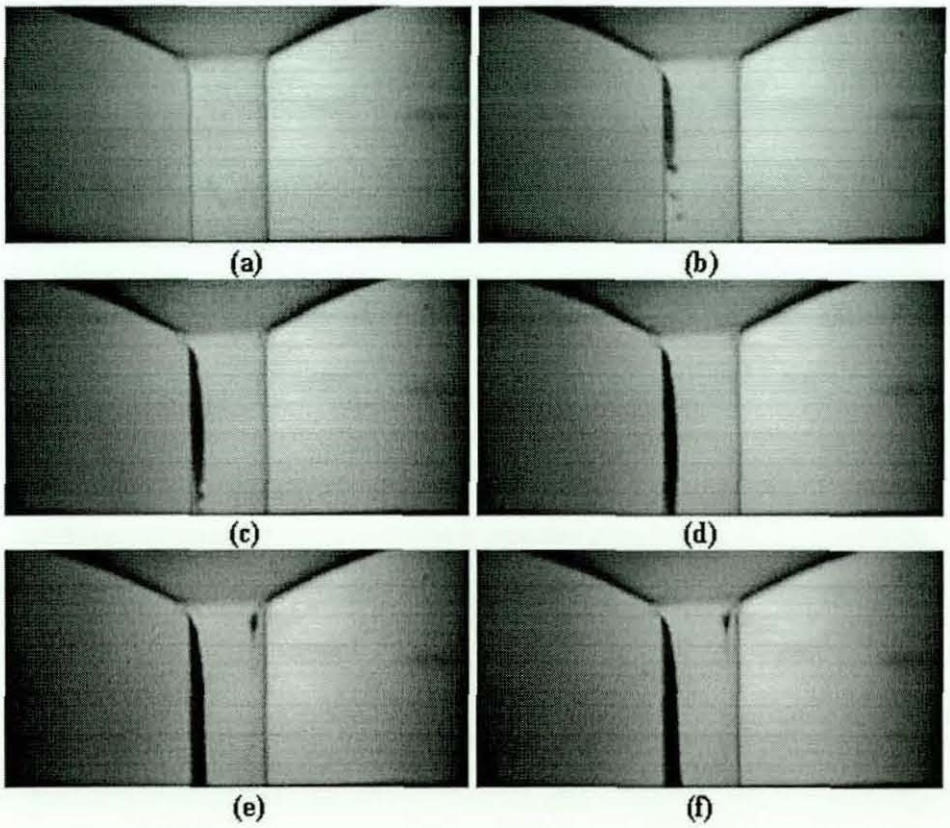

Figure 6.6 60° chamfered inlet orifice flow images at 10bar.

6.2.3 Discussion

The investigation of in-nozzle flow characteristics for the non-swirl injectors provided a useful insight of flow behaviour using different orifices and driving pressure conditions. The effect of cavitation on the sharp inlet nozzle (See

figure 6.3) was very dramatic, a small amount of cavitation caused a significant increase in the break-up of the spray, from 0° to 18°. However, with complete cavitation through the entire nozzle, this leads to hydraulic flip and effectively prevented any atomisation from occurring. This rapid transition from the initial onset of cavitation to the complete saturation of the nozzle made this process unstable and difficult to control the atomisation effect.

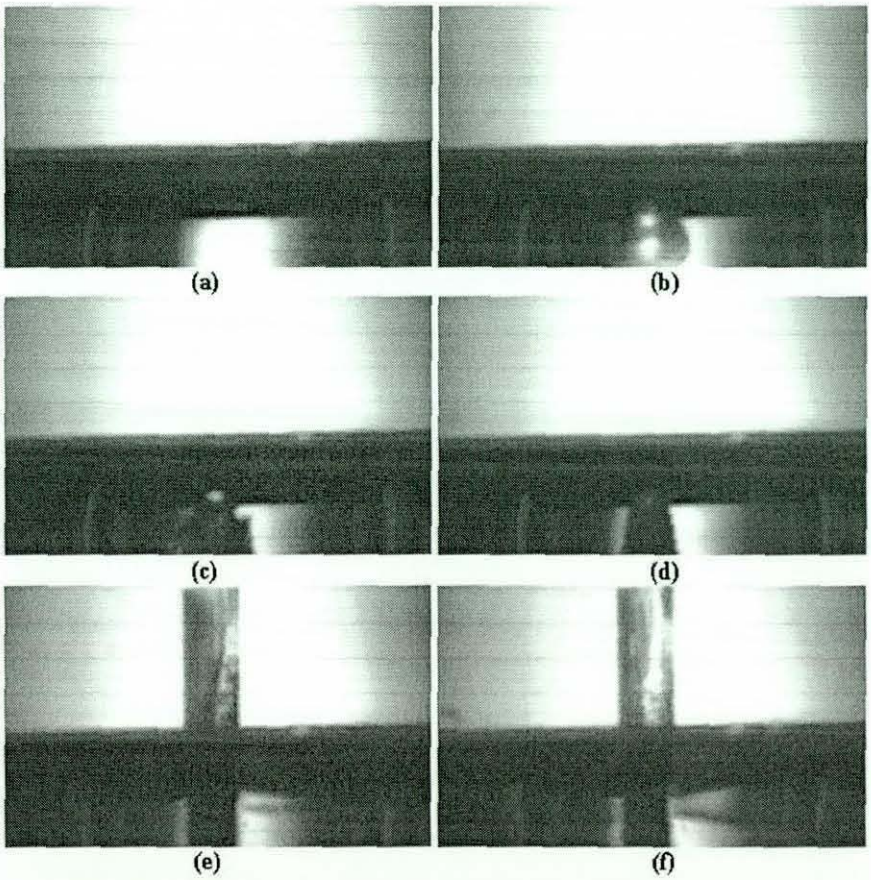

Figure 6.7 Internal and external flow regimes of a 30° chamfered inlet orifice with 50 bar driving pressure.

In the case of the chamfered inlet orifices, an interesting observation was that none of the orifices exhibited the hydraulic flip seen in the sharp inlet nozzle. Therefore, no straight and smooth jet was observed as the flow exited the three chamfered inlet orifices. The atomisation effect was also enhanced under high driving pressure conditions. The improvement in spray structures generated smaller droplets might improve combustion conditions in the case of a production engine. However, cavitation formation was noted to not only

sensitive to the change in geometry of the nozzle but also the surface imperfections in the nozzle shape highlighted in this study and by Allen *et al* [01]. They showed that any surface imperfections created localised cavitation.

Figures 6.7 and 6.8 show external flow structure images for 30° and 45° chamfered inlet orifices with 50 bar driving pressure. In the 40 bar driving pressure condition, the flow begins as the control valve was actuated. The flow began to open up as the flow reached peak pressure condition and cavitation develops. However the cavitated flow external spray structures does not differ much from non-cavitating condition, suggesting the atomised droplets are fairly large. With large atomised spray droplets, this will render PDA technique useless to measure large particle size in non-swirl orifices.

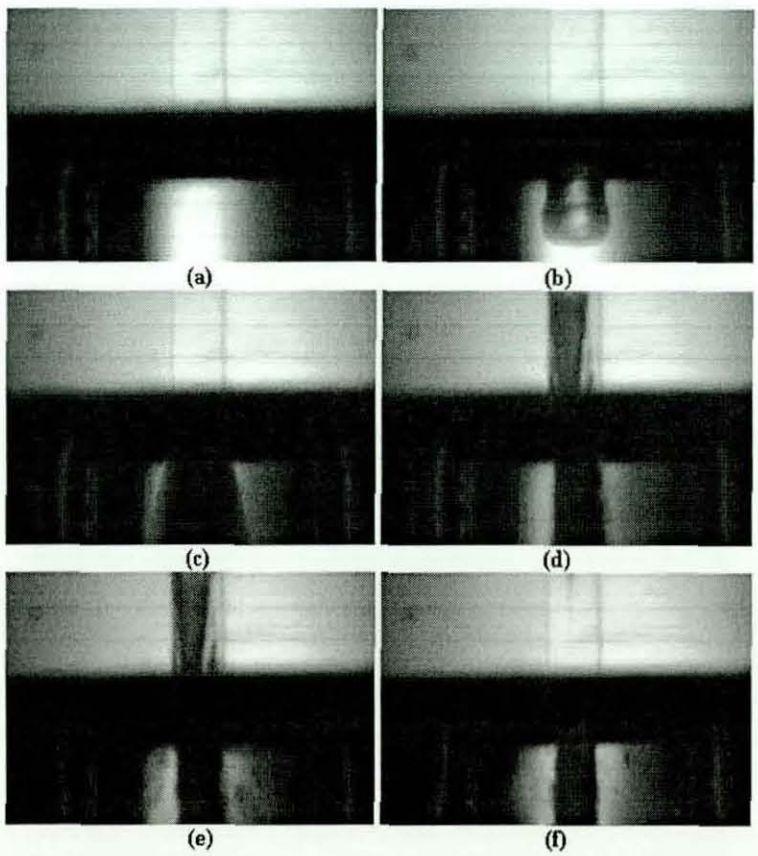

Figure 6.8 Internal and external flow regimes of a 45° chamfered inlet orifice with 50 bar driving pressure.

The study of flow structures from high speed flow visualisation provided a better understanding of the effects of the various orifice geometries on the

flow. However, the presence of cavitation structures would prevent the use of FPIV. To achieve this, any imperfection in the nozzle section of the orifice was required to be polished away. This was accomplished by using a thin wooden dowel with diamond solution and constantly polishes on the affected regions, until improvements were seen with high-speed flow visualisation. No further work to measure the spray droplet sizes of the atomised fluid using PDA technique were conducted due to the estimated large droplet sizes.

6.3 NON SWIRL INJECTORS STUDY (FPIV)

6.3.1 Introduction

Fluorescent particle image velocimetry was the next optical diagnostic tool used to quantify the in-nozzle flow for the three chamfered inlet orifices. This technique allowed the study of the flow velocity through different chamfered inlet sections and the nozzle sections of the orifices.

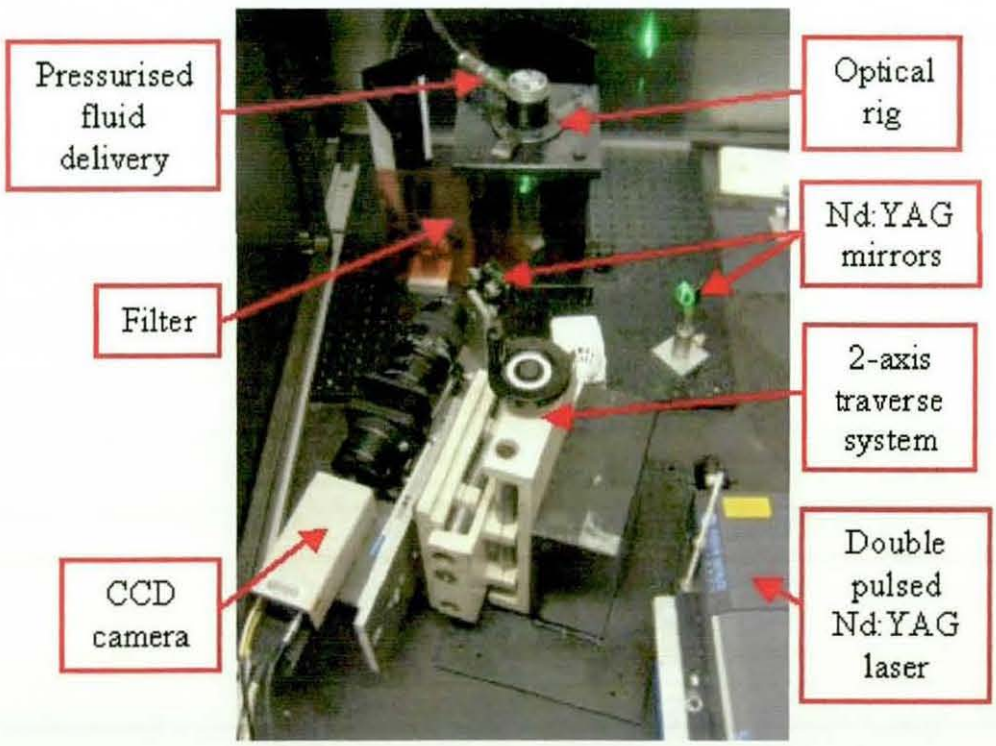

Figure 6.9 Fluorescent particle image velocimetry diagnostic setup.

The FPIV setup used in this study is presented in Figure 6.9. A doubled-pulsed Nd:YAG laser was used to provide the light source and aligned to illuminate the fluorescent seeding particles introduced into the flow as tracers. As mentioned in chapter 4, the fluorescent seeding particles used were 5 to 7 micron polyamide spheres with an encapsulated rhodamine laser dye (supplier: Brookhaven International). These particles were excited by the laser at 532 nm and emitted at a wavelength of 620 nm. Imaging through a 620 nm filter allowed the rejection of interference from unwanted scattering from injector and liquid surfaces. The twin-frame CCD camera with a 1μsec frame separation, records the fluorescence emitted by these particles. The doubled-pulsed laser images were then analysed using cross-correlation method with 32 x 32 and 64 x 64 pixels interrogation region and a 50% overlap. The size of the analysis region is dependent on the nozzle geometry investigated.

6.3.2 Results and Analysis

With the optical diagnostic setup for FPIV, the data collected was processed and analysed using Insight and Tecplot softwares [31]. The results are presented in the following order: starting with the 30° chamfered inlet nozzle and injector pressure ranging from 20 bar to 50 bar. This was followed by an example each from the 45° and 60° chamfered inlet orifices with injector pressure at 20 bar, with the rest listed in appendix A. These velocity profiles were also generated into graphs, showing the velocity flow through the centre of the nozzles with different driving pressures.

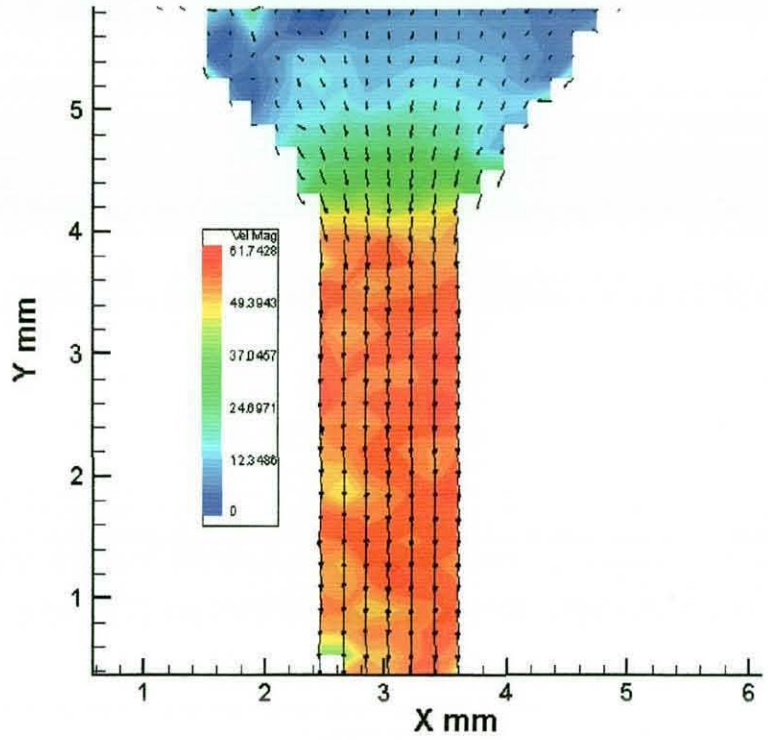

Figure 6.10 Average velocity magnitudes for 30° chamfered inlet orifice with 20bar driving pressure.

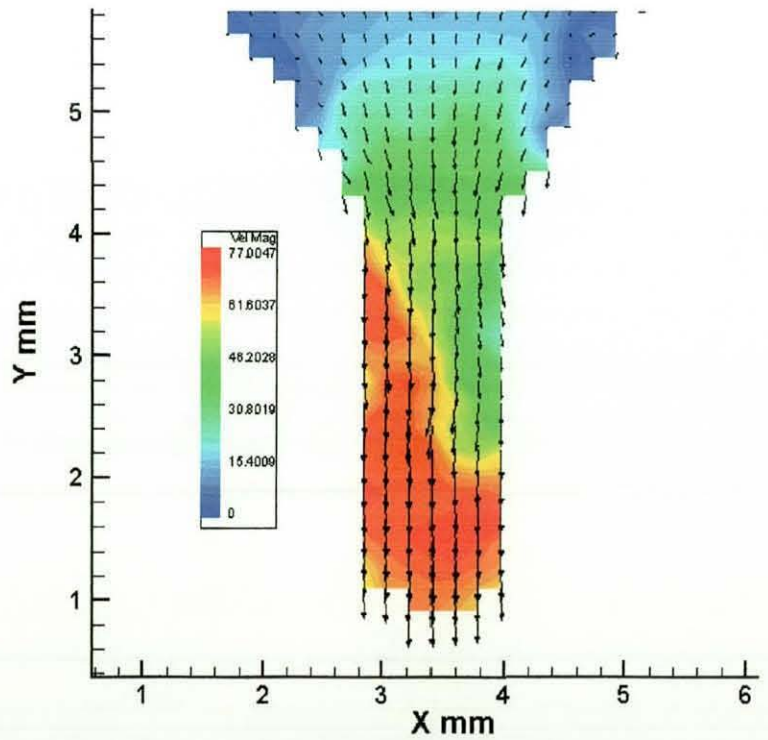

Figure 6.11 Average velocity magnitudes for 30° chamfered inlet orifice with 30bar driving pressure.

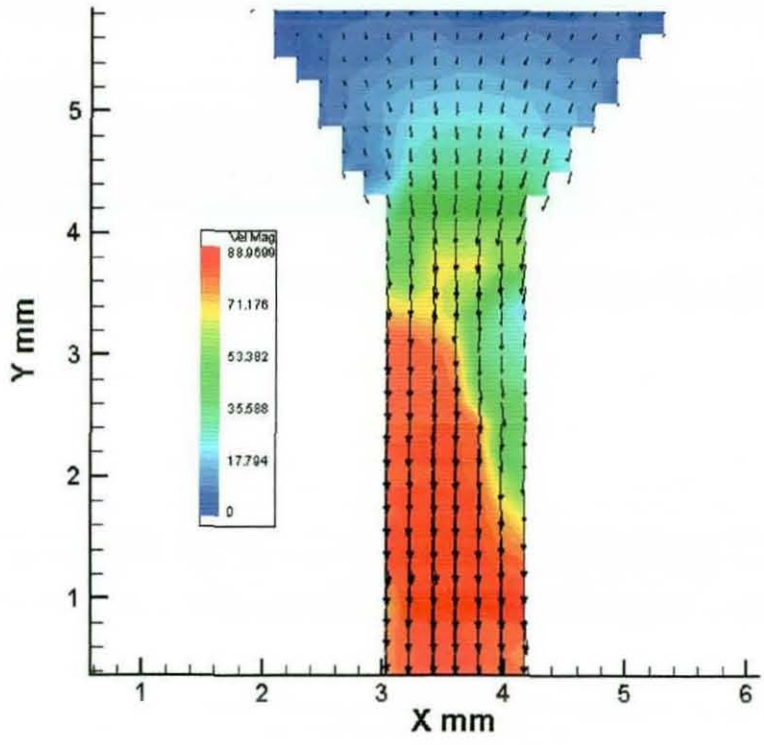

Figure 6.12 Average velocity magnitudes for 30° chamfered inlet orifice with 40bar driving pressure.

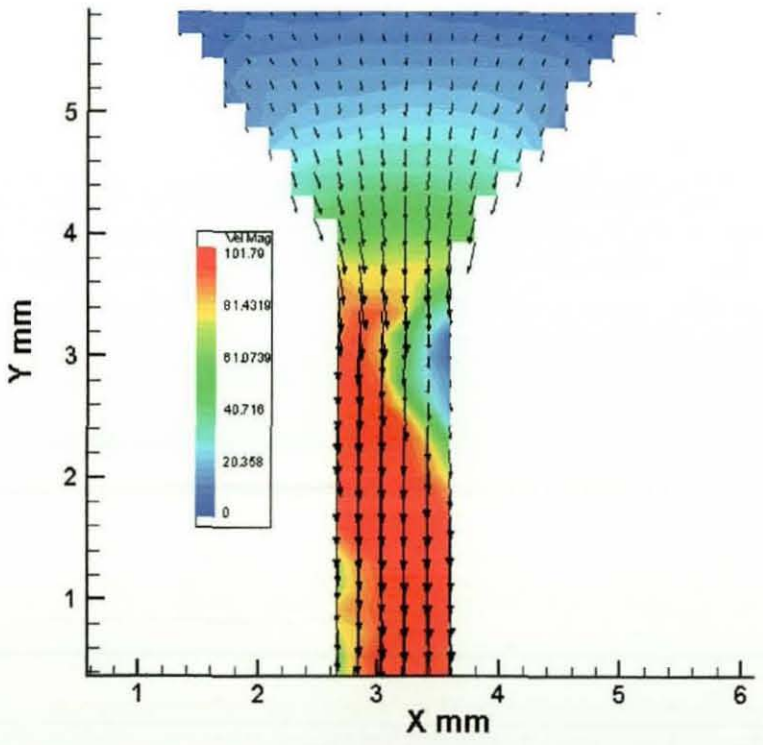

Figure 6.13 Average velocity magnitudes for 30° chamfered inlet orifice with 50 bar driving pressure.

Chamfered inlet orifices provided insight into flow velocity changes in the orifice with changing inlet angle. Figures 6.10 to 6.13 show the velocity profiles through the 30° chamfered inlet orifice with driving pressure range from 20 to 50 bar. These images show the flow from the chamfered inlet to the 1 mm nozzle and the colour coded bar indicates the velocity vector magnitude.

From these results, the injected fluid flow path was determined by the shape of the nozzle inlet. Low velocity vectors dominated the chamfered region of the nozzle when the flow enters from the reservoir and these velocity profiles increased as it reaches the straight region of the nozzle. Figure 6.10 velocity profile of the nozzle showed a more uniform velocity increment as compare to figures 6.11 to 6.13. These three figures flow velocity profile peaks at about 2 mm before the 1 mm nozzle exit.

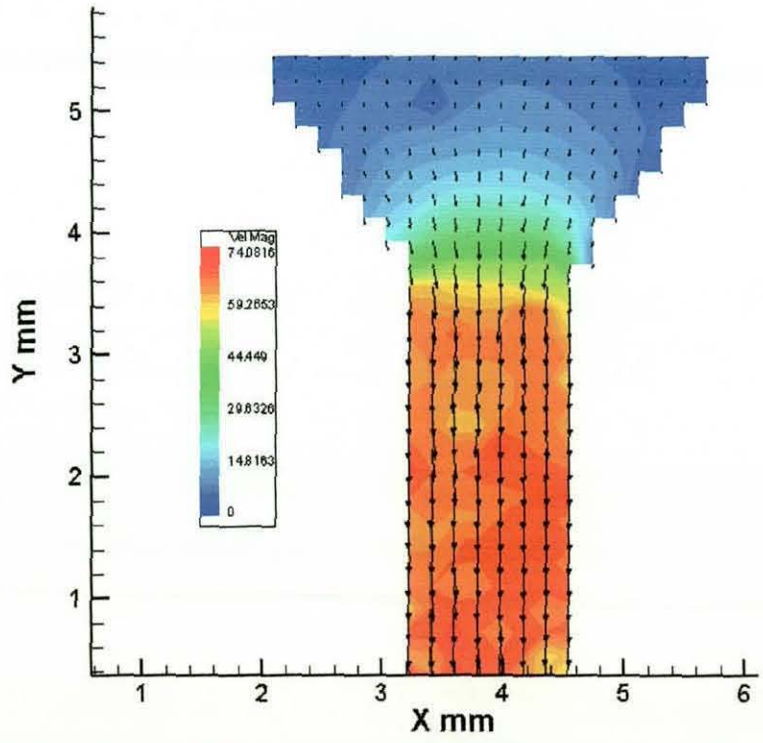

Figure 6.14 Average velocity magnitudes for 45° chamfered inlet orifice with 20 bar driving pressure.

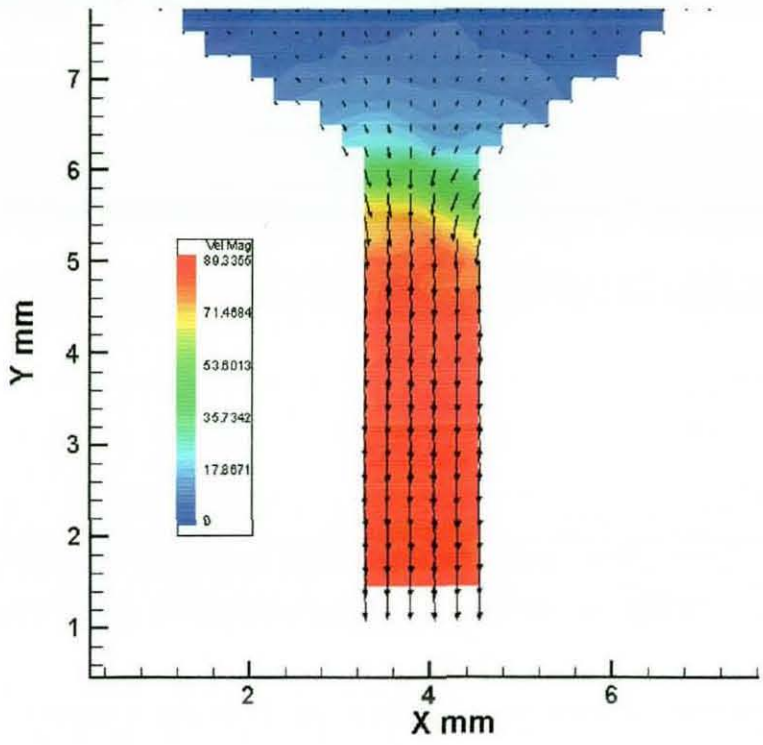

Figure 6.15 Average velocity magnitudes for 60° chamfered inlet orifice with 20 bar driving pressure.

Figures 6.14 and 6.15 show similar flow velocity trends for both 45° and 60° chamfered orifices as 30° chamfered inlet orifice for 20 bar driving pressure as shown in figure 6.10. Both show uniform increments in flow velocity as it surged into the 1 mm nozzle region. The peak velocity was observed to increase with increasing chamfered inlet nozzle. The maximum velocity shown for 30° and 45° orifices were 62 m/s and 74 m/s. In the case of the 60° orifice, there was an increase of more than 15 m/s from the 45° orifice. This profound increased in maximum flow velocity could be due to the shape of the 60° orifice. The larger chamfered inlet region required more flow into the 1 mm region of the nozzle.

To provide a better understanding of the flow velocity through the chamfered nozzles, the liquid flowing through the centre of the nozzle was plotted in three graphs, showing the velocity for each driving pressure. Figure 6.16 highlights the flow for the 30° chamfered orifice for injection pressure from 20 bar to 50 bar. The convergent section of the nozzle shows a linear velocity

increment into the straight section. Once the flow reached the convergent section, the velocity increases with injection pressure. The velocity for the 30 bar - 50 bar driving pressure was still increasing in the straight section of the nozzle. These increments straighten into a linear flow at about 1.5 mm into the straight section of the nozzle. The averaged velocities through the straight section of the chamfered nozzle are about 60 m/s with 20 bar injection pressure and this increased to 100 m/s for 50 bar injection pressure.

For the 45° chamfered inlet nozzles, the velocity trends are shown in figure 6.17. The velocity profile through the convergent section for 30 bar driving pressure is lower than the other driving pressures. The flow velocities were also slower in this chamfered inlet nozzle's convergent section when comparing to the 30° chamfered inlet nozzle. As with 30° chamfered inlet orifice the velocity continue to surge 1.5 mm into the straight section of the orifice, before the flow velocities stabilised into a steady-state flow. It should be noted that the data presented for 30bar driving pressure appears to be inconsistent and care should be taken in drawing conclusions from this data.

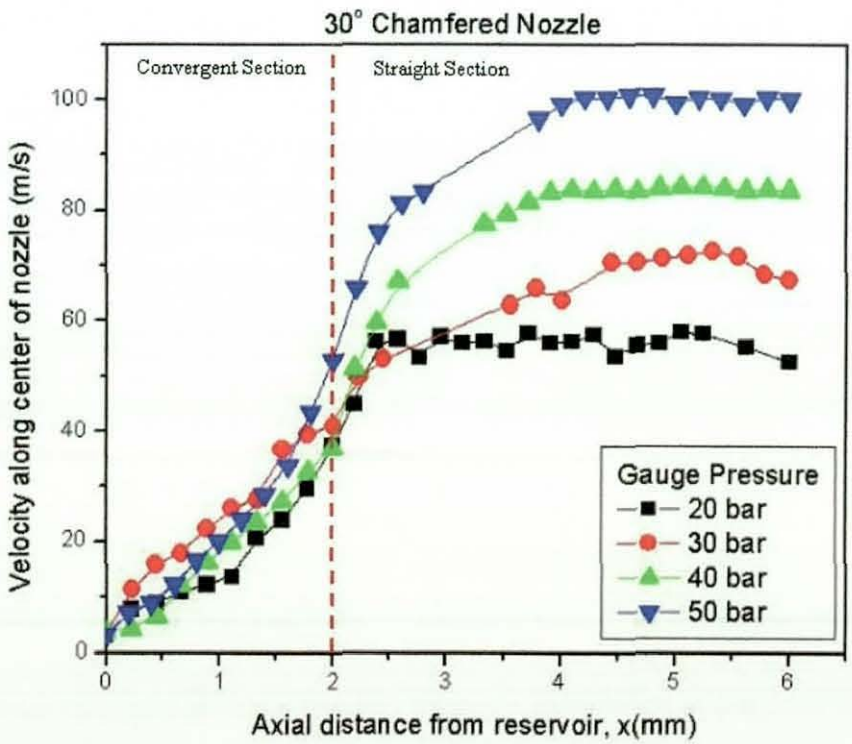

Figure 6.16 Velocity through the centre of a 30° chamfered inlet orifice.

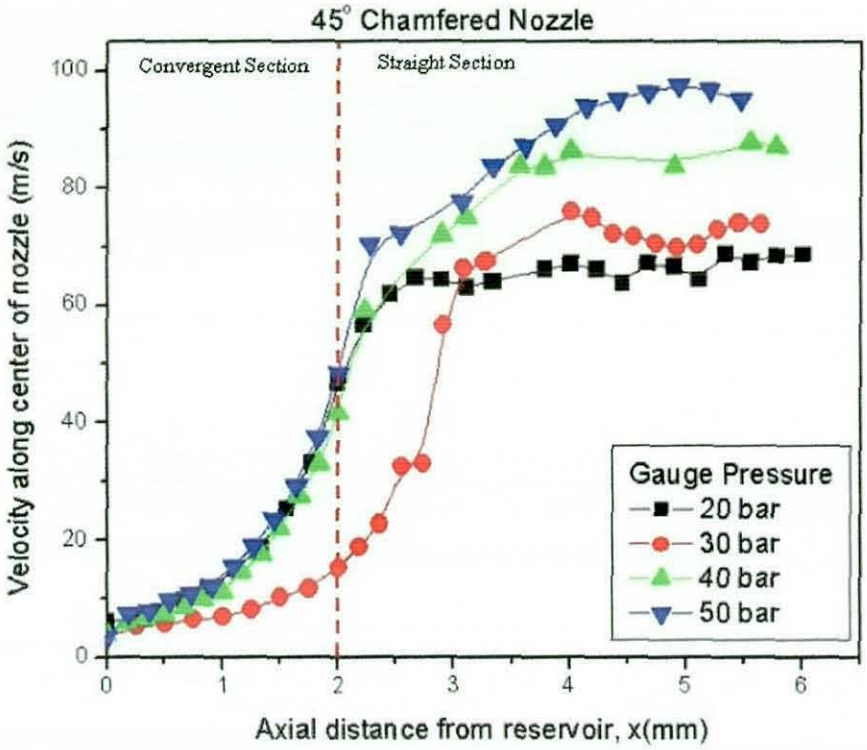

Figure 6.17 Velocity through the centre of a 45° chamfered inlet orifice.

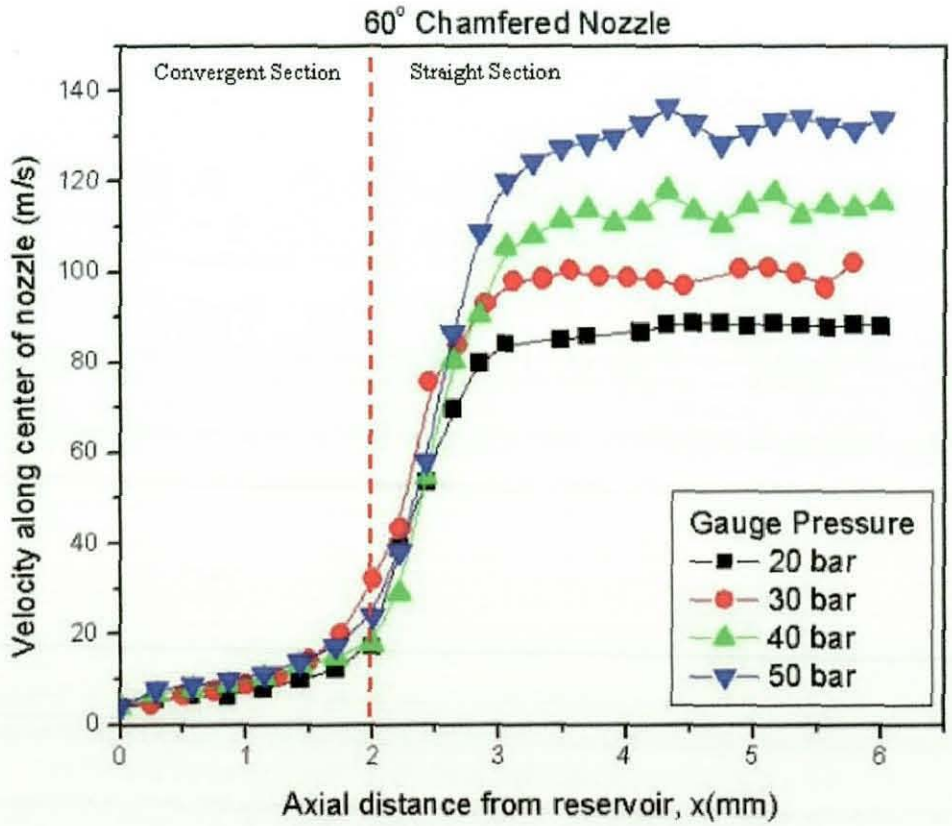

Figure 6.18 Velocity through the centre of a 60° chamfered inlet orifice.

With the higher chamfered inlet orifice of 60° angle, the velocity increments were more gradual initially in the convergent section of the nozzle. However, 1.5 mm into the convergent section, the flow velocity surged into the straight section for all injection pressure conditions before settling into a linear flow 1mm into the straight section. This orifice also recorded a higher averaged maximum velocity (135 m/s) for 50 bar injection pressure and this was considerably higher than the 100 m/s recorded for the other two orifices.

The flow velocity trends shown in figures 6.16, 6.17 and 6.18 provide a better insight and understanding of the flow behaviour under different driving pressure conditions. All the orifices showed the velocity profiles through the chamfered region in each nozzle were similar, regardless of the driving pressure. One notable difference between the three nozzles was the rate of flow from the chamfered inlet region to the 1 mm region of the nozzle. The rate of flow through these chamfered regions was observed to be lower with increasing chamfered inlet angle.

6.3.3 Discussion

The study of the non-swirl injector flows using FPIV allowed the velocity field to be quantified, providing a better understanding of the flow behaviour for different chamfered inlet orifices. From figures 6.10 to 6.15, it can be seen that the flow velocity is higher in the straight section of the orifice than the chamfered inlet region. These chamfered inlet regions assist the flow velocity to increase more gradually as oppose to the sharp inlet nozzle and thereby making the use of FPIV technique possible in the study of internal flow characteristics of optical nozzle. Without this chamfered region, supercavitation and hydraulic flip will dominate the flow regime for the internal and external flow of these nozzles.

Figures 6.16 to 6.18 provide the general flow trends through the center of the nozzle for increasing driving pressure. These figures also provide averaged velocities through these chamfered inlet nozzles. One notable observation is that the rate of flow through the chamfered region is slower for the 60° orifice

as compared to the 30° and 45° orifice. However, the rate of flow through the 60° orifice increased as it reaches the straight 1 mm diameter section. The likely cause for this sudden increased in flow velocity was the fact that the 60° orifice has a straighter inlet to the 1mm region as compared to the other two nozzles. Figure 6.16 shows the 30° orifice has a higher velocity through the chamfered region of the orifice, as compared to the gradual increase seen with the 60° orifice shown in figure 6.18.

Figures 6.19 to 6.22 show the velocity trends comparing three chamfered inlet orifices with the same driving pressure. They clearly show there is a distinct difference in the flow velocity through the centreline of the 60° chamfered inlet orifice with both the 30° and 45° chamfered inlet orifices. The 60° chamfered inlet orifice velocity increments are steeper when it enters the straight section of the nozzle, with the velocity rise shown clearly in the 1 mm of the straight section of the nozzle.

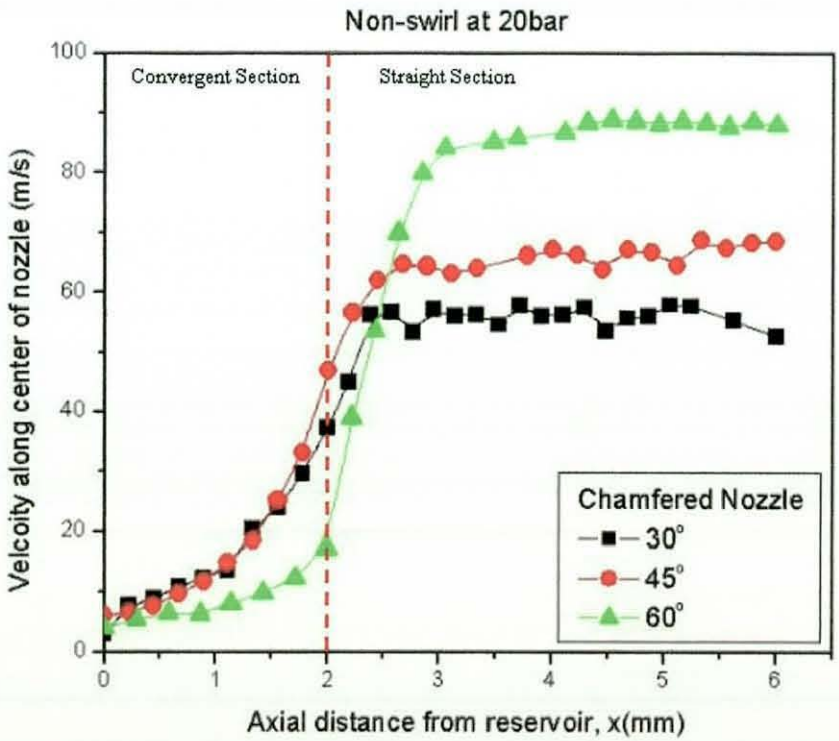

Figure 6.19 Comparison of different chamfered inlet orifices at 20bar.

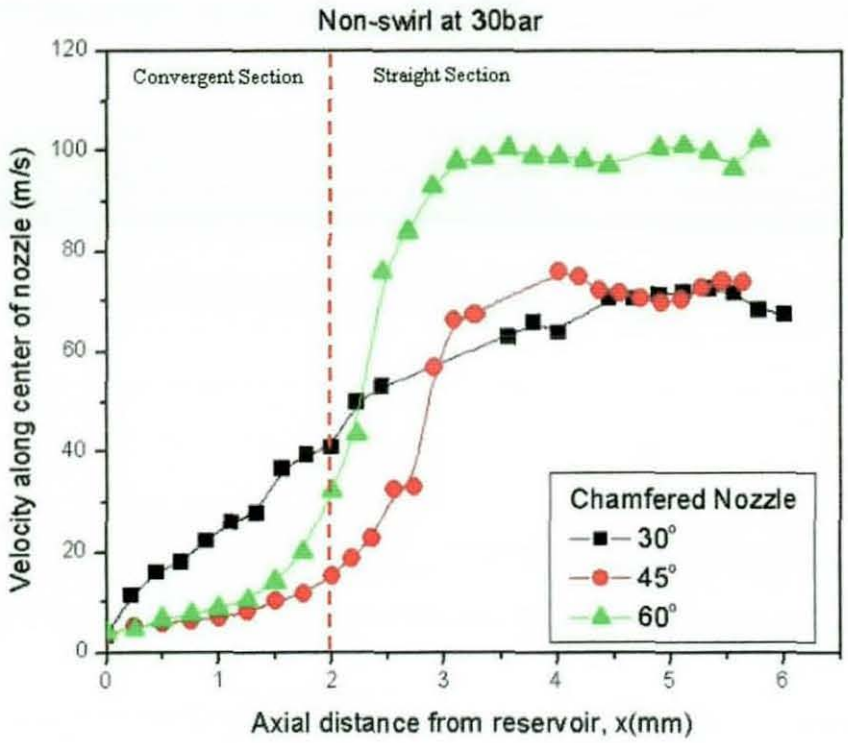

Figure 6.20 Comparison of different chamfered inlet orifices at 30bar.

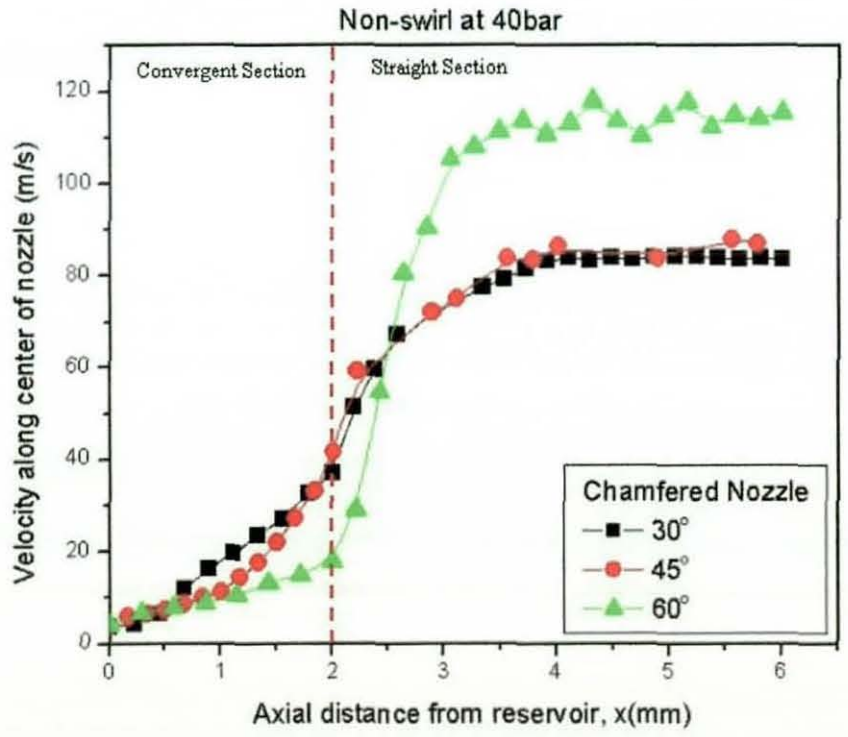

Figure 6.21 Comparison of different chamfered inlet orifices at 40bar.

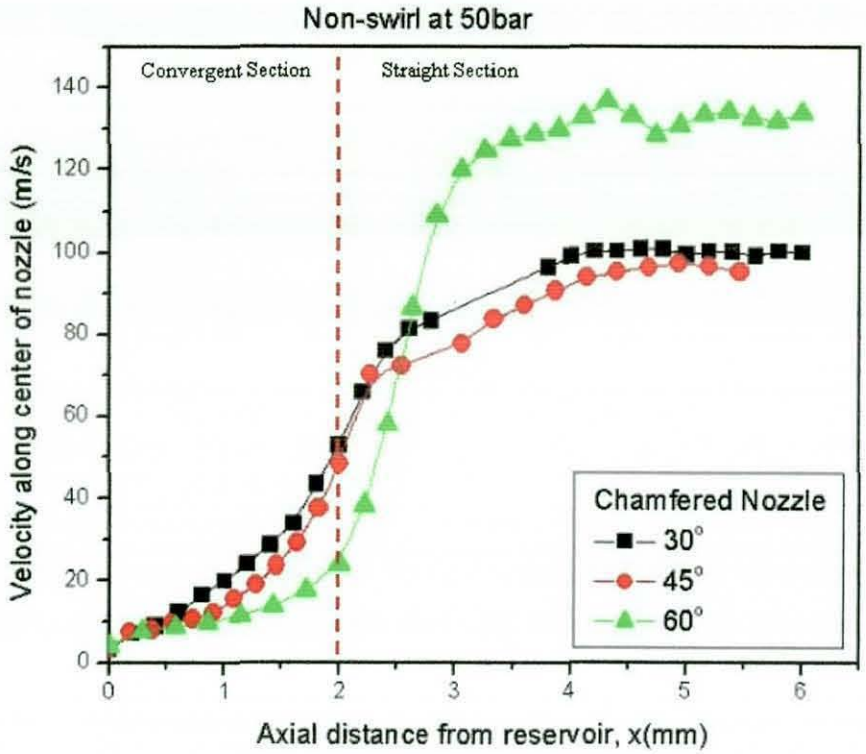

Figure 6.22 Comparison of different chamfered inlet orifices at 50bar.

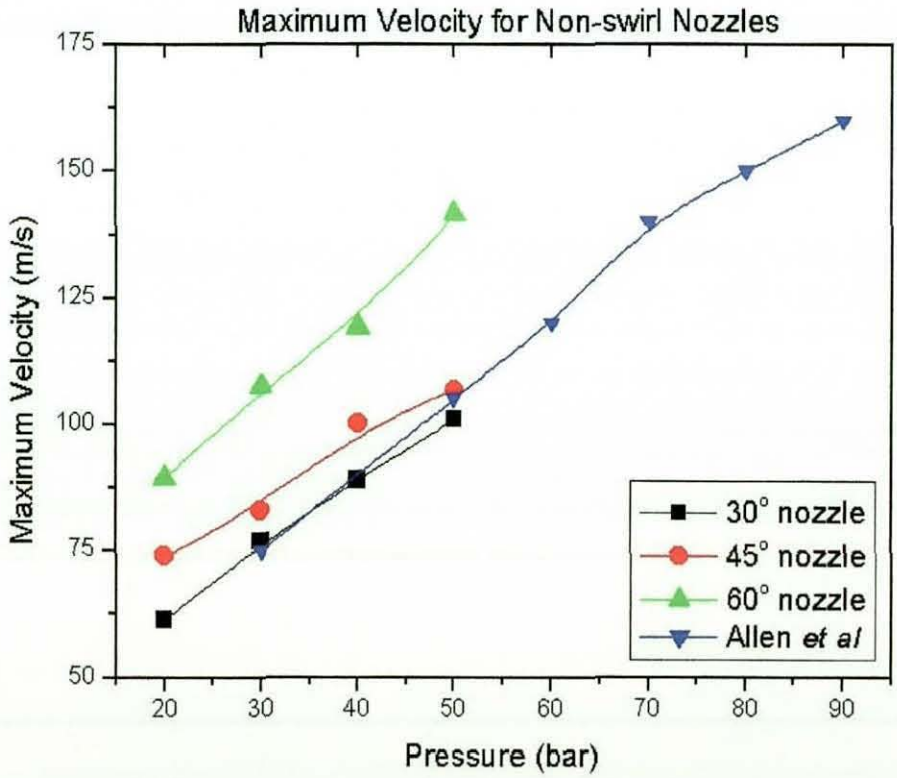

Figure 6.23 Maximum velocity for non-swirl orifices. [01]

Figure 6.23 provides further analysis of the flow, presenting the variation in maximum velocity for the three chamfered nozzles with driving pressure. The graph clearly shows that the pressure increase is linear with respect to the driving pressure, for all nozzles. This is particularly useful in predicting the likely maximum velocity at higher driving pressures. Included in this graph is the data from an earlier study by Allen *et al* [01], which provided internal velocity data for a 1 mm diameter nozzle with a 45° chamfered inlet orifice. The current data agrees well with the data of Allen et al. and demonstrates that the linear trend in velocity continues to a pressure in excess of 90 bar.

The study of non-swirl chamfered inlet orifices provides quantitative data for validation of Computational Fluid Dynamic (CFD) model, which will be presented in appendix C. This allowed the construction of a simple single-phase 3D mathematical model to provide an analytical description of the transient behaviour inside the nozzle of different chamfered inlet orifices. This is to facilitate any future modelling work involving swirl flow investigation. As mentioned, no PDA quantification will be investigated and examined due to the nature of the dense spray structures and large droplets generated by non-swirl flow study.

6.4 SWIRL INJECTORS STUDY (FLOW VISUALISATION)

6.4.1 Introduction

With the understanding of the internal flow regimes under non-swirl condition, the next investigation requires the use of swirl generators inserted into the same nozzle geometry to provide an insight on the new internal flow structures.

The basic principle of the pressure swirl atomiser was described in chapter 2 (section 2.1.3) and is reiterated in figure 6.24. The aim is to provide control of the swirl ratio and thereby control the size of the aircore and the thickness of the annular flow. This allows manipulation of the axial and tangential velocity

components at the nozzle exit to control the spray angle and break-up of the liquid sheet.

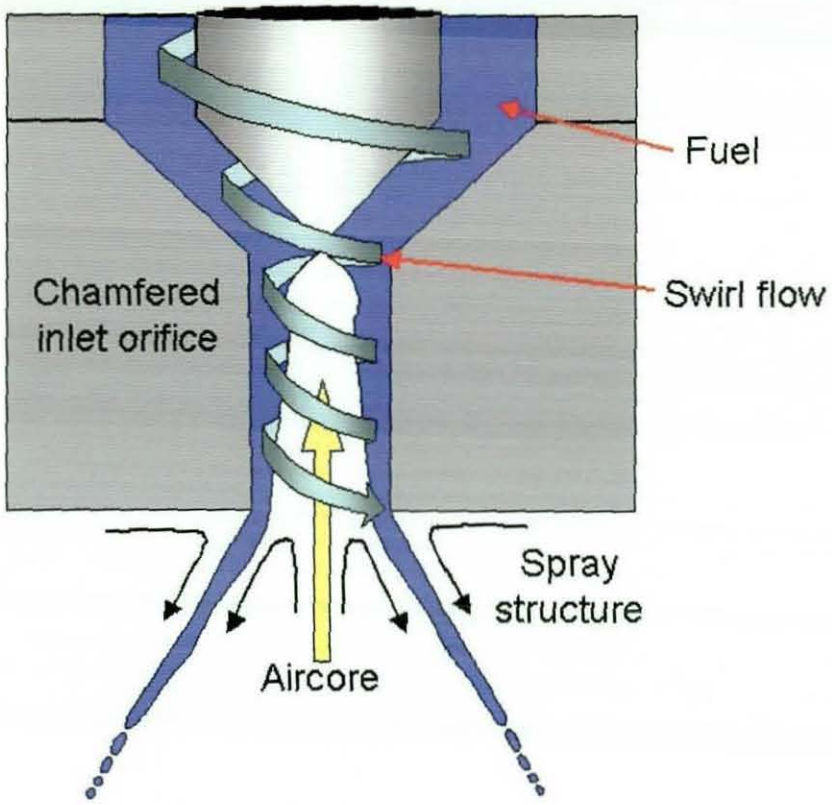

Figure 6.24 Basic principle of swirl orifice spray structure.

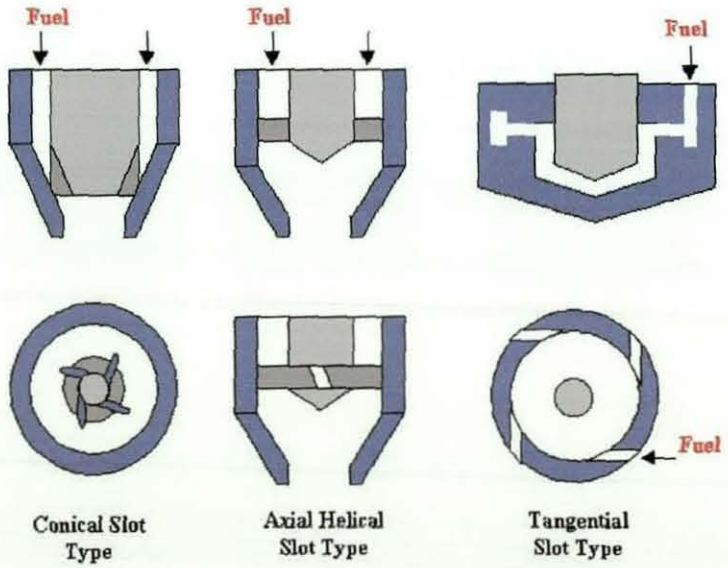

Figure 6.25 Commercial Swirl nozzles. [14]

There are many ways to generate a swirling flow through the nozzle and some of these are presented in figure 6.25. The choice of swirler is dependent on the fuel pressure available, the fuel flow rate and the swirl ratio required.

The geometry of the swirl generators chosen for the current study is presented in figures 6.26 and 6.27. The swirlers consist of a aluminium body with 1 mm x 1 mm flow channels machined into the surface and a pintle valve with a half angle of 15° running through the centre. The swirlers were inserted just above the optical orifices, allowing different swirl ratios to be generated. These different entry conditions allowed the same orifices to be studied as pressure swirl atomisers with varying flow rates and swirl ratios and also allows the accurate reproduction of real GDI nozzle geometries.

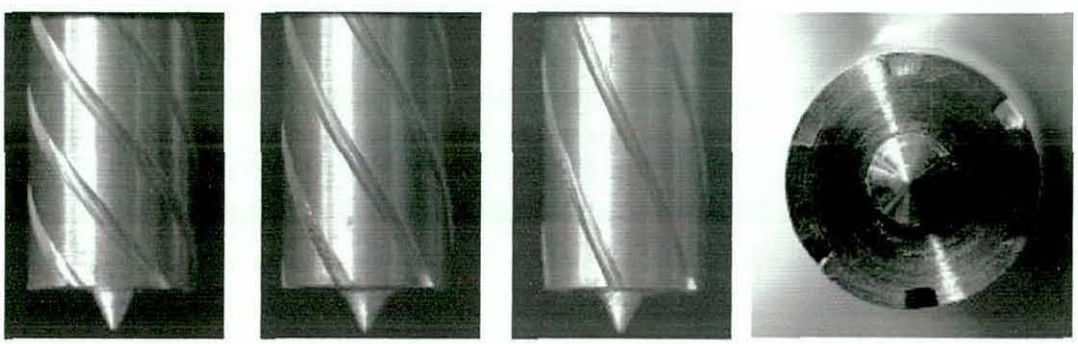

Figure 6.26 Three swirlers used in the experiments.

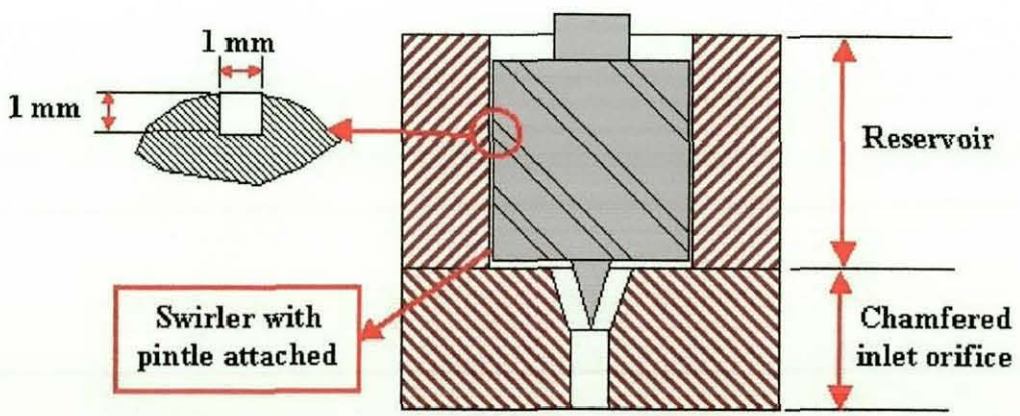

Figure 6.27 Swirler positioned into the chamfered inlet orifice.

6.4.2 In-nozzle Flow Results and Analysis

6.4.2.1 30° SWIRLER STUDY

A 30° swirler was used to investigate the flow characteristic of three chamfered inlet orifices. Each figure in this section presents a sequence of nine images of the flow development from atmospheric condition to the designated driving pressure, with the last image showing the fully developed flow. These flow images were taken at 9000 frames/sec using a high-speed Kodak camera. As the nozzle driving pressure increases, the swirl flow generated a vortex in the nozzle. This vortex grows in strength and draws a swirling aircore into the nozzle and attached to the pintle. This flow forces the exiting fuel flow into a thin annular region close to the wall.

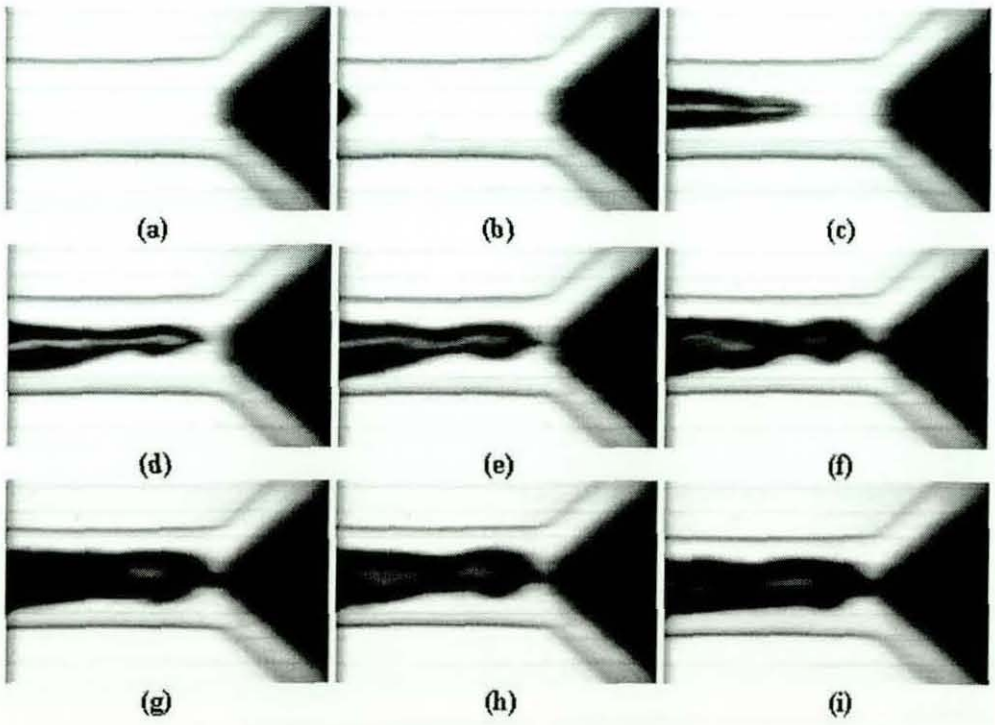

Figure 6.28 Flow images of 30° swirler with 30° chamfered inlet orifice at 20 bar pressure.

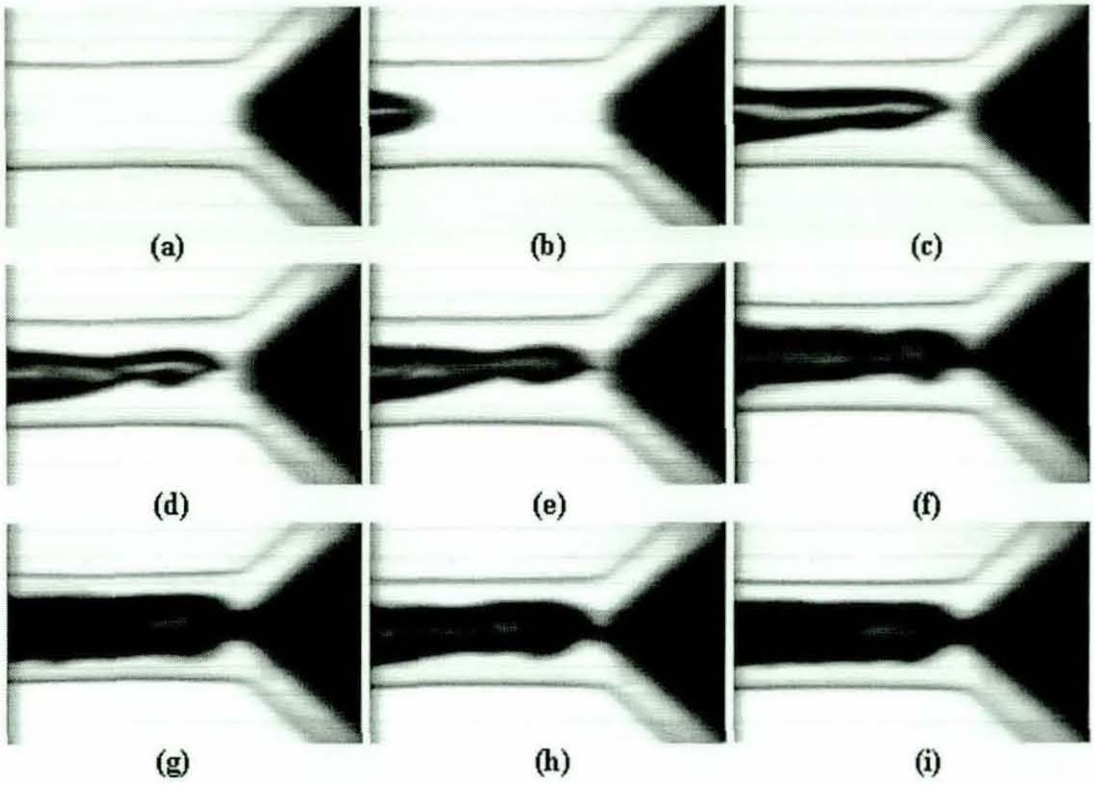

Figure 6.29 Flow images of 30° swirler with 30° chamfered inlet orifice at 30 bar pressure.

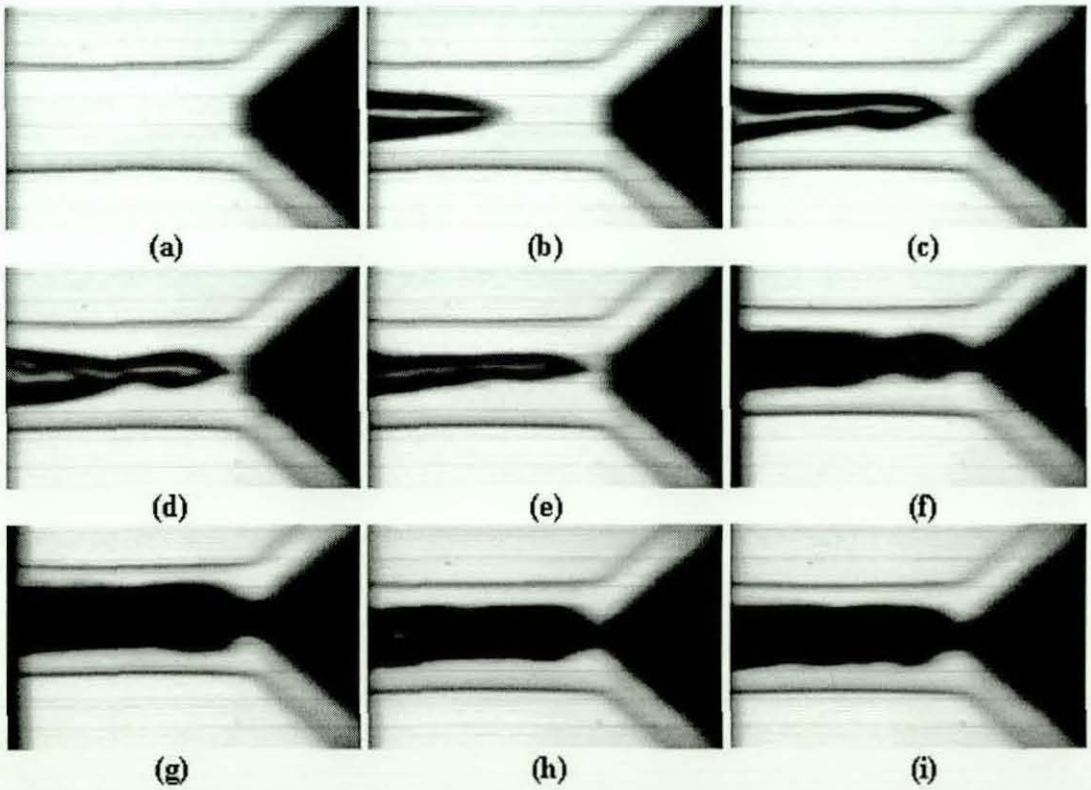

Figure 6.30 Flow images of 30° swirler with 30° chamfered inlet orifice at 40 bar pressure.

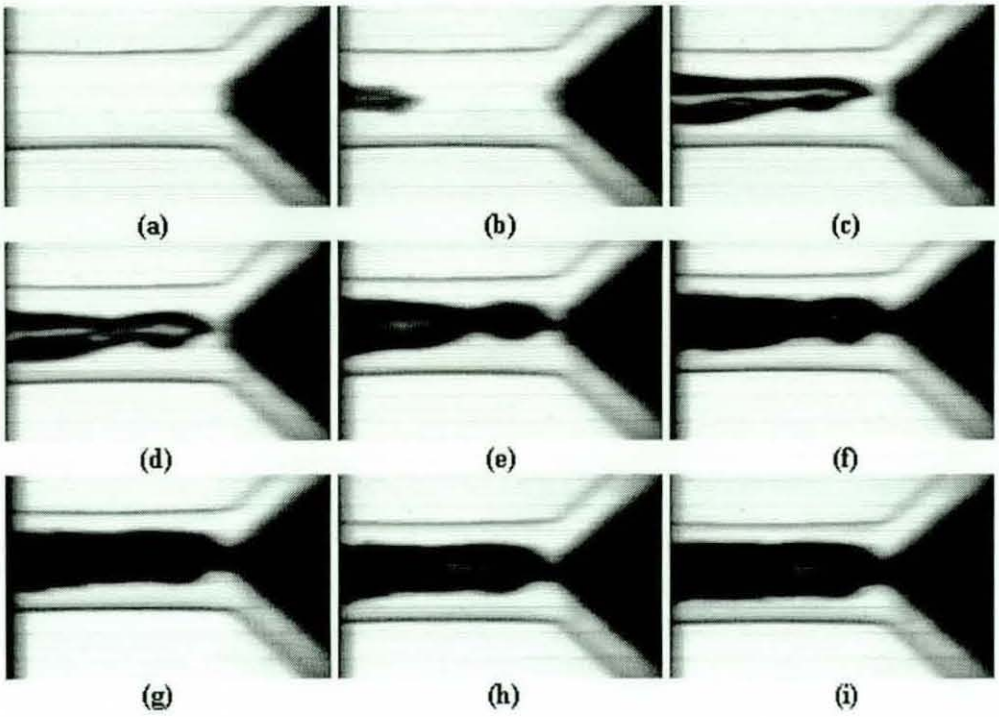

Figure 6.31 Flow images of 30° swirler with 30° chamfered inlet orifice at 50 bar pressure.

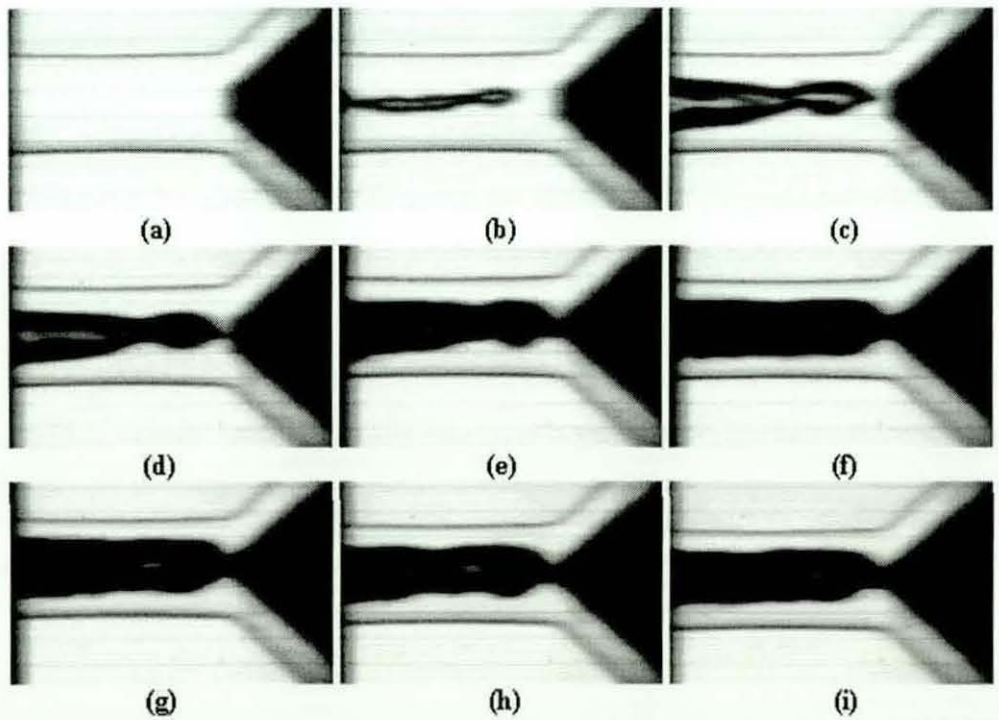

Figure 6.32 Flow images of 30° swirler with 30° chamfered inlet orifice at 60 bar pressure.

Figures 6.28 to 6.32 study the internal flow structures of a 30° chamfered inlet orifices with varying driving pressure. The visualised flow images showed the aircore developed as the pressurised fluid built up in the nozzle. The aircore travels up the nozzle and connects to the pintle as it reaches peak driving pressure. The visualised flow generated flow generated formed an almost perfect aircore from the pintle to the nozzle exit. The visualised aircore and annulus shown in these figures for all 30° chamfered inlet orifices look identical in all driving pressure ranges.

Figures 6.33 to 6.37 show the second study for 30° swirler with a 45° chamfered inlet orifice from 20 to 60 bar driving pressure. The aircore again was seen to travels up the nozzle and connects to the 30° angle pintle when it reaches peak pressure. The aircore structures formed a tapered shape leading from the pintle to the nozzle exit and one other noticeable difference is the necking in the aircore shown in these figures.

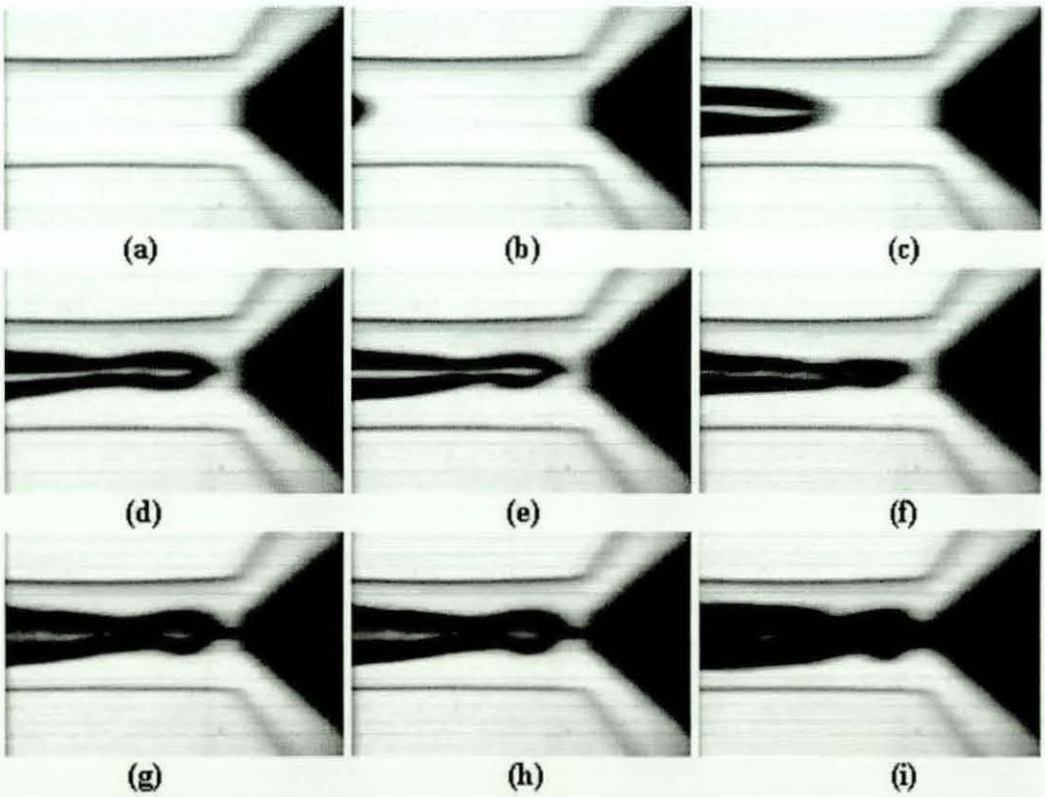

Figure 6.33 Flow images of 30° swirler with 45° chamfered inlet orifice at 20 bar pressure.

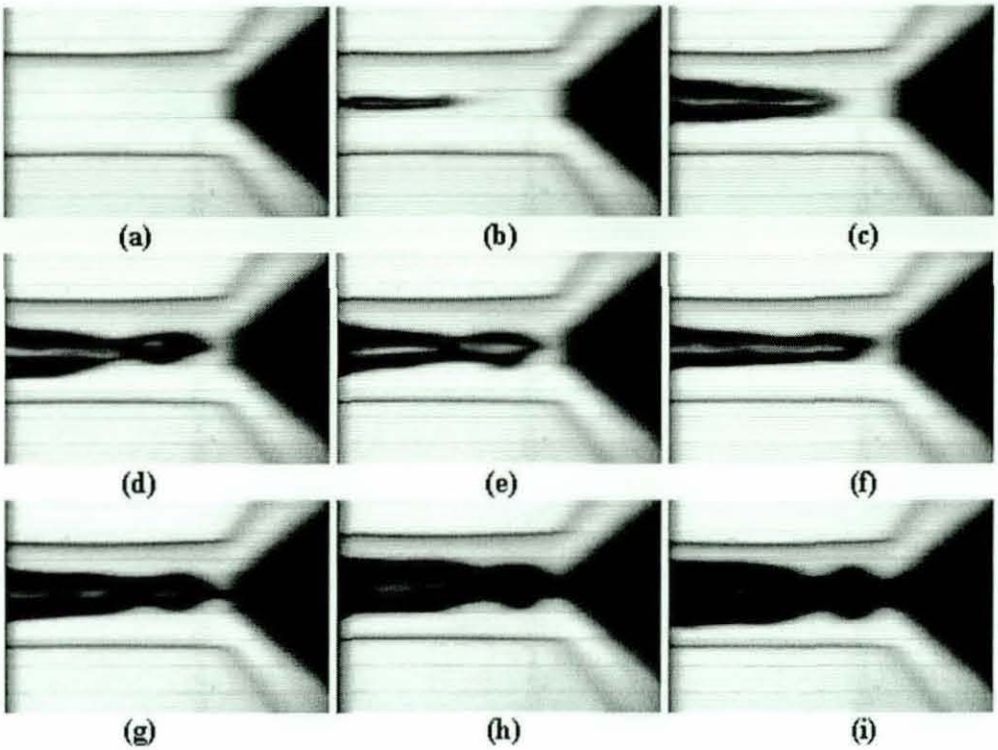

Figure 6.34 Flow images of 30° swirler with 45° chamfered inlet orifice at 30 bar pressure.

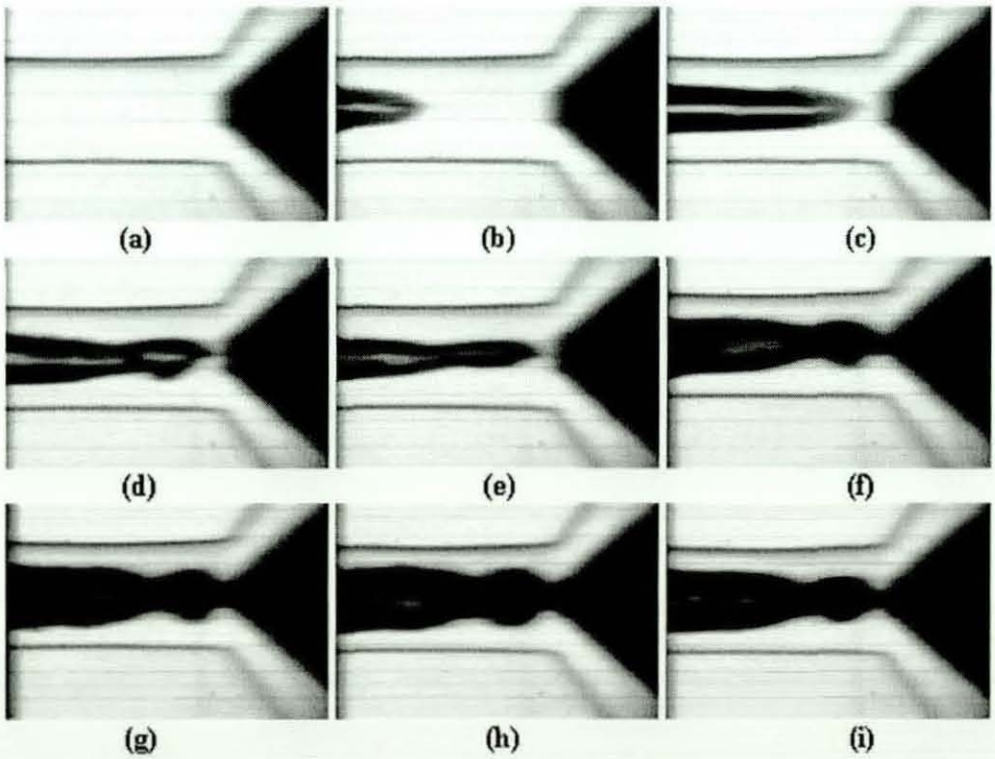

Figure 6.35 Flow images of 30° swirler with 45° chamfered inlet orifice at 40 bar pressure.

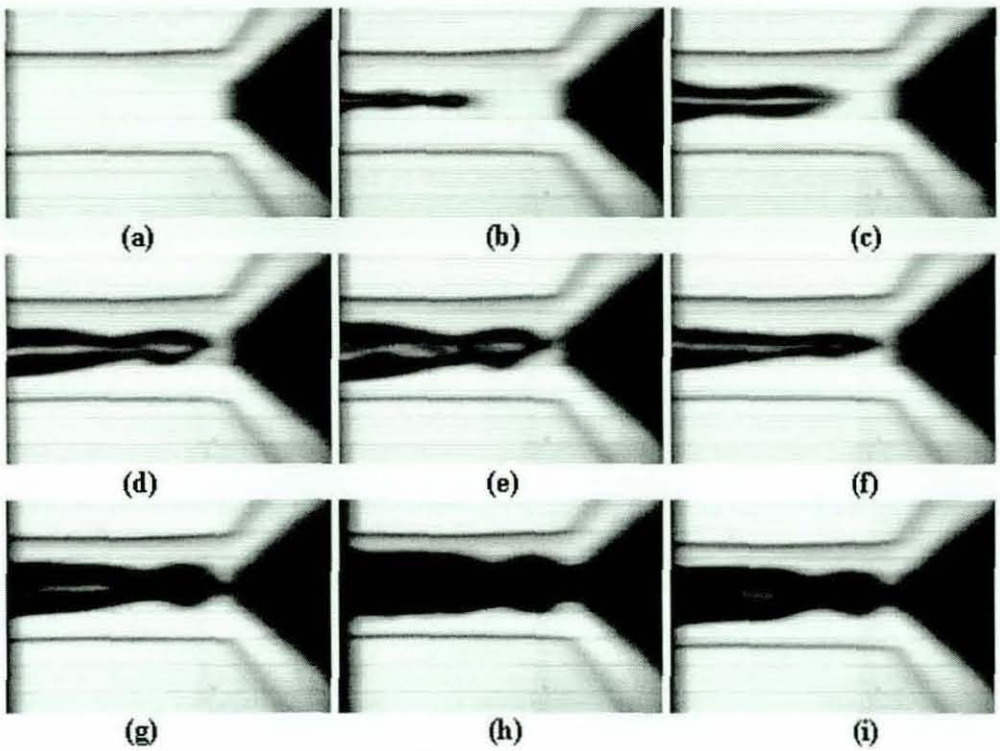

Figure 6.36 Flow images of 30° swirler with 45° chamfered inlet orifice at 50 bar pressure.

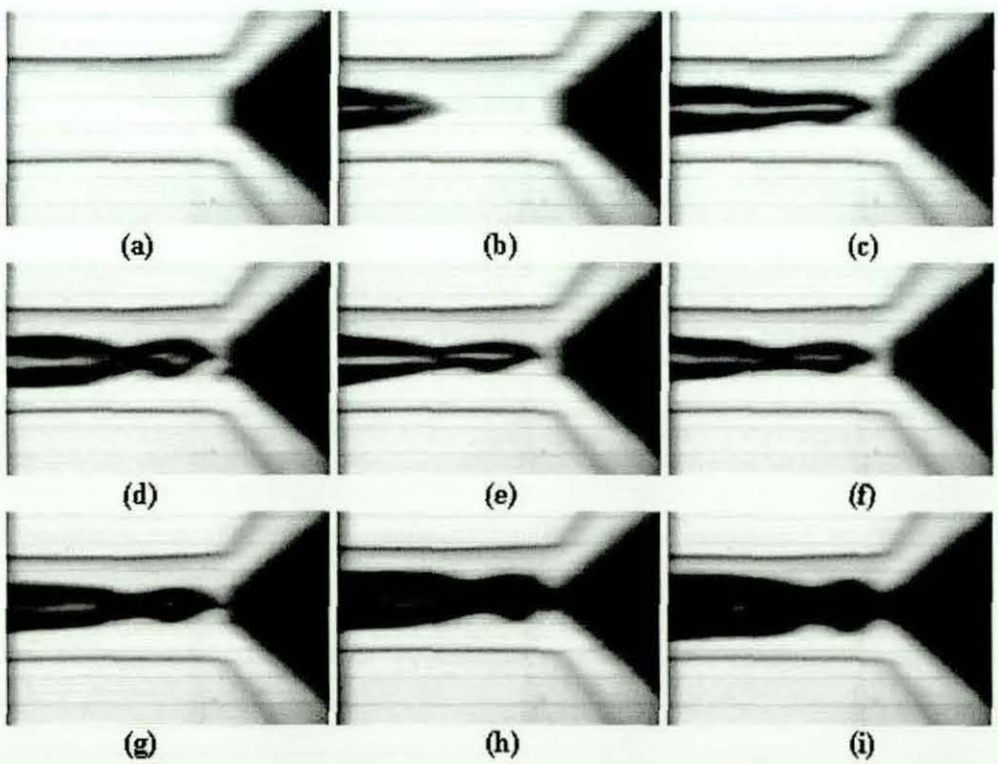

Figure 6.37 Flow images of 30° swirler with 45° chamfered inlet orifice at 60 bar pressure.

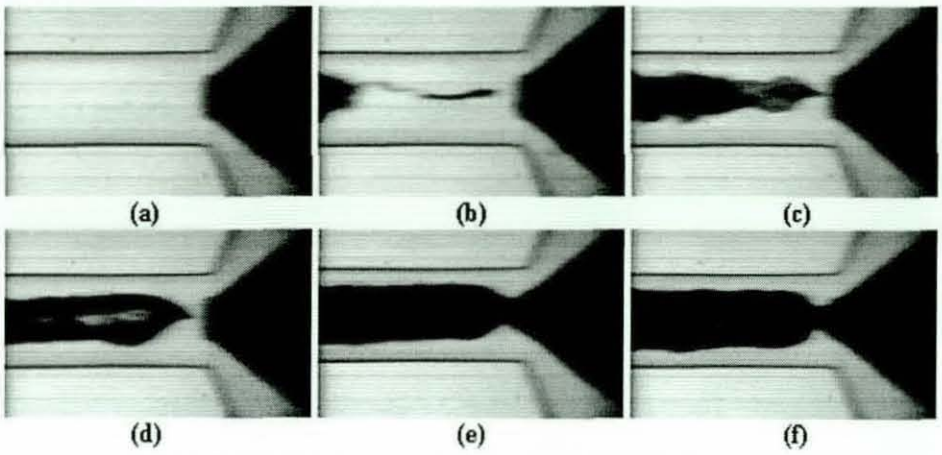

Figure 6.38 Flow images of 30° swirler with 60° chamfered inlet orifice at 20 bar pressure.

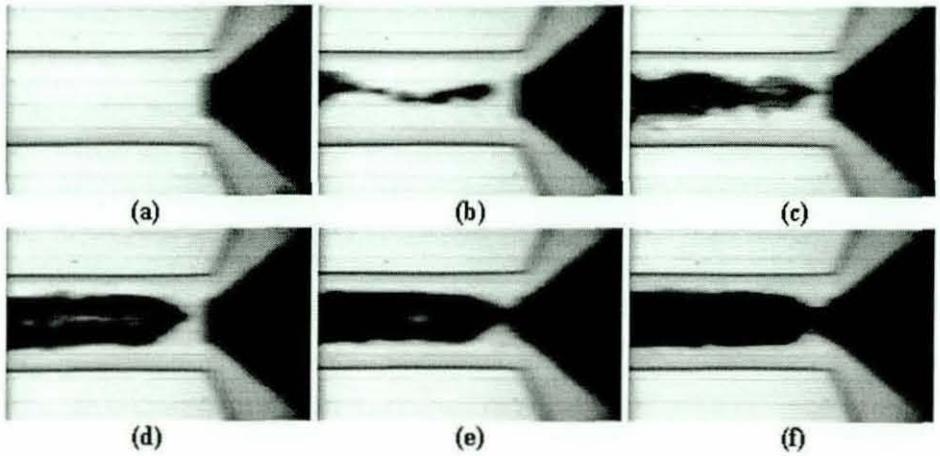

Figure 6.39 Flow images of 30° swirler with 60° chamfered inlet orifice at 30 bar pressure.

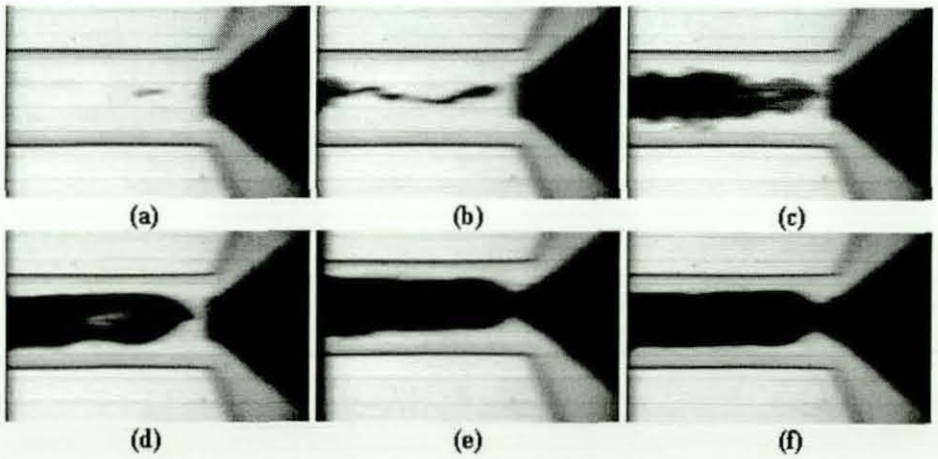

Figure 6.40 Flow images of 30° swirler with 60° chamfered inlet orifice at 40 bar pressure.

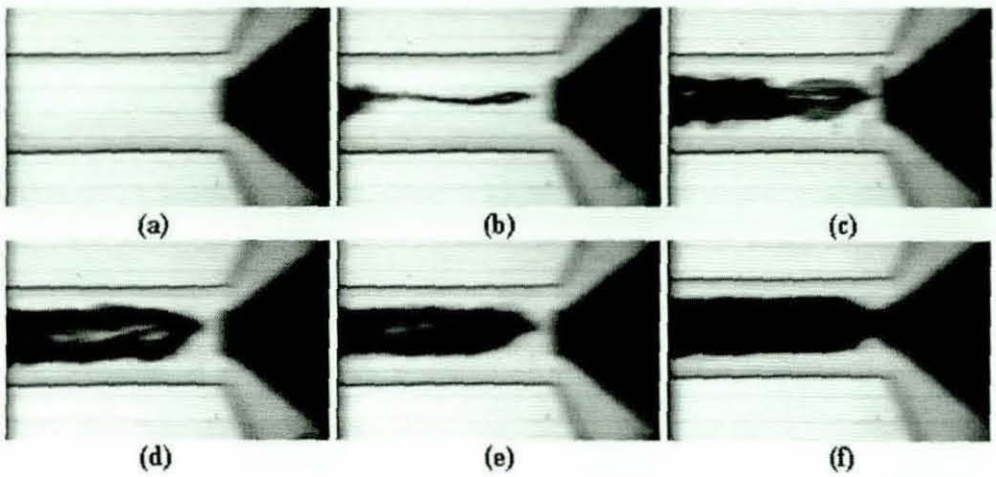

Figure 6.41 Flow images of 30° swirler with 60° chamfered inlet orifice at 50 bar pressure.

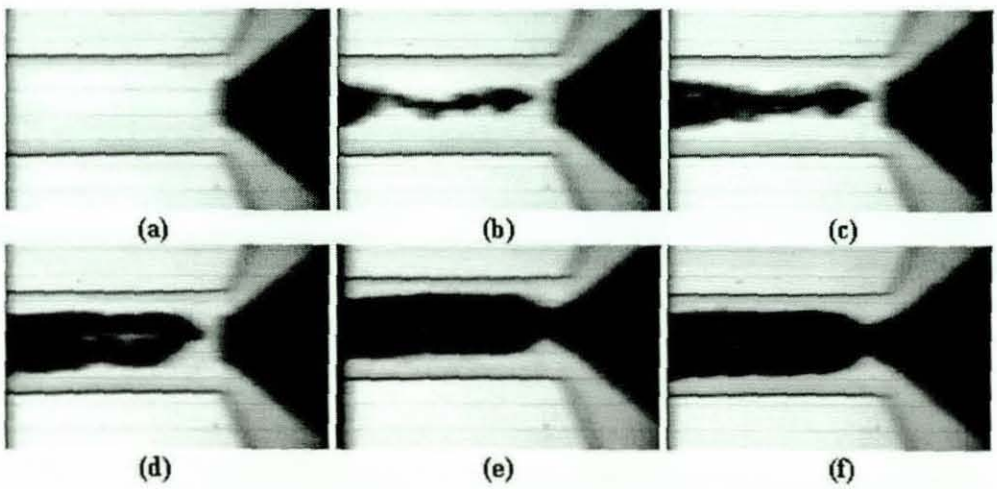

Figure 6.42 Flow images of 30° swirler with 60° chamfered inlet orifice at 60 bar pressure.

For figures 6.38 to 6.42, this again shows the 30° swirler but with a 60° chamfered inlet orifice from 20 to 60 bar driving pressure. With the 60° orifice, the aircore produced shows a uniform structure throughout the straight section of the orifice, regardless of the driving pressure used. This observation was similar with previous study for 30° swirler with a 30° chamfered inlet orifice. Both chamfered inlet orifices produced large and uniform aircore structure and a thin liquid film at the nozzle peripheral.

Observing the flow structures from the figures 6.28 - 6.42 for different chamfered inlet orifices helps to aid the understanding of the internal flow structures. To highlight the variation in the air core structure with changing flow geometry figure 6.43 presents data for the air core diameter and annular flow thickness for increasing driving pressure and increasing chamfered inlet orifice angles. The annulus thickness and air core diameter were measured from the high-speed video recordings and represent values at the nozzle exit for the steady state condition. The images provide a resolution of 15 μm. Figure 6.43 shows the variation of the annulus thickness and the air core diameter with driving pressure for nozzles with 30°, 45° and 60° chamfer inlets with a swirl angle of 30°. The annulus thickness displayed on the top graph shows it varies between 015 mm to 0.20 mm and also fluctuates from different injection pressure regardless of the chamfered orifices used. The aircore diameter graph also shows variation in the diameter sizes with injection pressures. *These graphs aircore diameter and annulus thickness are not* conclusive enough to show any variable trends.

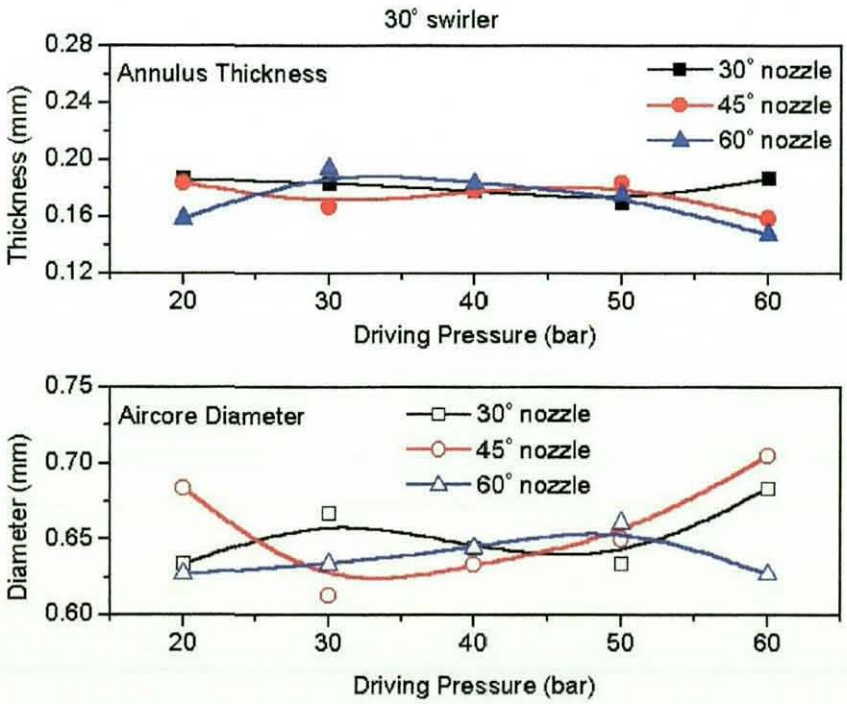

Figure 6.43 Variation of annulus thickness and aircore diameter at 30° swirler at the nozzle exit.

6.4.2.2 45° SWIRLER STUDY

The 45° swirler study also involved the use of 30°, 45° and 60° chamfered inlet orifices to investigate the flow structures in the straight section of the orifices. In this section, the images show only the fully developed flow structures for each driving pressure used. Figure 6.44 exhibits the fully developed flow for 30° chamfered inlet orifices. The flow structures showed a tapered shaped aircore with necking near the pintle. This tapered structures extends down the straight section of the orifice and to the orifice exit. The tapered shaped was observed to be increased in size with higher injection pressure. However, the aircore structures were similar in shape and size near the exit.

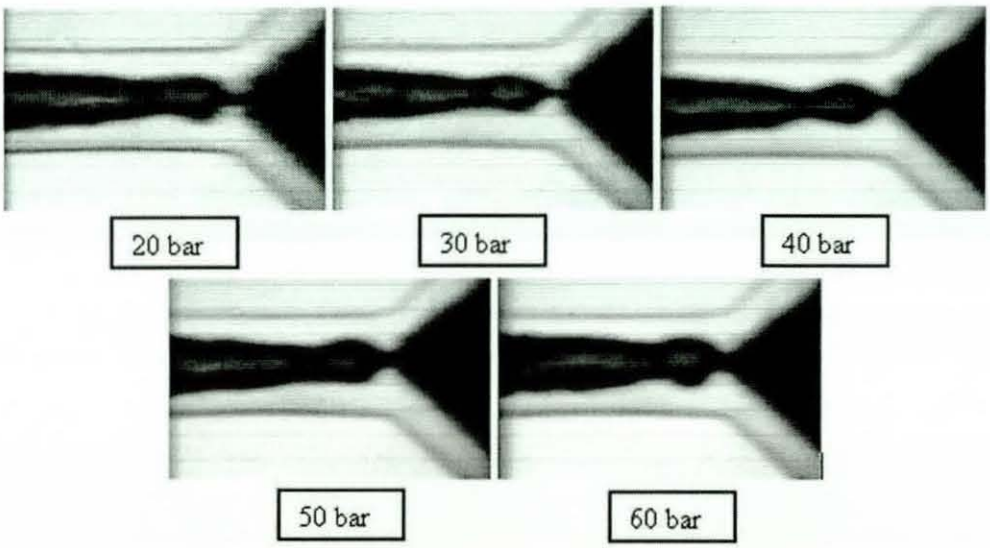

Figure 6.44 Flow images of 45° swirler with 30° chamfered inlet orifice.

Figure 6.45 shows the second study of the 45° swirler but with a 45° chamfered inlet orifice. The swirl flow structures also showed a tapered shaped aircore with necking near the pintle and larger aircore with each injection pressure increments. This was not the case with 60° chamfered inlet orifices shown in figure 6.46. The aircore structure generated connected to the pintle was much larger and uniformed in shaped. This uniform aircore structure extended through the straight section of the orifices and out to the orifice exit. As seen from previous studies, the aircore structure was again

remaining consistent with regardless of changes in injection pressure. The aircore structures displayed also looked to be closer to the topside of the orifice, suggesting the swirler located upstream dictated the swirl aircore position.

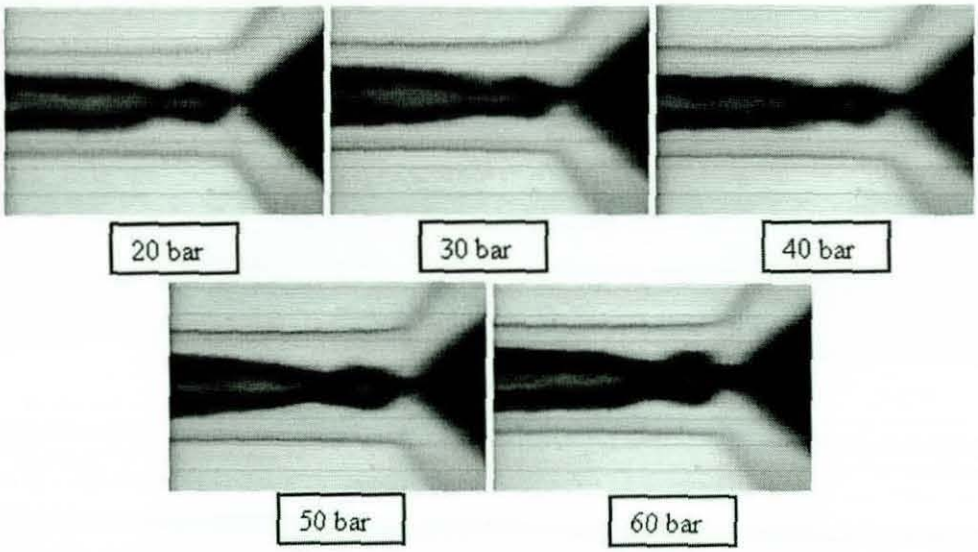

Figure 6.45 Flow images of 45° swirler with 45° chamfered inlet orifice.

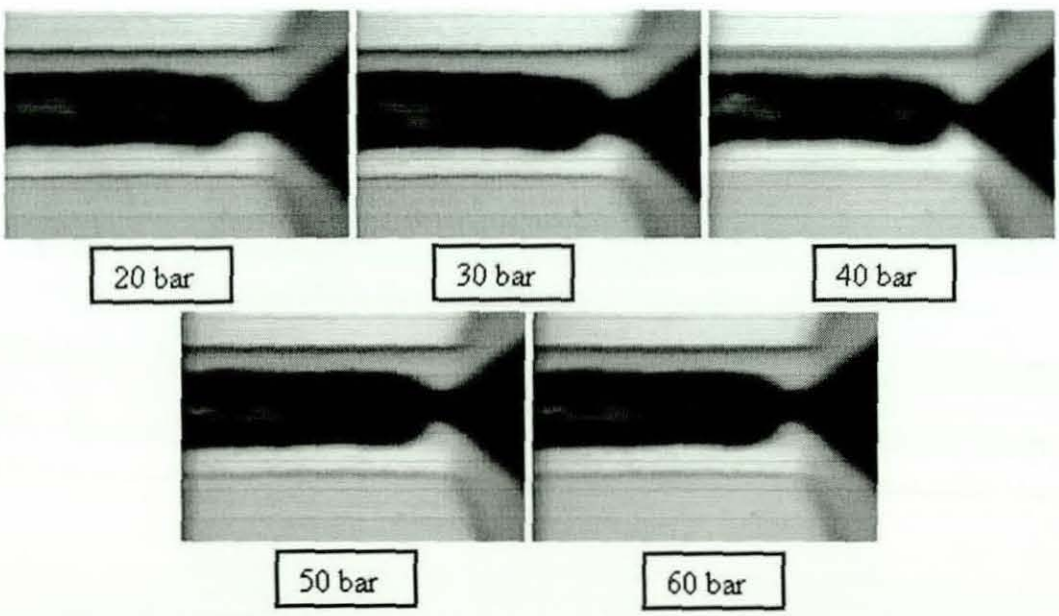

Figure 6.46 Flow images of 45° swirler with 60° chamfered inlet orifice.

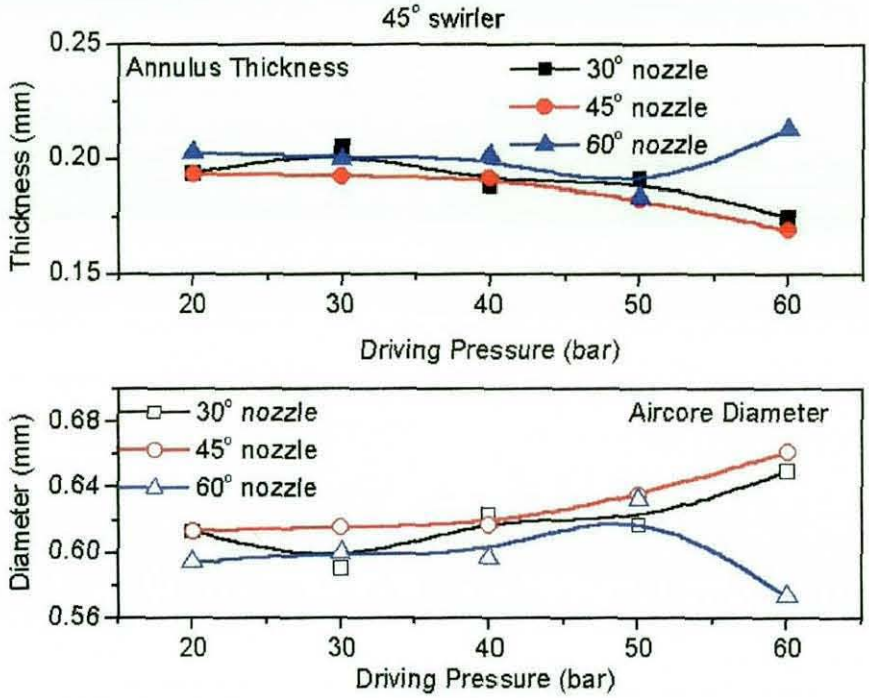

Figure 6.47 Variation of annulus thickness and aircore diameter at 45° swirler at the nozzle exit.

Figure 6.47 shows the annulus thickness and aircore diameter at the orifice exit. The 30° and 45° chamfered inlet orifice annulus thickness seen to be decreasing and the aircore diameter increasing with increasing driving pressure. The comparison of the three different chamfered inlet orifice results was not conclusive again for the 60° chamfered inlet orifice as the results varies from orifices as no distinctive trends were observed.

6.4.2.3 60° SWIRLER STUDY

The third study employed the same set of chamfered inlet orifices but with a 60° swirl generator. Figure 6.48 shows the aircore structures and liquid annulus for 30° chamfered inlet nozzle with 20 bar to 60 bar driving pressure. The aircore structure generated appeared slightly tapered with a necking effect appears at almost midpoint of the straight section of the nozzle. However, the 45° chamfered inlet nozzle necking effect on the aircore structure was much higher as seen in figure 6.49.

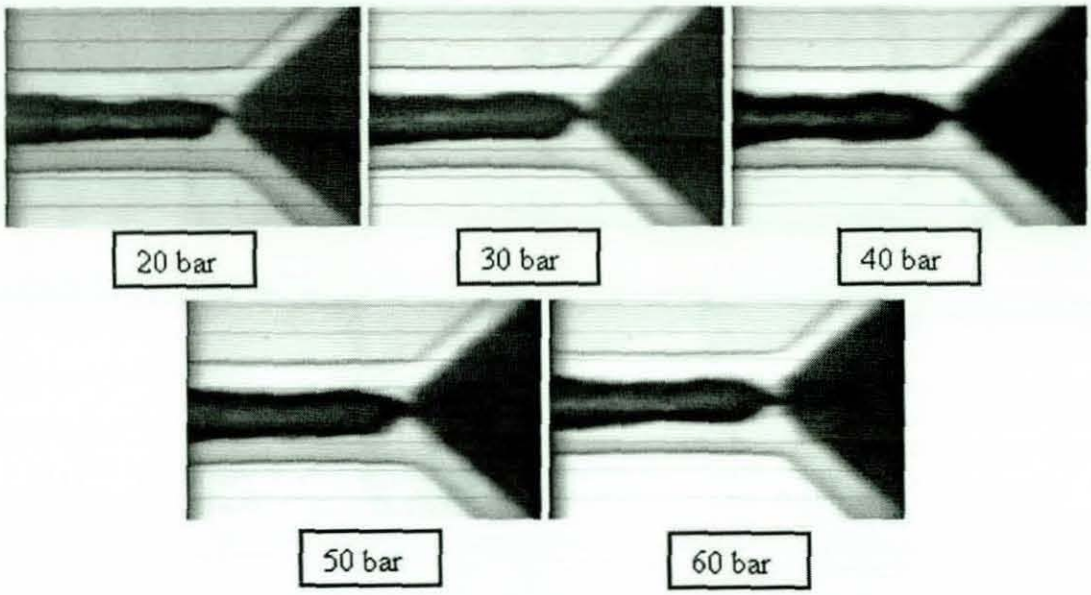

Figure 6.48 Flow images of 60° swirler with 30° chamfered inlet orifice.

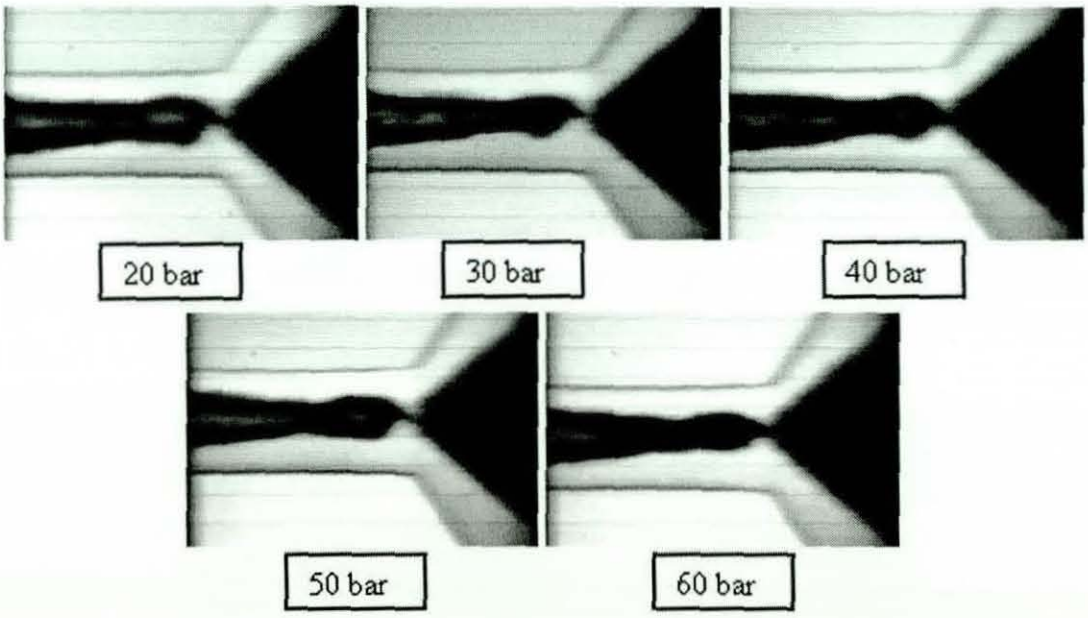

Figure 6.49 Flow images of 60° swirler with 45° chamfered inlet orifice.

In the case of the 60° chamfered inlet nozzle, it displays a uniform shaped aircore structure as seen on previous studies using the same chamfered inlet nozzle but with 30° and 45° swirl generators. All the flow structures also appeared similar regardless when compare to different driving pressure, which was also observed previously for both 30° and 45° swirler studies.

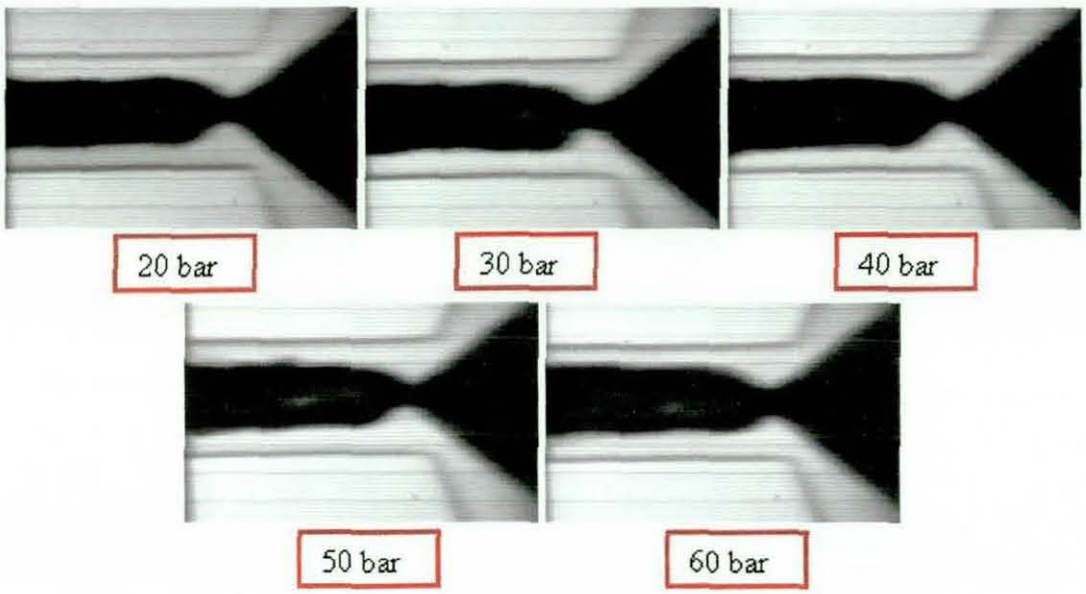

Figure 6.50 Flow images of 60° swirler with 60° chamfered inlet orifice.

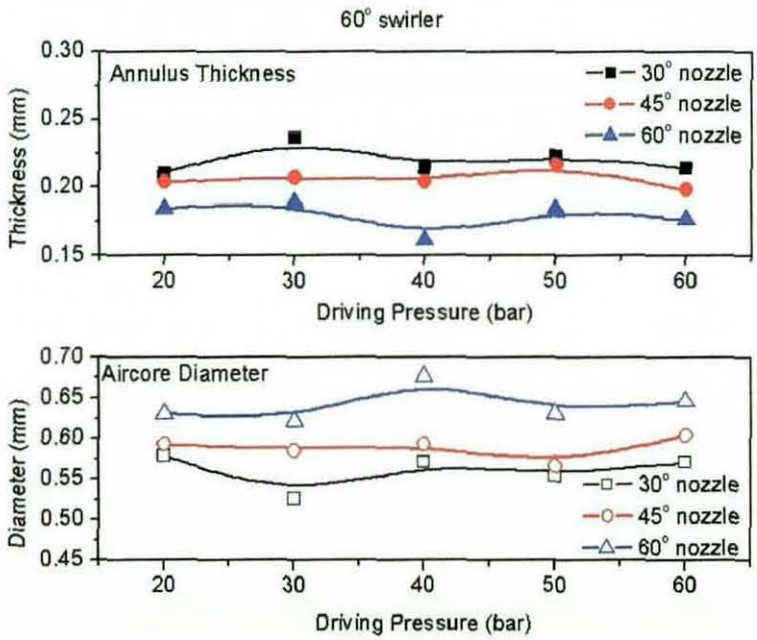

Figure 6.51 Variation of annulus thickness and aircore diameter at 60° swirler at the nozzle exit.

Figure 6.51 shows the variations in annulus thickness and aircore diameter with different chamfered inlet nozzles and driving pressures. The annulus thickness and aircore diameter remains fairly constant for the three chamfered inlet orifice despite an increase in driving pressure. The top graph shows the annulus thickness decreases with increasing chamfered inlet orifice. The 30°

orifice has an averaged annulus thickness of 0.22 mm and the 60° chamfered inlet orifice at about 0.18 mm. With a smaller annulus thickness at 60° chamfered inlet nozzle, the aircore diameter shown that the second graph is the biggest as expected.

6.4.3 External Flow Results and Analysis

The investigation of the internal flow structures is not complete without observing the external flow spray and atomisation. The aim of the study is to quantify the effect of nozzle geometry and internal flow structure on atomisation.

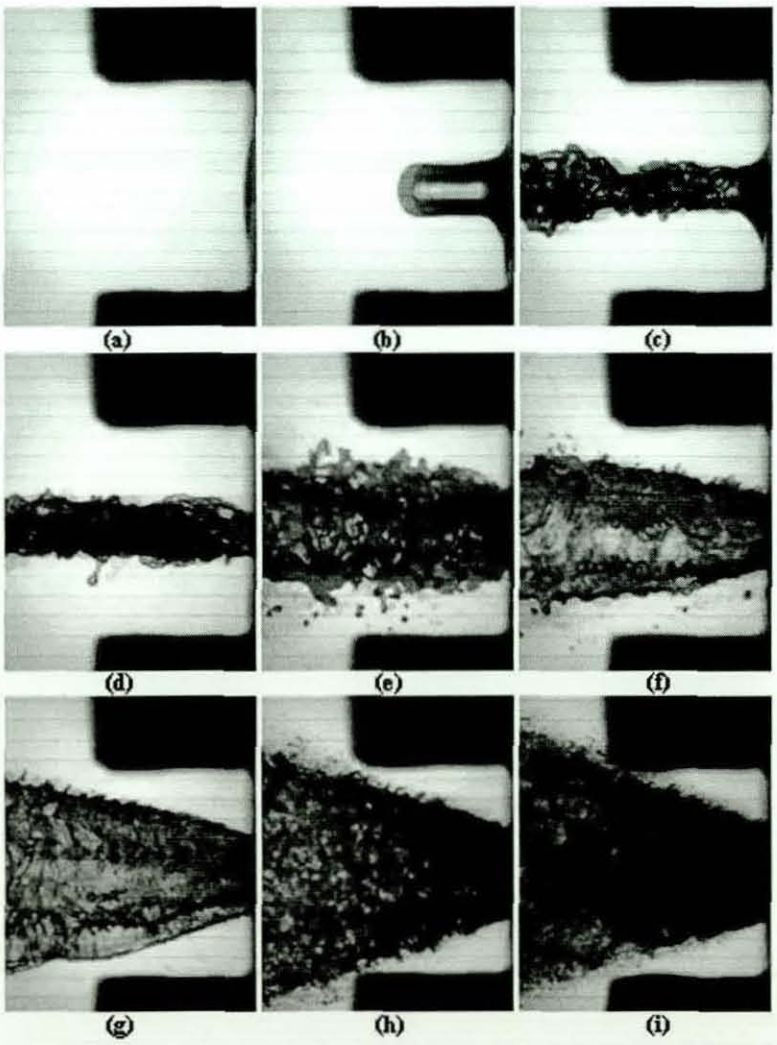

Figure 6.52 Sequential flow images of a 30° swirler with a 30° orifice at 30 bar driving pressure.

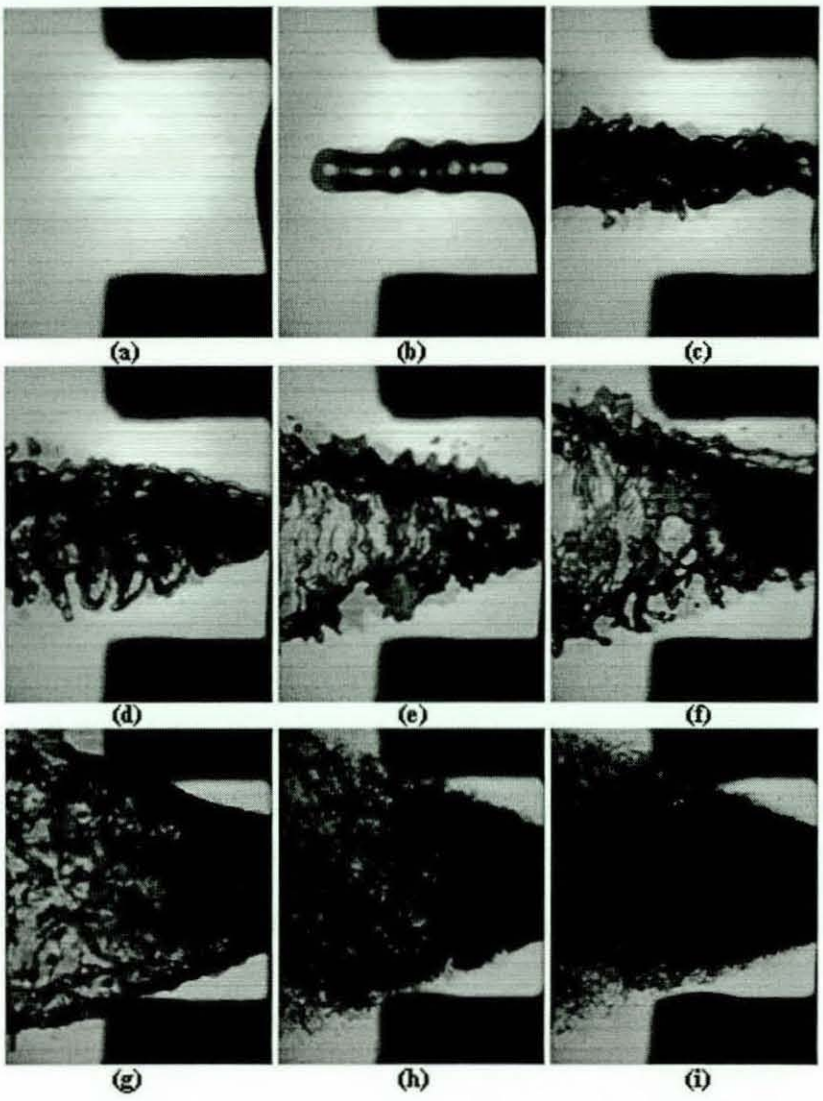

Figure 6.53 Sequential flow images of a 30° swirler with a 45° orifice at 30 bar driving pressure.

Figure 6.52 shows sequential images of a 30° swirler with a 30° chamfered inlet orifice at 30 bar driving pressure. When the injection activates, the pressurised fluid flows into the chamfered orifice before exiting the chamfered inlet orifice as a plug fluid flow. This external flow becomes more turbulent as the driving pressure builds up in the flow and develops into a hollowcone spray. As the driving pressure peaks, these hollowcone spray structures began to atomise into droplets. The figure shows this hollowcone sprays covers the full width of the orifice holder. The size of this hollowcone spray remains fairly consistent regardless of the driving pressure conditions. Further studies of the 30° swirler with 45° chamfered inlet orifice or 60° chamfered

inlet orifice with the same driving pressure condition (figure 6.53 and 6.54) also shows similar hollowcone spray and atomisation processes. This phenomena was also observed in the study of the 45° swirler and 60° swirler with the same set of chamfered inlet orifices. Further sequential images of these external flow structures are shown in Appendix B.

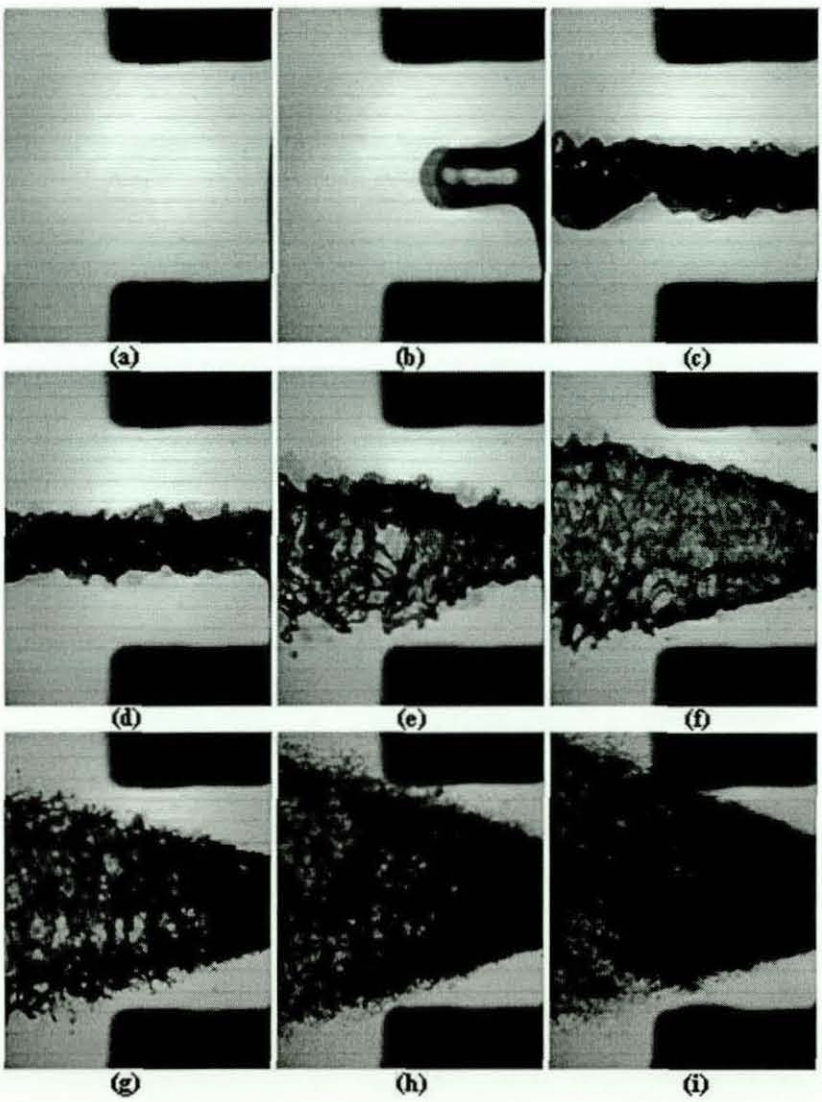

Figure 6.54 Sequential flow images of a 30° swirler with a 60° orifice at 30 bar driving pressure.

The investigation of both the internal and external flow regimes using high speed flow visualisation allows further quantification using both FPIV and PDA techniques. The FPIV provides further insight on the internal flow regimes and the PDA investigating the droplet sizes and momentum.

6.5 SWIRL INJECTORS STUDY (FPIV)

6.5.1 Introduction

Fluorescent particle image velocimetry was used to further the study of the swirl generators and chamfered inlet orifices by quantifying in-nozzle flow velocity. FPIV was ideal in the study of in-nozzle swirl flow structures as imaging through a 620 nm filter allowed the rejection of interference from unwanted scattering from injector and liquid surfaces. Figure 6.55 highlights the necessity of using FPIV to remove this unwanted scattering. The FPIV system setup was the same as shown in figure 6.9, consisting of a double pulsed Nd:YAG laser system and Kodak ES1.0 CCD camera with 1008 x 1018 pixels resolution. The images clearly show the seeding particles swirling along the aircore. It is noted that the seeding particles along the peripheral are flowing straight down to the nozzle exit. Therefore, it is possible to determine the radial and axial components of the velocity vectors along the centreline of the fluorescent seeding particle images from cross-correlation analysis. The velocity vector components shown in figure 6.56 present the measurement of the radial and axial velocity used. This will be presented later in the section in graphical form in terms of V (Axial) and U (Radial) velocity components.

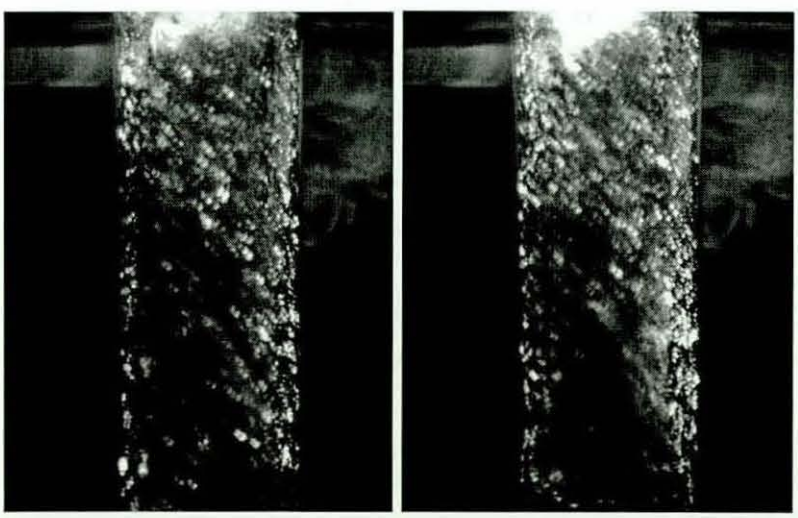

Figure 6.55 Two sequential fluorescent particles images showing swirl flow in the nozzle.

The swirl configuration study consisted of three swirlers and three chamfered inlet orifices. The following sub-sections showed the results and analysis based on the individual swirler with three chamfered inlet orifices used. However, only the 30° swirler study presents the full velocity plots for the three chamfered inlet orifices investigated. This was showed as velocity vectors through the orifices and also with graphs highlighting the flow velocity through the centre of the orifices. For the 45° and 60° swirlers study, the velocity plots for 20 bar driving pressure for the three chamfered inlet orifices and the flow velocity graph through the centreline of the orifices were presented, with the remaining plots accessible from appendix B.

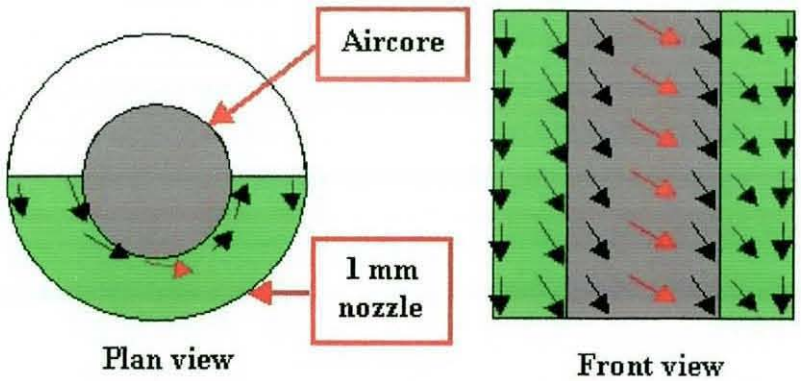

Figure 6.56 Laser illuminated (green colour) nozzle with true flow velocity vectors along the centreline of the aircore.

6.5.2 Results and Analysis

6.5.2.1 30° SWIRLER STUDY

The first set of flow velocity results showed the 30° swirl generators and 30° chamfered inlet orifice with 20 to 60bar driving pressure. With a known laser pulse separation of 1μsec, the fluid velocity was analysed and measured. Figure 6.57 displays a typical example of a derived flow velocity through the orifice at 20 bar driving pressure. The aircore can be easily identified by the swirl flow towards the centre of the nozzle, with the flow annular rushing straight out of the nozzle. With the flow moving from the chamfered section to

the straight section of the nozzle, the velocity vectors increases as it travels into the nozzle. This was highlighted by the change in the colour coded background. The legend shows a lower velocity was recorded in the chamfered inlet section, with the higher velocity vectors as the flow enters the straight section. The peak velocity recorded for this flow is 64 m/s and this was located at the centre line of the nozzle.

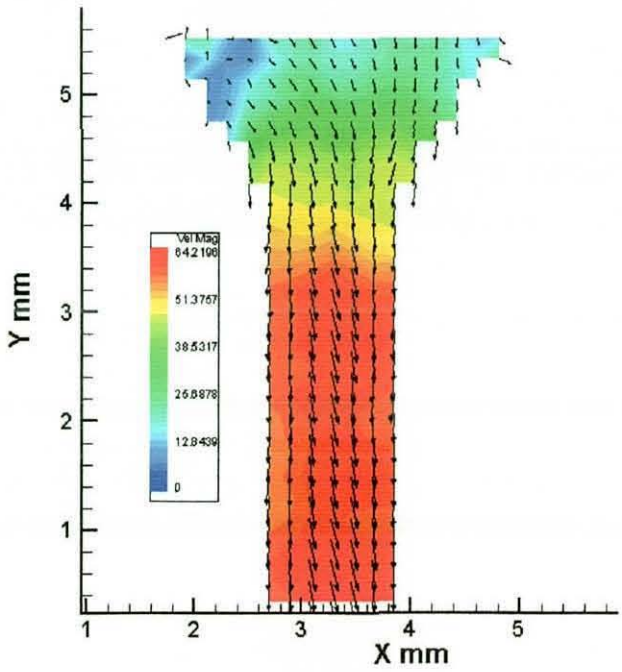

Figure 6.57 Average velocity magnitudes for 30° chamfered inlet orifice with 20 bar driving pressure.

Similar flow velocity vectors were also observed from figures 6.58 to 6.61 at higher injection pressures. The flow though the chamfered inlet orifice was seen to increase with each driving pressure used and this was observed by the increased swirl on the velocity vectors. Naturally, the peak velocity increases simultaneously with these increments in swirl flow. From this data, it was possible to quantify the flow velocity further by investigating the flow through the centreline of the orifice at different driving pressures. This study was highlighted in figure 6.62 with the radial and axial velocity values indicated by different driving pressure. These flow velocities along the centreline of the flow gives an indication on the kind of flow velocity through the chamfered inlet orifice. The radial velocity component is shown in the top

graph and the axial velocity component is shown in the bottom half of the graph.

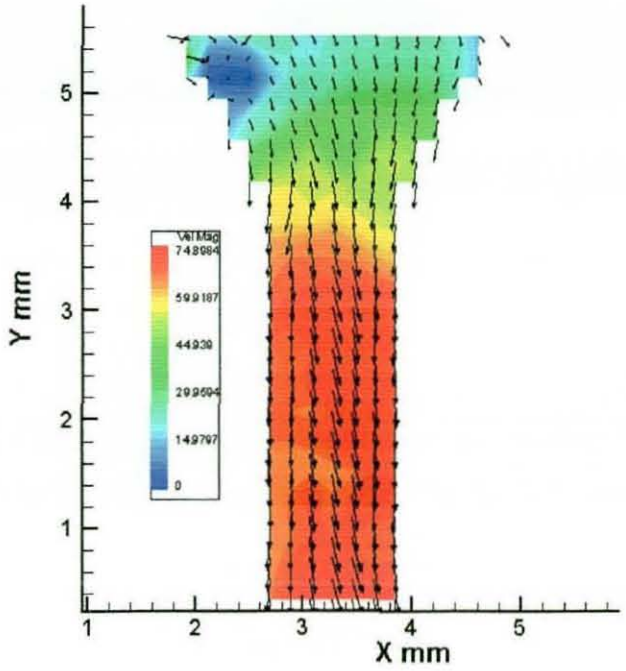

Figure 6.58 Average velocity magnitudes for 30° chamfered inlet orifice with 30 bar driving pressure.

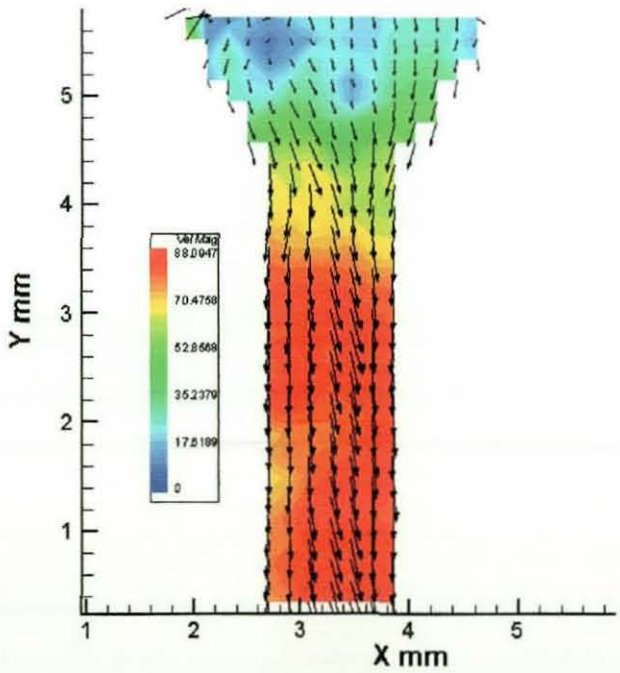

Figure 6.59 Average velocity magnitudes for 30° chamfered inlet orifice with 40 bar driving pressure.

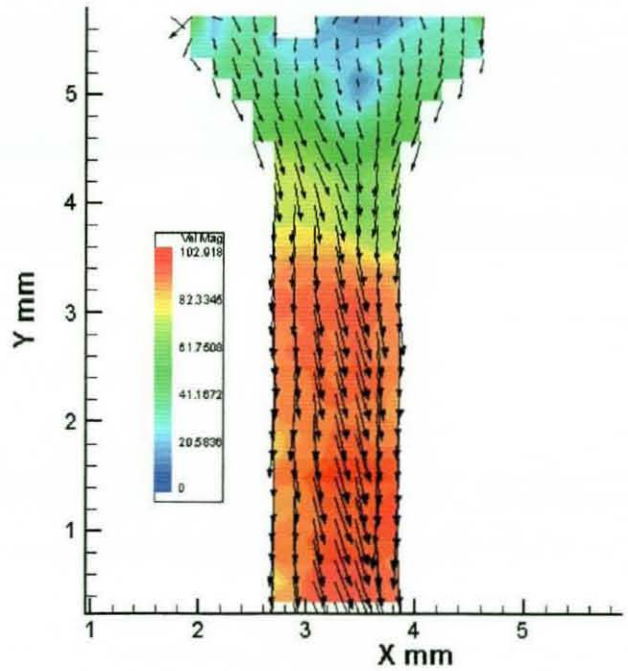

Figure 6.60 Average velocity magnitudes for 30° chamfered inlet orifice with 50 bar driving pressure.

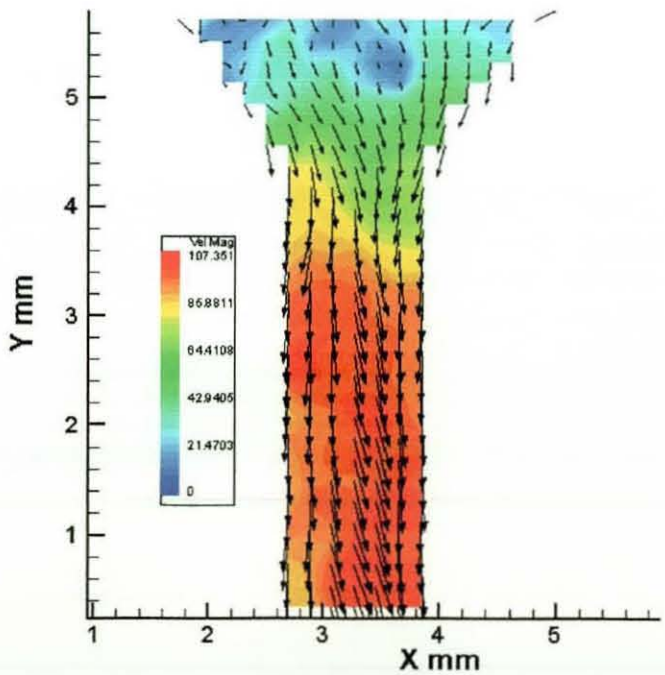

Figure 6.61 Average velocity magnitudes for 30° chamfered inlet orifice with 60 bar driving pressure.

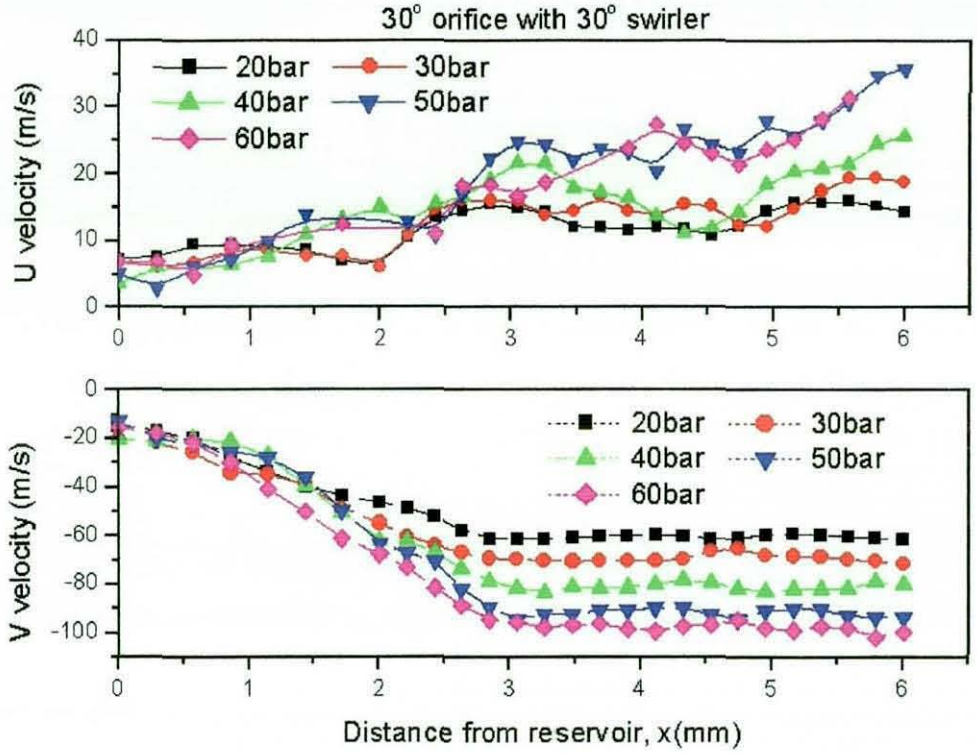

Figure 6.62 Velocity through the centreline of a 30° chamfered inlet orifice with a 30° swirler.

The radial graph shown in figure 6.62 shows gradual increments in velocity as the flow travels from the convergent section (0-2 mm) of the orifice and into the nozzle section. There are more distinctive flow increments in the axial velocity component shown on the second graph. The axial flow velocity increases linearly into the straight section of the orifice with higher driving pressures. The flow velocity then stabilised into a constant velocity at about 3mm into the chamfered inlet orifice. This clearly indicates the driving pressure used determines the flow velocity, with velocity increasing as the pressure rise from 20 bar to 60 bar.

For the 45° chamfered inlet orifices, figures 6.63 to 6.67 show the flow velocity for driving pressure ranging from 20 bar to 60 bar. Figure 6.63 again shows the flow velocity swirl into the chamfered inlet orifice, indicated by the velocity vectors entering the nozzle at an angle. This actually shows the fluid flow swirl into the nozzle at high speed but it was not possible to observe the flow

velocity regimes with the high-speed images. Similar flow velocity trend was also seen in higher driving pressure range.

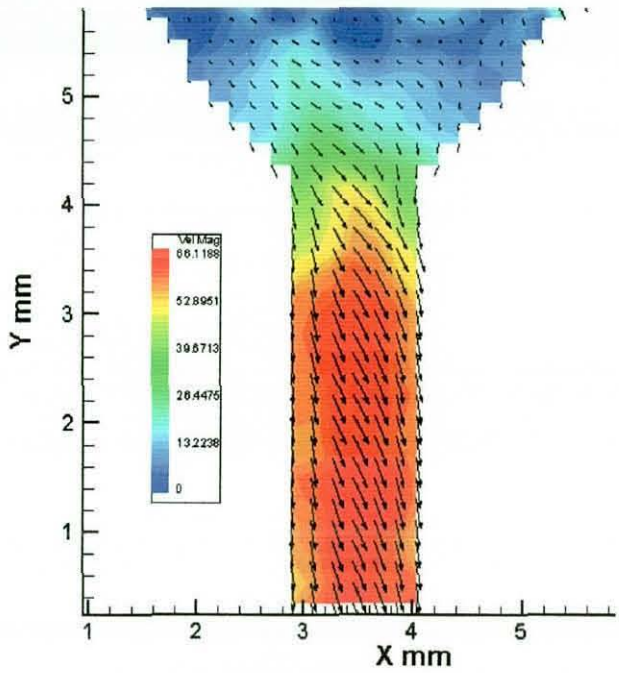

Figure 6.63 Average velocity magnitudes for 45° chamfered inlet orifice with 20 bar pressure.

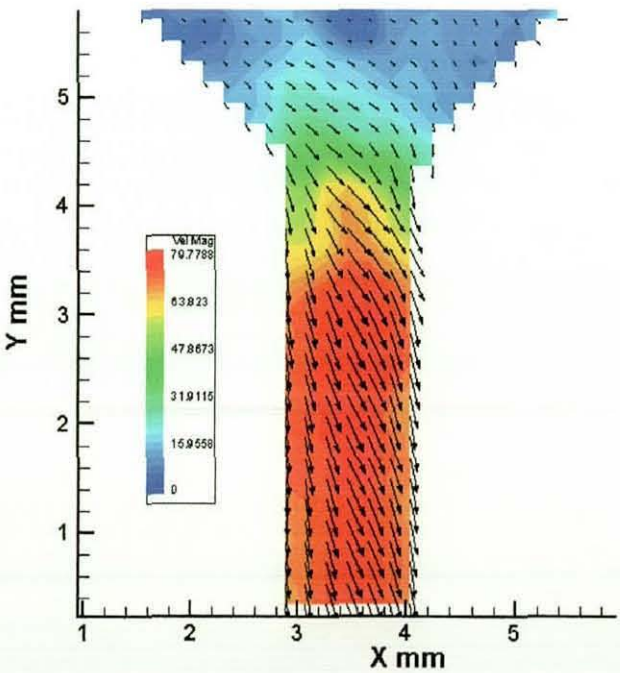

Figure 6.64 Average velocity magnitudes for 45° chamfered inlet orifice with 30 bar pressure.

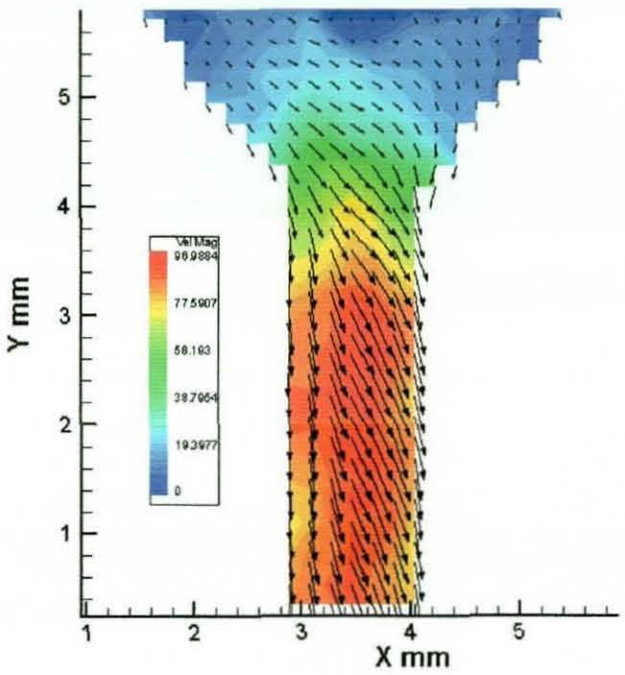

Figure 6.65 Average velocity magnitudes for 45° chamfered inlet orifice with 40 bar pressure.

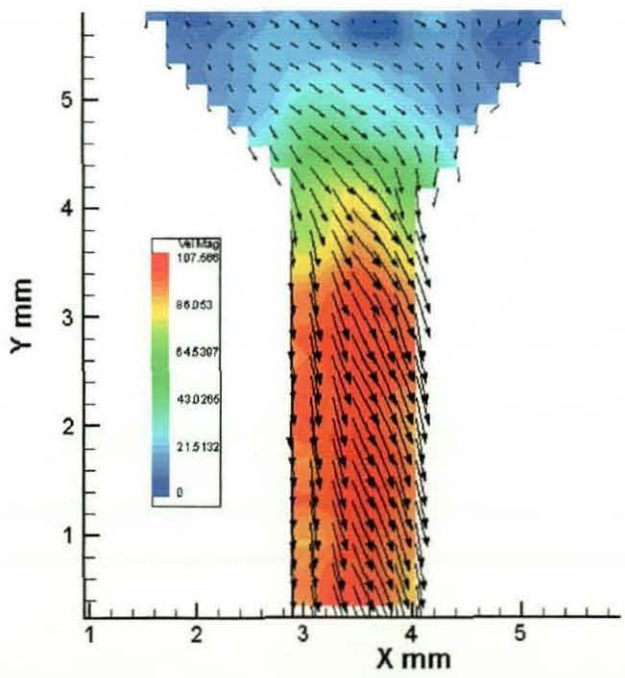

Figure 6.66 Average velocity magnitudes for 45° chamfered inlet orifice with 50 bar pressure.

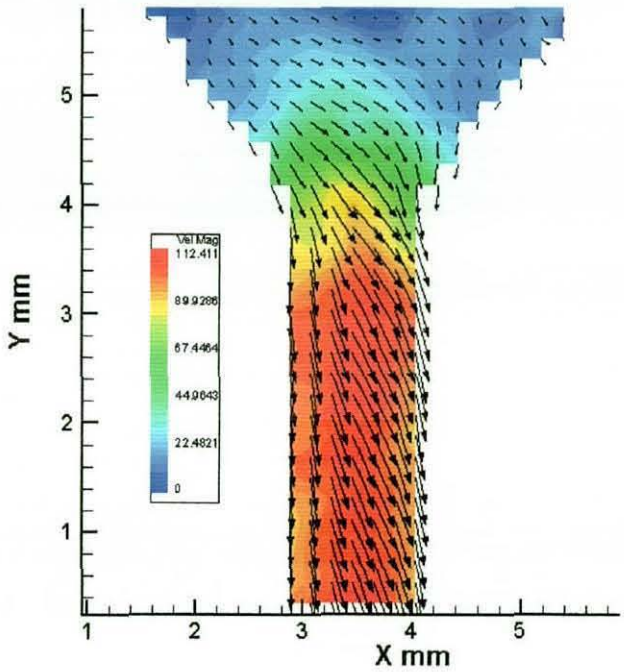

Figure 6.67 Average velocity magnitudes for 45° chamfered inlet orifice with 60 bar pressure.

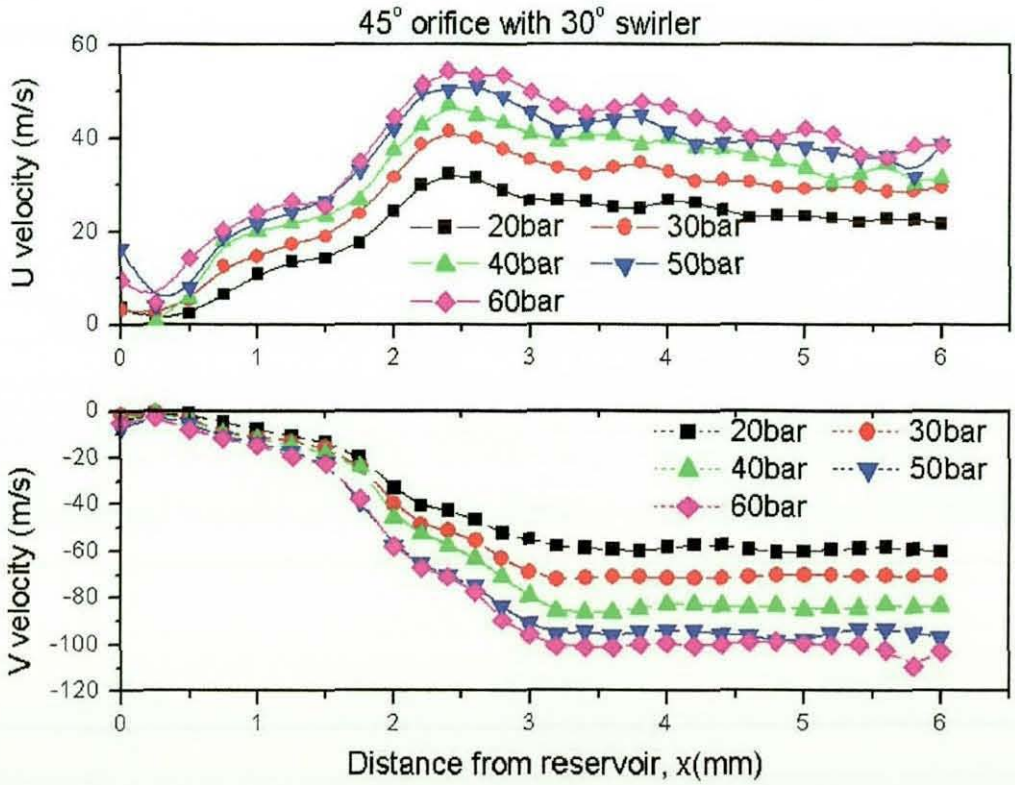

Figure 6.68 Velocity through the centreline of a 45° chamfered inlet orifice with a 30° swirler.

Figure 6.68 provides radial and axial velocity components for driving pressure ranging from 20 bar to 60 bar for 45° chamfered inlet orifice with a 30° swirler. The graphs show the radial and axial velocities increase gradually in the convergent section of the orifice. In the radial velocity graph, the lower driving pressure range remains constant in the nozzle section. However, the higher driving pressures (30 bar to 60 bar) appear to decrease slightly as the flow reaches the orifice exit. In the case of the axial velocity component, the velocity remains constant with increasing driving pressure in the nozzle section. The velocity in the straight section increases with each driving pressure. At 60 bar driving pressure, the average axial velocity is about 110 m/s in the nozzle section.

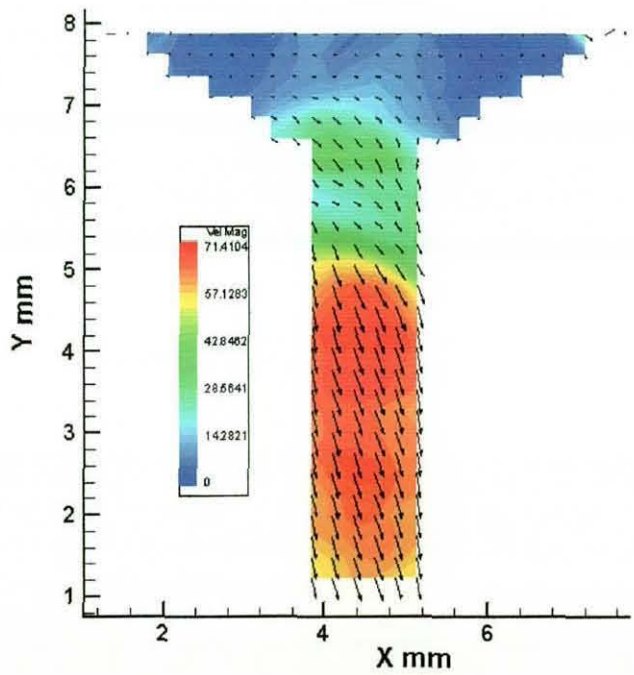

Figure 6.69 Average velocity magnitudes for 60° chamfered inlet orifice at 20 bar.

The last set of nozzles used in the 30° swirler study is the 60° chamfered inlet orifice shown from figures 6.69 to 6.73 under the same driving pressure conditions as the previous. The flow into the convergent section shows disruption in the flow as it moves into the nozzle section of the orifice. The

flow velocity decreases as it enters the straight section, before increasing again to higher velocity vectors.

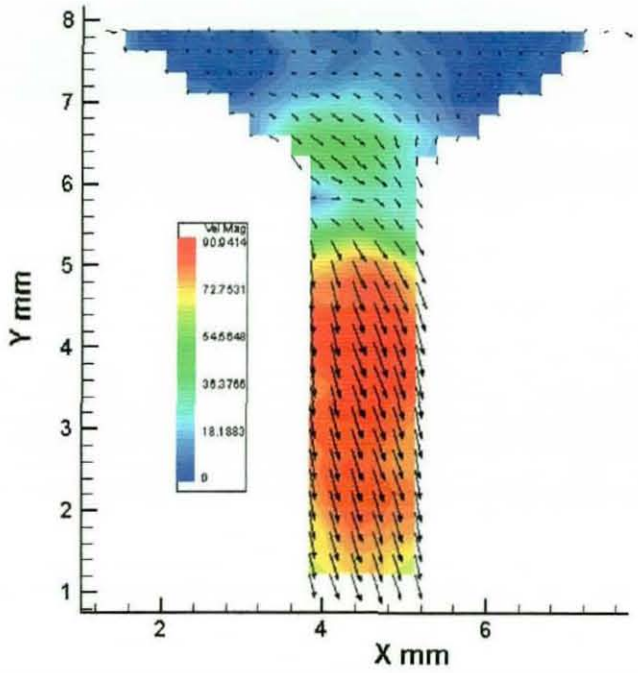

Figure 6.70 Average velocity magnitudes for 60° chamfered inlet orifice at 30 bar.

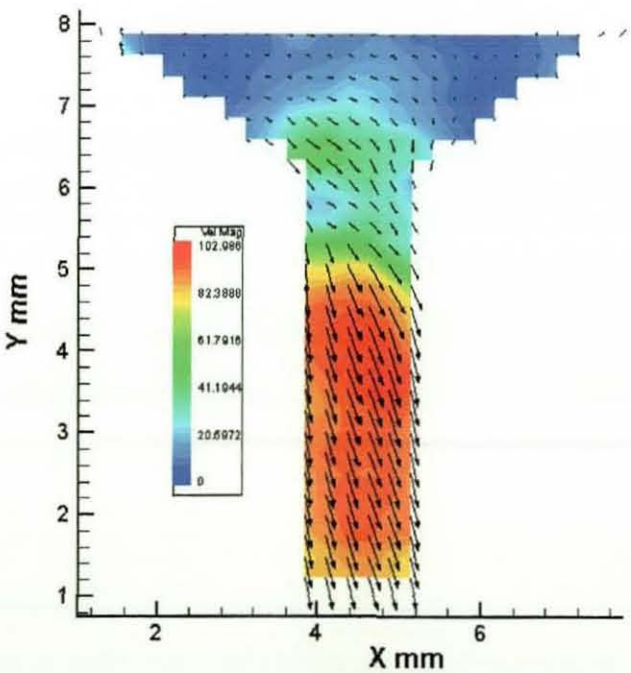

Figure 6.71 Average velocity magnitudes for 60° chamfered inlet orifice at 40 bar.

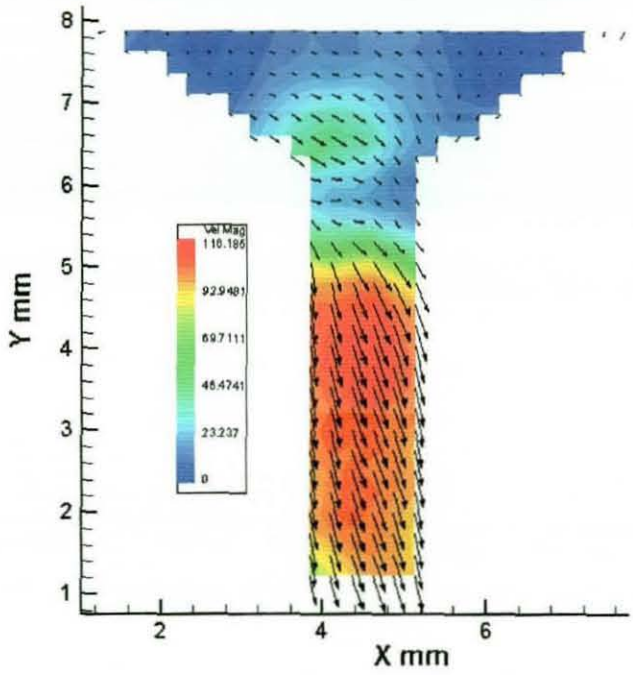

Figure 6.72 Average velocity magnitudes for 60° chamfered inlet orifice at 50 bar.

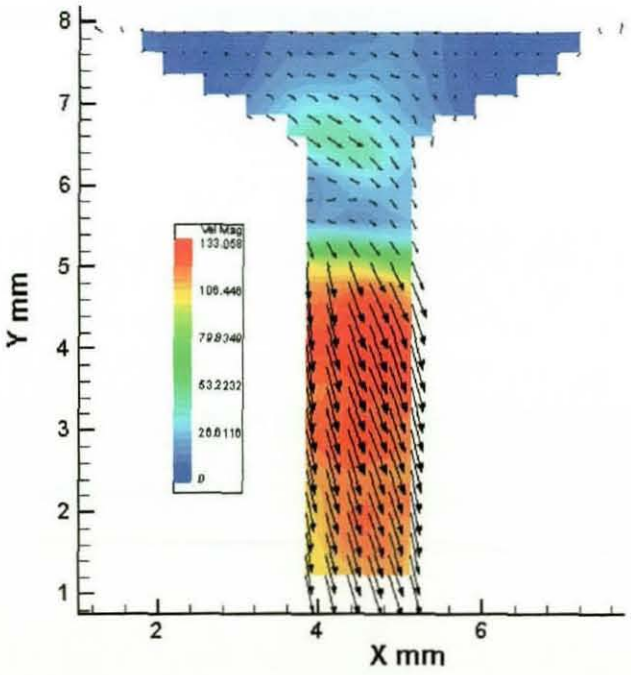

Figure 6.73 Average velocity magnitudes for 60° chamfered inlet orifice at 60 bar.

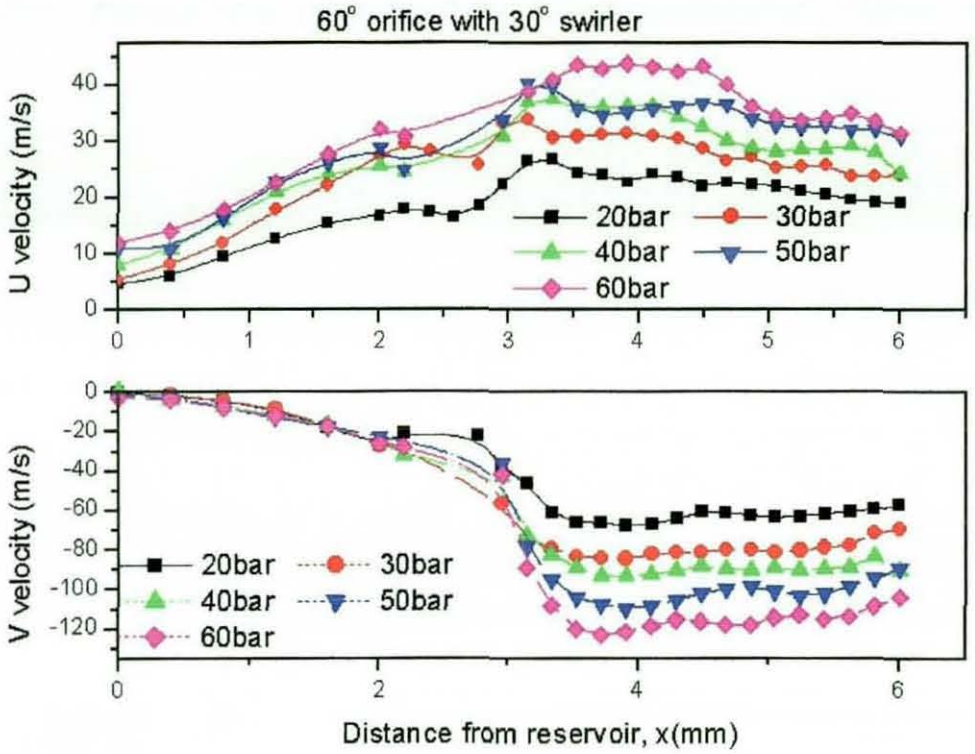

Figure 6.74 Velocity through the centreline of a 60° chamfered inlet orifice with a 30° swirler.

Figure 6.74 provides further evidence of the disruption in the flow in the axial graph (V velocity). The data shows that the rate of change of axial flow velocity in the convergent section of the nozzle is gradual, but these flow velocities suddenly increase as the flow enters the straight section. This is shown by a steep rise in flow velocities on the axial graph. All the flows velocities recorded an increase in velocity for about 1mm into the straight section before dropping slightly into a constant velocity to the nozzle exit. In the axial velocity components, the flow velocities increase are more gradual and they remains almost constant throughout the nozzle section. Both the graphs in figure 6.79 show similar trends to the previous two chamfered inlet orifices investigated under the same swirler.

6.5.2.2 45° SWIRLER STUDY

With the full display of the results for the 30° swirler, the next set of experimental results presents the 45° swirl generator study. In this section,

this study will only present the flow velocity vectors for 20 bar injection pressure since the results are similar from the previous swirl generator study. The rest of the 45° swirl generator results were attached in Appendix B. Only the results for the individual orifices through the centreline of the nozzle will be shown in the subsequent graphs from figures 6.75 to 6.77.

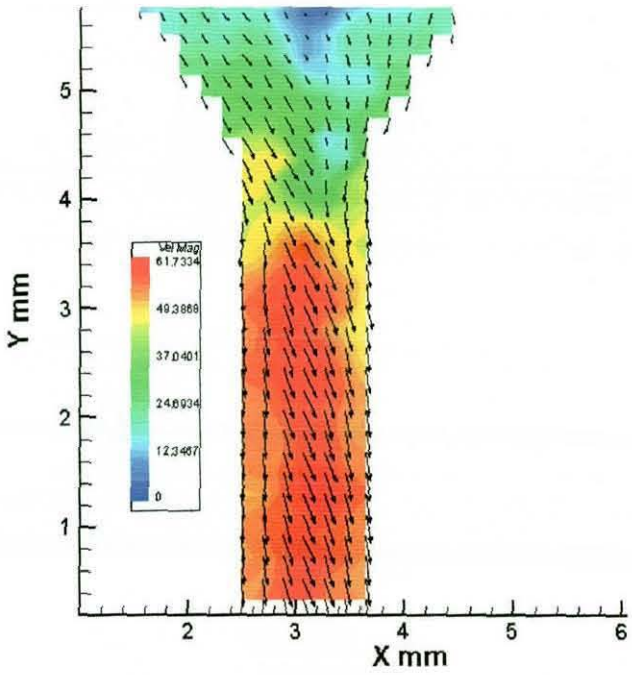

Figure 6.75 Average velocity magnitudes for 30° chamfered inlet orifice at 20 bar.

The 30° chamfered inlet orifice with an injection pressure of 20 bar is shown in figure 6.75. The diagram clearly shows the swirl flow entering the convergent section with the velocity vectors at an angle and into the straight section of the nozzle. The image also shows the velocity vectors flow smoothly into the straight section, indicating a smooth transition without any turbulent in the flow. The maximum averaged velocity recorded was 62 m/s. Figures 6.76 and 6.77 show the swirl velocity vectors for 45° and 60° chamfered inlet orifice at 20 bar pressure respectively. Both flows also show smooth transition from the convergent section of the nozzle into the straight section. The flow velocity in the convergent section has a lower flow velocity for both nozzles when compared with the 30° chamfered inlet nozzle at 20 bar driving pressure. The

maximum velocity recorded for 45° and 60° chamfered inlet nozzle were 55 m/s and 75 m/s respectively.

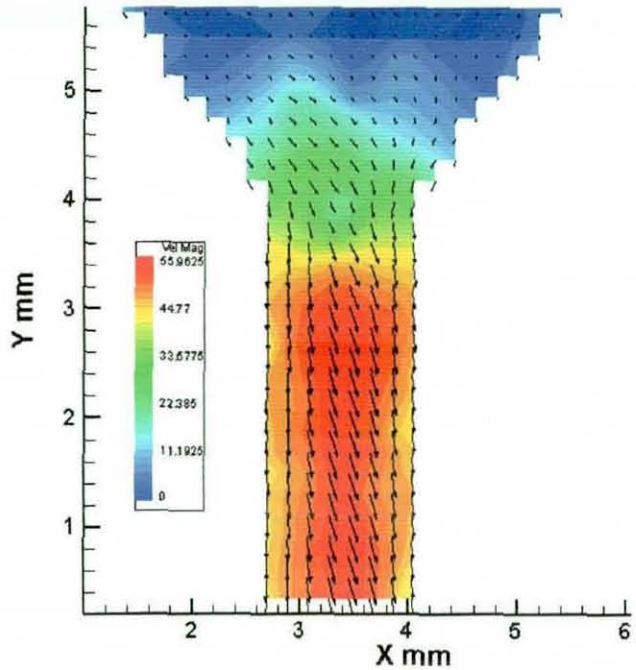

Figure 6.76 Average velocity magnitudes for 45° chamfered inlet orifice at 20 bar.

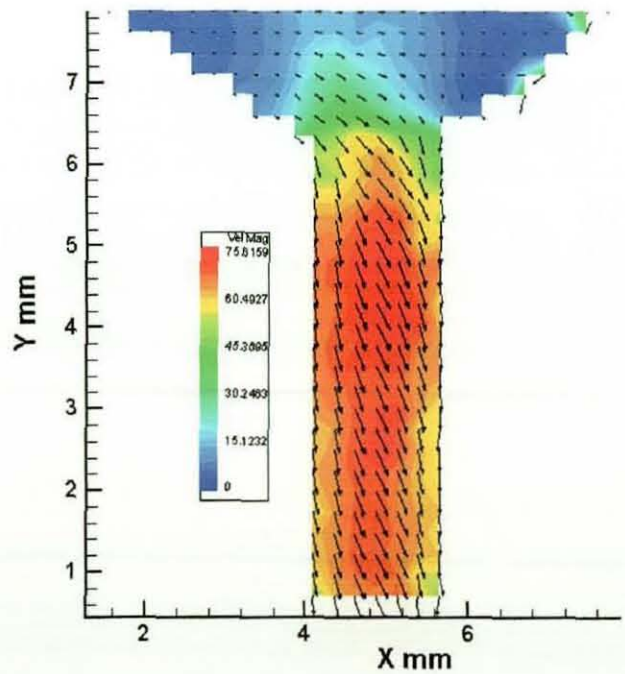

Figure 6.77 Average velocity magnitudes for 60° chamfered inlet orifice at 20 bar.

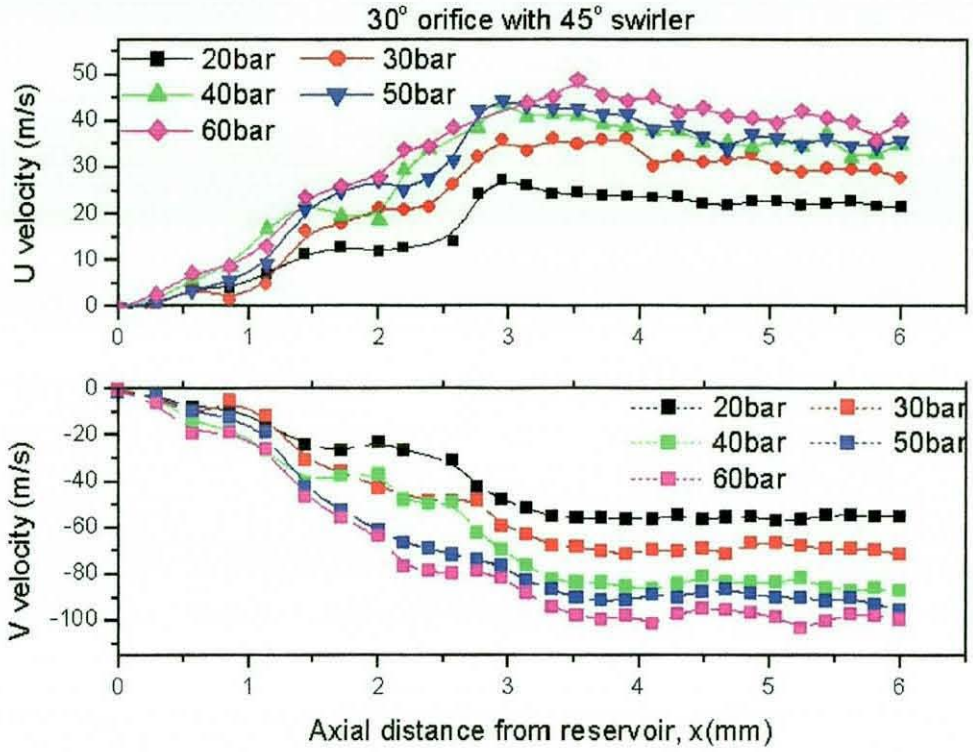

Figure 6.78 Velocity through the centreline of a 30° chamfered inlet orifice with a 45° swirler.

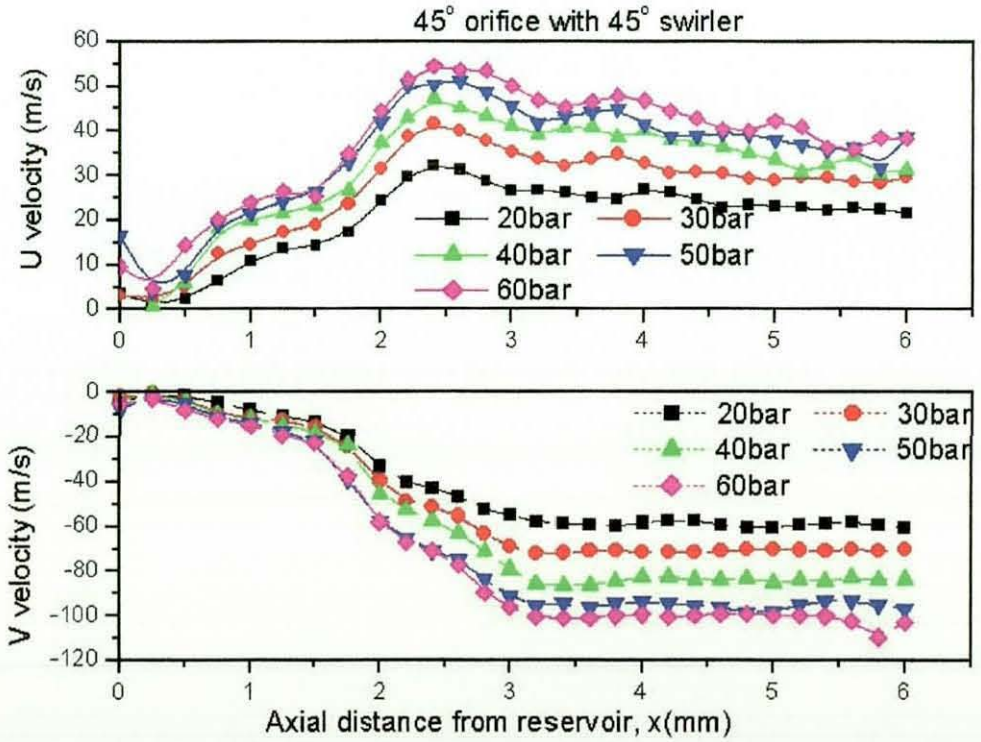

Figure 6.79 Velocity through the centreline of a 45° chamfered inlet orifice with a 45° swirler.

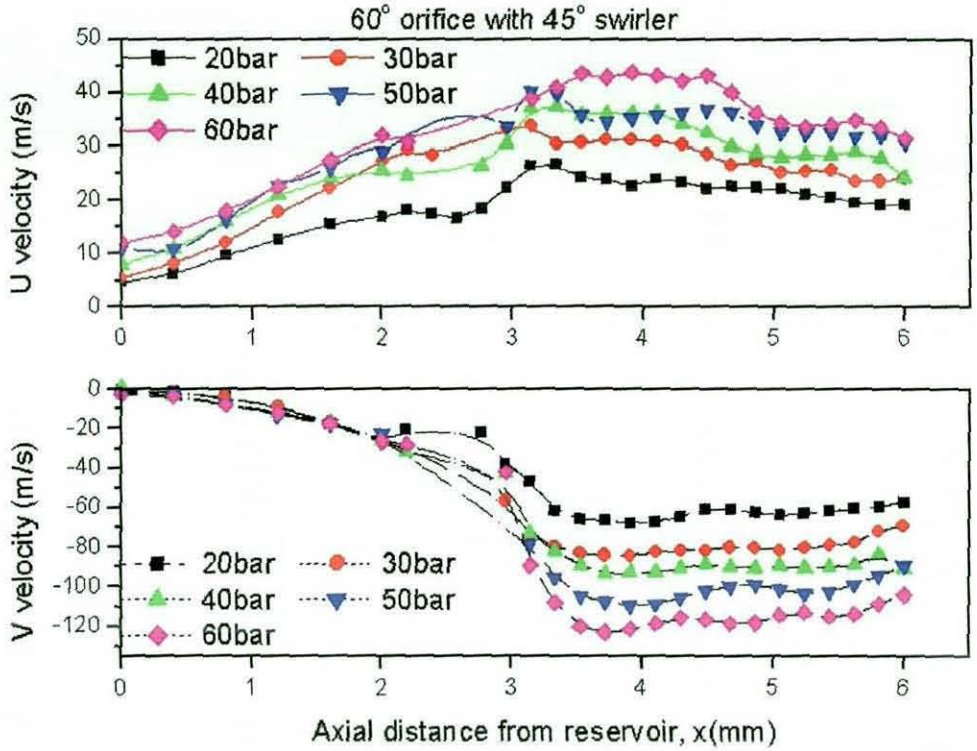

Figure 6.80 Velocity through the centreline of a 60° chamfered inlet orifice with a 45° swirler.

To understand the flow through the orifices, figures 6.78 to 6.80 show the velocity through the centreline of the orifices. For the 30° chamfered inlet orifice graph, it shows a gradual increase in both radial and axial velocities in the convergent section (0-2 mm) before settling to a constant velocity for the straight section. Both graphs also show the flow velocities increases with injection pressure and remain constant in the nozzle section of the orifice. In the 45° chamfered inlet orifice graphs shown in figure 6.79, both radial and axial flow velocities shows a steeper increase in the convergent section of the orifice. In the radial flow velocity graph, the velocities are observed to decrease slightly as the flow reaches the orifice exit. In the case of 60° chamfered inlet orifice graphs, the radial flow velocity shows a gradual increment in flow. However, the axial velocity components again appear to increase suddenly when it enters the straight section before remaining constant t the orifice exit. It is also noted that at 60 bar driving pressure, the velocity increases with increasing chamfered inlet orifice used.

6.5.2.3 60° SWIRLER STUDY

The last swirl generator used for the study of direct injection is the 60° swirler. This swirl generator was again attached to three chamfered inlet orifices for investigating the internal flow characteristics. The three velocity data sets presented in figures 6.81 to 6.83 show the in-nozzle flow velocity at a 20 bar driving pressure. Figure 6.81 displays the swirl flow structures in the 30° chamfered inlet orifice. The velocity vectors indicate the swirl flow moves from the convergent section into the straight section of the nozzle. The swirl flow seems to occur at the centre of the nozzle, with minimum or no swirl at the nozzle peripheral. The following velocity image (Figure 6.82) showing the 45° chamfered inlet orifice also exhibits a smooth transition from the convergent section of the orifice into the straight section. This was also the case in the 60° chamfered inlet orifice in figure 6.83 and this orifice also shows an increase in swirl velocity in the straight section. The peak velocity recorded as 73 m/s highlighted this increase in swirl velocity.

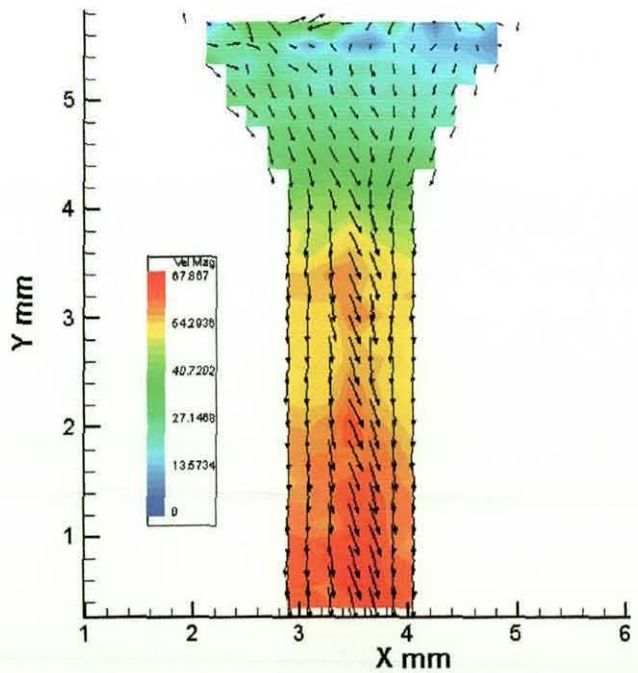

Figure 6.81 Average velocity magnitudes for 30° chamfered inlet orifice at 20 bar.

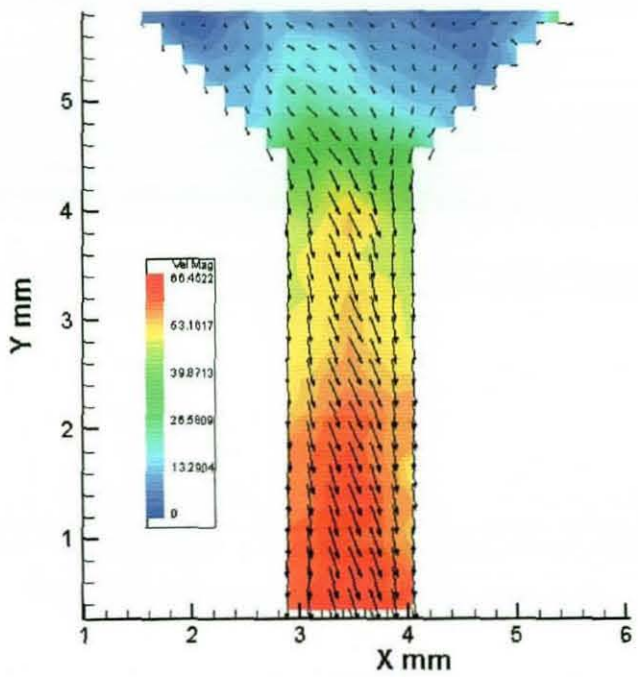

Figure 6.82 Average velocity magnitudes for 45° chamfered inlet orifice at 20 bar.

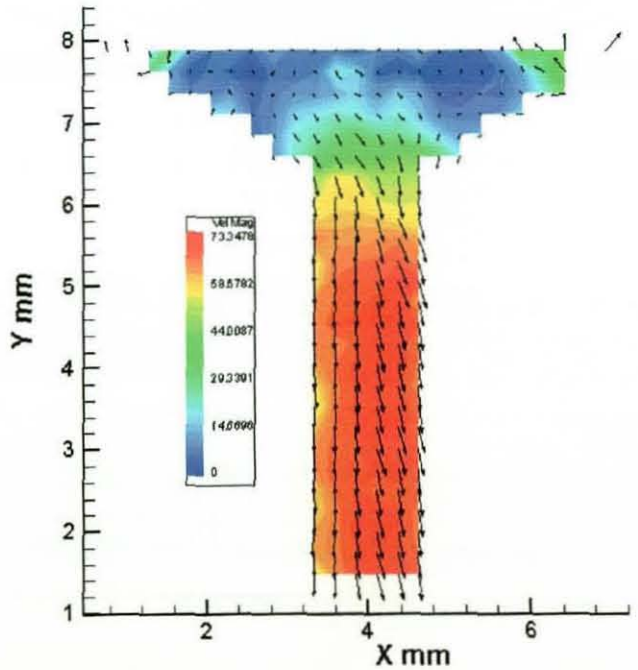

Figure 6.83 Average velocity magnitudes for 60° chamfered inlet orifice at 20 bar.

Figures 6.84 to 6.86 show the radial and axial flow velocity through the centreline of three chamfered inlet orifices with a 60° swirler. The 30°

chamfered inlet orifice displays in figure 6.84 shows fairly random radial velocity components as compare to the axial velocity. The axial velocity data shows a gradual increase in the velocity to the nozzle section of the orifice before stabilising to a constant velocity out through the orifice exit. In figure 6.85, it shows the radial velocity component enters the 45° chamfered inlet orifice at a more systematic increment with driving pressure when compared with the 30° chamfered inlet orifice. The axial velocity displays a more consistent and constant velocity in the nozzle section. For the 60° chamfered inlet orifice (Figure 6.86), the radial velocity component appears to increase from 20 bar to 30 bar but it remains the same from 30 bar to 60 bar driving pressure. As with the other axial flow velocity, the velocity remains constant in the nozzle section. The only notable difference between this orifice and the other two is the higher axial flow velocity recorded.

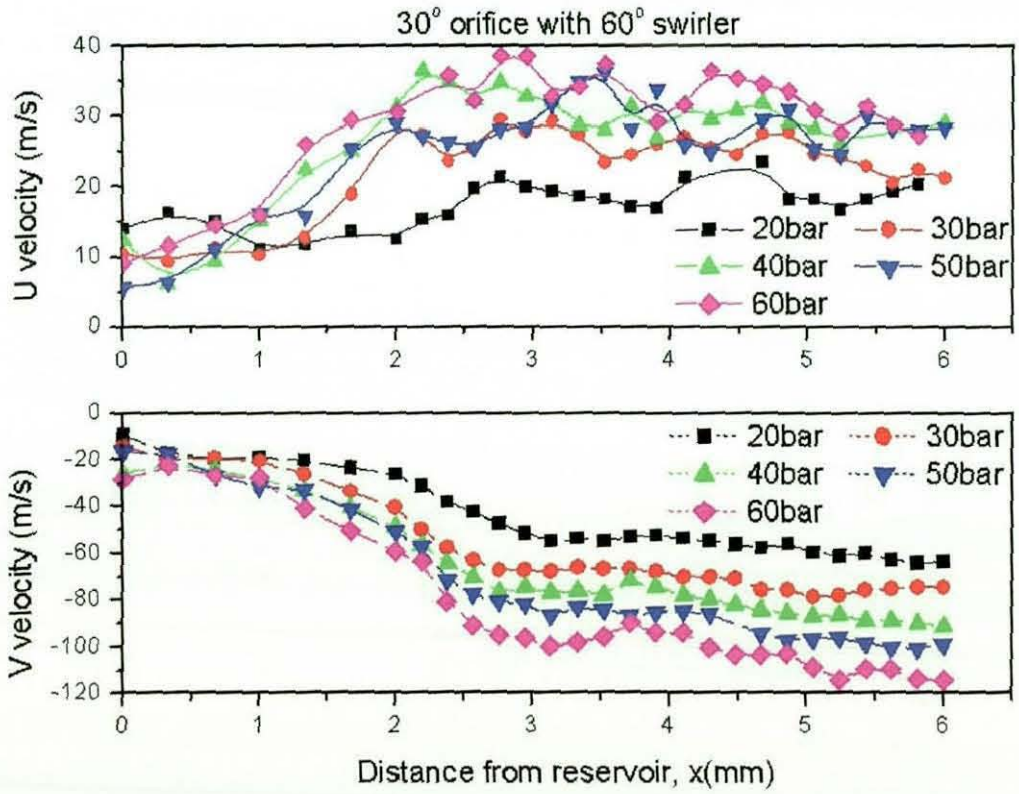

Figure 6.84 Velocity through the centreline of a 30° chamfered inlet orifice with a 60° swirler.

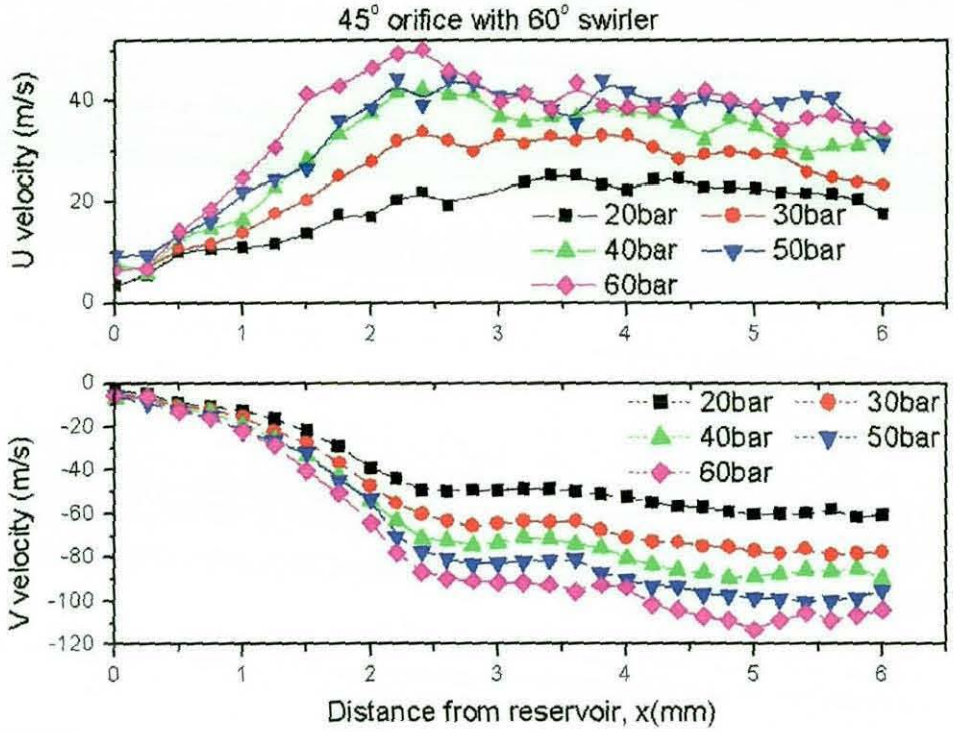

Figure 6.85 Velocity through the centreline of a 45° chamfered inlet orifice with a 60° swirler.

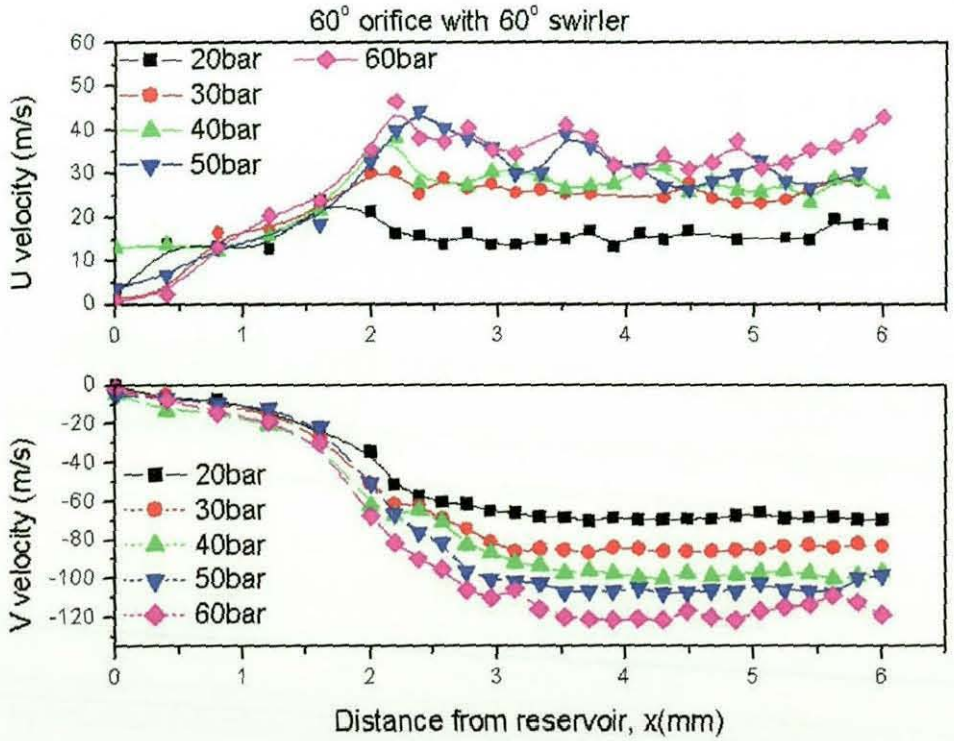

Figure 6.86 Velocity through the centreline of a 60° chamfered inlet nozzle with a 60° swirler.

6.6 SWIRL INJECTORS STUDY (PDA)

6.6.1 Introduction

The use of high speed flow visualisation and FPIV provided valuable insights and understanding of the effect of orifice geometries on flow characteristics. With the quantification of internal flow, the next logical step is to link this to the external spray. Figure 6.107 shows the PDA diagnostic technique used to quantify the external spray and atomisation. The optical rig was mounted on a 3-axis traverse system and placed in the path of the laser beams. The beams were aligned to pass through the centre of the optical orifice exit, which is located 88.9 mm above the crossed laser beams. As mentioned in chapter 4, the measurement begins just below the centre of the orifice exit and move along the x-axis out to the peripheral of the sprays. The data was then analysed to provide droplet size and velocity to quantify the sprays. This is an important experimentation as it provides a link from the study of internal flow structures to the external spray structures using the same set of orifice configurations, providing important understanding of the spray characteristics with respect to swirlers and orifice geometries.

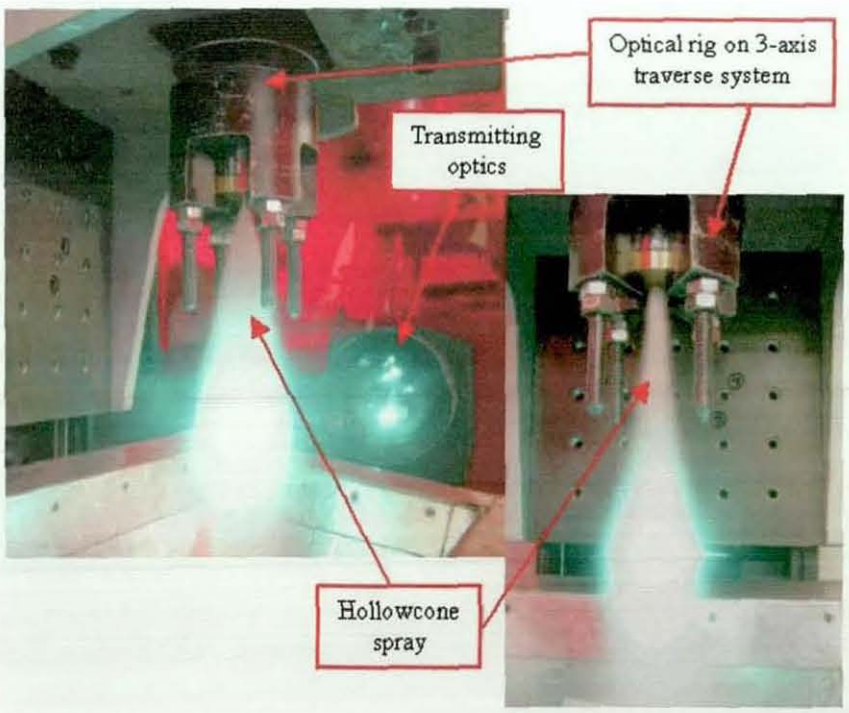

Figure 6.87 PDA setup show here with a hollowcone spray.

6.6.2 Results and Analysis

The following PDA results and analysis for the three swirl generators and three chamfered inlet orifices are sub-divided based on three swirler configurations, with each chamfered inlet orifice displayed in two graphs. The first graph provides the radial profile of droplet sizes and second graph the radial profile of droplet velocity. Data is presented for driving pressures from 20 bar to 60 bar. In these graphs the zero point represents the centre of the nozzle.

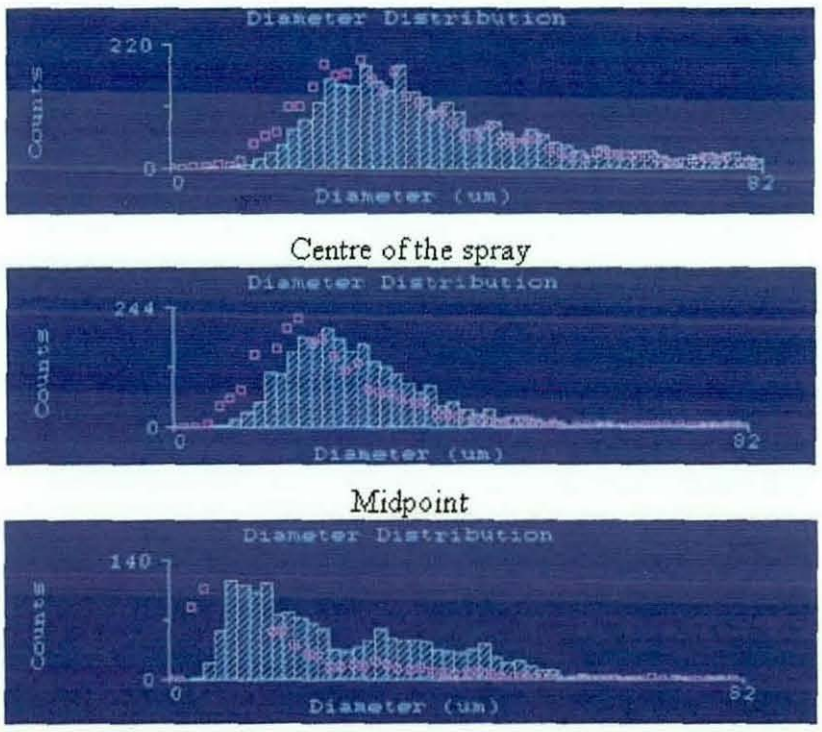

Figure 6.88 45° swirler with 30° chamfered inlet orifice at 30 bar driving pressure.

Examples of the particle diameter distribution is presented in figure 6.88 for locations at the centre of the spray, midpoint and at the spray periphery. This data is typical of the size distributions for all configurations tested. The profiles are basically skewed normal distributions. At the centre and midpoint the skewed towards larger particle diameters, but at the outer edge of the spray a

distinctive twin-peak distribution is seen with a high concentration of small (less than 20 micron) droplets.

6.6.2.1 30° SWIRLER STUDY

Figures 6.89 and 6.90 show the Sauter mean diameter (SMD) and mean velocity results for the 30° degree chamfered inlet orifice. The measurements were taken from the centre of the orifice and moves radially outward to the spray peripheral. As the 3-axis traverse system uses imperial measurement, the distance increment is 1.27mm per point. The SMD results from the centre of the orifice were inconclusive as the sizes vary with different driving pressures. However the SMD sizes decreases with increasing pressure as it reached the peripherals except the data recorded for 30 bar driving pressure that seems to over predict when compared with the 40 bar driving pressure. With the increase in SMD sizes at the peripherals, the mean axial velocity decreases with increase injection pressure.

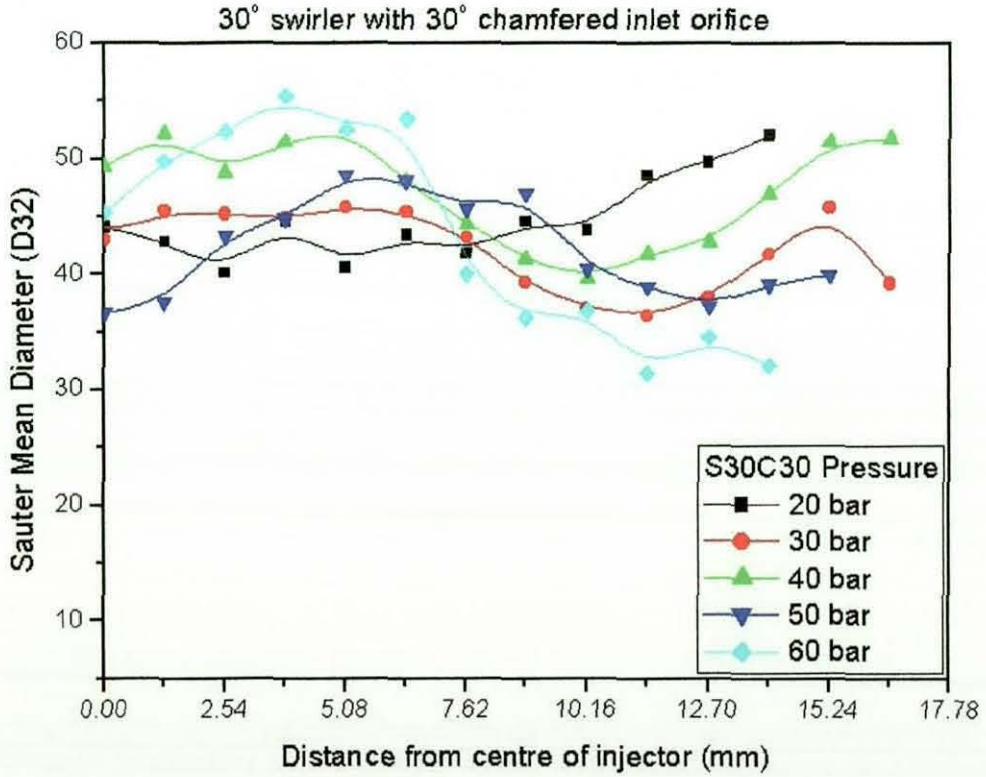

Figure 6.89 SMD for 30° swirler with 30° chamfered inlet orifice at 90 mm downstream.

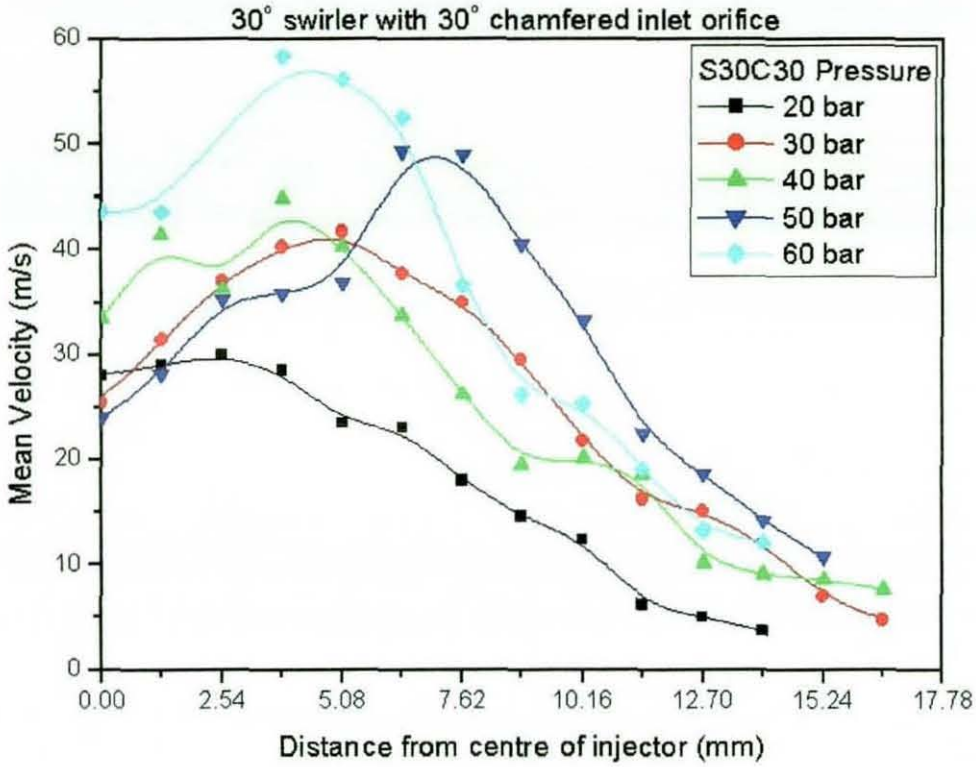

Figure 6.90 Mean axial velocity for 30° swirler with 30° chamfered inlet orifice at 90 mm downstream.

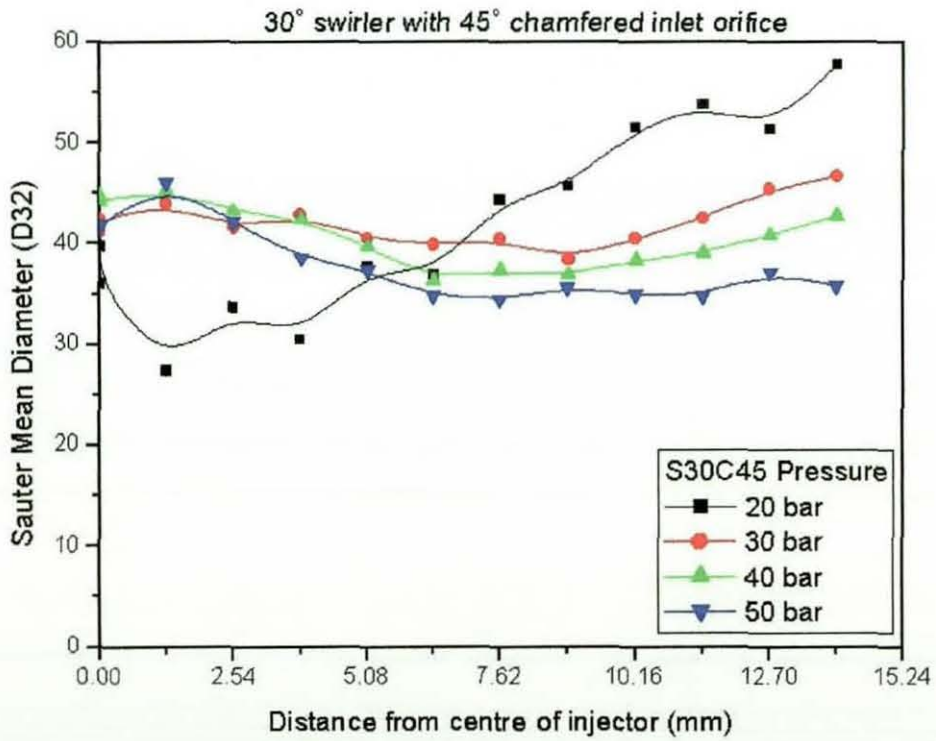

Figure 6.91 SMD for 30° swirler with 45° chamfered inlet orifice at 90 mm downstream.

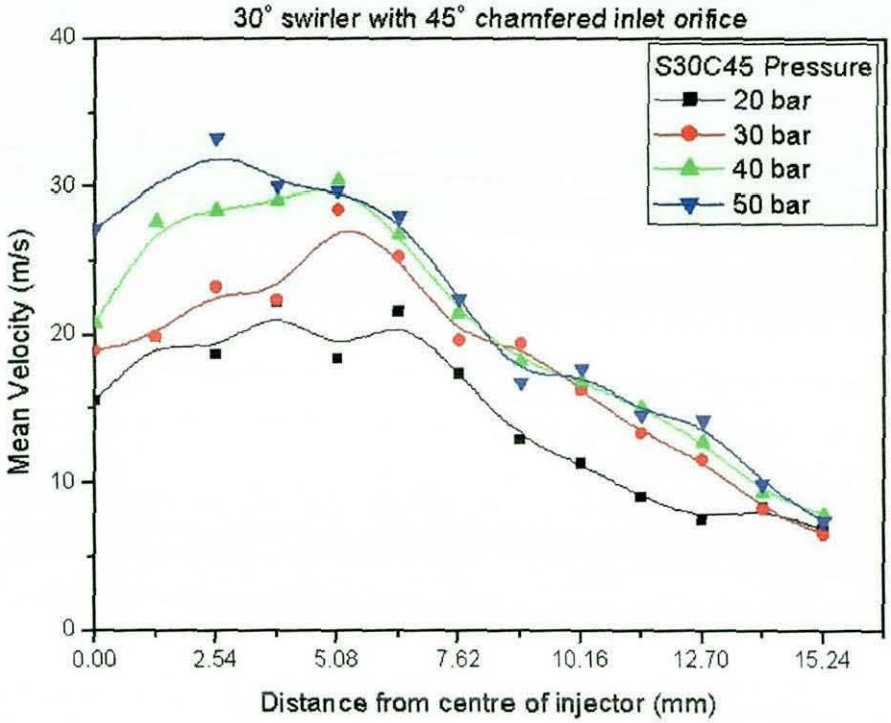

Figure 6.92 Mean axial velocity for 30° swirler with 45° chamfered inlet orifice at 90 mm downstream.

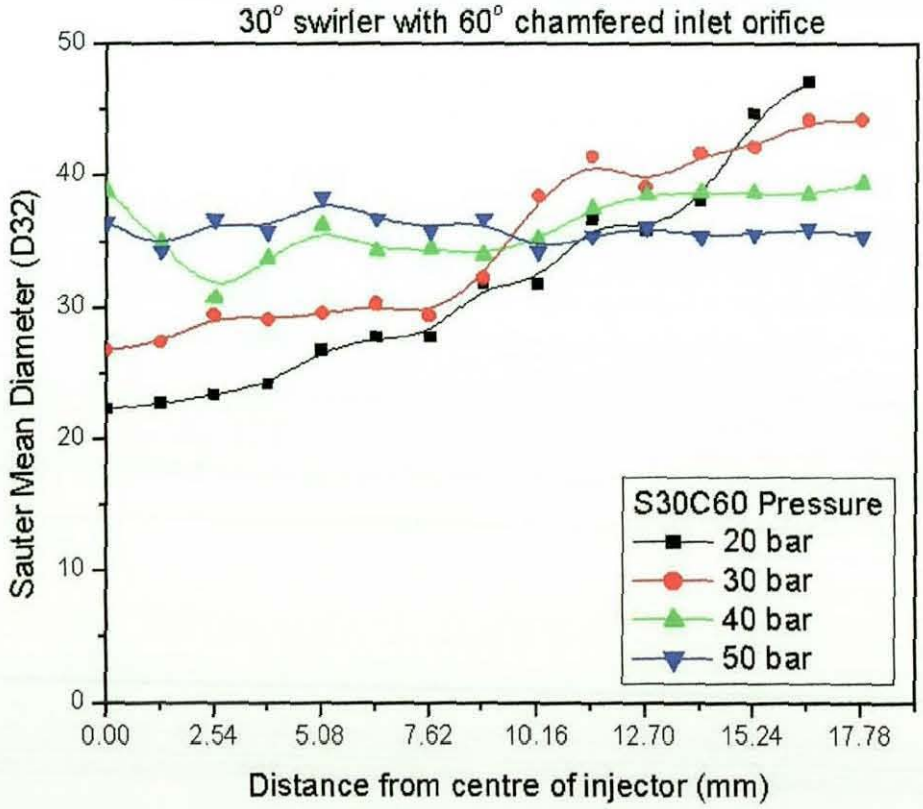

Figure 6.93 SMD for 30° swirler with 60° chamfered inlet orifice at 90 mm downstream.

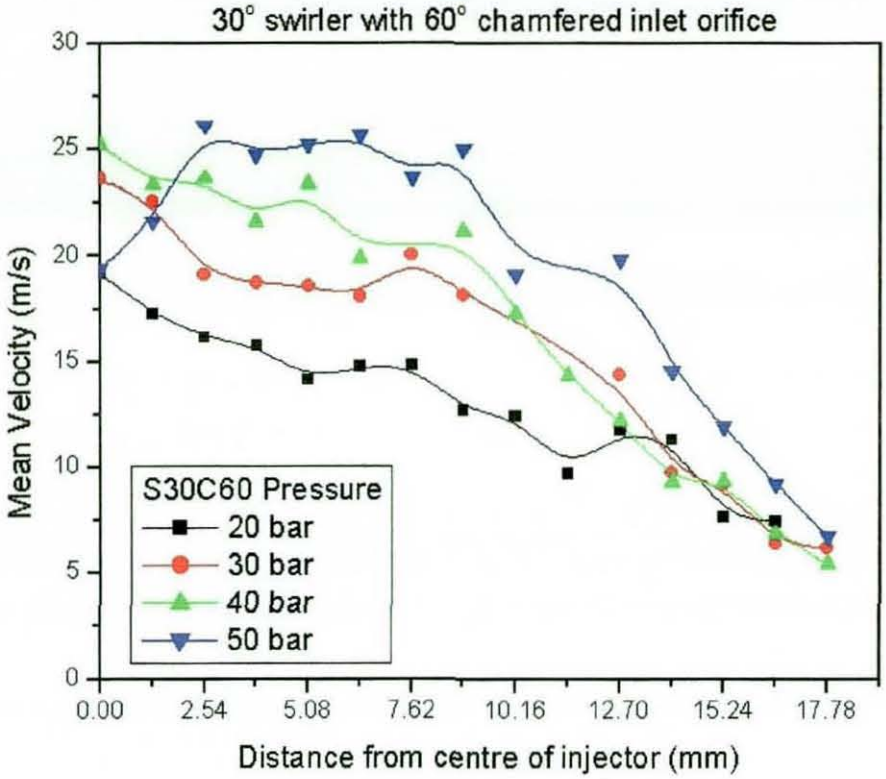

Figure 6.94 Mean axial velocity for 30° swirler with 60° chamfered inlet orifice at 90 mm downstream.

For 45° degree chamfered inlet orifice (figure 6.91 and 6.92), similar trends in SMD sizes were also observed. Increase in driving pressure resulted in smaller SMD sizes as the droplets reached the spray peripherals. However, the mean velocity of these droplets seems to converge to the same value of 7 m/s at the periphery. This trend is again seen in figures 6.93 and 6.94 for 60° degree chamfered inlet orifice study with both droplet SMD sizes and mean velocity for the same driving pressure range.

6.6.2.2 45° SWIRLER STUDY

The 45° swirler study for three chamfered inlet orifices were shown from figures 6.95 to 6.96. The SMD graph for 30° degree chamfered inlet orifice (Figure 6.95) showed the droplet sizes are almost similar beneath the orifice exit. However the droplets size for 20 bar driving pressure at the periphery were the largest, before decreasing as the driving pressure increases. In the axial velocity graph shown in figure 6.96, the plots clearly show an increase in

mean velocity 3.81 mm from the centre of the orifice before decreasing to the same velocity at the periphery.

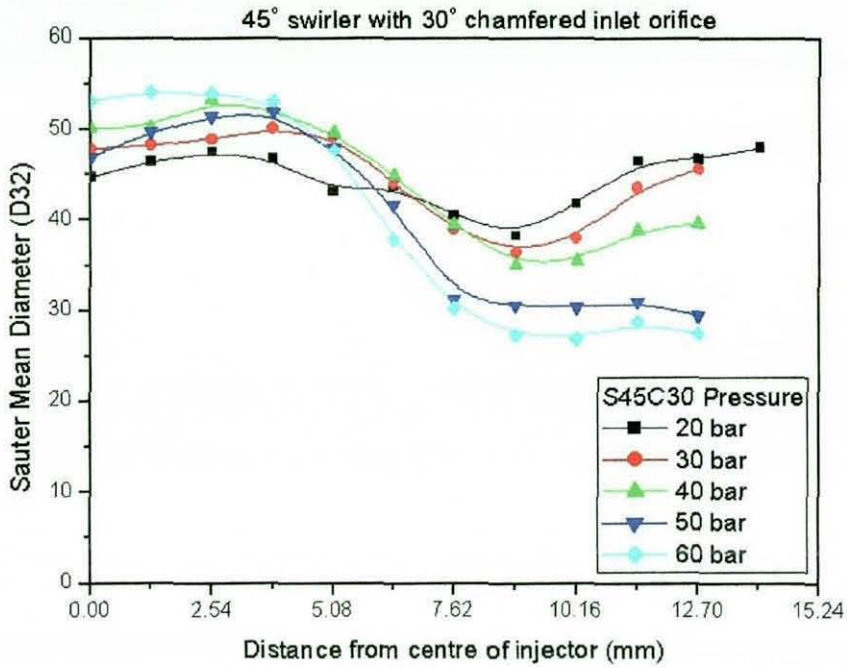

Figure 6.95 SMD for 45° swirler with 30° chamfered inlet orifice at 90 mm downstream.

Figures 6.97 and 6.98 present the droplet size and mean velocity for 45° degree chamfered inlet orifice with driving pressure ranging from 20 bar to 50 bar. The droplets size just beneath the orifice exit was inconsistent but this was not the case at the spray peripheral. The graph clearly shows the lower driving pressure displayed large droplet size compare with higher driving pressure. In the case for the mean velocity, the plots show inconsistent mean flow velocity below the orifice exit but all these velocity plots converge to the same velocity at the edge of the spray.

The last set of 45° swirler study results highlighted the use of the 60° chamfered inlet orifice with 20 bar to 50 bar driving pressure. The droplets size plots for this orifice remain fairly constant from the orifice exit to the peripheral. A decrease in droplet size was also observed with increase driving pressure. In the mean velocity plots, the results were inconsistent near the orifice exit as seen from the other two orifices.

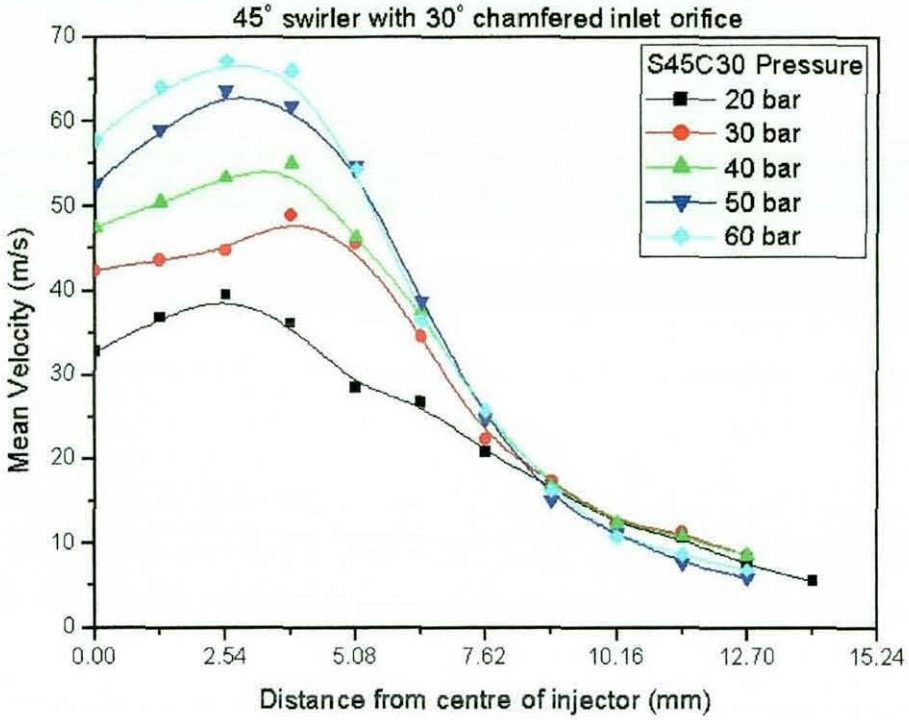

Figure 6.96 Mean axial velocity for 45° swirler with 30° chamfered inlet orifice at 90 mm downstream.

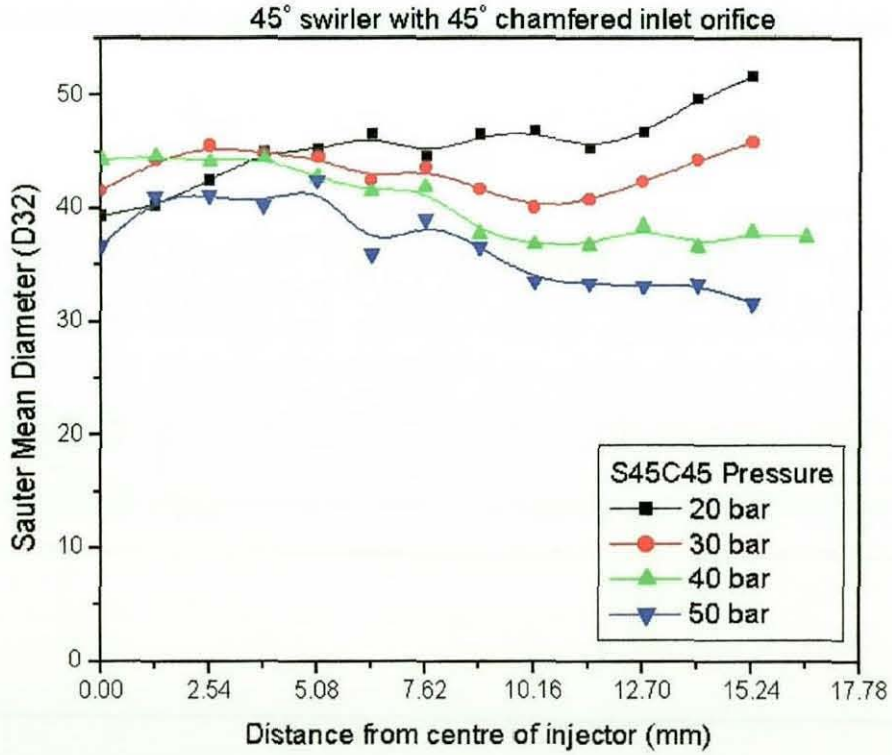

Figure 6.97 SMD for 45° swirler with 45° chamfered inlet orifice at 90 mm downstream.

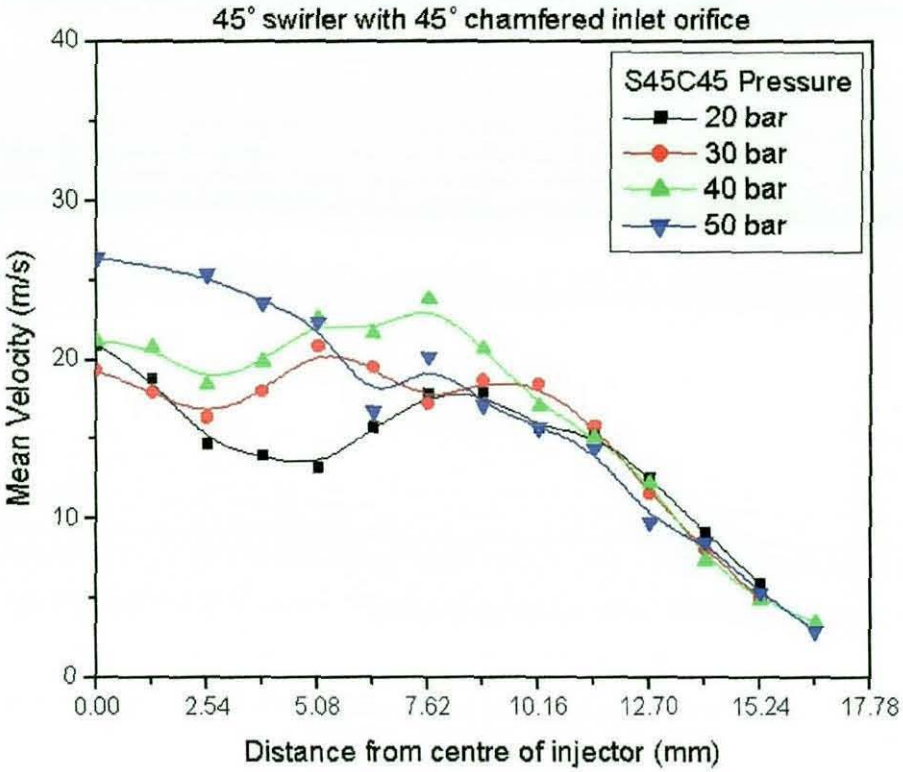

Figure 6.98 Mean axial velocity for 45° swirler with 45° chamfered inlet orifice at 90 mm downstream.

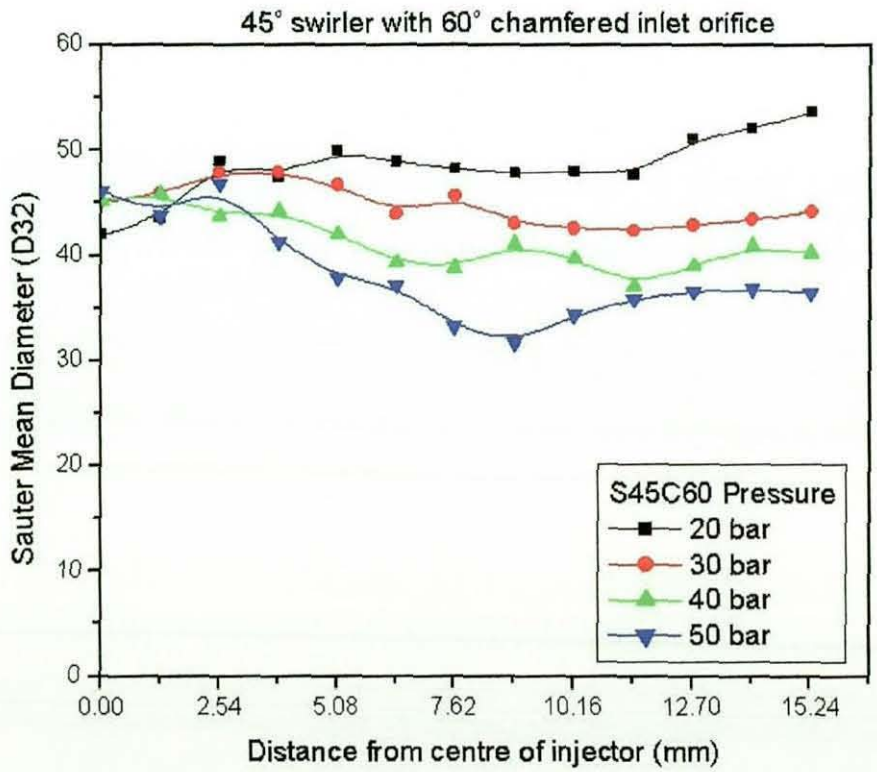

Figure 6.99 SMD for 45° swirler with 60° chamfered inlet orifice at 90 mm downstream.

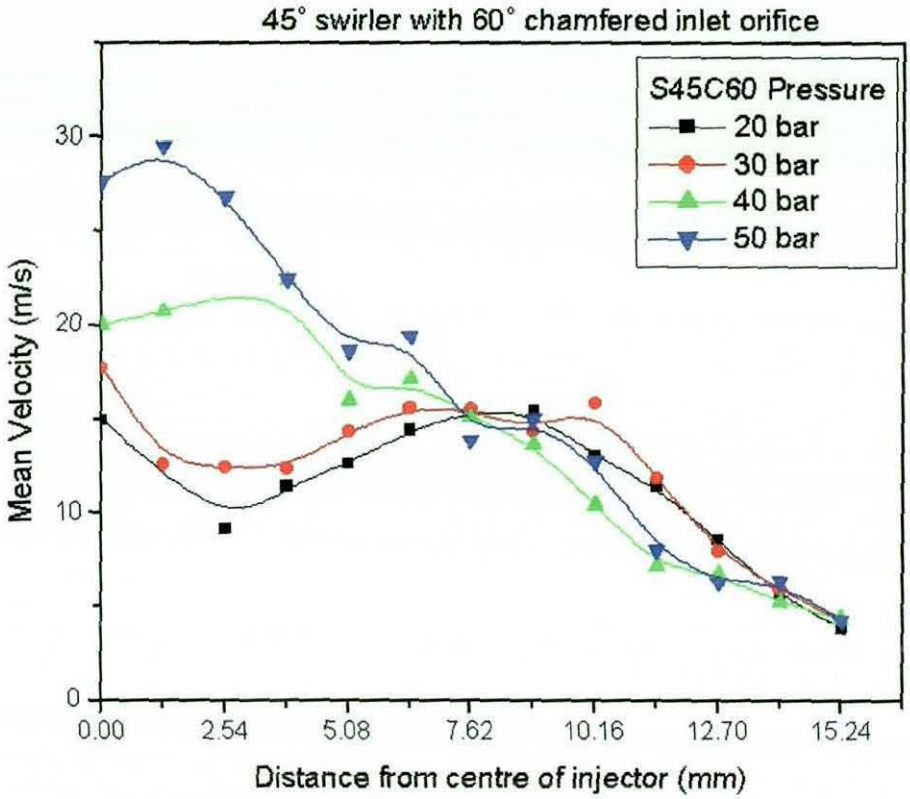

Figure 6.100 Mean axial velocity for 45° swirler with 60° chamfered inlet orifice at 90 mm downstream.

6.6.2.3 60° SWIRLER STUDY

The last set of PDA result involved the 60° swirler with the three chamfered inlet orifices. The first 2 figures show the 30° chamfered inlet orifice (Figures 6.101 and 6.102) with driving pressure range from 20 bar to 60 bar. The droplet size increases as it reaches the spray peripheral at 20 bar driving pressure. The droplet sizes for the other four driving pressures remain constant throughout the hollow cone spray. The mean velocity for all driving pressure conditions shows a linear decrease from the centre of the spray to the peripheral.

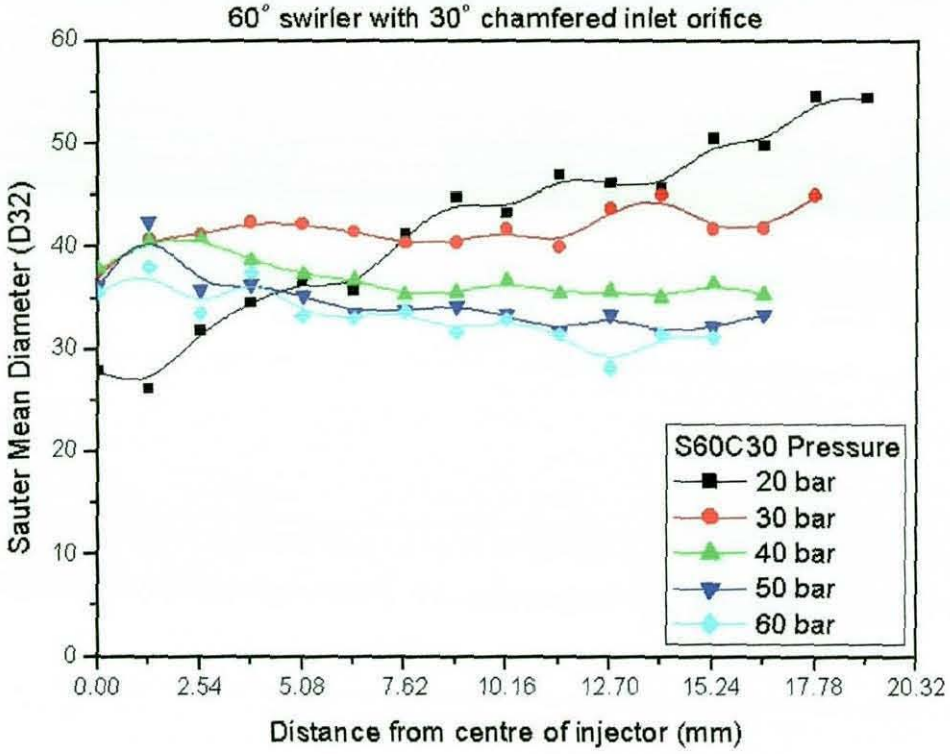

Figure 6.101 SMD for 60° swirler with 30° chamfered inlet orifice at 90 mm downstream.

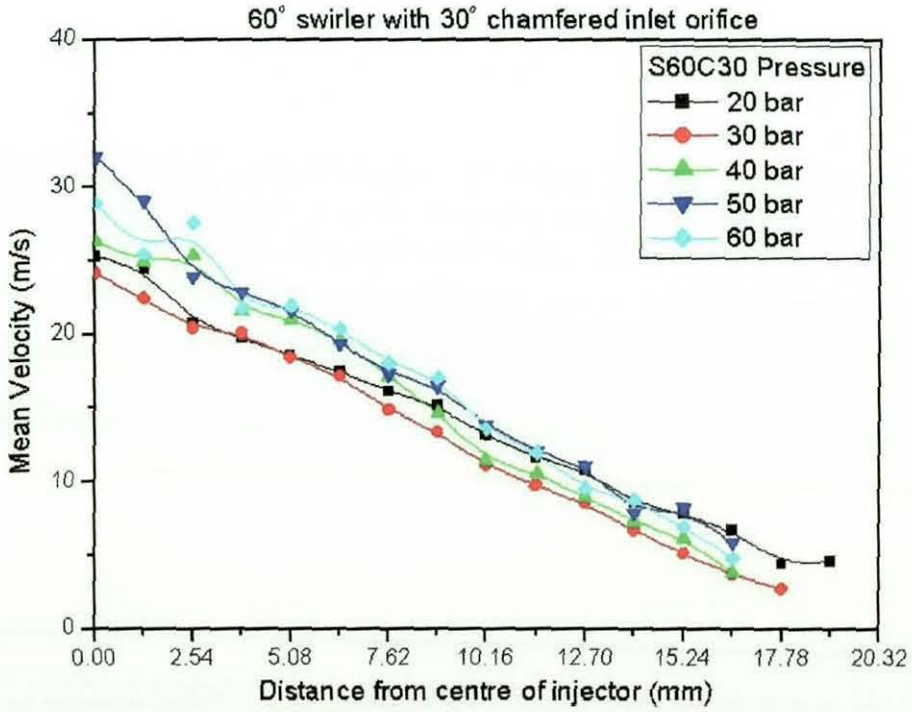

Figure 6.102 Mean axial velocity for 60° swirler with 30° chamfered inlet orifice at 90 mm downstream.

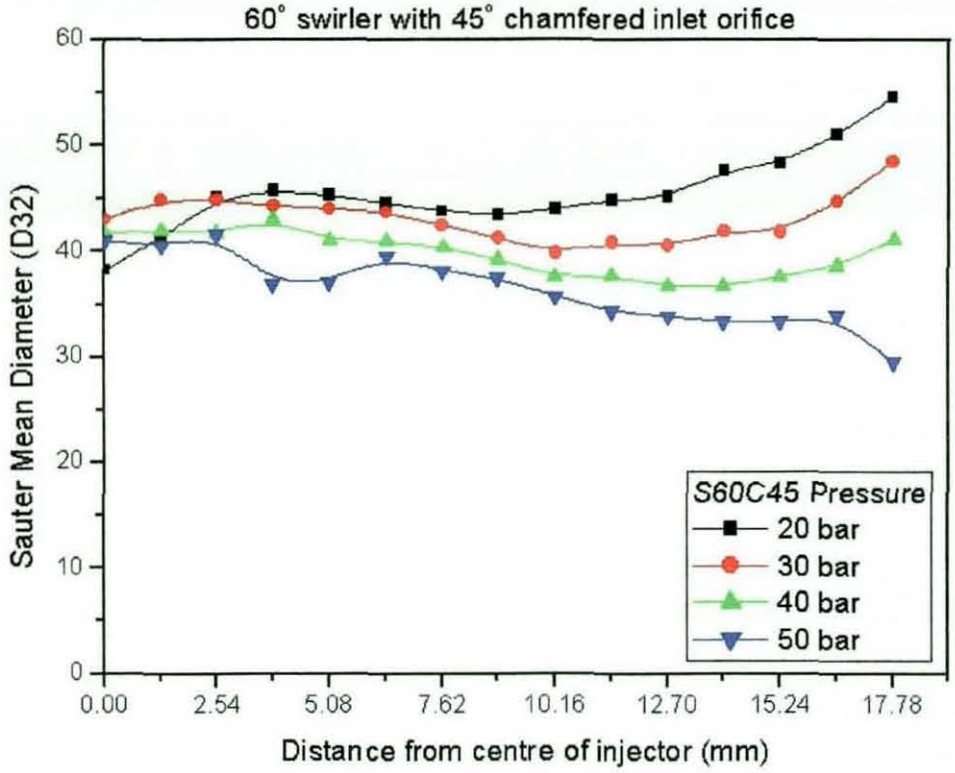

Figure 6.103 SMD for 60° swirler with 45° chamfered inlet orifice at 90 mm downstream.

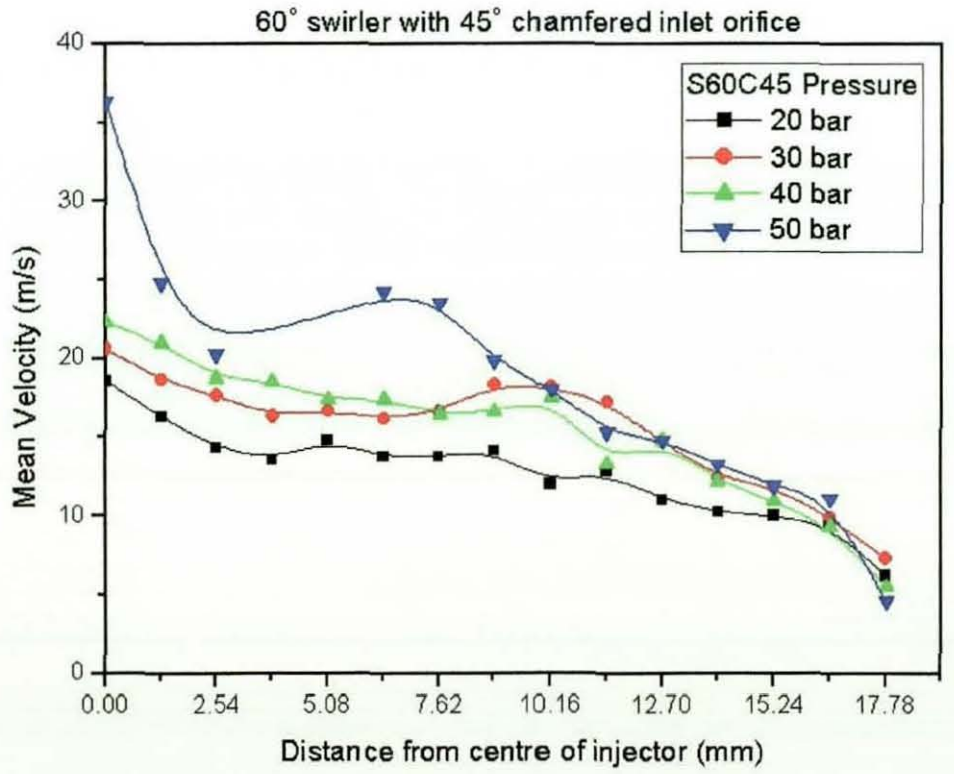

Figure 6.104 Mean axial velocity for 60° swirler with 45° chamfered inlet orifice *at 90 mm downstream.*

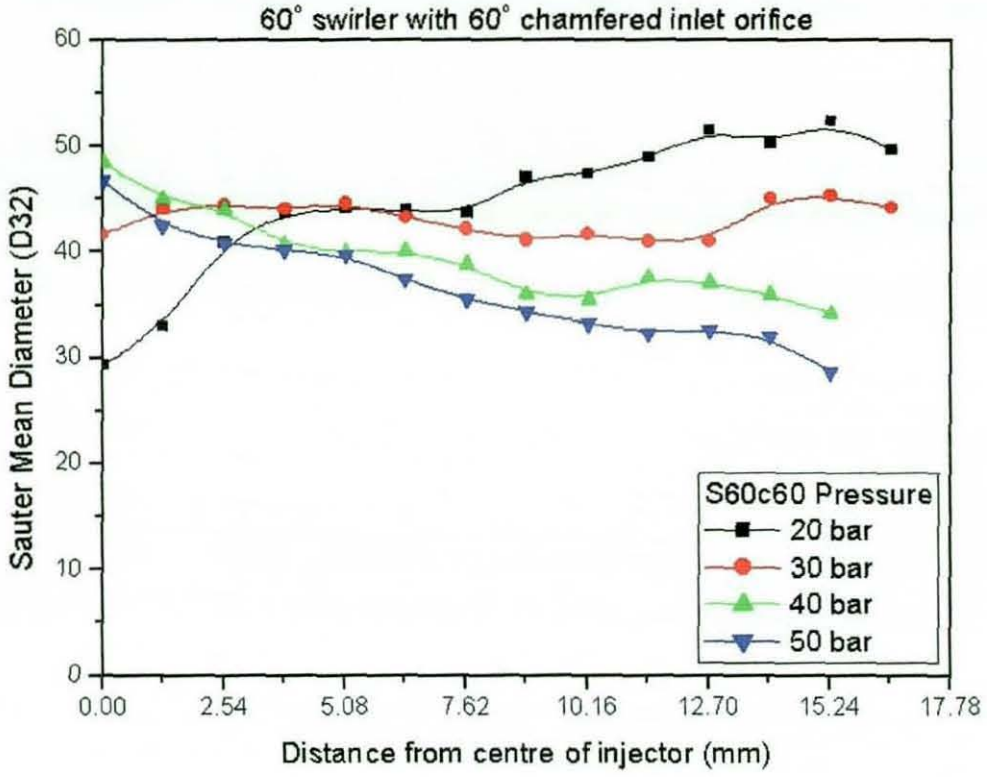

Figure 6.105 SMD for 60° swirler with 60° chamfered inlet orifice at 90 mm downstream.

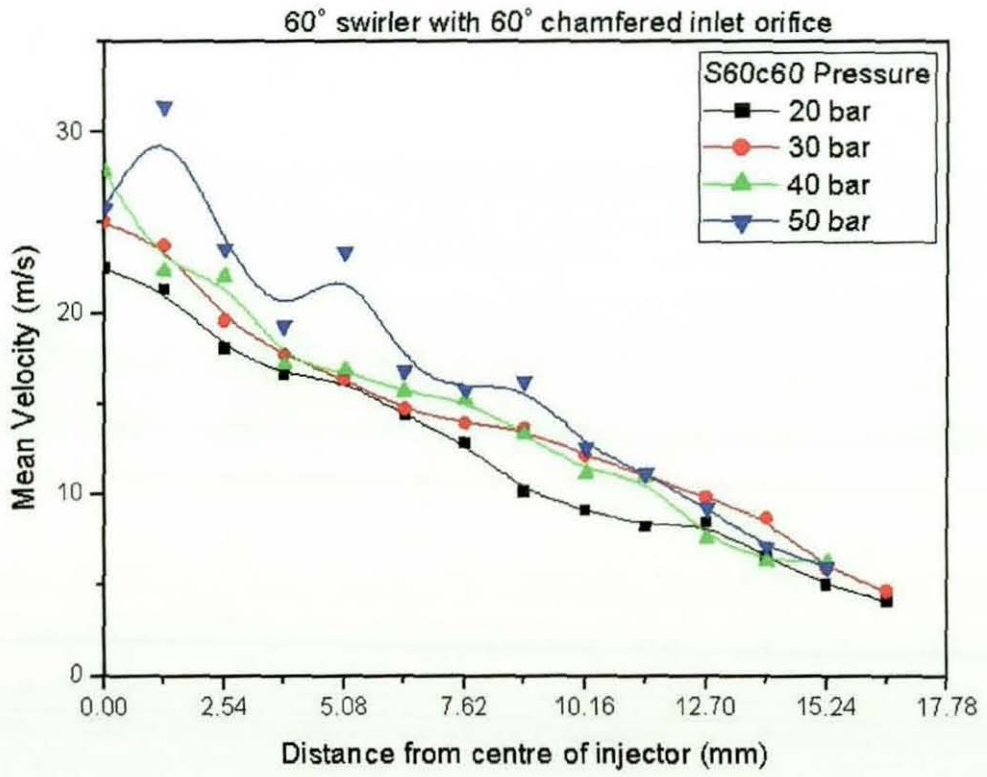

Figure 6.106 Mean axial velocity for 60° swirler with 60° chamfered inlet orifice at 90 mm downstream.

The droplets size for both 45° and 60° chamfered inlet orifice (figure 6.103 and 6.106) also showed a decrease in SMD size at higher injection pressure. The mean velocity for 45° and 60° chamfered inlet orifice appears to be similar regardless of the driving pressure used. These results seem to show similar trends to the 30° chamfered inlet orifice of the same swirl configurations.

6.7 SWIRL STUDY DISCUSSION

6.7.1 Flow Visualisation

The variations in the aircore structure and annular flow thickness presented in the study of the swirl generators in section 6.4 highlighted the importance of understanding the internal flow structure. To quantify the variation with geometry of the internal flow structure, the following figures present data for the aircore diameter and annular flow thickness for both increasing swirl angle and increasing chamfered inlet orifice angle.

Figure 6.107 displays results for the annular flow thickness and aircore diameter at a driving pressure of 20 bar. The 30° and 45° chamfered inlet orifices show a gradual increase in annulus thickness as the swirl angle increases from 30° and 60° angle. This was not the case for 60° chamfered inlet orifice, showing a maximum annulus thickness (minimum air core diameter) for the 45° swirl angle.

Figures 6.108 – 6.111 present the results for 30 bar to 60 bar driving pressure. The 30° and 45° chamfered inlet orifices all show an increase in annulus thickness as the swirl angle increases. With the annulus thickness increasing, the aircore diameter naturally decreases with increasing swirl angles. However, the variation of annulus thickness with swirl angle for the 60° chamfered inlet orifice shows a different trend. For all driving pressures, the annulus thickness shows a maximum with a 45° inlet swirl angle.

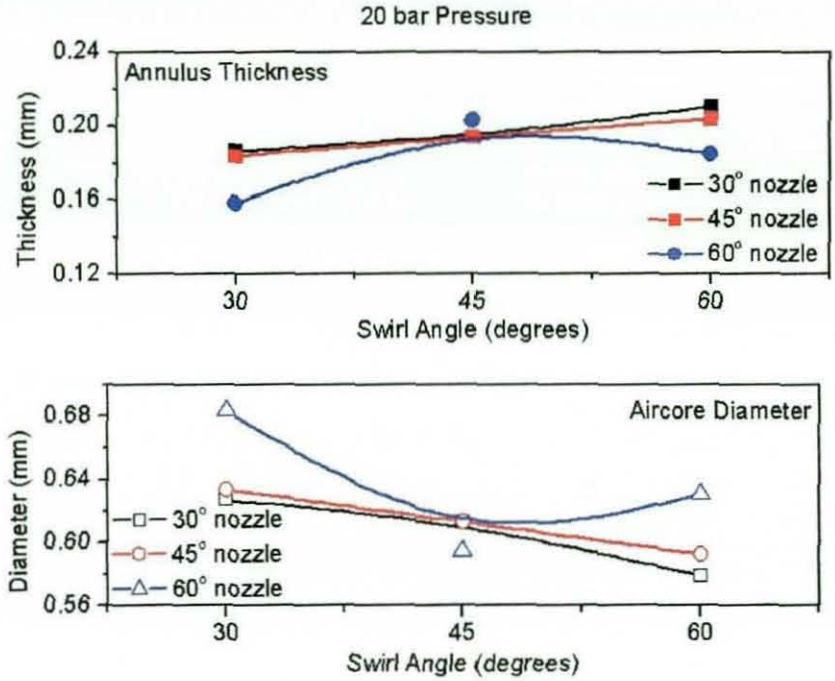

Figure 6.107 Swirler comparison for three chamfered inlet orifices at 20 bar pressure and at nozzle exit.

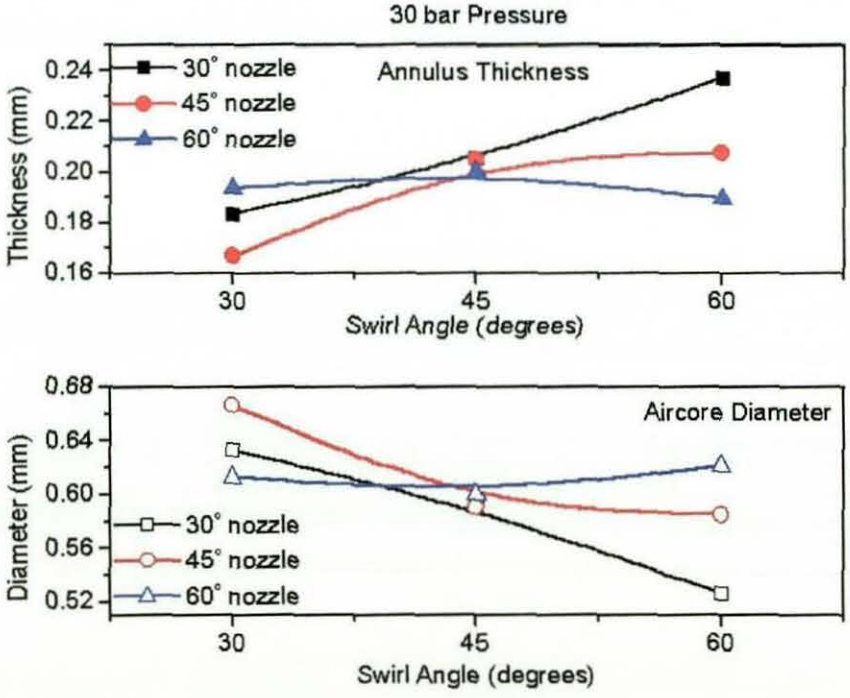

Figure 6.108 Swirler comparisons for three chamfered inlet orifices at 30 bar pressure and at nozzle exit.

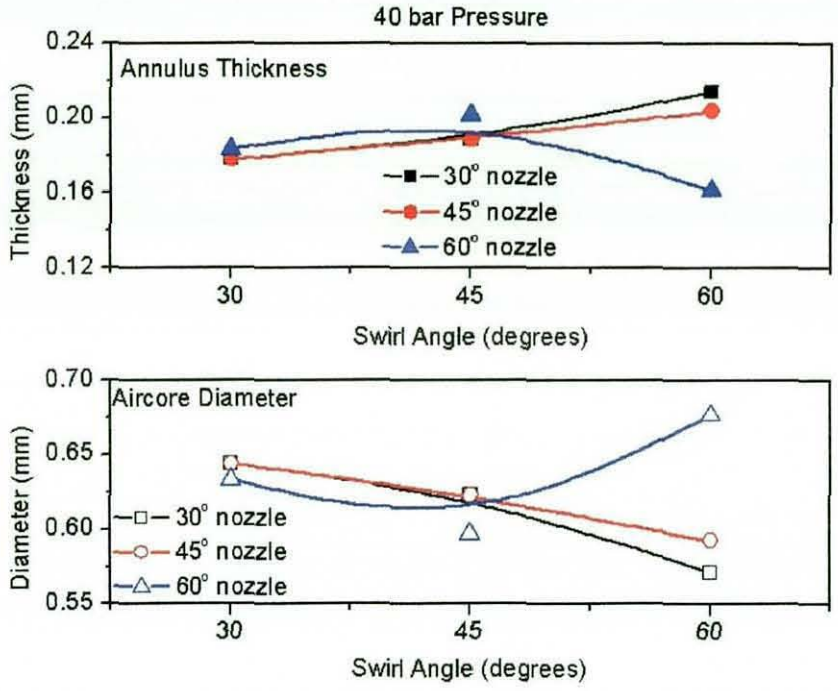

Figure 6.109 Swirler comparisons for three chamfered inlet orifices at 40 bar pressure and at nozzle exit.

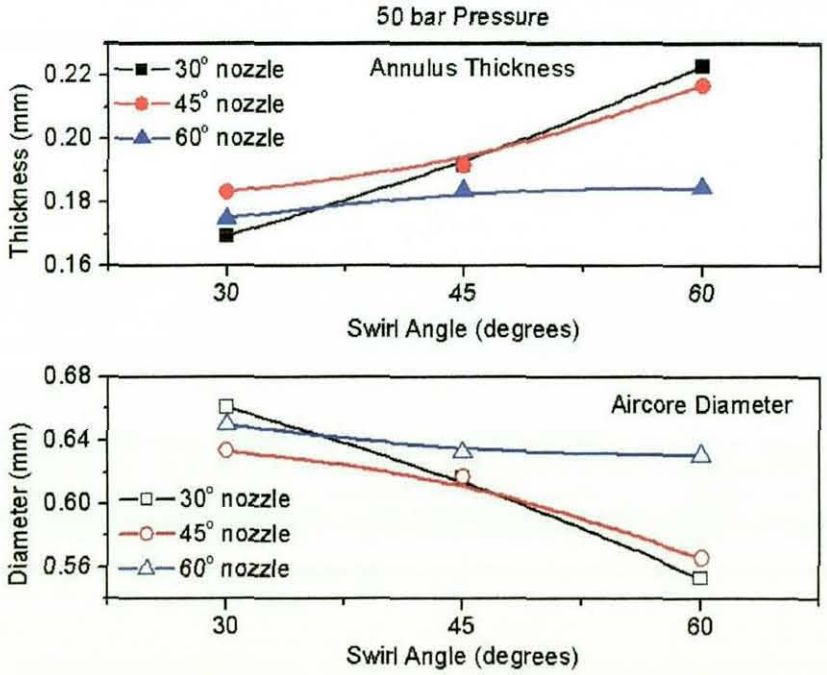

Figure 6.110 Swirler comparisons for three chamfered inlet orifices at 50 bar pressure and at nozzle exit.

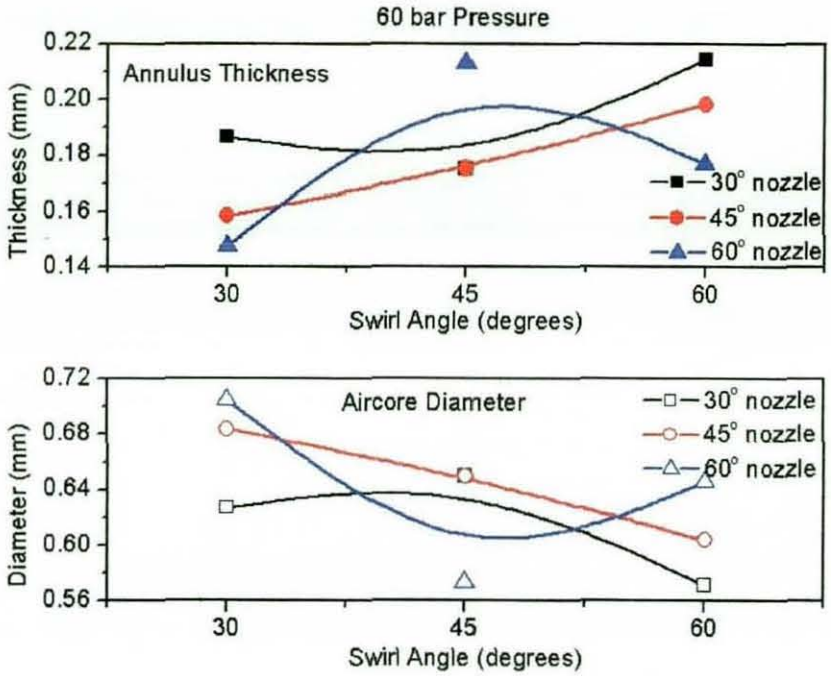

Figure 6.111 Swirler comparisons for three chamfered inlet orifices at 60 bar pressure and at nozzle exit.

Referring to Figures 6.107 and 6.111, it is clear that there is very little variation the exit aircore diameter and exit annulus thickness with driving pressure. This finding is in agreement with the data presented by Gavaises *et al* [11] for a pressure swirl atomiser (nominal size 1 mm) and may be attributed to the fact that the radial (swirl) to axial velocity ratio is independent of the driving pressure. The ratio is only a function of the geometry of the swirler and thereby the imposed tangential velocity at the inlet to the nozzle. As the driving pressure is increased, the total flow velocity increases, but the swirl motion remains the same and it is this that controls the aircore development.

Several authors have provided relationships for the calculation of annulus thickness for pressure swirl atomisers [16, 09]. According to Dorfner *et al* [05, 09], the film annulus thickness, h_o, at the nozzle exit is given by:

$$h_o = \left[3.66 \frac{\dot{m}_l d_o \mu_l}{\rho_l \Delta P_l} \right]^{0.25} \qquad (6.1)$$

where $\dot{m}_l$ is the liquid mass flow rate, d_o is the nozzle exit diameter, μ_l and ρ_l are the liquid viscosity and density. The pressure difference across the nozzle is given as ΔP_l. The Dorfner equation is an empirical relationship derived from experimental data taken on nozzles with diameters from 0.57 to 1.27 mm.

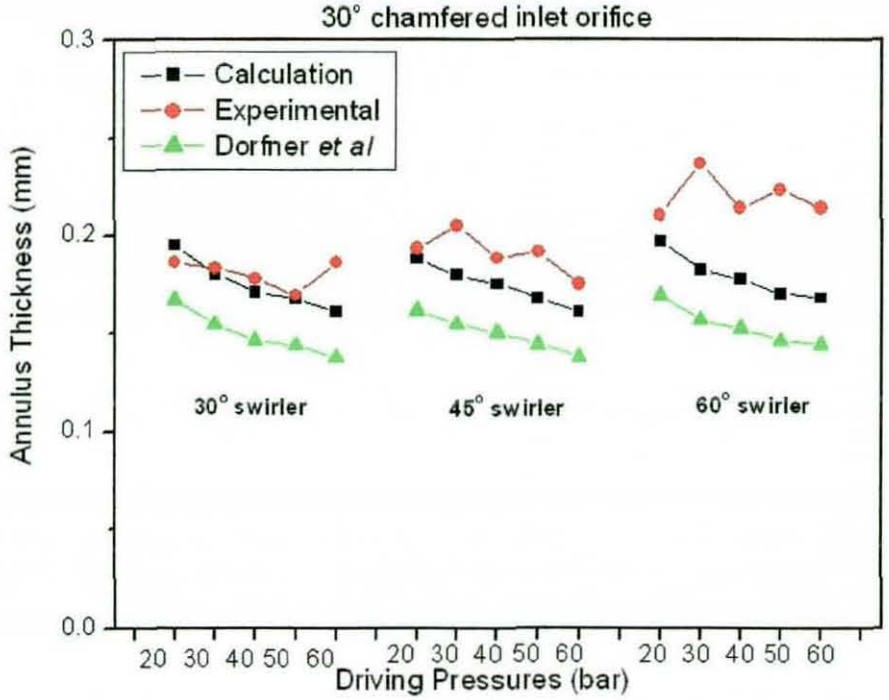

Figure 6.112 Experimental and calculated annulus thickness comparisons with a 30° chamfered inlet orifice at nozzle exit. [09]

Figure 6.112 presents annulus thickness data for all three swirlers, with a 30° chamfered inlet orifice and driving pressure from 20 to 60 bar. Comparison of the current data with the relationship provided by Dorfner *et al* [09] (equation 6.1) shows that the constant of 3.66 significantly under-predicts the experimental results. By increasing the constant value in equation 6.1 from 3.66 to 6, the calculated annulus thickness values fit better to the experimental data for the 30° swirler configuration. However, the equation still under-predicts the annulus thickness for the 45° and 60° swirlers. Clearly the thickness is a function of the swirler geometry, but this is not accounted for in the Dorfner *et al* [09] relationship.

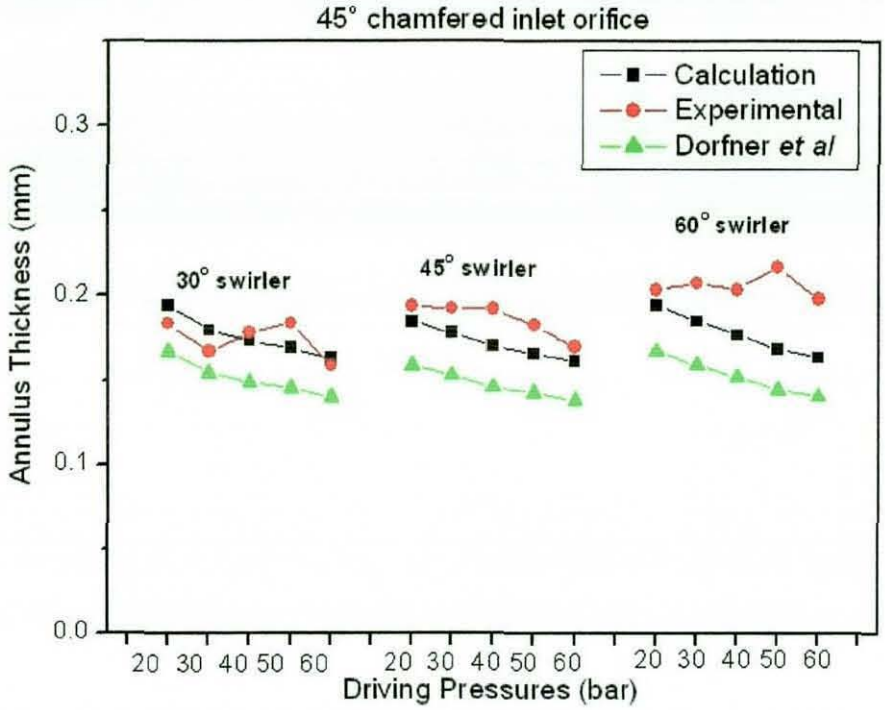

Figure 6.113 Experimental and calculated annulus thickness comparisons with a 45° chamfered inlet orifice at nozzle exit. [09]

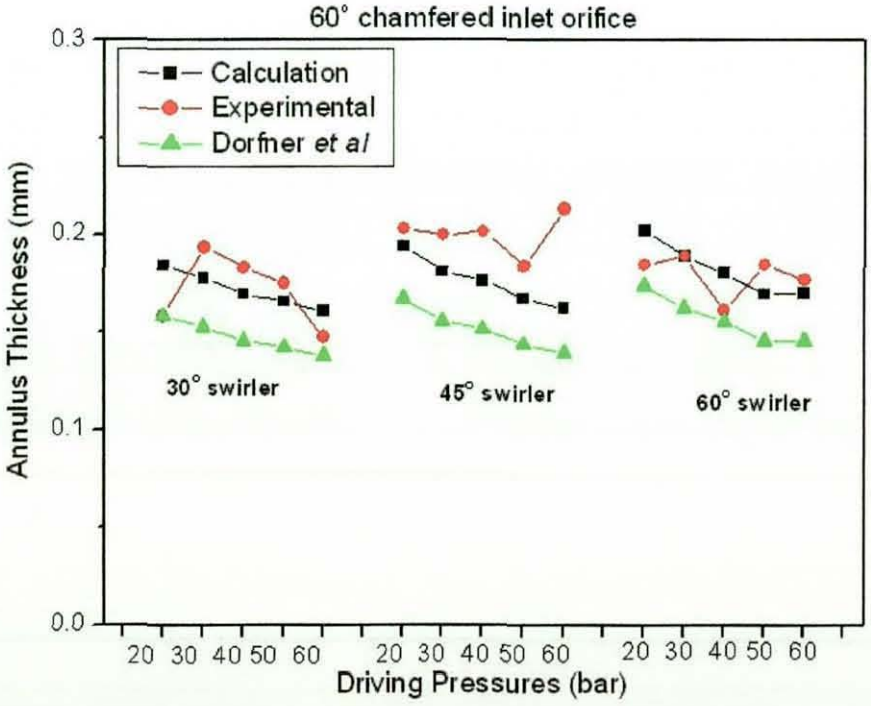

Figure 6.114 Experimental and calculated annulus thickness comparisons with a 60° chamfered inlet orifice at nozzle exit. [09]

Further comparisons can be seen in figure 6.113 and 6.114 with data being presented for the 45° and 60° chamfered inlet orifices. In a similar way to the 30° nozzle, the Dorfner *et al* [09] relationship with a 3.66 constant is lower than the experimental results and a constant of 6.0 provides better agreement.

Data for the variation in annulus thickness along the length of the injector is presented in figures 6.115, 6.116 and 6.117 for 30°, 45° and 60° swirlers, respectively. Two different types of aircore were observed in this study, tapered and uniform structure. The tapered aircore structure was seen in all the 45° chamfered inlet orifice studies, regardless of the change in swirl generators. 30° and 60° chamfered inlet orifice exhibits a more uniform aircore structure in the nozzle.

The data shows that for all configurations, the annulus thickness decreases along the nozzle. This finding is supported by the experimental work of Cooper *et al* [07] and the numerical modelling work of Shaikh *et al* [26]. However, this is in contradiction to the data provided by Gavaises *et al* [11], which showed an increase in film thickness along the nozzle. They attributed their finding to the fact that there will be frictional losses between the liquid and the wall resulting in a small decrease in flow velocity and a corresponding increase in film thickness as a result of the continuity equation. As will be shown in the next section, the velocity does not always show a decrease along the nozzle, but is a function of the nozzle and swirler geometry.

It is interesting to note the shape of the liquid annulus. There is clear evidence for all nozzle geometries of the formation of a wave-like structure in the annular flow. This is similar to that noted in the experimental work of Cooper *et al* [07]. The wave structures are a result of the radial velocity component imparted by the contraction from the reservoir into the nozzle. The flow enters the nozzle with a significant inward radial velocity causing the liquid surface to rise; decreasing the aircore and increasing film thickness. As flow progresses along the nozzle the relatively small radial momentum is redirected by the

large tangential and radial components. In this way the annulus thickness reduces along the nozzle all the way to the exit.

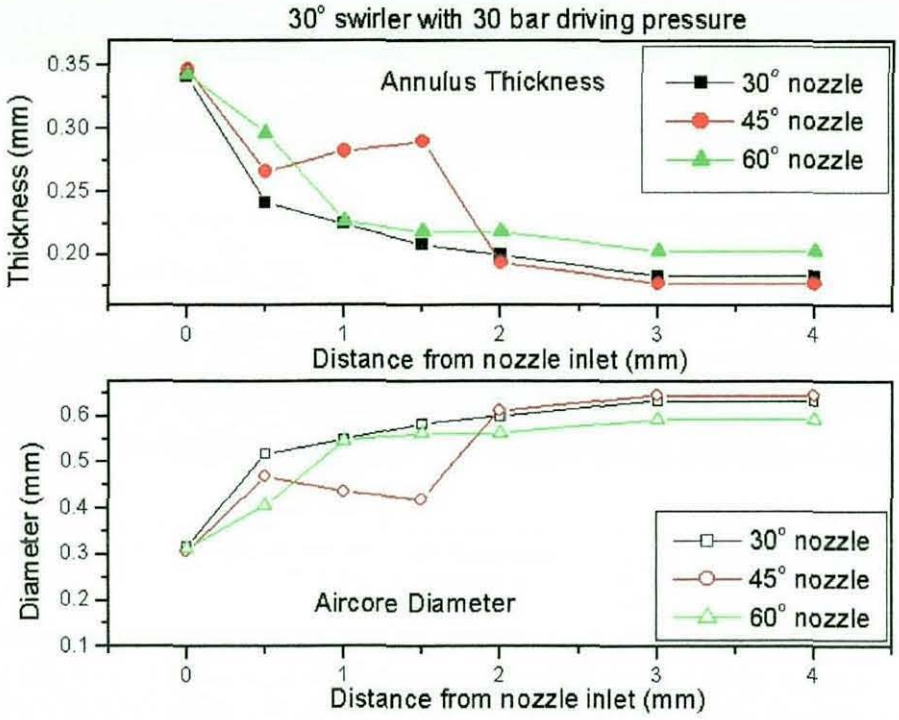

Figure 6.115 Annulus thickness and aircore diameter along 30° swirler.

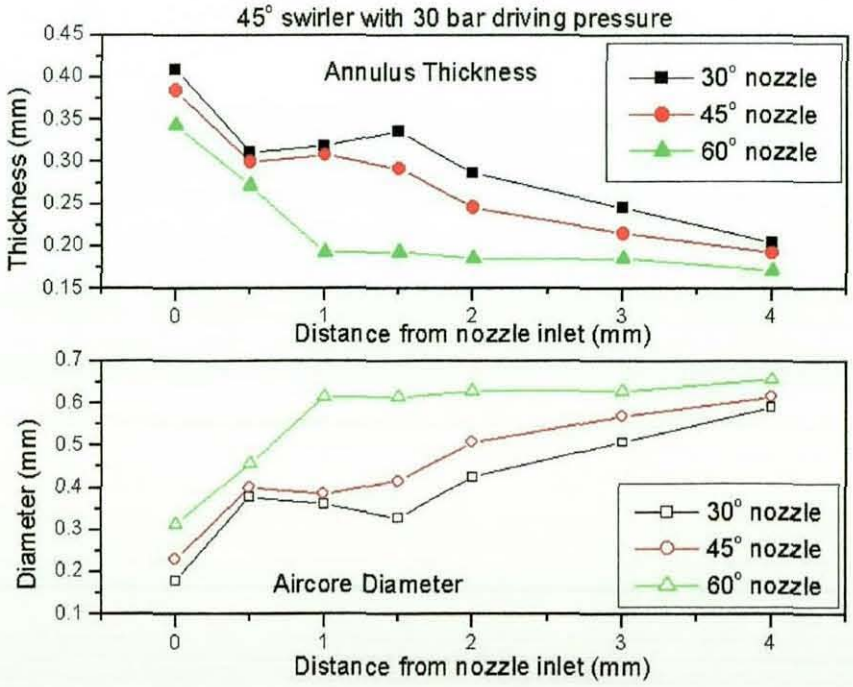

Figure 6.116 Annulus thickness and aircore diameter along 45° swirler.

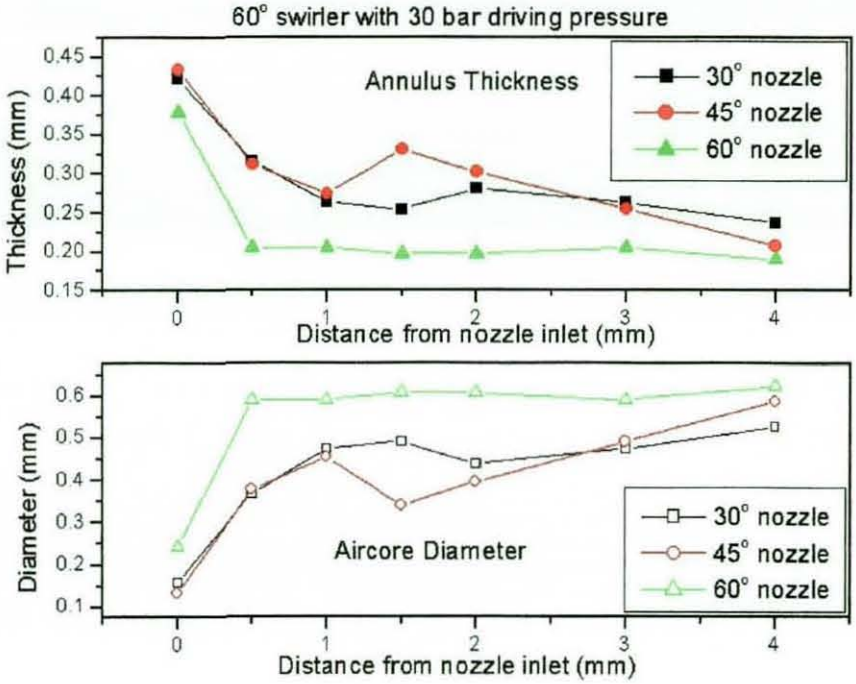

Figure 6.117 Annulus thickness and aircore diameter along a 60° swirler.

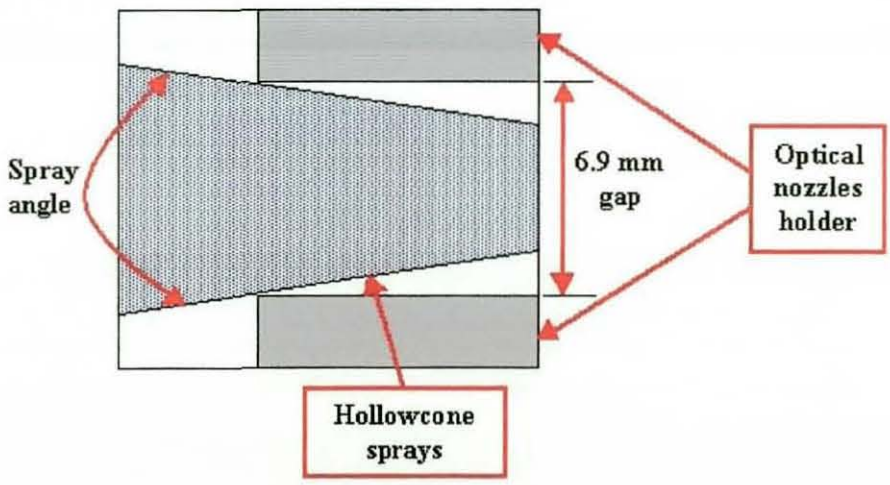

Figure 6.118 Schematic of spray angle measurement.

From the external flow images, it is possible to determine the spray angle. This allows the quantification of the effect of nozzle geometries on the hollowcone spray. Figure 6.118 shows a schematic of the measurement of spray angle from the orifice exit. The data provided in figure 6.119, shows the full spray angle for a 30 bar driving pressure. The experimentally measured swirl angle shows that the 45° swirler has the largest angle in all three

chamfered inlet orifices, with the biggest spray angle of 43° recorded with a 45° chamfered inlet orifice. The smallest spray angle recorded was for a 30° swirler with a 30° chamfered inlet orifice.

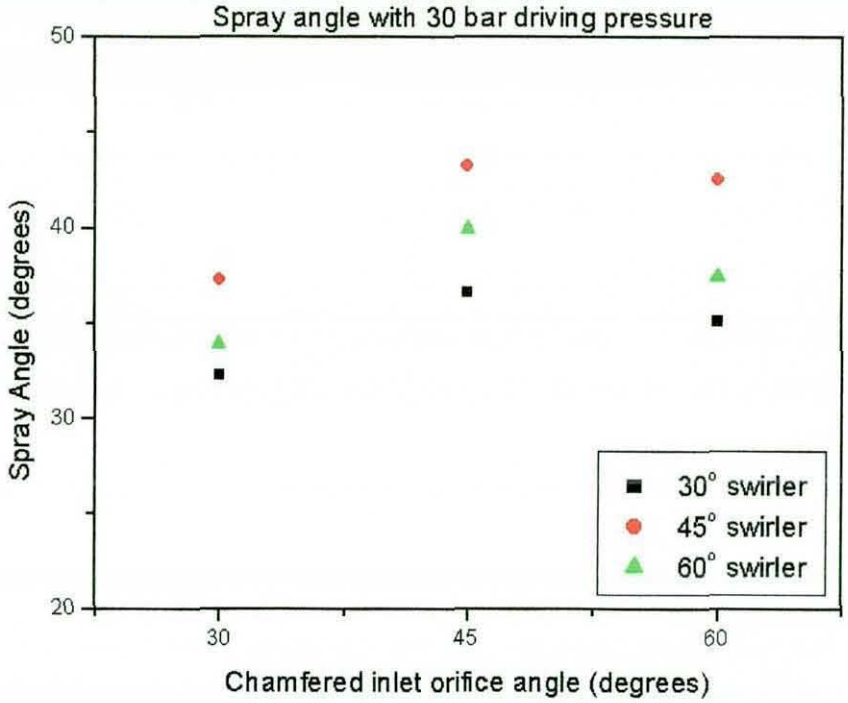

Figure 6.119 Spray angle for three swirlers and three chamfered inlet orifices at 30 bar driving pressure.

Figure 6.120 presents data for the variation with chamfer inlet orifice and swirler geometry of the spray cone angle. In this figure, the experimental data is compared with the empirical relationship provided by Ren *et al* [22, 23]:

$$Spray\ angle,\ \theta = C_{spray} \times \arctan\left(\frac{U}{V}\right) \qquad (6.2)$$

This equation relates the spray angle to the nozzle exit radial (U) and axial (V) components of velocity. The empirical constant, C_{spray}, was given by Ren *et al* [23] as 2.0. However, in the later paper (Ren *et al* [22]), after comparison with new experimental, this value was reduced to 0.79. However, in the current

work the original value for the empirical constant (C_{spray} = 2.0) was found to be in good agreement with experimental spray angles.

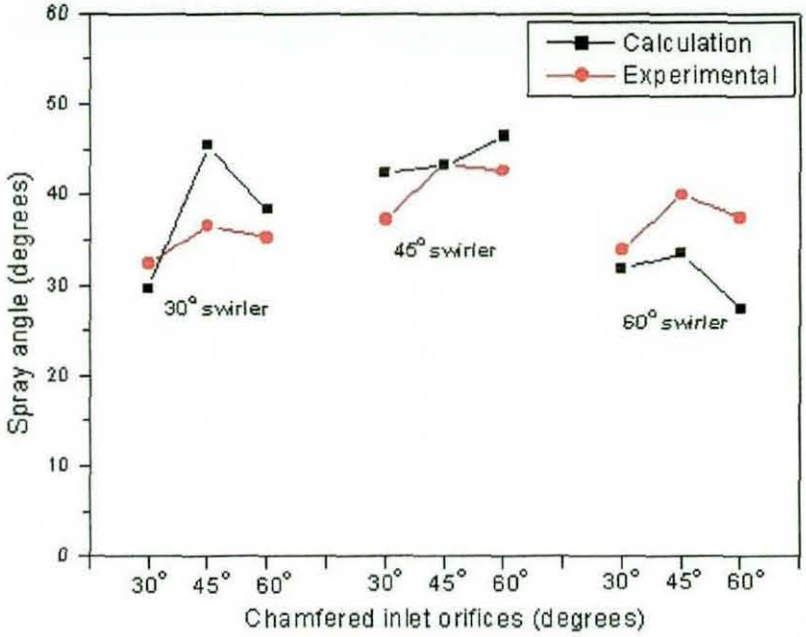

Figure 6.120 Experiment and calculation spray angle comparison. [23]

6.7.2 Fluorescent Particle Image Velocimetry

The use of FPIV to quantify the internal fluid flow of swirl atomisers provides a valuable insight into methodologies for the control of internal flow structure by variation in nozzle geometry. To further our understanding of the effects of the swirler and driving pressure on the flow, the following figures were used to provide a comparison of velocity between different orifice geometries.

Figure 6.121 shows the velocity magnitude along the centreline of a 30° chamfered inlet orifice with a 30° swirler and 20 bar driving pressure. In the convergent section of the orifice, it can be seen that the velocity increases linearly. The flow then stabilised to a constant velocity at about 1 mm into the straight section of the orifice.

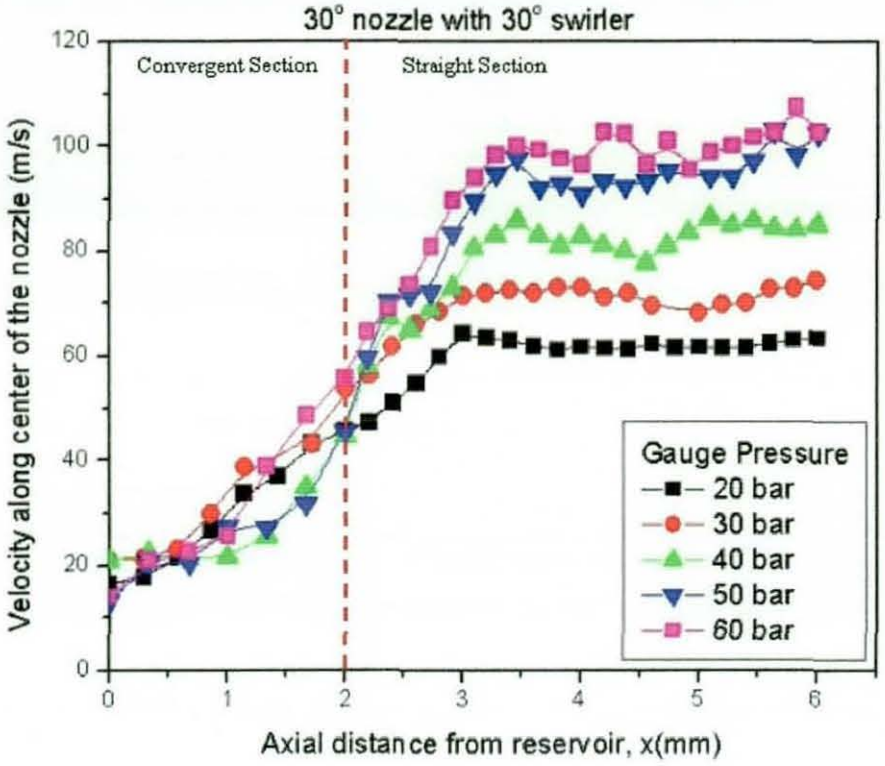

Figure 6.121 Velocity through the centreline of a 30° chamfered inlet orifice with a 30° swirler.

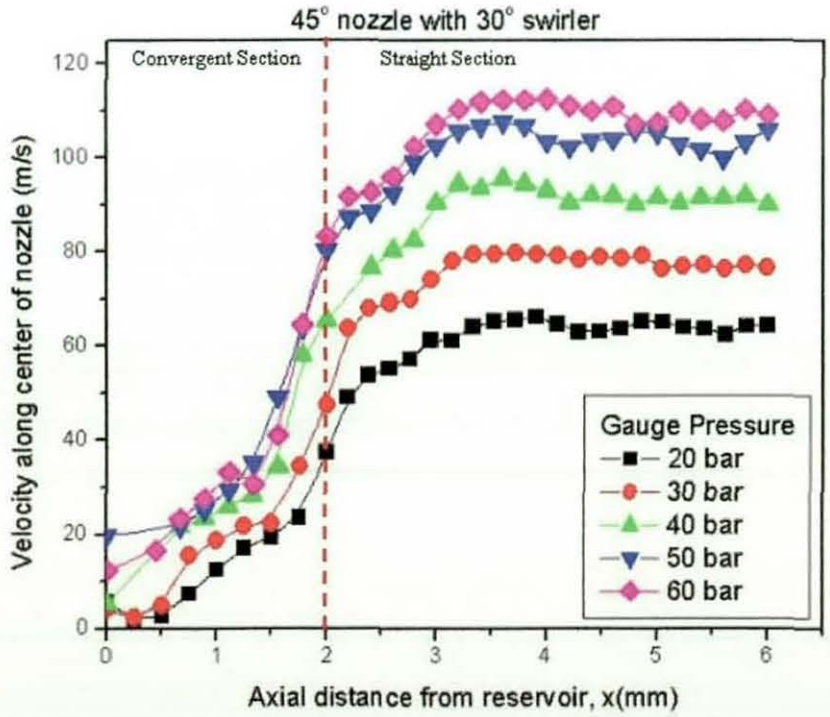

Figure 6.122 Velocity through the centreline of a 45° chamfered inlet orifice with a 30° swirler.

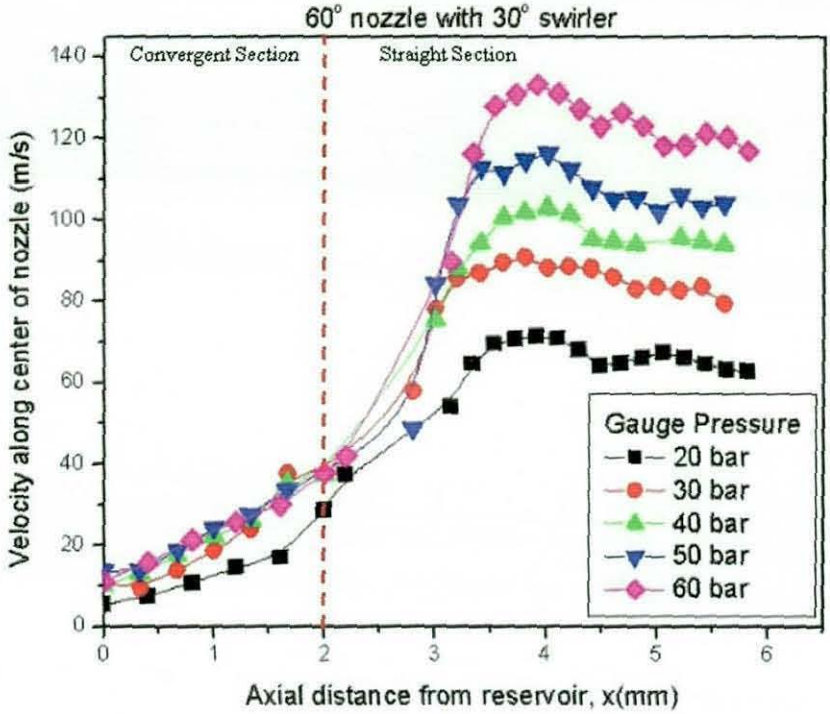

Figure 6.123 Velocity through the centreline of a 60° chamfered inlet orifice with a 30° swirler.

Figures 6.122 and 6.123 show the 30° swirl generator with 45° and 60° chamfered inlet orifice respectively. The 45° chamfered inlet orifice shows the flow velocity from the convergent section of the orifice increases steeply into the nozzle section. When the flow enters the nozzle section, the flow levels off to an almost constant velocity. The graph also shows the flow velocity in the nozzle section increases with increasing driving pressure. Figure 6.123 shows the 60° chamfered inlet orifice increases gradually in the convergent section of the orifice. The flow then suddenly surges in the nozzle section for about 1mm before levelling off to a constant velocity.

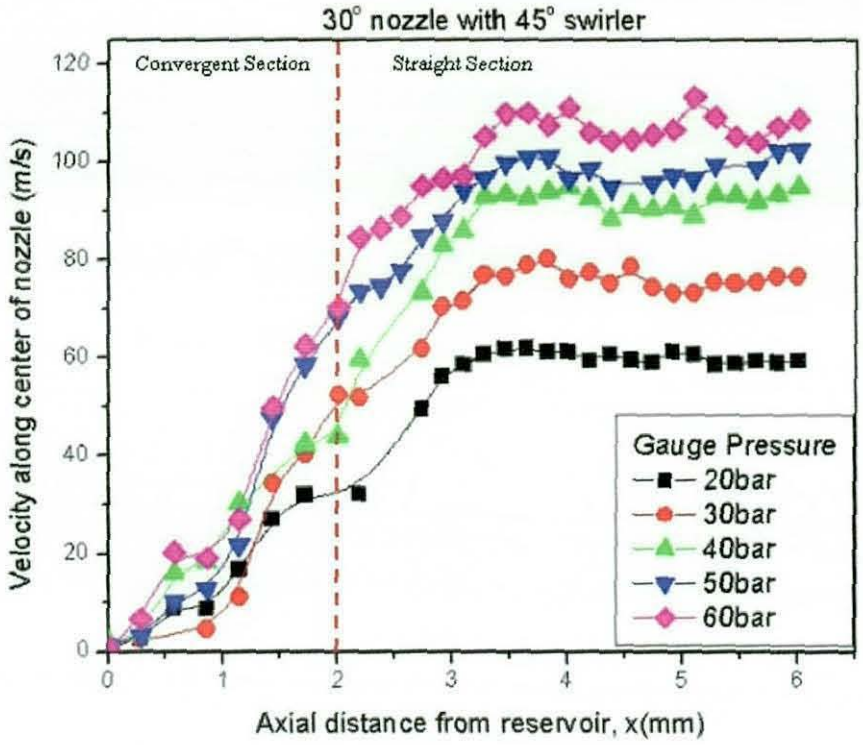

Figure 6.124 Velocity through the centreline of a 30° chamfered inlet orifice with a 45° swirler.

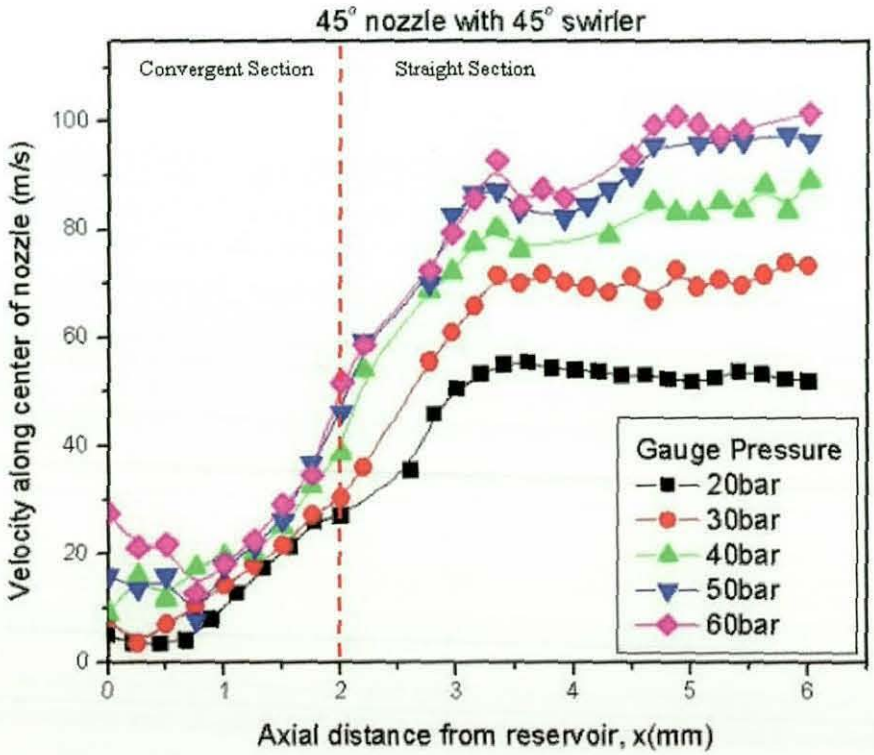

Figure 6.125 Velocity through the centreline of a 45° chamfered inlet orifice with a 45° swirler.

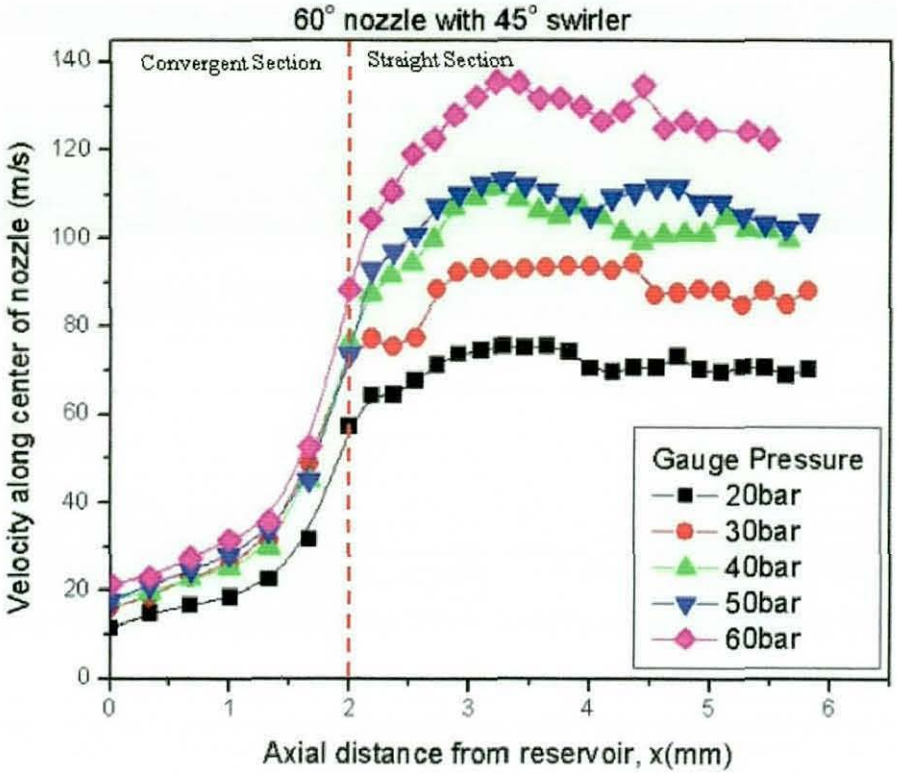

Figure 6.126 Velocity through the centreline of a 60° chamfered inlet orifice with a 45° swirler.

Figures 6.124 to 6.126 show further velocity magnitudes through the centreline of the orifices. For the 30° chamfered inlet orifice graph, it shows a steep increment in velocity in the convergent section before settle down into a constant velocity for the straight section. The flow velocity also increases with injection pressure. In the 45° chamfered inlet orifice graph shown in figure 6.125, the flow velocity shows a more gentle flow in the straight section of the nozzle. As seen in figure 6.125, the maximum velocity for this orifice is less than the 30° chamfered inlet orifice. In the case of 60° chamfered inlet orifice graph, the flow velocity started with a gradual flow before increasing sharply into the straight section of the nozzle.

Figures 6.127 to 6.129 highlight the flow velocity through the centreline of three chamfered inlet orifice with 60° swirler. The 30° chamfered inlet orifice (Figure 6.127) shows the flow velocity magnitude enters the convergent section of the orifice at about 20 m/s for all injection pressure conditions. The velocity magnitude increases gradually from the convergent section into the

straight section. Once the flow enters the nozzle section, the bulk flow velocity remains almost constant. In the 45° chamfered inlet orifice (Figure 6.128), the bulk velocity entering the convergent section of the orifice was lower than the 30° chamfered inlet orifice. However, the rise of the velocity magnitude into the nozzle section was steeper before settling down into a constant velocity magnitude. The increase in flow velocity in the 60° chamfered inlet orifice (Figure 6.129) was also similar to the 45° chamfered inlet orifice and the velocity magnitude also remains fairly constant into the straight section of the orifice. The notable difference between these two orifices was the higher velocity magnitude recorded in the 60° chamfered inlet orifice.

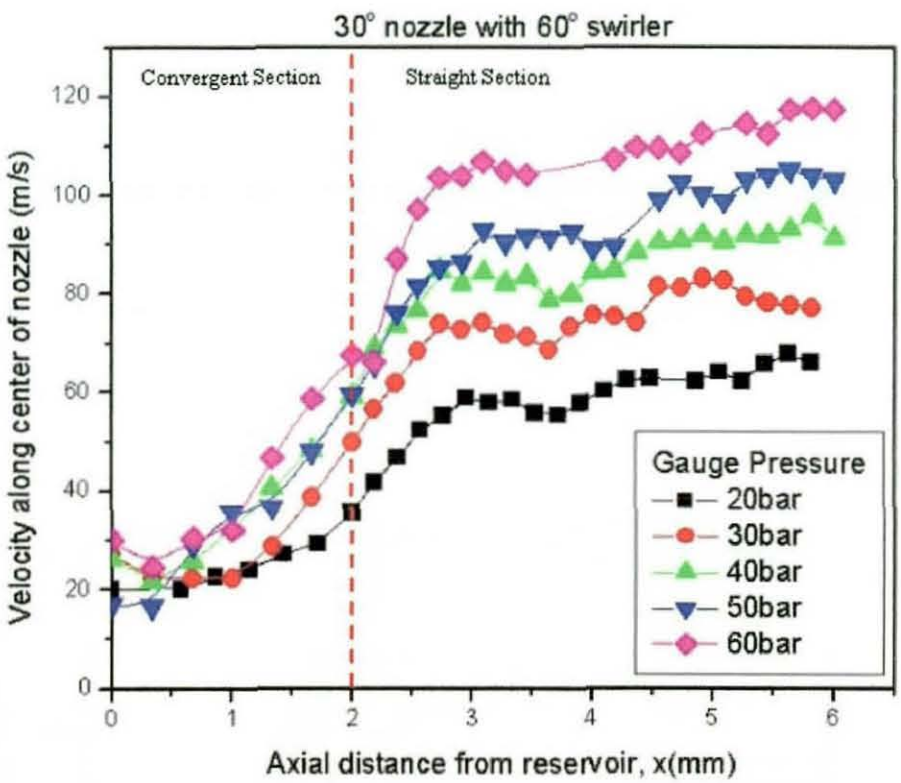

Figure 6.127 Velocity through the centreline of a 30° chamfered inlet orifice with a 60° swirler.

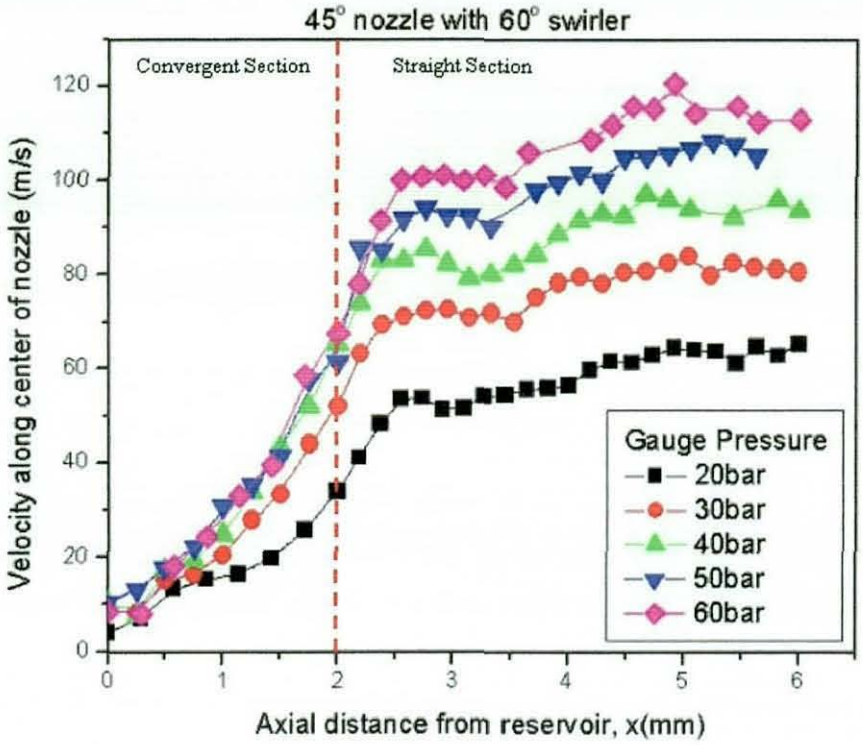

Figure 6.128 Velocity through the centreline of a 45° chamfered inlet orifice with a 60° swirler.

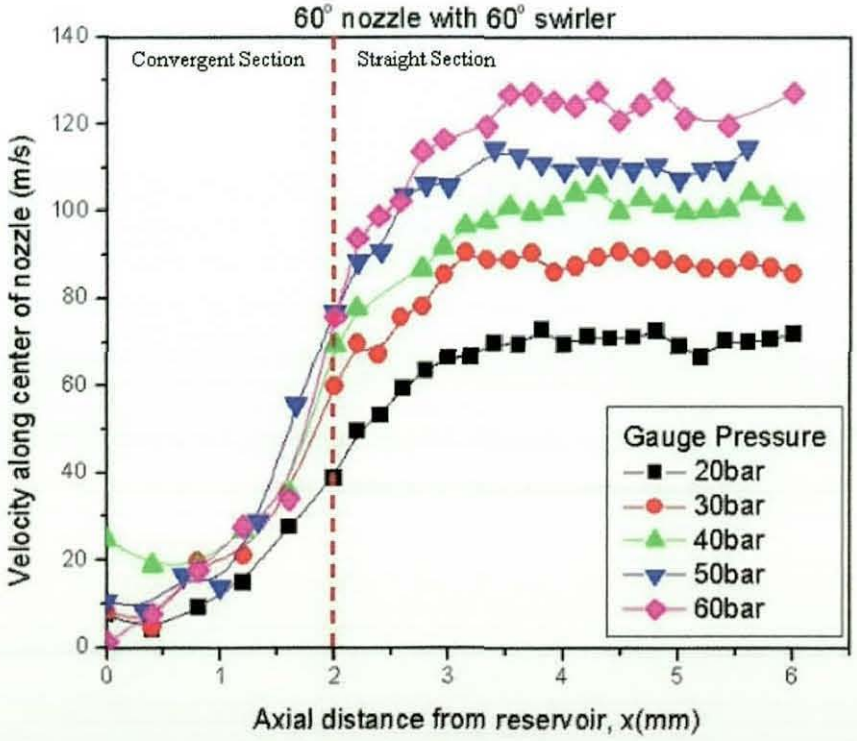

Figure 6.129 Velocity through the centreline of a 60° chamfered inlet nozzle with a 60° swirler.

Dorfner et al [09] and Chryssakis [05] provided a relationship to determine the total exit velocity. This is given by:

$$U = K_v \left(\frac{2\Delta P_l}{\rho_l} \right)^{0.5} \tag{6.3}$$

where $\dot{m}_l$ is the liquid mass flow rate, d_o is the nozzle exit diameter, μ_l and ρ_l are the liquid viscosity and density. The pressure difference across the nozzle is given as ΔP_l. K_v is the nozzle coefficient, which was defined by Lefebvre [16] as:

$$K_v = 0.00367 K^{0.29} \left(\frac{\Delta P_l \rho_l}{\mu_l} \right)^{0.2} \tag{6.4}$$

where K is the atomiser constant, $K = \dfrac{A_p}{d_o D_s}$.

A_p is the tangential inlet port, d_o is the orifice diameter and D_s is the swirl chamber diameter. For the injectors used in the current study, the A_p values are known (6 x 1 mm by 1mm ports) and d_o is known (1 mm). However, it is not clear how to define D_s. It should also be noted that the velocity coefficient K_v given by Lefebvre [16] is not dimensionally balanced [09] and is completely dependent on the actual nozzle geometry. Thus, following the methodology of Lefebvre [16], it was not possible to satisfactorily define the atomiser constant, K, for the current injector geometries.

So, for the data presented in figures 6.130 to 6.132, a best fit of equation 6.3 to the experimental data was defined by varying the value of K in equation 6.4. The K values used to provide the best fit are given in Table 6.2.

Figures 6.130 to 6.132 show the experimental and calculated exit velocities for three different chamfered inlet orifices. With the above K values, the

calculated exit velocities matched those of the experimental results. All the figures show linear trend in exit velocities with increasing driving pressure. From this study, the K and K_v values will provide a useful reference for future study of the same orifice configurations.

	30° orifice	45° orifice	60° orifice
30° swirler	1.67	2.00	1.67
45° swirler	2.00	1.67	2.14
60° swirler	2.14	2.14	2.73

Table 6.1 K values for each swirler and nozzle configurations.

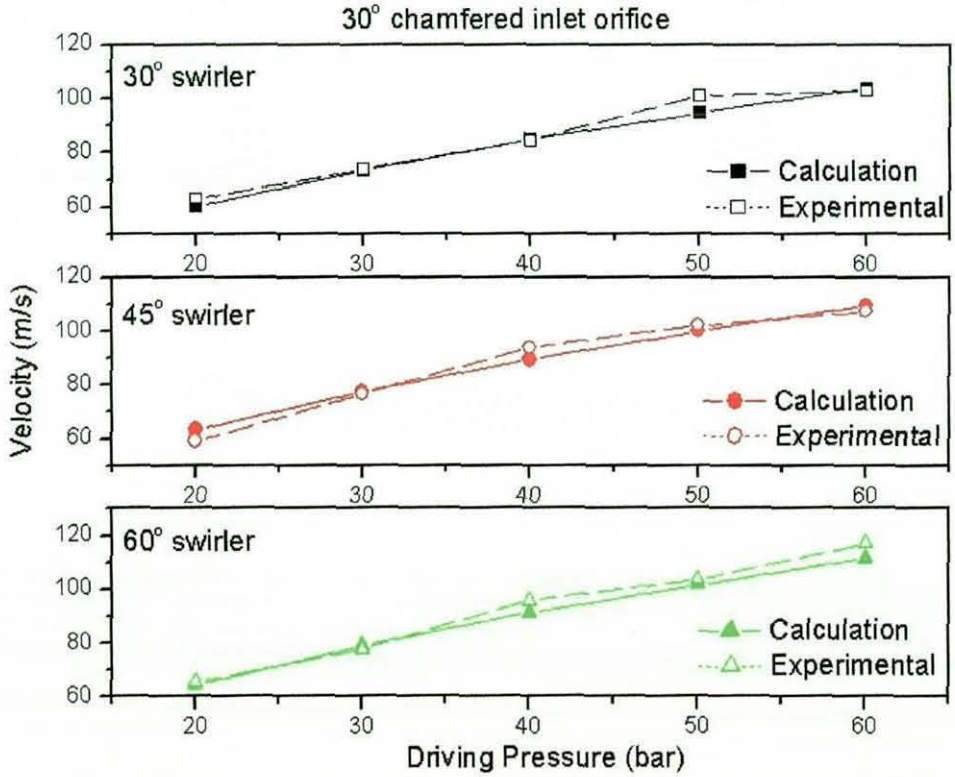

Figure 6.130 Exit velocities for a 30° chamfered inlet orifice. [09]

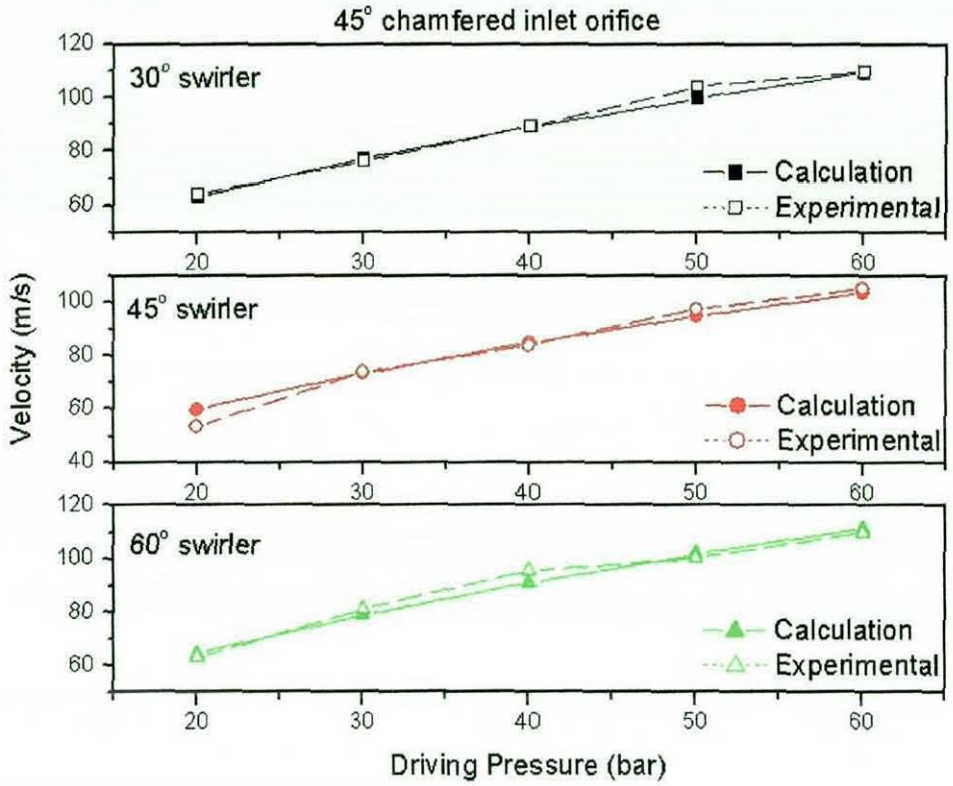

Figure 6.131 Exit velocities for a 45° chamfered inlet orifice. [09]

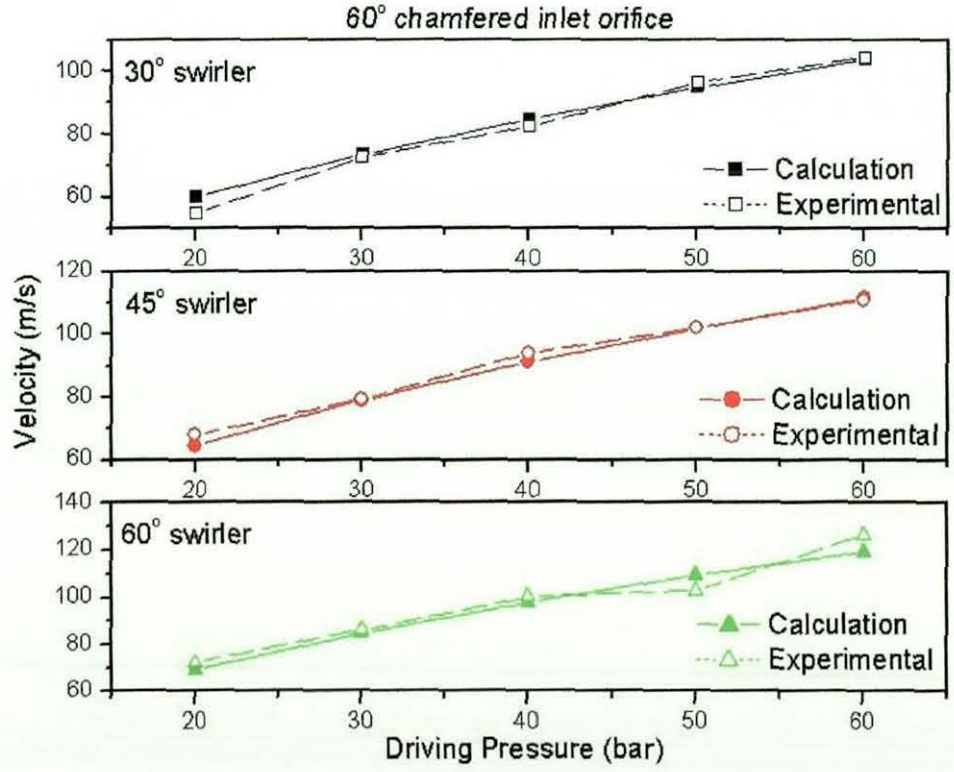

Figure 6.132 Exit velocities for a 60° chamfered inlet orifice. [09]

Figure 6.130 highlights the maximum velocity for different swirlers with a 30° chamfered inlet orifice and the plots displayed almost linear trend. The 60° chamfered inlet orifice exhibits a higher peak velocity at about 135 m/s compared with a 30° and 45° chamfered inlet orifice at 105 m/s and 100 m/s respectively. This high peak velocity magnitude by the 60° chamfered inlet orifice was also observed with 30° and 45° swirl generators in figure 6.132. The results in this study are in good agreement with Allen and Hargrave [02] using a chamfered inlet orifice with a commercial GDI swirl generator.

6.7.3 Phase Doppler Anemometry

PDA study results were presented and the data trend varies under different driving pressure conditions. However, some obvious trends still present in the hollowcone spray study. The hollowcone spray generated in this study appears to have the same spray angle as seen in the high-speed flow visualisation for all conditions. This can be seen by the spray periphery recorded in almost all the PDA study. Although the SMD sizes for the three swirlers and chamfered inlet orifices varies directly under the orifice exit, all the data shows that lower driving pressure produced the largest droplet size at the peripherals of the spray. 20 bar driving pressure have an averaged SMD size of about 50 μm as compared to 30 μm for 60 bar driving pressure.

SMD size can be quantified by comparing the experimental results with calculated results and literature papers. Ren *et al* [22 and 23] provided a relationship for calculating Sauter mean diameter from his model. Ren equation for SMD is given by:

$$SMD = C_{SMD}\left\{\frac{24\pi\sigma^2 h^*}{\rho_a^2 V^2 W^2}\right\}^{1/3} \qquad (6.5)$$

W is the radial velocity, V is the axial velocity, σ is the liquid surface tension (25×10^{-3} N/m), ρ_g is density of gas, λ is the wavelength of dominant wave, h^* is

the sheet thickness at break-up location and C_{SMD} was given by Ren *et al* [22] as 0.63. The sheet thickness at break-up location, h^*, is given by:

$$h^* = \frac{(r_o + r_{ac})h}{r_o + r_{ac} + 2L\sin\theta} \tag{6.6}$$

where h is the sheet thickness, r_{ac} is radius of aircore, r_o is radius of orifice and θ is the spray angle. L is the break-up length and this can be define by:

$$L = C_L\left(\frac{\rho_l h\cos\theta}{\rho_a^2 V_r^2}\right)^{1/2} \tag{6.7}$$

ρ_l is the density of the liquid. The constant C_L is given as 1.7.

Figures 6.136 to 6.138 shows the variation in Sauter mean diameter with driving pressure for three different chamfered inlet orifices. Each plot shows the particle sizes for experimental and the calculated SMD using the Ren equation (equation 6.5) with the constant C_{SMD} = 0.63. It can be seen that the Ren equation over-predicts the Sauter mean diameter for the current data for all geometries. Included in the figures are calculated SMD for a modified Ren equation where the constant C_{SMD} was changed to provide a best fit to the experimental data. The modified equation C_{SMD} values are presented in Table 6.2. It can be seen that a constant of C_{SMD} = 0.4 provide a good fit for the 30° and 45° chamfer inlet orifices, but for the 60° nozzles the constant is dependent on the inlet swirl angle. These values provide a new calculated SMD that fits the experimental data better than Ren *et al* [22]. Most of the plots show a slight decrease in experimental SMD sizes with increasing pressure.

	30° orifice	45° orifice	60° orifice
30° swirler	0.4	0.4	0.33
45° swirler	0.4	0.4	0.45
60° swirler	0.4	0.4	0.35

Table 6.2 Coefficient C_{SMD} values for each swirler and nozzle configurations.

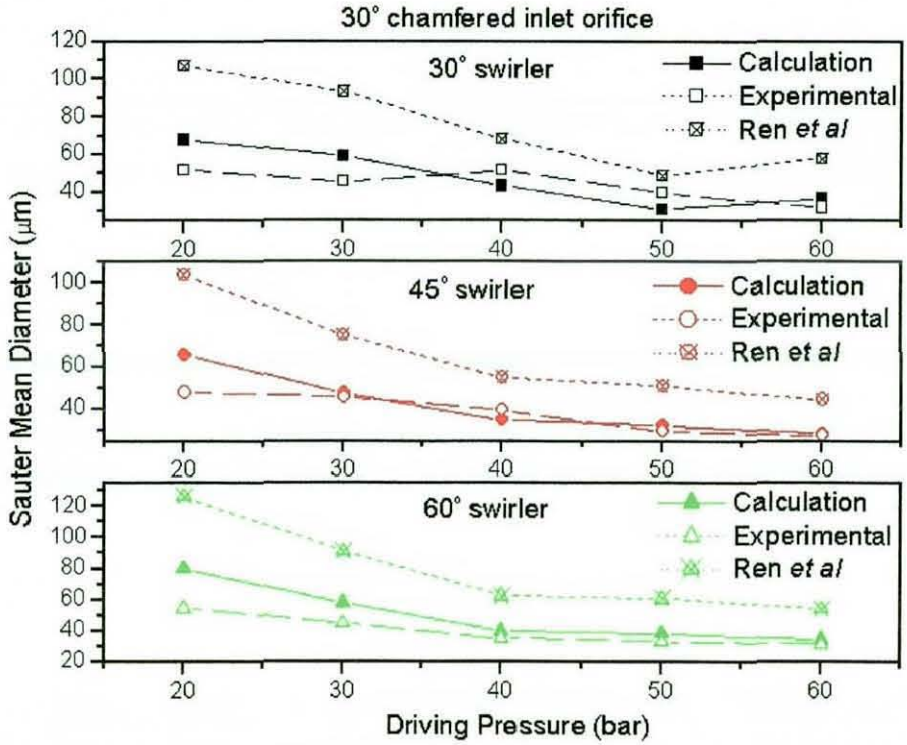

Figure 6.136 Sauter Mean Diameter comparisons for a 30° chamfered orifice with Ren *et al.* [22]

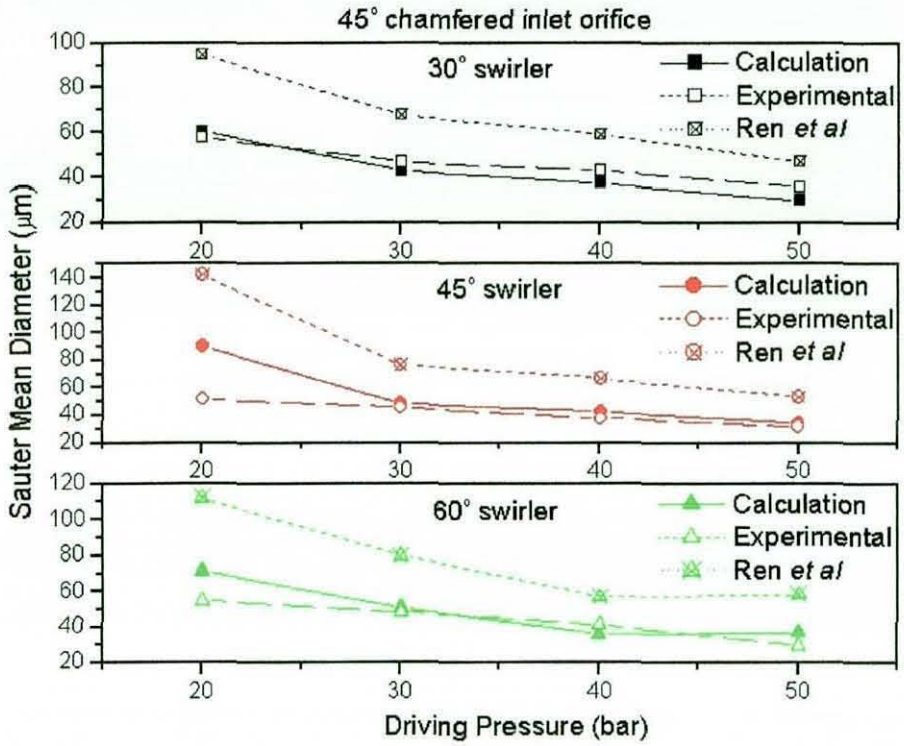

Figure 6.137 Sauter Mean Diameter comparisons for a 45° chamfered orifice with Ren *et al.* [22]

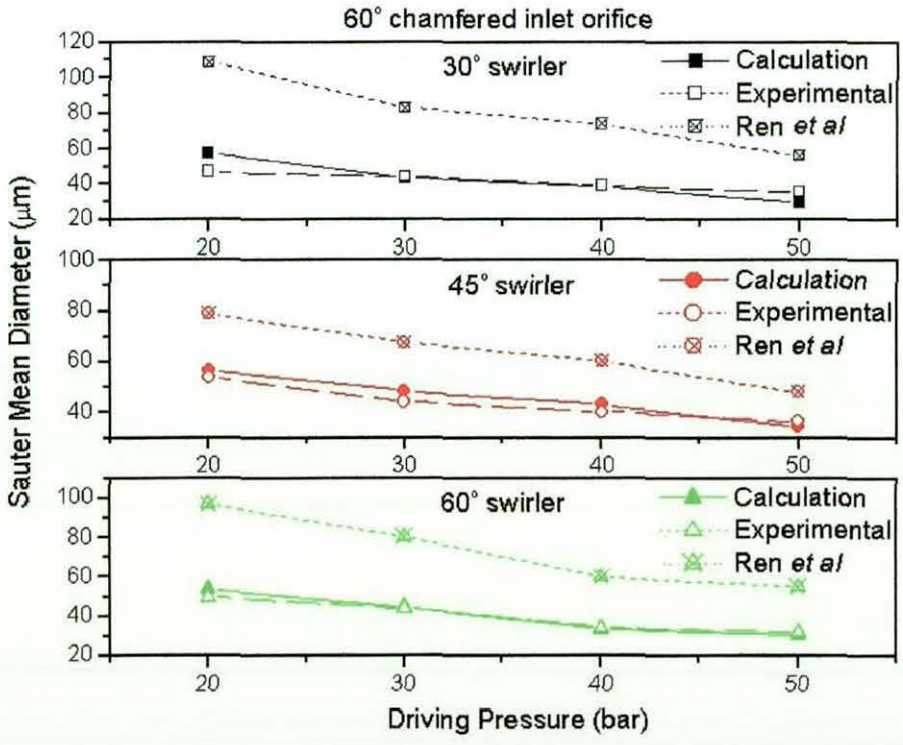

Figure 6.138 Sauter Mean Diameter comparisons for a 60° chamfered orifice with Ren *et al.* [22]

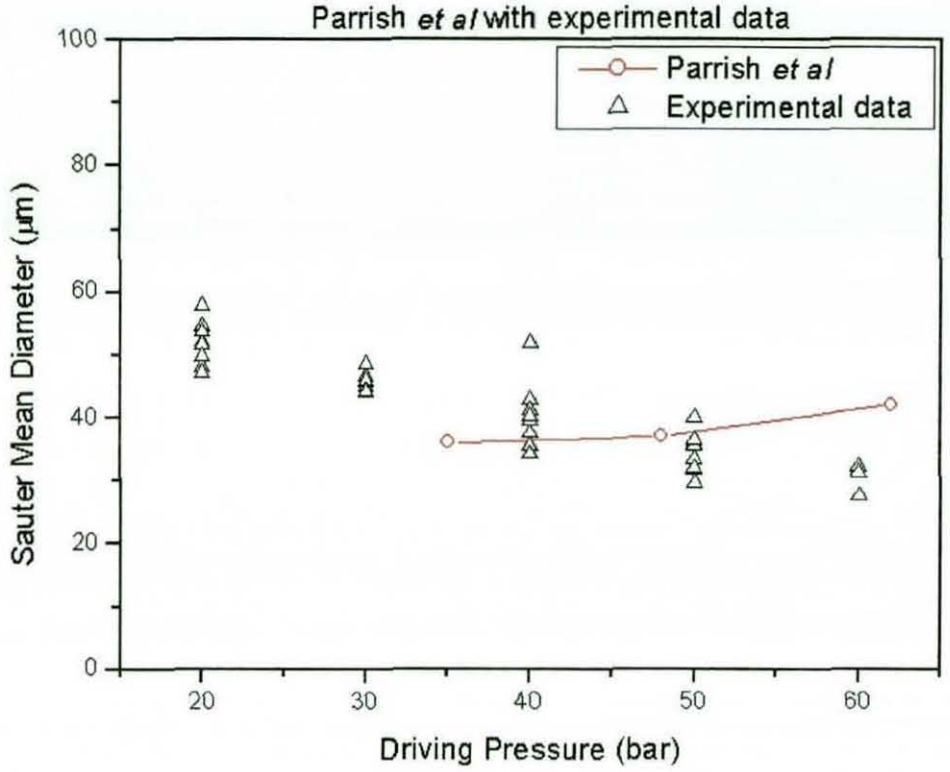

Figure 6.139 Parrish data comparison with experimental results. [19]

Comparison of the current data with that of Parrish *et al* [19] is provided in figure 6.139. The figure shows the variation of Sauter mean diameter with driving pressure. It can be seen that the data provided by Parrish *et al* [19] also shows similar SMD sizes for driving pressure ranging from 30 to 50 bar. However, their data shows a slight increase in SMD sizes with driving pressure compared with the decrease noted in the current experimental data.

6.8 SUMMARY

The study of non-swirl flow gave an insight into the flow characteristics through three different chamfered inlet orifices with different driving pressures. It was shown that with sharp-edged inlets that cavitation develops rapidly and completely controls the flow development. It was also shown that even for chamfered inlet nozzles that tiny imperfections in the nozzle surface finish can lead to severe cavitation. However cavitation was eliminated by careful polishing of the nozzle to remove any surface perturbations facilitating the use of FPIV to quantify the internal flow. The flow for non-swirl chamfered inlet orifices showed a linear variation in velocity with increase driving pressure.

The incorporation of three different swirl generators to the chamfered inlet orifices allowed further investigation on the flow behaviour. The initial study involved the use of high-speed flow visualisation to study the in-nozzle flow characteristics. Two different types of aircore were observed in this study, tapered and uniform structure. The tapered aircore structure was seen in all the 45° chamfered inlet orifice studies, regardless of the change in swirl generators. 30° and 60° chamfered inlet orifice exhibits a more uniform aircore structure in the nozzle. Comparing aircore diameter and liquid annulus, both 30° and 45° chamfered inlet orifice showed an increase in liquid annulus thickness with increasing swirl angle, and a corresponding decrease for aircore diameter. However, for the 60° chamfered inlet orifice a maximum annulus thickness was seen for the 45° swirl angle.

The Fluorescent Particle Image Velocimetry (FPIV) provided further information about the flow structure for the three chamfered inlet orifices and swirl generators. The results clearly showed that the flow through the 1mm nozzle section of the orifice increases with increasing driving pressure. This was also the case under same swirl generator and driving pressure, with flow velocity increasing with chamfered inlet orifice angle. The maximum velocity for each swirl and orifice conditions increased almost linearly with increasing driving pressure.

Phase Doppler Anemometry (PDA) highlighted the droplet sizes and external flow velocity. The investigation of the internal flow to the external flow provides valuable analysis of different geometry changes. The SMD size decreases at the hollowcone spray periphery with increasing driving pressure.

This study provides quantitative and qualitative results to provide further understanding of both non-swirl and swirl flow. The non-swirl data will provide validation of CFD model which will be presented in appendix C.

6.9 REFERENCES

[01] Allen, J., Hargrave, G.K., *Fundamental Study of In-nozzle fluid flow and it effect on liquid jet breakup in Gasoline Direct Injectors*, 16th ILASS, Darmstadt, Germany, 2000.

[02] Allen, J. and Hargrave, G. K., *Investigation of internal fluid flow in real sized pressure swirl gasoline direct injectors.* ImechE Conference Transactions Fuel Injection systems, Page 83-94, London, UK, 26-27th November 2002

[03] Allen, J, Heath, J., Hargrave, G.K., Wigley, G., *Comparison of the Spray Characteristics of Alternative GDI Fuel Injection Systems Under Atmospheric and Elevated Pressure Operation*, 15th International Combustion Engine Symposium, 9935086, Seoul (South Korea), July 1999, ISBN 4-915219-25-9

[04] Chigier, N., *Energy, Combustion, and Environment*, McGraw-Hill Series in Energy, Combustion, and Environment, McGraw-Hill Book company, 1981, ISBN 0-07-010766-1

[05] Chryssakis, C.A., *Modelling Gasoline Sprays Emerging from High-pressure Swirl Injectors for DISI engines*, Master Thesis, University of Michigan, August 2002

[06] Chryssakis, C.A., Assanis, D.N., Lee, J.K., Nishida, K., *Fuel Spray Simulation of High-Pressure Swirl Injector for DISI Engines and Comparison with Laser Diagnostic Measurements*, SAE 2003-01-0007, 2003

[07] Cooper, D., Yule, A.J., *Waves on the Aircore/Liquid Interface of a Pressure Swirl Atomiser*, ILASS-Europe, Zurich (Switzerland), September 2001

[08] Cousin, J., Ren, W.M., Nally, S., *Recent Developments in Simulations of Internal Flows in High Pressure Swirl Injectors*, Page 227-231, Oil & Gas Science and Technology, Vol. 54, No.2, 1999

[09] Dorfner, V., Domnick, J., Durst, F., Köhler, R., *Viscosity and Surface Tension Effects in Pressure Swirl Atomization*, Atomization and Sprays Journal, Volume 5, No.3, pp 261-285, 1995

[10] Ferguson, C.R., *Internal Combustion Engines*; Applied Thermosciences, John Wiley & Sons, 2001, ISBN 0471356174

[11] Gavaises, M., Abo-serie, E., Arcoumanis, C., *Nozzle Hole Film Formation and its link to Spray Characteristics in Swirl-Pressure Atomizers for Direct Injection Gasoline Engines*, SAE 2002-02-1136, SP-1693, 2002

[12] Heywood, J.B., *Internal Combustion Engine Fundamentals,* McGraw-Hill Book Company, 1988, ISBN 0-07-100499-8

[13] Huang, Z., Shao, Y.M., Shiga, S., Nakamura, H., Karasawa, T., *The role of orifice flow pattern in fuel atomization*, Paper I-12, ICLASS, Rouen (France), July 1994

[14] Iwamoto, Y., Noma, K., Nakayama, O., Yamauchi, T., Ando, H., *Development of Gasoline Direct Injection Engine*, SAE 970541, 1997

[15] Karl, G., Kemmler, R., Bargende, M., Abthoff, J., *Analysis of a Direct Injected Gasoline Engine*, SAE 970624, 1997

[16] Lefebvre, A.H., *Atomization and Sprays*, Combustion: An International Series, Hemisphere Publishing Corporation, 1989, ISBN 0-89116-603-3.

[17] Munson, B.R., Young, D.F., Okiishi, T.H., *Fundamentals of Fluid Mechanics*, John Wiley & Sons Inc, 1998, ISBN 0-471-17024-0

[18] Ohrn, T.R., Senser, D.W., Lefebvre, A.H., *Geometrical effects on discharge coefficicents for plain-orifice atomisers*, Atomization and Sprays Journal, Volume 1, No.2, pp 137-153, 1991

[19] Parrish, S.E., Farrell, P.V., *Transient Spray Characteristics of a Direct-Injection Spark-Ignited Fuel Injector*, SAE 970629, 1997

[20] Ramamurthi, K., Nandakumar, K., *Effect of injector orifice configurations on atomization*, Paper III-2, ICLASS, Rouen (France), July 1994

[21] Ramamurthi, K., Patnaik, S.R., *Influence of periodic disturbances on inception of cavitation in sharp-edged orifices*, Experiments in Fluids Journal, Volume 33, pp 720-727, 2002

[22] Ren, W.M., Nally Jr, J.F., *Computations of Hollow-Cone Sprays From A Pressure-Swirl Injector*, SAE 982610, 1998

[23] Ren, W.M., Shen, J., Nally Jr, J.F., *Geometrical Effects Flow Characteristics of a Gasoline High Pressure Swirl Injector*, SAE 971641, SP-1279, 1997

[24] Schmidt, D.P., Corradini, M.L., *Analytical prediction of the exit flow of cavitating orifices*, Atomization and Sprays Journal, Volume 17, No.6, 1997

[25] Schmidt, D.P., Corradini, M.L., *One-dimensional analysis of cavitating orifices*, 9th ILASS, San Francisco (USA), 1996

[26] Shaikh, S., Banaszak, U., Von Lavante, E., Cooper, D., Yule, A.J., *CFD prediction of the Effects of Viscosity on the Internal Flow of a Scale*

Pressure-swirl Atomiser, 19th ILASS-Europe, Nottingham (United Kingdom), 6-8 September 2004

[27] Spicher, U., Reissing, J., Kech, J.M., Gindele, J., *Gasoline Direct Injection (GDI) Engines - Development Potentialities*, SAE 1999-01-2938, SP-1469, 1999

[28] Tamaki, N., Nishida, K., Hiroyasu, H., *Promotion of the atomisation of a liquid jet by cavitation in a nozzle hole*, ILASS-Europe, Manchester (UK), July 1998

[29] Tamaki, N., Shimizu, M., Hiroyasu, H., *Enhanced Atomisation of a liquid jet by cavitation in a nozzle hole*, 8th ICLASS, Pasadena (USA), July 2000

[30] Tamaki, N., Shimizu, M., Hiroyasu, H., *Atomisation of super-high injection pressure liquid jet*, ILASS-Europe, Zurich (Switzerland), September 2001

[31] TSI Incorporated, *Insight: Particle Image Velocimetry Software*, version 3.3, Dec 2000, P/N 1990010

CHAPTER 7

CONCLUSIONS

7.1 OVERVIEW

This thesis has presented the results from experimental investigations to quantify the internal and external flow fields of both Diesel and gasoline injectors.

The Diesel injector study consisted of the application of high-speed, laser-illuminated flow visualisation to study the effect of injector geometry on the internal flow field and the near-field external spray structure. A series of real-sized, optically accessible sapphire Diesel injectors, capable of operating at realistic driving pressures, were constructed. These consist of a sac reservoir, microhole nozzle and external counterbore, with a total of 32 different configurations. The internal flow study was concerned with understanding the effect of different microhole nozzle geometries on the flow characteristics. The external flow investigated the effect of different counterbore geometries on the spray structure.

The gasoline study characterised the internal and external flow field of both non-swirl and swirl flow orifices. The non-swirl study used high-speed flow visualisation to observe the internal flow structure leading into a sharp inlet nozzle and three different chamfered orifices. This technique was also used to observe the spray exiting these nozzles. Fluorescent particle image velocimetry (FPIV) was then used to quantify the internal flow velocity of the chamfered inlet orifices and the data was used to validate CFD models.

The experimental investigation for high-press swirl injectors consisted of flow visualisation, fluorescent particle image velocimetry and phase Doppler anemometry. The internal flow regimes studies consisted of three chamfered inlet orifices and three swirl generators. These flow regimes were quantified

by flow visualisation and fluorescent particle image velocimetry. The external flow regimes were visualised using by high-speed flow visualisation and phase Doppler anemometry was used to quantify the droplets size and velocity.

The main findings of the Diesel and gasoline studies are summarised in the following sections. A final section has been devoted to continuation work in the future.

7.2 DIESEL INJECTION STUDY

The characterisation of Diesel injector flow was achieved by the use of a novel, optically accessible sapphire nozzle rig providing injector flow imaging at pressures up to 1750 bar through orifice nozzles of 0.15 mm and 0.3 mm diameter. The findings for the Diesel study can be summarised as follows:

(a) Cavitation is a predominant phenomenon in sharp inlet nozzles. This cavitation was observed in some of the initial few microholes but it was removed after repetitive fuel injections.

(b) The current study operating with driving pressures in excess of 1000 bar showed that cavitation at such high pressures is minimal or non-existent.

(c) Different microhole nozzles diameters and inlet radius did not have a significant affect on the observed internal flow and external spray structure.

(d) Both 0.15 mm and 0.3 mm diameter microhole nozzles had little effect on the spray angle under atmospheric charge back pressure condition and with no counterbore attached.

(e) The interaction of the counterbore increases with higher driving pressure, but close observation of the spray structure exiting the counterbore showed no changes on spray angle and atomisation.

(f) A graphical comparison of the variation of spray angle with density ratio shows that both 0.15 and 0.3 mm microhole nozzles, with driving pressure of 1050 bar and without counterbore, agrees well with the empirical relation provided by Heywood [05].

(g) A 0.3 mm diameter microhole nozzle without counterbore had a higher spray angle then with counterbore at the same driving pressure and charge air back pressure. At operating pressure of 1050 bar, density ratio of 140, the microhole nozzle without counterbore has a spray angle of 38° compared with 15° when a counterbore was inserted.

(h) Both 0.15 and 0.3 mm diameter microhole nozzles (without counterbore) shows good comparison with Chaves *et al* [01] data for all charge air back pressure conditions.

(i) The study showed that operating an injector with a counterbore provides a methodology for controlling spray angle.

7.3 GASOLINE DIRECT INJECTION STUDY

The aim of the gasoline injector study was to develop and apply innovative measurement techniques to provide data to link the internal flow structure to the external spray development. The study has provided high quality data to improve our understanding of the internal flow structure of GDI injectors. This will help to develop a system for engineers and scientists to conduct a comprehensive investigation of injectors that will provide qualitative and quantitative data for future engine development.

To aid the study a series of real-sized (1 mm diameter) optical nozzles were designed and manufactured. The nozzles were operated in both non-swirl and

swirl mode and with sharp-edged and chamfered nozzle inlets of 30°, 45° and 60°. Non-intrusive optical diagnostics were applied to quantify flow structure (aircore diameter and annulus film thickness), internal and external flow velocities and spray droplet sizes. The findings can be summarised as follows:

NON-SWIRL INJECTORS

(a) Optical orifices manufactured from fused silica were able to withstand the real injector driving pressures (up to 70 bar) and high quality data of internal flow velocity was measured using FPIV.

(b) Cavitation was seen in sharp inlet nozzles under all driving pressure condition. The cavitation developed into hydraulic flip effect when the flow falls below the vapour pressure.

(c) The study of non-swirl flow injectors gave an insight into the flow characteristics through three different chamfered inlet orifices with different driving pressures. It was shown that with sharp-edged inlets that cavitation develops rapidly and completely controls the flow development. It was also shown that even for chamfered inlet nozzles that tiny imperfections in the nozzle surface finish can lead to severe cavitation.

(d) For all chamfered inlet nozzles (30°, 45° and 60°), the FPIV data showed that the total velocity increased linearly with driving pressure. This trend was shown to agree well with data provided in literature.

SWIRL INJECTORS

(a) It was observed that in high-pressure swirl injectors, as the swirling liquid flows through the nozzle and exits the orifice, a vortex is formed which draws air into the centre of the nozzle. This generates an aircore which grows against the outflow until it connects with the pintle, forcing the liquid into a thin annular region on the nozzle wall. Two different types of aircore were observed from this study;

(i) Tapered aircore structures were seen in all the 30° and 45° chamfered inlet orifice studies, regardless of the change in swirl generators.

(ii) Parallel aircores were seen for the 60° chamfered inlet orifices.

(b) Evidence was found for the formation of a wave-like structure in the annular flow of the swirl injectors as a result of the radial velocity component imparted by the contraction from the reservoir into the nozzle. The flow entered the nozzle with a significant inward radial velocity causing the liquid surface to rise; locally decreasing the aircore width and increasing film thickness

(c) Annular film thickness ranging from 180 μm to 200 μm were measured. The film thickness was dependent of driving pressure and nozzle geometry. The annulus film thickness showed good agreement with Dorfner *et al* [02] empirical equation.

(d) For all chamfered inlet orifices the 45° swirler produced the highest spray angle. Measured spray angles ranged from 32° to 44° and were dependent on the injector geometry.

(e) Fluorescent particle image velocimetry (FPIV) was used to provide high quality data for the internal flow field for the full range of injector geometries studied.

(f) The data was compared with a semi-empirical relationship provided by Dorfner *et al* [02] and empirical constants modified to fit the current experimental results.

(g) For all injectors studied, phase Doppler anemometry (PDA) was used to provide profiles of particle size in the external spray.

(h) Particle SMD was compared with semi-empirical relationships provided by Ren *et al* [06, 07] and empirical constants tuned to the current data. The data was also compared with particle size result available in literature and good agreement was obtained.

7.4 OBJECTIVES REALISED

Two major objectives have been realised in this study. Firstly, data has been obtained in real-sized optical Diesel injectors operating at realistic driving pressures. To the author knowledge this is the first time that such information has been obtained at pressures up to 1750 bar. Secondly, velocity data has been gathered from real-sized gasoline injectors, operating at real driving pressures. A unique data set has been presented, which will provide the basis for CFD models of pressure swirl atomisers.

(a) Two optically accessed nozzle flow rigs were designed and built to allow the investigation of flow phenomena in both Diesel and Gasoline injectors using laser-based optical diagnostic techniques.

(b) The optical diagnostic techniques used were flow visualisation, particle image velocimetry (PIV) and phase Doppler anemometry (PDA). The applications of such optical diagnostic techniques help to provide new insights into the flow behaviour, allowing better definition of the internal flow structure. The data also provided an understanding of the link between internal flow structure and external flow spray characteristics. This will allow future engine designers and researchers to develop more efficient and also environmentally friendly engines.

(c) The understanding of flow and atomisation processes gained from the experimental findings was used to aid the development and validation of Computational Fluid Dynamics (CFD) codes and provide a predictive tool for GDI injector development. This is important for designers and

engineers to meet the challenges posed by the Euro IV emissions standards and beyond.

7.5 FUTURE WORK

The Diesel research work provided an in-depth understanding on the internal flow regimes in microhole nozzles under high pressure injection conditions. However, further improvement in the optical quality of the sapphire plates is crucial to provide better flow investigation into these optical orifices. One other important work is to link the internal flow structure with the developing fuel spray. The next stage is to use another optical diagnostic technique such as phase Doppler anemometry (PDA) to measure the droplet sizes and velocity at elevated charge back pressure condition. This would allow this study to link the internal flow structure with the developing fuel spray.

For the high-pressure swirl injectors used for GDI applications the next stage of the research should focus on the transient behaviour. Much of the current study has been aimed at investigating the steady-state part of the injection cycle. This is important since for much of the fuel mass is injected during the steady-state region. However, the transient periods, particularly during injector opening are important and experimental data is required.

Another important aspect of these swirl injectors is the structure of the aircore. More detailed measurement of the radial component of velocity, generated through the contraction from the reservoir to the exit nozzle, would provide data for the modelling of the wave-like structures formed on the aircore surface. This would provide a more accurate prediction of the nozzle discharge coefficients.

Further refinements of the optical diagnostics, such as higher resolution imaging and time-resolved FPIV would provide more information about the internal flow structure and the temporal development of the internal flow and the external spray.

Computational Fluid Dynamics (CFD) provides numerical simulation which can be used to predict internal and external flows, involving fluid and heat transfer. This technique is so useful and versatile that it covers a wide range of industrial to research based applications. A preliminary investigation into the application of CFD to aid the understanding of the internal flows in injectors was carried out as part of this research work and the results are presented in Appendix C. The CFD work conducted in this research is very useful for future study involving other non-swirl and swirl injectors' studies. The full study is not possible in this instance due to the amount of time required to understand and apply the various codes. The full CFD modelling work in creating the orifice geometry and validating these models itself is a PhD thesis.

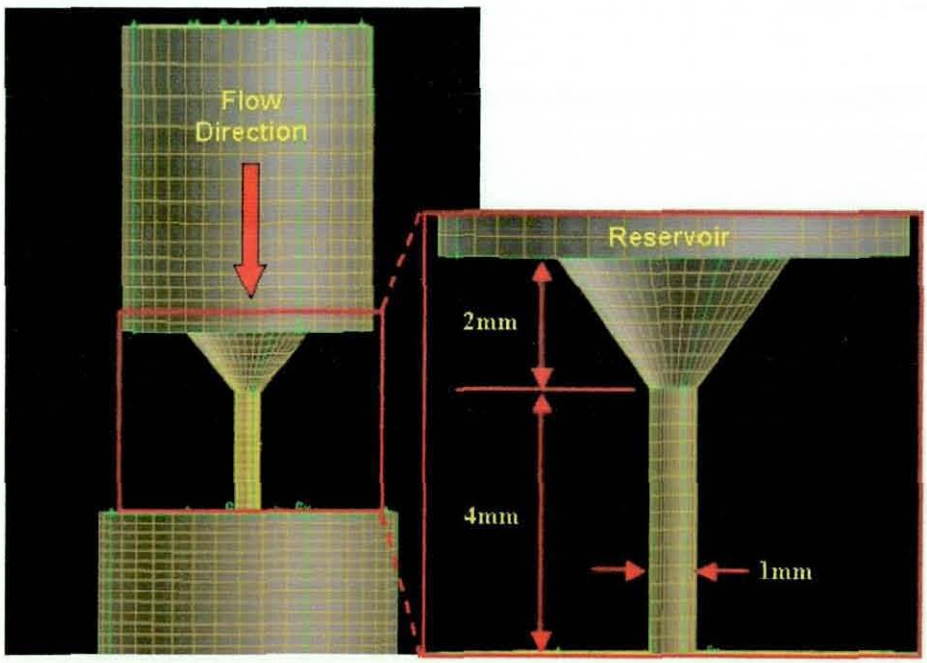

Figure 7.1 Gambit design software showing a 45° chamfered inlet orifice.

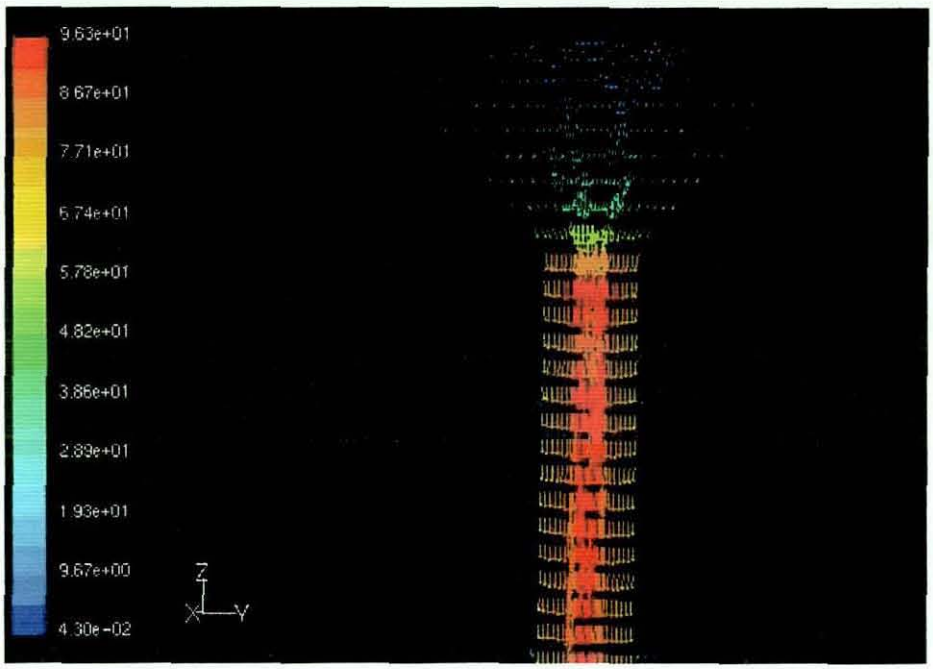

Figure 7.2 45° chamfered inlet orifice at 40 bar driving pressure.

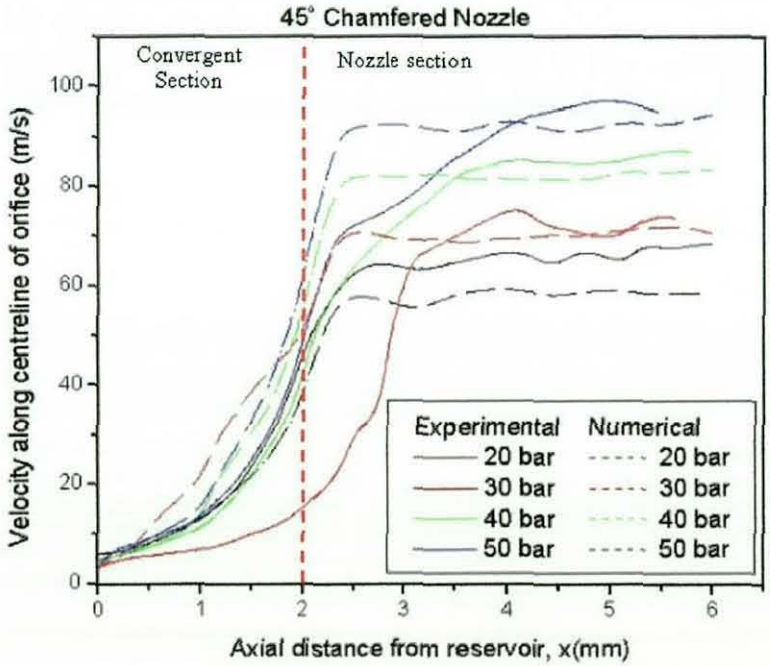

Figure 7.3 Experimental and numerical velocity profile along centreline of 45° chamfered inlet orifice.

Examples of the grid generation, velocity results and centreline velocity profiles are given in figures 7.1 to 7.3, for a non-swirl, 45° chamfered inlet

orifice operating at 40 bar. It can be seen from figure 7.3 that the agreement between experimental data and theoretical results is very good.

The application of CFD modelling in conjunction with experimental investigation has numerous significant advantages. The modelling tool helps to reduce the time and cost of designing and can help validate designs. Future work in this project will extend the CFD modelling to the high-pressure, swirl atomiser and validation can be provided by the extensive experimental data provided in this thesis.

7.6 REFERENCE

[01] Chaves, H., Knapp, M., Kubitzek, A., Obermeier, F., Schneider, T., *Experimental Study of Cavitation in the Nozzle Hole of Diesel Injectors Using Transparent Nozzles*, SAE 950290, SP-1101, 1995

[02] Dorfner, V., Domnick, J., Durst, F., Köhler, R., *Viscosity and Surface Tension Effects in Pressure Swirl Atomization*, Atomization and Sprays Journal, Volume 5, No.3, pp 261-285, 1995

[03] Fluent Inc., *Fluent 5.4 Documentation*, CD-Rom, April 2000

[04] Fluent Inc., *Gambit 1.3 Documentation*, CD-ROM, June 2000

[05] Heywood, J.B., *Internal Combustion Engine Fundamentals,* McGraw-Hill Book Company, 1988, ISBN 0-07-100499-8

[06] Ren, W.M., Nally Jr, J.F., *Computations of Hollow-Cone Sprays From A Pressure-Swirl Injector*, SAE 982610, 1998

[07] Ren, W.M., Shen, J., Nally Jr, J.F., *Geometrical Effects Flow Characteristics of a Gasoline High Pressure Swirl Injector*, SAE 971641, SP-1279, 1997

BIBLIOGRAPHY

[01] Adrian, R.J., *Scattering particle characteristics and their effect on pulsed laser measurements of fluid flow: speckle velocimetry vs particle image velocimetry*, Applied Optics, Vol. 24, Pg 1690-1691, 1984

[02] Alloca, L., Corcione, F.E., Valention, G., *Study of the Atomisation Process in a GDI Spray by Laser Light Extinction and Phase Doppler Techniques*, ILASS Europe, Zurich (Switzerland), Sept 2001

[03] Allen, J., Hargrave, G.K., *Fundamental Study of In-nozzle fluid flow and it effect on liquid jet breakup in Gasoline Direct Injectors*, 16th ILASS, Darmstadt, Germany, 2000.

[04] Allen, J. and Hargrave, G. K., *Investigation of internal fluid flow in real sized pressure swirl gasoline direct injectors.* ImechE Conference Transactions Fuel Injection systems, Page 83-94, London, UK, 26-27th November 2002

[05] Allen, J, Heath, J., Hargrave, G.K., Wigley, G., *Comparison of the Spray Characteristics of Alternative GDI Fuel Injection Systems Under Atmospheric and Elevated Pressure Operation*, 15th International Combustion Engine Symposium, 9935086, Seoul (South Korea), July 1999, ISBN 4-915219-25-9

[06] Abo-Serie, E., Arcoumanis, C., Gavaises, M., Argueyrolles, B., Galzin, F., *Structure of Sprays Generated by Pressure Swirl Injectors for Direct-Injection Gasoline Engines*, ILASS-Europe, Toulouse (France), July 1999

[07] Arcoumanis, C., Gavaises, M., French, B., *Effect of Fuel Injection Processes on the Structure of Diesel Sprays*, SAE 970799, SP-1219, 1997

[08] Arcoumanis, C., Gavaises, M., Argueyrolles, B., Galzin, F., *Modeling of Pressure-Swirl Atomisers for GDI Engines*, SAE 1999-01-0500, 1999

[09] Bae, C., Kang, J., *Diesel Spray Development of VCO Nozzles for High Pressure Direct-Injection*, SAE 2000-01-1254, SP-1498, 2000

[10] Bae, C., Yu, J., Kang, J., Kong, J., Lee, K.O., *Effect of Nozzle Geometry on the Common-Rail Diesel Spray*, SAE 2002-01-1625, SP-1713, 2002

[11] Badock, C., Wirth, R., Fath, A., Leipertz, A., Application of Laser Light Sheet Technique for the Investigation of Cavitation Phenomena in Real Size Diesel Injection Nozzles, ILASS-Europe, Manchester(UK), July 1998

[12] Balachandran, W., Hu, D., Yule, A.J., Shrimpton, J.S., Watkins, A.P., *Electrostatically produced Fuel Sprays for Combustion applications*, Paper XII-2, ICLASS, Rouen (France), July 1994

[13] Baumgarten, C., Shi, Y., Busch, R., Merker, G.P. *Numerical and Experimental Investigations of Cavitating Flow in High Pressure Diesel Nozzles*, ILASS Europe, Zurich (Switzerland), Sept 2001

[14] Asian Development Bank, *Vehicle Emissions*. (http://www.adb.org/documents/guidelines/Vehicle_Emissions/im_ch03.pdf), 2003. [19.11.2003]

[15] BBC News, Fuel-cell car hopes played down. (http://newsvote.bbc.co.uk/mpapps/pagetools/print/news.bbc.co.uk/1/hi/sci.../2840191.st), 11.03.2003. [13.03.2003]

[16] BBCi News, *The long road for hydrogen*.

(http://news.bbc.co.uk/1/hi/sci/tech/2705607.stm), 29.01.2003. [13.03.2003]

[17] Bella, G., Rocco, V., Ubertini, S., *Combustion and Spray Simulation of a DI Turbocharged Diesel Engine*, SAE 2002-01-2776, SP-1720, 2002

[18] Bergwerk, W., *Flow Pattern in Diesel Nozzle Spray Holes*, Proceedings of the Institution of Mechanical Engineers, Vol. 173, Pg 655-660, 1959

[19] Bunnell, R.A., Heister, S.D., Yen, C., Collicott, S.H., *Cavitating Injector Flows: Validation of Numerical Models and Simulations of Pressure Atomizers*, Atomization and Sprays Journal, Volume 9, No.5, pp 445-465, 1999

[20] Castagne, M., Cheve, E., Dumas, J.P., Henriot, S., *Advanced Tools for Analysis of Gasoline Direct Injection Engines*, SAE 2000-01-1903, 2000

[21] Caterpillar Inc, *A Guide to Using CADeTWin*, version 2.78, Measurement Systems Development, 1997-2001

[22] Caterpillar News, *CAT engines with ACERT technology* (http://www.cat.com/about_cat/news/03_products_n_services/getprdata.html?file=enginesepgindustrial051909114.dat&callingdoc=/about_cat/news/03_products_n_services/products_n_services.html&init_section=newsparts&origindoc=/products/engines_n_power_systems/service_n_support/01_press_releases/press_releases.html), 13.05.2003. [16.12.2003]

[23] Caterpillar: HEUI Fuel Systems (http://www.caterpillar.com/products/shared/parts_n_service/03_engine_parts/03_spec_sheet_library/pdf/pehp9526.pdf), 1999, [03.05.2004]

[24] Chang, C.T., Farrell, P.V., *A Study on the Effects of Fuel Viscosity and Nozzle Geometry on High Injection Pressure Diesel Spray Characteristics*, SAE 970353, SP-1219, 1997

[25] Chang, J.C., Chu, C.S., Chen, C.Y., *The Study of Effects of the Refractive Index Changing on a Phase Doppler Particle Analyser*, 8th ICLASS, Pasadena (USA), July 2000

[26] Chaves, H., Knapp, M., Kubitzek, A., Obermeier, F., Schneider, T., *Experimental Study of Cavitation in the Nozzle Hole of Diesel Injectors Using Transparent Nozzles*, SAE 950290, SP-1101, 1995.

[27] Chigier, N., *Combustion Measurements*, Combustion: An International Series, Hemisphere Publishing Corporation, 1991, ISBN 1-56032-028-1

[28] Chigier, N., *Energy, Combustion, and Environment*, McGraw-Hill Series in Energy, Combustion, and Environment, McGraw-Hill Book company, 1981, ISBN 0-07-010766-1

[29] Cho, Y.C., *Digital image Velocimetry*, Applied Optics, Vol.28, No.4, Pg 740-748, February 1989

[30] Christopher Outwater & Van Hamersveld, *Practical Holography* (http://www.holo.com/holo/book/book1.html#def), Jan2002 [09.01.2004]

[31] Chryssakis, C.A., *Modelling Gasoline Sprays Emerging from High-pressure Swirl Injectors for DISI engines*, Master Thesis, University of Michigan, August 2002

[32] Chryssakis, C.A., Assanis, D.N., Lee, J.K., Nishida, K., *Fuel Spray Simulation of High-Pressure Swirl Injector for DISI Engines and Comparison with Laser Diagnostic Measurements*, SAE 2003-01-0007, 2003

[33] Coldren, D.R., Schuricht, S.R., Smith, R.A., *Hydraulic Electronic Unit Injector with Rate Shaping Capability*, SAE 2002-01-2890, 2002

[34] Comer, M.A., Bowen, P.J., Bates, C.J., Sapsford, S.M., *CFD Modelling of Direct Injection Gasoline Sprays*, ILASS-Europe, Toulouse (France), July 1999

[35] Comer, M.A., Bowen, P.J., Bates, C.J., Sapsford, S.M., Johns, R.J.R., *Transient 3D Analysis of a DI Gasoline Injector Spray, Atomization and Sprays*, Vol.9, No.5, Pg 467-482, 1999

[36] Comer, M.A., Bowen, P.J., Sapsford, S.M., Bates, C.J., *Influence of Ambient Pressure on Transient GDI Sprays*, ILASS-Europe, Zurich (Switzerland), September 2001

[37] Cooper, D., Yule, A.J., *Waves on the Aircore/Liquid Interface of a Pressure Swirl Atomiser*, ILASS-Europe, Zurich (Switzerland), September 2001

[38] Coupland, J.M., Halliwell, N.A., *Particle image velocimetry: rapid transparency analysis using optical correlation*, Applied Optics, Vol. 27, No.10, Pg 1919-1921, 1988

[39] Coupland, J.M., C.J.D., Pickering, *Particle image velocimetry: Estimation of Measurement Confidence at Low Seeding Densities*, Optics and laser in Engineering, Vol. 9, Pg 20-210, 1988

[40] Cousin, J., Nuglisch, H.J., *Prediction of Characterisation of Sprays Produced by High Pressure Swirl Injectors*, ILASS-Europe, Toulouse (France), July 1999

[41] Cousin, J., Ren, W.M., Nally, S., *Recent Developments in Simulations of Internal Flows in High Pressure Swirl Injectors*, Page 227-231, Oil & Gas Science and Technology, Vol. 54, No.2, 1999

[42] Damaschke, N., Nobach, H., Tropea, C., Optical limits of particle concentration for multi-dmensional particle sizing techniques in fluid mechanics, Experimental in fluids, Vol.32, Pg 143-152, 2002

[43] Dan, T., Yamamoto, T., Senda, J., Fujimoto, H., *Effect of Nozzle Configurations for Characteristics of Non—Reacting Diesel Fuel Spray*, SAE 970355, SP-1219, 1997

[44] De Vita, A., Di Angelo, L., Alloca, L., Alfuso, S., *Spray Characteristics of a High Pressure Injection for GDI Engines*, 9th International Symposium on Flow Visualisation, Edinburgh (UK), 2000

[45] Dieselnet, *Emission Standards: European Union*. (http://www.dieselnet.com/standards/eu/ld.html), March 2003. [19.11.2003]

[46] Dorfner, V., Domnick, J., Durst, F., Köhler, R., *Viscosity and Surface Tension Effects in Pressure Swirl Atomization*, Atomization and Sprays Journal, Volume 5, No.3, pp 261-285, 1995

[47] Dudderar, T.D., Simpkins, P.G., *Laser Speckle photography in a fluid medium*, Nature, Vol. 270, Pg 45-47, 1977

[48] Durst, F., *Fluid Mechanics Developments and Advancements in the 20th Century*, 10th International Symposium on Application Laser Technology to Fluid Mechanics, Lisbon (Portugal), July 2000

[49] Durst, F., Melling, A., Whitelaw.J.H., *Principles and practice of laser-Doppler Anemometry*, Academic Press Inc (London) Ltd, 1976, ISBN 0-12-225250-0

[50] Egermann, J., Ipp, W., Rabenstein, F., Wensing, M., Leipertz, A., *Spray Formation and Evaporation of High Pressure Swirl Atomizers for Gasoline Direct Injection*, ILASS-Europe, Toulouse (France), July 1999

[51] El-Beshbeeshy, M.S., Hodges, J.T., Corradini, M.L., *Image Analysis of Diesel Sprays*, SAE 921628, 1992

[52] El-Hannouny, E.M., Lee, T.W., Farrell, P.V., Reitz, R.D., *An Experimental and Numerical Study of Injector Behavior for HSDI Diesel Engines*, SAE 2003-01-0705, SP-1739, 2003

[53] Evers, L.W., *Characterization of the Transient Spray from a High Pressure Swirl Injector*, SAE 940188, SP-1026, 1994

[54] Faure, M.A., Sandler, M., Oversby, K.K., Stokes, J., Begg, S.M., Pommier, L.S., Heika, M.R., *Application of LDA and PIV Techniques to the Validation of a CFD Model of a Direct Injection Gasoline Engine*, SAE 982705, 1998

[55] Ferguson, C.R., *Internal Combustion Engines*; Applied Thermosciences, John Wiley & Sons, 2001, ISBN 0471356174

[56] Fluent Inc., *Fluent 5.4 Documentation*, CD-Rom, April 2000

[57] Fluent Inc., *Gambit 1.3 Documentation*, CD-ROM, June 2000

[58] Fry, M., King, J., White, C., *A Comparison of Gasoline Direct Injection Systems and Discussion of Development Techniques*, SAE 1999-01-0171, SP-1416, 1999

[59] Ganippa, L.C., Bark, G., Andersson, S., Chomiak, J., *The Structure of Cavitation and its Effect on the Spray Pattern in a Single-Hole Diesel Nozzle*, SAE 2001-01-2008, SP-1630, 2001

[60] Gavaises, M., Abo-serie, E., Arcoumanis, C., *Nozzle Hole Film Formation and its link to Spray Characteristics in Swirl-Pressure Atomizers for Direct Injection Gasoline Engines*, SAE 2002-02-1136, SP-1693, 2002

[61] Goney, K.H., Corradini, M.L., *Isolated Effects of Ambient Pressure, Nozzle Cavitation and Hole Inlet Geometry on Diesel Injection Spray Characteristics*, SAE 2000-01-2043, 2000

[62] Gong, Y., Liu, C., Huang, Y., Peng Z., *An Experimental Study on Droplet Size Characteristics and Air Entrainment of Elliptic Sprays*, SAE 982546, 1998

[63] Han, J.S., Lu, P.H., Xie, X.B., Lai, M.C., Henein, N.A., *Investigation of Diesel Spray Primary Break-up and Development for Different Nozzle Geometries*, SAE 2002-01-2775, 2002.

[64] Han, J.S., Wang, T.C., Xie, X.B., Lai, M.C., Henein, N.A., Harringon, D.L., Pinso, J., Miles, P., *Dynamics of Multiple-Injection Fuel Sprays in a small-bore HSDI Diesel Engine*, SAE 2000-01-1256, SP-1498, 2000

[65] Harding, S.C., Farrugia, N., Le Gal, P., Nimmo, G.A., Greenhalgh,D.A., *Fuel Flux, Droplet Size and Velocity Measurements made on Pintle and Airspray Injectors*, ILASS-Europe, Manchester(UK), July 1998

[66] Heikal, M., Pethers, P., Gill, S., Shillington, S., Jackson, N., Stone, R., *Future Engine and System Technologies : The Euro IV Challenge*, IMechE Seminar Publication, 1997. ISBN 1-86058-166-8

[67] Heywood, J.B., *Internal Combustion Engine Fundamentals,* McGraw-Hill Book Company, 1988, ISBN 0-07-100499-8

[68] Huang, Z., Shao, Y.M., Shiga, S., Nakamura, H., Karasawa, T., *The role of orifice flow pattern in fuel atomization*, Paper I-12, ICLASS, Rouen (France), July 1994

[69] Iwamoto, Y., Noma, K., Nakayama, O., Yamauchi, T., Ando, H., *Development of Gasoline Direct Injection Engine*, SAE 970541, 1997

[70] Jacobsson, L., Winklhofer, E., Chomiak, J., *Injection Orifice Shape: Effects on Spray Characteristics and Heat-Release Rate in a Large-Size Single-Cylinder Diesel Engine*, SAE 1999-01-3490, 1999

[71] Jeong, K.S., Jermy, M.C., Greenhalgh, D.A., *Laser Sheet Dropsizing in Evaporating Sprays using Laser Induced Exciplex Fluorescence*, 9th International Symposium on Flow Visualisation, Edinburgh (UK), 2000

[72] Kamimoto, T., Yokota, H., Kobayashi, H., *A New Technique for the Measurement of Sauter Mean Diameter of Droplets in Unsteady Dense Sprays*, SAE 890316, 1989

[73] Karl, G., Kemmler, R., Bargende, M., Abthoff, J., *Analysis of a Direct Injected Gasoline Engine*, SAE 970624, 1997

[74] Khavkin, Y., *Can Atomization be Improved by Viscosity Increase?*, 8th ICLASS, Pasadena, California (USA), July 2000

[75] Kim, M., Park, J., Lee, N., Choi, K., *Analysis of In-cylinder Flow in a Spark-Ignited Direct Injection Engine Using PIV and CFD*, 15th International Combustion Engine Symposium, 9935031, Seoul (South Korea), July 1999, ISBN 4-915219-25-9

[76] Kirby, R.S, Withington, S., Darling A.B., Kilgour, F.G., *Engineering in History*, McGraw-Hill Book Company Inc, 1956,LCCN 55-8287

[77] Knapp, R.T., Daily, J.W., Hammitt, F.G., *Cavitation*, McGraw-Hill Inc, 1970, LCCN 77-96428

[78] Koivula, T.S., Ellman, *Cavitation Behaviour of Hydraulic Orifices and Valves*, SAE 982038, SP-1380, 1998

[79] Konig, G., Anders, K., Frohn, A., *A New Light-scattering Technique to Measure the Diameter of Periodically generated Moving Droplets*, Journal of Aerosol Science, Vol.17, No.2, Pg 157-167, 1986

[80] Kufferath, A., Wende, B., Leuckel, W., *Influence of Liquid Flow Conditions on Spray Characteristics of Internal Mixing Twin Fluid Atomisers*, ILASS-Europe, Manchester (UK), July 1998

[81] Kunkulagunta, K.R., *Video Imaging and Analysis of Common Rail Sprays in an Optical Engine using Shadowgraphy Technique*. SAE 2000-01-1255, SP-1498, 2000

[82] Kusakabe, T., Tsue, M., Kadota, T., *Visualization of Diesel Spray by Laser Sheet Method*, SAE 941920, 1994

[83] Kuwahara, K., Ando, H., *Diagnostic of in-cylinder flow, mixing and combustion in gasoline engines*, Measurement Science and Technology Journal, R95-R111, 2000

[84] Lading, L., Wigley, G., Buchhave, P., *Optical Diagnostics for Flow Processes*, Plenum Press, 1994, ISBN 0-306-44817-3

[85] Lake, T.H., Stokes, J., Whitaker, P.A., Crump, J.V., *Comparison of Direct Injection Gasoline Combustion Systems*, SAE 980154, 1998

[86] Laoonual, Y., Yule, A.J., Walmsley, S.J., *Internal Fluid Flow and Spray Visualization for a Large Scale Valve Covered Orifice (VCO) Injector Nozzle*, ILASS Europe, Zurich (Switzerland), Sept 2001

[87] Le Gal, P., *Development of a Laser Sheet Dropsizing Technique for Sprays*, PhD Thesis, School of Mechanical Engineering, Cranfield University, 1999

[88] Lefebvre, A.H., *Atomization and Sprays*, Combustion: An International Series, Hemisphere Publishing Corporation, 1989, ISBN 0-89116-603-3

[89] Lindsay, R.B., *Lord Rayleigh: The Man and his Works*, Pergamon Press, 1970, ISBN 08-006821-9

[90] Maunoury, B., Duverger, T., Mokaddem, K., Lacas. F., *Optical Investigation of Diesel Spray and Auto-ignition in a Small Direct-injected Diesel Engine*, ILASS Europe, Zurich (Switzerland), Sept 2001

[91] Mitsubishi Technology, *Gasoline Direct Injection Engines* (URL:http://www.mitsubishi-motors.co.jp/inter/technology/GDI/page1.html), 1996, [28.07.2001]

[92] Miyamoto, T., Kobayashi, T., Matsumoto, Y., *Structure of Sprays from an Air-Assist Hollow-Cone Injector*, SAE 960771, SP-1132, 1996

[93] Motion Analysis Systems, *Kodak Ektapro HS Motion Analyser: User's Manual Model 4540*, 1993, P/N 91000046-001

[94] Munson, B.R., Young, D.F., Okiishi, T.H., *Fundamentals of Fluid Mechanics*, John Wiley & Sons Inc, 1998, ISBN 0-471-17024-0

[95] Nasr, G.G., Yule, A.J., Bendig, L., *Industrial sprays and atomisation: design, analysis and application*, Springer publishing, 2002, ISBN 1852334606

[96] Noma, K., Iwamoto, Y., Murakami, N., Lida, K., Nakayama, O., *Optimised Gasoline Direct Injection Engine for the European Market*, SAE 980150, 1998

[97] Nogi, T., Shiraishi, T., Nakayama, Y., Ohsuga, M., Kurihara, N., *Stability Improvement of Direct Fuel Injection Engine under Lean Combustion Operation*, Direct Injection: Engines, Emissions and Aftertreatment, SAE Inc Publishing, SAE 982703, SP-1399, 1998, ISBN 0-7680-0313-X

[98] Nouri, J.M., Brehm, C., Whitelaw, J.H., *The Spray From A Gasoline Direct Injector*, 15th Intl. Liquid Atomisation and Spray Systems (Europe), Toulouse (France), July 1999

[99] Nurick, W.H., *Orifice Cavitation and its Effect on Spray Mixing*, Trans ASME Journal of Fluids Engineering, Volume 98, No.4, pp 681-687, 1976

[100] Ohrn, T.R., Senser, D.W., Lefebvre, A.H., *Geometrical effects on discharge coefficicents for plain-orifice atomisers*, Atomization and Sprays Journal, Volume 1, No.2, pp 137-153, 1991

[101] Parrish, S.E., Farrell, P.V., *Transient Spray Characteristics of a Direct-Injection Spark-Ignited Fuel Injector*, SAE 970629, 1997

[102] Pickering, C.J.D., Halliwell, N.A., *Laser speckle photography and particle image velocimetry: photographic film noise*, Applied Optics, Vol.23, No.17, Pg 2961-2969, September 1984

[103] Queiroz, C., Tomanik, E., *Gasoline Direct Injection Engines - A Bibliographical Review*, SAE 973113, 1997

[104] Raffel, M., Willert, C.E., Kompenhans, J., *Particle Image Velocimetry: A Practical Guide*, Springer ,1998, ISBN 3-540-63683

[105] Raffelsberger, P., Dolenc, A., Kordesch, V., *Fuel System for the Future High Speed Long Life DI Diesel Engines with Suitable Electronic Control*, SAE 951855, 1995

[106] Ramamurthi, K., Nandakumar, K., *Effect of injector orifice configurations on atomization*, Paper III-2, ICLASS, Rouen (France), July 1994

[107] Ramamurthi, K., Patnaik, S.R., *Influence of periodic disturbances on inception of cavitation in sharp-edged orifices*, Experiments in Fluids Journal, Volume 33, pp 720-727, 2002

[108] Rashkovan, A., Kholmer, V., Sher, E., *Gas-dissolved Gasoline Spray – An Experimental Study*, ILASS-Europe, Zurich (Switzerland), September 2001

[109] Reitz, R.D., Bracco, F.V., *Ultra-high-speed filming of atomising jets*, Physics of Fluids, Volume 22, Pg 1054-1064 ,June 1979

[110] Reitz, R.D., Bracco, F.V., *Ultra-high-speed filming of atomising jets*, Physics of Fluids, Volume 25, Pg 1730-1742 ,October 1982

[111] Ren, W.M., Nally Jr, J.F., *Computations of Hollow-Cone Sprays From A Pressure-Swirl Injector*, SAE 982610, 1998

[112] Ren, W.M., Shen, J., Nally Jr, J.F., *Geometrical Effects Flow Characteristics of a Gasoline High Pressure Swirl Injector*, SAE 971641, SP-1279, 1997

[113] Richter, M., Axelsson, B., Alden, M., Josefsson, G., Carlsson, L.O., Dahlberg, M., Nisbet, J., Simonsen, H., *Investigation of the Fuel Distribution and the In-cylinder Flow Field in a Stratified Charge Engine*

Using Laser Techniques and Comparison with CFD Modelling, SAE 1999-01-3540, 1999

[114] Sasaki, S., Akagawa, H., Tsujimura, K., *A Study on Surrounding Air Flow Induced by Diesel Sprays*, SAE 980805, SP-1316, 1998

[115] Schmidt, D.P., Corradini, M.L., *Analytical prediction of the exit flow of cavitating orifices*, Atomization and Sprays Journal, Volume 7, No.6, 1997

[116] Schmidt, D.P., Corradini, M.L., *One-dimensional analysis of cavitating orifices*, 9th ILASS, San Francisco (USA), 1996

[117] Schwalb, J.A., Ryan III, T.W., Dodge, L.G., *Investigation of Diesel Spray Structure and Spray/Wall Interactions in a Constant Volume Pressure Vessel*, SAE 941918, 1994.

[118] Settles, G.S., *Schlieren and Shadowgraph Techniques*, Springer publishing, 2001, ISBN 3-540-66155-7

[119] Shaikh, S., Banaszak, U., Von Lavante, E., Cooper, D., Yule, A.J., *CFD prediction of the Effects of Viscosity on the Internal Flow of a Scale Pressure-swirl Atomiser*, 19th ILASS-Europe, Nottingham (United Kingdom), 6-8 September 2004

[120] Shiraishi, T., Nakayama, Y., Nogi, T., Ohsuga, M., *Effect of Spray Characteristics on Combustion in a Direct Injection Spark Ignition Engine*, SAE 980156, 1998

[121] Sirignano, W.A., *Fluid Dynamics and Transportation of Droplets and Sprays*, Cambridge University Press, 1999, ISBN 0-521-63036-3

[122] Spicher, U., Reissing, J., Kech, J.M., Gindele, J., *Gasoline Direct Injection (GDI) Engines - Development Potentialities*, SAE 1999-01-2938, SP-1469, 1999

[123] Soteriou, C., Smith, M., Andrews, R., *Diesel injection – laser light sheet illumination of the development of cavitation in orifices*, Combustion Engines and Hybrid Vehicles Conference, Professional Engineering Publishing Limited, pp137-158, 1998, ISBN 1-86058-143-9

[124] Soteriou, C., Andrews, R., Smith, M., *Direct Injection Diesel Sprays and the Effect of Cavitation and Hydraulic Flip on Atomization*, SAE 950080, SP-1065, 1995

[125] Soteriou, C., Andrews, R., Smith, M., *Further Studies of Cavitation and Atomization in Diesel Injection*, SAE 1999-01-1486, SP-1460, 1999

[126] Stumpp, G., Ricco, M., *Common Rail-An Attractive Fuel Injection System for Passenger Car DI Diesel Engines*, SAE 960870, SP-1132, 1996

[127] Takeda, K., Sugimoto, T., Tsuchiya, T., Ogawa, M., Ueda, S., Yoneshige, K., *Slit Nozzle Injector for a New Concept of Direct Injection SI Gasoline Engine*, SAE 2000-01-1902, 2000

[128] Tamaki, N., Nishida, K., Hiroyasu, H., *Promotion of the atomisation of a liquid jet by cavitation in a nozzle hole*, ILASS-Europe, Manchester(UK), July 1998

[129] Tamaki, N., Shimizu, M., Hiroyasu, H., *Enhanced Atomisation of a liquid jet by cavitation in a nozzle hole*, 8th ICLASS, Pasadena (USA), July 2000

[130] Tamaki, N., Shimizu, M., Hiroyasu, H., *Atomisation of super-high injection pressure liquid jet*, ILASS-Europe, Zurich (Switzerland), September 2001

[131] Topenot, E., Le Visage, D., Radenac, C., Tremouliere, G., Carreau, J.L., *Experimental and Numerical Study of Atomisation of Hollow Cone Sheet. Application to Gasoline Direct Injection*, ILASS Europe, Zurich (Switzerland), Sept 2001

[132] Tropea, C., Damaschke N., Nobach, H., Semidetnov, N., *Multidimensional Particle Sizing Techniques for Two-Phase Flows*, 10th International Symposium on Flow Visualisation, Kyoto (Japan), August 26-29, 2002

[133] TSI Incorporated, *Insight: Particle Image Velocimetry Software*, version 3.3, Dec 2000, P/N 1990010

[134] US Department of Energy, *FreedomCar and Fuel Initiative*. (http://www.eere.energy.gov/hydrogenfuel/), 05.02.2003. [13.03.2003]

[135] VanDerWege, B.A., Lounsberry, T.H., Hochgreb, S., *Numerical Modelling of Fuel Sprays in DISI Engines under Early-Injection Operating Conditions*, SAE 2000-01-0273, SP-1512, 2000

[136] Walther, J., Schaller, J.K., Wirth, R., Tropea, C., *Investigation of Internal Flow in Transparent Diesel Injection Nozzles using Fluorescent Particle Image Velocimetry (FPIV)*, 8th ICLASS, Pasadena, California (USA), July 2000

[137] Wicker, R.B., Loya, H.I., Hutchison, P.A., Sakakibara, J., *SIDI Fuel Spray Structure Investigation Using Flow Visualization and Digital Particle Image Velocimetry*, SAE 1999-01-3535, 1999

[138] Wigley, G., Hargrave, G.K., Heath, J., *A High Power, High Resolution LDA/PDA System Applied to Dense Gasoline Direct Injection Spray*, 9th International Symposium on Application Laser Technology to Fluid Mechanics, Paper 9.4, Lisbon (Portugal), 1998

[139] Wirth, M., Piock, W.F., Fraidl, G.K., Schoeggl, P., Winklhofer, E., *Gasoline DI Engines: The Complete System Approach By Interaction of Advanced Development Tools*, SAE 980492. SP-1314, 1998

[140] Wu, K.J., Su, C.C., Steinberger, R.L., Santavicca, D.A., Bracco, F.V., *Measurement of the Spray Angle of Atomizing Jets*, Journal of Fluids Engineerng, Volume 107, Pg 406-413, December 1983

[141] Xu, M., Markle, L.E., *CFD-Aided Development of Spray for an Outwardly Opening Direct Injection Gasoline Injector*, SAE 980493, 1998

[142] Yamakawa, M., Isshiki, S., Lee, J., Nishida, K., *3-D PIV Analysis of Structural Behaviour of D.I. Gasoline Spray*, SAE 2001-01-3669, SP-1640, 2001

[143] Yoda, T., Tsuda, T., *Influence of Injection Nozzle Improvement on DI Diesel Engine*, SAE 970356, SP-1219, 1997

[144] Young, F.R., *Cavitation*, McGraw-Hill Book Company (UK) Limited, 1989, ISBN 0-07-707094-1

[145] Zhao, F.Q., Yoo, J.H., Liu, Y., Lai, M.C., *Spray Dynamics of High Pressure Fuel Injectors for DI Gasoline Engines*, SAE 961925, 1996

APPENDIX A

NON-SWIRL FLOW STUDY

A.1 FLOW VISUALISATION

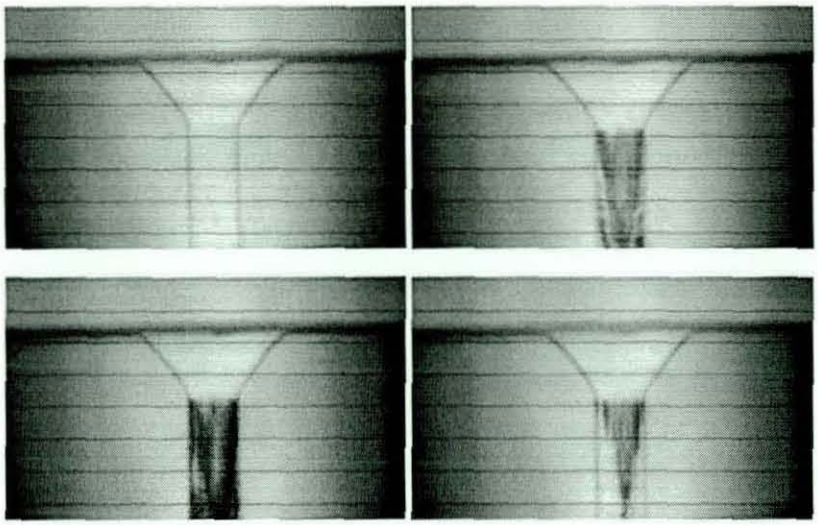

Figure A.1 30° chamfered inlet orifice with 30 bar driving pressure.

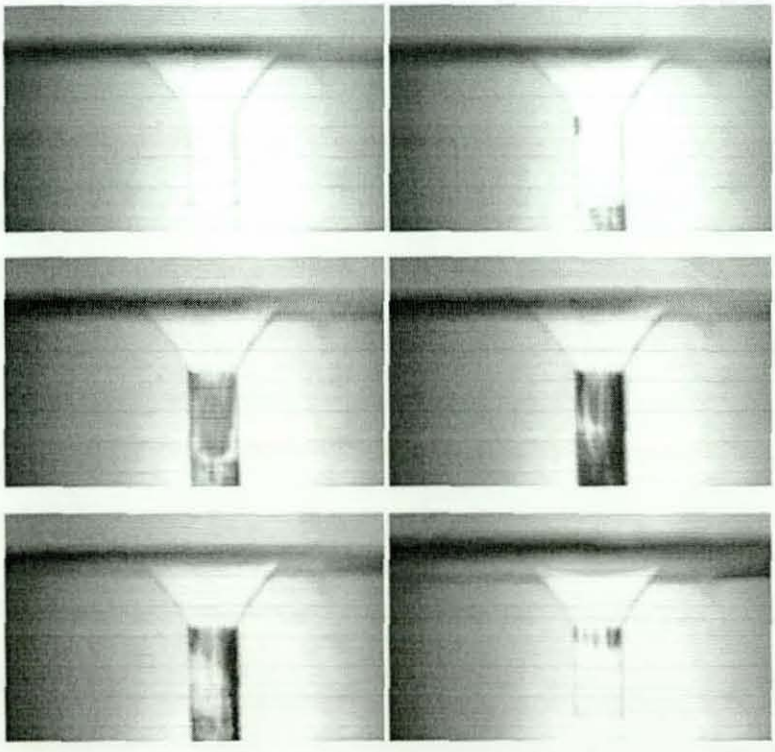

Figure A.2 30° chamfered inlet orifice with 40 bar driving pressure.

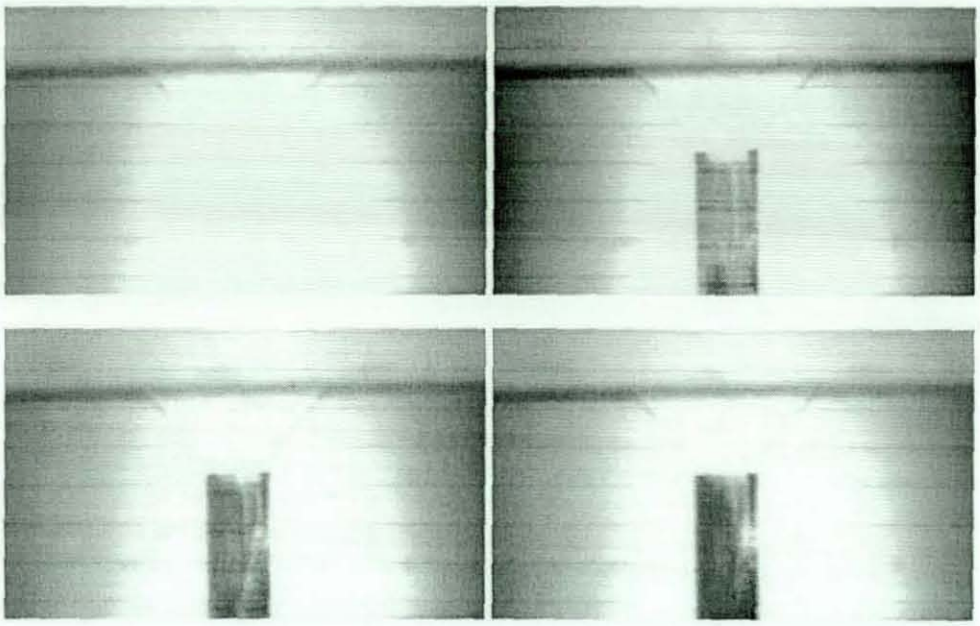

Figure A.3 30° chamfered inlet orifice with 50 bar driving pressure.

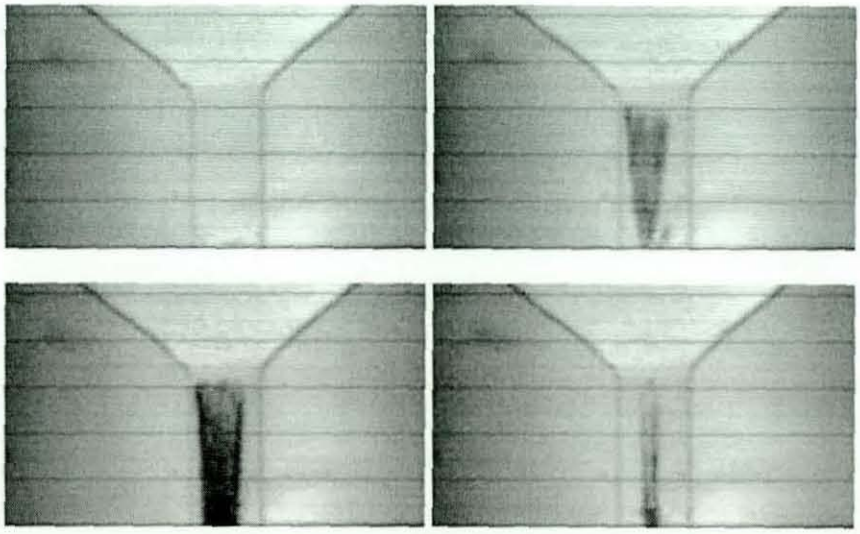

Figure A.4 45° chamfered inlet orifice with 20 bar driving pressure.

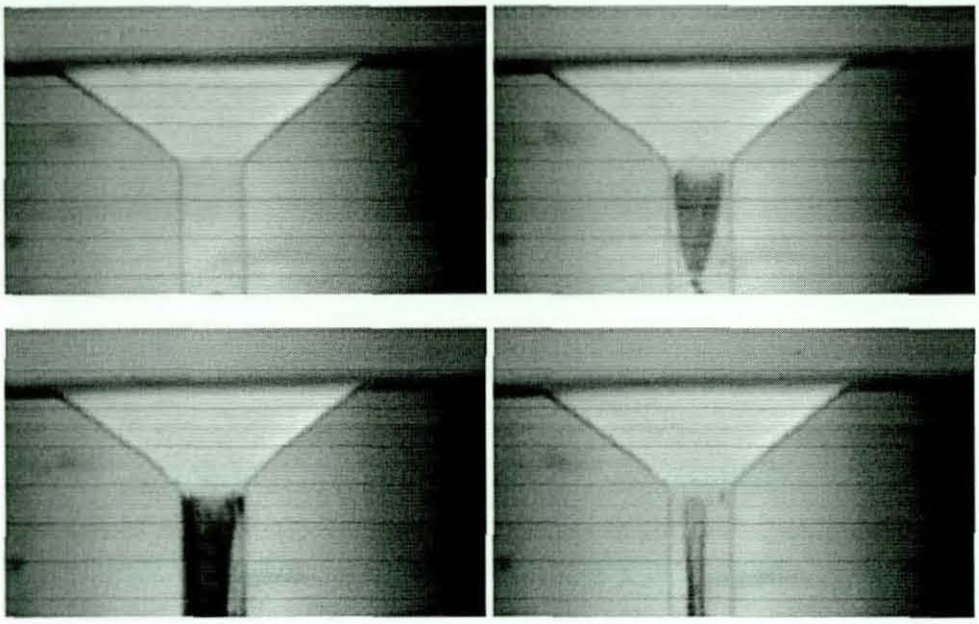

Figure A.5 45° chamfered inlet orifice with 40 bar driving pressure.

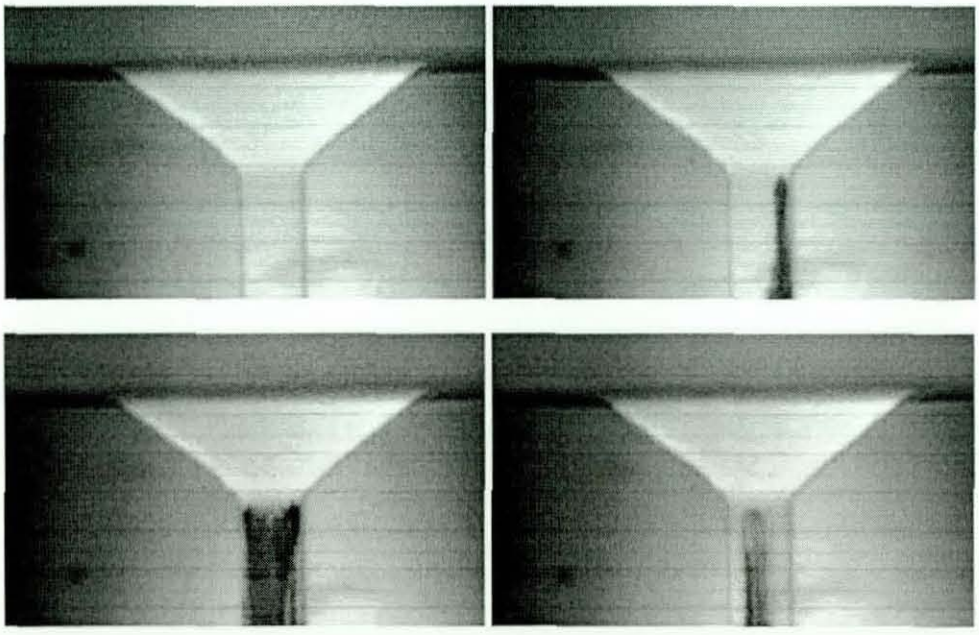

Figure A.6 45° chamfered inlet orifice with 50 bar driving pressure.

A.2 FLUORESCENT PARTICLE IMAGE VELOCIMETRY

A.2.1 45° Chamfered Inlet Nozzle

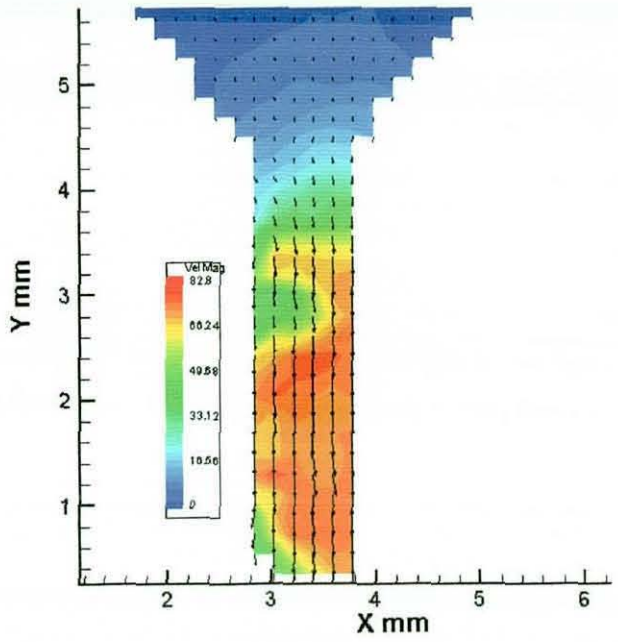

Figure A.7 Average velocity magnitudes for 45° chamfered inlet orifice with 30 bar driving pressure.

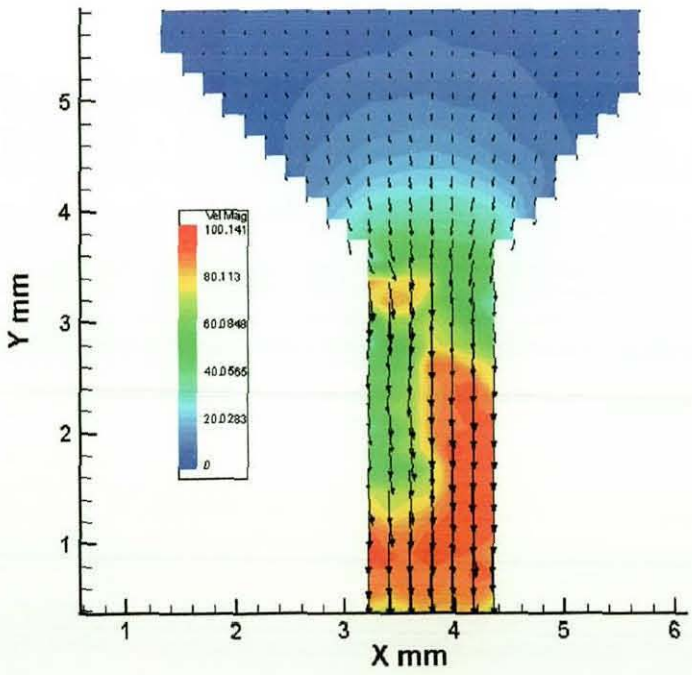

Figure A.8 Average velocity magnitudes for 45° chamfered inlet orifice with 40 bar driving pressure.

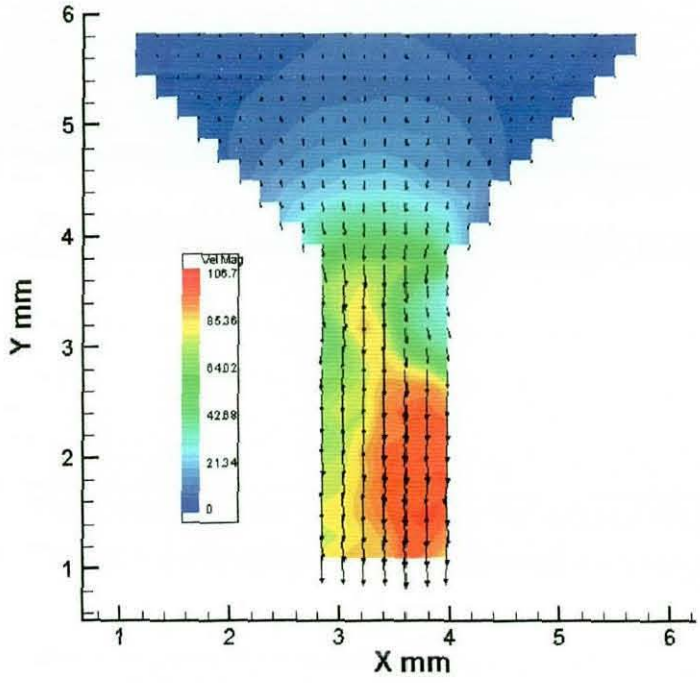

Figure A.9 Average velocity magnitudes for 45° chamfered inlet orifice with 50 bar driving pressure.

A.2.2 60° Chamfered Inlet Nozzle

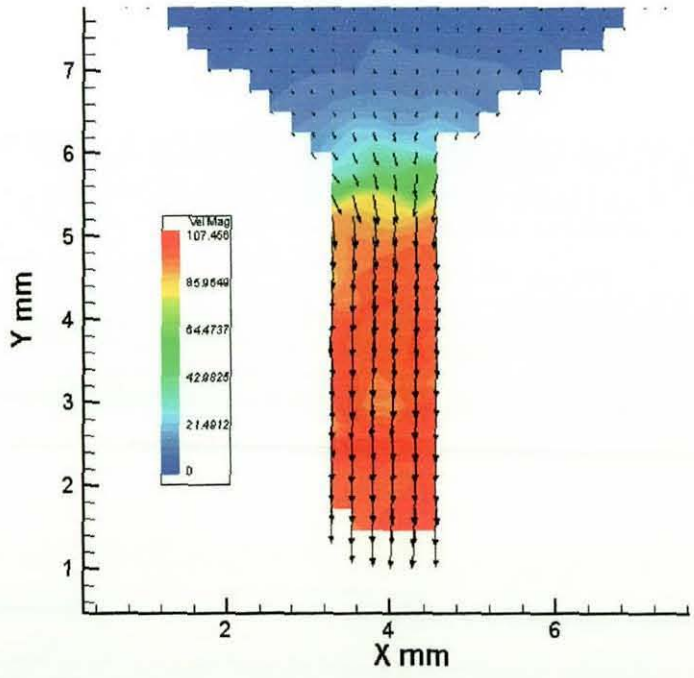

Figure A.10 Average velocity magnitudes for 60° chamfered inlet orifice with 30 bar driving pressure.

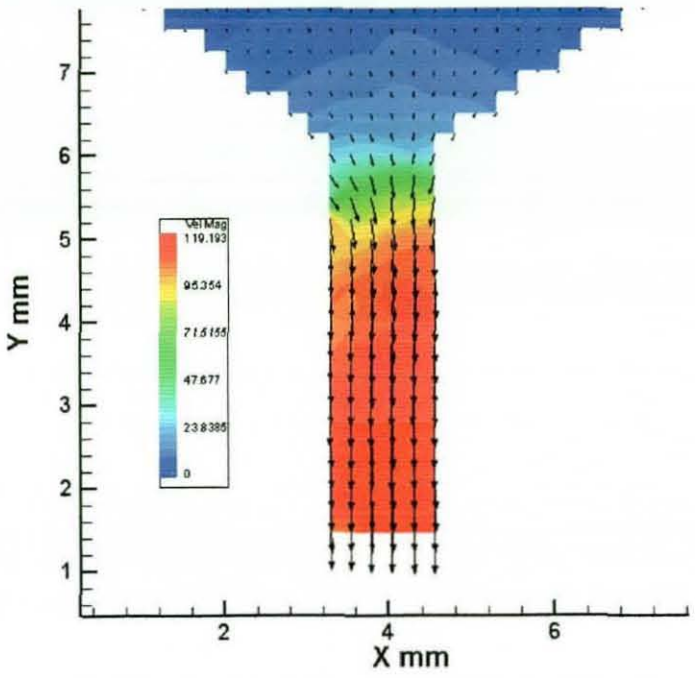

Figure A.11 Average velocity magnitudes for 60° chamfered inlet orifice with 40 bar driving pressure.

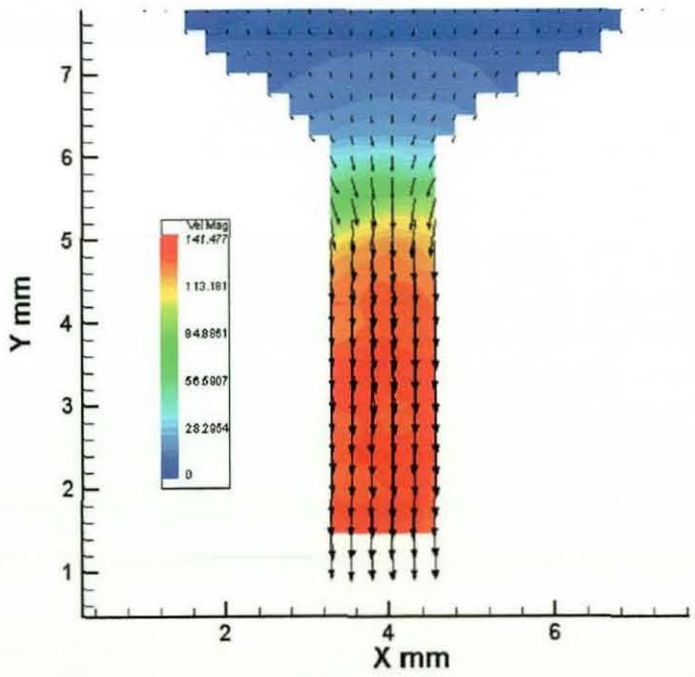

Figure A.12 Average velocity magnitudes for 60° chamfered inlet orifice with 50 bar driving pressure.

APPENDIX B

SWIRL INJECTORS STUDY

B.1 FLOW VISUALISATION

B.1.1 In-nozzle Flow Profile for a 45° Swirler

B.1.1.1 30° CHAMFERED INLET ORIFICE

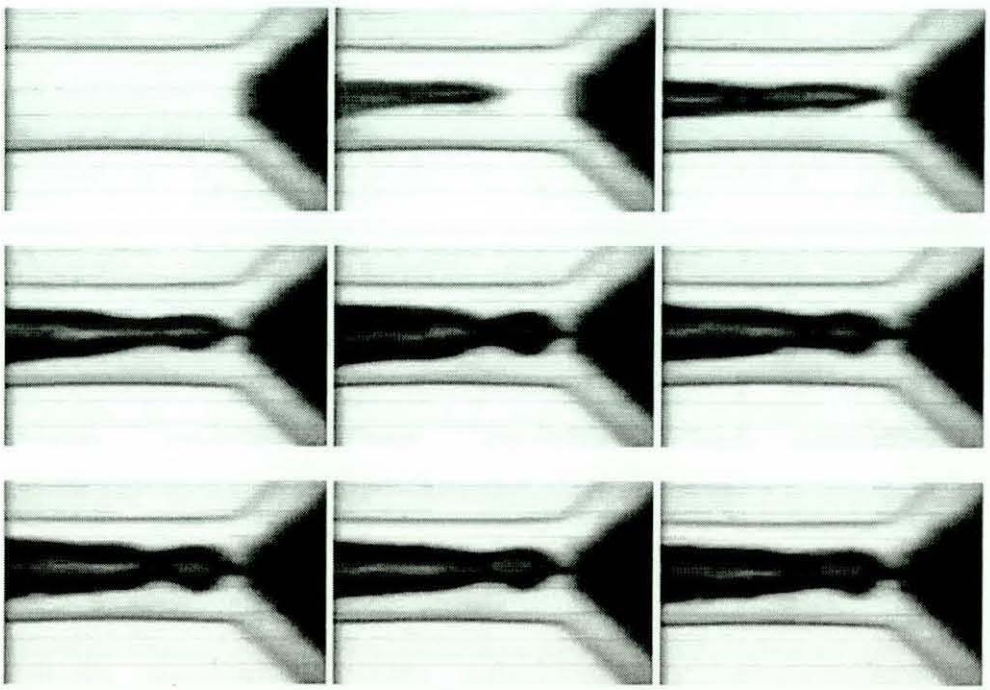

Figure B.1 Flow images of 45° swirler with 30° chamfered inlet orifice at 20 bar driving pressure.

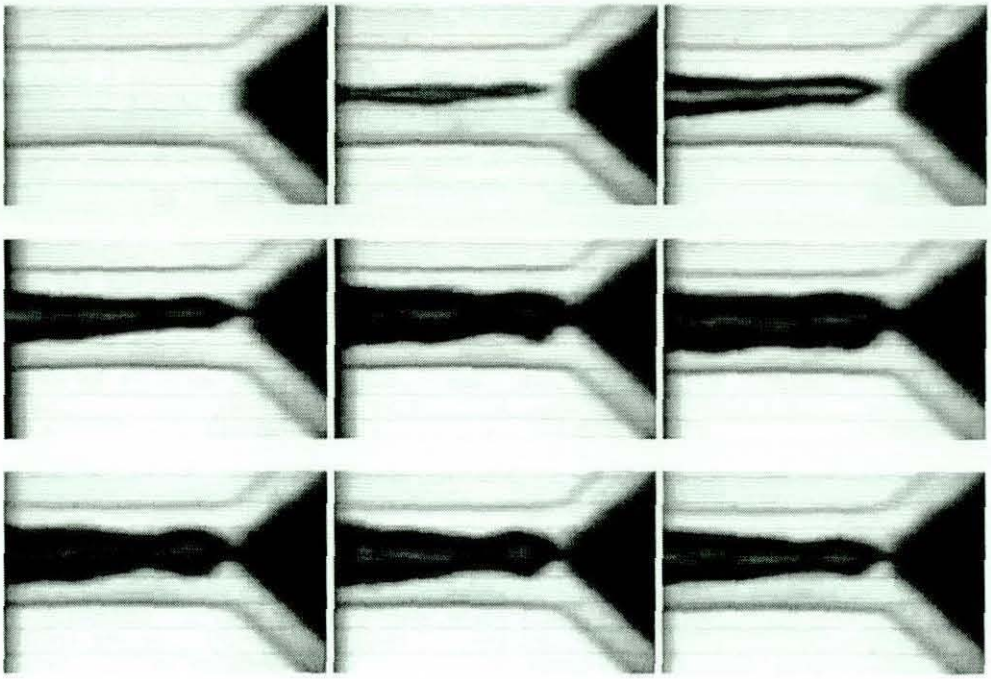

Figure B.2 Flow images of 45° swirler with 30° chamfered inlet orifice at 30 bar driving pressure.

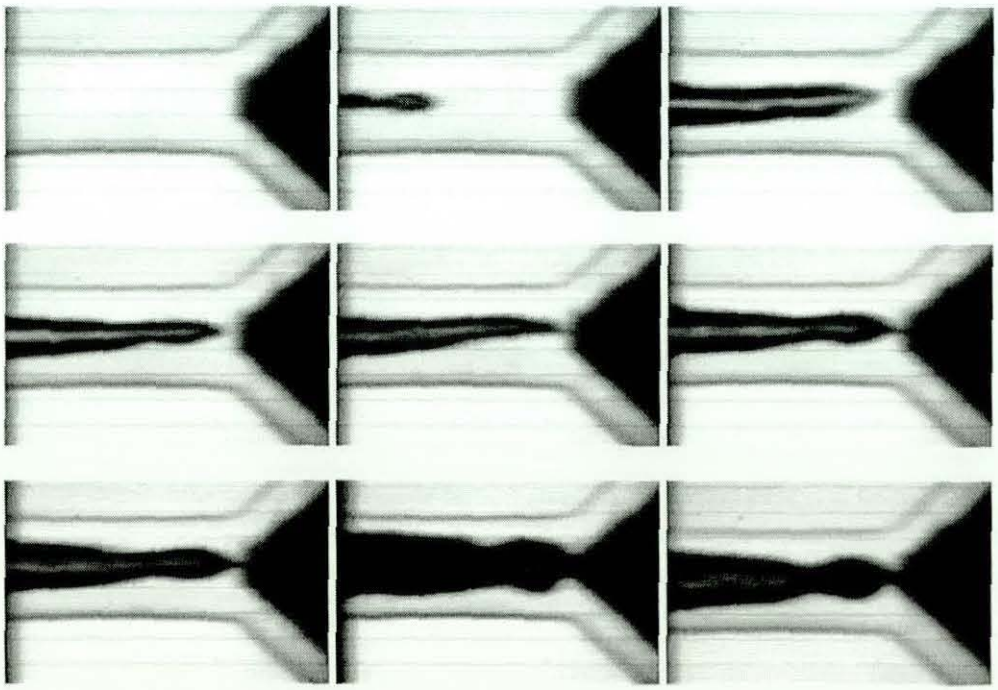

Figure B.3 Flow images of 45° swirler with 30° chamfered inlet orifice at 40 bar driving pressure.

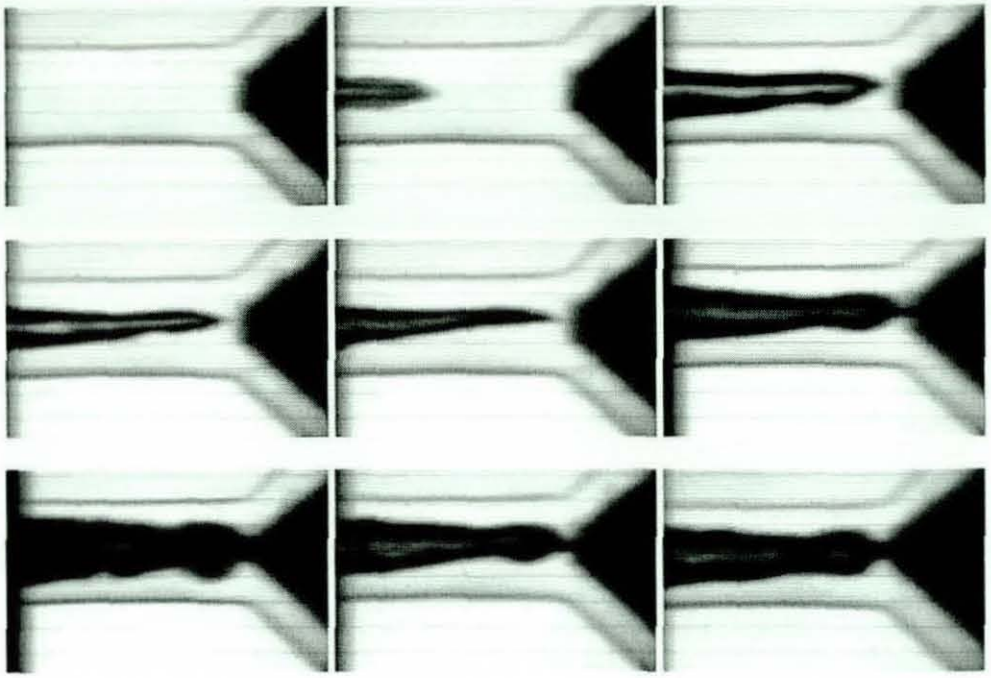

Figure B.4 Flow images of 45° swirler with 30° chamfered inlet orifice at 50 bar driving pressure.

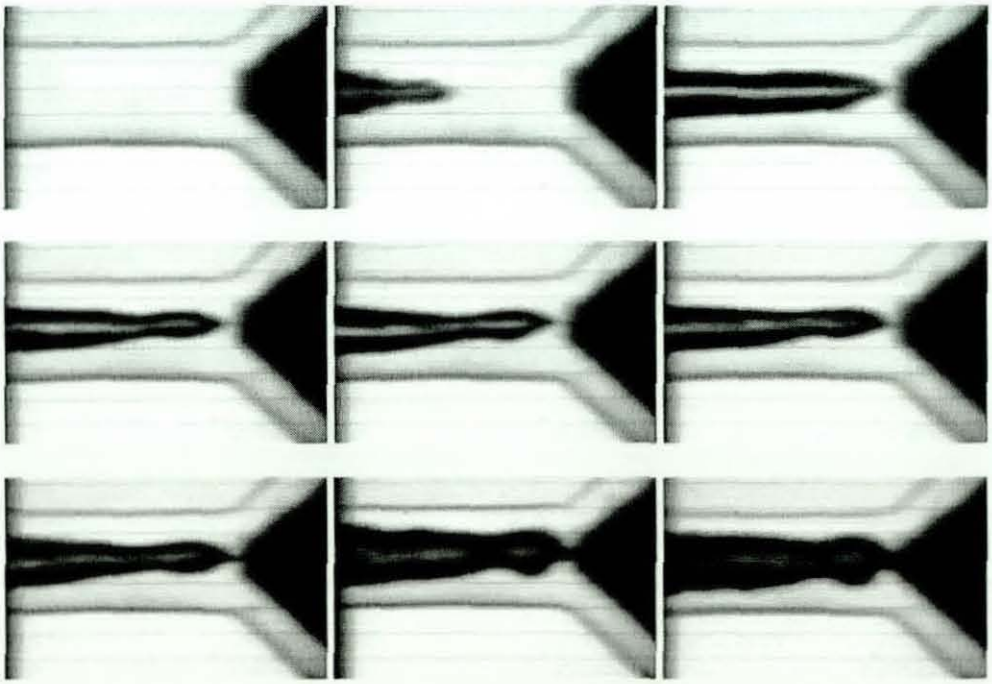

Figure B.5 Flow images of 45° swirler with 30° chamfered inlet orifice at 60 bar driving pressure.

B.1.1.2 45° CHAMFERED INLET ORIFICE

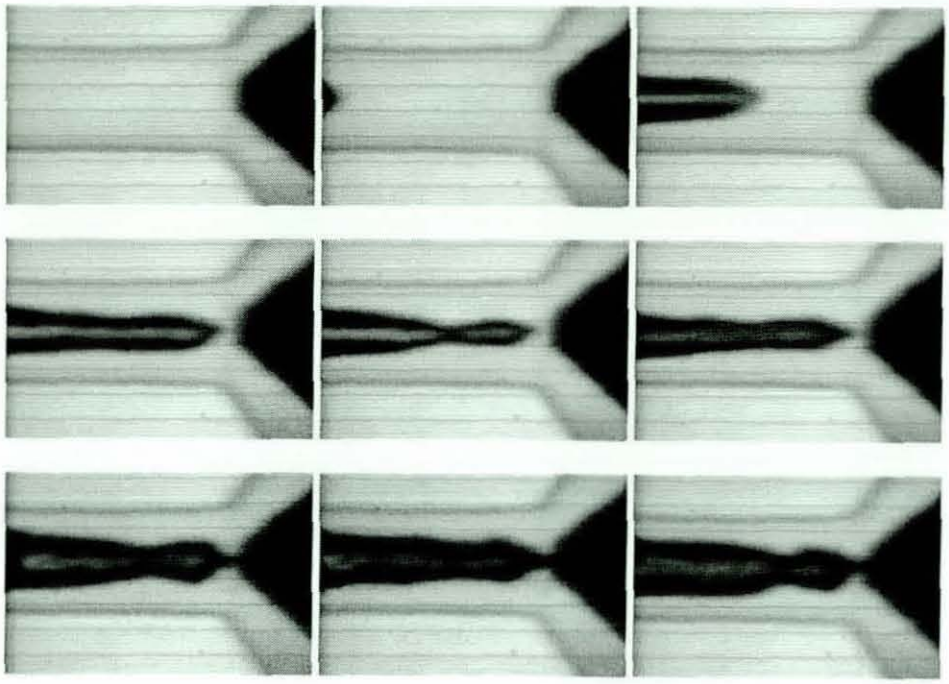

Figure B.6 Flow images of 45° swirler with 45° chamfered inlet orifice at 20 bar driving pressure.

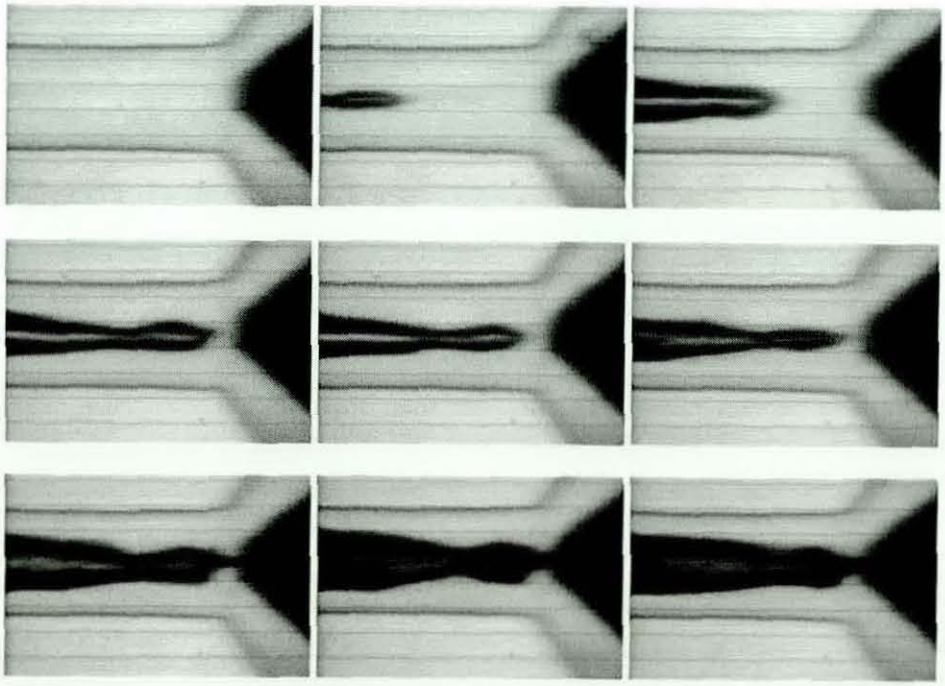

Figure B.7 Flow images of 45° swirler with 45° chamfered inlet orifice at 30 bar driving pressure.

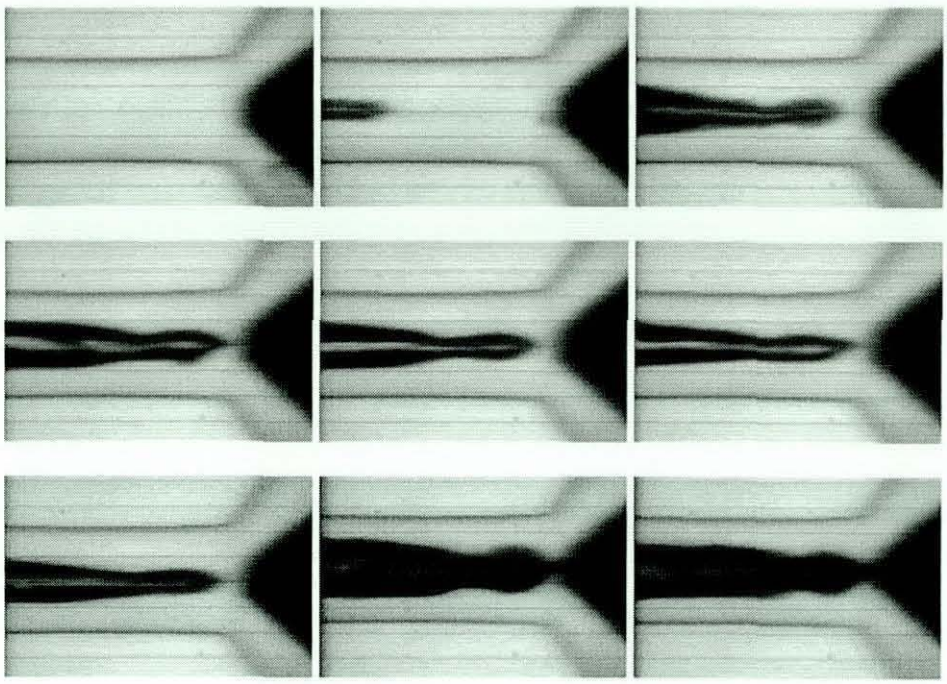

Figure B.8 Flow images of 45° swirler with 45° chamfered inlet orifice at 40 bar driving pressure.

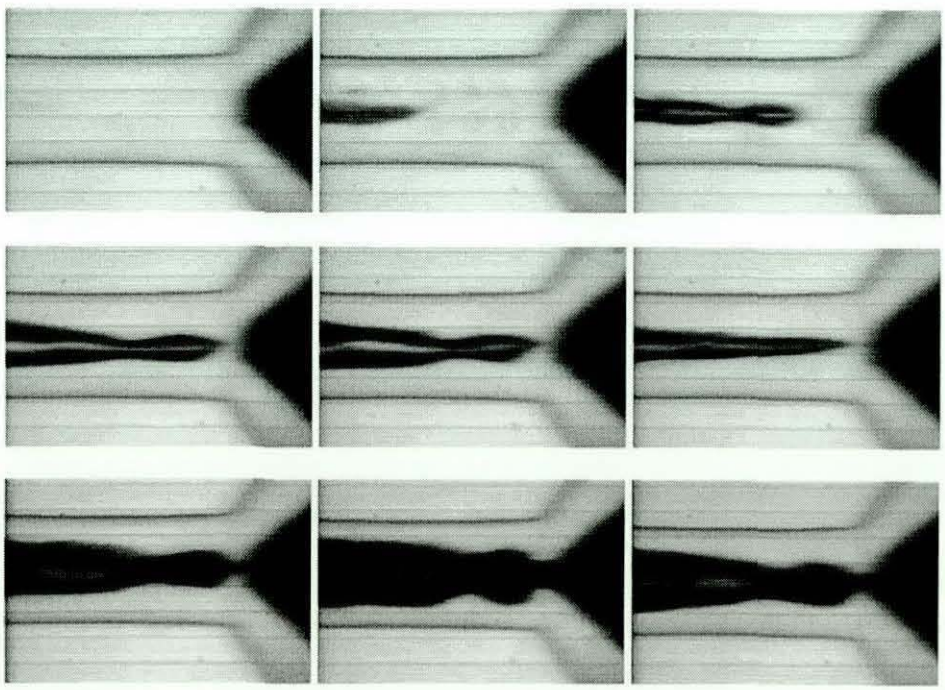

Figure B.9 Flow images of 45° swirler with 45° chamfered inlet orifice at 50 bar driving pressure.

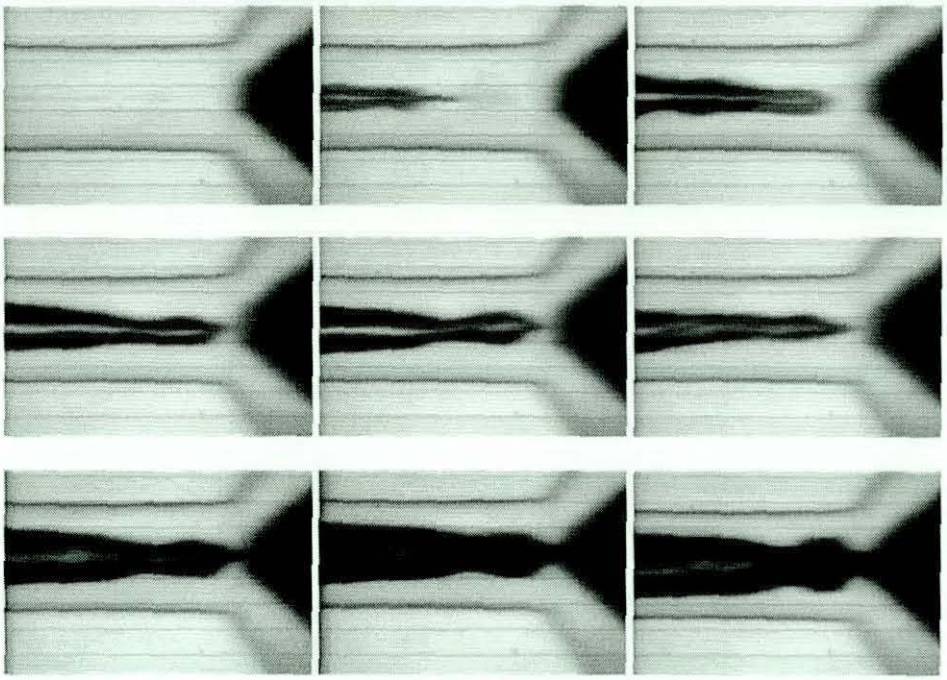

Figure B.10 Flow images of 45° swirler with 45° chamfered inlet orifice at 60 bar driving pressure.

B.1.1.3 60° CHAMFERED INLET ORIFICE

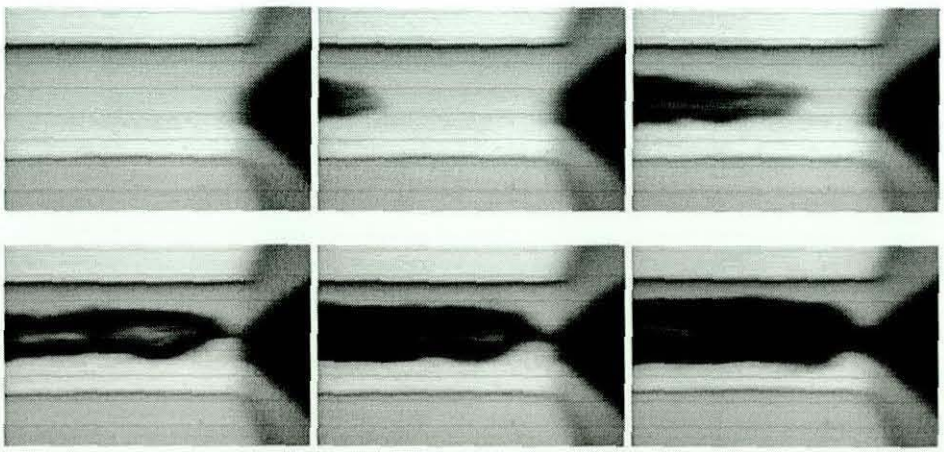

Figure B.11 Flow images of 45° swirler with 60° chamfered inlet orifice at 20 bar driving pressure.

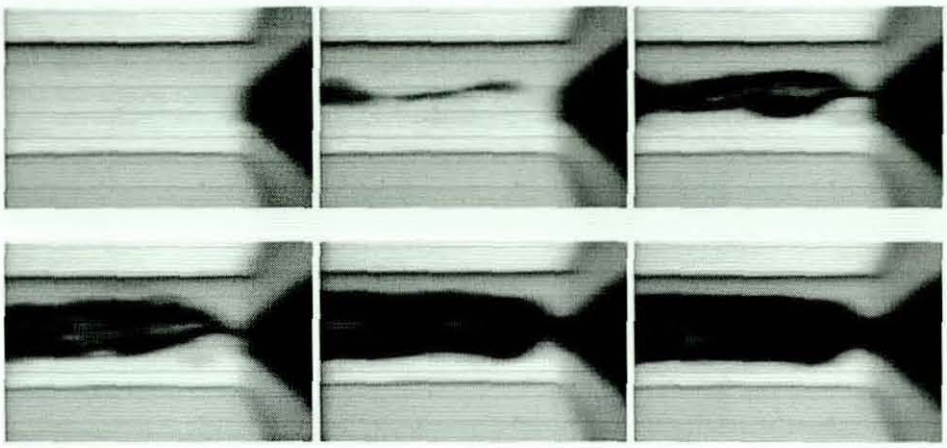

Figure B.12 Flow images of 45° swirler with 60° chamfered inlet orifice at 30 bar driving pressure.

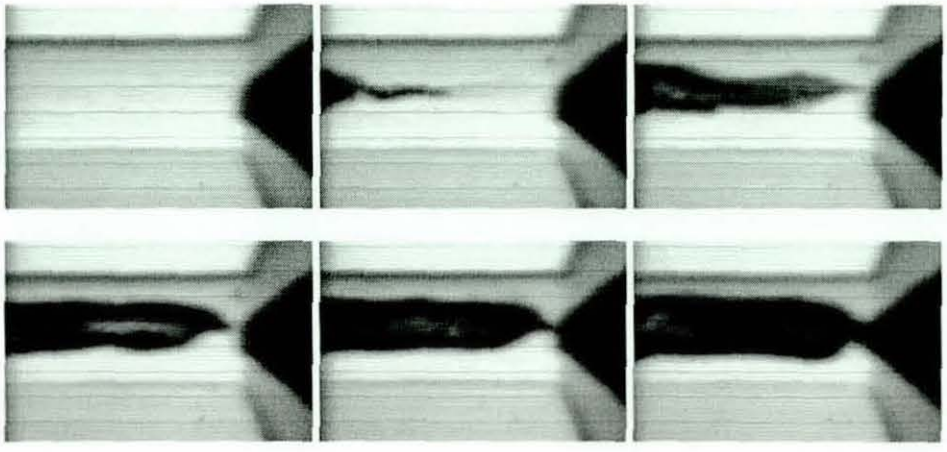

Figure B.13 Flow images of 45° swirler with 60° chamfered inlet orifice at 40 bar driving pressure.

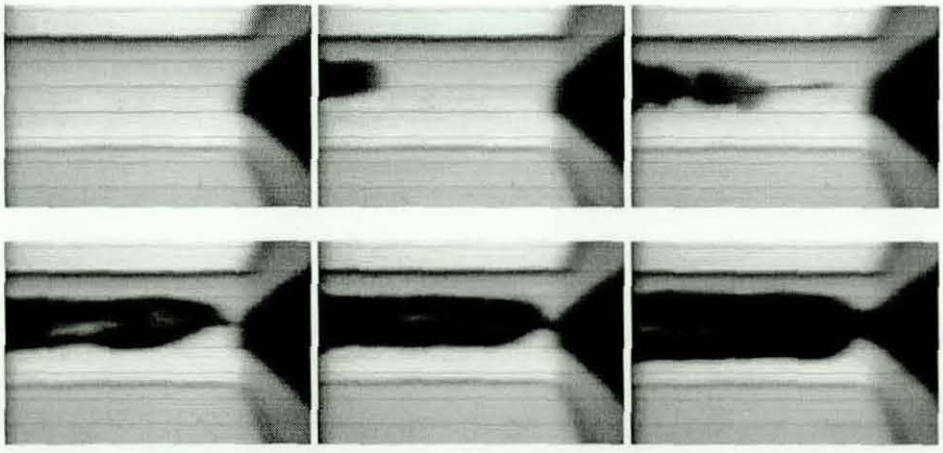

Figure B.14 Flow images of 45° swirler with 60° chamfered inlet orifice at 50 bar driving pressure.

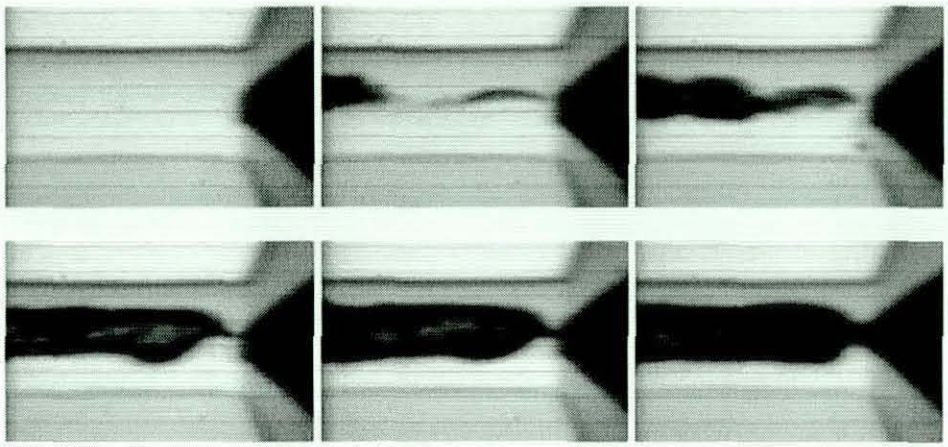

Figure B.15 Flow images of 45° swirler with 60° chamfered inlet orifice at 60 bar driving pressure.

B.1.2 In-nozzle Flow Profile for a 60° Swirler

B.1.2.1 30° CHAMFERED INLET ORIFICE

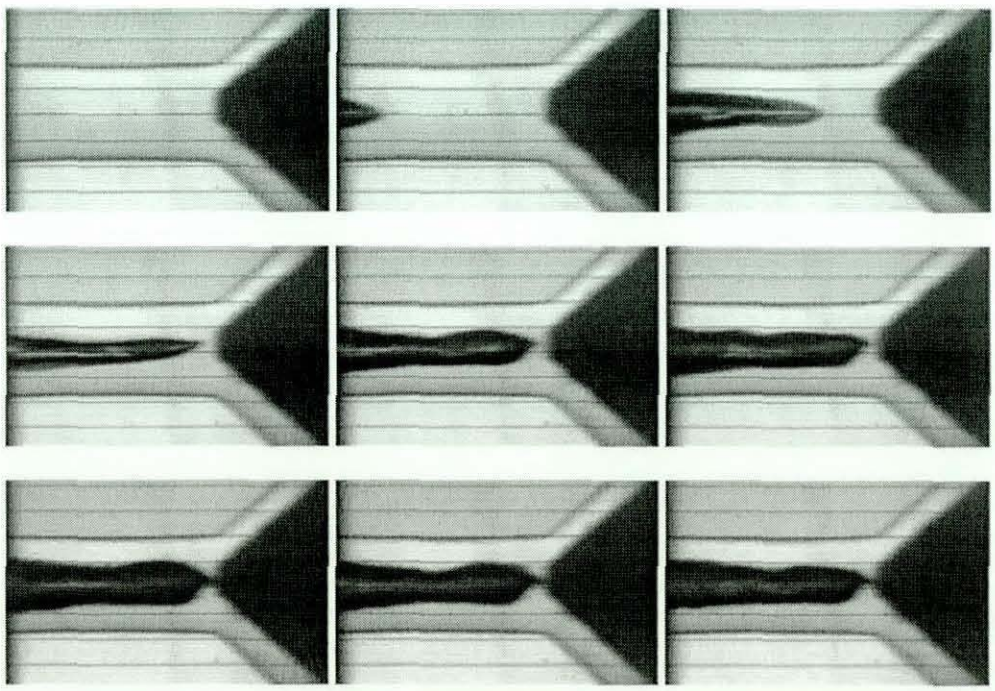

Figure B.16 Flow images of 60° swirler with 30° chamfered inlet orifice at 20 bar driving pressure.

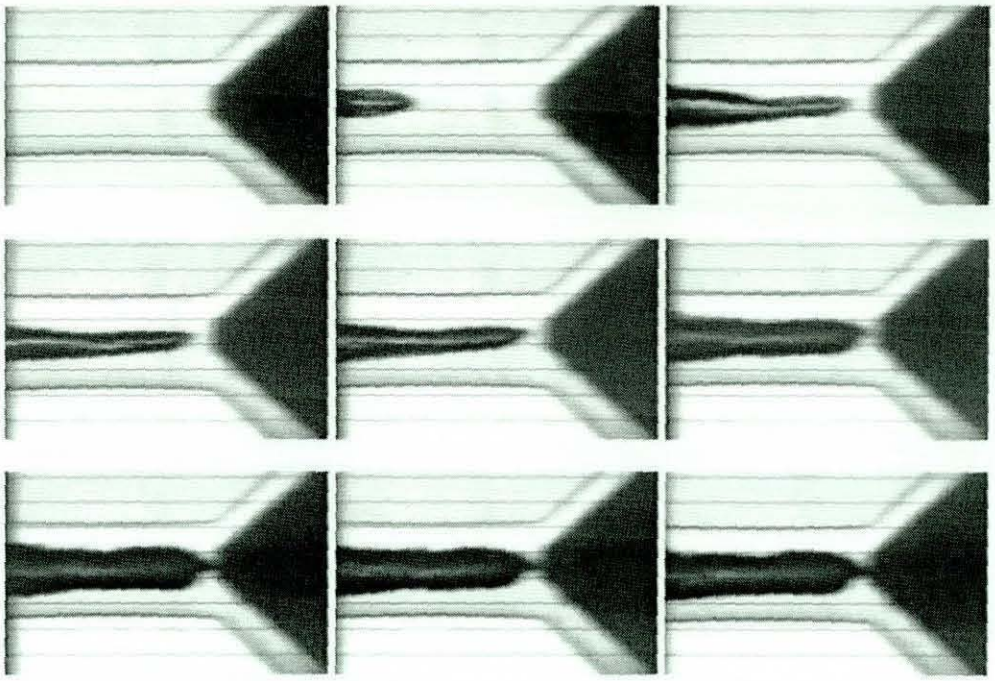

Figure B.17 Flow images of 60° swirler with 30° chamfered inlet orifice at 30 bar driving pressure.

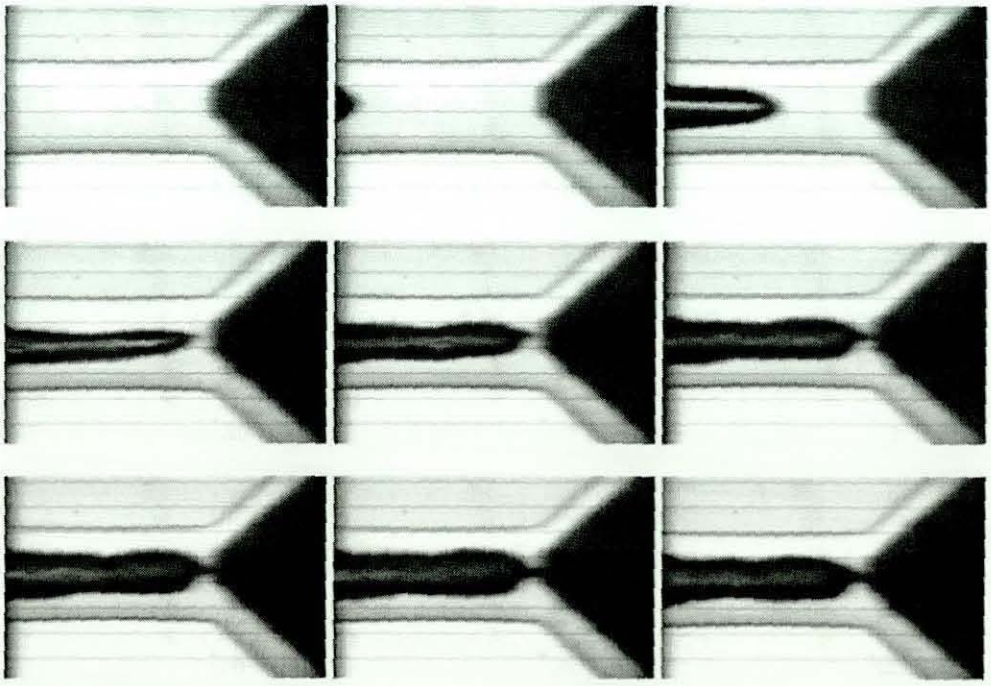

Figure B.18 Flow images of 60° swirler with 30° chamfered inlet orifice at 40 bar driving pressure.

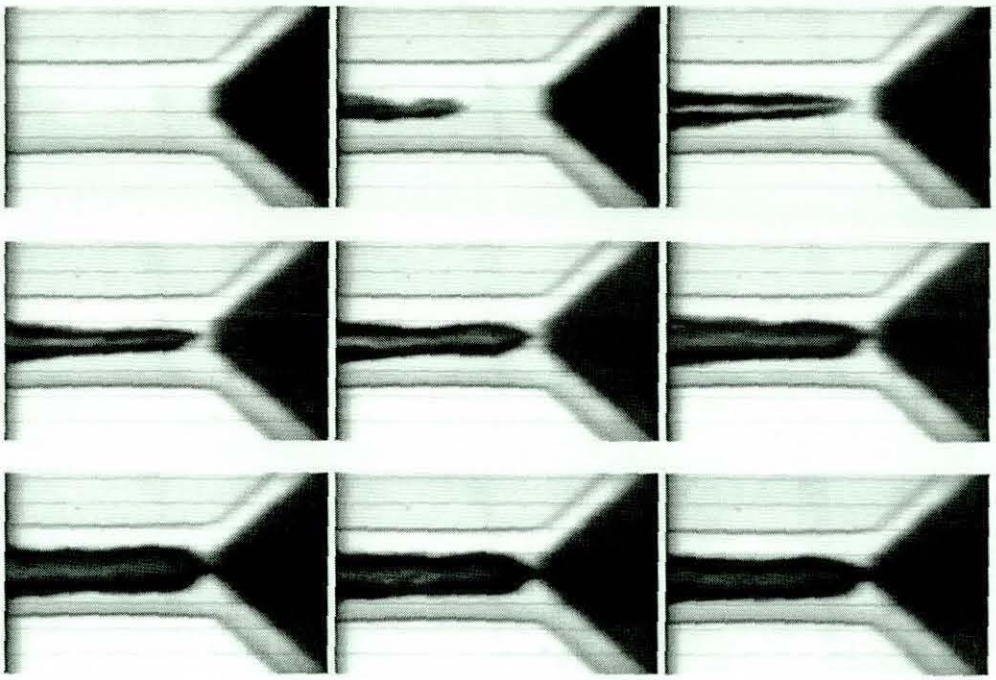

Figure B.19 Flow images of 60° swirler with 30° chamfered inlet orifice at 50 bar driving pressure.

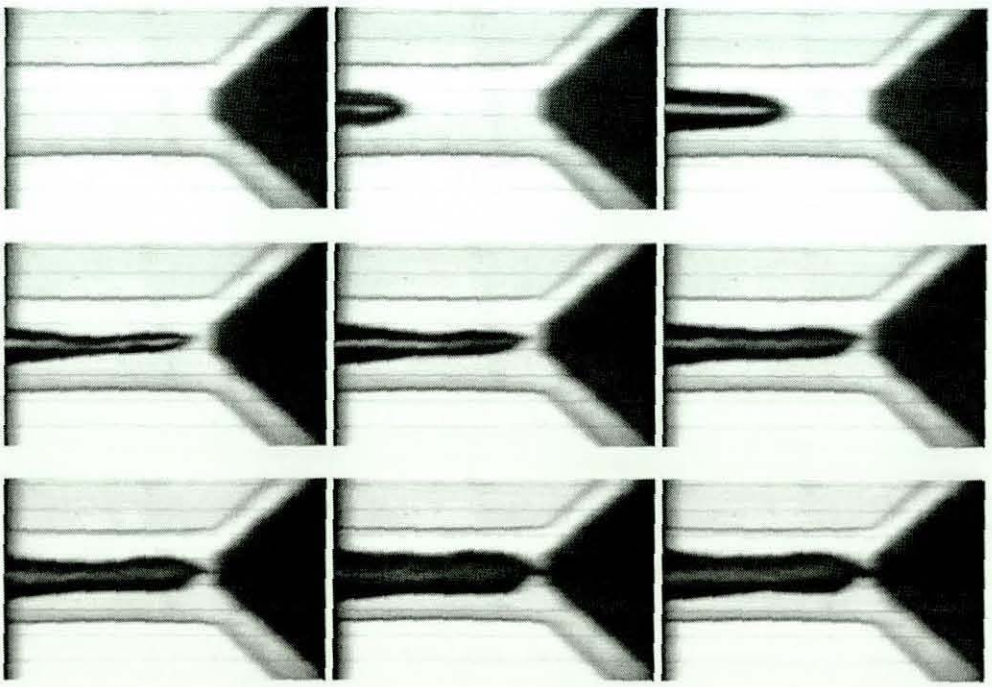

Figure B.20 Flow images of 60° swirler with 30° chamfered inlet orifice at 60 bar driving pressure.

B.1.2.2 45° CHAMFERED INLET ORIFICE

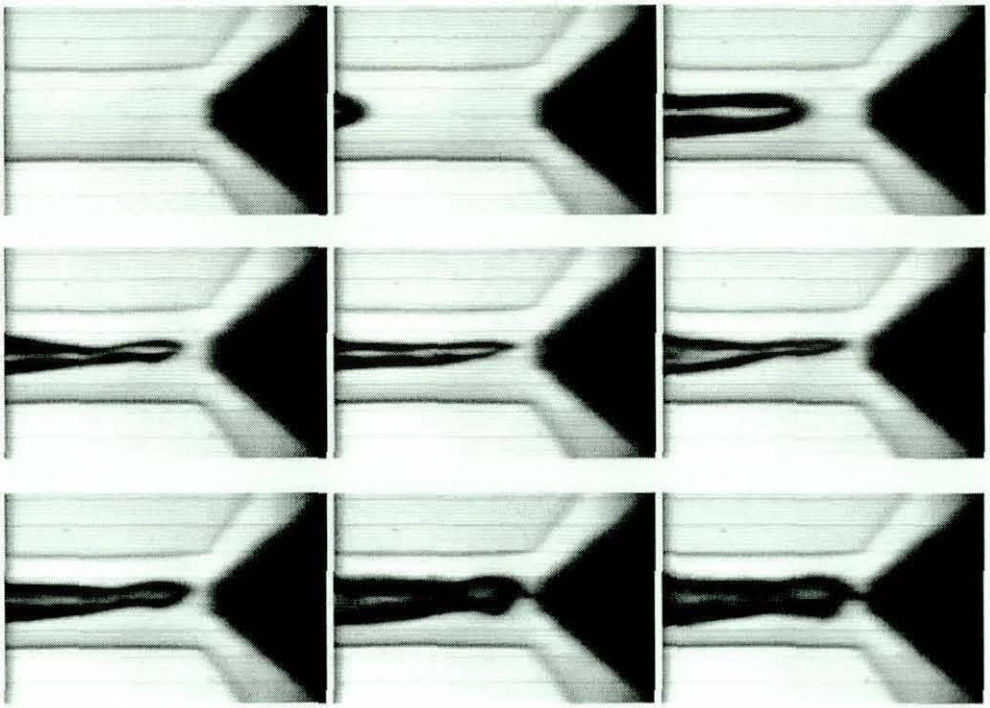

Figure B.21 Flow images of 60° swirler with 45° chamfered inlet orifice at 20 bar driving pressure.

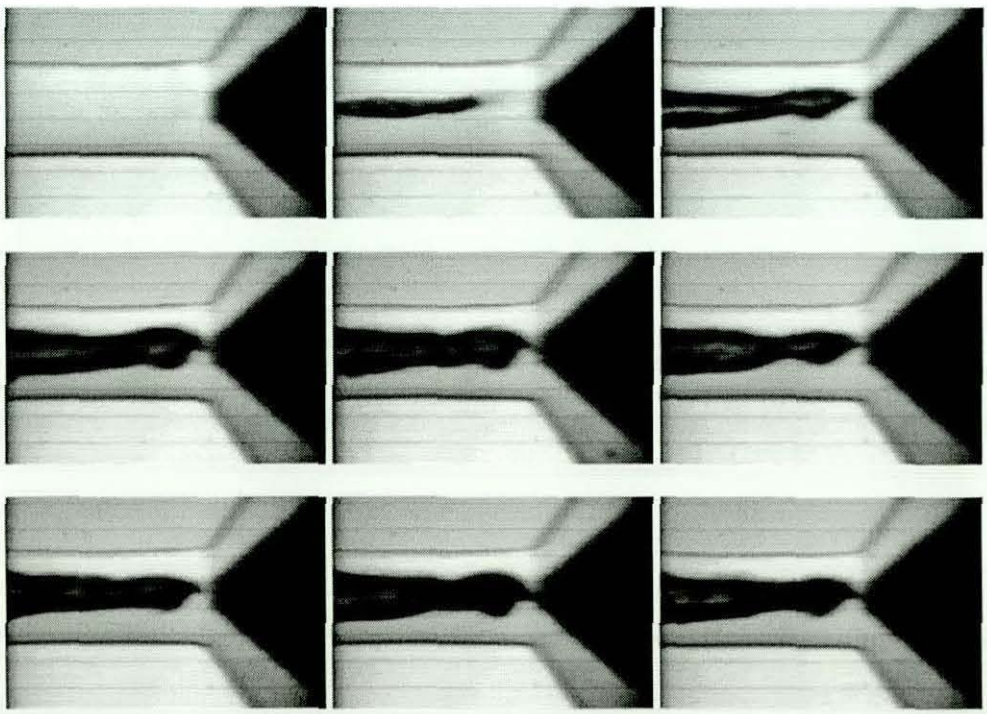

Figure B.22 Flow images of 60° swirler with 45° chamfered inlet orifice at 30 bar driving pressure.

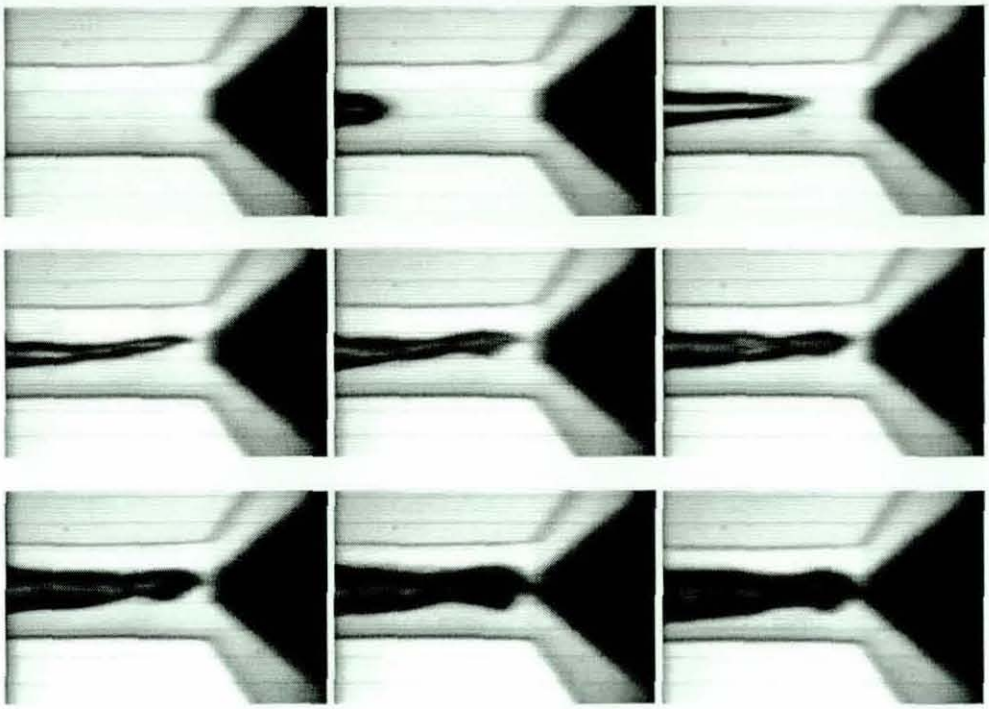

Figure B.23 Flow images of 60° swirler with 45° chamfered inlet orifice at 40 bar driving pressure.

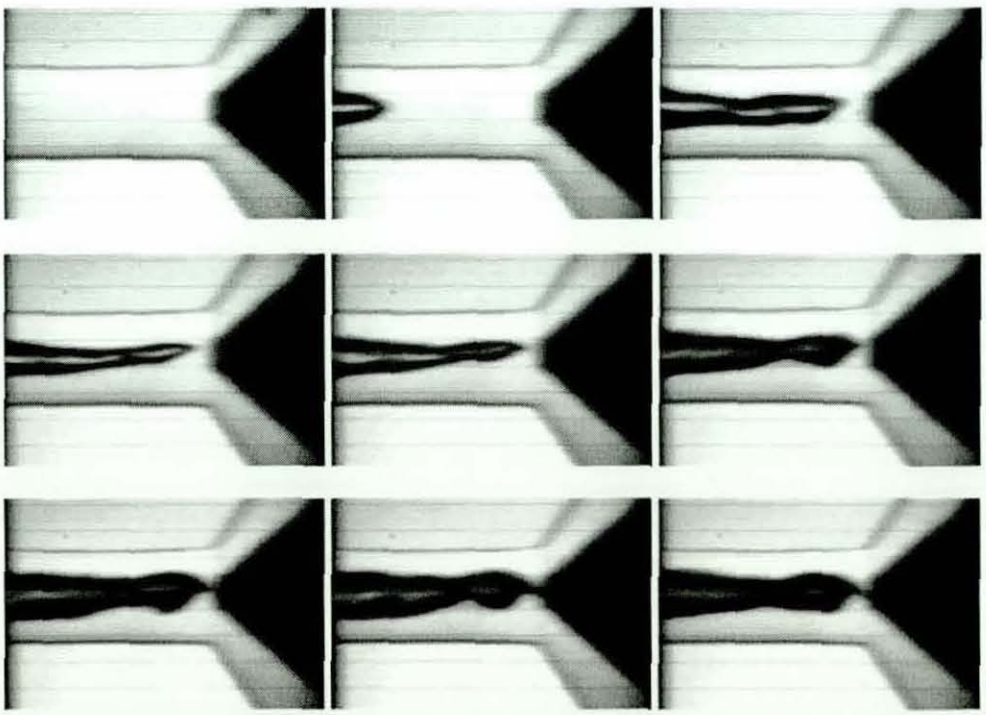

Figure B.24 Flow images of 60° swirler with 45° chamfered inlet orifice at 50 bar driving pressure.

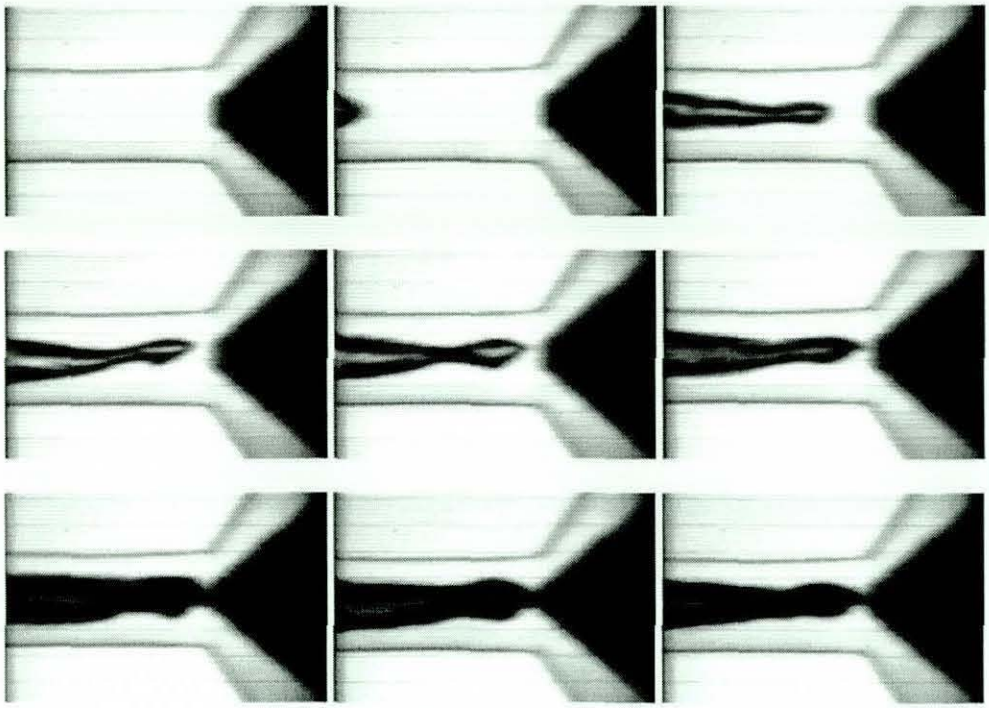

Figure B.25 Flow images of 60° swirler with 45° chamfered inlet orifice at 60 bar driving pressure.

B.1.2.3 60° CHAMFERED INLET ORIFICE

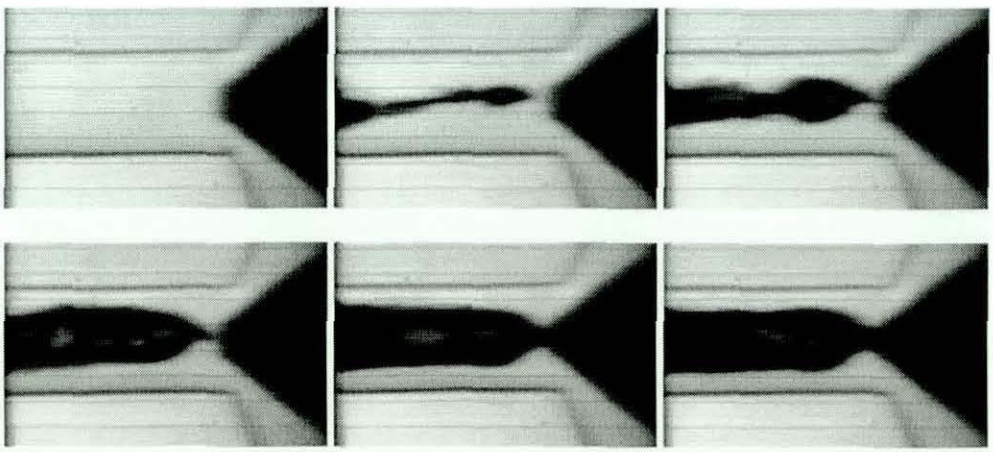

Figure B.26 Flow images of 60° swirler with 60° chamfered inlet orifice at 20 bar driving pressure.

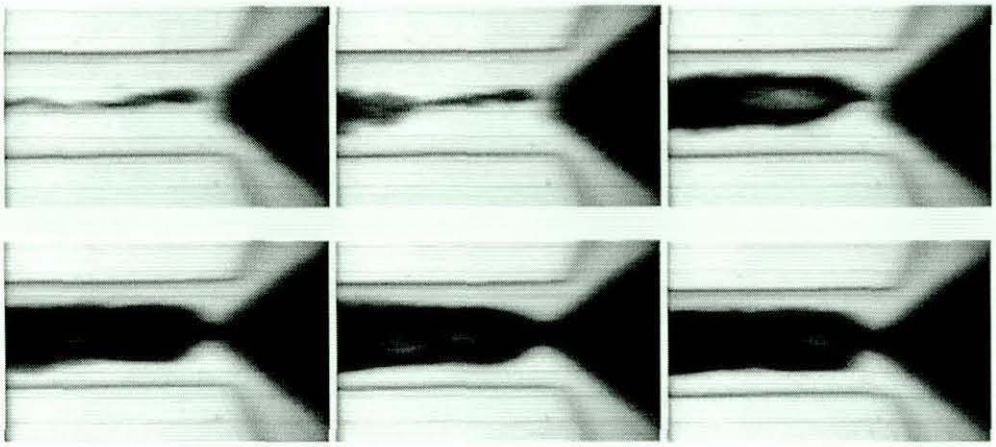

Figure B.27 Flow images of 60° swirler with 60° chamfered inlet orifice at 30 bar driving pressure.

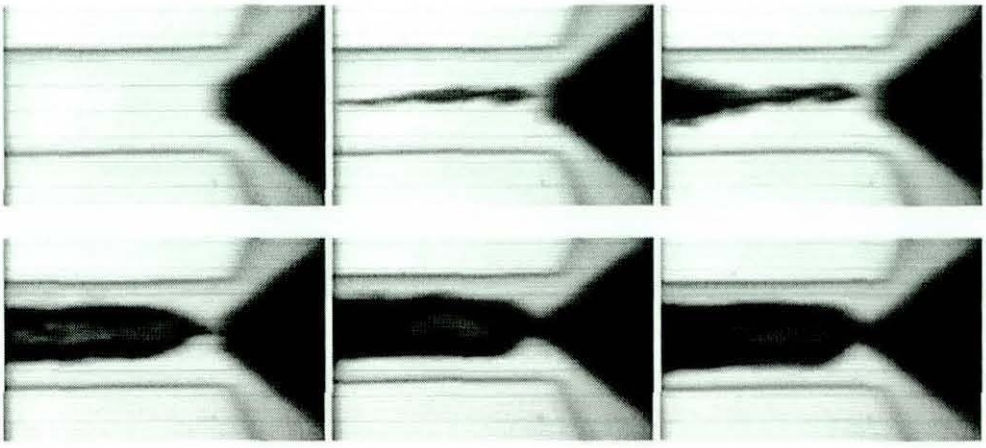

Figure B.28 Flow images of 60° swirler with 60° chamfered inlet orifice at 40 bar driving pressure.

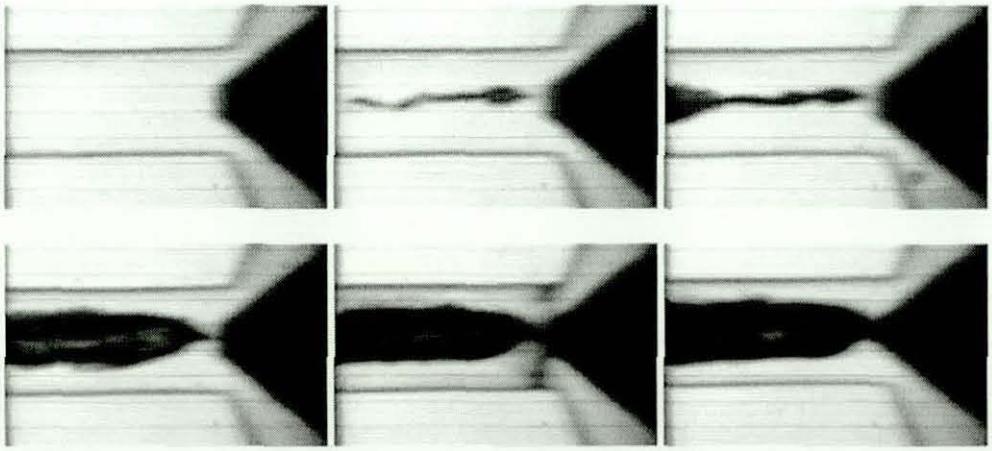

Figure B.29 Flow images of 60° swirler with 60° chamfered inlet orifice at 50 bar driving pressure.

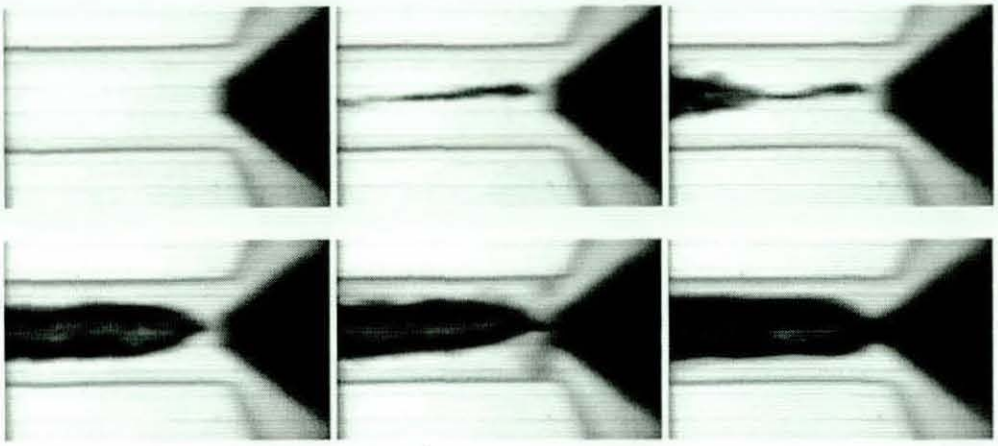

Figure B.30 Flow images of 60° swirler with 60° chamfered inlet orifice at 60 bar driving pressure.

B.1.2 External Flow Profile

B.1.2.1 45° SWIRLER

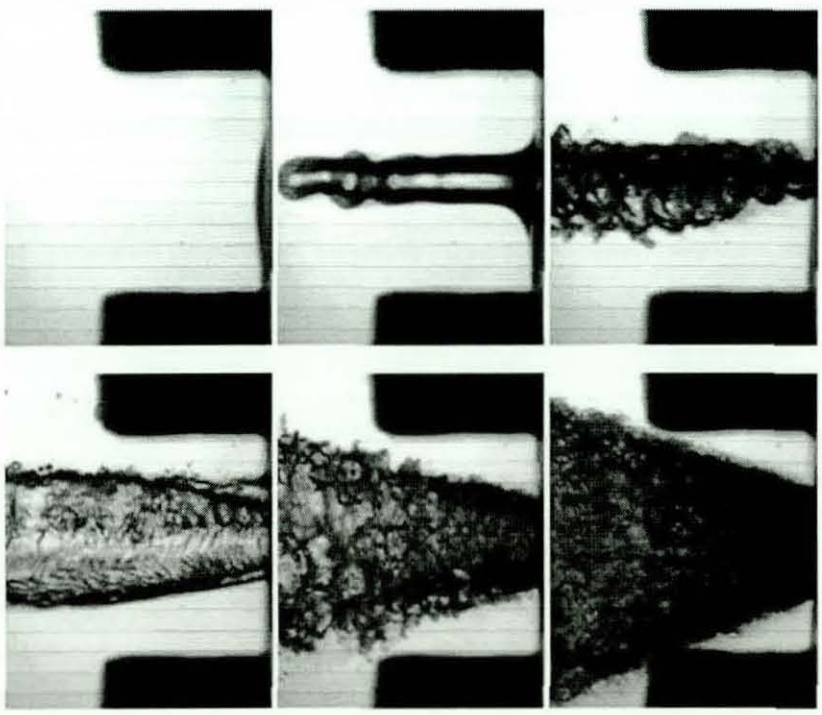

Figure B.31 Sequential flow images of a 45° swirler with a 30° orifice at 30 bar driving pressure.

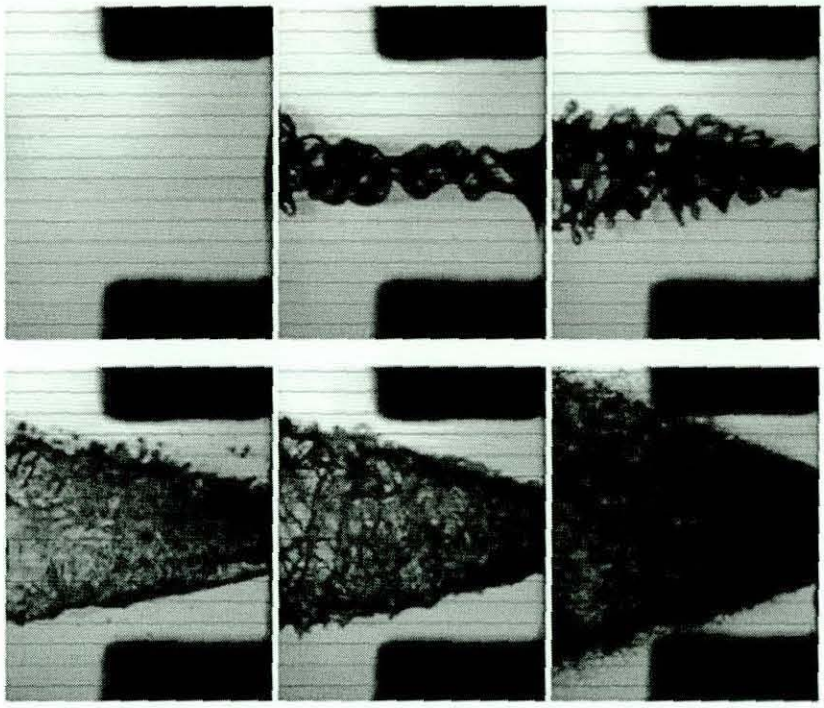

Figure B.32 Sequential flow images of a 45° swirler with a 45° orifice at 30 bar driving pressure.

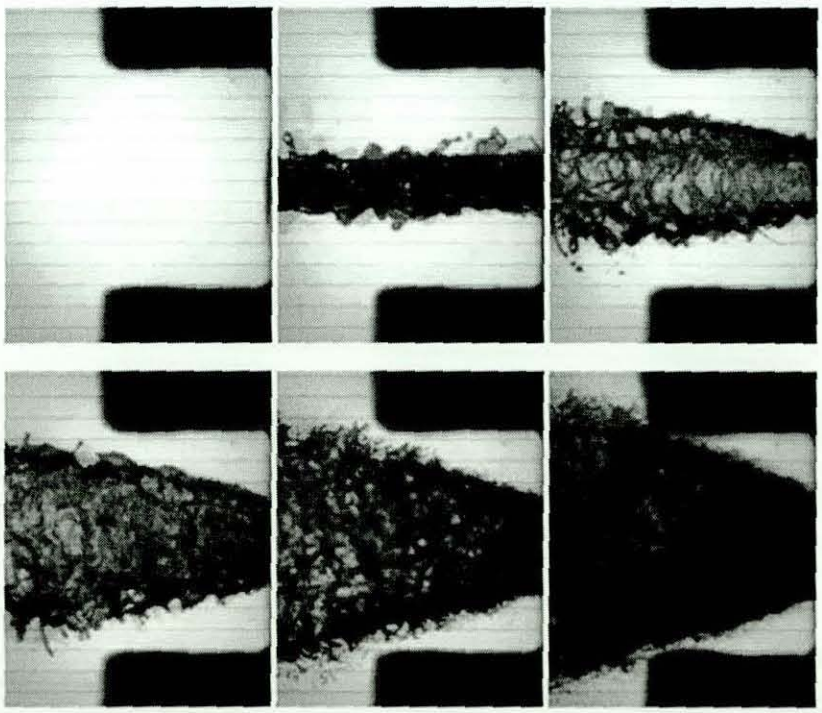

Figure B.33 Sequential flow images of a 45° swirler with a 60° orifice at 30 bar driving pressure.

B.1.2.2 60° SWIRLER

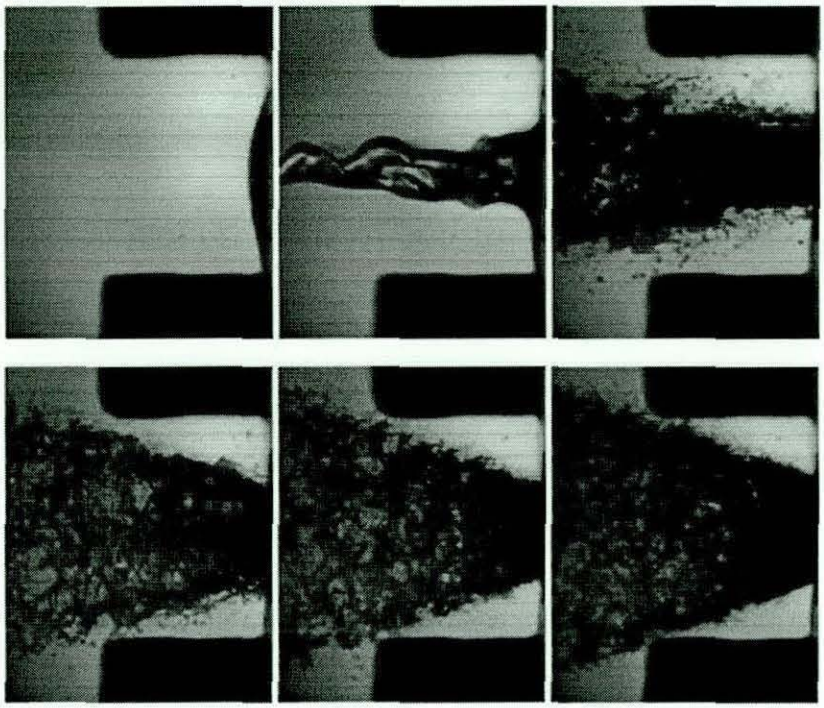

Figure B.34 Sequential flow images of a 60° swirler with a 30° orifice at 30 bar driving pressure.

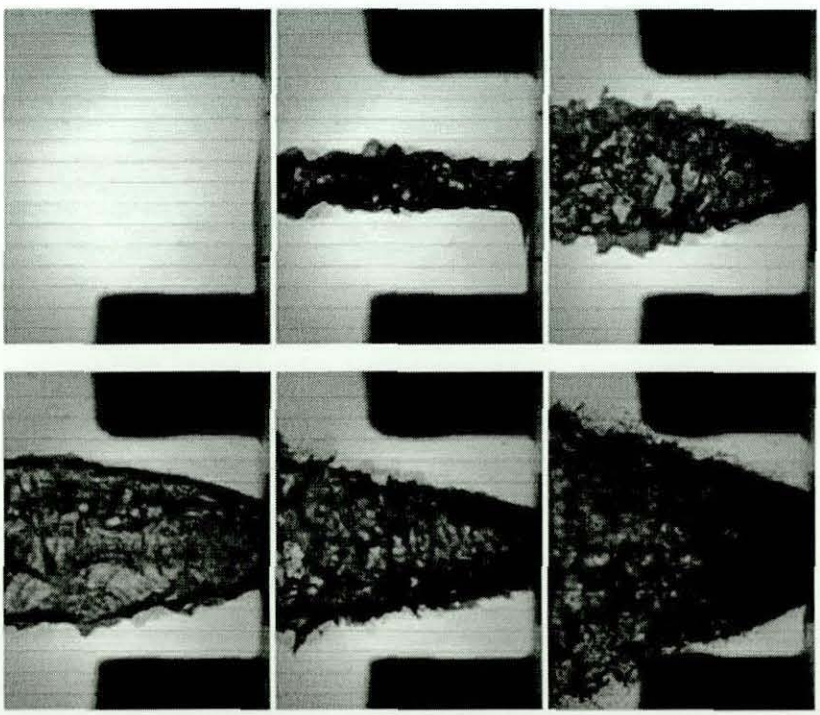

Figure B.35 Sequential flow images of a 60° swirler with a 45° orifice at 30 bar driving pressure.

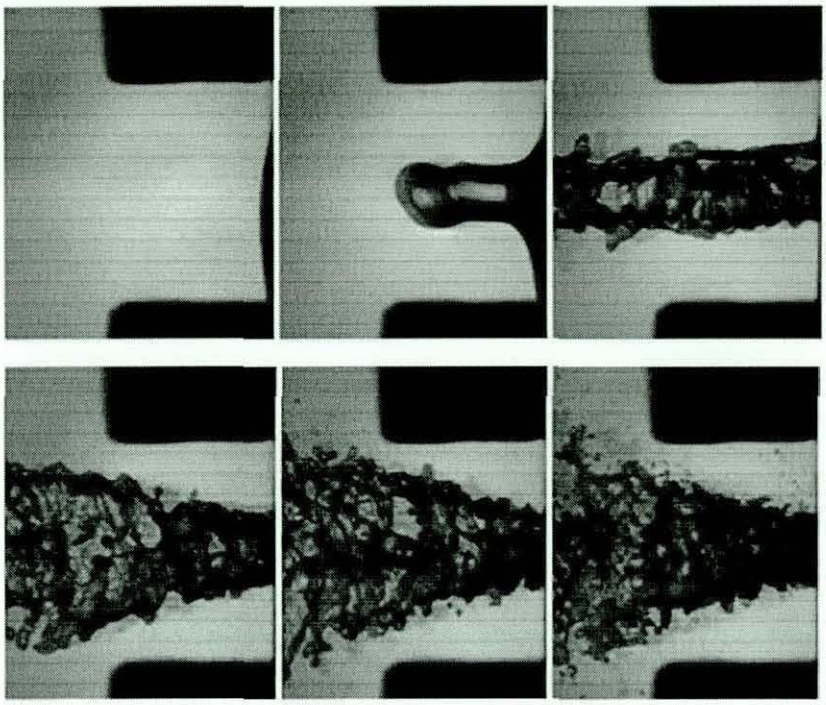

Figure B.36 Sequential flow images of a 60° swirler with a 60° orifice at 30 bar driving pressure.

B.2 FLUORESCENT PARTICLE IMAGE VELOCIMETRY

B.2.1 45° Swirler Velocity Profile

B.2.1.1 30° CHAMFERED INLET ORIFICE

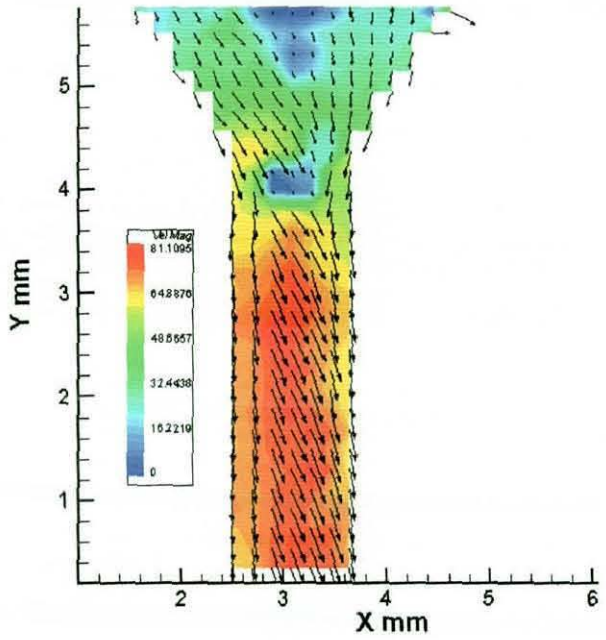

Figure B.37 Average velocity magnitudes for 30° chamfered inlet orifice at 30 bar driving pressure.

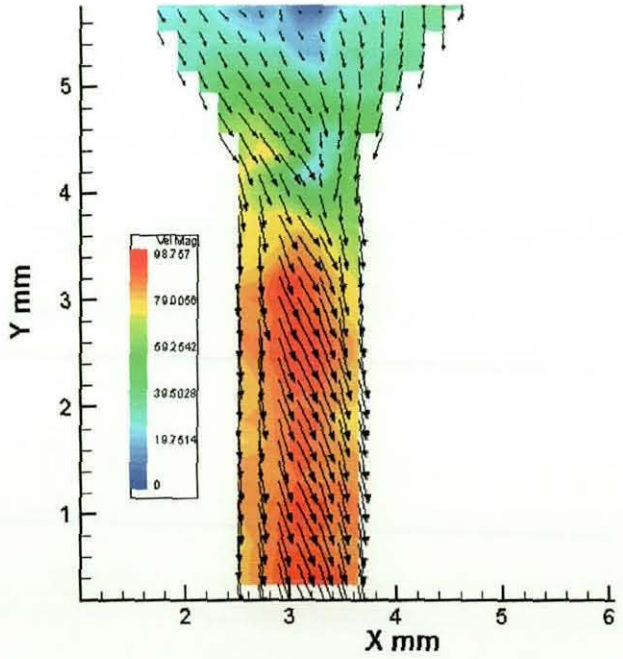

Figure B.38 Average velocity magnitudes for 30° chamfered inlet orifice at 40 bar driving pressure.

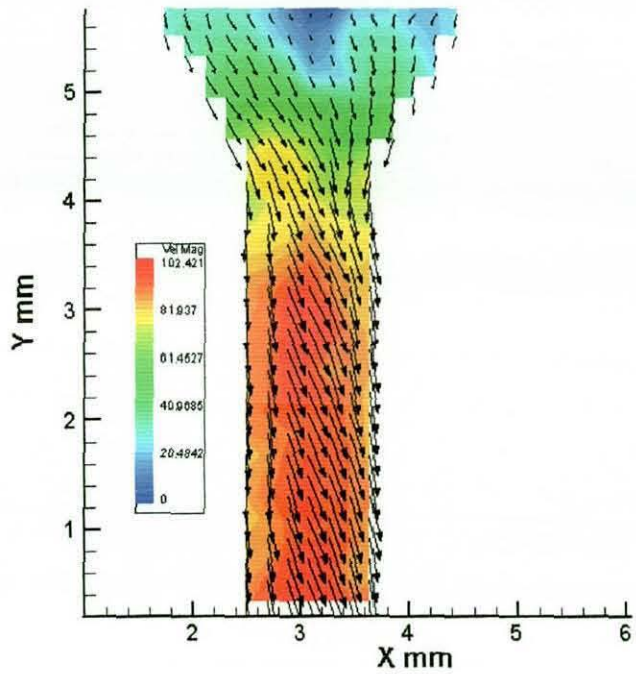

Figure B.39 Average velocity magnitudes for 30° chamfered inlet orifice at 50 bar driving pressure.

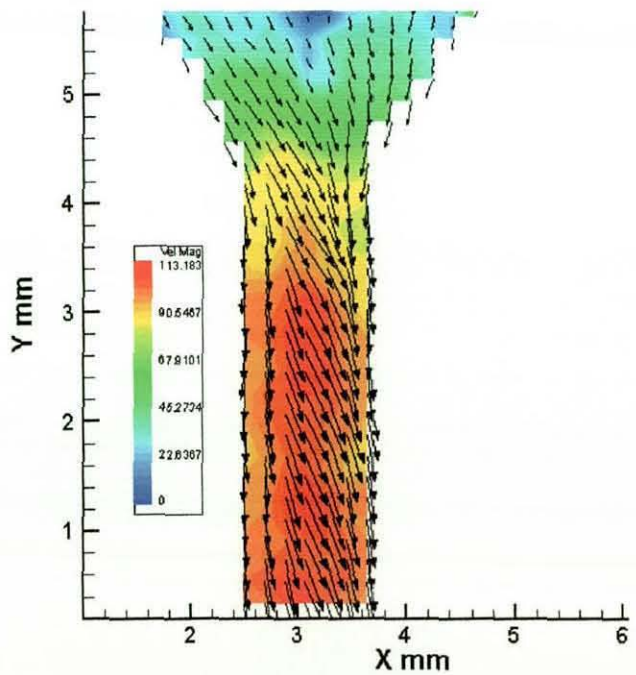

Figure B.40 Average velocity magnitudes for 30° chamfered inlet orifice at 60 bar driving pressure.

B.2.1.2 45° CHAMFERED INLET ORIFICE

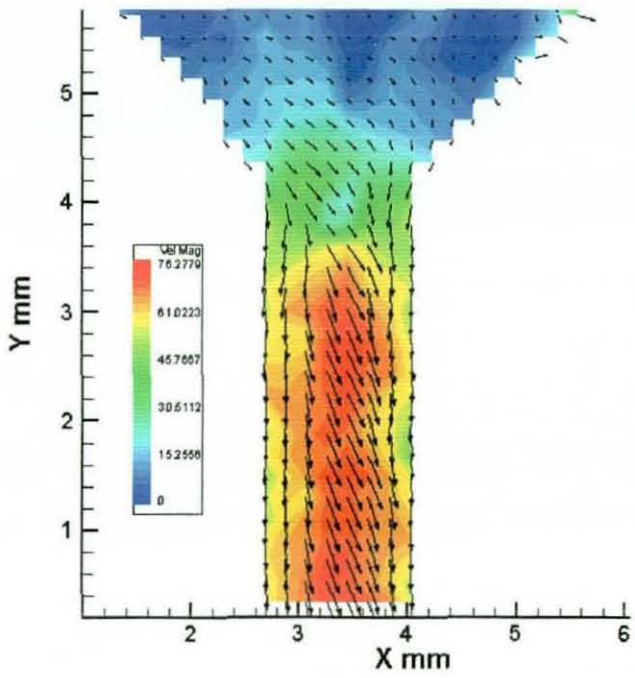

Figure B.41 Average velocity magnitudes for 45° chamfered inlet orifice at 30 bar driving pressure.

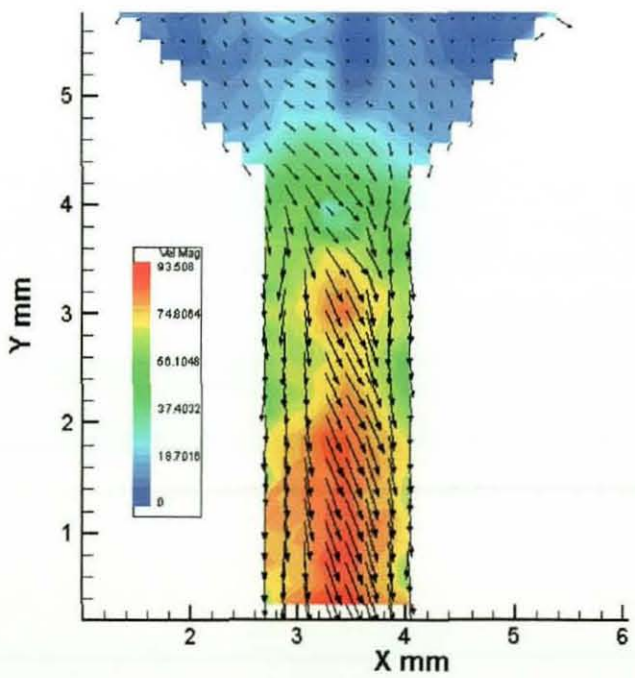

Figure B.42 Average velocity magnitudes for 45° chamfered inlet orifice at 40 bar driving pressure.

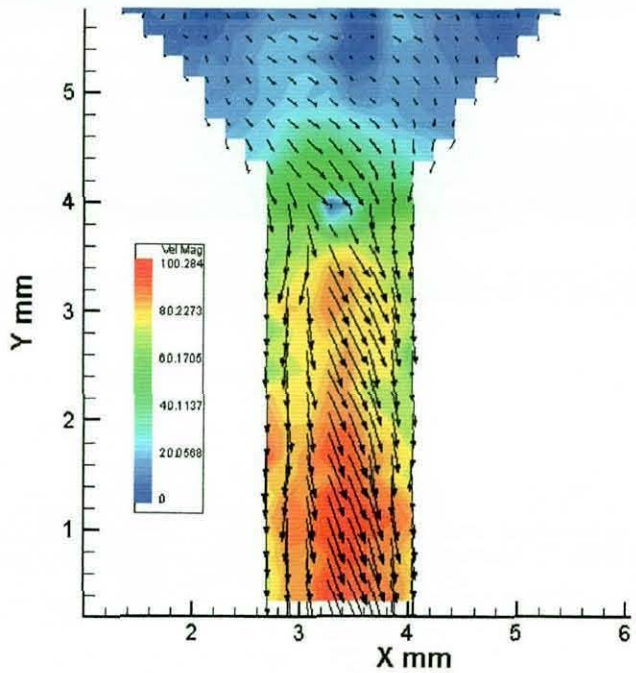

Figure B.43 Average velocity magnitudes for 45° chamfered inlet orifice at 50 bar driving pressure.

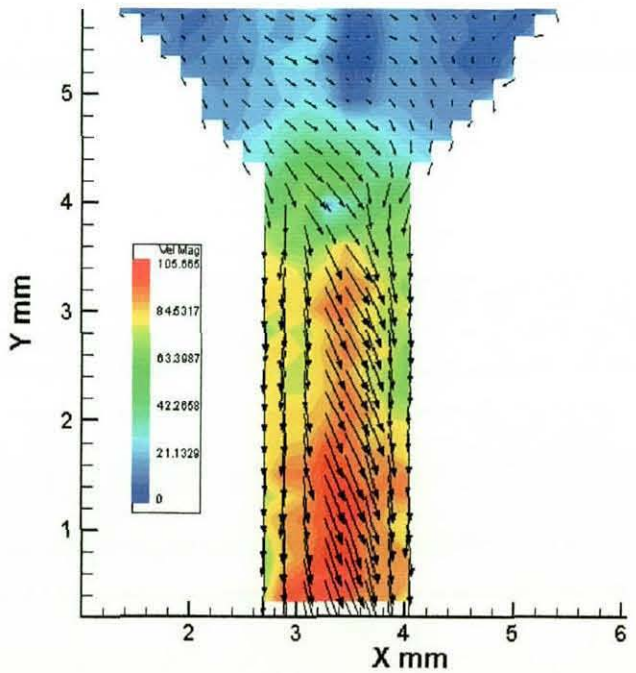

Figure B.44 Average velocity magnitudes for 45° chamfered inlet orifice at 60 bar driving pressure.

B.2.1.3 60° CHAMFERED INLET ORIFICE

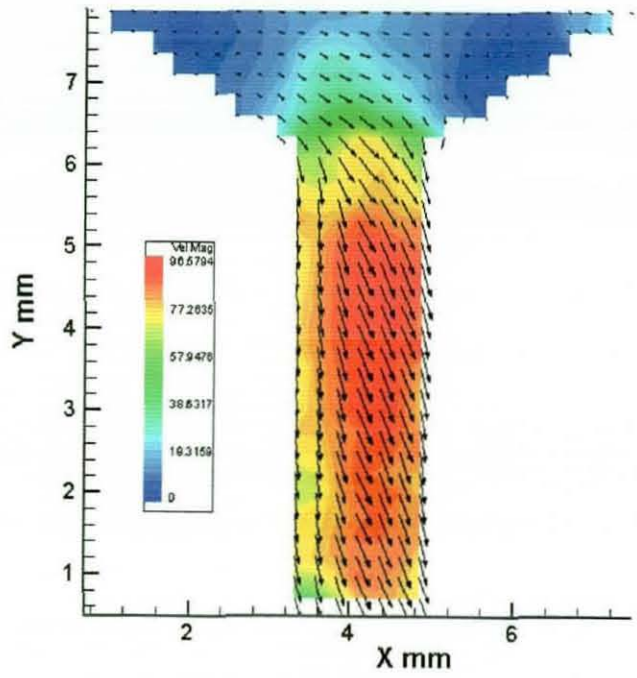

Figure B.45 Average velocity magnitudes for 60° chamfered inlet orifice at 30 bar driving pressure.

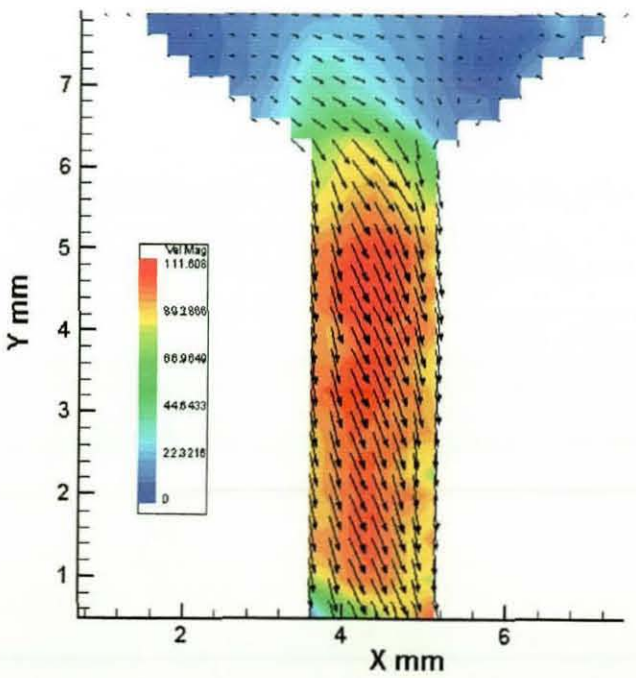

Figure B.46 Average velocity magnitudes for 60° chamfered inlet orifice at 40 bar driving pressure.

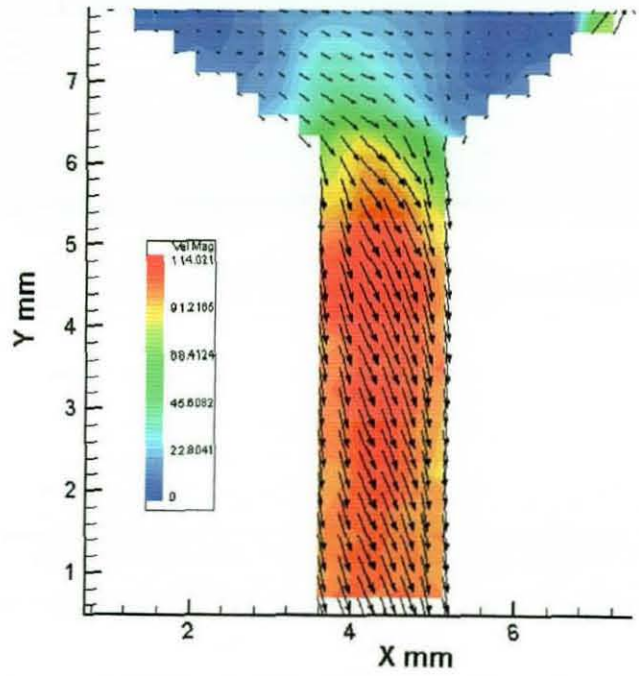

Figure B.47 Average velocity magnitudes for 60° chamfered inlet orifice at 50 bar driving pressure.

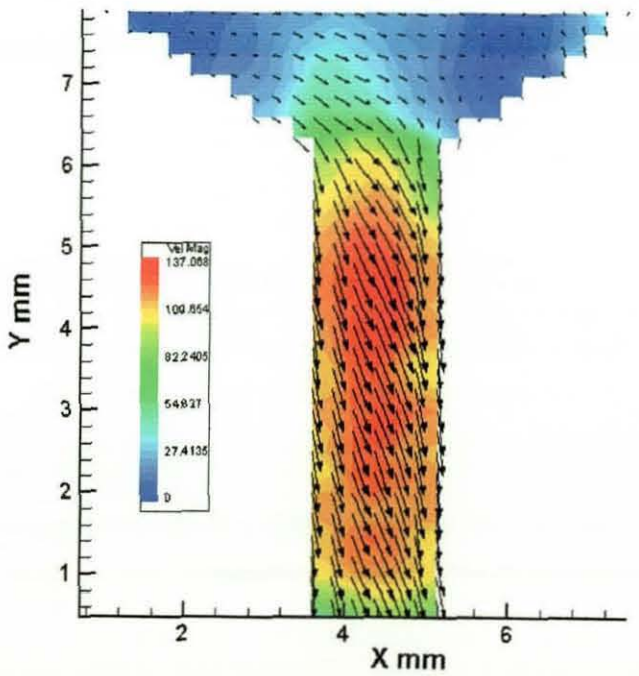

Figure B.48 Average velocity magnitudes for 60° chamfered inlet orifice at 60 bar driving pressure.

B.2.2 60° Swirler Velocity Profile

B.2.2.1 30° CHAMFERED INLET ORIFICE

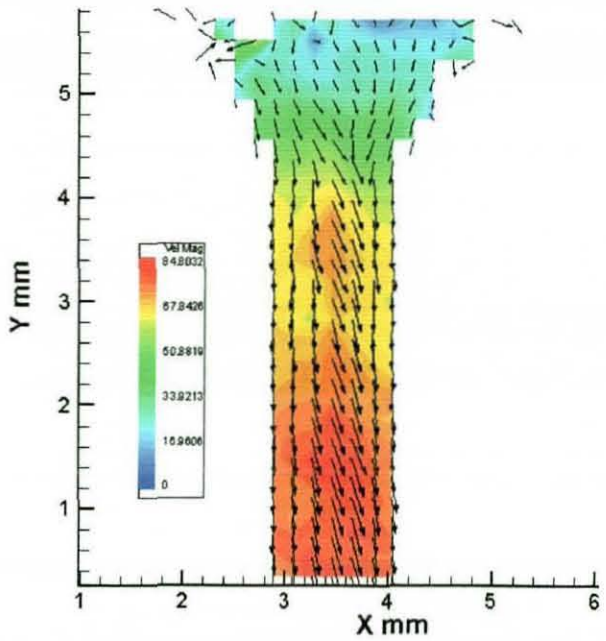

Figure B.49 Average velocity magnitudes for 30° chamfered inlet orifice at 30 bar driving pressure.

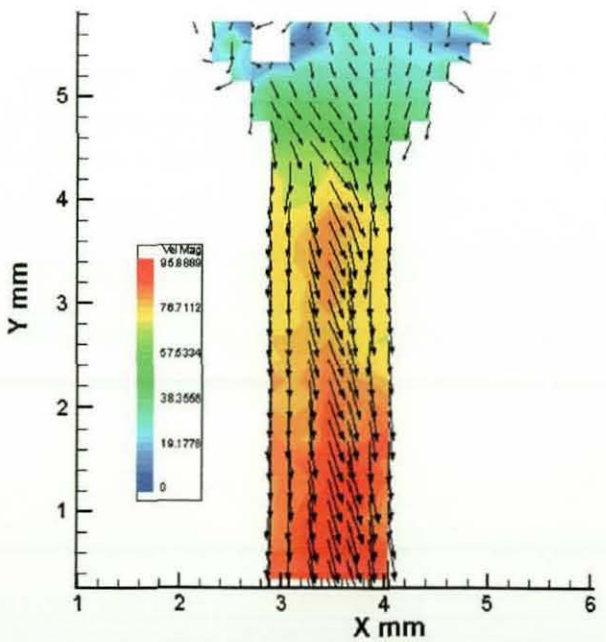

Figure B.50 Average velocity magnitudes for 30° chamfered inlet orifice at 40 bar driving pressure.

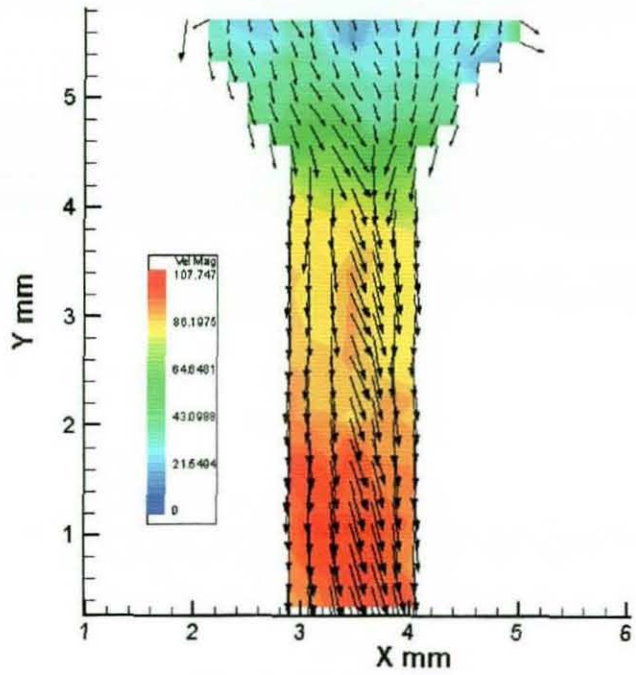

Figure B.51 Average velocity magnitudes for 30° chamfered inlet orifice at 50 bar driving pressure.

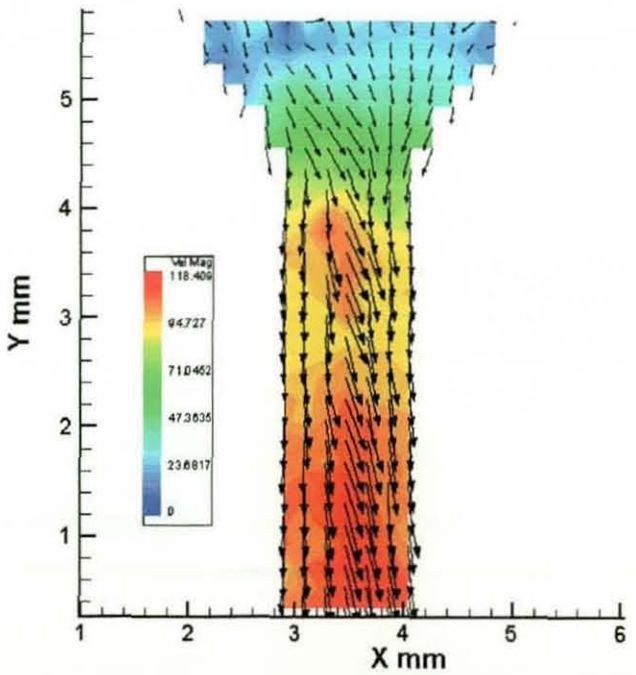

Figure B.52 Average velocity magnitudes for 30° chamfered inlet orifice at 60 bar driving pressure.

B.2.2.2 45° CHAMFERED INLET ORIFICE

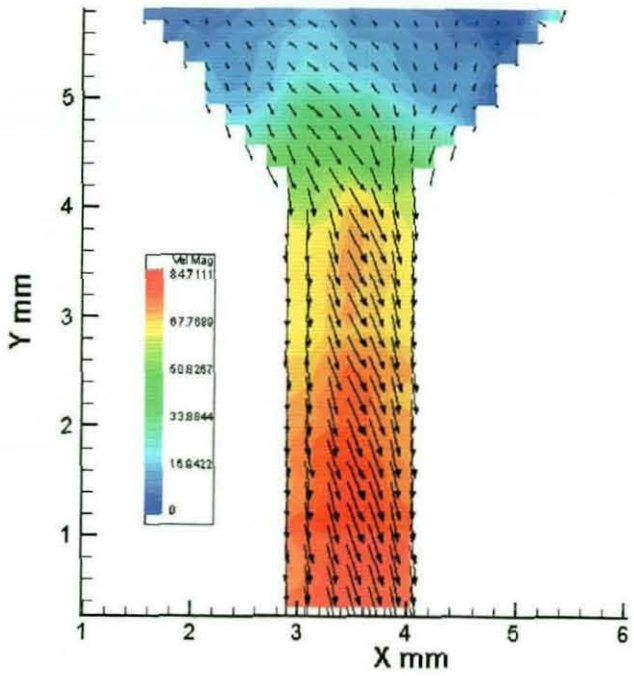

Figure B.53 Average velocity magnitudes for 45° chamfered inlet orifice at 30 bar driving pressure.

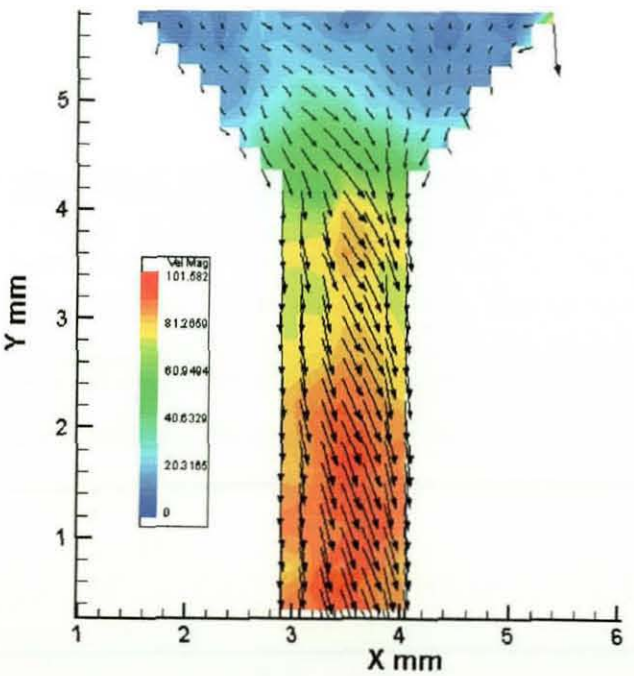

Figure B.54 Average velocity magnitudes for 45° chamfered inlet orifice at 40 bar driving pressure.

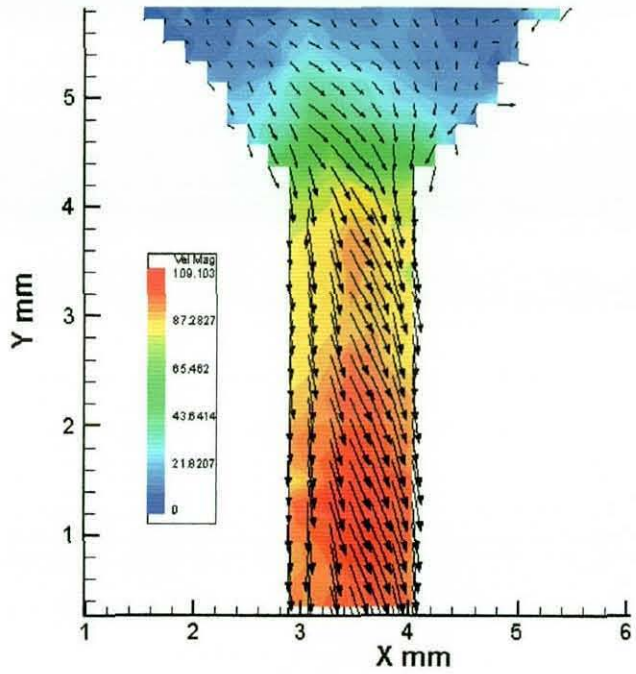

Figure B.55 Average velocity magnitudes for 45° chamfered inlet orifice at 50 bar driving pressure.

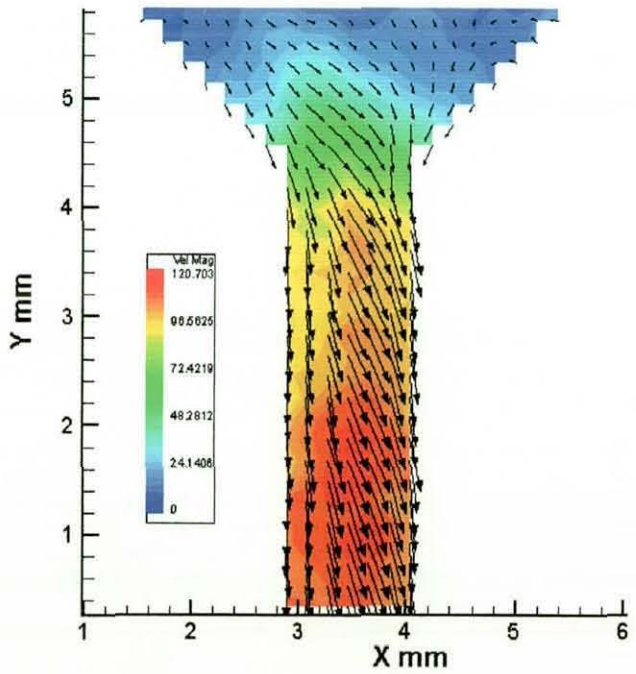

Figure B.56 Average velocity magnitudes for 45° chamfered inlet orifice at 60 bar driving pressure.

B.2.2.3 60° CHAMFERED INLET ORIFICE

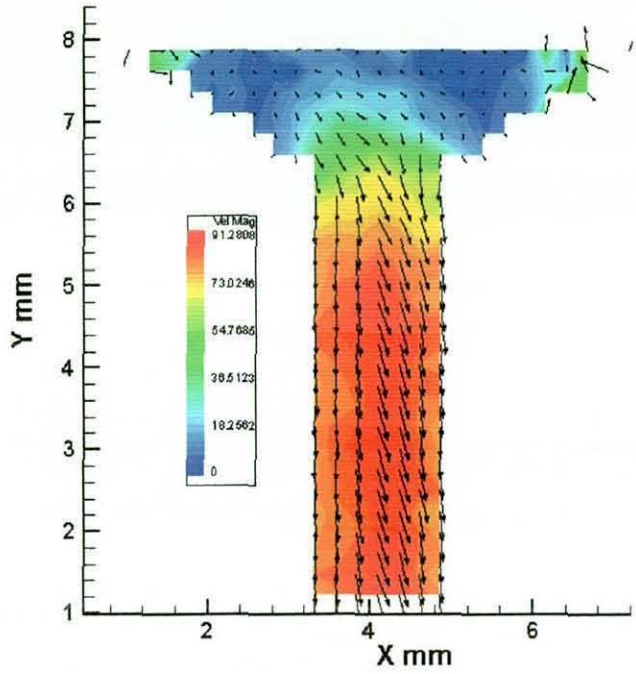

Figure B.57 Average velocity magnitudes for 60° chamfered inlet orifice at 30 bar driving pressure.

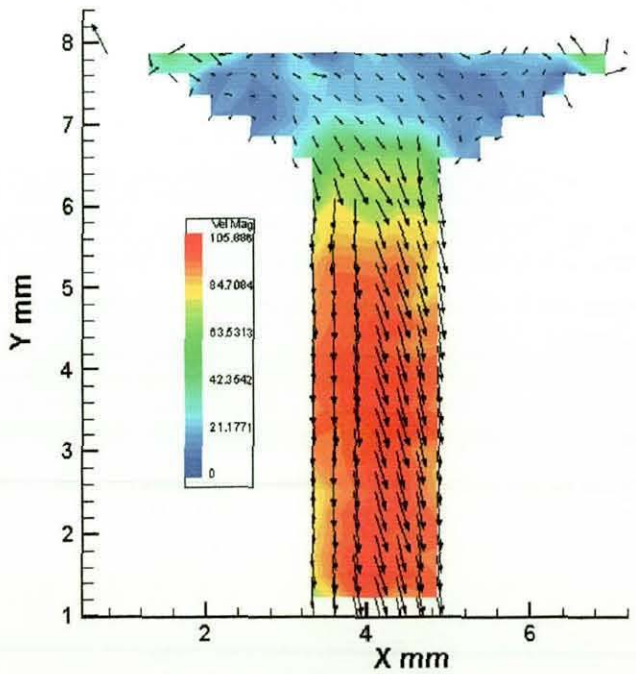

Figure B.58 Average velocity magnitudes for 60° chamfered inlet orifice at 40 bar driving pressure.

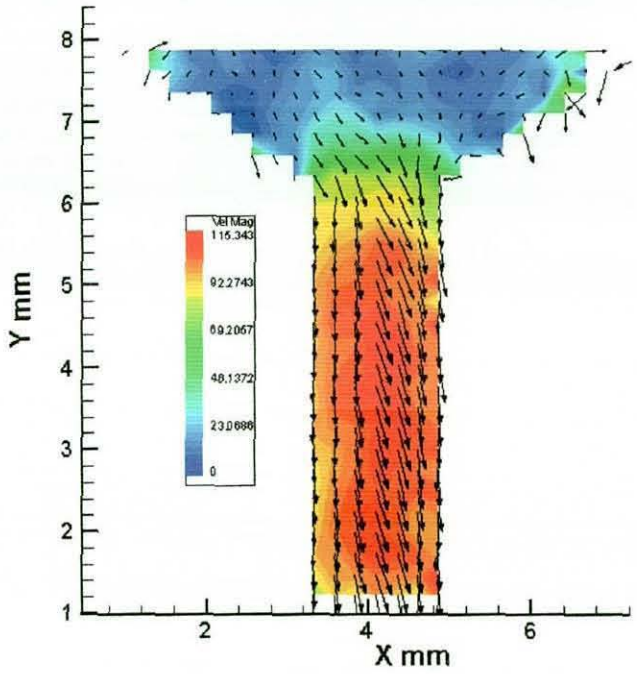

Figure B.59 Average velocity magnitudes for 60° chamfered inlet orifice at 50 bar driving pressure.

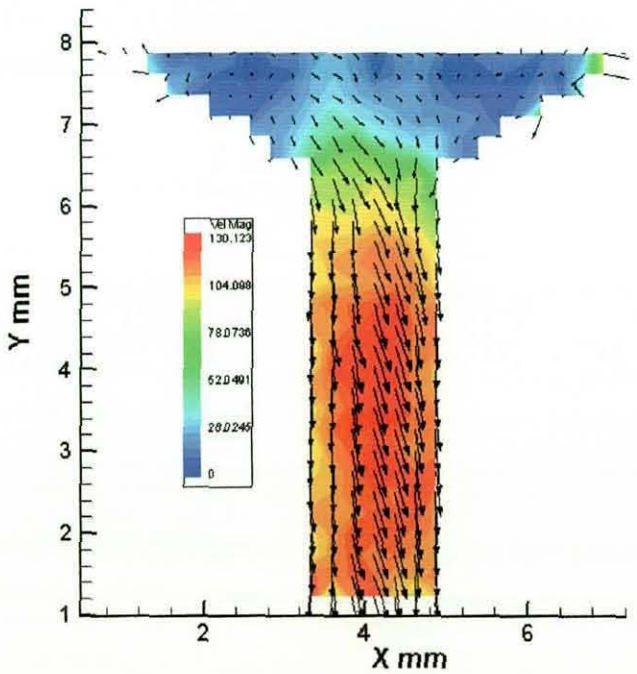

Figure B.60 Average velocity magnitudes for 60° chamfered inlet orifice at 60 bar driving pressure.

B.2.3 Velocity through centreline of the Orifice

B.2.3.2 30° SWIRLER

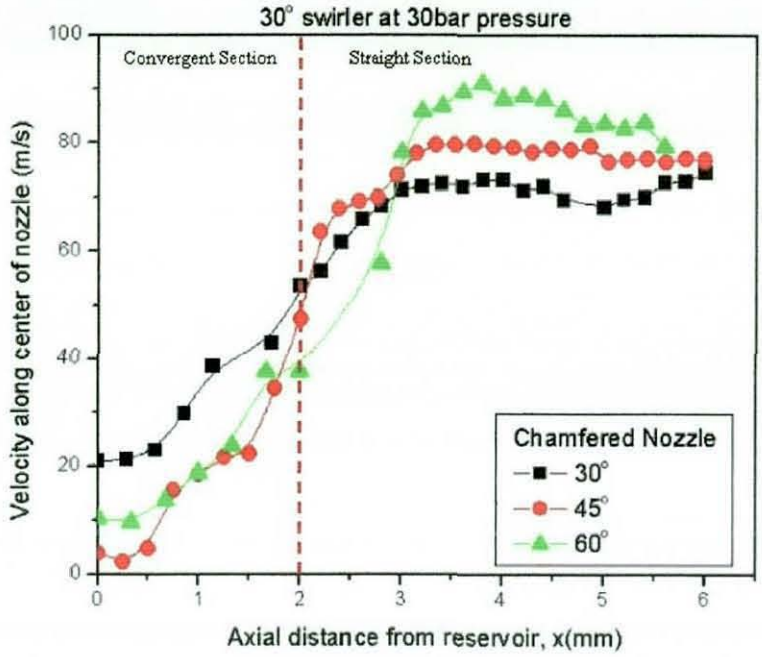

Figure 6.61 Velocity through the centreline of the different chamfered inlet. orifice with 30° swirler at 30 bar driving pressure.

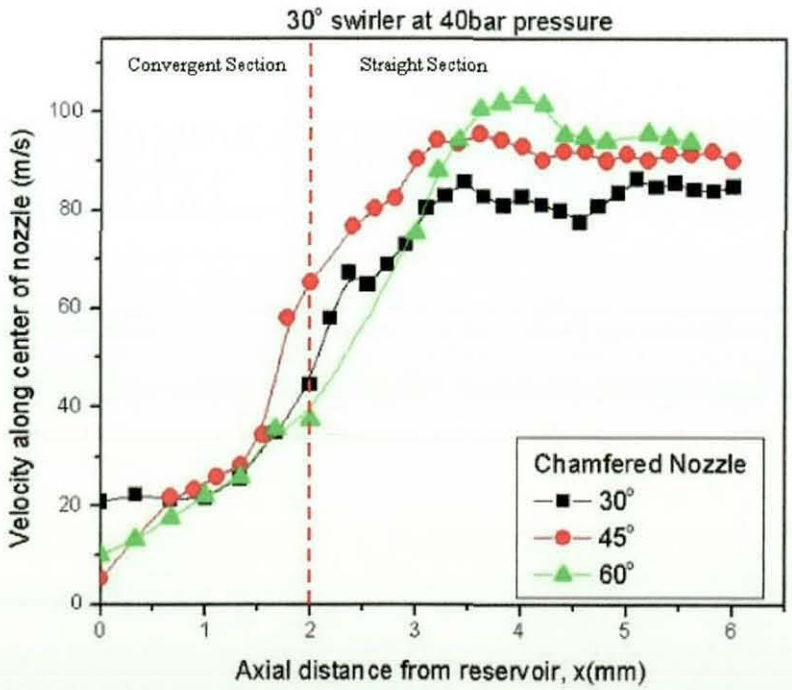

Figure 6.62 Velocity through the centreline of the different chamfered inlet orifice with 30° swirler at 40 bar driving pressure.

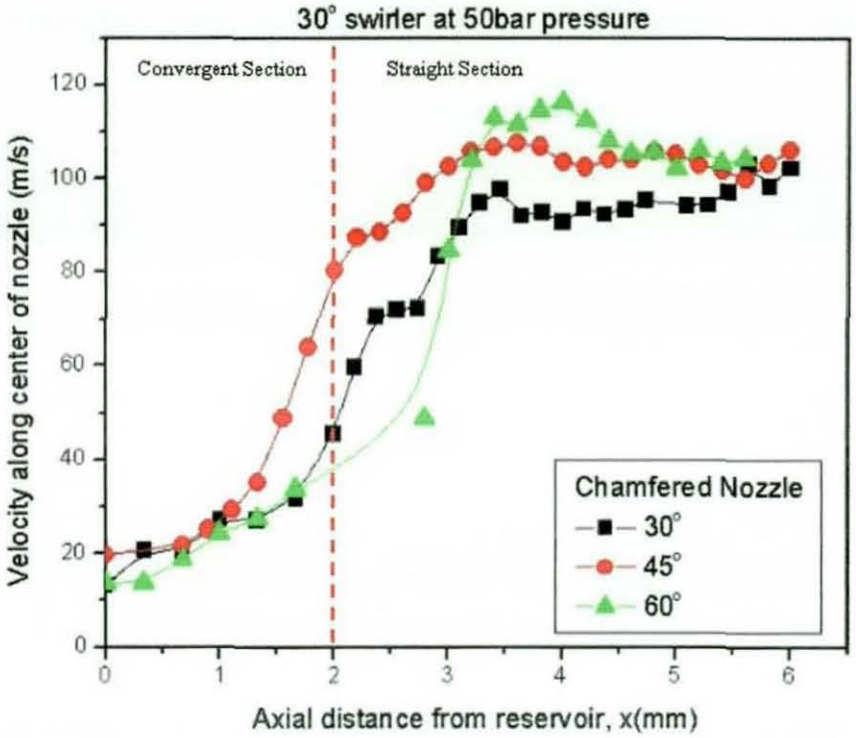

Figure 6.63 Velocity through the centreline of the different chamfered inlet orifice with 30° swirler at 50 bar driving pressure.

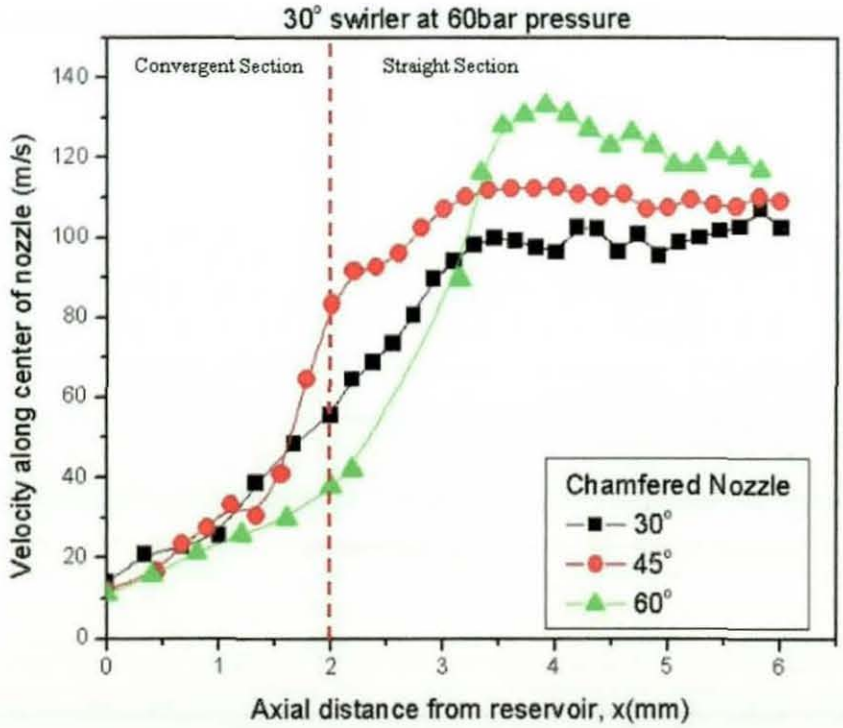

Figure 6.64 Velocity through the centreline of the different chamfered inlet orifice with 30° swirler at 60 bar driving pressure.

B.2.3.2 45° SWIRLER

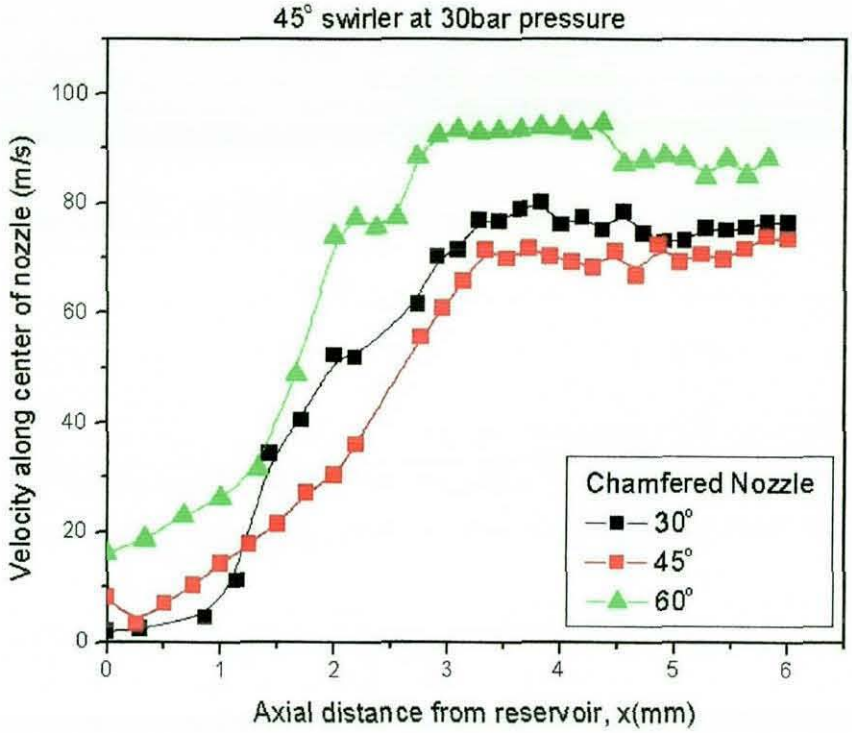

Figure B.65 Velocity through the centreline of the different chamfered inlet orifice with 45° swirler at 30 bar driving pressure.

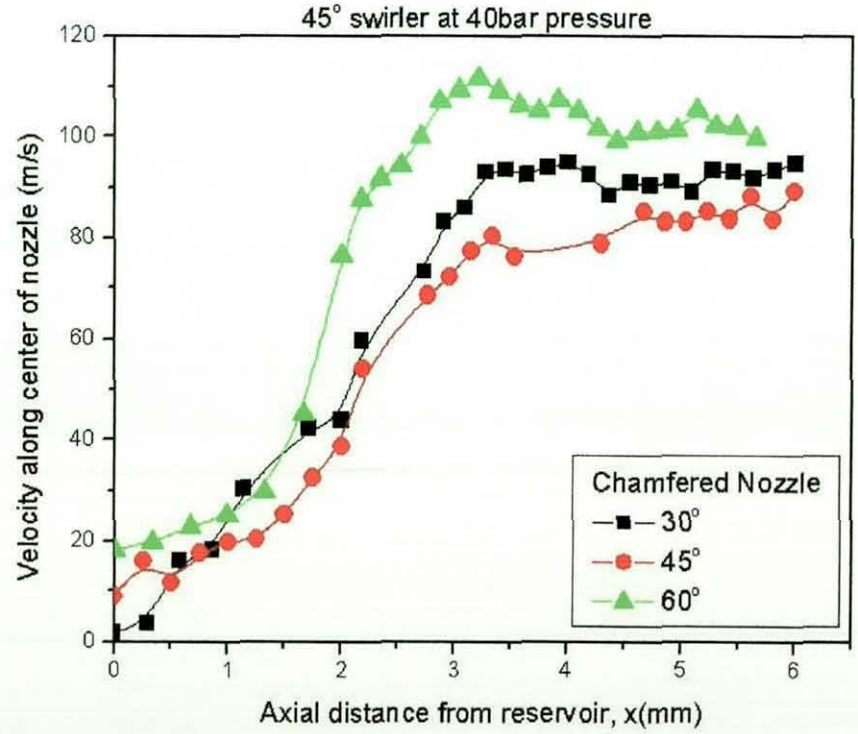

Figure B.66 Velocity through the centreline of the different chamfered inlet orifice with 45° swirler at 40 bar driving pressure.

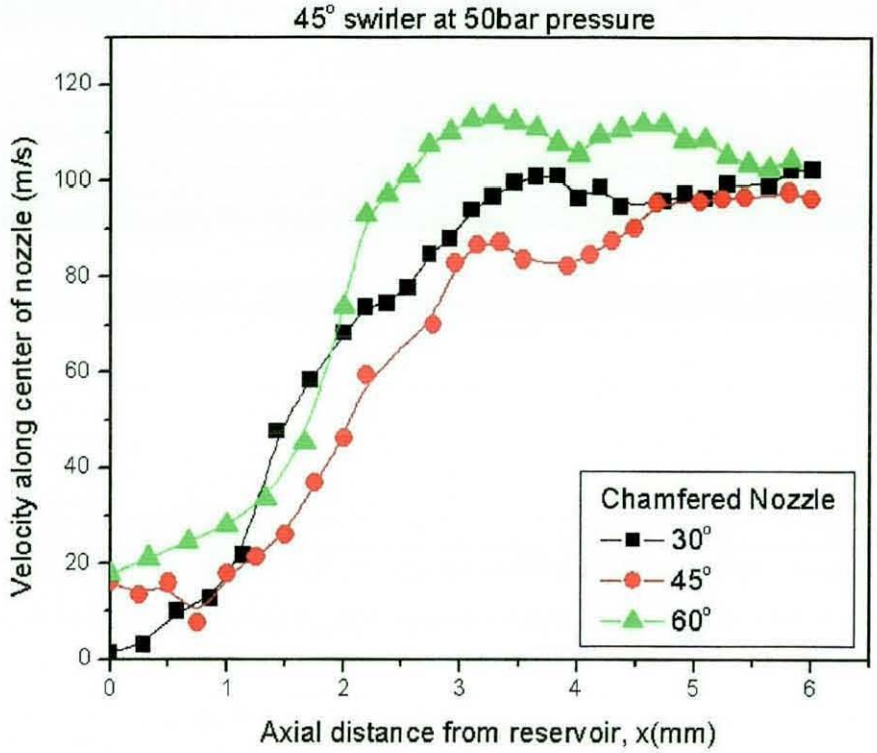

Figure B.67 Velocity through the centreline of the different chamfered inlet orifice with 45° swirler at 50 bar driving pressure.

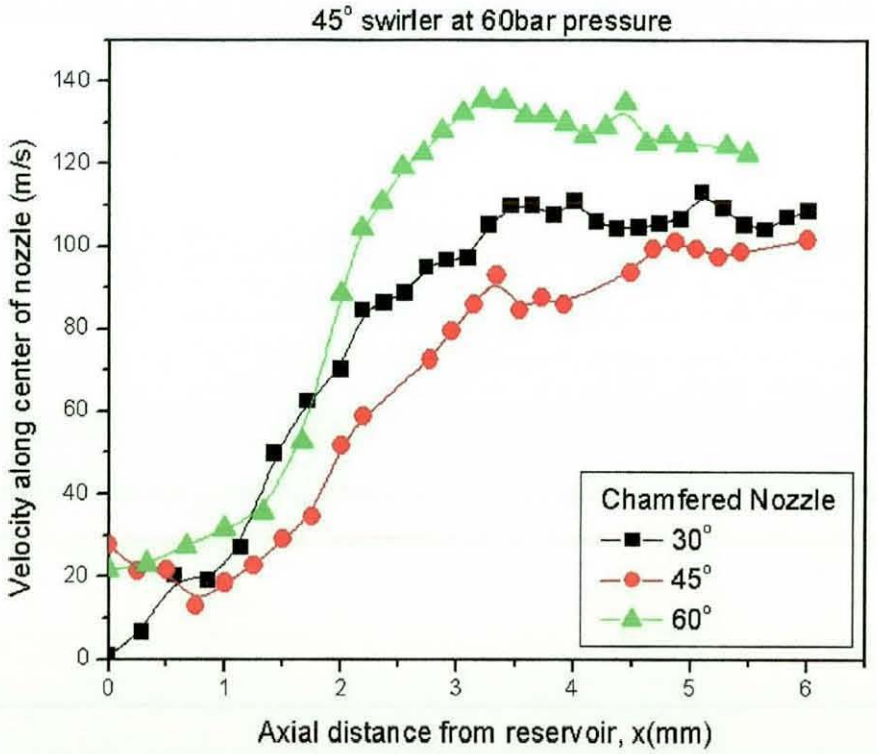

Figure B.68 Velocity through the centreline of the different chamfered inlet orifice with 45° swirler at 60 bar driving pressure.

B.2.3.3 60° SWIRLER

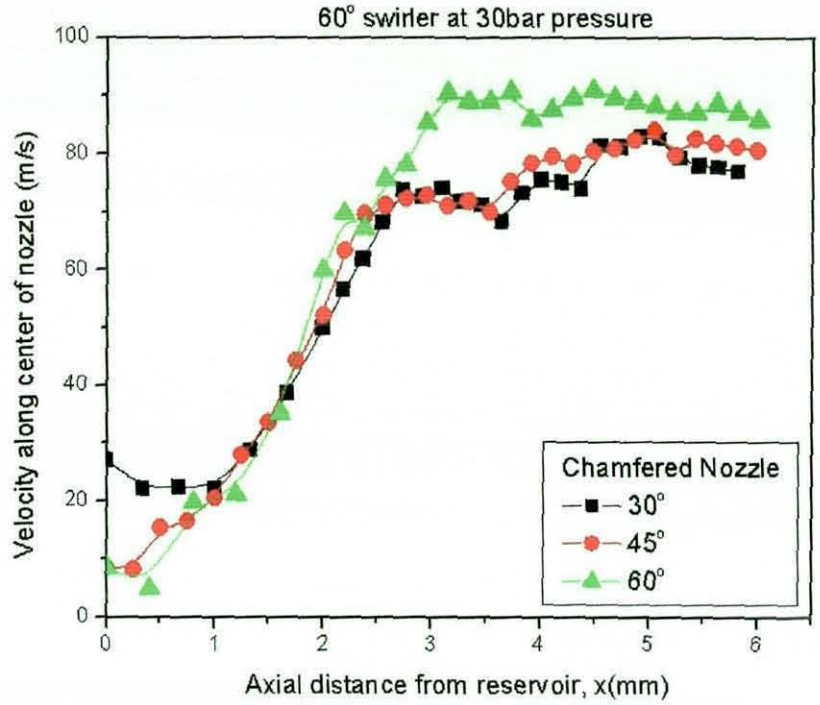

Figure B.69 Velocity through the centreline of the different chamfered inlet orifice with 60° swirler at 30 bar driving pressure.

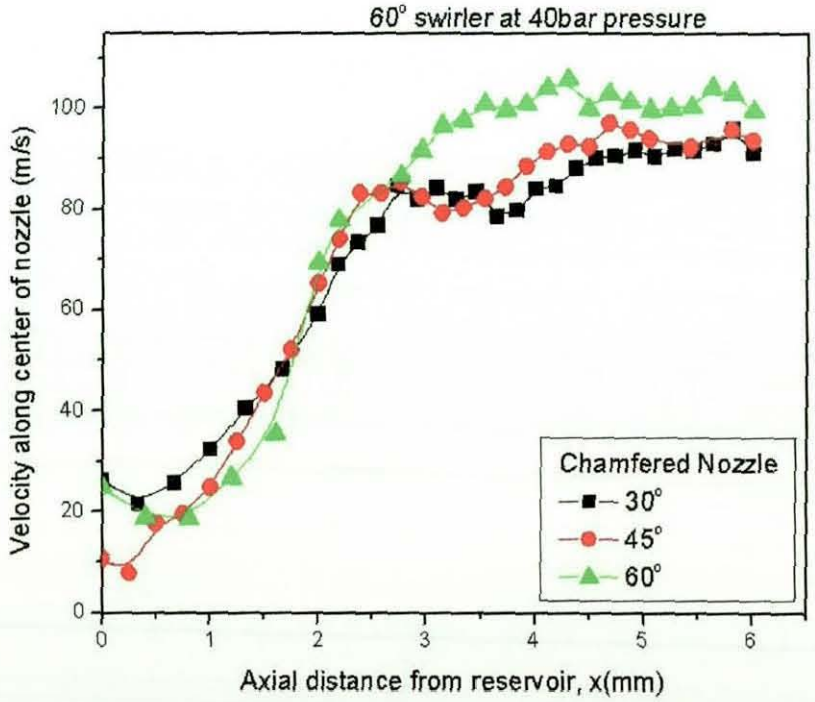

Figure B.70 Velocity through the centreline of the different chamfered inlet orifice with 60° swirler at 40 bar driving pressure.

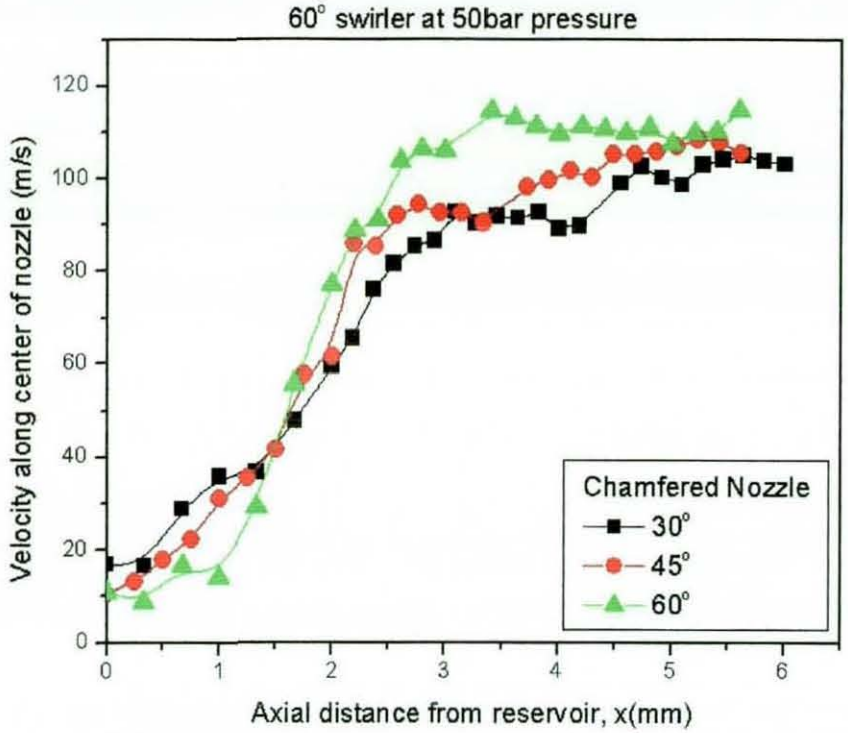

Figure B.71 Velocity through the centreline of the different chamfered inlet orifice with 60° swirler at 50 bar driving pressure.

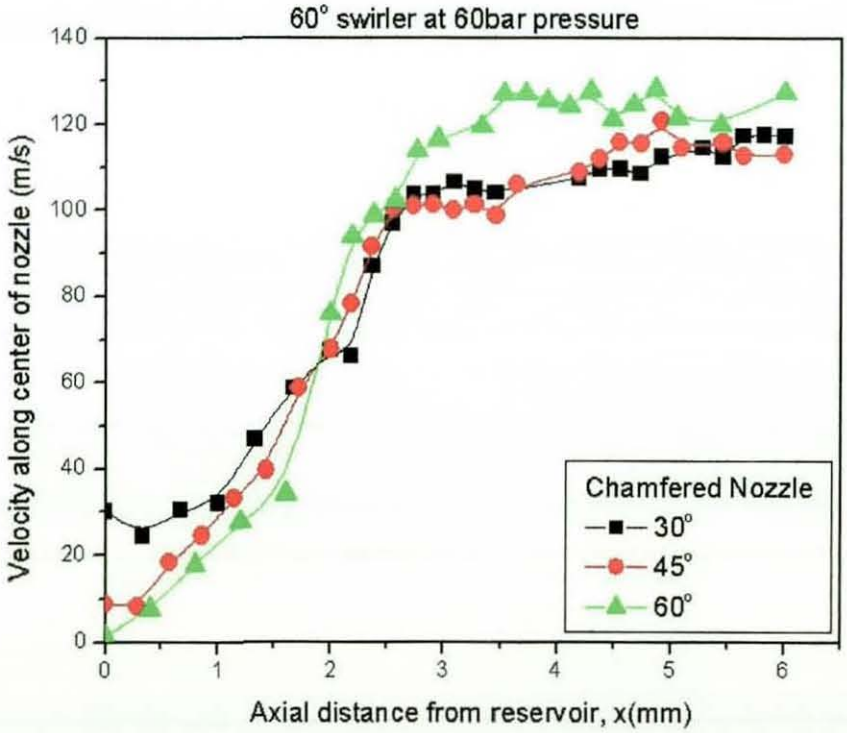

Figure B.72 Velocity through the centreline of the different chamfered inlet orifice with 60° swirler at 60 bar driving pressure.

APPENDIX C

COMPUTATIONAL FLUID DYNAMICS

C.1 INTRODUCTION

In the early 21st century, NASA was sourcing for different approaches to develop a high manoeuvrability, next generation aircraft with the use of supercomputers. This was because existing wind tunnel facilities were unable to perform simultaneous simulation of high Mach numbers and high flow field temperatures encountered by trans-atmospheric aircraft. This led to the development of Computational Fluid Dynamics (CFD) as the "third approach", to compliment the other two approaches of pure theory and pure experiment.

CFD provides numerical simulation which can be used to predict internal and external flows, involving fluid and heat transfer. This technique is so useful and versatile that it covers a wide range of industrial to research based applications. These examples [04] include the aerodynamics of aircraft and vehicles in terms of lift and drag (shown in figure C.1), hydrodynamics of ships, investigation of internal combustion engines and gas turbines, turbomachinery and other marine engineering.

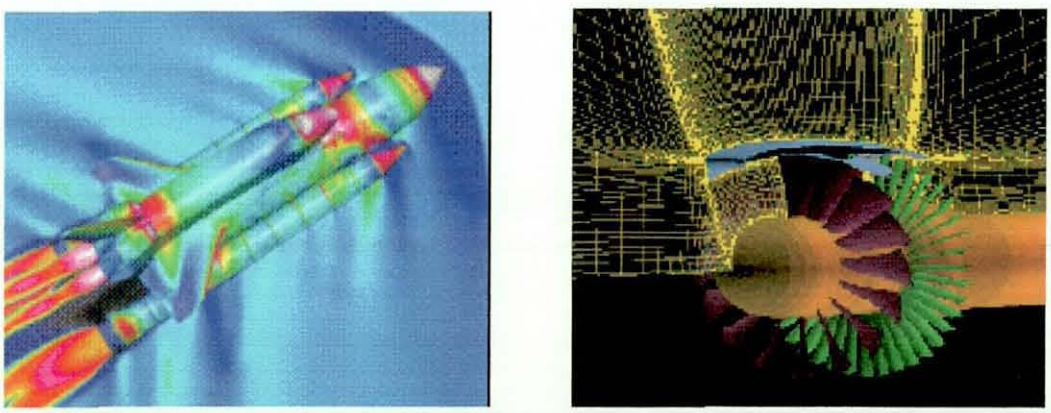

Figure C.1 The drag and lift effect on the space shuttle, flow around a turbomachinery. [01]

The application of CFD modelling has numerous significant advantages over conventional testing and experimentation. The modelling tool helps to reduce the time and cost of designing and installing expensive or large-scale equipment. It can validate the designs, perform changes and ensure the system performs prior to installations, therefore reducing the requirement for physical testing and help to gain insight into complex flows and chemical reaction processes. It also helps to diagnose and understand the risk involves on health and safety ground, if any troubleshooting on the equipment was needed.

There are several numerical tools available to assist in the study of engines and injectors. The most commonly used tools are Ricardo VECTIS, KIVA, FLUENT, FIRE and STAR-CD codes, and the application of these codes was discussed in the literature review in chapter 2. Although CFD codes have been around for decades, one common practice by most researchers is the use of both experiments and numerical simulation simultaneously to provide validation of theoretical results. Subsequent follow-on research work will rely heavily on the numerical tools as this is less timing consuming and more efficient.

This chapter provides a simple numerical method for investigating three non-swirl orifices. This is used to validate the non-swirl data presented in the previous chapter for the same set of orifices. This numerical work will provide a platform for developing the modelling tool for a swirl orifice study.

C.2 CFD WORKING PRINCIPLES

CFD is a numerical tool based on the three fundamental governing equations of fluid dynamics: the continuity, momentum and energy equations. They are based on the three physical principles that: Mass is conserved, Newton's second law (F = ma) and Energy is conserved. By applying these physical principles to a suitable flow model, it is possible to form mathematical equations into suitable forms for the numerical tool to model. The numerical

codes generally consist of three main elements [04]: a pre-processor, ii) a solver and iii) a post-processor.

The pre-processing consists of the parameters of a flow problem input by the operator into the programs. These include defining the fluid properties, domain geometry, grid generation or meshing and appropriate boundary conditions into the solver. These pre-processors also consist of libraries of material properties for common fluids and facility for physical alterations of these properties.

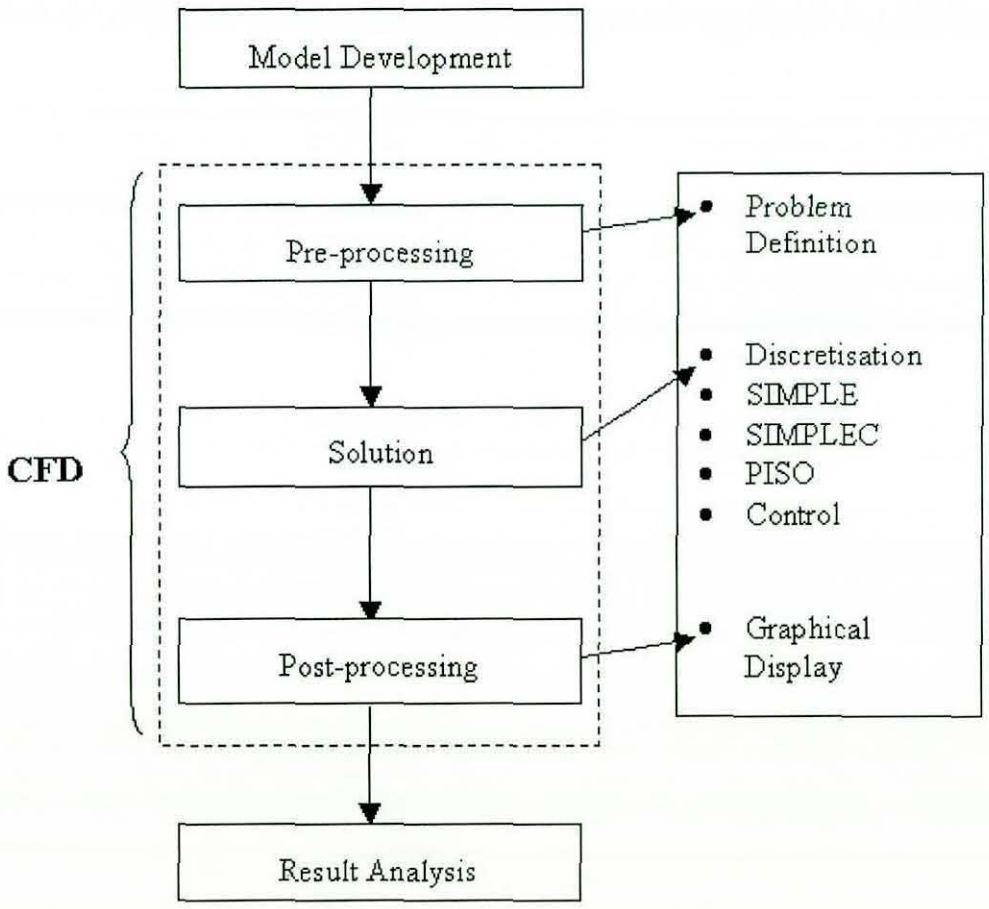

Figure C.2 Flow diagrams for numerical simulations.

As the name implies, the solver uses three distinctive techniques to solve the operator's flow problems:

i) Finite difference methods: Using Taylor series expansion to generate the unknown point of the flow problem, by means of point sample at the nodes of the grid of co-ordinate lines.

ii) Finite Element Method: Using simple piecewise functions valid on elements to describe any local variations of unknown flow variables.

iii) Spectral Method: This method approximates the unknowns in the grid of the flow problems by means of truncated Fourier series or series of Chebyshev polynomials. Unlike the previous two methods, the approximation is valid throughout the entire computational domain.

The post-processor is equipped with many versatile data visualisation tool to aid the extraction of useful results. These tools include:

i) Domain geometry and grid display
ii) Vectors plots
iii) Line and shaded contour plots
iv) 2D and 3D surface plots
v) Particle tracking
vi) View manipulation
vii) Colour postscript output

Figure C.2 shows that these three main elements form the basis of the numerical tool, but there are also two other elements that are essential in this instance. In the figure, the flow diagram shows "Model Development" as the first step before using the codes. This can be any design software, as long as it allows the integration of the mesh into the numerical tool. The mesh generated is important as it determines whether the simulations will work once it is incorporated into the numerical tool. As for "Results Analysis", this is to analyse the output results from the post-processing to fit into the work studied.

C.3 MODELLING SETUP

The numerical model provided in Fluent software allows both 2D and 3D grid setup. As mentioned, the pre-processor is the first step that helps to define the nozzle geometry, grid or mesh generation and the appropriate boundary for the flow regions. These parameters were generated using the Gambit 1.3 design software, which is integrated with the Fluent package and works in conjunction with the processing tool.

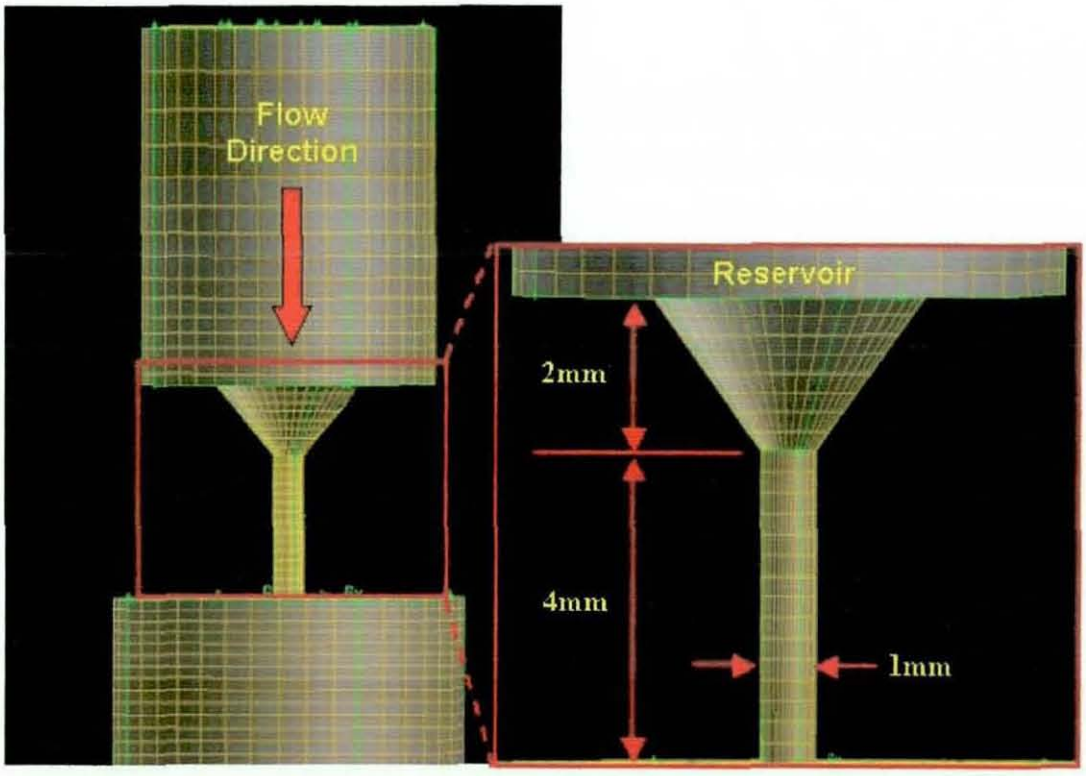

Figure C.3 Gambit design software showing a 45° chamfered inlet orifice.

Gambit 1.3 is the grid designing software used to create model geometry and grids for engineering analysis. Its advanced geometry and meshing tools can dramatically reduce pre-processing time. In this study, Gambit was used to develop and create complex 3D mesh grids, to model the non-swirl nozzles used in our study, 30°, 45° and 60° chamfered inlet orifices. The meshes were generated from equally spaced nodes on each plane. The mesh was closely packed at the orifice, as that is the most important aspect of this simulation and it allows the flows to be fully developed in the simulation.

In this study, reservoir and atmospheric mesh grids were created. The reservoir was defined as the inlet region before the fluid flow into the orifices and had a diameter of 6mm and was 10 mm deep for 30° and 45° chamfered inlet orifices. The atmospheric mesh is shown as an outlet region for simulating the flow out into atmospheric conditions. Figure C.3 shows an example of the geometry created with the gambit software. This is the grid generated for the 45° chamfered inlet orifice (1mm diameter) with the inlet and outlet regions. The insert shows that the length of the chamfered section as 2mm long and the nozzle section with a L/D ratio of 4. A reservoir was created and defined as the inlet region and to simulate fluid flow into the orifices. This was to allow the flow to be fully developed before entering the orifices. The reservoir had a cylindrical radius of 5 mm and was 10 mm long. The region beyond the orifice was the atmospheric area to simulate the fluid flowing out of the orifice. This outlet region had a diameter of 12 mm and a length of 10 mm to simulate the atmospheric conditions. With the setup completed, the gambit geometry was exported into the Fluent numerical tool for incorporating parameters requires for simulations.

In the fluent software program, the orifice's mesh was imported and loaded. The mesh was displayed and inspected for any errors. Figure C.4 shows the fluent operating window used for setting up and processing. The solver is defined as a 3D segregated with steady state conditions using the $k - \varepsilon$ turbulence model. In defining the fluid used in this numerical simulation, there was no white spirit available in the materials list, the next closest on the list is turpentine. It has the same chemical formula ($C_{10}H_{16}$), density and viscosity matched those of white spirit. Since the pre-programmed fluids do not include the white spirit used in the experiments, the next closest fluid called Turpentine was selected, as the fluid properties are almost identical. Operating condition was for the simulation was set as atmospheric with reference based on the surrounding in experiments.

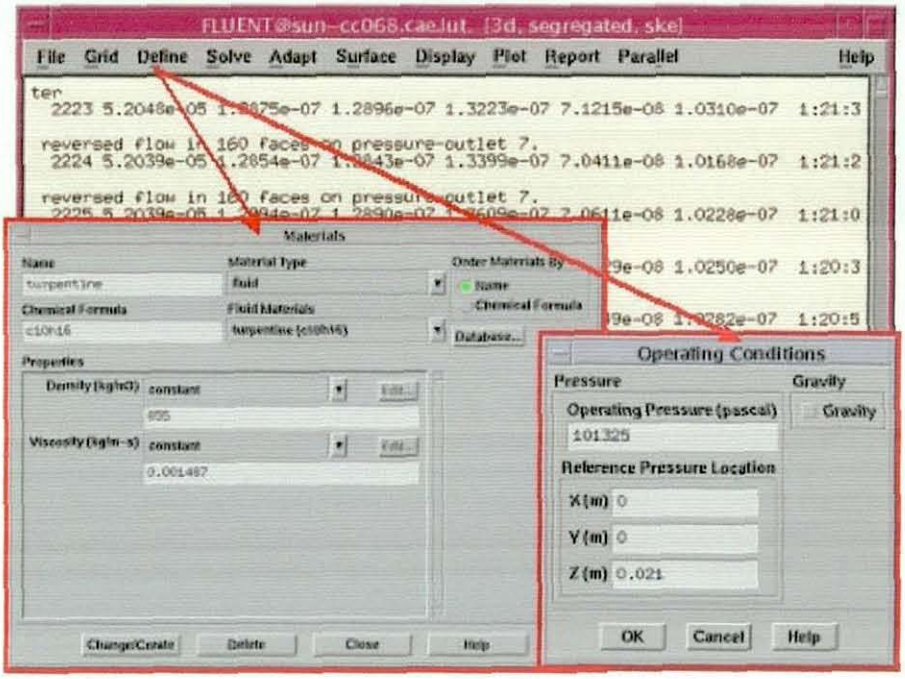

Figure C.4 Fluent software windows for defining materials used and operating conditions.

Under the boundary conditions window, there are several zones generated from the mesh for easy identification, but only three main zones are required. These are the fluid, inlet and outlet as shown in figure C.5. As mentioned previously, the fluid was defined as Turpentine, with the inlet and outlet defined as pressure conditions, similar to the actual experimentation. This allowed the inlet driving pressure to be set from 20 bar to 50 bar, depending on the tests. Since the flow was observed to be turbulent from the high-speed videos, the intensity and length scale method was selected to improve the numerical calculations during iterations. The turbulence intensity was set to 10% with the turbulence length scale as 0.001 m. For the outlet, the backflow turbulence intensity was 1% and a backflow length scale of 0.002 m. With the boundary condition parameters defined, the next step is to set the solutions control and the under-relaxation factors are shown in Figure C.6.

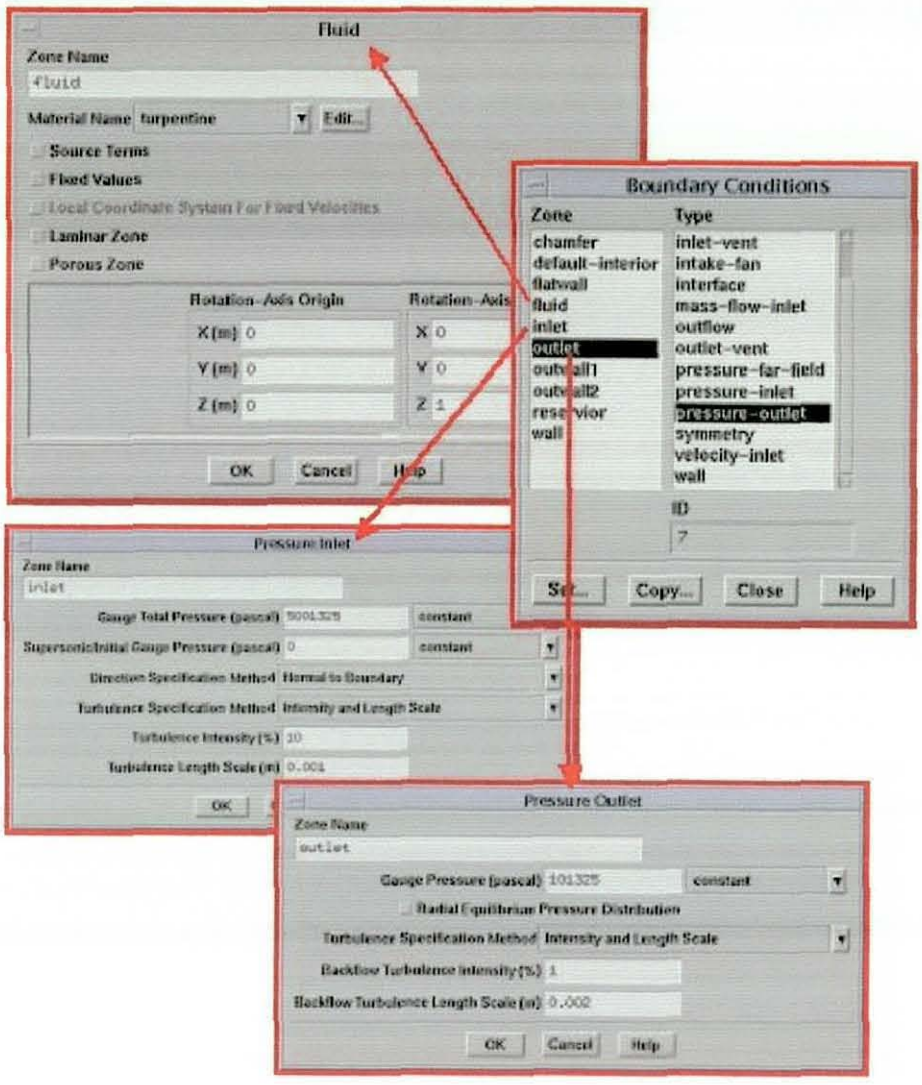

Figure C.5 Boundary conditions operating window with the various sub-windows.

Pressure	Density	Body Forces	Momentum	Turbulence Kinetic Energy	Turbulence Dissipation Rate	Turbulence Viscosity
0.3	1	1	0.7	0.8	0.8	1

Table C.1 Under-Relaxation Factors values used.

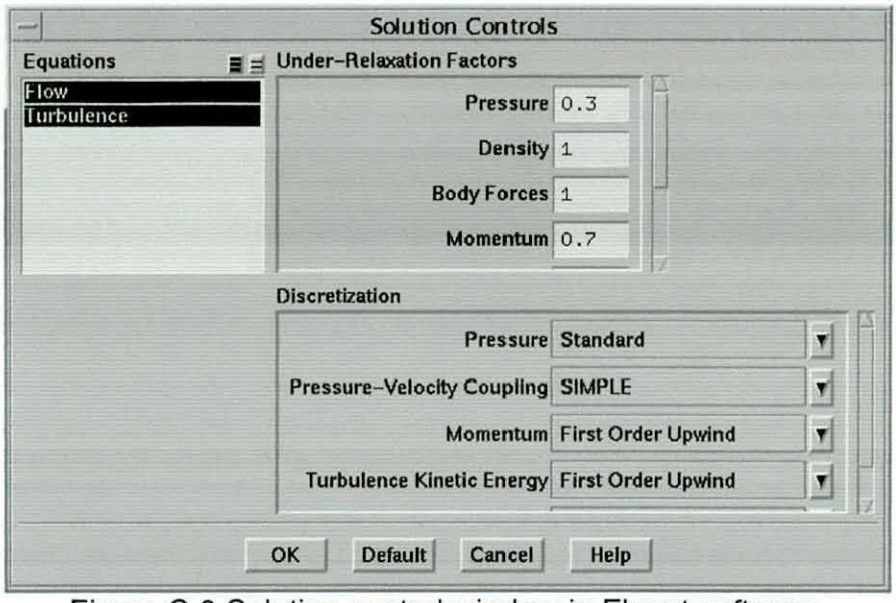

Figure C.6 Solution control window in Fluent software.

Pressure	Pressure-Velocity Coupling	Momentum	Turbulence Kinetic Energy	Turbulence Dissipation Rate
Standard	SIMPLE	First Order Upwind	First Order Upwind	First Order Upwind

Table C.2 Discretization window values

This window also shows the discretization window inputs as seen in table C.2 and this can be alter if required. A good example is by altering the values for momentum and turbulence kinetic energy if the "First Order Upwind" method fails to converge for the flow studied, a "Second Order" is available to improve the iterations.

Figure C.7 shows the iteration process as the simulation converges. As mentioned previously, there are several options available to present the output data under the post-processing element. In this research study, the results were presented in 2D and 3D plots for flow velocity and also close-up views of the different chamfered inlet orifice flow characteristics. Figure C.8 shows a three dimension velocity plot of the chamfered inlet orifice. Different colour coded vectors represent the velocity range calculated from the simulations.

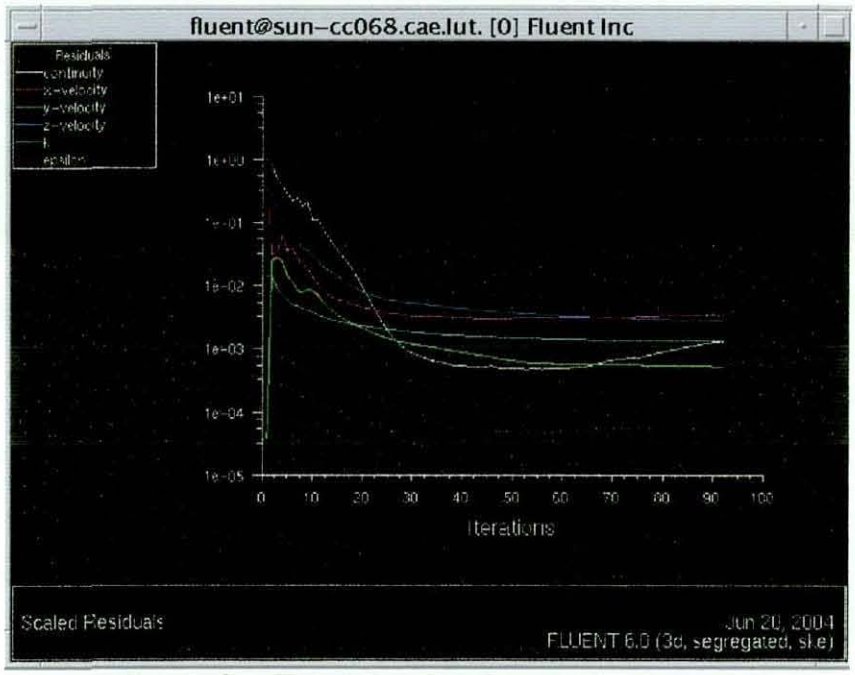

Figure C.7 Example of an iterations window.

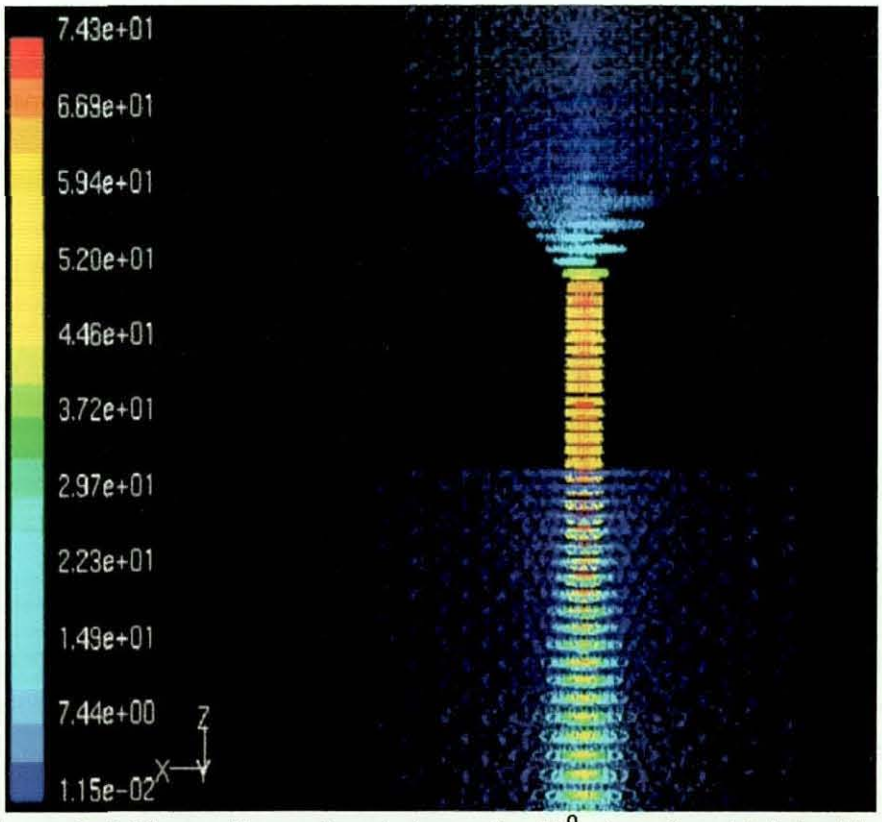

Figure C.8 Three dimensional view of a 45° chamfered inlet orifice.

The following sections will presents the results of the three chamfered inlet orifices at different driving pressure conditions. The results will then be compared with the experimental data from the non-swirl flow study in

chapter 6. A comparison will also be made on the maximum velocity at different driving pressures.

C.4 MODELLING RESULTS

C.4.1 30° Chamfered Inlet Orifice

The first set of results presented is from the 30° chamfered inlet orifice with driving pressure ranging from 20 to 50 bar. Figure C.9 shows the meshing grid imported from the Gambit meshing software, with the boundary of the model, the reservoir and the atmospheric boundary visible in the figure. Figure C.10 displays the velocity plot with a 20 bar driving pressure and the velocity range shown on the legend located on the left. The flow velocity appears to increase steadily as it enters the chamfered section of the orifice. This flow velocity begins to peak as it enters the nozzle section of the orifice, shown by the red velocity vectors. Similar flow trends were also observed, with velocity increasing as the driving pressure increases. The velocity graph shows a maximum velocity of 104 m/s with 50 bar driving pressure.

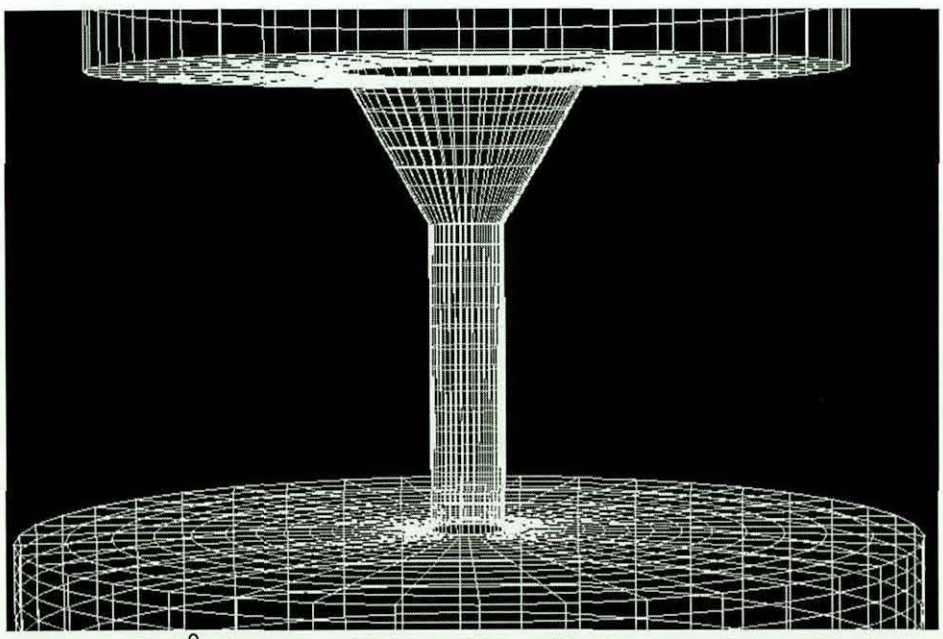

Figure C.9 30° chamfered inlet orifice with the boundary grid shown.

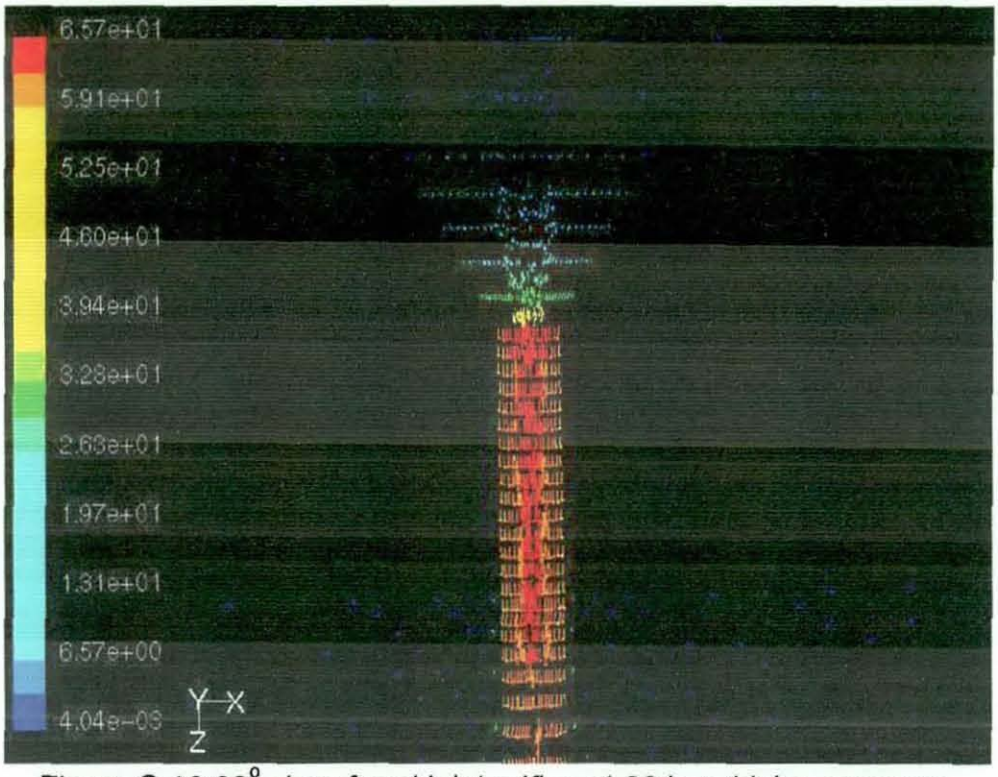

Figure C.10 30° chamfered inlet orifice at 20 bar driving pressure.

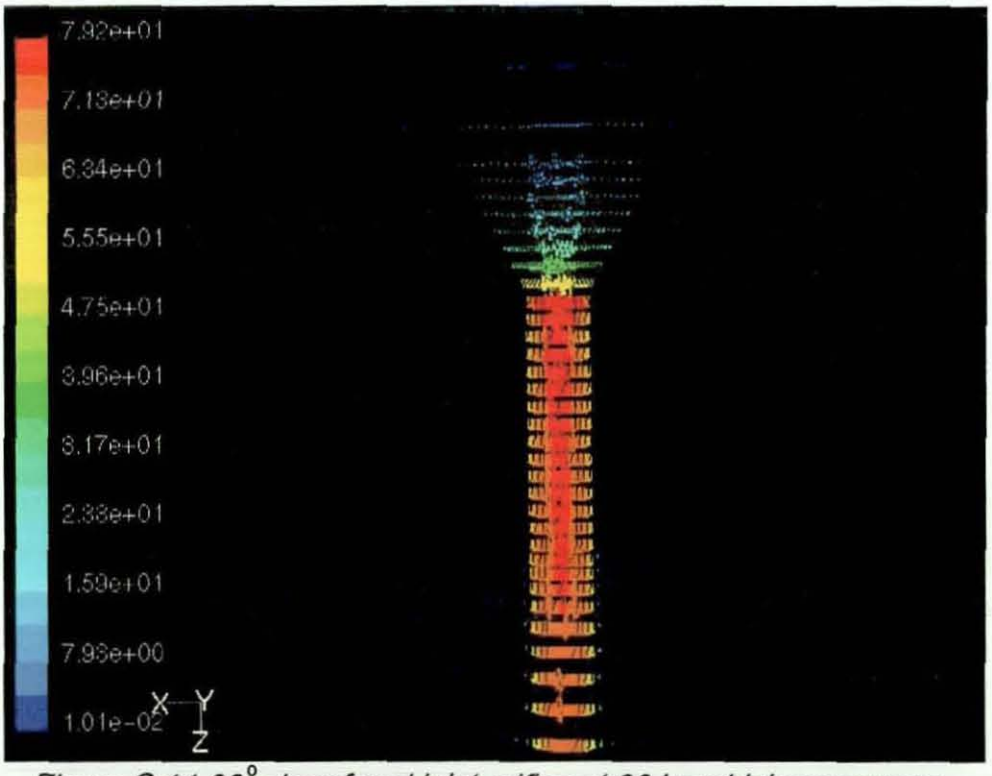

Figure C.11 30° chamfered inlet orifice at 30 bar driving pressure.

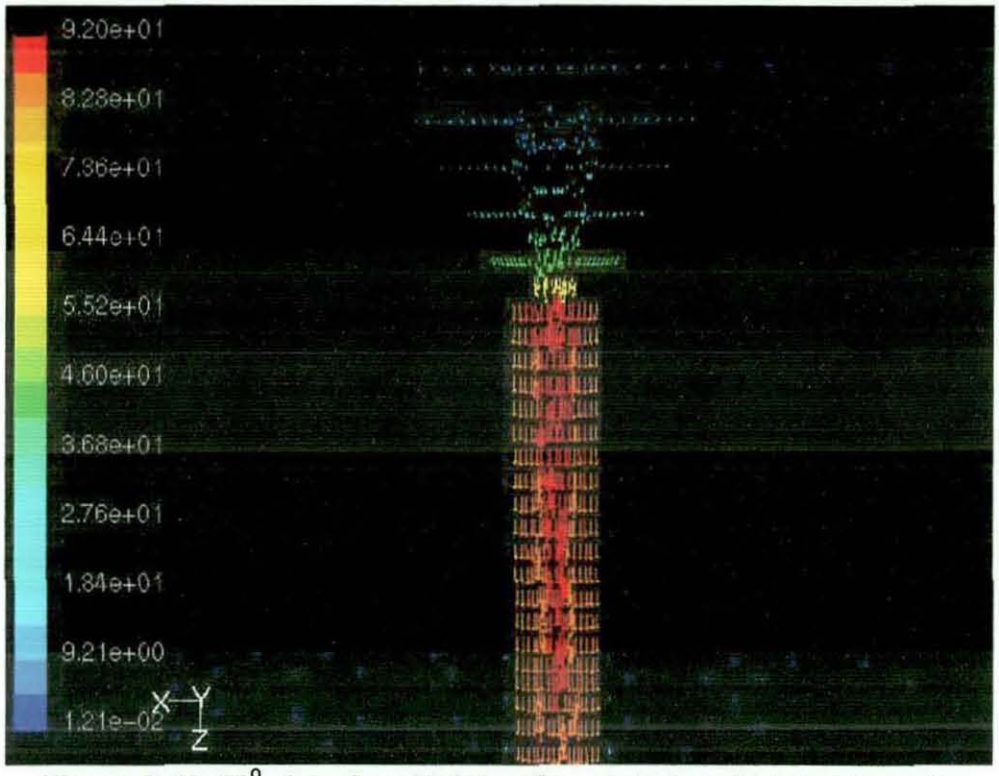

Figure C.12 30° chamfered inlet orifice at 40 bar driving pressure.

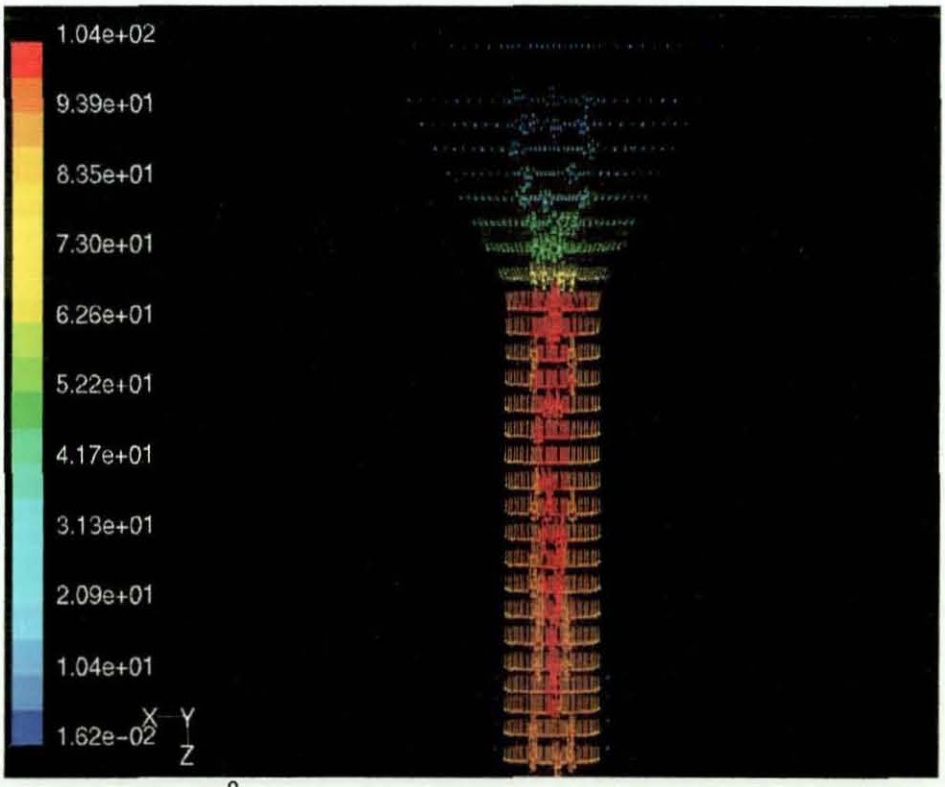

Figure C.13 30° chamfered inlet orifice at 50bar driving pressure.

C.4.2 45° Chamfered Inlet Orifice

The mesh grid for the 45° chamfered inlet orifice is shown in figure C.14. Figure C.15 shows the velocity vectors in the chamfered section of the orifice flowing into the nozzle section. The peak velocity shown here is 67 m/s with a 20 bar driving pressure. Figures C.16 to C.18 show higher velocity vectors with the higher driving pressure used. A low velocity field is seen to be located at the near wall as compared to the centre in the nozzle section of the orifice. In the 45° chamfered inlet orifice study, the velocity range from 66.6 m/s to about 96.3 m/s with driving pressure ranging from 20 to 50 bar.

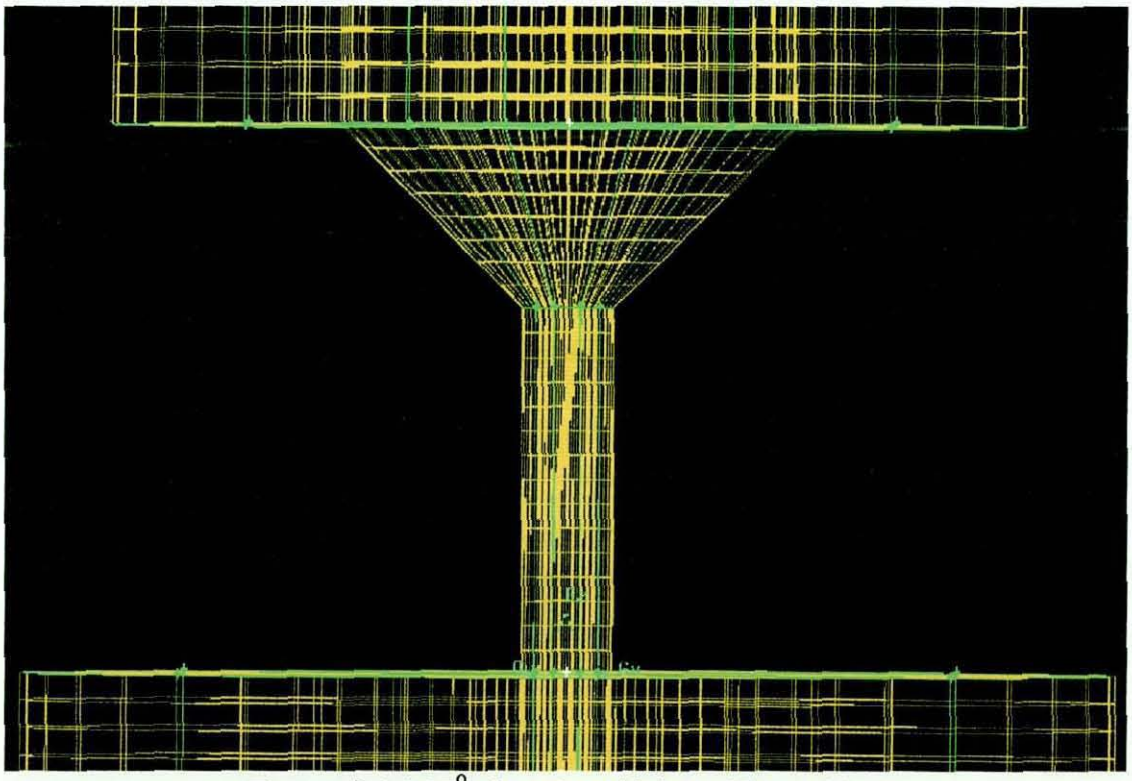

Figure C.14 45° chamfered inlet orifice grid.

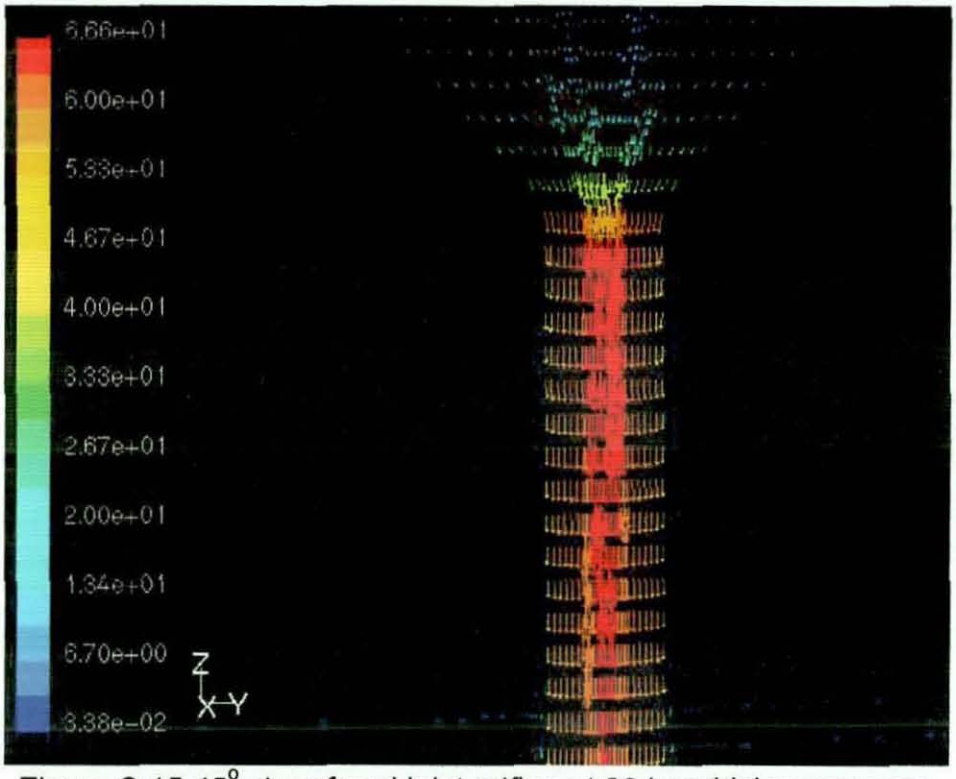

Figure C.15 45° chamfered inlet orifice at 20 bar driving pressure.

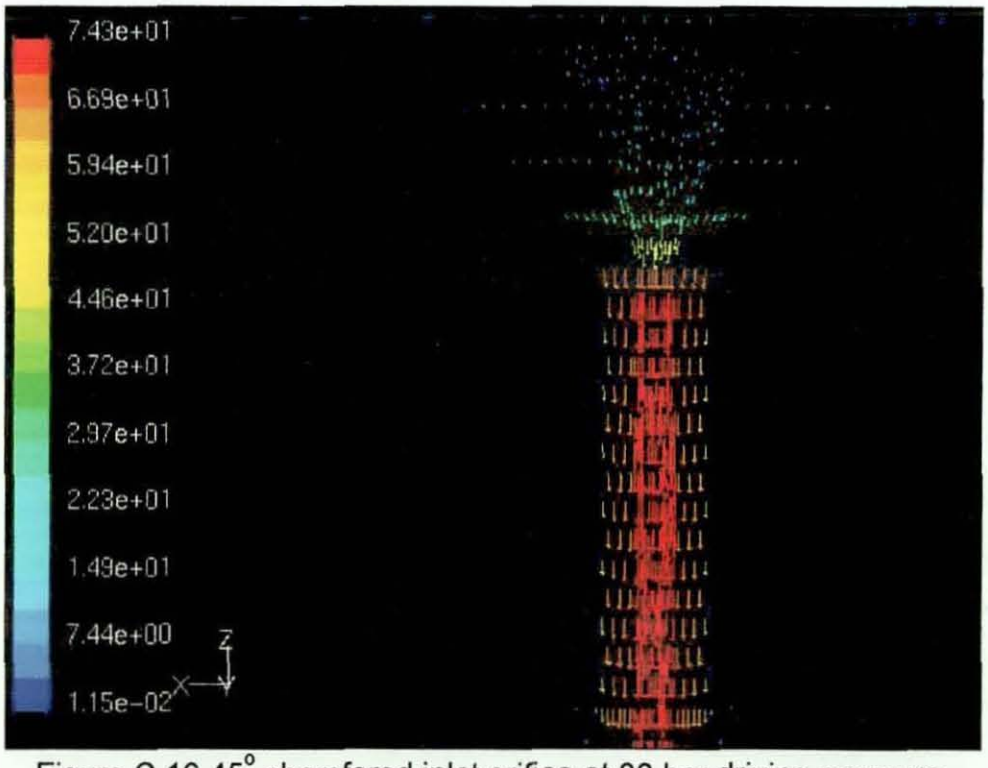

Figure C.16 45° chamfered inlet orifice at 30 bar driving pressure.

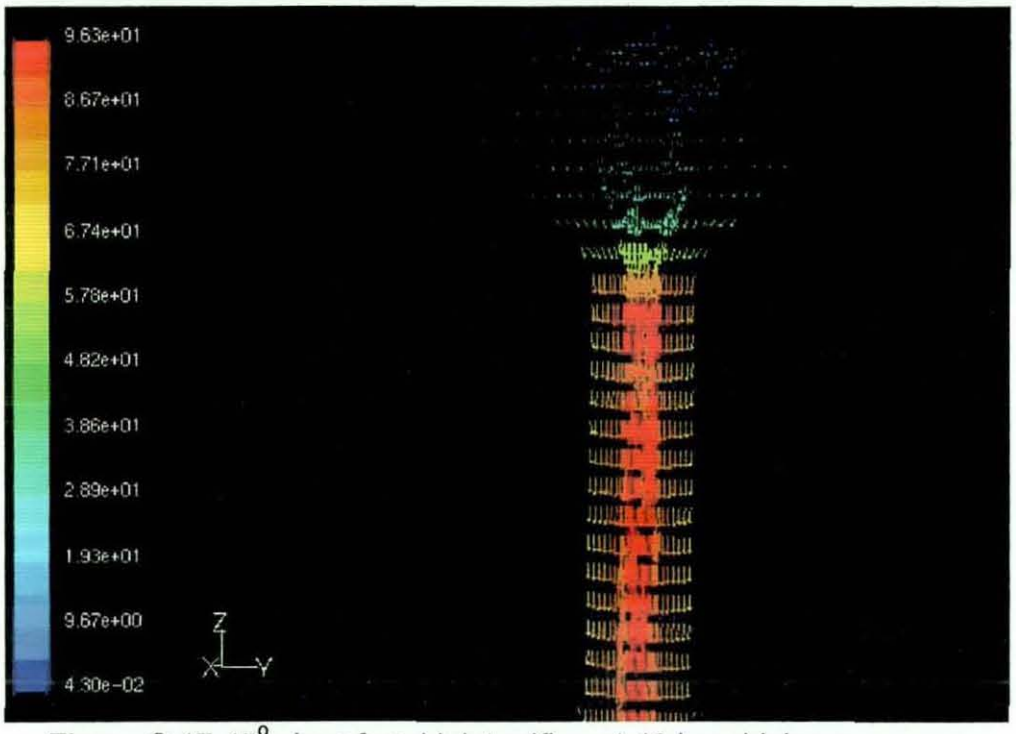

Figure C.17 45° chamfered inlet orifice at 40 bar driving pressure.

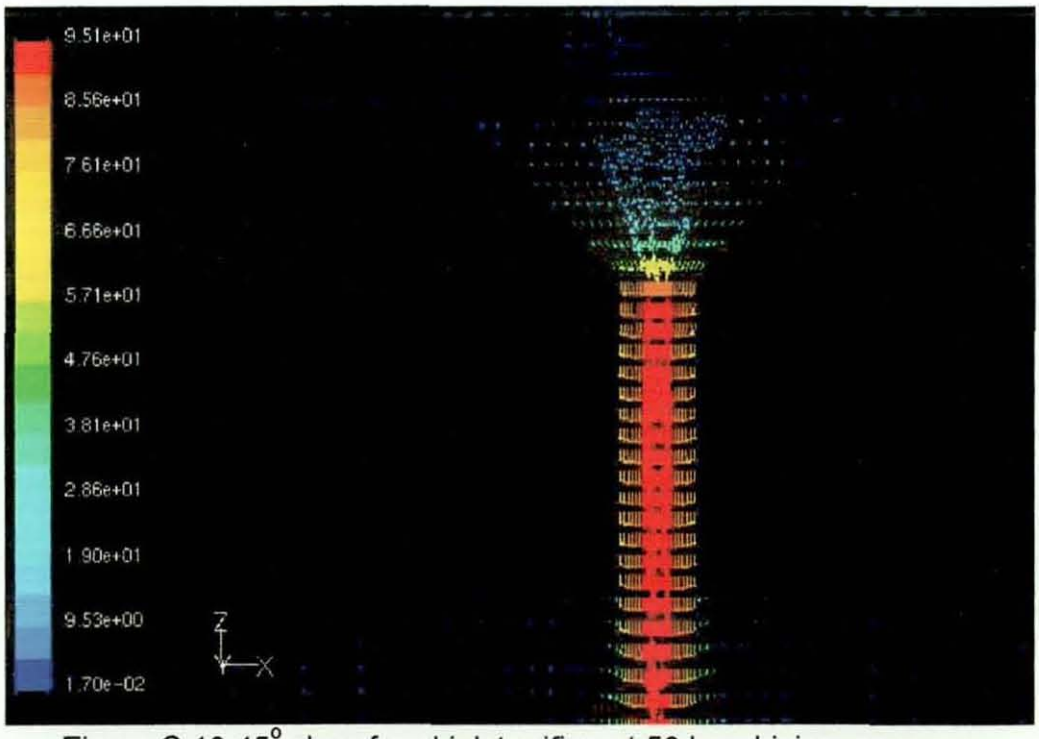

Figure C.18 45° chamfered inlet orifice at 50 bar driving pressure.

C.4.3 60° Chamfered Inlet Orifice

The 60° chamfered inlet orifice studied has the widest chamfered inlet angle as compared to the other two orifices. Figure C.19 shows the boundary mesh

geometry for this orifice, with the reservoir, orifice and the atmospheric boundary. Figures C.20 to C.23 shows the velocity graphs for a driving pressure ranging from 20 to 50 bar. These figures show the flow velocity increases as it enters the orifice and into the nozzle section. The peak velocity range from 61.4 m/s at 20 bar driving pressure to 96.1 m/s at 50 bar.

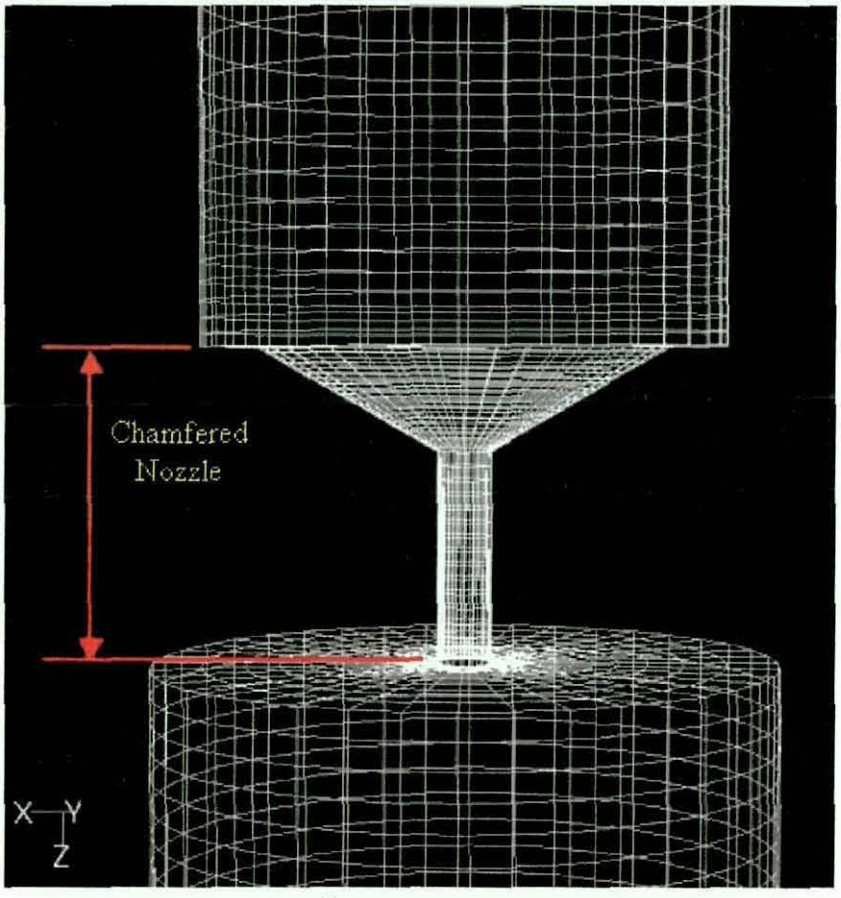

Figure C.19 60° chamfered inlet orifice grid.

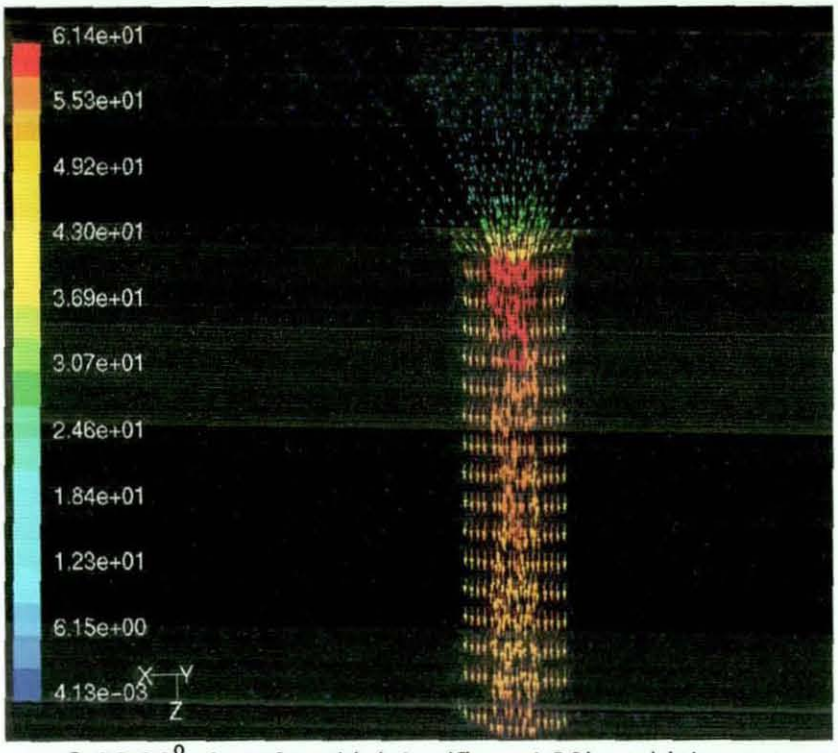

Figure C.20 60° chamfered inlet orifice at 20bar driving pressure.

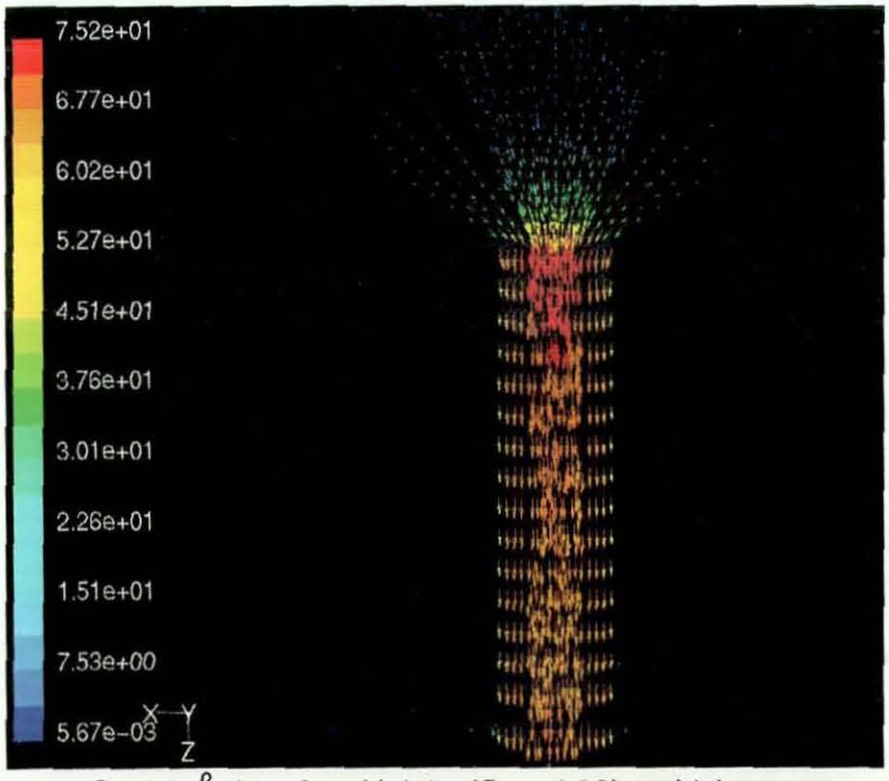

Figure C.21 60° chamfered inlet orifice at 30bar driving pressure.

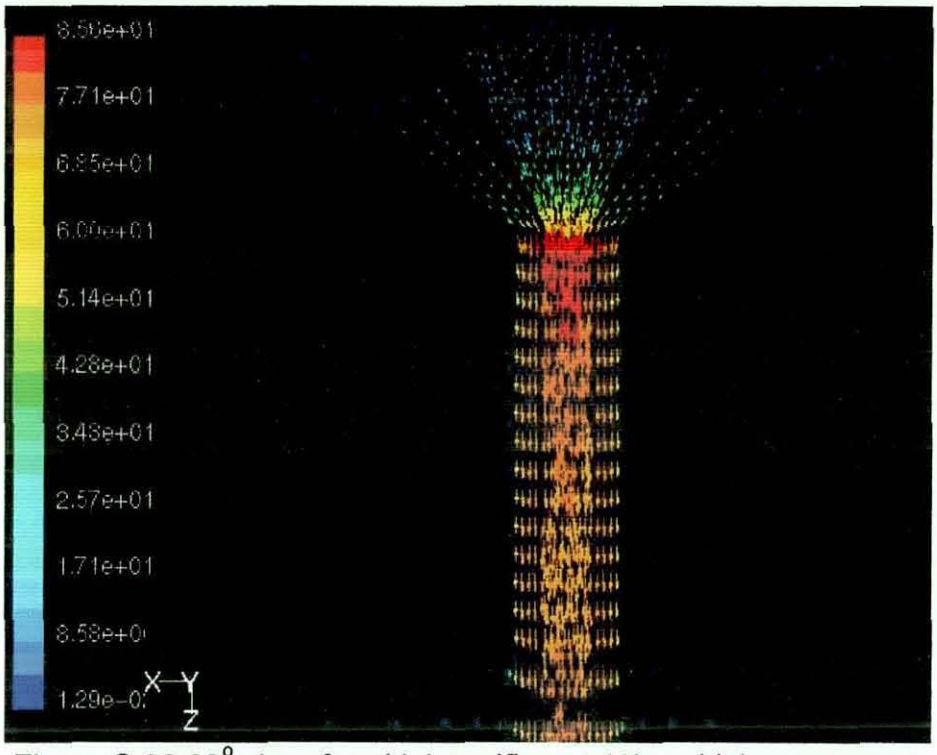

Figure C.22 60° chamfered inlet orifice at 40bar driving pressure.

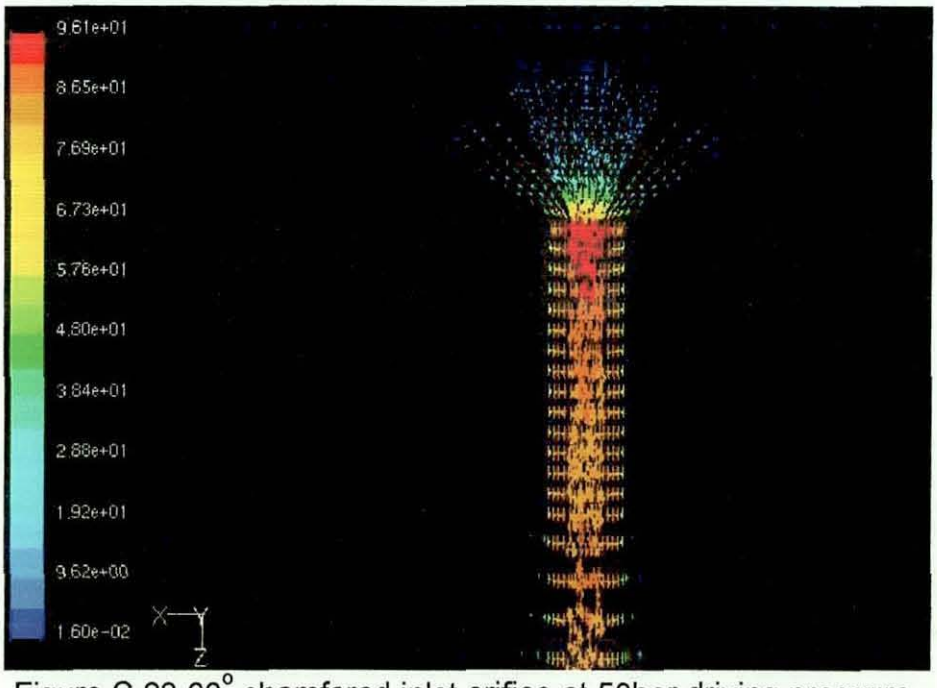

Figure C.23 60° chamfered inlet orifice at 50bar driving pressure.

C.5 SUMMARY

The simulated results provided an initial study of modelling technique on three chamfered inlet orifice. The flows in the orifices peripheral have a lower velocity compared to those at the centre. All the results from the three orifices

showed the peak velocity increases with higher driving pressure. The results also show the 30° chamfered inlet orifice has a higher peak velocity at 50 bar driving pressure compared to the other two orifices.

Figures C.24 to C.26 present numerical and experimental results for the axial variation in velocity along the centreline for three chamfered inlet orifices, with 20 bar to 50 bar driving pressure. In the 30° and 45° chamfered inlet orifices, these velocity flow profiles show a high degree of similarity between experimental and numerical results. At the 2 mm point of the nozzle, the flow surges into the straight section of the orifice. This was due to the change in orifice geometry from the convergent section into the nozzle section. Once the flow has entered the nozzle section of the orifice, the flow velocity remains almost constant. For the 60° chamfered inlet orifices, the velocity in the convergent section of the orifice over-predicted in all cases. Although the flow velocity remains constant in the nozzle section, the numerical results under-predict the velocity by about 30%.

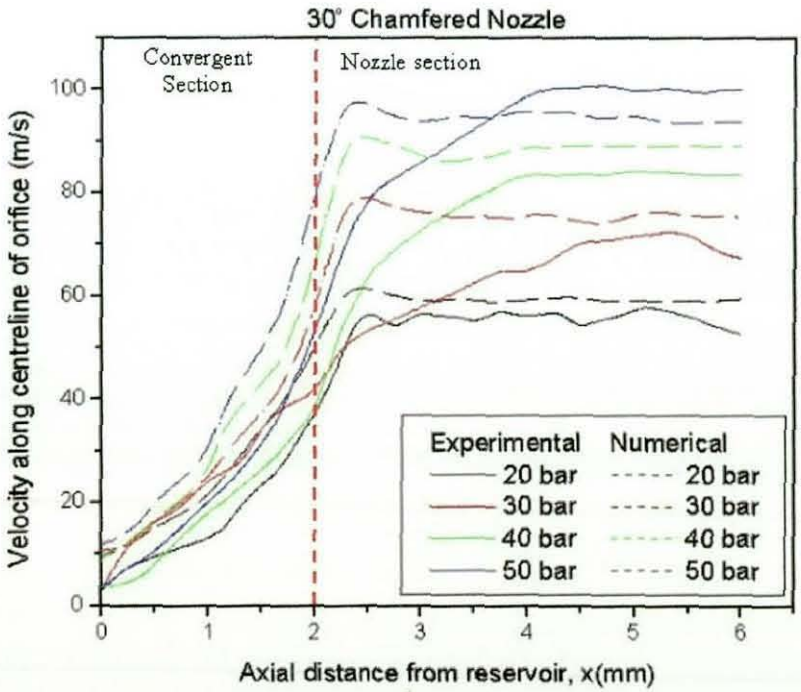

Figure C.24 Experimental and numerical velocity profile along centreline of 30° chamfered inlet orifice

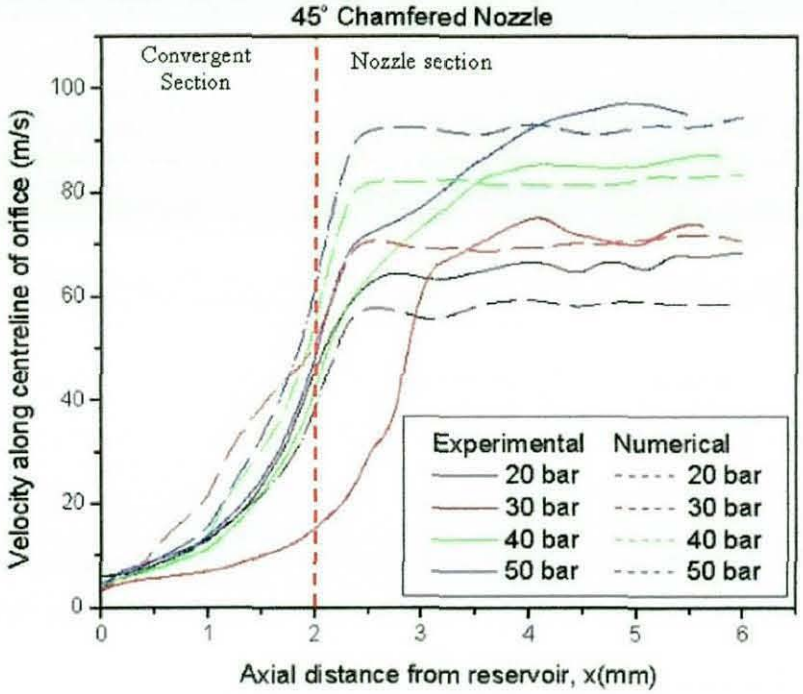

Figure C.25 Experimental and numerical velocity profile along centreline of 45° chamfered inlet orifice

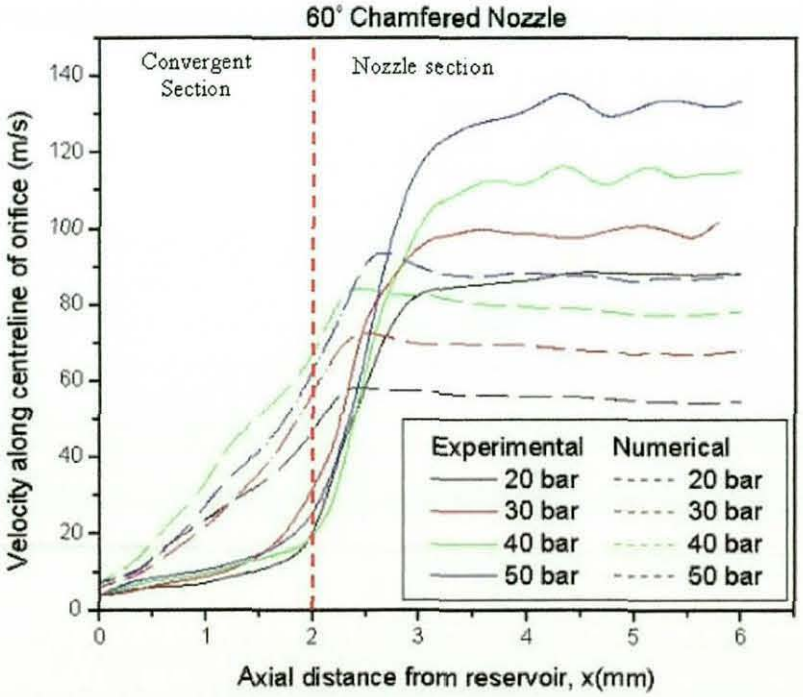

Figure C.26 Experimental and numerical velocity profile along centreline of 60° *chamfered inlet orifice*

Figure C.27 shows a comparison of maximum velocity between the numerical and experiment results. The numerical results from the graph shows the

maximum velocity trend was linear with increasing driving pressure but the numerical results under predicted the maximum velocity. However, the difference was not great apart from 60° chamfered inlet orifice and it was about 10% less than the actual experimental data. The 60° chamfered inlet orifice geometry is close to a sharp inlet orifice, therefore further improvements in generating the geometry mesh is required to allow the simulation to match those of the experimental data.

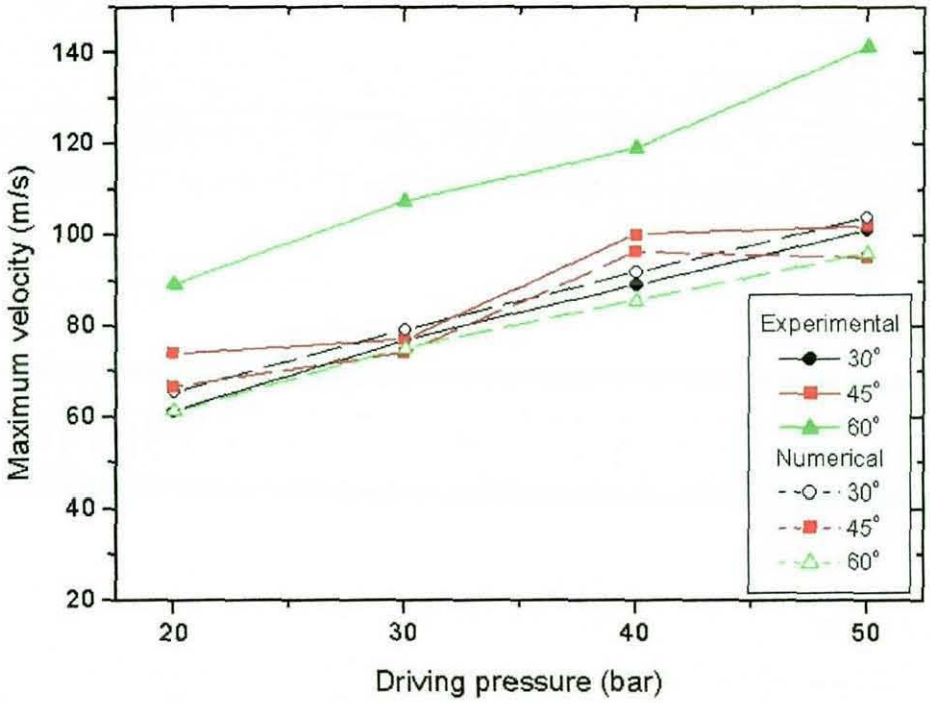

Figure C.27 Numerical and experimental maximum velocity.

These modelling results provided an insight into the capabilities of using modelling in future studies. Improvement in the modelling geometry mesh and solver is required to model results that match those of the experimental. As mentioned previously, this modelling work provides a simple tool to validate experimental results for non-swirl study. No further work was conducted due to amount of time required to conduct a full experimental investigation before setting up the validating procedures. However, this initial study proves this modelling tool is capable to be used to model swirl injection study for future study.

C.6 REFERENCES

[01] Cambridge University Press, *Computational Gasdynamics* (http://capella.colorado.edu/~laney/home.html), [30.08.2001]

[02] Fluent Inc., *Fluent 5.4 Documentation*, CD-Rom, April 2000

[03] Fluent Inc., *Gambit 1.3 Documentation*, CD-ROM, June 2000

[04] Versteeg, H.K., Malalasekera, W., *An Introduction of Computational Fluid Dynamics :The Finite Volume Method,* Prentice Hall, 1995, ISBN 0-582-21884-5

APPENDIX D

FUEL PHYSICAL PROPERTIES

D.1 DIESEL

Physical state:	Liquid State
Colour:	Light amber
Odour:	Gas oil-like
Density:	820 – 845 kg/m^3 @ 15°C
Boiling point/range:	160 – 385°C
Kinematics viscosity:	2 – 4.5 mm^2/s @ 40°C
Flash point (PMC):	60°C min
Explosion:	0.6 – 6.5%
Solubility in water:	low solubility
Partition Coefficient:	>3 $Log_{10}P_{ow}$ (n-octanol/water)

D.2 GASOLINE

Physical state:	Liquid State
Colour:	Clear
Odour:	Hydrocarbon or rotten egg
Density:	750 kg/m^3 @ 15°C
Boiling point/range:	30 – 230°C
Dynamic viscosity:	0.55 mPa.s @ 20°C
Flash point (PMC):	-40°C
Explosion:	0.8 – 7.6%
Solubility in water:	immiscible
Partition Coefficient:	5.15 $Log_{10}P_{ow}$ (n-octanol/water)

D.3 WHITE SPIRIT

Physical state:	Liquid State
Colour:	Clear and colourless
Odour:	Characteristic Odour
Density:	765 – 795 kg/m^3 @ 15°C
Boiling point/range:	130 - 200°C
Kinematics viscosity:	0.74 – 1.65 cps @ 25°C
Flash point (PMC):	21 - 55°C
Explosion:	0.6 – 8%
Solubility in water:	< 0.1%